

# **Fullerene-Grafted Polymers and Block Copolymers: Design, Structure Formation and Charge Transport**

DISSERTATION

zur Erlangung des akademischen Grades  
eines Doktors der Naturwissenschaften (Dr. rer. nat.)  
im Promotionsprogramm Polymer Science  
der Bayreuther Graduiertenschule für Mathematik und Naturwissenschaften  
an der Universität Bayreuth

vorgelegt von

**Martin Hufnagel**

Geboren in Sulzbach-Rosenberg / Deutschland

Bayreuth, 2015



This doctoral thesis was prepared in the group "Applied Functional Polymers" at the department of Macromolecular Chemistry I at the University of Bayreuth from June 2012 to December 2015 and was supervised by Prof. Dr. Mukundan Thelakkat.

This is a full reprint of the dissertation submitted to obtain the academic degree of Doctor of Natural Sciences (Dr. rer. nat.) and approved by the Bayreuth Graduate School of Mathematical and Natural Sciences (BayNAT) of the University of Bayreuth.

Date of submission: 01.12.2015

Date of defence: 20.05.2016

Acting director: Prof. Dr. Stephan Kümmel

Doctoral committee:

Prof. Dr. Mukundan Thelakkat (1<sup>st</sup> reviewer)

Prof. Dr. Hans-Werner Schmidt (2<sup>nd</sup> reviewer)

Prof. Dr. Jürgen Senker (chairman)

Prof. Dr. Georg Papastavrou

(3rd reviewer: Prof. Dr. Ullrich Scherf, Bergische Universität Wuppertal)



*Für meine Familie*



## Table of contents

Summary / Zusammenfassung .....	1
1 Introduction .....	7
Objective .....	41
2 Overview of the thesis.....	43
Individual contributions to joint publications .....	57
3 Fullerene-grafted copolymers exhibiting high electron mobility without nanocrystal formation .....	61
4 Donor-acceptor block copolymers carrying pendant PC <sub>71</sub> BM fullerenes with ordered nanoscale morphology .....	97
5 Influence of fullerene grafting density on structure, dynamics and charge transport in P3HT-b-PPC <sub>61</sub> BM block copolymers .....	137
6 Influence of composition on structure formation and charge transport in P3HT-b-PPC <sub>71</sub> BM block copolymers .....	181
7 Simultaneous morphological stability and high charge carrier mobilities in donor-acceptor block copolymer/PCBM blends.....	217
8 Appendix: Nanoscale morphology from donor-acceptor block copolymers: Formation and functions .....	251
List of publications.....	291
Danksagung.....	293
(Eidesstattliche) Versicherungen und Erklärungen.....	295



## Summary

This thesis addresses the preparation and in-depth characterization of new fullerene-based electron transport polymers and their integration into well-defined donor-acceptor block copolymers. In particular for organic photovoltaic devices, these semiconducting block copolymers hold great promise for improved long-term stability based on a stable nanoscale morphology. While theoretical studies predict their advantageous morphological and photophysical properties, the experimentally observed solar cell performance often remains below the expectations. This discrepancy can be understood and solved only by unraveling the complexity of interdependencies between polymer design, structure formation and electronic properties.

First, a feasible method was developed to synthesize fullerene polymers in a controlled way which circumvents cross-linking and multi-addition of fullerenes. Controlled polymerization techniques such as nitroxide-mediated radical polymerization (NMRP) or reversible addition-fragmentation chain transfer (RAFT) polymerization have been used to synthesize the precursor poly(4-methoxystyrene-*stat*-4-hydroxystyrene). The monomer ratio decides about the final grafting density after the polymer-analogous esterification with phenyl-C<sub>61</sub>-butyric acid (PC<sub>61</sub>BA) or its C<sub>70</sub> analogue PC<sub>71</sub>BA. This route yields well-soluble fullerene polymers (PPCBM, denotes PPC<sub>61</sub>BM or PPC<sub>71</sub>BM in general) incorporating up to 64 wt% PCBM with defined molecular weights and narrow dispersities. The PPCBMs retain the optical and electrochemical properties of the incorporated PCBM independent of the fullerene fraction. For PC<sub>61</sub>BM contents between 30 to 50 wt% the PPC<sub>61</sub>BM exhibit bulk electron mobilities up to  $1 \times 10^{-4} \text{ cm}^2 \text{ V}^{-1} \text{ s}^{-1}$  measured by space-charge limited current (SCLC). The structural analysis confirmed the homogeneous and amorphous nature of PPCBM and revealed a glass transition temperature which is strongly increasing with the grafting density.

A modular strategy for donor-acceptor block copolymers has been developed based on a poly(3-hexylthiophene) (P3HT) donor block and PPCBM as acceptor block. The combination of Kumada catalyst-transfer polycondensation (KCTP), NMRP or RAFT, azide-alkyne cycloaddition for polymer coupling and fullerene grafting provides a versatile toolbox for precisely tailored block copolymers. Specifically the grafting density and the donor-acceptor composition in P3HT-b-PPCBM has been systematically tuned to scrutinize the consequences on structure formation and charge transport. The block copolymers

show a periodic donor-acceptor nanostructure in the range of 30-40 nm following the molecular weight trend. Interestingly, the observed nanostructures are identical in bulk and in films and even independent of the processing method, *i.e.* from solution or melt-crystallization. Small angle X-ray scattering indicates a microphase separated morphology in the melt and upon cooling and crystallization of the P3HT. Though, the absence of long-range ordered microdomains is attributed to the high glass transition temperature of PPCBM which is likely pinning the structural evolution in an incomplete microphase separated state. This constraint becomes even more critical when the donor-acceptor composition is shifted towards high contents of PPCBM suppressing both crystallization of P3HT and microphase separation.

To identify the optimum polymer design for ambipolar and balanced charge transport, the block copolymers have been studied in organic field-effect transistors (OFET). The grafting density in P3HT-b-PPC<sub>61</sub>BM block copolymers turned out as a key factor to improve the electron mobility by orders of magnitude without sacrificing the hole transport. Tuning the donor-acceptor composition in a series of P3HT-b-PPC<sub>71</sub>BM revealed the significance of a roughly balanced composition which is required for bicontinuous percolation paths. Polymer design alone was not sufficient to realize balanced mobilities, therefore, blending with PCBM was investigated as an alternative approach. The blend of donor-acceptor block copolymer P3HT-b-PPC<sub>61</sub>BM and PC<sub>61</sub>BM (60:40, wt:wt) showed enhanced electron mobilities of  $\mu_e=(3.2 \pm 1.7) \times 10^{-4} \text{ cm}^2 \text{ V}^{-1} \text{ s}^{-1}$  and a hole mobility of  $\mu_h=(1.8 \pm 0.6) \times 10^{-3} \text{ cm}^2 \text{ V}^{-1} \text{ s}^{-1}$ . Thereby, the block copolymer blend provides similarly high mobilities compared to a P3HT:PC<sub>61</sub>BM blend, but exhibits exceptionally stable transport even for prolonged thermal annealing at high temperatures. The operational stability in OFETs originates from the long-term stable nanostructure comprising P3HT and PCBM-enriched acceptor phases templated by the block copolymer structure.

In conclusion, this thesis comprises a novel route for the synthesis of fullerene-grafted donor-acceptor block copolymers allowing the fine-tuning of composition, grafting density and molecular weights. The systematic investigation of polymer design, structure formation and charge transport contributed significantly to resolve the fundamental issues in structure-property relationships and it opens new perspectives for future application in optoelectronic devices.

## Zusammenfassung

Die vorliegende Dissertation beschäftigt sich mit der Synthese und detaillierten Untersuchung neuer Elektronentransport-Polymere auf der Basis von Fullerenen sowie deren Verwendung in wohldefinierten Donor-Akzeptor Blockcopolymeren. Für die Anwendung in der organischen Photovoltaik sind diese Blockcopolymere sehr vielversprechend im Hinblick auf eine verbesserte Langzeitstabilität aufgrund ihrer stabilen Nanostruktur. Obwohl theoretische Untersuchungen eine vorteilhafte Morphologie und günstige photo-physikalische Eigenschaften vorhersagen, erfüllen die experimentellen Ergebnisse bei Solarzellen die Erwartungen meistens nicht. Um die Kluft zwischen Theorie und Experiment zu verstehen und Lösungen entwickeln zu können, ist es zwingend notwendig, die vielschichtigen Wechselwirkungen zwischen Polymerdesign, Strukturbildung und elektronischen Eigenschaften dieser Blockpolymere systematisch aufzuklären.

Zunächst wurde eine geeignete Methode entwickelt, um fullerenhaltige Polymere auf kontrollierte Weise herzustellen ohne dass Vernetzungsreaktionen stattfinden oder Multiaddukte mit Fullerenen entstehen können. Kontrollierte radikalische Polymerisationsmethoden wie die Nitroxid-vermittelte Polymerisation (nitroxide mediated radical polymerization, NMRP) oder die reversible Addition-Fragmentierung Kettenübertragungspolymerisation (reversible addition-fragmentation chain transfer, RAFT) wurden zur Synthese des Precursors Poly(4-methoxystyrol-*stat*-4-hydroxystyrol) verwendet. Das eingebaute Monomerverhältnis legt die spätere Funktionalisierungsdichte mit Fullerenen nach der polymer-analogen Veresterung mit den Fullerenderivaten Phenyl-C<sub>61</sub>-Buttersäure (phenyl-C<sub>61</sub>-butyric acid, PC<sub>61</sub>BA) oder dem C<sub>70</sub>-Analogon PC<sub>71</sub>BA fest. Diese Syntheseroute erzeugt gut lösliche Fullerenpolymere (PPCBM, allgemein für PPC<sub>61</sub>BM oder PPC<sub>71</sub>BM), die bis zu 64 Gew.-% PCBM enthalten können und dabei definierte Molmassen mit niedriger Dispersität aufweisen. Die PPCBMs behalten die optischen und elektrochemischen Eigenschaften des eingebauten PCBM unabhängig vom Massenanteil des Fullerenes. Bei einem PC<sub>61</sub>BM-Gehalt zwischen 30 und 50 Gew.-% zeigen die PPC<sub>61</sub>BM eine Elektronenmobilität im Bulk von bis zu  $1 \times 10^{-4} \text{ cm}^2 \text{ V}^{-1} \text{ s}^{-1}$  bei SCLC-Messungen (space-charge limited current, SCLC). Die Strukturuntersuchungen belegen die homogenen und amorphen Eigenschaften der PPCBMs und zeigen eine deutlich steigende Glasübergangstemperatur mit wachsender Funktionalisierungsdichte.

Basierend auf Poly(3-hexylthiophen) (P3HT) als Donorblock und PPCBM als Akzeptorblock wurde in dieser Arbeit eine modulare Synthesestrategie entwickelt. Die Kombination von "Kumada catalyst transfer polycondensation" (KCTP), NMRP oder RAFT, Azid-Alkin-Cycloaddition zur Kopplung der Polymere sowie die polymer-analoge Fulleren-Funktionalisierung bietet vielseitige Varianten zur Synthese maßgeschneiderter Blockcopolymerer. Insbesondere wurde in dieser Arbeit die Funktionalisierungsdichte mit Fullerenen sowie das Donor-Akzeptor-Verhältnis in den P3HT-b-PPCBM Blockcopolymeren systematisch variiert, um deren Auswirkung auf Strukturbildung und Ladungstransport zu untersuchen. Die Blockcopolymerer zeigen eine periodische Donor-Akzeptor Nanostruktur in der Größe von 30 bis 40 nm, wobei die Domänengröße mit dem Molekulargewicht wächst. Auffallend ist, dass die Nanostrukturen im Bulk und im Dünnschicht identisch sind und sich zudem unabhängig von der Verarbeitungsmethode zeigen, d.h. gleiche Strukturen in lösungsprozessierten und schmelzkristallisierten Proben. Die Röntgenkleinwinkelstreuung deutet auf eine Mikrophasenseparation in der Polymerschmelze hin, die bei Abkühlen und Kristallisation von P3HT erhalten bleibt. Als Ursache für die Abwesenheit von langreichweitig geordneten Mikrodomänen wird die hohe Glasübergangstemperatur des PPCBM-Blocks vermutet, die die Strukturbildung in einer unvollständigen Mikrophasenseparation fixiert. Diese Einschränkung wird besonders kritisch, wenn das Donor-Akzeptor-Verhältnis im Blockcopolymer zugunsten des PPCBM-Blocks verändert wird und damit sowohl die Kristallisation des P3HT-Blocks als auch eine Mikrophasenseparation vollständig unterdrückt wird.

Um das optimale Polymerdesign für ambipolare und ausgewogene Ladungsträgermobilitäten zu finden, wurden die Blockcopolymerer in organischen Feldeffekttransistoren (OFET) untersucht. Dabei zeigte sich die Funktionalisierungsdichte mit Fullerenen in P3HT-b-PPC<sub>61</sub>BM als entscheidender Faktor, um die Elektronenmobilität um mehrere Größenordnungen zu verbessern ohne dabei die Lochmobilität einzuschränken. Die Variation des Donor-Akzeptor-Verhältnisses in einer Serie von P3HT-b-PPC<sub>71</sub>BM unterstrich die Bedeutung einer etwa gleichen Zusammensetzung zwischen Donor- und Akzeptorblock, um eine Morphologie mit bikontinuierlichen Ladungstransportwegen zu erzielen. Das Ziel eines ausgewogenen Ladungstransports ließ sich allein durch Polymerdesign nicht realisieren, deswegen wurde das Zumischen (Blending) von PCBM als alternativer Ansatz untersucht. Der Blend aus P3HT-b-PPC<sub>61</sub>BM und PC<sub>61</sub>BM (60:40, m:m) verfügt über eine deutlich höhere Elektronenmobilität von  $\mu_e = (3.2 \pm 1.7) \times 10^{-4} \text{ cm}^2 \text{ V}^{-1} \text{ s}^{-1}$  und

eine Lochmobilität von  $\mu_h=(1.8 \pm 0.6) \times 10^{-3} \text{ cm}^2 \text{ V}^{-1} \text{ s}^{-1}$ . Damit bietet der Blockcopolymerblend ähnlich hohe Ladungsträgermobilitäten wie ein P3HT:PC<sub>61</sub>BM Blend, zeichnet sich aber durch seinen außergewöhnlich stabilen Ladungstransport aus, der selbst nach langem Tempern bei hohen Temperaturen erhalten bleibt. Die Funktionsstabilität der OFETs beruht dabei auf der stabilen Nanostruktur aus P3HT-Domänen und PCBM-angereicherten Akzeptor-Domänen, die durch die Struktur des Blockcopolymers vorgegeben ist.

Diese Dissertation umfasst eine neuartige Syntheseroute zur Herstellung von fullerenhaltigen Donor-Akzeptor Blockcopolymeren, die eine präzise Einstellung von Donor-Akzeptor-Verhältnis, Funktionalisierungsdichte und Molekulargewichten ermöglicht. Die systematische Untersuchung von Polymerdesign, Strukturbildung und Ladungstransport ist ein wesentlicher Beitrag zum Verständnis der grundlegenden Struktur-Eigenschafts-Beziehungen und eröffnet dieser Materialklasse neue Perspektiven für optoelektronische Anwendungen.



# 1 Introduction

## 1.1 Semiconducting polymers in organic photovoltaic devices

The discovery of electrically conducting polymers in the 1970s initiated a rapidly growing field of research dedicated to the development of solution-processable, lightweight and mechanically flexible, carbon-based semiconductors. Alan J. Heeger, Alan MacDiarmid and Hideki Shirakawa observed that the conductivity in  $\pi$ -conjugated macromolecules, *e.g.* polyacetylene, can be tuned from a semiconductor to a highly conducting material by introducing permanent charge carriers (doping).<sup>[1]</sup> Since that time numerous conjugated polymers have been synthesized with manifold structural variations to improve solubility, stability, charge carrier transport and optical properties.<sup>[2]</sup> This new generation of polymer materials is particularly attractive as it exhibits metallic or semiconducting properties while retaining the mechanical properties and processing advantages of polymers.<sup>[3]</sup> Therefore, conjugated polymers gradually enter our daily life as they are applied in antistatic coatings,<sup>[4]</sup> corrosion protection,<sup>[5]</sup> chemical and biological sensors,<sup>[6,7]</sup> or in "plastic electronics" such as organic light emitting diodes (OLED),<sup>[8,9]</sup> organic field-effect transistors (OFET)<sup>[10]</sup> or organic photovoltaics (OPV).<sup>[11,12]</sup> Due to the impact of this fundamental discovery Heeger, MacDiarmid and Shirakawa were awarded with the Nobel Prize in chemistry in 2000.<sup>[13]</sup>

Since Ching W. Tang's initial work on multilayer organic solar cells in 1986,<sup>[14]</sup> extensive research activities have been devoted to conjugated polymer-based organic solar cells<sup>[15–20]</sup> reaching nowadays power conversion efficiencies of over 10%.<sup>[21]</sup> One of the best studied material systems in OPV is poly(3-hexylthiophene) (P3HT) as electron donor and phenyl-C<sub>61</sub>-butyric acid methyl ester (PCBM) as electron acceptor material.<sup>[20]</sup> Organic semiconductors typically exhibit low dielectric constants and inherent energetic and structural disorder. In contrast to inorganic semiconductors, the absorption of light in the photoactive layer generates localized excited states of tightly bound hole and electron pairs. The so-called excitons have rather strong binding energies resulting in short lifetime and short exciton diffusion length around 10 nm. Therefore, the exciton dissociation is a key issue for efficient photocurrent generation. The formation of a bulk heterojunction (BHJ) as photoactive layer, *i.e.* the intimate mixture of donor and acceptor phases on the nanoscale, has proven to facilitate exciton diffusion to the donor-acceptor interface, dissociation and charge generation. A schematic illustration of such a blend

solar cell in conventional configuration is depicted in Figure 1.1a. The acceptor material can be distinguished from the donor by its higher electron affinity, leading to a highest occupied molecular orbital (HOMO) and a lowest unoccupied molecular orbital (LUMO) which are lower in energy compared to the donor. It is further inevitable that the donor/acceptor phases form a bicontinuous morphology to enable charge transport through the active layer to the corresponding electrodes.

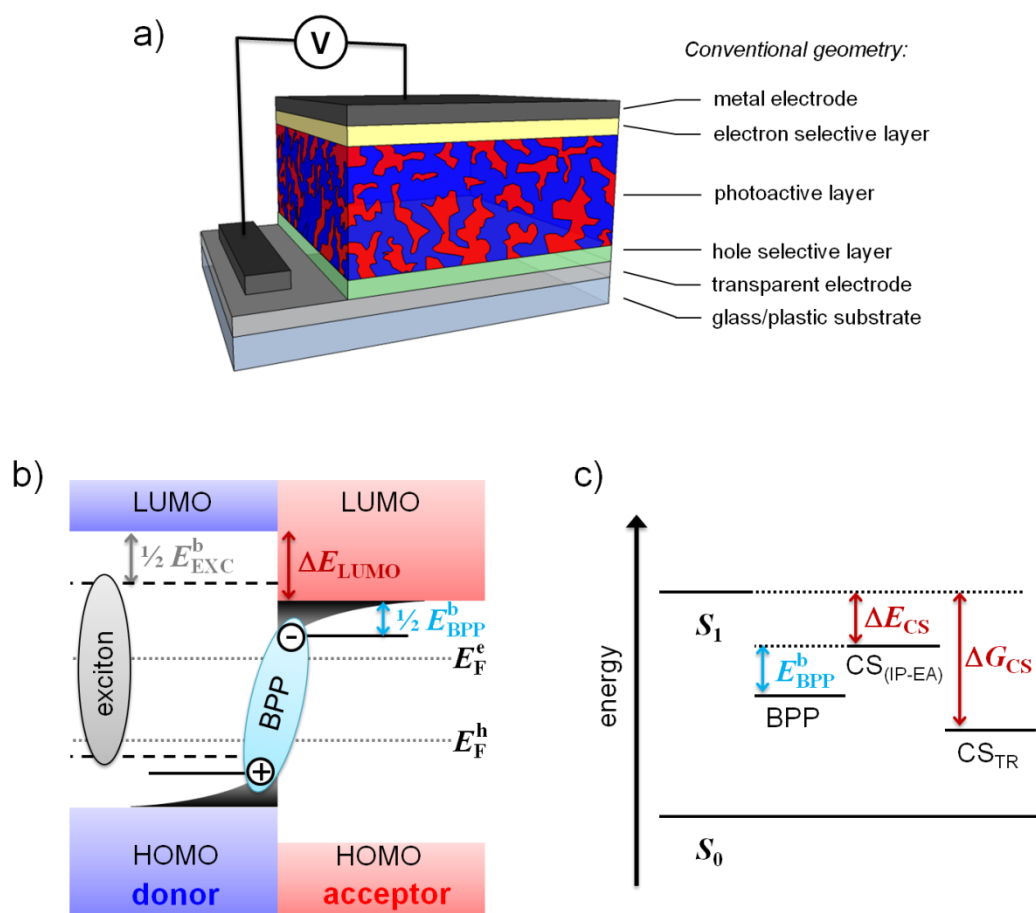


**Figure 1.1.** (a) Schematic illustration of a bulk heterojunction solar cell with a blend bulk-heterojunction as photoactive layer. (b) Electronic orbital energy diagram and (c) state energy diagram for a donor-acceptor interface describing the energetics of charge separation in organic solar cells. HOMO is the highest occupied molecular orbital; LUMO is the lowest unoccupied molecular orbital; BPP is the bound polaron pair with a binding energy  $E_{\text{BPP}}^b$ ; the singlet exciton binding energy is  $E_{\text{EXC}}^b$ ;  $E_F^e$  and  $E_F^h$  denote the quasi-Fermi levels of electrons and holes;  $S_0$  is the singlet exciton energy level;  $S_1$  is the ground state;  $\Delta E_{\text{CS}}$  is the enthalpy difference between the singlet exciton energy  $E_{S_1}$  and the energy of the charge separated state  $CS_{(\text{IP-EA})}$ ;  $\Delta G_{\text{CS}}$  is the overall free energy difference after charge photogeneration between the singlet exciton energy  $E_{S_1}$  and the thermally relaxed charge separated state  $CS_{\text{TR}}$ . Figures b and c adapted from Durrant et al.<sup>[22]</sup>

The working principle of organic solar cells and the corresponding energetics have been outlined by Brédas *et al.*,<sup>[23]</sup> Dyakonov *et al.*,<sup>[24]</sup> Marks *et al.*,<sup>[25]</sup> Durrant *et al.*,<sup>[22]</sup> and Ratner *et al.*<sup>[26]</sup> The basic operation principle of an organic solar cell is characterized by a cascade of four subsequent processes: 1. Absorption of an incident photon and formation of an exciton, 2. Diffusion of the exciton to a donor-acceptor interface, 3. Dissociation of the exciton into free charge carriers and 4. Percolation of the charges and collection at the electrodes. While the short circuit current  $I_{sc}$  in organic solar cells mainly depends on light harvesting efficiency (band gap) and charge carrier mobility, the open circuit voltage  $V_{oc}$  is influenced by the difference between the HOMO of the donor and the LUMO of the acceptor. One limiting factor for photocurrent generation is the formation of coulombically bound charges at the interface, referred to as bound polaron pair (BPP), at the donor-acceptor interface with binding energies far above the thermal activation energy. The rapid charge recombination of these BPP states is regarded as a key limitation for charge separation and photocurrent generation in organic solar cells. The energy level diagram of a donor/acceptor interface is illustrated Figure 1.1b as an electronic orbital picture. Here, the driving force for charge separation is the energy offset  $\Delta E_{LUMO}$  which represents the difference of donor and acceptor LUMO levels. An empirical value frequently reported is  $\Delta E_{LUMO} > 0.3$  eV that is required to overcome the exciton binding energy  $E_{EXC}^b$ . At the donor-acceptor interface the formation of a BPP state occurs with a corresponding binding energy of  $E_{BPP}^b$ . Figure 1.1c represents a state energy diagram to describe the energetics of charge separation. Here, the measure for the energy offset is the enthalpy difference  $\Delta E_{CS} = (IP - EA) - E_{S1}$  between the donor exciton with  $E_{S1}$  and the polaron energies IP and EA. Note that the blend band gap is  $(IP - EA)$  with the electron donor ionization potential IP and the electron acceptor electron affinity EA.  $\Delta E_{CS}$  is related to  $\Delta E_{LUMO}$  considering the exciton binding energy,  $\Delta E_{CS} = \Delta E_{LUMO} - E_{EXC}^b$ . The voltage output of the device is governed by the splitting of the quasi-Fermi levels  $E_F^e$  and  $E_F^h$  upon light irradiation. The thermalisation of electron and holes with the Fermi levels corresponds to the energy level  $CS_{TR}$  and the corresponding overall energy loss during the charge separation process into these thermalized polarons is expressed by  $\Delta G_{CS}$ .

Generally, the morphology of the active layer of organic solar cells has to fulfill two fundamental requirements: a) domain size in the range of the exciton diffusion length of 5-10 nm and b) an interpenetrating network of percolation paths that enable charge transport to the respective electrodes. The thin active layer, typically smaller than 200 nm,

is governed by the trade-off between optical density which is increasing with film thickness and recombination losses that can be minimized by decreasing the film thickness.

The fabrication of a bilayer morphology comprising a simple donor-acceptor stack is the most simple realization of a donor-acceptor heterojunction (Figure 1.2).<sup>[27]</sup> This, however, creates a relatively small interface available for exciton dissociation and allows only very thin films with limited photon absorption. Increasing the film thickness in bilayer solar cells would drastically reduce the quantum efficiency due to geminate recombination losses which originate from the short exciton diffusion length. Besides, the bilayer morphology often requires a vacuum deposition of fullerene or small molecules which is not suited for cost-effective solution-processing on an industrial scale.

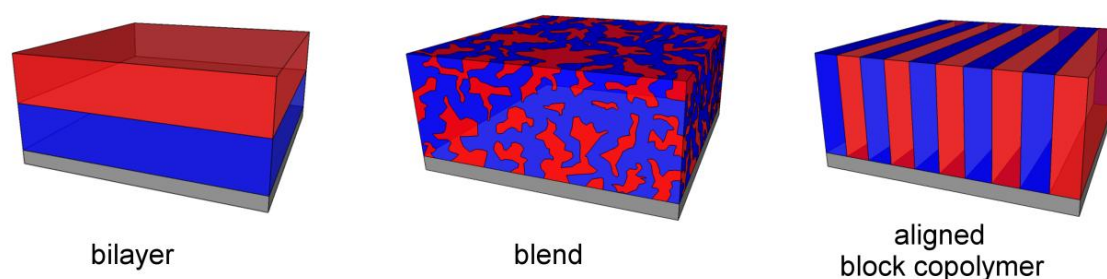


**Figure 1.2.** Active layer morphologies for organic solar cells: Bilayer structure, donor-acceptor blend and vertical lamellae of an aligned donor-acceptor block copolymer.

Another approach is the physical mixture of a donor and acceptor blend generating a bicontinuous morphology, also known as bulk-heterojunction (BHJ, Figure 1.2), which is the most common fabrication method to achieve high performance polymer solar cells.<sup>[28,29]</sup> The blend morphology of conjugated polymers and fullerene derivatives was extensively optimized by adequate processing conditions, processing additives or post-preparation thermal treatments.<sup>[30–36]</sup> However, such optimized, kinetically frozen mesostructures are in a non-equilibrium state, thus, it is a big challenge to control the size and long-term stability of such mesostructures. A frequent problem is to maintain the scale of phase separation which suffers from coarsening processes with time, leading to growing domain sizes due to continuous (macro) phase separation<sup>[37,38]</sup> or unfavorable phase segregation towards a specific electrode.<sup>[39,40]</sup> Controlling the blend morphology is in particular critical for transferring the small area, lab-scale processing of OPV devices to a large scale roll-to-roll fabrication which requires totally different drying or annealing procedures.<sup>[41]</sup> In consequence, several strategies have been developed to stabilize the

blend nanomorphology towards enhanced long-term stability, *e.g.* by cross-linking of either donor or acceptor material,<sup>[42,43]</sup> increasing the glass transition temperature<sup>[44]</sup> or by compatibilization of the blend using suitable block copolymers.<sup>[45–51]</sup>

An ideal solution to obtain long-term stable two-phase morphologies is the development of dual-function, nanostructured single-component materials in thermodynamic equilibrium. One approach is the use of a single polymeric material consisting of both donor and acceptor functions, known as donor-acceptor block copolymer, with the capability to self-assemble into the desired nanostructures. Microphase separation in block copolymers generates a rich variety of equilibrium morphologies with domain sizes on the nanoscale that are tunable both in size and shape simply by variation of the degree of polymerization, Flory-Huggins interaction parameter and volume fraction.<sup>[52,53]</sup> Donor-acceptor block copolymers as single material in OPV attract notable attention as the microphase separated morphology provides a large donor-acceptor interface with domain sizes in the range of the diffusion lengths of the excitons. This seems beneficial for the exciton dissociation and efficient charge generation. Further, block copolymer microdomains provide long-range percolation paths for charge carriers which is supposed to improve charge collection and reduce recombination losses. Theoretical studies on block copolymer systems comprising donor and acceptor blocks further predict an improved device performance for vertically aligned nanostructures as depicted in Figure 1.2.<sup>[54,55]</sup> It must be emphasized that the orientation of block copolymer nanostructures with respect to the substrate/electrode is a fundamental issue.<sup>[56]</sup> While a vertical alignment of nanostructure (drawn in Figure 1.2) provides perfect charge percolation pathways, the horizontal alignment of lamellae completely blocks charge transport to the electrodes causing a severe solar cell device failure. Nevertheless, donor-acceptor block copolymers are attractive candidates for OPV application owing to their capability to form self-assembled and long-term stable nanostructures with favorable photophysical properties. Comprehensive reviews about donor-acceptor block copolymers for organic photovoltaics have been published by Darling *et al.*,<sup>[57]</sup> Thelakkat *et al.*,<sup>[58]</sup> Hiorns *et al.*,<sup>[59]</sup> Horowitz *et al.*<sup>[60]</sup> and Mori *et al.*<sup>[61]</sup> in recent years.

## 1.2 Self-assembly and morphology of block copolymers

Block copolymers are macromolecules comprising two or more homopolymer chains that are covalently bound together at the chain ends. The most common class is the com-

bination of two chemically different polymer blocks, known as diblock copolymers (Figure 1.3a). The bulk structure of these diblock copolymers is driven by the interaction between the two blocks, thermodynamically described by the product of the degree of polymerization  $N$  and the Flory-Huggins interaction parameter  $\chi$ .<sup>[62–64]</sup> Hence,  $\chi N$  represents the segregation strength of the two chemically different chains. Weakly segregating block copolymers with  $\chi N < 10$  favor an isotropic, disordered morphology since the thermodynamic driving force is not sufficient to overcome the entropic chain stretching energy required for demixing. A strong incompatibility between both blocks, typically for  $\chi N > 10$ , will force the block copolymer to self-assemble into nanoscopic domains since a bulk (macro) phase separation is prevented by the covalent bond that keeps the polymer blocks together. This self-assembly process is referred to as microphase separation, which arises from the fact that the typical domains sizes are in the range of nanometers rather than micrometers (macrophase-separation).

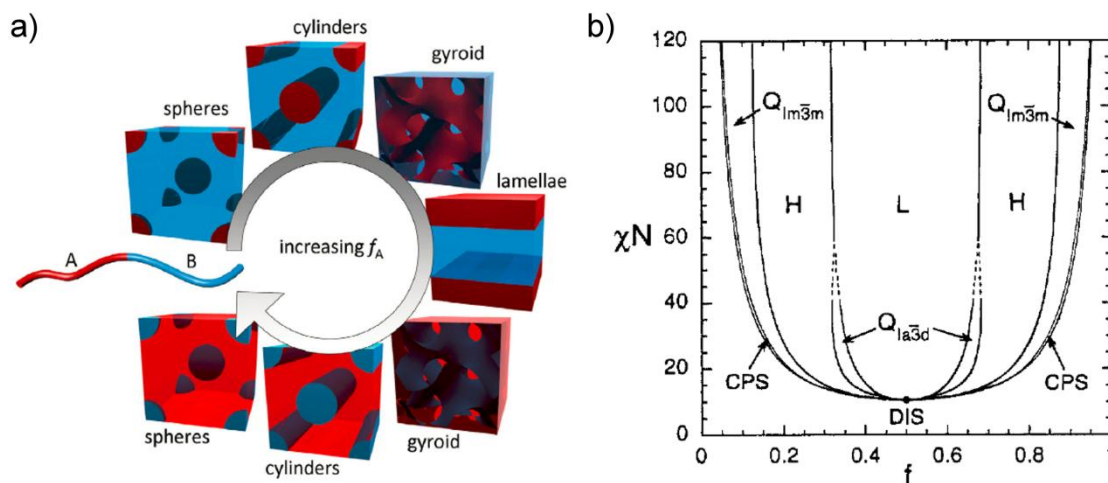


**Figure 1.3.** (a) Equilibrium morphologies of coil-coil block copolymers formed by microphase separation in the bulk as a function of the volume fraction of  $f_A$ . (b) Phase diagram for conformationally symmetric diblock copolymer melts. The phases are labeled as L (lamellar), H (hexagonally packed cylinders),  $Q_{1a3d}$  (bicontinuous cubic/gyroid),  $Q_{1m3m}$  (body-centered cubic spheres), CPS (close-packed spheres) and DIS (disordered). Figures reproduced from Darling et al.<sup>[66]</sup> and Bates et al.<sup>[52]</sup>

The type of nanoscale morphology depends on the ratio of volume fractions ( $f_A$ ,  $f_B$ ) of the blocks A and B and the product  $\chi N$  (Figure 1.3b). Frequently observed diblock copolymer morphologies are body-centered cubic spheres, hexagonally ordered cylinders, gyroid, and lamellae (Figure 1.3a). Block copolymers with more than two polymer blocks exhibit a variety of more complex morphologies.<sup>[65]</sup> The size of the domains formed by microphase separation is dictated by the molecular weight of the respective polymer

block, thus, providing a useful tool to the polymer chemist to precisely adjust the domains size according to a specific demand.

The process of microphase separation becomes more complicated considering conjugated polymer blocks. While the flexible chains ("coils") typically adopt an amorphous, "random-walk" conformation, the rigid and stiff conjugated polymers ("rod") exhibit anisotropic forces from  $\pi$ - $\pi$  interactions which often result in crystallization.<sup>[67]</sup> Specifically block copolymers for optoelectronic applications usually incorporate a conjugated polymer block as semiconductor.<sup>[60,68,69]</sup> Whereas the self-assembly behavior of coil-coil block copolymers is well understood and mainly driven by the immiscibility between the polymer segments,<sup>[52,70]</sup> conjugated rod-coil block copolymers indicate more complex phase diagrams which is attributed to additional driving forces influencing the structure formation.<sup>[71]</sup> Apart from the segregation strength  $\chi N$  and the relative volume fractions of the blocks ( $f$ ), the Maier-Saupe potential, describing the orientational ordering between liquid crystalline rod molecules, as competing driving force for the self-assembly of rod-coil block copolymers is currently under debate.<sup>[72]</sup> Further, the anisotropic rod-like nature of conjugated polymers is associated to form more planar domains. In general, the crystallization of one (or more) blocks in a block copolymer can occur in different modes: 1. In break-out crystallization the driving force for crystallization overwhelms the microphase separation and generates large crystalline microdomains that destroy the nanoscale order from phase-separation. 2. Confined crystallization occurs when the driving force for microphase separation is stronger than the crystallization. This leads to a crystallization confined to the microdomains which have been formed by microphase separation.<sup>[67]</sup> 3. In some cases crystallization of one polymer block can also initiate the formation of microdomains in a disordered block copolymer melt.<sup>[73]</sup> Recent reports also demonstrate that double-crystalline block copolymers such as P3HT-b-poly(perylene acrylate) can adopt block copolymer nanostructures very similar to amorphous coil-coil systems.<sup>[73]</sup>

### 1.3 Donor-acceptor block copolymers

Donor-acceptor block copolymers are composed of two polymer blocks with different electronic functionalities: While the electron donor block with its low ionization potential acts as a hole transport material, the electron acceptor block has a high electron affinity and acts as an electron transport material.

Several concepts have been reported to realize this dual functionality in block copolymers and the materials can be classified based on their structure: coil-coil block copolymers, rod-coil block copolymers and rod-rod block copolymers (Figure 1.4). While in coil-coil block copolymers the donor and acceptor moieties are attached as pendant side groups to the non-conjugated, flexible main chain, rod-coil block copolymers contain one  $\pi$ -conjugated main chain and a side-chain functionalized coil block. The rod-rod block copolymers are composed of two different  $\pi$ -conjugated main chains and are also known as all-conjugated block copolymers.

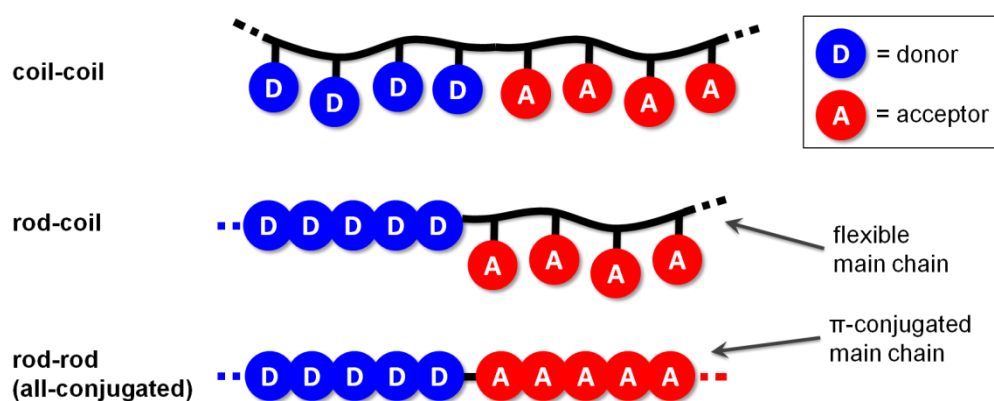


**Figure 1.4.** Different types of donor-acceptor block copolymers classified as coil-coil, rod-coil and rod-rod (all-conjugated) block copolymer.

Regarding the synthesis of such block copolymers, convenient routes for coil-coil systems are available from established preparative methods for classical block copolymers. Introducing a conjugated polymer block, however, requires appropriate strategies to combine polymer blocks synthesized by different routes, *e.g.* polycondensation and anionic/cationic/radical polymerization. An important milestone was the discovery of chain-growth Kumada catalyst transfer polycondensation (KCTP) of P3HT which paved the way for a large variety of well-defined rod-coil diblock copolymers containing P3HT as conjugated donor block. The synthesis of all-conjugated block copolymers has been progressively reported in recent years. However, the synthesis of acceptor blocks using KCTP is still a challenging issue. Therefore, many of the all-conjugated donor-acceptor block copolymers comprise acceptor blocks that were obtained from uncontrolled conventional polycondensation. The poor control over molecular weight, dispersity and end groups in conventional polycondensations of conjugated polymers is an unsolved issue and thus severely limits the availability of well-defined, all-conjugated donor-acceptor block copolymers.

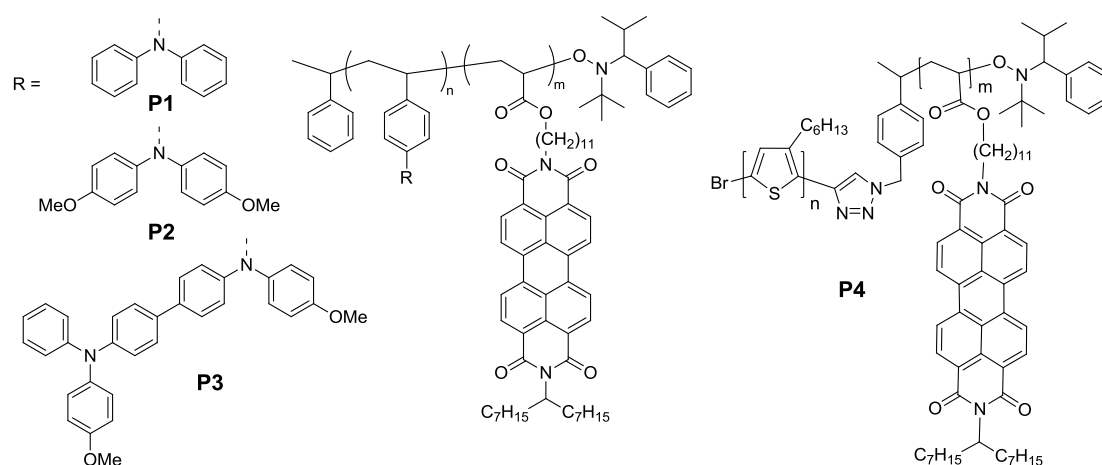
Due to the large diversity of chemical structures and plenty of publications in this field, the overview focuses on some of the representative examples of donor-acceptor block copolymers. In the following they are categorized with respect to the type of acceptor used; that is a) non-fullerene acceptors such as perylene bisimides and conjugated polymers (Figure 1.5) or b) pendant fullerene polymers (Figure 1.8). While the non-fullerene block copolymers are only briefly introduced, the fullerene-grafted polymers are discussed in detail covering synthesis, morphological aspects, charge transport and their application in OPV.

### 1.3.1 Non-fullerene donor-acceptor block copolymers

A general trend in material science for OPV is the development of suitable non-fullerene acceptors as a cost-effective replacement for fullerenes and due to their finely tunable electronic properties, optical properties and better availability.<sup>[74]</sup> Another important advantage of acceptors like perylene bismides (PBI) is a facile grafting *via* polymer-analogous reactions<sup>[75,76]</sup> or the possibility to synthesize vinyl or acrylate monomers which can be polymerized radically. In our research group, Lindner and Sommer *et al.* utilized this strategy to build up the first coil-coil type donor-acceptor block copolymers poly(bisphenyl-4-vinylphenylamine)-block-poly(perylen bisimide acrylate) **P1**, poly(bis(4-methoxyphenyl)-4'-vinylphenylamine)-block-poly(perylen bisimide acrylate) **P2** and poly(*N,N'*-bis(4-methoxyphenyl)-*N*-phenyl-*N'*-4-vinylphenyl-(1,1'-biphenyl)-4,4'-diamine)-block-poly(perylen bisimide acrylate) **P3**.<sup>[77,78]</sup> The functional triphenylamine- and PBI-based monomers were polymerized radically *via* nitroxide-mediated radical polymerization (NMRP) in subsequent steps. Sommer and Lohwasser *et al.* developed a macroinitiator route to combine the conjugated donor polymer poly(3-hexylthiophene) with a poly(perylen bisimide acrylate) block forming the rod-coil block copolymer **P4** with outstanding control over molecular weight and narrow polydispersity.<sup>[73,79]</sup> A controlled microphase separation leading to lamellar and cylindrical structures were also demonstrated in these systems.

Apart from the perylene bismides as acceptors, many electron-deficient conjugated polymers have been designed to replace fullerenes as acceptor materials in OPV. Their combination with donor polymers result in the class of all-conjugated block copolymers shown in Figure 1.5b. This topic has been reviewed by Scherf *et al.*,<sup>[80]</sup> Hawker *et al.*<sup>[81]</sup> and very recently by Gomez *et al.*<sup>[82]</sup>

a) Side-chain functionalized donor-acceptor block copolymers:



b) All-conjugated donor-acceptor block copolymers:

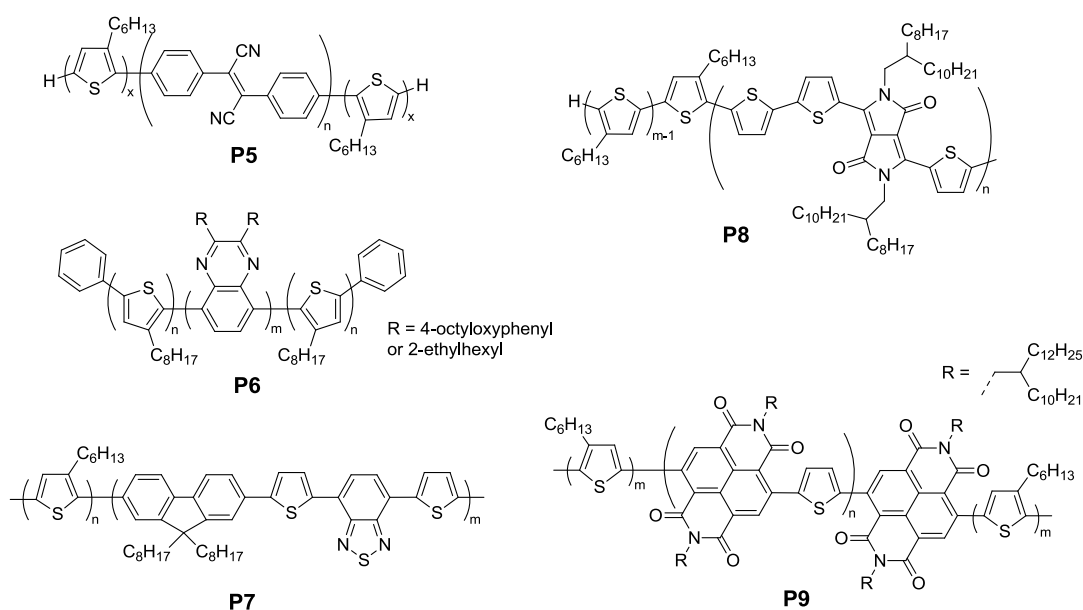


**Figure 1.5.** Overview on non-fullerene donor-acceptor block copolymers (a) carrying pendant functional moieties in a coil-coil **P1-3**<sup>[78]</sup> or rod-coil architecture **P4**<sup>[73]</sup> and (b) as all-conjugated block copolymer **P5-9**.<sup>[83,84,86,87,90]</sup>

One of the first reports was by Scherf *et al.* showing a facile one-pot synthesis of conjugated D-A-D triblock copolymers based on P3HT as donor and various cyano-substituted poly(phenylene vinylene) acceptor blocks **P5**.<sup>[83]</sup> Herein, the acceptor middle block was prepared by Yamamoto coupling of dibromo-functionalized monomers with a subsequent end-capping of the polycondensation using bromine-monoterminated P3HT. A similar D-A-D triblock structure was achieved by Collard *et al.* with poly(quinoline) as

acceptor and P3HT as donor in **P6** using a combination of preformed P3HT and Yamamoto polycondensation for the acceptor block.<sup>[84]</sup> Another example for this D-A-D triblock copolymer architecture incorporating a conjugated poly(naphthalene bisimide thiophene) as acceptor and P3HT **P9** was presented by Nakabayashi *et al.*<sup>[85]</sup> and Wang *et al.*<sup>[86]</sup> A prominent all-conjugated block copolymer is poly(3-hexylthiophene)-b-poly((9,9-dioctylfluorene)-2,7-diyl-alt-[4,7-bis(thiophen-5-yl)-2,1,3-benzothiadiazole]-2',2''-diyl) (P3HT-b-PFTBT) **P7** which has been synthesized by several groups including Verduzco *et al.*, Sommer *et al.* and Scherf *et al.*<sup>[87-89]</sup>

Another conjugated acceptor block was introduced by Hawker *et al.* using a poly(diketopyrrolopyrrol-terthiophene) as acceptor in conjunction with P3HT **P8**.<sup>[90]</sup> Despite the large variety of chemical structures accessible in all-conjugated block copolymers the synthetic challenges remain a difficult issue. Usually the combination of Grignard metathesis polymerization (GRIM) and step-growth polycondensations like Suzuki-Miyaura, Stille or Yamamoto coupling result in relatively low molecular weight block copolymers with broad distribution and often generate a mixture of homopolymers, diblock and triblock copolymers which require tedious purification procedures for separation.<sup>[87,88]</sup> The limitations regarding the control over molecular weight, dispersity and purity of the polymers are unfavorable to obtain sufficiently well-defined diblock copolymers which exhibit the desired block copolymer morphologies with nanoscale donor/acceptor domain sizes.

### 1.3.2 Fullerene-grafted donor-acceptor block copolymers

The integration of fullerenes into (block) copolymers attracts notable attention since C<sub>60</sub> and its derivatives are the state-of-the-art acceptor material in polymer solar cells (Figure 1.8). The unique electron-accepting and transporting capability<sup>[15]</sup> of fullerenes is employed to create novel polymeric acceptors by covalent attachment of fullerene moieties to polymer chains. While the electronic properties of such side chain polymers can be tuned by the type of attached fullerene derivative, the thermal and mechanical properties are determined by the nature of the polymer backbone. Generally, different routes for the preparation of pendant fullerene polymers have been reported: Either the polymerization of fullerene-derivatized monomers such as ring-opening metathesis polymerization (ROMP) of norbornenes<sup>[91-95]</sup> and copper(I)-catalyzed azide-alkyne click polymerization of fullerene bisalkynes<sup>[96]</sup> or the polymer-analogous modification of polymers with

fullerenes. These polymer-analogous synthesis routes rely on functional polymers, which are decorated with fullerene derivatives in a further step. Among the manifold reactions applicable to fullerene molecules,<sup>[97]</sup> only a few types of reactions have been utilized to attach C<sub>60</sub> covalently to functional polymers including the addition of amines,<sup>[98]</sup> atom transfer radical addition (ATRA),<sup>[99]</sup> [3+2]-cycloaddition with azides,<sup>[100,101]</sup> [3+2]-cycloaddition with tosylhydrazones,<sup>[48]</sup> Bingel reaction,<sup>[102]</sup> Friedel-Crafts type reactions,<sup>[103]</sup> and nucleophilic addition of lithiated compounds<sup>[104]</sup> (Figure 1.6). Since all these methods are based on the reaction with double bonds, C<sub>60</sub> acts as an inherently multifunctional reactant. In particular for high fullerene loads, this fact leads to multiple additions, polymer cross-linking and in consequence to diminished solubility or even insoluble products. Monofunctionalized fullerene derivatives have been designed to circumvent the issue of multiaddition and cross-linking and were grafted to the polymers by (Steglich) esterification procedures,<sup>[105–107]</sup> copper(I) catalyzed azide-alkyne cycloaddition<sup>[108–110]</sup> or Williamson etherification<sup>[51]</sup> (Figure 1.7).

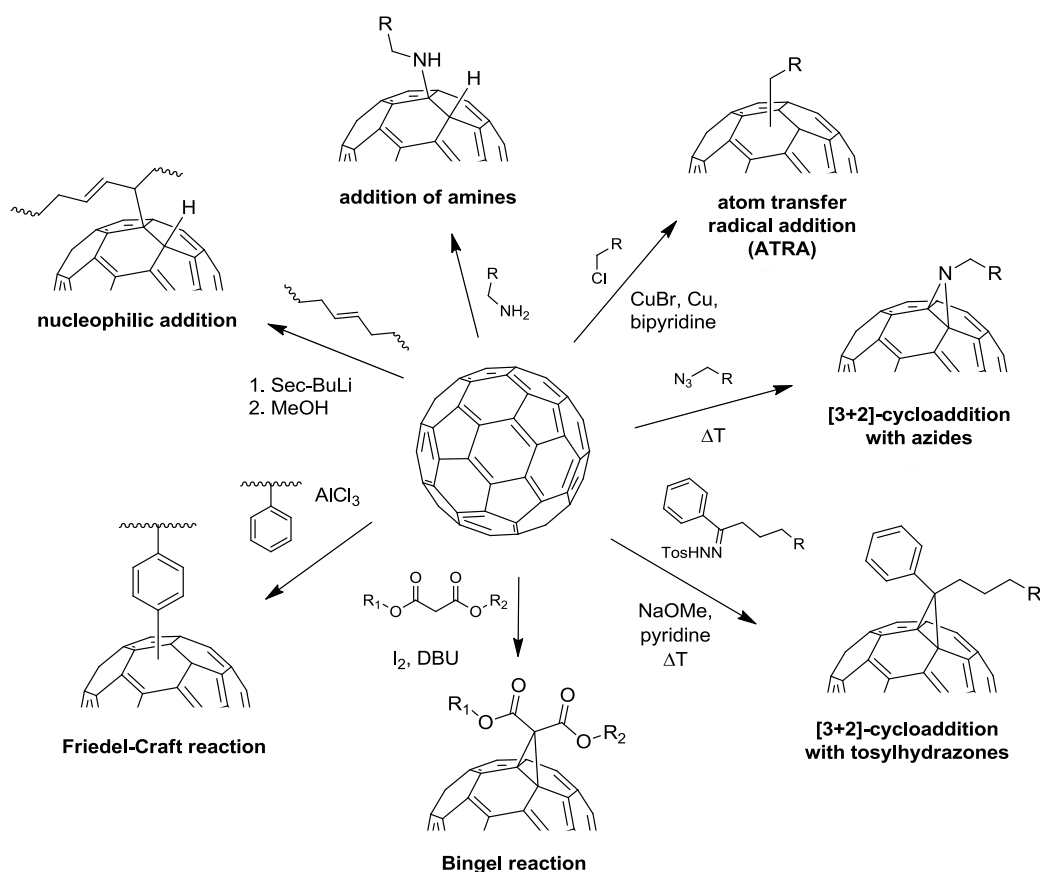


**Figure 1.6.** Reactions for polymer-analogous attachment of C<sub>60</sub> fullerenes to functional polymers.<sup>[48,98–104]</sup> The inherent multifunctional character of C<sub>60</sub> can lead to multiple additions and cross-linking as side reaction.

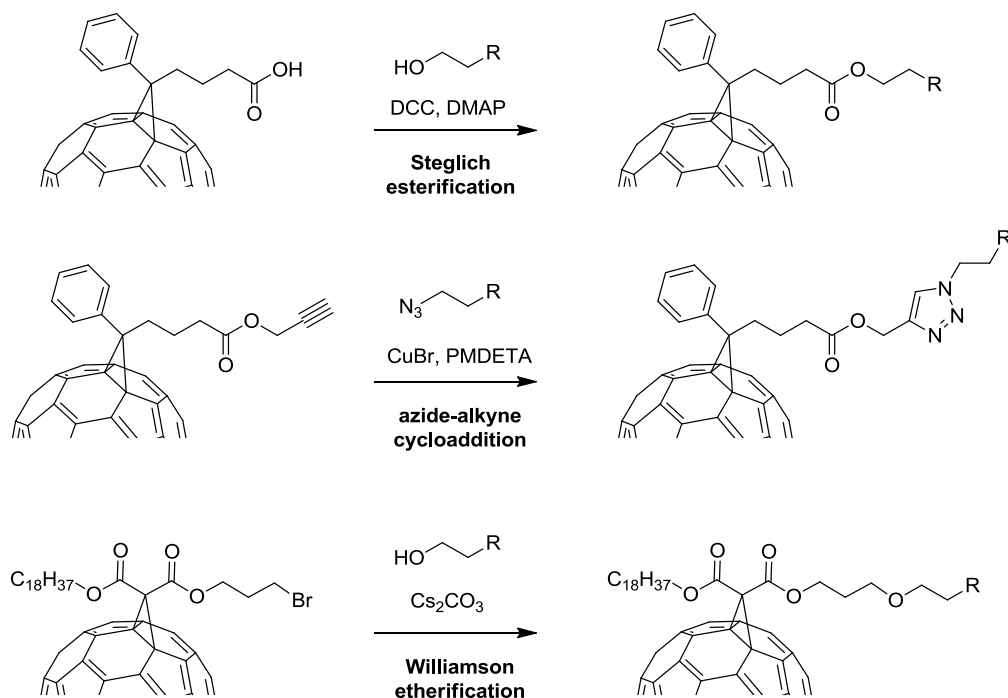


**Figure 1.7.** Reactions for polymer-analogous attachment of  $C_{60}$  derivatives to functional polymers.<sup>[51,105,108]</sup> The monofunctional character of the  $C_{60}$  derivatives facilitates excellent control of the grafting reaction without generating multiadducts or cross-linking.

A general issue in fullerene-grafted polymers is the choice of suitable diluting monomers since a fully functionalized fullerene polymer is insoluble. Substituted acrylates, styrenes and norbornenes have been used as comonomers to keep the resulting fullerene copolymers soluble allowing roughly 60 wt% of attached  $C_{60}$  at the polymer backbone. This implies that the acceptor block is to be diluted in almost all cases.

Indeed, the fullerene-grafted polymers adopt the electron transporting capability of the fullerene molecules showing a correlation of increasing electron mobility with increasing  $C_{60}$  content in the polymer.<sup>[111]</sup> Detailed studies on pendant  $C_{60}$  polystyrenes have been presented by Alberola and Flandin *et al.* to clarify the interplay between charge transport, percolation threshold and aggregation in these systems.<sup>[112,113]</sup> For a  $C_{60}$  content of 23-60 wt%, a rather low electron mobility of  $10^{-9}$  to  $10^{-7}$   $cm^2 V^{-1} s^{-1}$  was determined by the space charge limited current (SCLC) method. Further, these fullerene polymers exhibit a  $C_{60}$  aggregation starting at a threshold of only 12-13 vol% of incorporated  $C_{60}$ . Confined organization of fullerene moieties along the polymer chain resulting in improved electron mobility has been found by Bao *et al.* for pendant  $C_{60}$  polynorbornenes in organic field effect transistors (OFET).<sup>[94]</sup> The application of pendant fullerene polymers as plausible

acceptor material in polymer solar cells was successfully demonstrated by Do et al in a polymer-polymer blend with P3HT yielding a power conversion efficiency of 1.5%.<sup>[93]</sup>

The variety of rod-coil block copolymers incorporating fullerenes is large since the conjugated polymer block, in most cases P3HT, can be combined with well-established polymerization methods such as reversible addition-fragmentation chain transfer (RAFT), nitroxide mediated radical polymerization (NMRP) or atom transfer radical polymerization (ATRP, Figure 1.8). These methods are applicable to a broad range of monomers with manifold options for polymer-analogous modification. The very first reports on fullerene-grafted block copolymers such as **P10** carrying a poly(p-phenylene vinylene) (PPV) conjugated block and a fullerene pendant block are related to the work of Hadziioannou *et al.* in 2000.<sup>[99,101,114,115]</sup> A parallel development by Wudl *et al.* and Fréchet *et al.* was the polymerization of fullerene-derivatized norbornene monomers using ROMP which allows the synthesis of copolymers<sup>[91,92]</sup> and block copolymers.<sup>[95]</sup> As shown for **P12**, the donor polymer P3HT was introduced as side chains in the first block and a Bingel-type C<sub>60</sub> monomer in the acceptor block.<sup>[45]</sup>

Recent advances in the synthesis of  $\pi$ -conjugated polymers, *e.g.* Kumada catalyst transfer polymerization (KCTP),<sup>[118–120]</sup> considerably enhanced the ability to prepare conjugated polymers by chain-growth type polycondensations with high end group fidelity, specifically for P3HT.<sup>[121]</sup> This has opened new perspectives for the development of rod-coil block copolymers comprising fullerene-grafted acceptor blocks. A variety of C<sub>60</sub>-decorated block copolymers such as **P11** has been reported.<sup>[47,48,51,122]</sup> Holdcroft *et al.* synthesized graft-type polymers **P13** with a P3HT main chain and poly(styrene) side chains carrying C<sub>60</sub> or PCBM moieties.<sup>[117,123,124]</sup> Recent developments in the field of donor-acceptor block copolymers are focussing on more controlled fullerene grafting methods as shown in polymer **P14** by Jo *et al.*<sup>[105]</sup> using a Steglich esterification procedure or in **P15** by Hashimoto *et al.* using click chemistry.<sup>[108,110]</sup>

An important question to be addressed is the structure formation of the synthesized donor-acceptor block copolymers. Unlike classical coil-coil block copolymers, the aforementioned donor-acceptor block copolymers typically have at least one crystallizable block that can affect the block copolymer self-assembly. Generally, the crystallization in rod-coil block copolymers depends on the block copolymer composition and the interplay between crystallization temperature, glass transition of the amorphous block and the order-disorder transition.<sup>[67]</sup> Owing to this complexity and the difficulty to prepare these

type of block copolymers with sufficiently narrow dispersity, the observation of highly ordered microphase separation is rather rare. Reports for donor-acceptor block copolymers show either complete loss of the nanoscale structure as observed for **P10**<sup>[116]</sup> or only weak evidence for a segregated donor-acceptor nanostructure based on atomic force microscopy, electron microscopy or X-ray scattering experiments.<sup>[105,110,117,125–127]</sup>

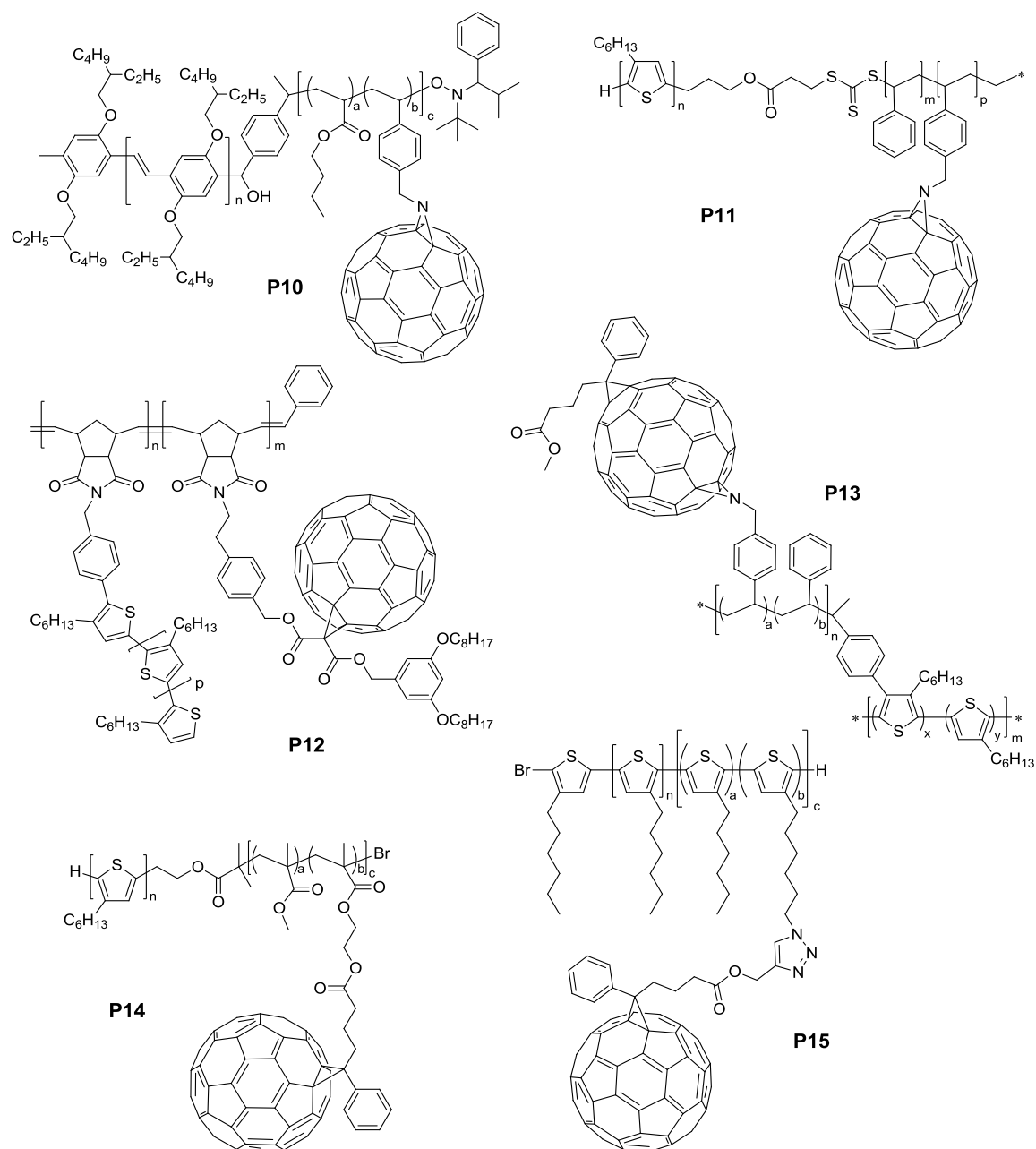


**Figure 1.8.** Overview on pendant fullerene donor-acceptor block (graft) copolymers **P10-15**.<sup>[45,48,105,108,116,117]</sup>

However, Lohwasser *et al.* have recently reported microphase separation similar to classical coil-coil block copolymers in a double-crystalline P3HT-b-poly(perylene bismide) donor-acceptor block copolymer with lamellar or cylindrical morphology in the range of tens of nanometers.<sup>[73]</sup> The microstructure in all-conjugated block copolymers observed by Verduzco *et al.* is heavily dependent on the annealing conditions, thermal or in solvent-vapour, intermolecular  $\pi$ - $\pi$  stacking and liquid-crystalline interactions and can reach a certain degree of long-range order.<sup>[87,126,127]</sup>

The aforementioned block copolymers have been widely employed as compatibilizers for donor:acceptor blends which was recently reviewed by Chen *et al.*<sup>[128]</sup> In general, the block copolymer additives stabilize the optimized blend morphology and retard or even suppress a macrophase separation of the blend upon annealing or device operation.<sup>[51]</sup> In some cases, the addition of block copolymer compatibilizers to bulk heterojunction solar cells increased the operational stability.<sup>[45,49,129–131]</sup>

The application of donor-acceptor block copolymers in solar cells is of course the central target and has been elucidated since many years. After the first rather poor attempts with power conversion efficiencies far below 1%,<sup>[77,78,132]</sup> the materials as well as understanding for appropriate postproduction treatments have notably improved the performance in recent years. Hashimoto *et al.* could demonstrate in a valuable comparison of the donor-acceptor block copolymer **P15** with its random copolymer analogue the importance of phase-separated donor/acceptor domains leading to a superior device performance up to 2.46%.<sup>[110]</sup> Further, such a block copolymer nanostructure exhibits excellent long-term operation characteristics with only negligible performance loss compared to a blend system even after 80 hours of thermal annealing.<sup>[108]</sup> Verduzco *et al.* reported for the all-conjugated block copolymer **P7** a power conversion efficiency of ~3% which is so far the record efficiency in the field of donor-acceptor block copolymers.<sup>[126]</sup> The good device performance was assigned to the self-assembly of the block copolymer into a lamellar microstructure of 18 nm in a vertical orientation to the substrate, thus, providing a domain size in the range of the exciton diffusion length and charge transport paths to the respective electrodes.

Despite a few encouraging results the research on donor-acceptor block copolymers containing fullerene moieties often lacks an in-depth analysis of structure formation, charge transport and device application studies. The individual design of the functional polymer blocks, the composition of the blocks, crystallization and glass transition aspects

can be controlled in many cases by polymer synthesis. Understanding the basic principles between polymer design and structure as well as the consequences on charge transport and device operation is of fundamental importance to achieve progress in this field. Especially, the advantages of a vertical alignment of nanostructures is still to be elucidated.

## 1.4 Controlled synthesis methods for functional polymers

### 1.4.1 Kumada catalyst transfer polycondensation (KCTP)

The Kumada catalyst-transfer polycondensation (KCTP) is a rapidly developing method with great potential for the synthesis of conjugated polymers and block copolymers. The scope of monomers was steadily growing in recent years covering now thiophene-, fluorene-, phenylene- and pyrrole-based conjugated polymers.<sup>[133]</sup> Further, low bandgap systems, all-conjugated block copolymers, gradient polymers and brush polymer prepared by KCTP have been reported. The discovery of the chain-growth mechanism by Yokozawa and McCollough demonstrated the unique character of Nickel-catalyzed KCTP among other transition-metal catalyzed polycondensations.<sup>[118,119,134]</sup> The preparation of poly(3-hexylthiophene) (P3HT) is the most prominent application for KCTP since it allows excellent control over regioregularity, molecular weight, narrow polydispersity and well-defined chain ends.<sup>[120,135]</sup>

For KCTP the active Grignard monomer is formed *in situ* from the dihalide monomer **1** via a Grignard metathesis reaction leading to the regioisomers **2a** and **2b** (Figure 1.9). The desired active Grignard monomer **2b** is formed in large excess of roughly 75% due to the steric hindrance by the 3-hexyl chain. After addition of the Nickel catalyst, *e.g.* dichloro(1,3-bis(diphenylphosphino)propane)nickel (Ni(dppp)Cl<sub>2</sub>), two subsequent transmetallation steps generate the bithiophene-Ni complex **3** which instantaneously forms the initiating species **4** via an intramolecular Ni transfer. The chain growth proceeds in a sequence of transmetallation **5**, reductive elimination **6** and oxidative addition **7** steps. Most importantly, the Ni catalyst should not be released from the polymer chain end during the chain growth. Otherwise, the controlled growth is lost and the polymerization follows a step-growth polycondensation. It is worth to note that KCTP follows not only a chain-growth mechanism but even exhibits the characteristics of a living polymerization process because one equivalent of Ni catalyst initiates one polymer chain. This

highly controlled preparation method for P3HT paves the way for the design of new materials for optoelectronic applications with superior material properties.<sup>[136,137]</sup>

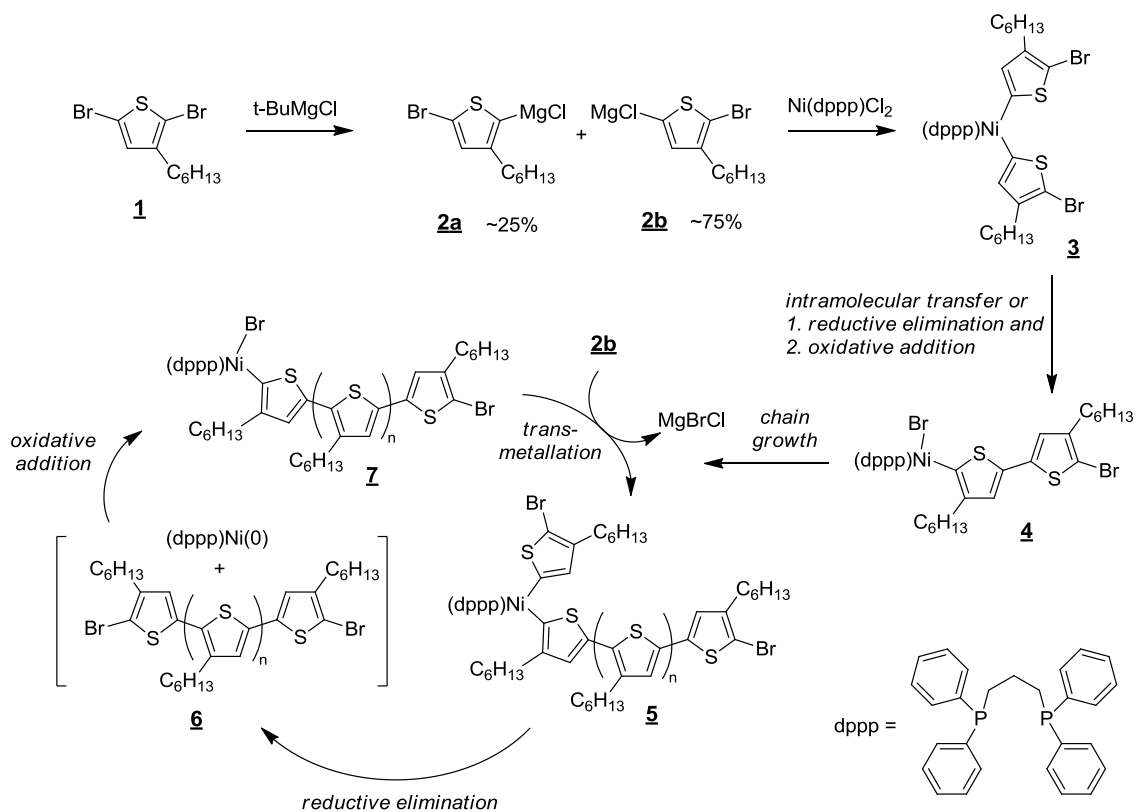


**Figure 1.9.** Grignard metathesis reaction for the formation of the active Grignard monomer and proposed mechanism of the Kumada catalyst-transfer polycondensation (KCTP). Adapted from McCullough *et al.*<sup>[118]</sup>

#### 1.4.2 Reversible addition-fragmentation chain transfer (RAFT) polymerization

RAFT polymerization has emerged as a versatile tool for controlled/living radical polymerization, providing excellent control over molecular weight and narrow distribution.<sup>[138–140]</sup> In particular, the use of thiocarbonylthio compounds as chain transfer agents (CTA), first reported in 1998 by Thang *et al.*,<sup>[141]</sup> notably extended the potential applications for RAFT. It is compatible with the most monomer types such as (meth)acrylates, (meth)acrylamides, acrylonitrile, styrenes, dienes and vinyl monomers in a wide range of reaction conditions. Another striking advantage is the tolerance of unprotected functionalities in the monomer and the solvent (*e.g.* OH, NR<sub>2</sub>, COOH, CONR<sub>2</sub>, SO<sub>3</sub>H). The living character of the RAFT polymerization enables also the precise introduction of functional end groups. Therefore, RAFT polymerization evolved into a powerful synthesis method to generate complex macromolecular architectures like block, graft, comb and star polymers.<sup>[142]</sup>

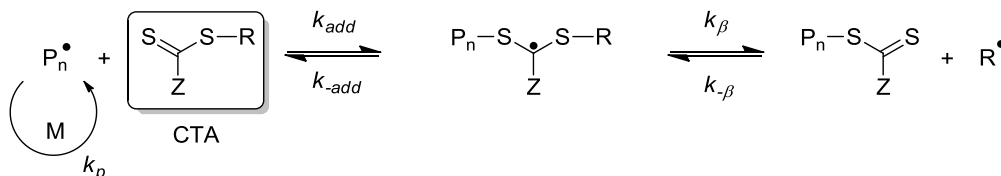
Basically, the control over chain growth in the RAFT process is gained by a reversible termination of the propagating radical. Chain transfer agents (CTA) such as dithioesters, trithiocarbonates, dithiocarbamates and dithiocarbonates (xanthates) act as transfer reagents by a two-step addition-fragmentation mechanism. They all possess a C=S double bond that is reactive towards radical addition and a substituent  $Z$  that determines the reactivity towards propagating radicals. The  $Z$  group is responsible for addition and fragmentation rates of the CTA. The  $R$  group is a homolytic leaving group with a corresponding radical  $R\cdot$  which must be capable of efficiently re-initiating the polymerization. The generally accepted mechanism of RAFT polymerization is shown in Figure 1.9 and includes several steps of (re)initiation and addition-fragmentation equilibria.<sup>[141]</sup>

First, conventional radical initiators are used to create the primary radicals  $I\cdot$  which form the polymer radicals  $P_n\cdot$  after consumption of  $n$  monomers. Addition of this propagating radical  $P_n\cdot$  to the CTA gives a polymeric RAFT agent that releases a new radical  $R\cdot$  after the homolytic dissociation of the weak S-R bond. The subsequent re-initiation by  $R\cdot$  forms a new propagating radical  $P_m\cdot$ . The rapid equilibria between the active propagating radicals  $P_n\cdot$  and  $P_m\cdot$  and their corresponding dormant species guarantee equal probability for all chains to grow. This is crucial for narrow molecular weight distributions. When the polymerization is stopped or complete, each polymer chain will carry a thiocarbonylthio end group. On the one hand, the CTA end-capped polymers can then be re-initiated to form more complex macromolecules and end functional polymers. On the other hand, the presence of the thiocarbonylthio group can be detrimental *e.g.* for electronic applications due to its colour and limited stability, hence, several procedures to remove the CTA after polymerization have been reported.<sup>[143,144]</sup> Similar to other controlled radical polymerization techniques the RAFT process faces limitations by irreversible bimolecular recombination, specifically for high monomer conversion, high initiator concentration and high molecular weights ( $>100 \text{ kg mol}^{-1}$ ).

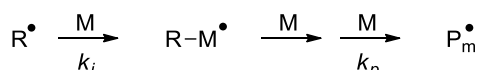
Initiation:



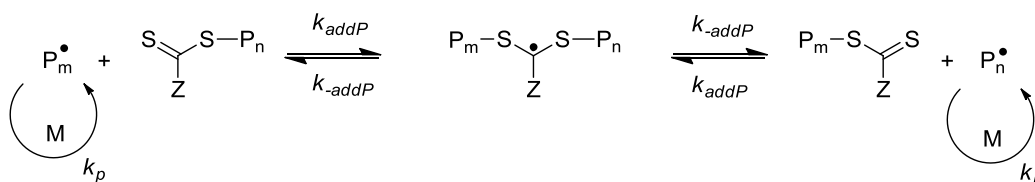
Reversible chain transfer / propagation:



Reinitiation:



Chain equilibration / propagation:



Termination:

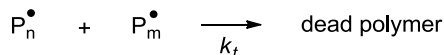


**Figure 1.10.** Mechanism of RAFT polymerization. The chain transfer agent (CTA) is commonly a dithioester carrying a leaving group R and a stabilizing group Z. Adapted from Moad *et al.*<sup>[140]</sup>

### 1.4.3 Nitroxide mediated radical polymerization (NMRP)

NMRP is another controlled radical polymerization method with the ability to produce well-defined polymers in a facile, thermally controlled process. The identification of alkoxyamines which are able to act as unimolecular agents was an important milestone for the development of NMRP. Alkoxyamines provide both the reactive initiating radical and the persistent nitroxide radical (Figure 1.11a).<sup>[145]</sup> In 1999, Hawker *et al.* reported a universal NMRP alkoxyamine initiator which permits the polymerization of a wide range of monomers including acrylates, acrylamides, acrylonitrile-based monomers, styrenes and vinyl monomers.<sup>[146]</sup> The living character of NMRP, the tolerance against various functional groups and control over end groups allow the synthesis of complex macromo-

lecular architectures such as block, cyclic, star, graft, comb and hyperbranched polymers.<sup>[147]</sup>

The mechanism of NMRP is based on a reversible termination between the growing propagating (macro)radical and the nitroxide. The nitroxide radical is a persistent radical which does not self-terminate. The predominant species after initiation is the dormant (macro)alkoxyamine which is in equilibrium with the propagating radical and the nitroxide by a simple homolytic cleavage (Figure 1.11b). The activation-deactivation equilibrium is established only upon heating of the system which is necessary to break up the alkoxyamine bond. Hence, the polymerization kinetics is governed by the equilibrium constant ( $K = k_d/k_a$ ) and the persistent radical effect of the nitroxide.<sup>[148]</sup>

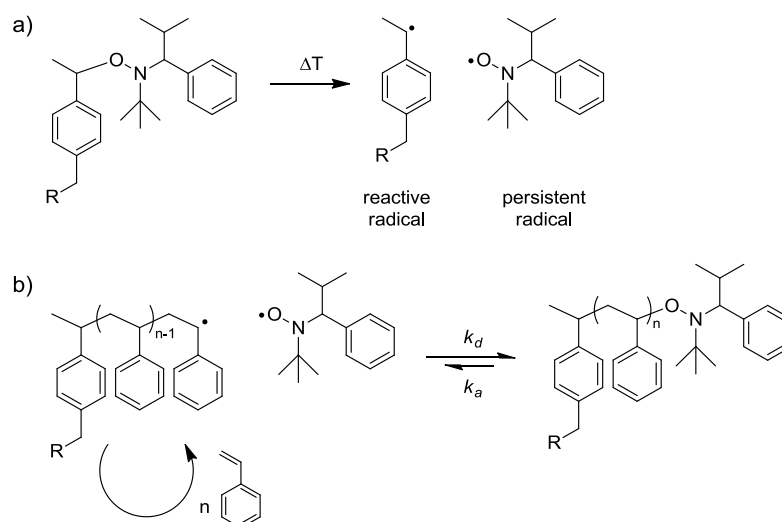


**Figure 1.11.** Mechanism of nitroxide mediated radical polymerization. (a) Formation of radicals by thermal decomposition of an alkoxyamine into a reactive and a persistent radical. (b) Activation-deactivation equilibrium: The reactive radical initiates the polymerization and starts chain growth while the persistent radical mediates the reaction by deactivation of the propagating radical into a dormant species.

#### 1.4.4 Copper-catalyzed azide-alkyne cycloaddition (CuAAC)

Copper-catalyzed azide-alkyne cycloaddition (CuAAC), initially developed by Sharpless *et al.*,<sup>[149,150]</sup> has evolved into a powerful tool in polymer and materials chemistry.<sup>[151,152]</sup> The copper(I)-catalyzed Huisgen 1,3-dipolar cycloaddition reaction between azides and terminal alkynes exhibits outstanding advantages like high reaction rates, excellent regioselectivity, near-quantitative yield and a remarkable tolerance towards various solvents (including water) and functional groups. These properties are in particular

interesting for the synthesis of novel polymer materials since conventional polymer-analogous reactions are often confronted with insufficient reaction yields.

The proposed reaction mechanism of the CuAAC is depicted in Figure 1.12. The initial steps of the catalytic cycle include the formation of a copper(I) acetylide between the  $[\text{CuL}_x]$  complex and the terminal alkyne and the subsequent coordination of the organic azide to the copper(I) acetylide. The C-N bond is formed based on the nucleophilic vinylidene-like  $\beta$ -carbon of the copper(I) acetylide and the electrophilic terminal nitrogen of the coordinated azide resulting in a 5-triazoyl copper intermediate. After regioselective formation of the 1,4-disubstituted 1,2,3-triazole the copper(I) catalyst is recovered to start a new reaction cycle.

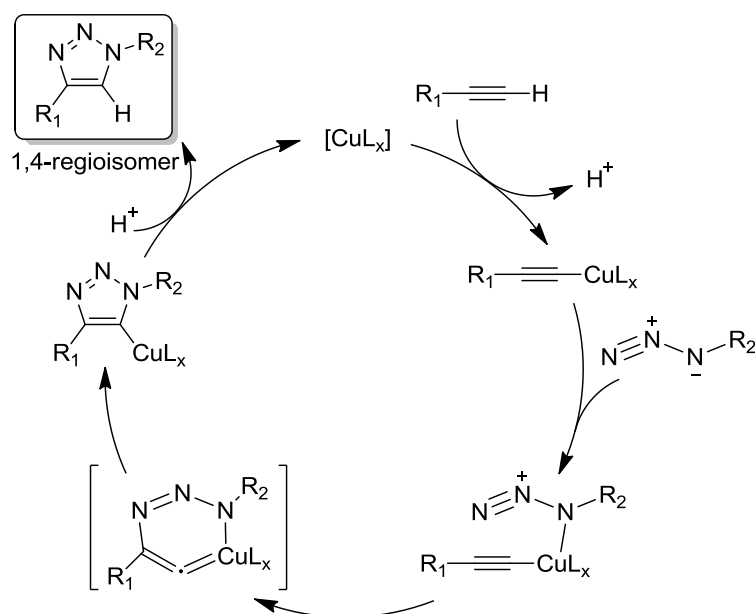


**Figure 1.12.** Proposed mechanism for the copper(I)-catalyzed azide-alkyne cycloaddition generating the 1,4-disubstituted regioisomer of 1,2,3-triazole at room temperature in excellent yields. Adapted from Fokin et al.<sup>[153]</sup>

## 1.5 Charge transport in organic semiconductors

One of the key parameters driving the performance of optoelectronic devices such as organic light-emitting diodes (OLED), organic photovoltaics (OPV) or organic field-effect transistors (OFET) is the charge carrier mobility. When charge carriers, electrons or holes, are generated in a semiconductor by exciton dissociation or by injection from an electrode, they will move under the influence of an electrical field  $F$ . The charge carrier mobility  $\mu$  indicates how fast the charge carrier can travel through the semiconductor. The mobility  $\mu$  is defined as the effective drift velocity  $v$  of charge carriers per unit electric field  $E$ :<sup>[154]</sup>

$$\mu = vF^{-1} \quad (1)$$

Further, the electrical current  $j$  in a device is described in a simplified way by  $j = env = en\mu F$ , with  $n$  the number of charge carriers and  $e$  the elementary charge. Taking Ohm's law into account,  $j = \sigma_c F$ , the conductivity  $\sigma_c$  of a semiconductor is expressed by following equation:<sup>[154]</sup>

$$\sigma_c = en\mu \quad (2)$$

In general, organic semiconductors exhibit relatively low charge carrier mobilities compared to single-crystalline inorganic semiconductors such as silicon or gallium-arsenide. The reason for this low mobility is associated to the disordered nature of organic materials (glasses or polymers), the amount and nature of charge traps, the energetic and structural disorder due to their inhomogeneity what makes charge transport different from the band-like transport in inorganic materials. The prevailing charge transport model attributed to disordered organic semiconductors like polymers is the disorder-controlled transport or hopping transport.<sup>[154]</sup> Here, the charge transport is no longer described by band motion but by localized charge carriers at individual sites which can proceed by a sequence of non-coherent transfer events (hopping). In other words, charges in organic semiconductors can move from one molecule to another by a series of thermally activated electron transfers. The corresponding charge carrier mobility  $\mu$  depends on temperature  $T$  and the electrical field  $F$ , which is expressed by the Pool-Frenkel equation,<sup>[155]</sup>

$$\mu(F, T) = \mu(0, T) \exp[\gamma(T)\sqrt{F}] \quad (3)$$

with the zero-field mobility  $\mu(0, T)$  and the material parameter  $\gamma(T)$  describing the field-dependence of the mobility.

### 1.5.1 Space-charge limited current (SCLC) method

To determine the charge carrier mobility of a semiconductor in bulk space-charge limited current (SCLC) measurement is a feasible method. The device setup is a simple diode where the semiconductor material to be probed is placed between two electrodes (Figure 1.13a). The choice of electrodes is important: First, the electrode from which charges are injected must form an Ohmic contact with the semiconductor allowing a space-charge limited current instead of an injection-limited current. Second, the work function of the electrodes must adopt the type of charge carrier transport either through the HOMO level of a hole conductor or the LUMO level of an electron conductor. This is experimentally realized by different device configurations, *e.g.* glass/ITO/PEDOT:PSS/semiconductor/Au for hole-only devices or glass/ITO/ZnO/semiconductor/Ca/Al for electron-only devices.

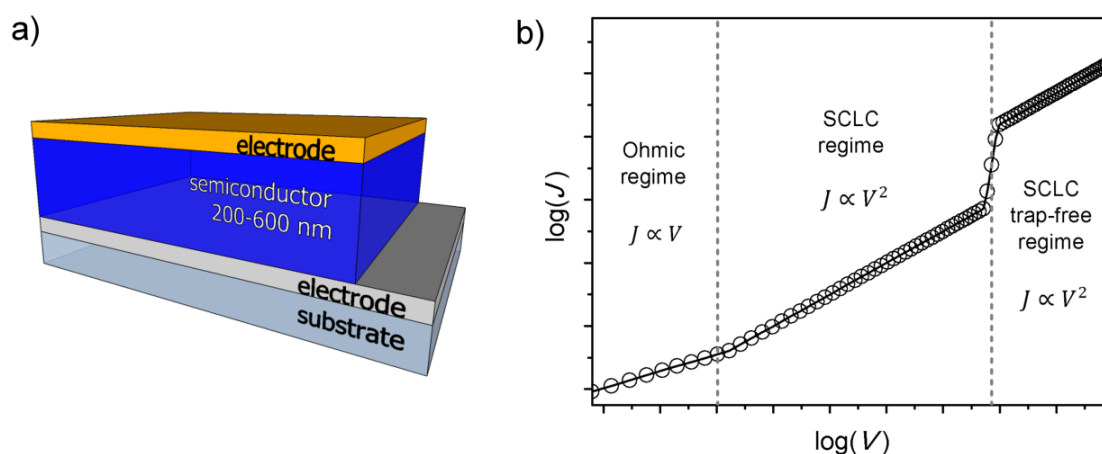


**Figure 1.13.** (a) Simplified SCLC device configuration and (b) schematic  $J$ - $V$  characteristics of an SCLC device in log-log plot showing the different voltage-dependent operating regimes. Figure (b) redrawn from Ostroverkhova *et al.*<sup>[156]</sup>

The current-voltage  $J$ - $V$  characteristics are measured in dark and follow in the SCLC regime the Mott-Gurney law,<sup>[157]</sup>

$$J = \frac{9}{8} \varepsilon \varepsilon_0 \mu \frac{V^2}{L^3} \quad (4)$$

with the dielectric constant  $\varepsilon$  ( $\sim 3$  for organic semiconductors), the permittivity of free space  $\varepsilon_0$ , the charge carrier mobility  $\mu$ , the effective voltage  $V$  and the active layer thickness  $L$ . It is important to verify the space-charge limited character of the measured current  $J$ , which has to obey the inverse cubic thickness dependence  $J \propto L^{-3}$  and the quadratic voltage dependence  $J \propto V^2$ . SCLC devices can be operated in different regimes, *i.e.*

Ohmic regime, SCLC regime and trap-free SCLC regime (Figure 1.13b), thus a careful data analysis is indispensable.

Quite frequently organic semiconductors exhibit a field-dependent mobility, described by the Pool-Frenkel equation (5). For this case, the  $J$ - $V$  characteristics of a SCLC device is better described by the empirical Murgatroyd equation,<sup>[158]</sup>

$$J = \frac{9}{8} \varepsilon \varepsilon_0 \mu_0 e^{(0.89\gamma\sqrt{F})} \frac{V^2}{L^3} \quad (5)$$

with the zero field charge carrier mobility  $\mu_0$  and the parameter  $\gamma$  that represents the field-dependence of the mobility. The effective voltage  $V$  is obtained by correction of the applied voltage  $V_{appl}$  with the built-in voltage  $V_{bi}$ , originating from the differences in work function of the two electrodes, and the voltage drop  $V_r$  from the internal resistance  $R_s$ , *i.e.*  $V = V_{appl} - V_{bi} - IR_s$ . The contact resistance  $R_s$  is usually determined from a reference device without semiconductor layer.

### 1.5.2 Organic field-effect transistor (OFET)

In contrast to the bulk mobility which can be determined with SCLC, the organic field-effect transistor (OFET) delivers a charge carrier mobility  $\mu_{FET}$  that is measured in a very thin sheet of a few nanometers at the semiconductor-dielectric interface. Thus, the extracted mobility is strongly dependent on the morphology at the interface (*e.g.* face-on or edge-on orientation of conjugated semiconductors), the properties of the dielectric material and the configuration of the OFET itself.<sup>[154,159]</sup>

The general device geometry for an OFET in bottom-contact, bottom-gate configuration is depicted in Figure 1.14a. A thin semiconductor layer is deposited in-between to coplanar electrodes, source and drain, and separated from the gate electrode by an insulating dielectric layer. For instance, a highly n-doped silicon substrate is used as substrate and gate electrode with a silicon oxide layer of about 200 nm as dielectric. Typically, the silanol groups of the SiO<sub>2</sub> layer are passivated by a silanization treatment with alkyl trichlorosilanes to avoid charge trapping at the surface. Gold electrodes are deposited on the gate insulating layer, the gap between the source and drain electrodes is the channel length  $L$  (up to 100  $\mu\text{m}$ ), the contact zone between both electrodes is the channel width  $W$  ( $\sim 1$  mm).

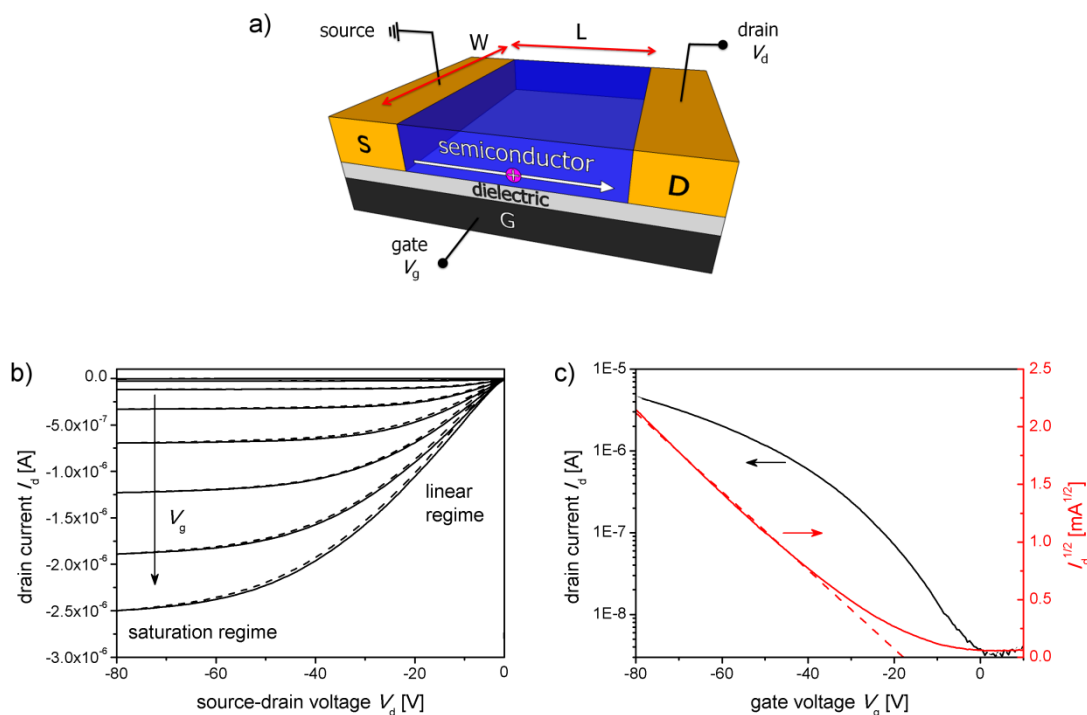


**Figure 1.14.** (a) Schematic illustration of an organic field-effect transistor (OFET) in bottom-contact, bottom-gate configuration.  $S$  denotes source electrode,  $D$  drain electrode,  $G$  gate electrode,  $W$  channel width and  $L$  the channel length. (b) Representative current-voltage characteristics of a p-type OFET showing the output characteristics with linear and saturation regime. (c) Corresponding transfer characteristics in the saturation regime (black) and square-root drain current  $I_d^{1/2}$  (red) with a linear fit (dashed).

The operation principle of an OFET is simply by measuring the source-drain current  $I_d$  as a function of the gate voltage  $V_g$  which is applied perpendicularly to the source-drain voltage  $V_d$ . The gate voltage generates an unipolar capacitor charge at the semiconductor-dielectric interface that moves along the interface due to the applied source-drain voltage  $V_d$ . However, the presence of charge traps in the semiconductor cause a threshold voltage  $V_{th}$  for the gate which must be exceeded to generate an accumulation layer of mobile charges. The transistor obeys Ohm's law as long as  $V_d \ll V_g - V_{th}$  leading to a linearly increasing drain current  $I_d$  with the source-drain voltage  $V_d$ , the so-called linear regime (Figure 1.14b). When  $V_d$  is equal to  $V_g - V_{th}$  the concentration of mobile charges at the drain electrode becomes zero, this point is known as pinch-off point. Further increase of  $V_d$ , i.e.  $V_d > V_g - V_{th}$ , results in a saturation of the drain current  $I_d$  since the pinch-off point gradually moves towards the source electrode. This operation mode is referred to as saturation regime. The current-voltage characteristics of an OFET can be described for the different operation regimes. An important assumption is that the electrical field per-

pendicular to the transistor plane (gate field) is much larger than the source-drain field (gradual channel approximation). This condition is experimentally realized with a channel length  $L$  that is at least 10 fold larger than the thickness of the dielectric layer. The drain current  $I_d$  can be described by following equation:

$$I_d = \frac{W}{L} \mu C_i \left[ (V_g - V_{th}) V_d - \frac{1}{2} V_d^2 \right] \quad (6)$$

$C_i$  is the capacitance of the dielectric. In the saturation regime, where  $V_d$  must be replaced by the potential of the pinch-off point  $V_g - V_{th}$ , the saturation drain current  $I_d$  is

$$I_{d,sat} = \frac{W}{2L} \mu C_i (V_g - V_{th})^2 \quad (7)$$

In the saturation regime, the square root of the saturation current is directly proportional to the gate voltage. Hence, the charge carrier mobility can be extracted from the transfer characteristics by plotting the square-root drain current  $I_d^{1/2}$  versus gate voltage  $V_g$  (Figure 1.14c). By determination of the slope of the linear fit the OFET saturation mobility  $\mu_{sat}$  can be calculated using following expression:

$$\mu_{sat} = \left( \frac{\partial \sqrt{I_d}}{\partial V_g} \right)^2 \frac{2L}{WC_i} \quad (8)$$

## 1.6 Structural elucidation using X-ray scattering techniques

X-ray scattering is a technique for studying the structural features of materials based on the interaction of electromagnetic radiation with condensed matter. The elastic scattering is following a reciprocity law which causes an inverse relationship between the structure size and the scattering angle. While colloidal or nanoscale dimensions are huge compared to the X-ray wavelength (*e.g.*  $\text{CuK}\alpha = 0.154 \text{ nm}$ ), the corresponding angular range of the observed scattering pattern is very small and therefore known as small-angle X-ray scattering (SAXS). Vice versa, periodic structures on the atomic or intermolecular scale generate a scattering pattern in the wide-angle range, known as wide-angle X-ray scattering (WAXS). Unlike transmission/scanning electron microscopy (TEM/SEM) or atomic force microscopy (AFM), which provide a rather localized structural information, the X-ray scattering techniques deliver a statistically averaged information of the morphology in bulk. SAXS is in particular helpful to investigate the structure of block copolymers in solid state or in solution. The morphologies of block copolymers, typically induced by microphase separation and/or crystallization, usually show dimensions in the range of 1-

100 nm. SAXS analysis provides a detailed insight into the type of periodic microdomain structure with long-range order, the size of microdomains and the kinetics of structure formation and phase transitions. Further, colloidal-sized supramolecular structures of block copolymers can be studied to understand the self-assembly in solution.<sup>[160]</sup> Going down the length scale towards (sub-) nanometer structures requires the application of WAXS experiments. Specifically for polymers, the WAXS technique reveals information on the crystalline arrangement of chain segments, *i.e.* lattice type and lattice constants, the degree of crystallinity and an estimation of the crystal sizes.<sup>[161]</sup> In-between both angular regions, SAXS and WAXS, distinct scattering patterns of liquid-crystalline materials or rigid-rod polymers can be found. Hence, the combination of X-ray scattering methods covering different angular regions allow a systematic investigation of the structure over a broad range of length scales from nanostructures down to the intermolecular or atomic level (Figure 1.15).<sup>[162]</sup>

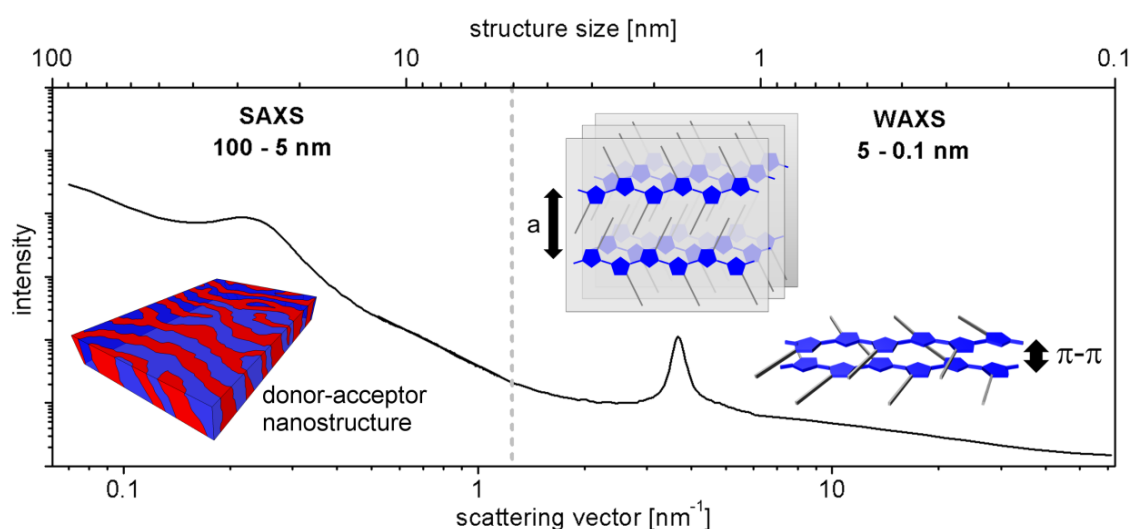


**Figure 1.15.** Length scales accessible by X-ray scattering experiments in different angular regions. Small angle X-ray-scattering (SAXS) for periodic structures on the nanoscale and wide-angle X-ray scattering (WAXS) to unravel crystalline features of semiconducting polymers.

Grazing incidence small-angle X-ray scattering (GISAXS) and wide-angle X-ray scattering (GIWAXS) are advanced scattering techniques based on synchrotron radiation for the analysis of thin film structures.<sup>[163,164]</sup> In contrast to surface-sensitive methods such as AFM or SEM, GISAXS/GIWAXS provide an insight into the inner morphology of thin films which is particularly interesting for the characterization of active layer materials for OPV.<sup>[165]</sup> Owing to the large surface area probed by GISAXS/GIWAXS, the results have much larger statistical significance compared to AFM. An additional information ad-

dressable by grazing-incidence scattering is the orientation of structures relative to the substrate or film-air interface, *e.g.* the orientation of nanoscale microdomains in block copolymers films by GISAXS or crystalline regions by GIWAXS. Both methods have emerged as indispensable tools to develop a general understanding of material properties like charge transport or the performance of OPV devices and the orientation of structures in thin films.<sup>[166–168]</sup>

## REFERENCES

- [1] H. Shirakawa, E. J. Louis, A. G. MacDiarmid, C. K. Chiang, A. J. Heeger, *J. Chem. Soc. Chem. Commun.* **1977**, 578.
- [2] X. Guo, M. Baumgarten, K. Müllen, *Prog. Polym. Sci.* **2013**, *38*, 1832.
- [3] A. J. Heeger, *Chem. Soc. Rev.* **2010**, *39*, 2354.
- [4] S. Kirchmeyer, K. Reuter, *J. Mater. Chem.* **2005**, *15*, 2077.
- [5] P. P. Deshpande, N. G. Jadhav, V. J. Gelling, D. Sazou, *J. Coatings Technol. Res.* **2014**, *11*, 473.
- [6] H. Bai, G. Shi, *Sensors* **2007**, *7*, 267.
- [7] P. Lin, F. Yan, *Adv. Mater.* **2012**, *24*, 34.
- [8] G. Gustafsson, Y. Cao, G. M. Treacy, F. Klavetter, N. Colaneri, A. J. Heeger, *Nature* **1992**, *357*, 477.
- [9] OLED-info. The OLED experts, Web 08.20.2015, <www.oled-info.com>.
- [10] S. Holliday, J. E. Donaghey, I. McCulloch, *Chem. Mater.* **2014**, *26*, 647.
- [11] G. Li, R. Zhu, Y. Yang, *Nat. Photonics* **2012**, *6*, 153.
- [12] F. C. Krebs, N. Espinosa, M. Hösel, R. R. Søndergaard, M. Jørgensen, *Adv. Mater.* **2014**, *26*, 29.
- [13] A. J. Heeger, *Angew. Chem. Int. Ed.* **2001**, *40*, 2591.
- [14] C. W. Tang, *Appl. Phys. Lett.* **1986**, *48*, 183.
- [15] N. S. Sariciftci, L. Smilowitz, a. J. Heeger, F. Wudl, *Science* **1992**, *258*, 1474.
- [16] G. Yu, J. Gao, J. C. Hummelen, F. Wudl, a J. Heeger, *Science* **1995**, *270*, 1789.
- [17] J. J. M. Halls, C. A. Walsh, N. C. Greenham, E. A. Marseglia, R. H. Friend, S. C. Moratti, A. B. Holmes, *Nature* **1995**, *376*, 498.
- [18] B. A. Gregg, B. A. Gregg, *J. Phys. Chem. B* **2003**, *107*, 4688.
- [19] C. J. Brabec, S. Gowrisanker, J. J. M. Halls, D. Laird, S. Jia, S. P. Williams, B. C. J. Brabec, *Adv. Mater.* **2010**, *22*, 3839.
- [20] M. T. Dang, L. Hirsch, G. Wantz, *Adv. Mater.* **2011**, *23*, 3597.
- [21] Y. Liu, J. Zhao, Z. Li, C. Mu, W. Ma, H. Hu, K. Jiang, H. Lin, H. Ade, H. Yan, *Nat. Commun.* **2014**, *5*, 5293.
- [22] S. D. Dimitrov, J. R. Durrant, *Chem. Mater.* **2014**, *26*, 616.
- [23] J.-L. Brédas, J. Norton, J. Cornil, V. Coropceanu, *Acc. Chem. Res.* **2009**, *42*, 1691.
- [24] C. Deibel, V. Dyakonov, *Reports Prog. Phys.* **2010**, *73*, 096401.
- [25] J. D. Servaites, M. a. Ratner, T. J. Marks, *Energy Environ. Sci.* **2011**, *4*, 4410.
- [26] B. M. Savoie, N. E. Jackson, T. J. Marks, M. a Ratner, *Phys. Chem. Chem. Phys.* **2013**, *15*, 4538.
- [27] K. H. Lee, P. E. Schwenn, A. R. G. Smith, H. Cavaye, P. E. Shaw, M. James, K. B. Krueger, I. R. Gentle, P. Meredith, P. L. Burn, *Adv. Mater.* **2011**, *23*, 766.
- [28] K. M. Coakley, M. D. McGehee, *Chem. Mater.* **2004**, *16*, 4533.
- [29] J. Peet, A. J. Heeger, G. C. Bazan, *Acc. Chem. Res.* **2009**, *42*, 1700.

- [30] J. K. J. Van Duren, X. Yang, J. Loos, C. W. T. W. T. Bulle-Lieuwma, A. B. a. B. Sieval, J. C. J. C. Hummelen, R. a. J. a J. Janssen, J. K. J. van Duren, X. Yang, J. Loos, C. W. T. W. T. Bulle-Lieuwma, A. B. a. B. Sieval, J. C. J. C. Hummelen, R. a. J. a J. Janssen, *Adv. Funct. Mater.* **2004**, *14*, 425.
- [31] W. Ma, C. Yang, X. Gong, K. Lee, A. J. Heeger, *Adv. Funct. Mater.* **2005**, *15*, 1617.
- [32] T. Erb, U. Zhokhavets, G. Gobsch, S. Raleva, B. Stühn, P. Schilinsky, C. Waldauf, C. J. Brabec, *Adv. Funct. Mater.* **2005**, *15*, 1193.
- [33] J. K. Lee, W. L. Ma, C. J. Brabec, J. Yuen, J. S. Moon, J. Y. Kim, K. Lee, G. C. Bazan, A. J. Heeger, *J. Am. Chem. Soc.* **2008**, *130*, 3619.
- [34] J. Peet, M. L. Senatore, A. J. Heeger, G. C. Bazan, *Adv. Mater.* **2009**, *21*, 1521.
- [35] X. Yang, J. Loos, M. Control, *Macromolecules* **2007**, *40*, 1353.
- [36] M. T. Dang, L. Hirsch, G. Wantz, J. D. Wuest, *Chem. Rev.* **2013**, *113*, 3734.
- [37] B. a. Collins, J. R. Tumbleston, H. Ade, *J. Phys. Chem. Lett.* **2011**, *2*, 3135.
- [38] S. Bertho, G. Janssen, T. J. Cleij, B. Conings, W. Moons, A. Gadisa, J. D'Haen, E. Goovaerts, L. Lutsen, J. Manca, D. Vanderzande, *Sol. Energy Mater. Sol. Cells* **2008**, *92*, 753.
- [39] I. T. Sachs-Quintana, T. Heumüller, W. R. Mateker, D. E. Orozco, R. Cheacharoen, S. Sweetnam, C. J. Brabec, M. D. McGehee, *Adv. Funct. Mater.* **2014**, *24*, 3978.
- [40] S. S. van Bavel, M. Bärenklau, G. de With, H. Hoppe, J. Loos, *Adv. Funct. Mater.* **2010**, *20*, 1458.
- [41] F. C. Krebs, *Sol. Energ. Mat. Sol. C.* **2009**, *93*, 394.
- [42] G. Wantz, L. Derue, O. Dautel, A. Rivaton, P. Hudhomme, C. Dagron-Lartigau, *Polym. Int.* **2014**, *63*, 1346.
- [43] J. W. Rumer, I. McCulloch, *Mater. Today* **2015**, *18*, 425.
- [44] C. Müller, *Chem. Mater.* **2015**, *27*, 2740.
- [45] K. Sivula, Z. T. Ball, N. Watanabe, J. M. J. Fréchet, *Adv. Mater.* **2006**, *18*, 206.
- [46] M. Urien, H. Erothu, E. Cloutet, R. C. Hiorns, L. Vignau, H. Cramail, *Macromolecules* **2008**, *41*, 7033.
- [47] F. Richard, C. Brochon, N. Leclerc, D. Eckhardt, T. Heiser, G. Hadziioannou, *Macromol. Rapid Commun.* **2008**, *29*, 885.
- [48] C. Yang, J. K. Lee, A. J. Heeger, F. Wudl, *J. Mater. Chem.* **2009**, *19*, 5416.
- [49] J. U. Lee, J. W. Jung, T. Emrick, T. P. Russell, W. H. Jo, *Nanotechnology* **2010**, *21*, 105201.
- [50] V. Gernigon, P. Lévêque, C. Brochon, J.-N. Audinot, N. Leclerc, R. Bechara, F. Richard, T. Heiser, G. Hadziioannou, *Eur. Phys. J. Appl. Phys.* **2011**, *56*, 34107.
- [51] M. Heuken, H. Komber, T. Erdmann, V. Senkovskyy, A. Kiriya, B. Voit, *Macromolecules* **2012**, *45*, 4101.
- [52] M. W. Matsen, F. S. Bates, *Macromolecules* **1996**, *29*, 1091.
- [53] F. H. Schacher, P. a. Rugar, I. Manners, *Angew. Chem. Int. Ed.* **2012**, *51*, 7898.
- [54] M. Shah, V. Ganesan, *Macromolecules* **2010**, *43*, 543.
- [55] G. a. Buxton, N. Clarke, *Phys. Rev. B* **2006**, *74*, 085207.
- [56] C. R. Singh, G. Gupta, R. Lohwasser, S. Engmann, J. Balko, M. Thelakktat, T. Thurn-Albrecht, H. Hoppe, *J. Polym. Sci. Part B Polym. Phys.* **2013**, *51*, 943.
- [57] S. B. Darling, *Energy Environ. Sci.* **2009**, *2*, 1266.
- [58] M. Sommer, S. Huettner, M. Thelakktat, *J. Mater. Chem.* **2010**, *20*, 10788.
- [59] P. D. Topham, A. J. Parnell, R. C. Hiorns, *J. Polym. Sci. Part B Polym. Phys.* **2011**, *49*, 1131.
- [60] A. Yassar, L. Miozzo, R. Gironda, G. Horowitz, *Prog. Polym. Sci.* **2013**, *38*, 791.

- [61] K. Nakabayashi, H. Mori, *Materials* **2014**, *7*, 3274.
- [62] P. J. Flory, *Principles of Polymer Chemistry*; Cornell University Press: Ithaca, New York, 1953.
- [63] P.-G. De Gennes, *Scaling Concepts in Polymer Physics*; Cornell University Press: Ithaca, New York, 1979.
- [64] F. S. Bates, *Science* **1991**, *251*, 898.
- [65] F. S. Bates, M. a. Hillmyer, T. P. Lodge, C. M. Bates, K. T. Delaney, G. H. Fredrickson, *Science* **2012**, *336*, 434.
- [66] I. Botiz, S. B. Darling, *Mater. Today* **2010**, *13*, 42.
- [67] W.-N. He, J.-T. Xu, *Prog. Polym. Sci.* **2012**, *37*, 1350.
- [68] C.-L. Liu, C.-H. Lin, C.-C. Kuo, S.-T. Lin, W.-C. Chen, *Prog. Polym. Sci.* **2011**, *36*, 603.
- [69] A. de Cuendias, R. C. Hiorns, E. Cloutet, L. Vignau, H. Cramail, *Polym. Int.* **2010**, *59*, 1452.
- [70] L. Leibler, *Macromolecules* **1980**, *13*, 1602.
- [71] M. Reenders, G. ten Brinke, *Macromolecules* **2002**, *35*, 3266.
- [72] B. Olsen, R. Segalman, *Mater. Sci. Eng. R Reports* **2008**, *62*, 37.
- [73] R. H. Lohwasser, G. Gupta, P. Kohn, M. Sommer, A. S. Lang, T. Thurn-Albrecht, M. Thelakkat, *Macromolecules* **2013**, *46*, 4403.
- [74] Y. Lin, X. Zhan, *Mater. Horizons* **2014**, *1*, 470.
- [75] A. S. Lang, M. Thelakkat, *Polym. Chem.* **2011**, *2*, 2213.
- [76] A. S. Lang, M.-A. Muth, C. D. Heinrich, M. Carassco-Orozco, M. Thelakkat, *J. Polym. Sci. Part B Polym. Phys.* **2013**, *51*, 1480.
- [77] S. M. Lindner, S. Hüttner, A. Chiche, M. Thelakkat, G. Krausch, *Angew. Chem. Int. Ed.* **2006**, *45*, 3364.
- [78] M. Sommer, S. M. Lindner, M. Thelakkat, *Adv. Funct. Mater.* **2007**, *17*, 1493.
- [79] M. Sommer, A. S. Lang, M. Thelakkat, *Angew. Chem. Int. Ed.* **2008**, *47*, 7901.
- [80] U. Scherf, A. Gutacker, N. Koenen, *Acc. Chem. Res.* **2008**, *41*, 1086.
- [81] M. J. Robb, S.-Y. Ku, C. J. Hawker, *Adv. Mater.* **2013**, *25*, 5686.
- [82] Y. Lee, E. D. Gomez, *Macromolecules* **2015**, 150915153648005.
- [83] G. Tu, H. Li, M. Forster, R. Heiderhoff, L. J. Balk, U. Scherf, *Macromolecules* **2006**, *39*, 4327.
- [84] K. B. Woody, B. J. Leever, M. F. Durstock, D. M. Collard, *Macromolecules* **2011**, *44*, 4690.
- [85] K. Nakabayashi, H. Mori, *Macromolecules* **2012**, *45*, 9618.
- [86] J. Wang, M. Ueda, T. Higashihara, *ACS Macro Lett.* **2013**, *2*, 506.
- [87] R. Verduzco, I. Botiz, D. L. Pickel, S. M. Kilbey, K. Hong, E. Dimasi, S. B. Darling, *Macromolecules* **2011**, *44*, 530.
- [88] M. Sommer, H. Komber, S. Huettner, R. Mulherin, P. Kohn, N. C. Greenham, W. T. S. Huck, *Macromolecules* **2012**, *45*, 4142.
- [89] R. C. Mulherin, S. Jung, S. Huettner, K. Johnson, P. Kohn, M. Sommer, S. Allard, U. Scherf, N. C. Greenham, *Nano Lett.* **2011**, *11*, 4846.
- [90] S.-Y. Ku, M. a Brady, N. D. Treat, J. E. Cochran, M. J. Robb, E. J. Kramer, M. L. Chabiny, C. J. Hawker, *J. Am. Chem. Soc.* **2012**, *134*, 16040.
- [91] N. Zhang, S. Schrick, F. Wudl, M. Prato, *Chem. Mater.* **1995**, *7*, 441.
- [92] J. J. Y. Kim, M. H. Yun, J. Lee, J. J. Y. Kim, F. Wudl, C. Yang, D. A. Links, *Chem. Commun.* **2011**, *47*, 3078.
- [93] M. Eo, S. Lee, M. H. Park, M. H. Lee, S. Yoo, Y. Do, *Macromol. Rapid Commun.* **2012**, *33*, 1119.
- [94] L. Fang, P. Liu, B. R. Sveinbjornsson, S. Atahan-Evrenk, K. Vandewal, S. Osuna,

- G. Jiménez-Osés, S. Shrestha, G. Giri, P. Wei, A. Salleo, A. Aspuru-Guzik, R. H. Grubbs, K. N. Houk, Z. Bao, *J. Mater. Chem. C* **2013**, *1*, 5747.
- [95] Z. T. Ball, K. Sivula, J. M. J. Fréchet, *Macromolecules* **2006**, *39*, 70.
- [96] Y.-G. Ko, S. G. Hahm, K. Murata, Y. Y. Kim, B. J. Ree, S. Song, T. Michinobu, M. Ree, *Macromolecules* **2014**, *47*, 8154.
- [97] A. Hirsch, *Synthesis* **1995**, 895.
- [98] K. E. Geckeler, A. Hirsch, *J. Am. Chem. Soc.* **1993**, *115*, 3850.
- [99] U. Stalmach, B. de Boer, C. Videlot, P. F. van Hutten, G. Hadziioannou, *J. Am. Chem. Soc.* **2000**, *122*, 5464.
- [100] C. J. Hawker, *Macromolecules* **1994**, *27*, 4836.
- [101] M. H. van der Veen, B. de Boer, U. Stalmach, K. I. van de Wetering, G. Hadziioannou, M. H. Van Der Veen, B. De Boer, K. I. Van De Wetering, *Macromolecules* **2004**, *37*, 3673.
- [102] M. Heuken, H. Komber, B. Voit, *Macromol. Chem. Phys.* **2012**, *213*, 97.
- [103] B. Liu, C. E. Bunker, Y.-P. Sun, *Chem. Commun.* **1996**, 1241.
- [104] L. Dai, A. Mau, H. Griesser, T. Spurling, *J. Phys. Chem.* **1995**, *99*, 17302.
- [105] J. U. Lee, A. Cirpan, T. Emrick, T. P. Russell, W. H. Jo, P. Russell, W. Ho, T. P. Russell, W. H. Jo, *J. Mater. Chem.* **2009**, *19*, 1483.
- [106] W.-B. Bin Zhang, J. He, X. Dong, C.-L. L. Wang, H. Li, F. Teng, X. Li, C. Wedemiotis, R. P. Quirk, S. Z. D. D. Cheng, *Polymer* **2011**, *52*, 4221.
- [107] J. Tisserant, R. Hany, E. Wimmer, A. Sa, J. Adamcik, F. Nu, D. Rentsch, A. Borgschulte, J. Heier, **2013**.
- [108] S. Miyanishi, Y. Zhang, K. Tajima, K. Hashimoto, *Chem. Commun.* **2010**, *46*, 6723.
- [109] X.-H. Dong, W.-B. Zhang, Y. Li, M. Huang, S. Zhang, R. P. Quirk, S. Z. D. Cheng, *Polym. Chem.* **2012**, *3*, 124.
- [110] S. Miyanishi, Y. Zhang, K. Hashimoto, K. Tajima, *Macromolecules* **2012**, *45*, 6424.
- [111] G. Adamopoulos, T. Heiser, U. Giovanella, S. Ouldsaad, K. Vandewetering, C. Brochon, T. Zorba, K. Paraskevopoulos, G. Hadziioannou, *Thin Solid Films* **2006**, *511-512*, 371.
- [112] A. Nourdine, L. Perrin, R. De Bettignies, S. Guillerez, L. Flandin, N. Alberola, *Polymer* **2011**, *52*, 6066.
- [113] L. Perrin, A. Nourdine, E. Planes, C. Carrot, N. Alberola, L. Flandin, *J. Polym. Sci. Part B Polym. Phys.* **2013**, *51*, 291.
- [114] B. de Boer, U. Stalmach, C. Melzer, G. Hadziioannou, *Synth. Met.* **2001**, *121*, 1541.
- [115] B. de Boer, U. Stalmach, P. F. van Hutten, C. Melzer, V. V. Krasnikov, G. Hadziioannou, B. De Boer, P. F. Van Hutten, *Polymer* **2001**, *42*, 9097.
- [116] S. Barrau, T. Heiser, F. Richard, C. Brochon, C. Ngov, K. van de Wetering, G. Hadziioannou, D. V. Anokhin, D. A. Ivanov, *Macromolecules* **2008**, *41*, 2701.
- [117] B. Gholamkhash, T. J. Peckham, S. Holdcroft, *Polym. Chem.* **2010**, *1*, 708.
- [118] E. E. Sheina, J. Liu, M. C. Iovu, D. W. Laird, R. D. McCullough, *Macromolecules* **2004**, *37*, 3526.
- [119] R. Miyakoshi, A. Yokoyama, T. Yokozawa, *J. Am. Chem. Soc.* **2005**, *127*, 17542.
- [120] R. H. Lohwasser, M. Thelakkat, *Macromolecules* **2011**, *1*, 3388.
- [121] N. V. Handa, A. V. Serrano, M. J. Robb, C. J. Hawker, *J. Polym. Sci. Part A Polym. Chem.* **2015**, *53*, 831.
- [122] M. Dante, C. Yang, B. Walker, F. Wudl, T.-Q. Nguyen, *Adv. Mater.* **2010**, *22*, 1835.

- [123] X. Chen, B. Gholamkhash, X. Han, G. Vamvounis, S. Holdcroft, *Macromol. Rapid Commun.* **2007**, *28*, 1792.
- [124] B. Gholamkhash, S. Holdcroft, *Chem. Mater.* **2010**, *22*, 5371.
- [125] R. C. Hiorns, E. Cloutet, E. Ibarboure, A. Khoukh, H. Bejbouji, L. Vignau, H. Cramail, *Macromolecules* **2010**, *43*, 6033.
- [126] C. Guo, Y.-H. Y. Lin, M. D. M. Witman, K. K. a Smith, C. Wang, A. Hexemer, J. Strzalka, E. D. Gomez, R. Verduzco, *Nano Lett.* **2013**, *13*, 2957.
- [127] Y.-H. Lin, K. G. Yager, B. Stewart, R. Verduzco, *Soft Matter* **2014**, *10*, 3817.
- [128] K. Yuan, L. Chen, Y. Chen, *Polym. Int.* **2014**, *63*, 593.
- [129] E. Biccocchi, M. Haeussler, E. Rizzardo, A. D. Scully, K. P. Ghiggino, *J. Polym. Sci. Part A Polym. Chem.* **2015**, *53*, 888.
- [130] E. F. Palermo, S. B. Darling, a J. McNeil, *J. Mater. Chem. C* **2014**, *2*, 3401.
- [131] S. Rajaram, P. Armstrong, B. J. Kim, J. M. J. Fréchet, *Chem. Mater.* **2009**, *21*, 1775.
- [132] C. R. Singh, M. Sommer, M. Himmerlich, A. Wicklein, S. Krischok, M. Thelakkat, H. Hoppe, *Phys. Status Solidi* **2011**, *5*, 247.
- [133] A. Kiriya, V. Senkovskyy, M. Sommer, *Macromol. Rapid Commun.* **2011**, *32*, 1503.
- [134] A. Yokoyama, R. Miyakoshi, T. Yokozawa, *Macromolecules* **2004**, *37*, 1169.
- [135] M. Jeffries-El, G. Sauvé, R. McCullough, *Macromolecules* **2005**, *38*, 10346.
- [136] *P3HT Revisited – From Molecular Scale to Solar Cell Devices*; Ludwigs, S., Ed.; Springer: Berlin, 2014.
- [137] T. Higashihara, M. Ueda, *Macromol. Res.* **2013**, *21*, 257.
- [138] C. Barner-Kowollik, T. P. Davis, J. P. A. Heuts, M. H. Stenzel, P. Vana, M. Whittaker, *Polymer* **2003**, *41*, 365.
- [139] G. Moad, Y. K. Chong, A. Postma, E. Rizzardo, S. H. Thang, *Polymer* **2005**, *46*, 8458.
- [140] G. Moad, E. Rizzardo, S. H. Thang, *Polymer* **2008**, *49*, 1079.
- [141] J. Chiefari, Y. Chong, F. Ercole, J. Krstina, J. Jeffery, T. P. T. Le, R. T. A. Mayadunne, G. F. Meijs, C. L. Moad, G. Moad, E. Rizzardo, S. H. Thang, *Macromolecules* **1998**, *31*, 5559.
- [142] A. Gregory, M. H. Stenzel, *Prog. Polym. Sci.* **2012**, *37*, 38.
- [143] H. Willcock, R. K. O'Reilly, *Polym. Chem.* **2010**, *1*, 149.
- [144] G. Moad, E. Rizzardo, S. H. Thang, *Polym. Int.* **2011**, *60*, 9.
- [145] C. J. Hawker, *J. Am. Chem. Soc.* **1994**, *116*, 11185.
- [146] D. Benoit, V. Chaplinski, R. Braslau, C. J. Hawker, *J. Am. Chem. Soc.* **1999**, *121*, 3904.
- [147] J. Nicolas, Y. Guillaneuf, C. Lefay, D. Bertin, D. Gimes, B. Charleux, *Prog. Polym. Sci.* **2013**, *38*, 63.
- [148] H. Fischer, *Chem. Rev.* **2001**, *101*, 3581.
- [149] H. C. Kolb, M. G. Finn, K. B. Sharpless, *Angew. Chem. Int. Ed.* **2001**, *40*, 2004.
- [150] V. V Rostovtsev, L. G. Green, V. V Fokin, K. B. Sharpless, *Angew. Chem. Int. Ed.* **2002**, *41*, 2596.
- [151] J.-F. F. Lutz, *Angew. Chem. Int. Ed.* **2007**, *46*, 1018.
- [152] W. H. Binder, R. Sachsenhofer, *Macromol. Rapid Commun.* **2007**, *28*, 15.
- [153] J. E. Hein, V. V Fokin, *Chem. Soc. Rev.* **2010**, *39*, 1302.
- [154] A. Köhler, H. Bässler, *Electronic Processes in Organic Semiconductors: An Introduction*; WILEY-VCH Verlag GmbH & Co. KGaA: Weinheim, Germany, 2015.
- [155] W. D. Gill, *J. Appl. Phys.* **1972**, *43*, 5033.
- [156] O. Ostroverkhova, *Handbook of Organic Materials for Optical and*

- (*Opto*)*Electronic Devices*; Woodhead Publishing: Cambridge (UK), 2013.
- [157] N. F. Mott, R. W. Gurney, *Electronic Processes in Ionic Crystals*; 1st Editio.; Oxford University Press, 1940.
- [158] P. N. Murgatroyd, *J. Phys. D. Appl. Phys.* **1970**, *3*, 151.
- [159] J. Zaumseil, H. Sirringhaus, J. Zaumseil, H. Sirringhaus, H. Sirringhaus, *Chem. Rev.* **2007**, *107*, 1296.
- [160] B. Chu, B. S. Hsiao, *Chem. Rev.* **2001**, *101*, 1727.
- [161] *Progress in understanding of polymer crystallization*; Reiter, G.; Strobl, G., Eds.; Springer: Berlin, 2007.
- [162] R.-J. Roe, *Methods of x-ray and neutron scattering in polymer science*; Oxford University Press: New York, 2000.
- [163] P. Müller-Buschbaum, *Anal. Bioanal. Chem.* **2003**, *376*, 3.
- [164] M. Ree, *Macromol. Rapid Commun.* **2014**, *35*, 930.
- [165] P. Müller-Buschbaum, *Adv. Mater.* **2014**, *26*, 7692.
- [166] J. R. Tumbleston, B. a. Collins, L. Yang, A. C. Stuart, E. Gann, W. Ma, W. You, H. Ade, *Nat. Photonics* **2014**, *8*, 385.
- [167] I. Botiz, N. Stingelin, *Materials* **2014**, *7*, 2273.
- [168] R. Noriega, J. Rivnay, K. Vandewal, F. P. V Koch, N. Stingelin, P. Smith, M. F. Toney, A. Salleo, *Nat. Mater.* **2013**, *12*, 1038.

## Objective

The aim of this thesis was the synthesis of new fullerene-based electron transport polymers and their integration into well-defined donor-acceptor block copolymers. Unraveling the complexity of interdependencies between polymer design, structure formation and physical properties such as charge transport was a key objective in this work.

A fundamental requirement was to develop controlled synthesis methods to prepare polymers with high loads of fullerenes, both  $C_{60}$  and  $C_{70}$ , while maintaining their solubility and processability. Moreover, suitable well-defined polymerization methods such as KCTP, RAFT, NMRP and click chemistry for block copolymer formation should be investigated in order to create finely tailored donor-acceptor block copolymers with desired molecular weights, donor-acceptor composition, copolymer ratio and grafting density.

Incorporating the highly crystalline fullerenes into an amorphous polymer environment raises a couple of intriguing questions regarding the aggregation of fullerenes, the morphology of the polymers, their glass transition temperature and the consequences on charge transport. These fundamental properties strongly depend on the individual design of the fullerene-grafted polymers and therefore demand for a systematic investigation.

Donor-acceptor block copolymers comprising a fullerene polymer and a conjugated polymer block such as P3HT are attractive materials due to their dual functionality and self-assembly properties for optoelectronic devices. Understanding the basic design principles and the corresponding influence on structure formation is of fundamental importance. This thesis should address in particular the effects of polymer design on nanoscale structures and microphase separation, film and bulk morphology and the influence of the processing method.

The charge transport properties of these block copolymers cannot be viewed singularly from design and structural features. This fact is reflected by the close interdependency between crystallization of the conjugated block and the dynamics of the block copolymer which is mostly governed by the high glass transition temperature of the fullerene polymers. Thus, an important target is to assess different approaches to tune the charge carrier mobility in the block copolymer in a way that hole and electron transport is balanced.

Donor-acceptor block copolymers represent a complex class of semiconducting materials and it is inevitable to resolve the fundamental structure-property relationships for future application in optoelectronic devices.



## 2 Overview of the thesis

This thesis focuses on the controlled synthesis and understanding of structure-property relationships in polymers carrying pendant fullerenes. The basic principle relies on the functionalization of a polymer backbone with fullerene molecules (PCBM) which possess electron accepting and electron transporting properties (Figure 2.1). The resulting acceptor polymer PPCBM represents a new semiconductor material based on fullerenes and opens new perspectives in materials chemistry. Further, the combination with a second polymer block with electron donating properties (donor) such as P3HT results in block copolymers, which are potentially attractive as an active layer material in organic photovoltaic devices.

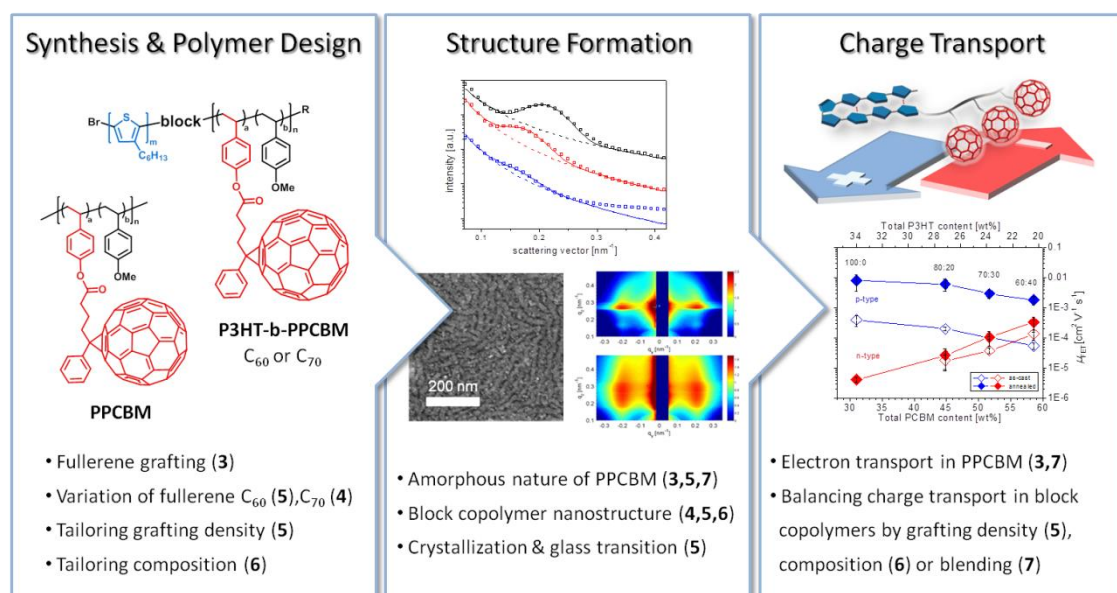


**Figure 2.1.** Overview of the thesis including the main topics i) synthesis and polymer design, ii) structure formation and iii) charge transport studies (chapters are given in brackets).

The donor-acceptor block copolymers P3HT-b-PPCBM are designed to self-assemble into temporally and thermodynamically stable, nanoscale equilibrium structures which are promising for improved charge generation and fast charge transport through the bi-continuous network of acceptor and donor domains. However, the complex cascade of photophysical and electronic processes during device operation places high demands on functionality of the active layer material. Specifically, a single material such as a donor-acceptor block copolymer has to comply with efficient light harvesting, a suitable nano-morphology enabling charge separation and high charge carrier mobility for both electrons and holes. In view of the complexity of material properties required for the applica-

tion in electronic devices, the thesis focuses on a fundamental understanding of structure-property relationships between polymer design, the consequences on structure formation and charge transport (Figure 2.1).

The first part of the thesis covers the synthesis and design of fullerene-grafted polymers: It is of fundamental importance to develop a preparative method for the controlled functionalization of polymers with fullerenes which avoids cross-linking and multi-addition of fullerenes. Additionally, polymers with high fullerene contents are targeted while maintaining the solubility of the synthesized materials. For this, a synthesis route based on well-defined statistical precursor copolymers poly(4-methoxystyrene-*stat*-4-hydroxystyrene) obtained by controlled radical polymerization (CRP) methods has been developed. Either reversible addition-fragmentation chain transfer (RAFT) polymerization or nitroxide-mediated radical polymerization (NMRP) were used to synthesize the statistical polystyrene copolymer with a tailored monomer ratio, molecular weight and a suitable end group for block copolymer preparation. Decoration with phenyl- $C_{61}$ -butyric acid ( $PC_{61}BA$ ) is performed in an efficient polymer-analogous esterification to yield highly soluble, fullerene-grafted copolymers ( $PPC_{61}BM$ , **Chapter 3**). Furthermore, suitable analytical methods for the determination of the exact fullerene weight fraction in the polymers were evaluated as the fullerene load is one of the key parameters driving the material properties in PPCBMs.

The precise control over end group fidelity paves the way towards integration of the acceptor polymer PPCBM into a block copolymer architecture. For this, an ethynyl-encapped P3HT using Kumada catalyst transfer polycondensation (KCTP) and a copolymer of styrene with an azide end group were synthesized. The donor-acceptor block copolymers P3HT-b-PPCBM are then obtained by coupling of the polystyrene copolymer precursor carrying hydroxy groups with the donor polymer P3HT using polymer-polymer click chemistry and subsequent esterification of the polystyrene block with fullerenes. This novel synthesis route was applied to block copolymers with  $C_{60}$  fullerenes  $PC_{61}BA$  (**Chapter 5**) as well as the  $C_{70}$  analogue  $PC_{71}BA$  (**Chapter 4**) attached to the polymer backbone. The modularity of this synthetic approach allows the combination of well-defined, preformed polymer blocks with tailored molecular weights, backbone composition and PCBM content. Based on this synthesis toolbox a variety of donor-acceptor block copolymers can be precisely designed to elucidate the fundamental structure-

property relationships between polymer design, structure formation and charge transport (**Chapter 5, 6**).

The second part of the thesis elucidates the consequences of fullerene grafting on the structure formation of the polymers. On the one hand, the fundamental morphological effects are examined that arise from the covalent bonding of the highly crystalline fullerene molecules to the polymer backbone in the PPCBM copolymers (**Chapter 3**). On the other hand, the structure formation in donor-acceptor block copolymers carrying pendant fullerenes is more complex. Although a two-phase nanostructure can be observed which is induced by the incompatibility of P3HT and PPCBM, the microphase separation seems incomplete due to restrictions in polymer dynamics (**Chapter 4, 5**). A central aspect regarding structure formation in crystalline-amorphous block copolymers is the interplay between crystallization of P3HT and the glass transition in the amorphous PPCBM polymer block (**Chapter 5**). The SAXS, WAXS and GIXRD measurements and analysis were done in collaboration with the group of Prof. Thurn-Albrecht at the University of Halle-Wittenberg.

The third part of the thesis deals with charge transport properties of the synthesized semiconducting polymers. PPCBM is a polymeric electron transporting material where we have studied the bulk mobility in a series of polymers in detail (**Chapter 3**). Regarding the donor-acceptor block copolymers there is a great interest for both high mobilities and balanced charge transport of holes and electrons which is favourable for the application in devices. To address the issue of balanced charge carrier mobilities three different approaches have been developed in this thesis: Tailoring the polymer design either by variation of fullerene grafting density (**Chapter 5**), by changing the composition of donor and acceptor moieties (**Chapter 6**) or by blending molecular PCBM with high mobility into the block copolymer (**Chapter 7**).

This thesis includes two published manuscripts (Chapter 3, 4), two submitted manuscripts (Chapter 5, 7) and one which is intended for submission (Chapter 6). A review/feature article submitted to *Advances in Polymer Science* summarizes the current state of research in the field of donor-acceptor block copolymers with emphasis on the work done in our research group and it is added to the appendix (Chapter 8).

### Fullerene-grafted copolymers exhibiting high electron mobility without nanocrystal formation (Chapter 3)

This fundamental work shows a feasible synthetic path towards a series of fullerene-grafted copolymers (PPC<sub>61</sub>BM) which incorporate high contents between 30 and 64 wt% of pendant phenyl-C<sub>61</sub>-butyric acid methyl ester (PC<sub>61</sub>BM) while maintaining the solubility of the polymers. For this, tailor-made precursor copolymers poly(4-methoxystyrene-*stat*-4-hydroxystyrene) obtained by RAFT polymerization were functionalized *via* an efficient polymer-analogous Steglich esterification with the carboxylic acid derivative PC<sub>61</sub>BA (Figure 2.2a). This controlled grafting method yields well-soluble PPC<sub>61</sub>BM polymers with narrow molecular weight distributions (Figure 2.2b). An important aspect is the absence of any cross-linking which was the main problem in obtaining soluble fullerene-grafted polymers earlier.

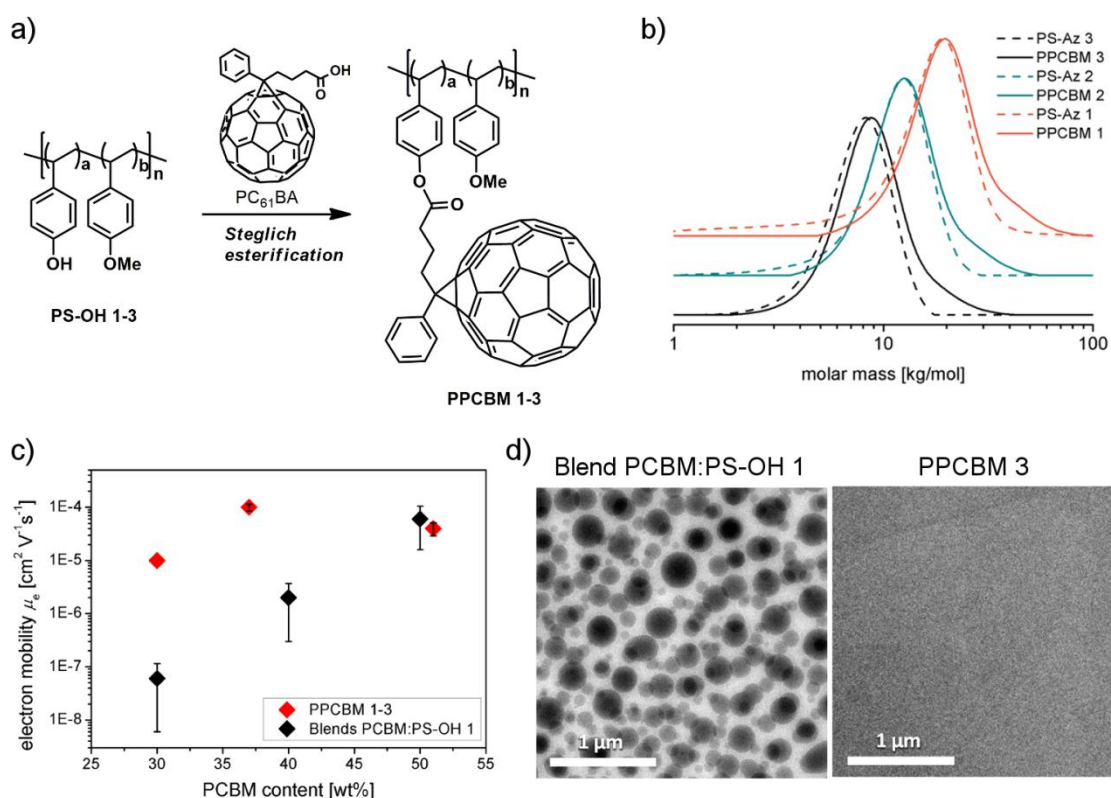


**Figure 2.2.** (a) Key step towards fullerene-grafted polystyrene copolymers: Polymer-analogous esterification with monofunctional phenyl-C<sub>61</sub>-butyric acid (PC<sub>61</sub>BA). (b) SEC traces of a series of PPC<sub>61</sub>BM 1-3 in comparison to the corresponding precursor copolymers PS-Az 1-3. (c) SCLC electron mobility in dependence of the PC<sub>61</sub>BM weight fraction of PPC<sub>61</sub>BM (red) and blends PC<sub>61</sub>BM:PS-OH 1 (black). (d) TEM images showing thin films of a PC<sub>61</sub>BM:PS-OH 1 blend with 50 wt% PC<sub>61</sub>BM (left) and a PPC<sub>61</sub>BM polymer with 51 wt% of covalently attached PC<sub>61</sub>BM (right).

The synthesized acceptor copolymers retain the optical and electrochemical properties of the incorporated PC<sub>61</sub>BM independent of the fullerene weight fraction. The bulk electron transport properties of the PPC<sub>61</sub>BM were studied by the space-charge limited current (SCLC) method. The maximum electron mobility  $\mu_e$  of  $1 \times 10^{-4} \text{ cm}^2 \text{ V}^{-1} \text{ s}^{-1}$  was achieved for only 37 wt% of incorporated PC<sub>61</sub>BM. In the range of 30 to 50 wt% of PC<sub>61</sub>BM, the acceptor polymers exhibit exceptional high charge carrier mobility compared to corresponding blends of molecular PC<sub>61</sub>BM and polystyrene copolymer having the same composition (Figure 2.2c). In contrast to the spinodal demixing of polystyrene:PC<sub>61</sub>BM blends, the PPC<sub>61</sub>BM polymers show a fully homogenous morphology in the TEM images (Figure 2.2d). Our detailed structural analysis of PPC<sub>61</sub>BM using AFM, TEM, XRD and DSC confirms the amorphous nature of the polymer in thin films and in bulk without the formation of any PC<sub>61</sub>BM nanocrystals. Thus, an efficient charge carrier percolation is facilitated by the homogeneous distribution of PC<sub>61</sub>BM in the copolymer. The crystallization of the PC<sub>61</sub>BM pendants is suppressed even upon thermal annealing of the PPC<sub>61</sub>BM samples, whereas blends undergo a macrophase separation.

#### **Donor-acceptor block copolymers carrying pendant PC<sub>71</sub>BM fullerenes with ordered nanoscale morphology (Chapter 4)**

This work demonstrates an elegant synthetic approach to integrate the acceptor polymers PPCBM from the previous chapter into block copolymers. Here, the preparation of a novel donor-acceptor block copolymer based on phenyl-C<sub>71</sub>-butyric methyl ester (PC<sub>71</sub>BM) and a regioregular poly(3-hexylthiophene) (P3HT) as donor is presented in detail (Figure 2.3a). First, a hydroxyl-functionalized polystyrene copolymer with an azide end group was synthesized *via* nitroxide-mediated radical polymerization (NMRP) and coupled with ethynyl-terminated P3HT using copper(I) catalyzed azide-alkyne cycloaddition (CuAAC). The polymer-analogous grafting reaction of phenyl-C<sub>71</sub>-butyric acid (PC<sub>71</sub>BA) to the hydroxyl groups of the polystyrene precursor was optimized to yield near-quantitative conversion which is further demonstrated for a PC<sub>71</sub>BM-grafted acceptor copolymer in detail using MALDI-TOF mass spectrometry, thermogravimetric analysis (TGA) and <sup>1</sup>H-NMR spectroscopy. Owing to the incorporation of C<sub>70</sub> instead of C<sub>60</sub>, the donor-acceptor block copolymer exhibits enhanced absorption from the UV range up to 600 nm. To illustrate the improved optical properties, the same block copolymer precursor has been grafted either with PC<sub>71</sub>BA or PC<sub>61</sub>BA fullerenes yielding P3HT-b-PPC<sub>71</sub>BM and P3HT-b-PPC<sub>61</sub>BM, respectively. Despite similar compositions of P3HT

and PC<sub>71</sub>BM or PC<sub>61</sub>BM in both polymers, the absorption spectra clearly show the notably increased optical density for the C<sub>70</sub> pendant block polymer (Figure 2.3b).

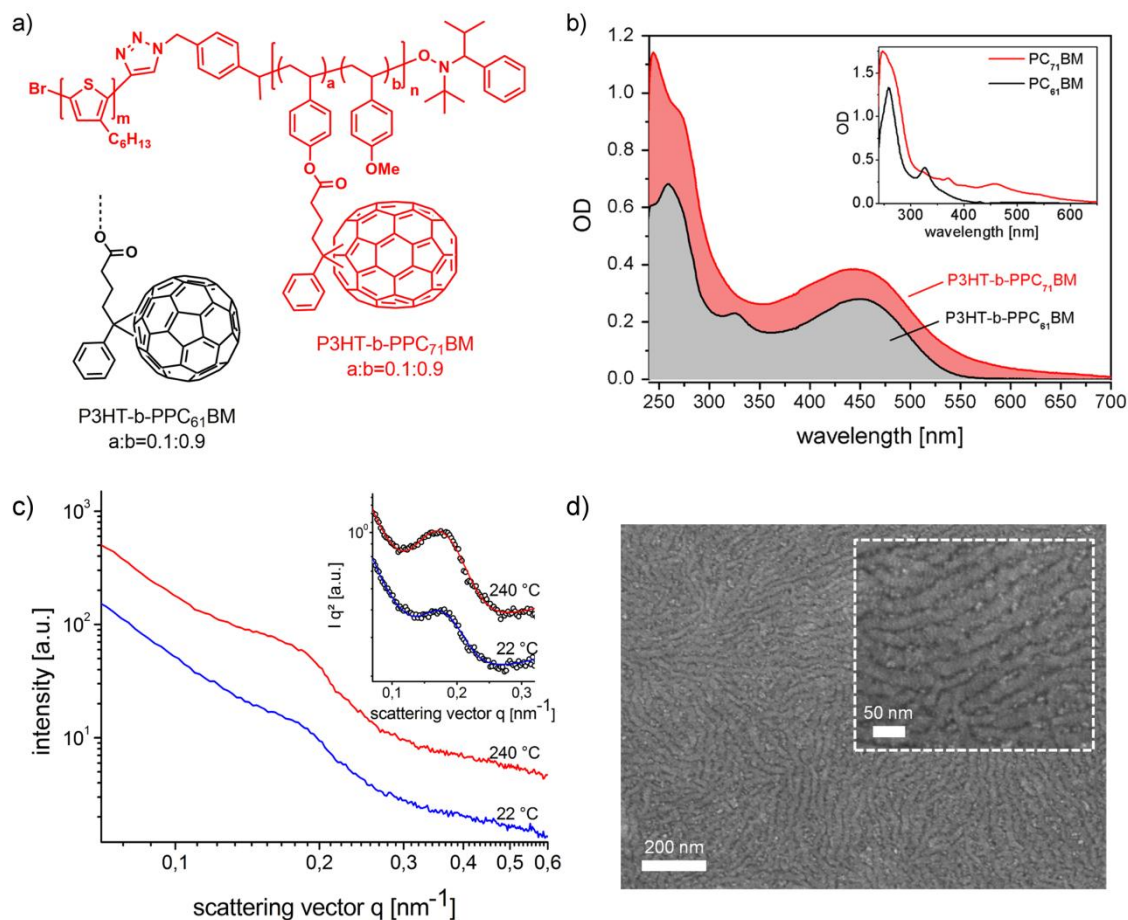


**Figure 2.3.** a) Chemical structure of the donor-acceptor block copolymer P3HT-b-PPC<sub>71</sub>BM and P3HT-b-PPC<sub>61</sub>BM. (b) Absorption spectra in chloroform solution comparing P3HT-b-PPC<sub>61</sub>BM (black), P3HT-b-PPC<sub>71</sub>BM (red) and the small molecule references PC<sub>61</sub>BM (inset, black) and PC<sub>71</sub>BM (inset, red). (c) SAXS curves for P3HT-b-PPC<sub>71</sub>BM indicating a periodic nanostructure in the melt at 240 °C and after cooling to room temperature. The inset shows the same data with a Lorentz corrected intensity scale. (d) SEM surface image of P3HT-b-PPC<sub>71</sub>BM prepared by drop-casting.

The thin film absorption spectra clearly indicate that crystallization of P3HT is occurring both in the P3HT-b-PS<sub>OH</sub> precursor as well as in the fullerene-grafted P3HT-b-PPC<sub>71</sub>BM block copolymer and can be improved by suitable thermal annealing procedures. The structural elucidation of the block copolymer P3HT-b-PPC<sub>71</sub>BM based on small-angle X-ray scattering in transmission (SAXS) and in grazing incidence geometry (GISAXS) gives clear evidence for the formation of a periodic donor-acceptor nanostructure of 37 nm in bulk and in thin films (Figure 2.3c). The SAXS analysis both in the melt and at room temperature after crystallization of the P3HT component suggest that the

nanostructure is already caused by a liquid-liquid phase separation in the melt. Further, scanning electron microscopy (SEM) of P3HT-b-PPC<sub>71</sub>BM films prepared by drop-casting supports the existence of a periodic donor-acceptor nanostructure (Figure 2.3d).

### Influence of fullerene grafting density on structure, dynamics and charge transport in P3HT-b-PPC<sub>61</sub>BM block copolymers (Chapter 5)

The block copolymer P3HT-b-PPC<sub>61</sub>BM structure offers a couple of tunable design parameters to the polymer chemist: These are the molecular weight of each polymer block, the weight ratio between both blocks, the monomer ratio in the polystyrene copolymer and the corresponding fullerene grafting density in PPC<sub>61</sub>BM. We define the grafting density as the weight content of fullerenes in the PPC<sub>61</sub>BM block, *i.e.* this parameter is a measure for the dilution of fullerene moieties along the polystyrene backbone. To study the impact of the grafting density on structure formation, dynamics and charge transport, a series of P3HT-b-PPC<sub>61</sub>BM block copolymers has been synthesized with accurately tuned grafting density between 26, 47 and 60 wt%. The chain length of the PPC<sub>61</sub>BM block was reduced at the same time to keep the overall ratio of P3HT and PPC<sub>61</sub>BM moieties roughly constant between 1:0.70 and 1:0.92 (Figure 2.4).

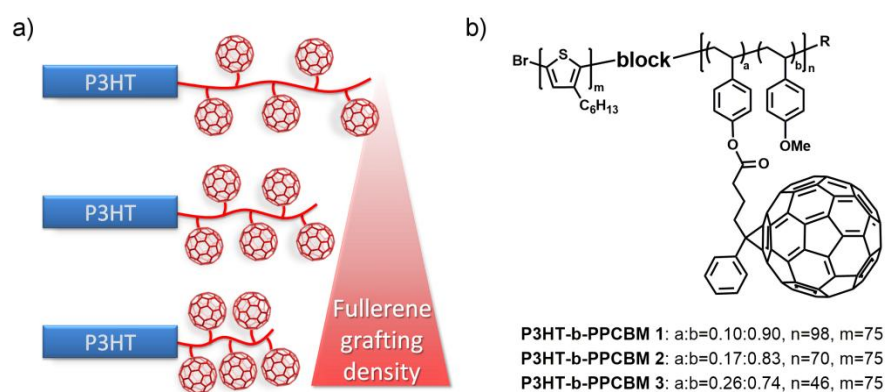


**Figure 2.4.** (a) Schematic illustration of the P3HT-b-PPC<sub>61</sub>BM block copolymer series with variation of the fullerene grafting density and chain length. (b) Chemical structure of P3HT-b-PPC<sub>61</sub>BM 1-3 consisting of the same P3HT block with 20 kg mol<sup>-1</sup> and a tailored PPC<sub>61</sub>BM block with an increasing grafting density of 27, 47 to 61 wt%, respectively.

The dual function block copolymer is designed to exhibit hole transport through P3HT and electron transport through the PPC<sub>61</sub>BM polymer phase. Thereby, the crystallization of the P3HT block is of fundamental interest, since it notably improves the hole mobility in P3HT. Detailed DSC studies confirm the crystallization of P3HT in the block copolymers P3HT-b-PPC<sub>61</sub>BM, however, the crystallization is likely restricted by the glass tran-

sition temperature of the amorphous PPC<sub>61</sub>BM block (Figure 2.5a). The investigation of a series of PPC<sub>61</sub>BM homopolymers revealed that the glass transition temperature increases considerably with increasing grafting density (Figure 2.5b). Thus, the restricted dynamics of PPC<sub>61</sub>BM seem to impose significant constraints for crystallization and structure formation in the block copolymers. Both SAXS and GISAXS measurements of P3HT-b-PPC<sub>61</sub>BM 1-3 revealed a donor-acceptor nanostructure of roughly 30 to 40 nm in bulk and in thin films (Figure 2.5c). This two-phase nanoscale morphology is further supported by transmission electron microscopy (TEM) and scanning electron microscopy (SEM). However, the high  $T_g$  of the amorphous PPC<sub>61</sub>BM block is suggested to trap the structural evolution in an incomplete microphase separated state impeding a long-range and well-ordered morphology of the block copolymer.

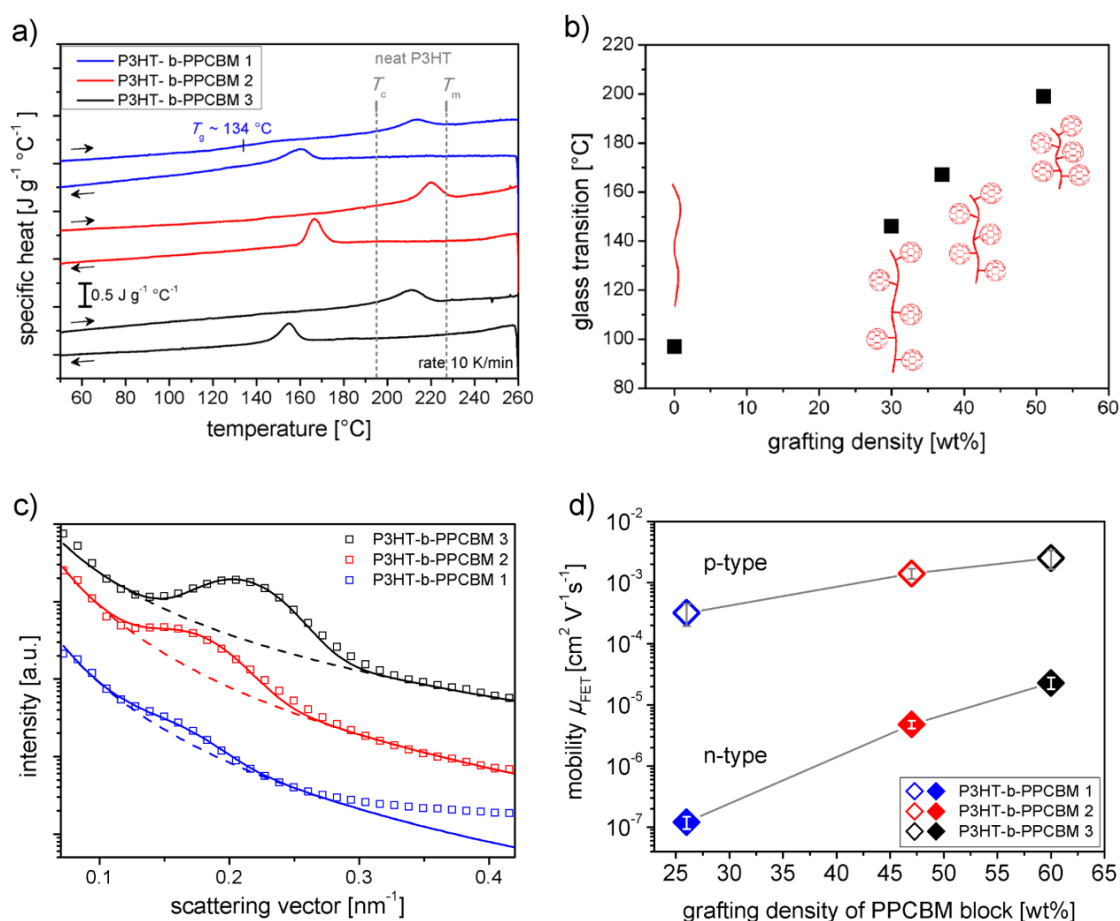


**Figure 2.5.** (a) DSC traces of P3HT-b-PPC<sub>61</sub>BM 1-3 showing the melting/crystallization of the P3HT block and a  $T_g$  for P3HT-b-PPC<sub>61</sub>BM 1. (b) Correlation between grafting density and glass transition temperature in PPC<sub>61</sub>BM homopolymers and a polystyrene precursor. (c) SAXS curves of the block copolymers in bulk indicating a periodic nanostructure of 31-42 nm. (d) Hole (p-type) and electron mobility (n-type) in field-effect transistors of P3HT-b-PPC<sub>61</sub>BM 1 (blue), 2 (red) and 3 (black) demonstrating the importance of grafting density for electron transport in the block copolymers.

Further, it is demonstrated that the fullerene grafting density is a key parameter in P3HT-b-PPC<sub>61</sub>BM block copolymers to improve the electron mobility by two orders of magnitude without sacrificing the hole transport. In organic field-effect transistors, the block copolymers exhibit ambipolar charge transport in particular for P3HT-b-PPC<sub>61</sub>BM 2 and 3 with high fullerene grafting density (Figure 2.5d).

### **Influence of composition on structure formation and charge transport in P3HT-b-PPC<sub>71</sub>BM block copolymers (Chapter 6)**

While the fullerene grafting density is a crucial factor to control charge carrier transport in the donor-acceptor block copolymers, the previous chapter has shown that tuning the grafting density is not sufficient to balance the mobilities. The variation of the donor-acceptor ratio by synthesis represents another approach towards balanced charge transport between holes and electrons in donor-acceptor block copolymers. By tailoring the molecular weights of the p-type P3HT block and the n-type PPCBM block, the donor-acceptor composition of the block copolymer can be fine-tuned. To study the composition dependence of charge transport and structure formation, a series of P3HT-b-PPC<sub>71</sub>BM block copolymers has been prepared with a high grafting density between 51 and 63 wt%. The composition of P3HT:PPC<sub>71</sub>BM in the block copolymers is varied between 1:0.43, 1:1.70 and 1:3.55 (wt:wt) by increasing the polymer chain length of the acceptor block PPC<sub>71</sub>BM (Figure 2.6).

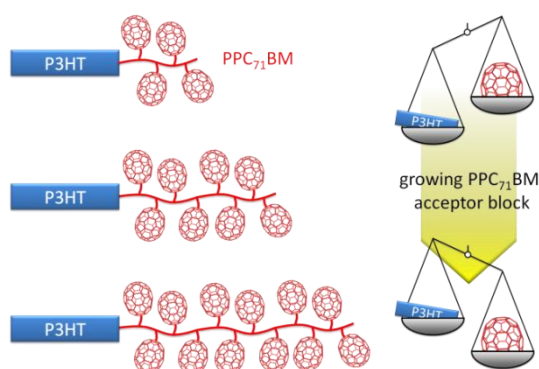


**Figure 2.6.** Schematic illustration of the P3HT-b-PPC<sub>71</sub>BM series with varied donor-acceptor ratio P3HT:PPC<sub>71</sub>BM=1:0.43, 1:1.70 and 1:3.55 (wt:wt).

This study reveals the consequences of the donor-acceptor composition on the crystallization of P3HT in bulk as well as in thin films and the structure formation using differential scanning calorimetry (DSC), absorption and photoluminescence (PL) spectroscopy and small angle X-ray scattering (SAXS). To find ideal conditions for crystallization of

the hole transporting P3HT block, various thermal annealing procedures have been screened in thin films. The thermally induced crystallization of one component further improves phase purity and phase separation of the donor and acceptor domains which is indicated in the photoluminescence quenching results (Figure 2.7). However, when the PPC<sub>71</sub>BM block becomes too large, the dynamics is frozen due to the expected high  $T_g$ . This results in an almost complete suppression of P3HT crystallization. Additionally, the structural investigation of the P3HT-b-PPC<sub>71</sub>BM series using SAXS clearly reveals the impact of chain length on microphase separation: While P3HT-b-PPC<sub>71</sub>BM 1 with a very short acceptor chain is most likely in the weak segregation regime and does not exhibit a clear microphase separation, P3HT-b-PPC<sub>71</sub>BM 2 with a medium sized acceptor block is microphase separated under the constraints of the high  $T_g$  of the PPCBM block. P3HT-b-PPC<sub>71</sub>BM 3 with the largest PPC<sub>71</sub>BM block, however, does not develop a periodic nanostructure which is associated to the dynamic restrictions arising from the high  $T_g$  majority phase of PPC<sub>71</sub>BM.

The composition dependence of charge transport in P3HT-b-PPC<sub>71</sub>BM block copolymers was studied using OFETs. With increasing PPC<sub>71</sub>BM chain length the P3HT weight fraction is reduced and, consequently, the hole mobility is decreasing (Figure 2.7b).

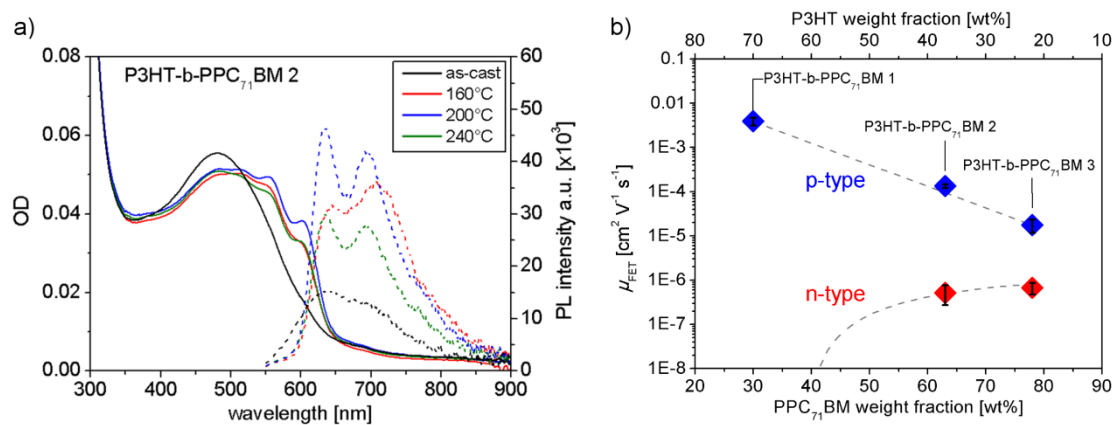


**Figure 2.7.** (a) Thin film absorption (solid lines) and photoluminescence spectra (dashed lines) for P3HT-b-PPC<sub>71</sub>BM 2 in as-cast and annealed samples at 160 °C (120 min), 200 °C (30 min) and 240 °C (5 min). (b) OFET hole (blue) and electron mobilities (red) of the block copolymers series P3HT-b-PPC<sub>71</sub>BM 1-3. The dashed lines are a guide to the eye.

P3HT-b-PPC<sub>71</sub>BM 1 with only 30 wt% of PPC<sub>71</sub>BM apparently does not offer connected percolation paths for electrons and therefore does not show any electron mobility. Despite the increasing PPC<sub>71</sub>BM fraction in the block copolymers 2 and 3, the electron mobility saturates at around  $7 \times 10^{-6} \text{ cm}^2 \text{ V}^{-1} \text{ s}^{-1}$ . Interestingly, the electron mobility of the

C<sub>70</sub>-grafted block copolymers is notably lower compared to the C<sub>60</sub>-grafted block copolymers.

This chapter is unraveling the significance of a roughly balanced composition of the P3HT-b-PPC<sub>71</sub>BM block copolymer in order to achieve the desired periodic donor-acceptor nanostructure induced by microphase separation. The corresponding network of donor/acceptor domains with rather high phase purity is crucial for any optoelectronic application. The charge transport, however, could not be balanced only by varying the composition. On the one hand, the C<sub>70</sub>-grafted block copolymers show in general low electron mobilities compared to P3HT. On the other hand, the correlation of composition and charge transport is strongly influenced by the structure formation in these block copolymers. With increasing PPC<sub>71</sub>BM content the morphology is first weakly segregated with rather isolated PPC<sub>71</sub>BM domains, then microphase separated with a donor-acceptor nanostructure and finally reaches a dynamically frozen state without nanoscale order. This work clearly shows the limitations and complexity of polymer design to tailor a specific material property. In particular, the high glass transition temperature of the PPC<sub>71</sub>BM block is a recurring issue that reinforces the need for tailoring the polymer backbone towards low  $T_g$  systems.

### **Simultaneous morphological stability and high charge carrier mobilities in donor-acceptor block copolymer/PC<sub>61</sub>BM blends (Chapter 7)**

The active layer in organic photovoltaics in particular requires a long-term stable morphology with nanoscale donor/acceptor domains and a balanced charge carrier transport for holes and electrons. The previous chapters have demonstrated that both fullerene grafting density and donor:acceptor composition are important parameters to control the charge carrier transport and structure in the donor-acceptor block copolymers. However, despite the enhancement of electron mobility through tailoring fullerene grafting density, the charge transport is not yet balanced. Therefore, an elegant approach has been developed to match hole and electron transport in P3HT-b-PPC<sub>61</sub>BM by blending molecular PC<sub>61</sub>BM into the block copolymer without causing any macrophase separation. It could be demonstrated that an insufficient electron mobility in the homopolymer PPC<sub>61</sub>BM (Figure 2.8a) can be compensated by blending with molecular PC<sub>61</sub>BM. The SCLC electron mobility in bulk is improved by two orders of magnitude to  $1.8 \times 10^{-4} \text{ cm}^2 \text{ V}^{-1} \text{ s}^{-1}$  for a blend ratio of PPC<sub>61</sub>BM:PC<sub>61</sub>BM=60:40 (Figure 2.8b). Using a

combination of XRD, AFM and DSC, the large miscibility of the PPC<sub>61</sub>BM:PC<sub>61</sub>BM blend up to 60 wt% PC<sub>61</sub>BM load could be verified (Figure 2.8c). The blend between PPC<sub>61</sub>BM homopolymer and PC<sub>61</sub>BM forms an amorphous, molecularly mixed fullerene phase without crystallization of the molecular fullerene component.

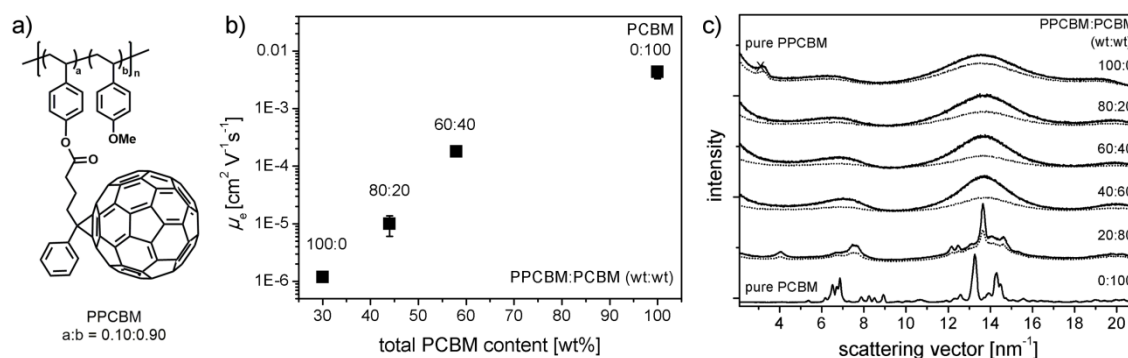


**Figure 2.8.** (a) PPC<sub>61</sub>BM polymer with 30 wt% pendant PC<sub>61</sub>BM. (b) SCLC electron mobility  $\mu_e$  in dependence of the total PC<sub>61</sub>BM content. (c) WAXS scattering curves of pure PPC<sub>61</sub>BM, the PPC<sub>61</sub>BM:PC<sub>61</sub>BM blends 80:20, 60:40, 40:60 and 20:80 and pure PC<sub>61</sub>BM as powder samples measured as-prepared (dotted lines) and after thermal annealing (solid lines).

The blending strategy is applicable to block copolymers as well: Blends of donor-acceptor block copolymer (BCP, Figure 2.9a) and PC<sub>61</sub>BM show substantially enhanced electron mobilities of  $\mu_e = (3.2 \pm 1.7) \times 10^{-4} \text{ cm}^2 \text{V}^{-1} \text{s}^{-1}$  and a hole mobility of  $\mu_h = (1.8 \pm 0.6) \times 10^{-3} \text{ cm}^2 \text{V}^{-1} \text{s}^{-1}$  for BCP:PC<sub>61</sub>BM=60:40 in field-effect transistors (Figure 2.9b). Thereby, the BCP:PC<sub>61</sub>BM blend provides a similarly high ambipolar charge transport compared to the established P3HT:PC<sub>61</sub>BM blend and exhibits exceptionally stable hole and electron mobilities even for prolonged thermal annealing. The operational stability of the OFETs is attributed to the long-term stable donor-acceptor nanostructure of the block copolymer consisting of a network of semi-crystalline P3HT and amorphous PCBM-enriched acceptor phases without macrophase separation (Figure 2.9c). This work demonstrates the feasibility of high charge transport and stable morphology in a donor-acceptor block copolymer by a blend approach.

An application and optimization of the donor-acceptor block copolymers or their blends in organic photovoltaics is not yet attempted due to the lack of vertical orientation of the nanostructures in thin films. Otherwise a thermal annealing usually leads to a non-desired alignment of the nanostructures parallel to the substrate, which does not favor charge carrier transport towards the electrodes in a sandwich geometry.

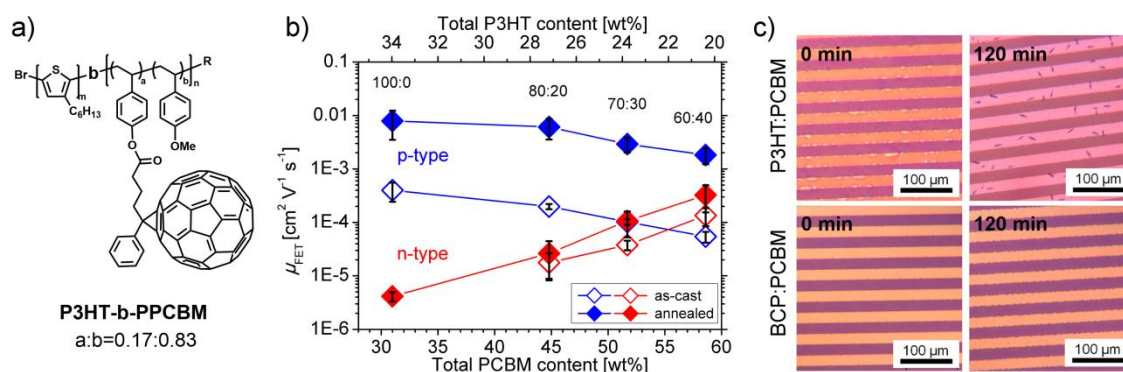


**Figure 2.9.** (a) Chemical structure of the P3HT-b-PPCBM block copolymer (BCP) used for the blend studies. (b) OFET hole (blue) and electron mobilities (red) of BCP:PCBM blends given in wt:wt ratio in as-cast (open symbols) and annealed devices (filled symbols). (c) Optical microscopy images of P3HT:PC<sub>61</sub>BM=1.0:0.8 (wt:wt) and BCP:PC<sub>61</sub>BM=60:40 (wt:wt) blend films showing a section of the interdigitating 20  $\mu\text{m}$  channel gold electrodes of the OFET devices. The images were taken in as-cast state, 0 min, and after 120 min of annealing at 160  $^{\circ}\text{C}$ .

### Appendix: Nanoscale morphology from donor-acceptor block copolymers: Formation and functions (Chapter 8)

This chapter gives a comprehensive overview on general design principles of donor-acceptor block copolymers with a specific focus on block copolymers carrying a P3HT donor block and acceptor blocks with pendant perylene bisimides (PPerAcr) or fullerene derivatives (PPCBM). The article was written based on results from a joint research project between the groups of Prof. Mukundan Thelakkat, Prof. Thomas Thurn-Albrecht and Dr. Harald Hoppe.

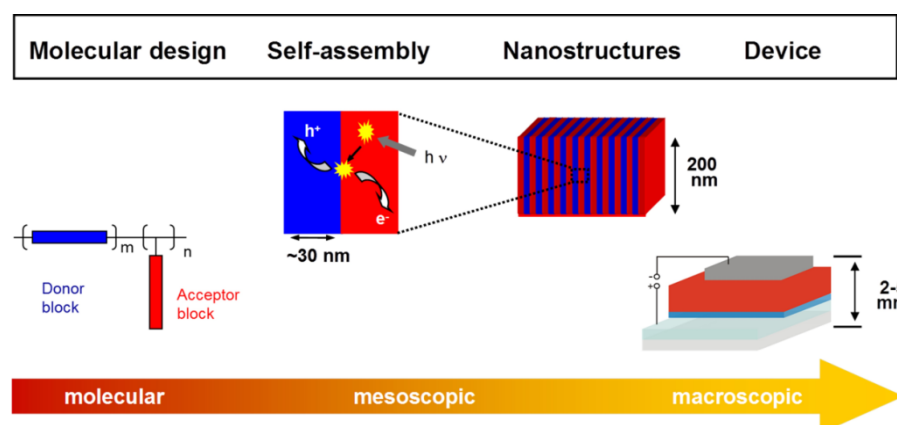


**Figure 2.10.** Concept for donor-acceptor block copolymers in photovoltaic devices: From molecular design of functional semiconducting block copolymers with the ability to self-assemble into a donor-acceptor nanostructure towards aligned functional structures on the mesoscale and their integration into macroscopic devices.

The review/feature article addresses the main issues from an interdisciplinary perspective including the synthetic challenges of the building blocks P3HT, PPerAcr and PPCBM used for the synthesis of the corresponding block copolymers, in-depth studies on structure formation and the consequences for charge transport and application in photovoltaic devices. In particular, we elaborate the implications of the double-crystalline or crystalline-liquid crystalline nature of the block copolymer P3HT-b-PPerAcr on structure in comparison to a crystalline-amorphous system such as P3HT-b-PPCBM. The review article highlights the considerable progress in the field of P3HT-b-PPerAcr block copolymers which exhibit microphase separation in the melt and confined crystallization of P3HT during cooling to room temperature. Similarly to classical coil-coil block copolymers, the type of morphology is determined by the respective volume fractions of P3HT and PPerAcr in the block copolymer and show long-range ordered lamellar or cylindrical microdomains.

## Individual contributions to joint publications

### CHAPTER 3

This manuscript is published in *Macromolecules* (2014, 47, 2324-2332) with the title:

"Fullerene-grafted copolymers exhibiting high electron mobility without nanocrystal formation"

by **Martin Hufnagel**, Mathis-Andreas Muth, Johannes C. Brendel and Mukundan Thelakkat

During the master thesis I synthesized the polymers and did the basic polymer characterization. In-depth analysis of the polymers and blends using transmission electron microscopy (TEM), X-ray diffraction (XRD), differential-scanning calorimetry (DSC) and cyclic voltametry (CV) and the preparation of the manuscript was done during my PhD thesis.

Mathis-Andreas Muth performed the SCLC charge transport measurements, characterized the thin films by AFM, carried out the SEC measurements and was involved in the scientific discussions.

Johannes C. Brendel was involved in the scientific discussion.

Mukundan Thelakkat supervised the project, was involved in the scientific discussion and corrected the manuscript.

### CHAPTER 4

This manuscript is published in *Polymer Chemistry* (2015, 6, 813-826) with the title:

"Donor-acceptor block copolymers carrying pendant PC<sub>71</sub>BM fullerenes with ordered nanoscale morphology"

by **Martin Hufnagel**, Matthias Fischer, Thomas Thurn-Albrecht and Mukundan Thelakkat

I synthesized and characterized all the polymer materials including optical characterization in solution/films and thermal analysis and I wrote the manuscript. Further, I performed initial SAXS experiments using the XRD facilities in the group of Prof. Thurn-Albrecht and prepared the thin films for GISAXS experiments at the European Synchrotron Radiation Facility in Grenoble.

Matthias Fischer characterized in detail the polymers using SAXS and GISAXS.

Thomas Thurn-Albrecht was involved in the scientific discussion and corrected the manuscript.

Mukundan Thelakkat supervised the project, was involved in the scientific discussion and corrected the manuscript.

## CHAPTER 5

This manuscript is under revision in *Macromolecules* with the title:

“Influence of fullerene grafting density on structure, dynamics and charge transport in P3HT-b-PPC<sub>61</sub>BM block copolymers”

by **Martin Hufnagel**, Matthias Fischer, Thomas Thurn-Albrecht and Mukundan Thelakkat

Two block copolymers have been synthesized during my master thesis. During my PhD thesis I developed a new synthetic route and prepared the third block copolymer. I characterized all the polymers and analyzed the material properties using DSC, optical and photoluminescence spectroscopy in solution/films, electron microscopy (TEM, SEM) and OFET. Additionally, I performed initial SAXS and WAXS experiments using the XRD facilities in the group of Prof. Thurn-Albrecht and prepared the thin films for GISAXS experiments at the European Synchrotron Radiation Facility in Grenoble. Further, I wrote the manuscript.

Matthias Fischer characterized in detail the block polymers using SAXS, WAXS and GISAXS and measured DSC for some of the polymers.

Thomas Thurn-Albrecht was involved in the scientific discussion and corrected the manuscript.

Mukundan Thelakkat supervised the project, was involved in the scientific discussion and corrected the manuscript.

**CHAPTER 6**

This manuscript is intended for submission with the title:

"Influence of composition on structure formation and charge transport in P3HT-b-PPC<sub>71</sub>BM block copolymers"

by **Martin Hufnagel**, Matthias Fischer, Anne Browa, Thomas Thurn-Albrecht and Mukundan Thelakkat

I synthesized and characterized all the polymer materials and performed the DSC, spectroscopy and OFET charge transport studies. Further, I wrote the manuscript.

Under my supervision, Anne Browa (practical student) did the spectroscopic characterization of the polymers and performed the preparation and characterization of the OFET devices.

Matthias Fischer contributed to the SAXS measurements and their analysis and was involved in the scientific discussion.

Thomas Thurn-Albrecht was involved in the scientific discussion and correction of the SAXS part of the manuscript.

Mukundan Thelakkat supervised the project, was involved in the scientific discussion and corrected the manuscript.

**CHAPTER 7**

This manuscript is submitted to *Journal of Polymer Science, Part B: Polymer Physics* with the title:

"Simultaneous morphological stability and high charge carrier mobilities in donor-acceptor block copolymer/PC<sub>61</sub>BM blends"

by **Martin Hufnagel** and Mukundan Thelakkat

I performed all the experiments including the structural investigation (XRD, AFM and optical microscopy), thermal analysis (DSC), optical and photoluminescence spectroscopy, SCLC and OFET device preparation and their analysis. Further, I wrote the full manuscript.

Mukundan Thelakkat supervised the project, was involved in the scientific discussion and corrected the manuscript.

**CHAPTER 8**

This review/feature article is submitted to *Advances in Polymer Science* to be published as book chapter with the title:

"Nanoscale morphology from donor-acceptor block copolymers: Formation and functions"

by David Heinrich, **Martin Hufnagel**, Chetan Raj Singh, Matthias Fischer, Shahidul Alam, Harald Hoppe, Thomas Thurn-Albrecht and Mukundan Thelakkat

I have written the sections "Acceptor building block: Poly(fullerenes)/PPCBM" and "Donor-acceptor block copolymer: P3HT-block-PPCBM" focusing on synthesis, structure formation and charge transport in these materials. Apart from highlighting the relevant results of my PhD, the article also provides a current overview on general synthetic strategies for fullerene-grafted polymers and corresponding material properties reported in this field of research.

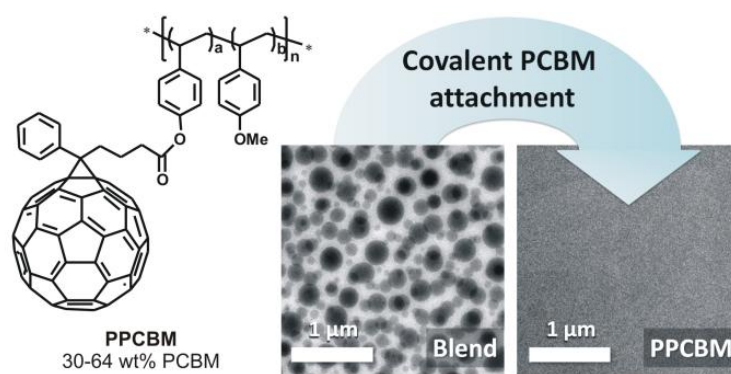
David Heinrich, Chetan Raj Singh, Matthias Fischer, Shahidul Alam contributed to the other sections of the article. Harald Hoppe, Thomas Thurn-Albrecht and Mukundan Thelakkat corrected the manuscript.

### 3 Fullerene-grafted copolymers exhibiting high electron mobility without nanocrystal formation

*Martin Hufnagel, Mathis-Andreas Muth, Johannes C. Brendel, Mukundan Thelakkat\**

Applied Functional Polymers, Department of Macromolecular Chemistry I  
University of Bayreuth, Universitaetsstr. 30, 95440 Bayreuth (Germany)

E-mail: [mukundan.thelakkat@uni-bayreuth.de](mailto:mukundan.thelakkat@uni-bayreuth.de)



**ABSTRACT**

Well-soluble fullerene-grafted copolymers PPCBMs with high contents of pendant phenyl-C<sub>61</sub>-butyric acid methyl ester (PCBM) between 30 and 64 wt% are reported. Herein, the tailor-made precursor copolymers poly(4-methoxystyrene-*stat*-4-*tert*-butoxystyrene) obtained by reversible addition fragmentation chain transfer (RAFT) polymerization are functionalized *via* an efficient polymer-analogous esterification. The synthesized acceptor copolymers retain the optical and electrochemical properties of the incorporated PCBM independent of their fullerene weight fraction. Their electron transport properties are studied by space-charge limited current (SCLC) method. The maximum electron mobility  $\mu_e$  of  $1 \times 10^{-4} \text{ cm}^2 \text{ V}^{-1} \text{ s}^{-1}$  is achieved for 37 wt% of incorporated PCBM. Below 50 wt% of PCBM, the acceptor polymers exhibit exceptional high charge carrier mobility compared to the corresponding blends of molecular PCBM and precursor copolymer. Detailed structural studies using AFM, TEM, and XRD are performed. We confirm amorphous morphology both in thin films and in bulk for the PPCBMs, which clearly indicates the absence of PCBM nanocrystals. Thus, an efficient charge carrier percolation is facilitated by the homogeneous distribution of PCBM in copolymer. Additionally, the absence of nanocrystal formation was demonstrated during thermal annealing.

**INTRODUCTION**

Buckminsterfullerene and its derivatives exhibit a unique electron-accepting/transporting capability<sup>[1]</sup> and their application as n-type semiconductors for organic photovoltaic (OPV) cells has been extensively studied.<sup>[2]</sup> Physically mixed blends of phenyl-C<sub>61</sub>-butyric acid methyl ester (PCBM) and poly(3-hexylthiophene) (P3HT) as donor material for bulk heterojunction (BHJ) solar cells have achieved power conversion efficiencies (PCEs) up to 5%.<sup>[3]</sup> This benchmark value was outperformed by the application of low-bandgap donor materials, yielding PCEs of more than 8% in single junction devices.<sup>[4]</sup>

A crucial requirement for high solar cell performance is an efficient but balanced charge transport of electrons and holes through the active layer of organic solar cells. Regarding the morphology in blend devices based on P3HT:PCBM or poly(p-phenylenevinylene):PCBM, it was found that PCBM forms a crystallization-induced network of PCBM-rich domains, which consist of PCBM nanocrystals.<sup>[5,6]</sup> In these blend systems the bulk electron mobility improved with an increasing fraction of crystalline

PCBM. With a sufficiently large content of PCBM, roughly 60-70 wt% in the blend, a dense network of percolation pathways is opened up which enables charge carrier transport over macroscopic distances.<sup>[7-10]</sup> Pure PCBM is a crystalline n-type semiconductor<sup>[11]</sup> and forms different crystal structures depending on the crystallization solvent.<sup>[12]</sup>

However, new concepts to overcome the inherent problem of limited thermodynamic stability of nanostructured blends direct towards a replacement of easily-diffusing small molecule acceptors by polymeric electron transport materials. We recently could show high bulk electron mobility in pendant perylene polymers.<sup>[13]</sup> Studies on side chain polymers carrying pendant C<sub>60</sub> show a correlation of increasing electron mobility with increasing C<sub>60</sub> content.<sup>[14,15]</sup> In these systems, for a C<sub>60</sub> content of 23-60 wt%, electron mobility of 10<sup>-9</sup> to 10<sup>-7</sup> cm<sup>2</sup> V<sup>-1</sup> s<sup>-1</sup> was reported.<sup>[14]</sup> Further a threshold for C<sub>60</sub> aggregation was found for 12-13 vol% of incorporated C<sub>60</sub>.<sup>[15]</sup> Fang *et al.* recently reported improved charge transport of pendant C<sub>60</sub> polynorbornene in organic field effect transistors attributed to the confined organization along the polymer chain.<sup>[16]</sup> Such detailed studies have not been reported in pendant PCBM polymers. However, the synthesis of PCBM pendant polymers and their potential applications in polymer solar cells were demonstrated recently.<sup>[17]</sup> Therefore, we were motivated to synthesize well-defined pendant PCBM copolymers in order to study the correlation of aggregate formation, morphology and electron transport in these systems.

While the electronic properties of side chain polymers can be tuned by the type of attached fullerene derivative, the physicochemical parameters are determined by the nature of the polymer backbone. Their preparation is achieved either by polymer-analogous modification or directly by polymerization of fullerene-derivatized monomers using organometallic catalysis.<sup>[16-19]</sup> Polymer-analogous synthetic routes rely on functionalized polymers, which are decorated with fullerene derivatives in a further step. Various types of reactions were reported to attach C<sub>60</sub> covalently to functional polymers including atom transfer radical addition (ATRA),<sup>[20]</sup> [3+2]-cycloaddition with azides,<sup>[21,22]</sup> Friedel-Crafts type reactions,<sup>[23]</sup> tosylhydrazone addition,<sup>[24]</sup> lithiation,<sup>[25]</sup> Bingel reaction<sup>[26]</sup> and azide-alkyne Huisgen cycloaddition.<sup>[27,28]</sup> Since all these methods are based on the reaction with double bonds, C<sub>60</sub> acts as an inherently multifunctional reactant. In particular for high fullerene loads, this fact leads to multiple additions, polymer cross-linking and diminished solubility. Therefore, selective grafting reactions with mono-functionalized C<sub>60</sub> derivatives are highly preferred. Jo *et al.* have presented such a well-controlled method to

prepare fullerene-grafted block copolymers by an efficient Steglich esterification with phenyl-C<sub>61</sub>-butyric acid (PCBA).<sup>[29]</sup>

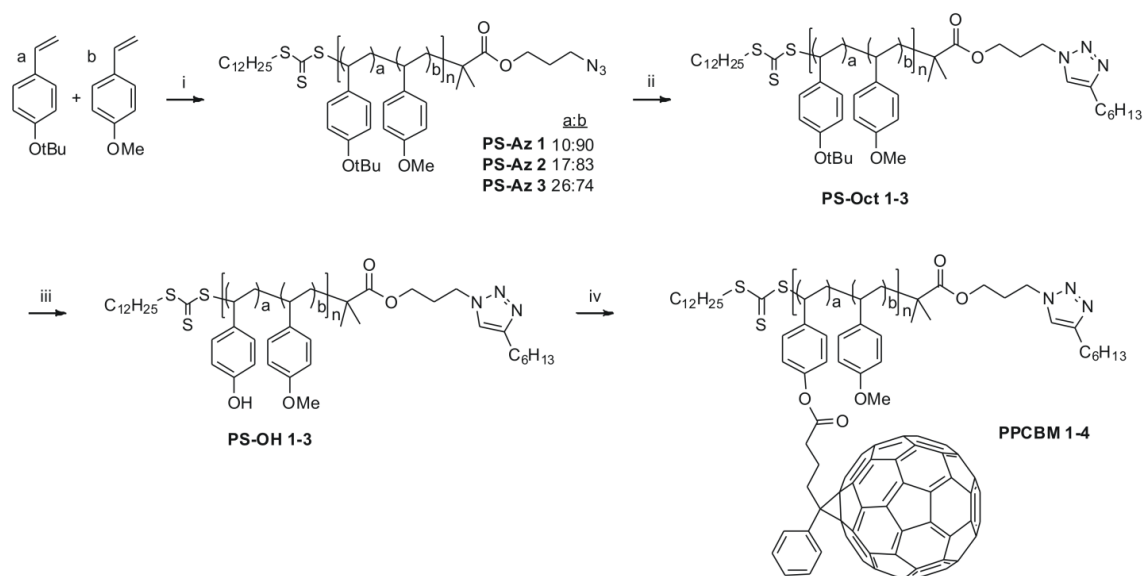
In this work we present a tailor-made synthesis for highly soluble PCBM-grafted copolymers without cross-linking. Further, the impact of covalent fullerene attachment to the polymer backbone is investigated with regard to morphology and fullerene nanocrystal formation and compared to blend systems. Here, we can demonstrate that efficient electron transport can be achieved, even if the pendant PCBM polymers do not show any indication for fullerene nanocrystal formation.

## RESULTS AND DISCUSSION

### Synthesis

The key aspect of our approach, depicted in Scheme 1, relies on the synthesis of a statistical precursor copolymer consisting of 4-methoxystyrene (MS) and 4-butoxystyrene (BS). The monomer BS can easily be deprotected to yield hydroxyl groups. In a subsequent step, the resulting 4-hydroxystyrene (HS) units were covalently linked to the C<sub>60</sub> fullerene derivative, phenyl-C<sub>61</sub>-butyric acid (PCBA). The proposed strategy provides both a precise tailoring of the overall number and density of the pendant fullerenes. Hence, there are two ways to tune the PCBM content in the copolymers: First, controlling the amount of grafted PCBM while the copolymer composition is kept the same. Second, varying the copolymer composition, or in other words changing the dilution of the HS monomer, followed by a complete grafting with PCBM. In this work, we followed the second route.

We applied a reversible addition fragmentation chain transfer (RAFT) polymerization for the synthesis of the precursor copolymer using an azide-derivatized trithiocarbonate chain transfer agent<sup>[30]</sup> (CTA). Thereby, an azide mono-terminated polymer is obtained that is giving access to a wide range of synthetic opportunities *via* click chemistry. Here, the RAFT polymerization was carried out with varying feed ratios of the monomers MS and BS in presence of the CTA and the initiator 2,2'-azobisisobutyronitrile (AIBN) in toluene at 80 °C. Samples for <sup>1</sup>H-NMR spectroscopy were periodically taken to monitor the progress of polymerization. We found first order polymerization kinetics and could prove that the consumption of both monomer species is equally fast (Fig. S1).



**Scheme 1.** Synthesis route towards PCBM-grafted copolymers. i) 3-azidopropyl-2-(((dodecylthio)carbonothioyl)thio)-2-methylpropanoate, AIBN, toluene, 80 °C; ii) 1-octyne, Cu/PMDETA, THF, room temperature, 24 h; iii) concentrated HCl, THF, 35 °C, 22h; iv) PCBA, DCC, DMAP, DMAP·HCl, DSC:CS<sub>2</sub>:AcN=3:3:1 (v:v:v), 40 °C, 72-91 h.

Therefore, we obtain statistical copolymers with a built-in ratio of BS:MS = 10:90, 17:83 and 26:74, respectively. The polymerization was stopped at around 50% total monomer conversion to ensure narrow molecular weight distributions. The synthesized precursor copolymers PS-Az 1, PS-Az 2 and PS-Az 3 differ both in monomer ratio and chain length (see Table 1). With increasing mole fraction of BS in the precursor copolymer, here 10 (PS-Az 1), 17 (PS-Az 2) and 26 mol% (PS-Az 3), the overall chain length was reduced from 117, 73 to 45 repeating units, respectively. Note that the number of BS units per chain is then 12 in all the copolymers according to our calculation based on the molecular weight which was determined by matrix-assisted laser desorption/ionization mass spectrometry with time of flight detection (MALDI-TOF MS). This number was selected to give appreciable amounts of fullerene in the final copolymer. The molecular weight distribution of the obtained copolymers measured by size exclusion chromatography (SEC) in THF is narrow, ranging from 1.09 to 1.11 (Table 1 and Fig. 1). Despite the calibration with polystyrene as standard, the apparent number average molecular weights  $M_n$  of 12.7 (PS-Az 1), 10.0 (PS-Az 2) and 6.9 kg mol<sup>-1</sup> (PS-Az 3) do not represent the theoretically expected values, which are considerably higher. This deviation is attributed to the increased polarity of the copolymer which influences the interactions with column material and the eluent.

The azide end group is relevant only for clicking functional moieties or a second polymer block. A further aim of this synthetic route with an azide end group is to attach a donor polymer with an alkyne end group. But this is not the subject matter of this manuscript. Therefore, we have deactivated it to avoid [3+2]-cycloaddition between the fullerenes and the azide end group<sup>[21]</sup>, which may lead to cross-linking of the PCBM-grafted copolymers. The Huisgen 1,3-dipolar cycloaddition (click chemistry)<sup>[31]</sup> is an elegant method to couple the azide end group with an alkyne reagent. Therefore, the precursor polymers PS-Az 1-3 were reacted with a ten-fold excess of 1-octyne in presence of 23 mol% CuI/PMDETA catalyst at room temperature. The success of this reaction was proved by Fourier-transform infrared (IR) spectroscopy, which is very sensitive towards azides due to its strong asymmetric vibration<sup>[32]</sup>. The azide vibration at 2098 cm<sup>-1</sup> disappears completely in the IR spectra of PS-Oct 1-3, indicating a quantitative end-capping of the azide end groups upon formation of a 1,2,3-triazole ring (Fig. S2). The analysis by SEC in THF shows only a negligible shift of  $M_n$ , but exhibit a very weak shoulder at approximately double weight  $2M_n$  (Fig. 1a). This polymer coupling is attributed to a transformation of the trithiocarbonate to a thiol end group by nucleophilic reagents, which can result in polymer-polymer disulfide formation.<sup>[33]</sup>

**Table 1.** Experimentally determined data of the synthesized copolymers.

Polymer	Molar ratio a:b	$M_n$ SEC <sup>a)</sup> [kg mol <sup>-1</sup> ]	$\mathcal{D}$	$M_n$ SEC <sup>b)</sup> [kg mol <sup>-1</sup> ]	$\mathcal{D}$	$M_n$ MALDI <sup>c)</sup> [kg mol <sup>-1</sup> ]	$M_p$	RU <sup>d)</sup> a:b	PCBM content <sup>e)</sup> [wt%]
PS-Az 1	10:90	12.3	1.11	12.7	1.37				
PS-OH 1	10:90	9.3	1.29			16.0	16.0	12:105	
PPCBM 1	10:90			17.2	1.27	35.1	22.9		30
PS-Az 2	17:83	9.0	1.11	10.0	1.18				
PS-OH 2	17:83	7.9	1.17			10.2	10.1	12:61	
PPCBM 2	17:83			11.6	1.21	25.8	16.1		37
PS-Az 3	26:74	5.7	1.09	6.9	1.14				
PS-OH 3	26:74	5.3	1.10			6.3	6.4	12:33	
PPCBM 3	26:74			7.6	1.21	19.6	13.0		51
PPCBM 4	26:74					25.2	17.8		64

a) SEC in THF as eluent. b) SEC in chlorobenzene as eluent. <sup>c)</sup> Peak maximum  $M_p$  determined by MALDI-TOF mass spectrometry. <sup>d)</sup> Repeating units determined by <sup>1</sup>H-NMR spectrometry and MALDI-TOF mass spectrometry. <sup>e)</sup> Determined by MALDI-TOF mass spectrometry.

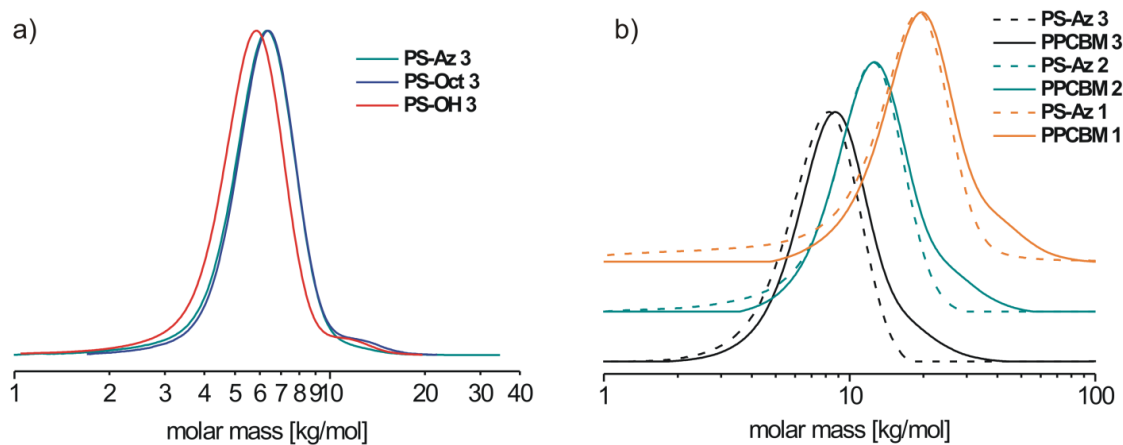


**Figure 1.** SEC traces (a) after each step during the postpolymerization modification of precursor copolymer PS-Az 3 (UV 254 nm, eluent THF) and (b) of the PCBM-grafted copolymers PPCBM 1-3 in comparison to their respective precursor copolymers PS-Az 1-3 (RI detector, eluent chlorobenzene).

The polymer-analogous cleavage of *tert*-butyl ether groups was carried out at very mild thermal conditions of 35 °C with an excess of hydrochloric acid. Quantitative conversion of *tert*-butyl ether to hydroxyl groups in PS-OH 1-3 was achieved after 22 h reaction time, which was evidenced by <sup>1</sup>H-NMR (Fig. S3). Exemplarily shown for PS-OH 2, the full conversion of BS to 4-hydroxystyrene is indicated by the integral ratio of the hydroxyl proton signal at  $\delta = 9.23\text{--}8.88$  ppm and the phenyl protons at  $\delta = 6.85\text{--}6.15$  ppm which matches perfectly the expected content of 17 mol% of HS (Fig. 2). For PS-OH 1 and PS-OH 3 the integral ratio corresponds to a HS content of 10 and 26 mol%, respectively. Accordingly, the strong singlet at  $\delta = 1.29$  ppm associated with the *tert*-butyl protons, is significantly decreased. The residual signal belongs to the remaining alkyl chains and methyl groups of the CTA. The SEC trace is shifted to lower molecular weight, which is in accordance with the expected weight loss (see Table 1) and can be seen in Fig.1 for PS-OH 3. Note that also the increased polarity of the polymers PS-OH 1-3 significantly affects the elution time, which is dependent on interactions between polymer and solvent or column material.

For the final step of fullerene attachment, we favored an efficient Steglich esterification procedure, which was reported recently for polymer-analogous functionalization with

PCBA by Russel *et al.*<sup>[29]</sup> PCBA can easily be prepared in high yields by ester hydrolysis from the commercially available PCBM.<sup>[34]</sup>

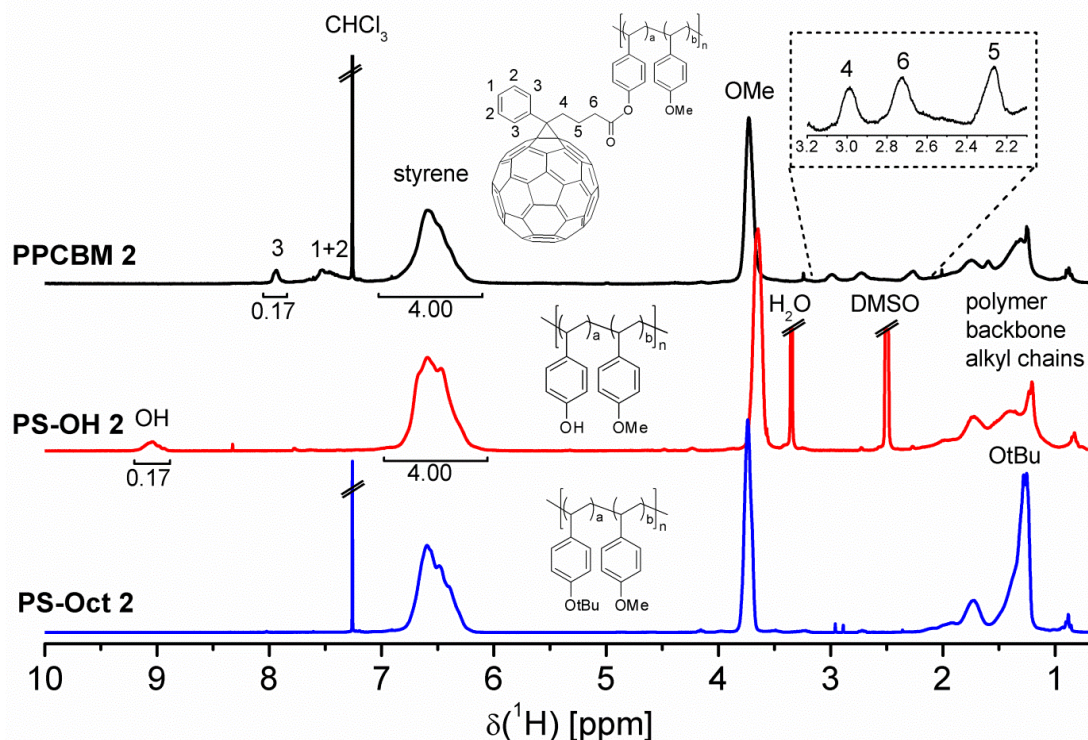


**Figure 2.** <sup>1</sup>H-NMR spectra of the octyl-encapped copolymer PS-Oct 2, deprotected copolymer PS-OH 2 and the PCBM-grafted copolymer PPCBM 2.

Steglich esterification of PS-OH 1-3 with PCBA was performed at 40 °C for 72-91 h in a solvent mixture of carbon disulfide (CS<sub>2</sub>), 1,2-dichlorobenzene (DCB) and acetonitrile (AcN) in the ratio 3:3:1 (v:v:v). Additional to *N,N'*-dicyclohexylcarbodiimide (DCC) and *N,N*-dimethyl-4-aminopyridine (DMAP), we further added the hydrochloride of DMAP, abbreviated as DMAP·HCl. This reagent can act as a proton source, which is supposed to enhance the yield of esterification by suppression of the side product formation of the *N*-acylurea.<sup>[35]</sup> An important aspect for fullerene grafting is the monomer ratio in the copolymers, since this parameter determines the maximum PCBM content of the copolymers. With increasing molar fraction of HS, the solubility of the obtained PCBM-grafted copolymers is diminished. While polymers with 30 (PPCBM 1) and 37 wt% PCBM (PPCBM 2) are well soluble in chloroform, 51 wt% PCBM (PPCBM 3) shows only limited solubility in chloroform, but good solubility in chlorobenzene (CB) and DCB. The copolymer with 64 wt% PCBM (PPCBM 4) already precipitated during

the esterification due to its high PCBM load. PPCBM 4 then could only be redissolved in DCB at 100 °C. In consequence, the maximum content of PCBM for solution processable copolymers was determined to be 64 wt%. The corresponding monomer ratio was HS:MS=26:74 and the number of repeating units HS:MS=11:34.

We applied an extensive purification for PPCBM 1-4 to guarantee that only covalently attached PCBM remains in the product. After precipitation twice into methanol, the residual low-molecular weight fullerene derivatives (*e.g.* the *N*-acylurea derivative of PCBA from Steglich esterification) were removed by precipitation the product into a mixture of toluene and methanol. The ratio of both solvents was adapted to the solubility of the PCBM-grafted copolymer, *i.e.* toluene:methanol 1:1 for PPCBM 1, 2:1 for PPCBM 2, 3:1 for PPCBM 3. While the low-molecular weight fullerene side products were efficiently dissolved, the PPCBMs precipitated. The absence of low-molecular weight impurities was carefully controlled by thin layer chromatography. Besides, any fullerene impurities would be easily visible in the NMR spectra due the sharp resonances from low molecular weight compounds.

According to the  $^1\text{H}$ -NMR spectrum in Fig. 2, all relevant proton signals which belong to the polymer backbone and the pendant PCBM are clearly evident. Whereas pure PCBM shows a distinct fine structure of the multiplet signals arising from the methylene protons, these proton resonances are strongly broadened in the PCBM-grafted copolymers. This is exemplarily shown for PPCBM 2 in Fig. 2. Here, the broad proton signals 4, 5 and 6 give clear evidence for the covalent attachment to the polymer backbone. The successful ester bond formation is further supported by the significant shift of the broadened proton signal 6 at  $\delta = 2.73$  ppm, which is adjacent to the ester bond, compared to the triplet proton signal at  $\delta = 2.53$  for pure PCBM (Fig. S4). We calculated the efficiency of the Steglich esterification from  $^1\text{H}$ -NMR spectroscopy and MALDI-TOF MS. According to this, the grafting process was incomplete for the copolymers PPCBM 1-3, achieving 56 to 67% esterification of the available HS units. In contrast, PPCBM 4 was fully derivatized with PCBA. In the series of PPCBM 1-4, the concentration of PCBM increases considerably while the overall molecular weight of the polymer backbone decreases. As a result, there is statistically one PCBM molecule for every 15, 10, 6 and 4 repeating units of the PCBM-grafted copolymers PPCBM 1-4. Apparently, steric hindrance regarding the bulky fullerene molecules is not the only limiting factor for polymer-analogous grafting. The difference in grafting yield can also be attributed to the differences in dilu-

tion of HS units (different monomer ratios) as well as the used solvent mixture, which may not be ideal for the desired high fullerene grafting. The SEC traces of the PCBM-grafted copolymers PPCBM 1-3 in CB (Fig. 1b) shift only marginally to higher molar masses compared to the precursor polymers PS-Az 1-3. This finding seems contradictory to the significant mass increase, which was evidenced by the MALDI-TOF mass spectra shown in Fig. S5. However, this observation is mostly attributed to a contractile effect of intrachain interaction of fullerenes, leading to a reduced hydrodynamic volume.<sup>[20]</sup> PPCBM 4 is not soluble in chlorobenzene and could not be characterized by SEC. In conclusion, we confirm the successful covalent linkage of the PCBA moieties to the precursor copolymer *via* esterification. As we applied an extensive purification of the PPCBMs to remove low-molecular weight fullerenes, we get a clear picture about the chemical composition of the PCBM-grafted copolymers. The covalent attachment of PCBA was evidenced by NMR (Fig. 2 and Fig. S4) and further supported by MALDI-TOF mass spectrometry (Fig. 3 and Fig. S5). Particularly, the distinct mass increase of the PCBM-grafted copolymer compared to the precursor in the expected range rules out any other possibilities than a grafted copolymer.

### Characterization

One of the most important parameters to be determined regarding fullerene polymers is the exact amount of covalently attached PCBM molecules. We have employed several complementary methods such as MALDI-TOF MS, <sup>1</sup>H-NMR spectroscopy, thermogravimetric analysis (TGA) and quantitative UV-vis spectroscopy to determine the PCBM content (Table 2). Analysis of the MALDI-TOF mass spectra give the mass differences  $\Delta M$  between PPCBM 1-4 and their corresponding precursors PS-OH 1-3 that are 6.9, 6.0, 6.6 and 11.4 kDa, respectively (Fig. S5). This approximately equals to 8, 7, 7 and 13 grafted PCBA molecules per chain. Accordingly, the content of pendant PCBM increases considerably as the molecular weight of the precursor copolymer is strongly reduced. As an example, the mass spectra of PS-OH 3 and PPCBM 3 are shown in Fig. 3. The mass difference  $\Delta M$  between the peak maxima  $M_p$  of the molecular weight distributions represent the amount of covalently attached PCBM. Then the PCBM content  $f_{\text{PCBM}}$  was calculated as  $f_{\text{PCBM}} = \Delta M / M_p$ , with  $M_p$  as peak maximum of the molecular weight distribution of the PCBM-grafted copolymers PPCBM 1-4 obtained by MALDI-TOF MS. These results are in good agreement with the values calculated from <sup>1</sup>H-NMR data.

**Table 2.** PCBM weight content of PPCBM 1-4 determined by various methods. Calculated values refer to a degree of 100% grafting of the available 4-hydroxystyrene repeating units and represent the maximum theoretical PCBM weight content possible.

Polymer	PCBM content [wt%]				
	theor.	MALDI	<sup>1</sup> H-NMR	TGA	UV-Vis
PPCBM 1	40	30	27	44	32
PPCBM 2	52	37	38	52	42
PPCBM 3	63	51	51	56	45
PPCBM 4	63	64	64	63	53

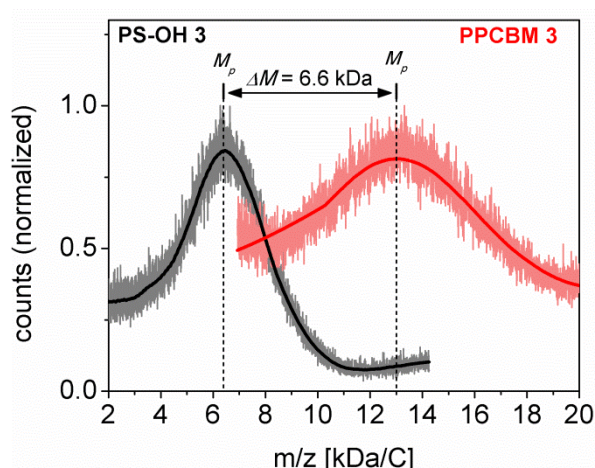


**Figure 3.** MALDI-TOF mass spectra of precursor copolymer PS-OH 3 (black) and PPCBM 3 (red) for the determination of the PCBM content. For better clarity, the mass spectra were smoothed and plotted as thick solid lines. The mass difference  $\Delta M$  represents the amount of PCBM, which was covalently attached by the esterification reaction.

A wide-spread method to determine  $f_{\text{PCBM}}$  is TGA.<sup>[20]</sup> Since the thermal decomposition of PCBM under nitrogen atmosphere is restricted to the loss of the tethered phenylbutyric acid at about 395 °C, the remaining char is roughly 90 wt%. Thus, the PCBM content of PPCBM 1-4 can be estimated from the char, as the polystyrene backbone is expected to decompose almost completely above 395 °C (Fig. 4). However, the precision of this method is restricted, because the residual char content is often too high. This effect is attributed to cross-linking during heating which hinders a neat thermal decomposition.<sup>[24]</sup> Consequently, the calculated values are generally overestimated. The TGA traces in Fig. 4 show two decomposition processes: The first at  $T_1 \approx 185$  °C is pre-

sumably related to the trithiocarbonate decomposition, the second at  $T_2 \approx 390$  °C can be attributed to the polystyrene backbone decomposition.

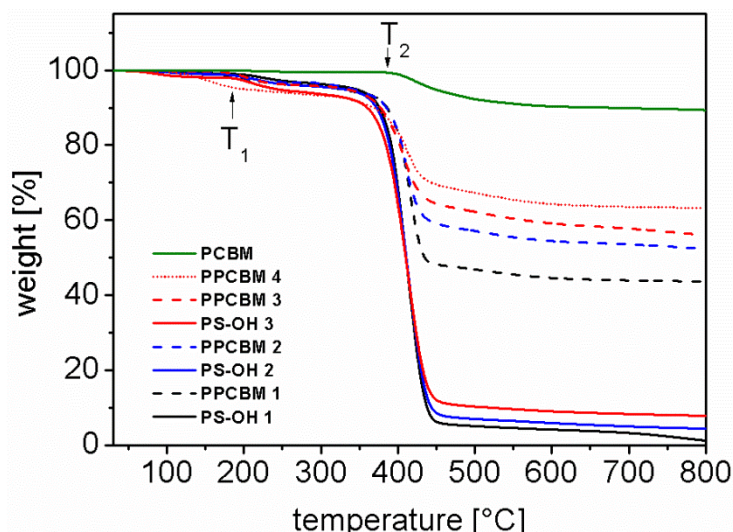


**Figure 4.** TGA weight loss curves (for heating under  $N_2$  atmosphere) of PCBM-grafted copolymers PPCBM 1-4, their corresponding precursor copolymers PS-OH 1-3 and pristine PCBM as reference. The copolymers show two decomposition processes at  $T_1 \approx 195$  °C, which is related to the trithiocarbonate decomposition, and  $T_2 \approx 390$  °C, which arises from the polymer backbone decomposition. Since degradation of PCBM is only marginal above 400 °C, the residual char of the PCBM-grafted copolymers indicates the PCBM weight content.

As an alternative method, quantitative UV-vis spectroscopy in solution is well described in literature for the precise determination of the molar or weight content of polymer-bound chromophores<sup>[36]</sup> and fullerenes.<sup>[28]</sup> The PCBM content is calculated by the ratio of the extinction coefficients of PPCBM 1-4 and pristine PCBM as  $f_{\text{PCBM}} = \varepsilon_{\text{Polymer}} / \varepsilon_{\text{PCBM}} \times 100$  wt% at the absorption maximum  $\lambda_{\text{max}}$  (Fig. S6). The obtained values  $f_{\text{PCBM}}$  deviate from MALDI-TOF MS and NMR values in particular for high fullerene loading. This might be due to interaction of the fullerene moieties in the polymer and in consequence a change in the molar extinction coefficients compared to pure PCBM. To conclude, the PCBM content was most accurately determined by MALDI-TOF mass spectra, which are consistent with NMR analysis. The other methods show partially significant deviations and thus are neglected for any further considerations.

To determine whether the properties of PCBM are affected by the incorporation into the precursor polymer we conducted UV-Vis measurements of PPCBM 1-4. Their absorption spectrum is dominated by the prominent fullerene absorption bands at 258 nm ( $\varepsilon_{258 \text{ nm}} = 0.0703 \text{ mL mg}^{-1} \text{ cm}^{-1}$ ) and 328 nm (Fig. S7). Since pristine PCBM exhibits

exactly the same absorption bands, the optical properties were not influenced by the covalent attachment to the copolymers.

Further, we studied the electrochemical characteristics by cyclic voltammetry (CV) measurements of PPCBM 1-3 (Fig. S8). PPCBM 1-3 undergo three reversible reductions up to -2.0 V, very similar to pure PCBM. The lowest unoccupied molecular orbital (LUMO) levels were calculated based on the onset reduction potential  $E_{\text{red}}$  using the following equation:  $E_{\text{LUMO}} = -e (E_{\text{red}} + 4.71 \text{ V})$ .<sup>[37]</sup> While the LUMO level of PCBM was determined as -3.82 eV, it is -3.79 eV for PPCBM 1 and -3.80 eV for PPCBM 2 and PPCBM 3. The negligible deviations lie within the range of measurement error, thus, the attachment of PCBM to the polymer backbone does not influence the LUMO level.

The thermal behavior of the synthesized polymers was investigated using differential scanning calorimetry (DSC, Fig. S9). Here, PS-OH 1-3 revealed a glass transition temperature  $T_g$  in the range of 93-95 °C, which is similar to poly(styrene). The grafting of 30, 37 and 51 wt% of PCBM onto the polymers leads both to a strong signal broadening and a temperature shift of  $T_g$  up to 144, 167 and 189 °C for PPCBM 1-3, respectively. This considerable decrease of molecular mobility is attributed to the sterical hindrance by the attached fullerene moieties and to the strong intermolecular interaction between the fullerenes.<sup>[15,21]</sup>

### Bulk electron mobility

We investigated the bulk electron mobility  $\mu_e$  of PPCBM 1-3 in comparison to blends of precursor polymer PS-OH 1 and PCBM. PPCBM 4 was not included in this study, since the degree of grafting deviates significantly from the other polymers, making the comparability difficult. We used the space-charge limited current (SCLC) method, as it enables the study of charge carrier mobility across the bulk in thin films.<sup>[38]</sup> The electrodes ITO/PEDOT:PSS and Ca/Al were selected to avoid any injection limited current. The active layer of the SCLC devices was prepared by blade-coating from DCB at 70°C of either PCBM-grafted copolymers PPCBM 1-3 or blends of PS-OH 1 and PCBM. The blend composition is 30 wt% PCBM for blend 1, 40 wt% PCBM for blend 2 and 50 wt% PCBM for blend 3. Finally, the electron mobility  $\mu_e$  can be extracted from the obtained current-voltage ( $J$ - $V$ ) curves and the Mott-Gurney equation (see experimental part for details). The  $J$ - $V$  characteristics of PPCBM 1-3 and the corresponding blends 1-3 are depicted in Fig. 5a.

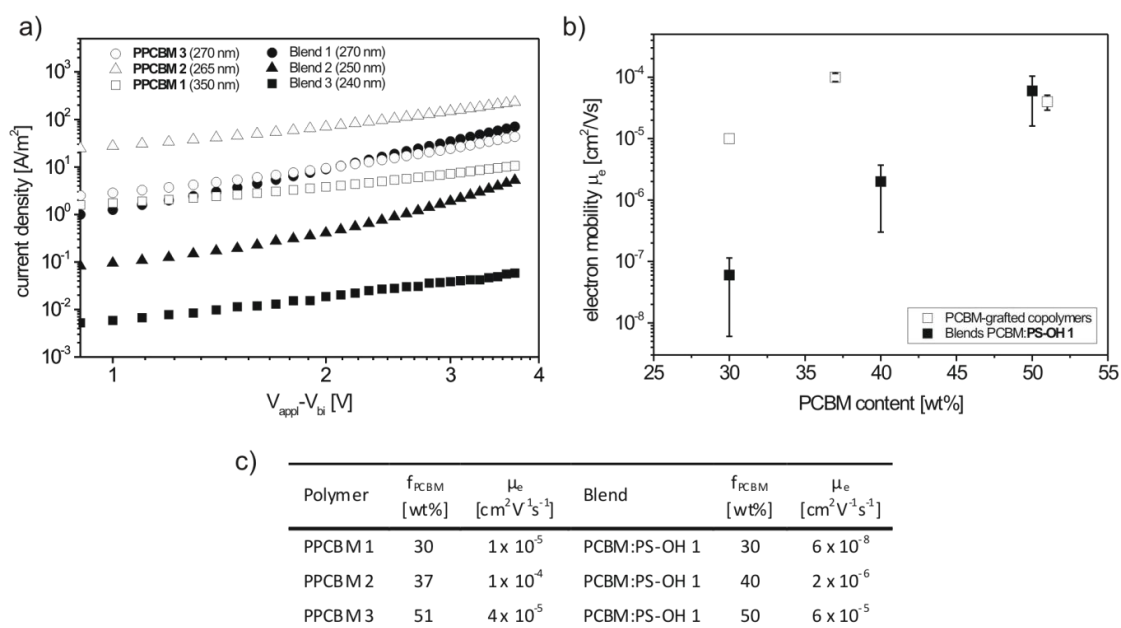


**Figure 5.** SCLC measurements of the PCBM-grafted copolymers PPCBM 1-3 in comparison to the blends of PCBM:PS-OH 1 showing (a) the  $J$ - $V$  curves with active layer thickness given in brackets and (b,c) the average electron mobility  $\mu_e$ . The error bars for the electron mobility correspond to the standard deviation from three measurements. The average electron mobility of pure PCBM was determined to be  $4 \times 10^{-3} \text{ cm}^2 \text{ V}^{-1} \text{ s}^{-1}$ .

To check the thickness scaling of the SCLC, the  $J$ - $V$  curves of each material with varied active layer thickness were measured (Fig. S10, S11). Within the experimental error, the electron mobility is found to be constant for each thickness (Table S2).

In general, the PCBM-grafted copolymers PPCBM 1-3 and the blends exhibit different electron transport values depending on the PCBM content (Fig. 5b). The blend devices show an exponential increase in electron mobility with increasing PCBM content. However, even blend 3 with 50 wt% of PCBM exhibits a low mobility ( $\mu_e = 6 \times 10^{-5} \text{ cm}^2 \text{ V}^{-1} \text{ s}^{-1}$ ) compared to pristine PCBM ( $\mu_e = 4 \times 10^{-3} \text{ cm}^2 \text{ V}^{-1} \text{ s}^{-1}$ ) that is two orders of magnitude higher (Fig. 5c). In contrast, the PCBM-grafted copolymers show a different trend in mobility. Here, the mobility remains rather constant and varies between  $1 \times 10^{-5}$  and  $1 \times 10^{-4} \text{ cm}^2 \text{ V}^{-1} \text{ s}^{-1}$  for a PCBM content in the range between 30 and 51 wt%. The maximum electron mobility of  $1 \times 10^{-4} \text{ cm}^2 \text{ V}^{-1} \text{ s}^{-1}$  was achieved for 37 wt% of incorporated PCBM. Remarkably, the pendant fullerene polymers show considerable better electron mobility compared to the blends for a PCBM content below 50 wt%. For example, PPCBM 1 with 30 wt% of incorporated PCBM exhibits three orders of magnitude higher mobility than the respective blend. PPCBM 3 with 51 wt% PCBM possess a simi-

lar electron mobility compared to its corresponding blend. The mobility dependence on the fullerene content in a C<sub>60</sub>-grafted polystyrene was investigated by Perrin *et al.*<sup>[15]</sup> and described using the statistical percolation theory.<sup>[39,40]</sup> Typically, a percolation threshold is observed for low amounts of the C<sub>60</sub> leading to a sharp increase in mobility, then the further increase in mobility with C<sub>60</sub> content is only marginal. If we apply this model, the weight fractions of PPCBM 1-3 between 30 and 51 wt% lie rather in the regime of constant mobility. Thus the improved performance of PPCBMs compared to the respective blends can be understood in terms of an enhanced percolation network in pendant fullerenes than in blend systems. Apart from the PCBM content, the copolymers PPCBM 1-3 exhibit different chain length and copolymer composition. So far, the influence of these parameters on mobility remains an open question.

### Film morphology

Here, we investigate any possible influence of morphology on charge carrier mobility. The film morphology of the SCLC devices was investigated after the initial SCLC characterization. Here, we present topographic AFM images as they provide a precise insight into the surface morphology of polymer films. The corresponding AFM phase images did not show any additional information. As depicted in Fig. 6, the films of PPCBM 1-3 are throughout smooth and featureless independent of the PCBM content. This indicates an effective suppression of fullerene aggregation realized by covalent attachment to the polymer backbone as well as the utilized dilution in the copolymers. At the same time, the blend films of PCBM and PS-OH 1 are heterogeneous and strongly dominated by PCBM clusters except the blend containing 30 wt% PCBM (Fig. 6). With increasing weight fraction of PCBM both number and size of the clusters is growing. The fullerene cluster size is estimated to be in the range of 60-70 nm for blend 2 and 100-110 nm for blend 3. Loos *et al.* have studied the phase separation and crystallization of PCBM in polymer blends in detail.<sup>[5,41]</sup> The formation of PCBM nanocrystals in polymer blends is thermodynamically favored but strongly depends on the solvent, the polymer and the preparation technique. Due to the spherical shape of the PCBM domains in the blends which we have observed in AFM (Fig. 6) and TEM (Fig. 7a), we suggest a spinodal-like phase separation.<sup>[42]</sup> The resulting PCBM clusters are as-cast in a glassy state (see XRD, Fig. 7c).

The observed charge transport in blends is strongly dependent on fullerene content. High electron mobility requires sufficient percolation pathways, therefore high PCBM

contents facilitate electron transport by an increasing number of PCBM clusters which are in close proximity. Conversely, the mobility is very low for a small PCBM content, when the phase separated fullerene clusters are isolated from each other.

In strong contrast to that, the PCBM-grafted copolymers PPCBM 1-3 do not show any visible PCBM clusters and hence, enable charge percolation *via* homogeneously distributed fullerene molecules. Even for a low PCBM content of 30 wt%, the distance between the fullerene molecules is apparently close enough to allow efficient electron transport through the bulk ( $10^{-5} \text{ cm}^2 \text{ V}^{-1} \text{ s}^{-1}$ ). For the corresponding blend 1 with the same PCBM content, the electron mobility is three orders of magnitude worse ( $10^{-8} \text{ cm}^2 \text{ V}^{-1} \text{ s}^{-1}$ ).

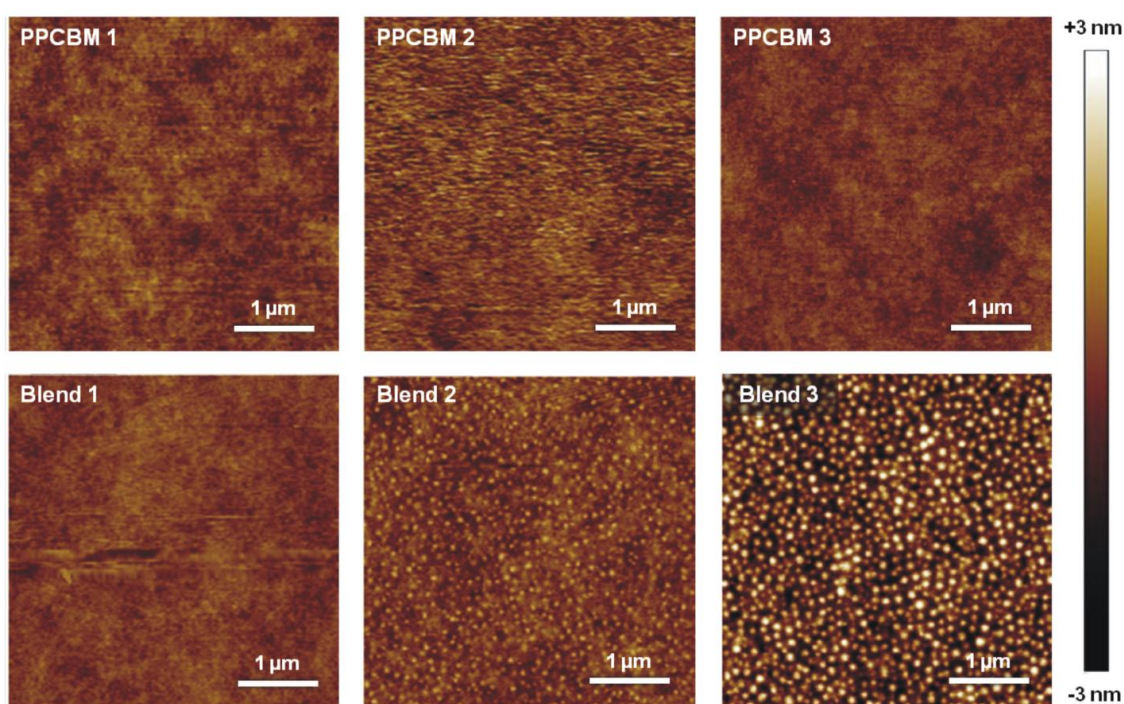


**Figure 6.** AFM topography images showing films of PPCBM 1-3 and blends of PCBM:PS-OH 1 in varying composition prepared for the SCLC measurements.

Clear evidence for the morphological difference between the blend system and the PCBM-grafted copolymers was obtained by transmission electron microscopy (TEM) of thin films. In case of blend 3 with 50 wt% of PCBM (Fig. 7a), a phase separated film with numerous PCBM clusters with a diameter in the range of 50 to 350 nm is observed. In contrast, the film of PPCBM 3 with 51 wt% of grafted PCBM is fully homogeneous without any visible nanocrystal or cluster formation (Fig. 7b). This obviously supports the observations in AFM regarding the absence of phase separation and PCBM clustering in PCBM-grafted copolymers. These findings are fully consistent with the powder X-ray

diffraction (PXRD) results shown in Fig. 7c. For this, we have collected the material as powder from films which were cast from DCB at 70 °C and investigated the structure with a Guinier diffraction system. The blend 3 shows a characteristic reflection at 9.62° additional to the amorphous scattering (Fig. 7c). This weak reflection indicates the existence of some PCBM nanocrystals in the amorphous polymer matrix, but the majority of PCBM seems to be in a glassy state. Upon annealing of the sample above  $T_g$  at 140 °C for 3 hours, the intensity of the crystalline reflections increased significantly. Since the diffusion of PCBM molecules is promoted during the annealing process, the crystallinity and size of the clusters can grow and yield a significant fraction of PCBM nanocrystals. Consequently, both the overall crystalline fraction in the blend is increasing and the reflections get sharper. In contrast, the PCBM-grafted copolymer PPCBM 3 remains completely amorphous, even after annealing for 3 hours at 140 °C. These results clearly demonstrate that the covalent attachment of PCBM to the polymer entirely suppresses the phase separation and clustering of the fullerenes leading to morphological stability.

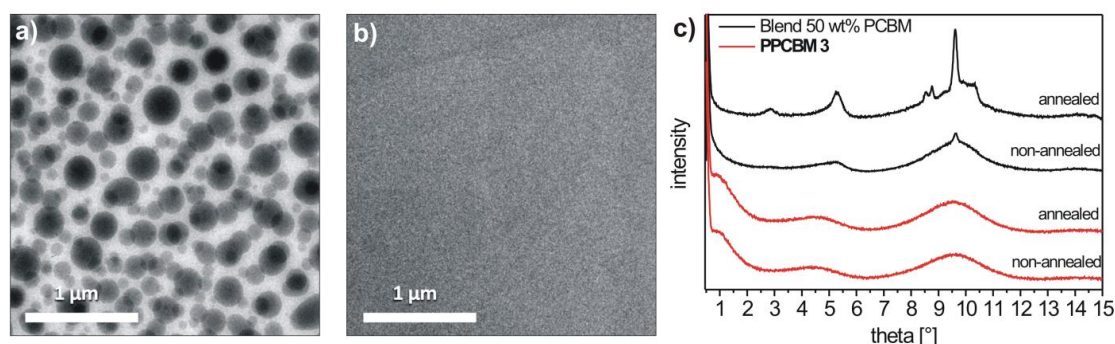


**Figure 7.** Transmission electron microscopy images of thin films made of (a) blend 3 with 50 wt% PCBM content and (b) PCBM-grafted copolymer PPCBM 3 with 51 wt% of incorporated PCBM. (c) Powder X-ray diffractograms of both samples before and after annealing at 140 °C for 3 hours.

## CONCLUSIONS

We have presented a successful synthesis strategy towards well-soluble fullerene side chain copolymers with high PCBM contents between 30 and 64 wt%. Both grafting density and PCBM content could easily be tuned by the monomer ratio in the precursor copolymers. The resulting PCBM-grafted copolymers exhibit low molecular-weight dispersity and no cross-linking owing to the controlled PCBM grafting by Steglich esterification. The PCBM-grafted copolymers retain the optical and electrochemical properties of the incorporated PCBM independently of their fullerene weight fraction. Electron

transport characteristics derived from SCLC show a maximum electron mobility  $\mu_e$  of  $1 \times 10^{-4} \text{ cm}^2 \text{ V}^{-1} \text{ s}^{-1}$  for 37 wt% of incorporated PCBM. Despite their low fullerene content, the PCBM-grafted copolymers exhibit exceptional high charge transport in reference to blend systems. For 30 wt% PCBM content, the grafted copolymer exhibits three orders of magnitude better mobility than the corresponding blend. Charge transport in the blends relies on nanocrystal formation and is improved with an increasing PCBM content. On the other hand, the PCBM-grafted copolymers exhibit excellent mobility and no nanocrystal formation even after thermal annealing. This can be of great advantage if issues of long term stability in devices have to be addressed using fullerene materials. The modular synthetic approach presented here can be extended to other fullerene derivatives.

## ASSOCIATED CONTENT

### Supporting Information

Experimental details, Fourier-transform infrared spectra, MALDI-TOF mass spectra, thermogravimetric analysis data, UV-Vis spectra, cyclic voltammetry curves, differential scanning calorimetry curves and current-voltage characteristics of the electron-only SCLC devices. This material is available free of charge *via* the Internet at <http://pubs.acs.org>.

## ACKNOWLEDGEMENT

We kindly acknowledge DFG (SPP1355) and EU LARGECELLS (Gr. No: 291936) for financial support of this project. M. Hufnagel also thanks the Elite Network Bavaria Macromolecular Science programme at the University of Bayreuth. We also acknowledge Melanie Förtsch for TEM measurements, Marina Behr for XRD and Katharina Neumann for SEC.

## REFERENCES

- [1] N. S. Sariciftci, L. Smilowitz, A. J. Heeger, F. Wudl, *Science* **1992**, *258*, 1474.
- [2] B. C. Thompson, J. M. J. Fréchet, *Angew. Chem. Int. Ed.* **2008**, *47*, 58.
- [3] W. Ma, C. Yang, X. Gong, K. Lee, A. J. Heeger, *Adv. Funct. Mater.* **2005**, *15*, 1617.
- [4] Z. He, C. Zhong, X. Huang, W.-Y. Wong, H. Wu, L. Chen, S. Su, Y. Cao, *Adv. Mater.* **2011**, *23*, 4636.
- [5] X. Yang, J. K. van Duren, R. A. Janssen, M. A. Michels, J. Loos, *Macromolecules* **2004**, *37*, 2151.
- [6] X. Yang, J. Loos, S. C. Veenstra, W. J. H. Verhees, M. M. Wienk, J. M. Kroon, M. a J. Michels, R. A. J. Janssen, *Nano Lett.* **2005**, *5*, 579.
- [7] T. Savenije, J. Kroeze, M. Wienk, J. Kroon, J. Warman, *Phys. Rev. B* **2004**, *69*, 155205.
- [8] E. von Hauff, J. Parisi, V. Dyakonov, *J. Appl. Phys.* **2006**, *100*, 043702.
- [9] V. D. Mihailetschi, H. X. Xie, B. de Boer, L. J. a. Koster, P. W. M. Blom, *Adv. Funct. Mater.* **2006**, *16*, 699.
- [10] V. D. Mihailetschi, L. J. a. Koster, P. W. M. Blom, C. Melzer, B. de Boer, J. K. J. van Duren, R. a. J. Janssen, *Adv. Funct. Mater.* **2005**, *15*, 795.
- [11] V. D. Mihailetschi, J. K. J. van Duren, P. W. M. Blom, J. C. Hummelen, R. a. J. Janssen, J. M. Kroon, M. T. Rispens, W. J. H. Verhees, M. M. Wienk, *Adv. Funct. Mater.* **2003**, *13*, 43.
- [12] M. T. Rispens, A. Meetsma, R. Rittberger, C. J. Brabec, N. S. Sariciftci, J. C. Hummelen, *Chem. Commun.* **2003**, 2116.
- [13] A. S. Lang, M.-A. Muth, C. D. Heinrich, M. Carasco-Orozco, M. Thelakkat, *J. Polym. Sci. Part B Polym. Phys.* **2013**, *51*, 1480.
- [14] G. Adamopoulos, T. Heiser, U. Giovanella, S. Ouldsaad, K. Vandewetering, C. Brochon, T. Zorba, K. Paraskevopoulos, G. Hadziioannou, *Thin Solid Films* **2006**, *511-512*, 371.
- [15] L. Perrin, A. Nourdine, E. Planes, C. Carrot, N. Alberola, L. Flandin, *J. Polym. Sci. Part B Polym. Phys.* **2013**, *51*, 291.
- [16] L. Fang, P. Liu, B. R. Sveinbjornsson, S. Atahan-Evrenk, K. Vandewal, S. Osuna, G. Jiménez-Osés, S. Shrestha, G. Giri, P. Wei, A. Salleo, A. Aspuru-Guzik, R. H. Grubbs, K. N. Houk, Z. Bao, *J. Mater. Chem. C* **2013**, *1*, 5747.
- [17] M. Eo, S. Lee, M. H. Park, M. H. Lee, S. Yoo, Y. Do, *Macromol. Rapid Commun.* **2012**, *33*, 1119.
- [18] N. Zhang, S. Schrick, F. Wudl, M. Prato, *Chem. Mater.* **1995**, *7*, 441.
- [19] J. J. Y. Kim, M. H. Yun, J. Lee, J. J. Y. Kim, F. Wudl, C. Yang, D. A. Links, *Chem. Commun.* **2011**, *47*, 3078.
- [20] U. Stalmach, B. de Boer, C. Videlot, P. F. van Hutten, G. Hadziioannou, *J. Am. Chem. Soc.* **2000**, *122*, 5464.
- [21] C. J. Hawker, *Macromolecules* **1994**, *27*, 4836.
- [22] M. H. van der Veen, B. de Boer, U. Stalmach, K. I. van de Wetering, G. Hadziioannou, M. H. Van Der Veen, B. De Boer, K. I. Van De Wetering, *Macromolecules* **2004**, *37*, 3673.
- [23] B. Liu, C. E. Bunker, Y.-P. Sun, *Chem. Commun.* **1996**, 1241.
- [24] C. Yang, J. K. Lee, A. J. Heeger, F. Wudl, *J. Mater. Chem.* **2009**, *19*, 5416.
- [25] L. Dai, A. Mau, H. Griesser, T. Spurling, *J. Phys. Chem.* **1995**, *99*, 17302.
- [26] M. Heuken, H. Komber, B. Voit, *Macromol. Chem. Phys.* **2012**, *213*, 97.
- [27] S. Miyanishi, Y. Zhang, K. Tajima, K. Hashimoto, *Chem. Commun.* **2010**, 46,

- 6723.
- [28] X.-H. Dong, W.-B. Zhang, Y. Li, M. Huang, S. Zhang, R. P. Quirk, S. Z. D. Cheng, *Polym. Chem.* **2012**, *3*, 124.
- [29] J. U. Lee, A. Cirpan, T. Emrick, T. P. Russell, W. H. Jo, P. Russell, W. Ho, T. P. Russell, W. H. Jo, *J. Mater. Chem.* **2009**, *19*, 1483.
- [30] S. R. Gondi, A. P. Vogt, B. S. Sumerlin, *Macromolecules* **2007**, *40*, 474.
- [31] W. H. Binder, R. Sachsenhofer, *Macromol. Rapid Commun.* **2007**, *28*, 15.
- [32] E. Lieber, C. N. R. Rao, T. Chao, C. Hoffman, *Anal. Chem.* **1957**, *29*, 916.
- [33] *Handbook of RAFT Polymerization*; Barner-Kowollik, C., Ed.; Wiley-VCH: Weinheim, Germany, 2008.
- [34] J. C. Hummelen, B. W. Knight, F. LePeq, F. Wudl, J. Yao, C. L. Wilkins, *J. Org. Chem.* **1995**, *60*, 532.
- [35] E. P. Boden, G. E. Keck, *J. Org. Chem.* **1985**, *50*, 2394.
- [36] M. Thelakkat, P. Pösch, H. W. Schmidt, *Macromolecules* **2001**, *34*, 7441.
- [37] Y. He, G. Zhao, B. Peng, Y. Li, *Adv. Funct. Mater.* **2010**, *20*, 3383.
- [38] V. Mihailetschi, J. Wildeman, P. Blom, *Phys. Rev. Lett.* **2005**, *94*, 126602.
- [39] S. Kirkpatrick, *Rev. Mod. Phys.* **1973**, *45*, 574.
- [40] F. Lux, *J. Mater. Sci.* **1993**, *28*, 285.
- [41] X. Yang, J. K. J. van Duren, M. T. Rispens, J. C. Hummelen, R. a. J. Janssen, M. a. J. Michels, J. Loos, *Adv. Mater.* **2004**, *16*, 802.
- [42] H. C. Wong, T. Cabral, *Macromolecules* **2011**, 4530.
- [43] A. S. Lang, M. Thelakkat, *Polym. Chem.* **2011**, *2*, 2213.
- [44] P. Blom, M. Vissenberg, *Mater. Sci. Eng.* **2000**, *27*, 53.
- [45] C. Goh, R. J. Kline, M. D. McGehee, E. N. Kadnikova, J. M. J. Fréchet, *Appl. Phys. Lett.* **2005**, *86*, 122110.

## SUPPORTING INFORMATION

### Experimental Section

#### Materials and Characterization

*Chemicals:* The reagents for the following synthetic procedures were purchased from different suppliers and used as received, if not stated otherwise. Sigma-Aldrich: 3-Chloropropanol, sodium azide, 4-dimethylaminopyridine, N,N'-dicyclohexylcarbodiimide, 4-methoxystyrene, 4-tert-butoxystyrene, 2-2'-azobisisobutyronitrile, 1-octyne, copper(I) iodide, N,N,N',N',N''-pentamethyldiethylenetriamine, anhydrous sodium sulfate, sodium hydrogencarbonate, basic and neutral alumina. abcr: 2-(((Dodecylthio)carbonothioyl)thio)-2-methylpropanoic acid. Solenne BV (Groningen, Netherlands): Phenyl-C<sub>61</sub>-butyric acid methyl ester (PCBM, purity 99 %). Solvents were either distilled at atmospheric pressure utilizing appropriate desiccants or purchased in p.a. (pro analysi) grade. Commercially available anhydrous solvents were purchased from Sigma Aldrich and Acros in sealed bottles with mole sieve. Prior to polymerization, 4-methoxystyrene (MS) and 4-tert-butoxystyrene (BS) were passed through a column of basic alumina to remove the inhibitor and stored at -18°C. DMAP·HCl was prepared by addition of 37 wt% HCl dropwise to a solution of DMAP in THF. The precipitated solid was collected by filtration, washed with THF and dried under vacuum at RT. The stock solution of 0.07 M CuI/PMDETA in THF was prepared according to a literature procedure<sup>[43]</sup> and stored at 5 °C under argon. The chain transfer agent (CTA) 3-azidopropyl-2-(((dodecylthio)carbonothioyl)thio)-2-methylpropanoate was prepared following a published synthesis route.<sup>[30]</sup> Phenyl-C<sub>61</sub>-butyric acid (PCBA) was also prepared according to a published synthesis protocol.<sup>[34]</sup>

*Instrumentation:* All <sup>1</sup>H-NMR spectra were measured with a Bruker Avance AC250 spectrometer at 300 MHz. The obtained spectra were calibrated to the corresponding residual solvent peak (CDCl<sub>3</sub>  $\delta$ =7.26 ppm, DMSO-D<sub>6</sub>  $\delta$ =2.50 ppm). Chemical shifts are given in ppm, coupling constants in Hertz. Ultraviolet-visible (UV-Vis) spectra were recorded on a Hitachi U-3000 spectrophotometer using quartz cuvettes with a path length of 1 cm. Fourier transform infrared (FTIR) spectra were recorded from solids on a Perkin Elmer Spectrum 100 FTIR spectrometer in attenuated total reflection (ATR) mode. Thermal gravimetry analysis (TGA) experiments were performed under continuous N<sub>2</sub> stream using a Mettler Toledo TGA/SDTA 851. The measurement range was 30-800 °C

with a heating rate of  $10 \text{ K min}^{-1}$ . The determined decomposition temperatures  $T_{\text{dec}}$  are onset temperatures. Differential scanning calorimetry (DSC) experiments were carried out on a Perkin Elmer Diamond DSC with a heating rate of  $10 \text{ K min}^{-1}$  under  $\text{N}_2$  atmosphere. From each sample three cycles were measured. Glass transition ( $T_g$ ) are given as half step temperature. Size exclusion chromatography (SEC) with stabilized THF as eluent was performed using a Waters 515-HPLC pump at a flow rate of  $0.5 \text{ mL min}^{-1}$ . A guard column (Varian,  $50 \times 0.75 \text{ cm}$ , ResiPore, particle size  $3 \mu\text{m}$ ) and two separation columns (Varian,  $300 \times 0.75 \text{ cm}$ , ResiPore, particle size  $3 \mu\text{m}$ ) are connected in series with a Waters UV detector at  $254 \text{ nm}$  and  $486 \text{ nm}$  calibrated in relation to polystyrene standards. 1,2-dichlorobenzene (DCB) was used as an internal standard. SEC with chlorobenzene (CB) as eluent were carried out at  $60 \text{ }^\circ\text{C}$  on an Agilent 1100 using two Polymer Laboratories mixed B columns in series. The refractive index detector was calibrated in relation to polystyrene standards. Matrix assisted laser desorption ionization mass spectroscopy with time of flight detection (MALDI-TOF MS) was performed on a Bruker Reflex III using trans-2-(3-(4-tert-butylphenyl)-2-methyl-2-propenylidene)malononitrile (DCTB) as matrix and silver trifluoroacetate as cationizing salt. Solutions in either THF or oDCB of polymer ( $0.01 \text{ mg } \mu\text{L}^{-1}$ ), matrix ( $0.02 \text{ mg } \mu\text{L}^{-1}$ ) and salt ( $0.01 \text{ mg } \mu\text{L}^{-1}$ ) were mixed in the ratio 5:20:1 (v:v:v) and spotted onto the MALDI target plate. In case of DCB, the MALDI target plate was dried at  $40 \text{ }^\circ\text{C}$  for 24 h prior to the measurement.

Electron-only devices for space-charge limited current (SCLC) measurements were fabricated using the following device structure: glass/ITO/PEDOT:PSS/active layer/Ca/Al. Commercial ITO coated glass substrates with a sheet resistance of  $13 \text{ Ohms per sq}$  (Lumtec) were cleaned using the following sequence in an ultrasonic bath: detergent, water, acetone and 2-propanol. After ozone treatment of the substrates for 10 min, PEDOT:PSS was spin-coated on the ITO surface and dried at  $130 \text{ }^\circ\text{C}$  for 30 min. All following steps were carried out under  $\text{N}_2$  atmosphere with water and oxygen levels  $\leq 0.1 \text{ ppm}$ . After cooling the substrate, the polymer layer was blade coated from oDCB solutions at  $70 \text{ }^\circ\text{C}$ . The substrates were then put in a thermal evaporation chamber to evaporate the top electrode ( $30 \text{ nm Ca/ } 100 \text{ nm Al}$ ) under high vacuum ( $1 \cdot 10^{-6} \text{ mbar}$ ) through a shadow mask (active area  $4 \text{ mm}^2$ ). The current-voltage characteristics of the devices were measured using a Keithley 2420 (J-V) Digital SourceMeter at  $25 \text{ }^\circ\text{C}$ . The electron mobility  $\mu_e$  was extracted from the obtained J-V curves using the following equation<sup>[44]</sup>,

$$J = \frac{9}{8} \varepsilon_r \varepsilon_0 \mu \frac{V^2}{L^3}$$

where  $J$  is the current density,  $\varepsilon_r$  the dielectric constant ( $\approx 3$  for organic semiconductors<sup>[45]</sup>),  $\varepsilon_0$  the permittivity of free space,  $\mu$  the charge carrier mobility,  $V$  the voltage and  $L$  the active layer thickness. Voltage  $V$  is a corrected value  $V = V_{\text{appl}} - V_{\text{built-in}}$ , resulting from the differences in work function of the Calcium and ITO/PEDOT:PSS contacts ( $\approx 2.2$  eV). Film thicknesses were determined on a Dektak ST surface profilometer. Atomic force microscopy (AFM) was applied on the SCLC devices using a Veeco Dimension Icon with Nanoscope V controller, in tapping mode. The used cantilevers were NSC15/AIBS from Mikromasch.

Cyclic voltammetry experiments were carried out at 25 °C in a mixture of *o*-dichlorobenzene and acetonitrile 5:1 (v:v) containing 0.1 M tetrabutylammonium hexafluorophosphate (TBAPF<sub>6</sub>) as the conducting electrolyte. Reduction potentials were measured with a glassy carbon disk electrode as the working electrode versus Ag/AgCl as the reference electrode.

Samples for transmission electron spectroscopy were prepared on mica substrates by spin-coating (1000 rpm, 30% acceleration, 120 s) of a 2 wt% solution in chloroform (PS-OH 1:PCBM=50:50, wt:wt) or by drop-casting from a 2 wt% solution in dichlorobenzene (PPCBM 3) with subsequent drying at 70 °C for 10 min on a precision hot stage. The thin films were floated on water, carefully collected on top of a TEM copper grid and dried under vacuum at room temperature. The measurement was carried out on a Zeiss EM922 Omega. Powder X-ray analysis (PXRD) was carried out with a Huber/Seifert Iso-Debyeflex 3003, using a Guinier diffractometer system (Cu K<sub>α</sub>: 1.5418 Å) with a sealed tube for temperature dependent measurements.

### General synthetic procedure for PS-Az 1-3

4-Methoxystyrene (MS) and 4-*tert*-butoxystyrene (BS) were added to a 10 mL schlenk tube under argon. The chain transfer agent (CTA) 3-azidopropyl-2-(((dodecylthio)carbonothioyl)thio)-2-methyl-propano-ate and 2-2'-azobisisobutyronitrile (AIBN) were each separately dissolved in 500 μL of dry toluene. To guarantee exact equivalents of both reagents, the recalculated amounts of these solutions were added to the reaction flask. The overall volume of dry toluene was filled up to the given amount. Then the reaction mixture was degassed by four freeze, pump and thaw cycles and

polymerization was started in a preheated oil bath at 80 °C. Samples were taken periodically by syringe to monitor the monomer conversion *via*  $^1\text{H-NMR}$  spectroscopy. When the desired monomer conversion was reached, the polymerization was quenched by cooling the solution rapidly to 0 °C in an ice bath and exposition to air. The resulting polymer was isolated by precipitation twice into 300 mL methanol and drying under vacuum.

### Synthesis of PS-Az 1

MS (4.377 g, 32.62 mmol, 253 equ.), BS (0.500 g, 2.84 mmol, 22 equ.), CTA (57.8 mg, 0.129 mmol, 1 equ.) and AIBN (4.2 mg, 0.026 mmol, 0.2 equ.) were used for polymerization in 3 mL toluene. After 27.5 h the monomer conversion was 48 % and the polymerization was stopped. Yield: 1.876 g of a pale yellow solid. The monomer ratio MS:BS was 90:10 in mol% ( $^1\text{H-NMR}$ ).  $M_n = 12.3 \text{ kg mol}^{-1}$ ,  $M_w/M_n = 1.11$  (THF),  $M_n = 12.7 \text{ kg mol}^{-1}$ ,  $M_w/M_n = 1.37$  (CB).  $^1\text{H-NMR}$  (300 MHz,  $\text{CDCl}_3$ ,  $\delta$ ): 6.85-6.15 (br m, 4(a+b)·H,  $H_{\text{ar}}$ ), 3.85-3.62 (br s, 3b·H,  $H_{\text{OMe}}$ ), 2.20-1.10 (br m,  $H_{\text{backbone}}$ ,  $H_{\text{tBu}}$ ,  $H_{\text{CTA}}$ ).

### Synthesis of PS-Az 2

MS (4.314 g, 32.15 mmol, 149 equ.), BS (1.000 g, 5.67 mmol, 26 equ.), CTA (96.4 mg, 0.215 mmol, 1 equ.) and AIBN (7.1 mg, 0.043 mmol, 0.2 equ.) were used for polymerization in 4 mL toluene. After 8.5 h the monomer conversion was 46 % and the polymerization was stopped. Yield: 2.114 g of a pale yellow solid. Monomer ratio MS:BS was 83:17 in mol% ( $^1\text{H-NMR}$ ).  $M_n = 9.0 \text{ kg mol}^{-1}$ ,  $M_w/M_n = 1.11$  (THF),  $M_n = 10.0 \text{ kg mol}^{-1}$ ,  $M_w/M_n = 1.18$ .  $^1\text{H-NMR}$  (300 MHz,  $\text{CDCl}_3$ ,  $\delta$ ): 6.85-6.15 (br m, 4(a+b)·H,  $H_{\text{ar}}$ ), 3.85-3.62 (br s, 3b·H,  $H_{\text{OMe}}$ ), 2.20-1.10 (br m,  $H_{\text{backbone}}$ ,  $H_{\text{OtBu}}$ ,  $H_{\text{CTA}}$ ).

### Synthesis of PS-Az 3

MS (3.823 g, 28.49 mmol, 88 equ.), BS (1.500 g, 8.51 mmol, 26 equ.), CTA (144.6 mg, 0.323 mmol, 1 equ.) and AIBN (10.6 mg, 0.065 mmol, 0.2 equ.) were used for polymerization in 2 mL toluene. After 5.0 h the monomer conversion was 46 % and the polymerization was stopped. Yield: 2.090 g of a pale yellow solid. Monomer ratio MS:BS was 74:26 in mol% ( $^1\text{H-NMR}$ ).  $M_n = 9.0 \text{ kg mol}^{-1}$ ,  $M_w/M_n = 1.11$  (THF),  $M_n = 6.9 \text{ kg mol}^{-1}$ ,  $M_w/M_n = 1.14$ .  $^1\text{H-NMR}$  (300 MHz,  $\text{CDCl}_3$ ,  $\delta$ ): 6.85-6.15 (br m, 4(a+b)·H,  $H_{\text{ar}}$ ), 3.85-3.62 (br s, 3b·H,  $H_{\text{OMe}}$ ), 2.20-1.10 (br m,  $H_{\text{backbone}}$ ,  $H_{\text{OtBu}}$ ,  $H_{\text{CTA}}$ ).

### General synthetic procedure for PS-Oct 1-3

A dry Schlenk flask was charged with 1.20 g (1 equ.) of PS-Az under argon atmosphere and dissolved in 70 mL of dry THF. After 10 equ. of 1-octyne was added, the reaction mixture was purged with argon for 25 min. Then, 0.23 equ. of a 0.07 M CuI/PMDETA stock solution were added *via* a syringe and stirred for 24 h at RT. The reaction mixture was passed through a column of neutral aluminium oxide to remove the catalyst. The obtained polymer was isolated by precipitation twice into 500 mL methanol and drying under vacuum.

#### Synthesis of PS-Oct 1

The reaction yielded 1.284 g of a pale yellow solid.  $^1\text{H-NMR}$  (300 MHz,  $\text{CDCl}_3$ ,  $\delta$ ): 6.85-6.15 (br m, 4(a+b)·H,  $\text{H}_{\text{ar}}$ ), 3.85-3.62 (br s, 3b·H,  $\text{H}_{\text{OMe}}$ ), 2.20-1.10 (br m,  $\text{H}_{\text{backbone}}$ ,  $\text{H}_{\text{OtBu}}$ ,  $\text{H}_{\text{CTA}}$ ,  $\text{H}_{\text{Octyl}}$ ).

#### Synthesis of PS-Oct 2

The reaction yielded 1.034 g of a pale yellow solid.  $M_n = 9.1 \text{ kg mol}^{-1}$ ,  $M_w/M_n = 1.10$  (THF),  $^1\text{H-NMR}$  (300 MHz,  $\text{CDCl}_3$ ,  $\delta$ ): 6.85-6.15 (br m, 4(a+b)·H,  $\text{H}_{\text{ar}}$ ), 3.85-3.62 (br s, 3b·H,  $\text{H}_{\text{OMe}}$ ), 2.20-1.10 (br m,  $\text{H}_{\text{backbone}}$ ,  $\text{H}_{\text{OtBu}}$ ,  $\text{H}_{\text{CTA}}$ ,  $\text{H}_{\text{Octyl}}$ ).

#### Synthesis of PS-Oct 3:

The reaction yielded 1.10 g of a pale yellow solid.  $M_n = 6.0 \text{ kg mol}^{-1}$ ,  $M_w/M_n = 1.08$  (THF),  $^1\text{H-NMR}$  (300 MHz,  $\text{CDCl}_3$ ,  $\delta$ ): 6.85-6.15 (br m, 4(a+b)·H,  $\text{H}_{\text{ar}}$ ), 3.85-3.62 (br s, 3b·H,  $\text{H}_{\text{OMe}}$ ), 2.20-1.10 (br m,  $\text{H}_{\text{backbone}}$ ,  $\text{H}_{\text{OtBu}}$ ,  $\text{H}_{\text{CTA}}$ ,  $\text{H}_{\text{Oct}}$ ).

### General synthetic procedure for PS-OH 1-3

A round bottom flask was charged with PS-Oct and dissolved in 100 mL THF for every 1.0 g of polymer. 12 mL of concentrated hydrochloric acid (37 wt%) for every 1.0 g of polymer was added dropwise *via* a syringe. After purging the reaction mixture with argon for 20 min, it was stirred at 35 °C for 22 h. All volatile components were removed under reduced pressure. The hydrolyzed polymer was isolated by precipitation twice into 500 mL water and freeze-drying from 1,4-dioxane.

### Synthesis of PS-OH 1

$M_n = 9.3 \text{ kg mol}^{-1}$ ,  $M_w/M_n = 1.29$ ,  $M_n = 16.0 \text{ kg mol}^{-1}$ ,  $M_p = 16.6 \text{ kg mol}^{-1}$  (MALDI-TOF MS),  $^1\text{H-NMR}$  (300 MHz, DMSO- $\text{D}_6$ ,  $\delta$ ): 9.20-8.90 (br, a·H, OH), 6.95-6.10 (br m, 4(a+b)·H,  $\text{H}_{\text{ar}}$ ), 3.80-3.50 (br s, 3b·H,  $\text{H}_{\text{OMe}}$ ), 2.20-1.10 (br m,  $\text{H}_{\text{backbone}}$ ,  $\text{H}_{\text{CTA}}$ ,  $\text{H}_{\text{Octyl}}$ ).  $T_{\text{dec},1} = 204 \text{ }^\circ\text{C}$ ,  $T_{\text{dec},2} = 388 \text{ }^\circ\text{C}$ ,  $T_g = 95 \text{ }^\circ\text{C}$ .

### Synthesis of PS-OH 2

$M_n = 7.9 \text{ kg mol}^{-1}$ ,  $M_w/M_n = 1.17$ ,  $M_n = 10.2 \text{ kg mol}^{-1}$ ,  $M_p = 10.1 \text{ kg mol}^{-1}$  (MALDI-TOF MS).  $^1\text{H-NMR}$  (300 MHz, DMSO- $\text{D}_6$ ,  $\delta$ ): 9.23-8.88 (br, a·H, OH), 6.85-6.15 (br m, 4(a+b)·H,  $\text{H}_{\text{ar}}$ ), 3.85-3.42 (br s, 3b·H,  $\text{H}_{\text{OMe}}$ ), 2.20-1.05 (br m,  $\text{H}_{\text{backbone}}$ ,  $\text{H}_{\text{CTA}}$ ,  $\text{H}_{\text{Octyl}}$ ).  $T_{\text{dec},1} = 191 \text{ }^\circ\text{C}$ ,  $T_{\text{dec},2} = 385 \text{ }^\circ\text{C}$ ,  $T_g = 95 \text{ }^\circ\text{C}$ .

### Synthesis of PS-OH 3:

$M_n = 5.3 \text{ kg mol}^{-1}$ ,  $M_w/M_n = 1.10$ ,  $M_n = 6.3 \text{ kg mol}^{-1}$ ,  $M_p = 6.4 \text{ kg mol}^{-1}$  (MALDI-TOF MS).  $^1\text{H-NMR}$  (300 MHz, DMSO- $\text{D}_6$ ,  $\delta$ ): 9.20-8.90 (br, a·H, OH), 6.85-6.15 (br m, 4(a+b)·H,  $\text{H}_{\text{ar}}$ ), 3.80-3.53 (br s, 3b·H,  $\text{H}_{\text{OMe}}$ ), 2.20-1.00 (br m,  $\text{H}_{\text{backbone}}$ ,  $\text{H}_{\text{CTA}}$ ,  $\text{H}_{\text{Octyl}}$ ).  $T_{\text{dec},1} = 191 \text{ }^\circ\text{C}$ ,  $T_{\text{dec},2} = 384 \text{ }^\circ\text{C}$ ,  $T_g = 95 \text{ }^\circ\text{C}$ .

### General synthetic procedure of PPCBM 1-4

A 500 ml schlenk flask was charged with PS-OH (1 equ. of 4-hydroxystyrene), PCBA (1.15 equ.), DMAP (3 equ.) and DMAP·HCl (2 equ.). The flask was degassed under high vacuum and backfilled with argon twice. 100 mL of dry oDCB:CS<sub>2</sub>:AcN (3:3:1/v:v:v) was added and stirred vigorously for 45 min at RT. In a separate 50mL schlenk flask under argon, DCC (7 equ.) was dissolved in 16.5 mL of the same solvent mixture. Then the DCC solution was added dropwise to the reaction mixture, which was stirred at 40 °C for 3-4 days. After removal of the solvents under reduced pressure, the crude product was redissolved in DCB and filtered. For polymer purification the filtrate was precipitated twice into 800 ml methanol from first DCB and second chloroform. To remove soluble fullerene derivatives, the polymer was precipitated from chloroform into 800 mL of a toluene:methanol mixture (1:1 for PPCBM 1, 2:1 for PPCBM 2, 3:1 for PPCBM 3). Purity of the obtained polymer was monitored by TLC (SiO<sub>2</sub>, toluene), where the polymer remains on the start line and the impurities show distinct spots. The product was once more precipitated from chloroform into 800 mL methanol and dried under high vacuum.

### Synthesis of PPCBM 1

$M_n = 17.2 \text{ kg mol}^{-1}$ ,  $M_w/M_n = 1.27$  (CB),  $M_n = 35.1 \text{ kg mol}^{-1}$ ,  $M_{p,1} = 22.9 \text{ kg mol}^{-1}$ ,  $M_{p,2} = 45.2 \text{ kg mol}^{-1}$  (MALDI-TOF MS).  $^1\text{H-NMR}$  (300 MHz,  $\text{CDCl}_3$ ,  $\delta$ ): 8.00-7.87 (br m, 2a·H, *Ph*-( $\text{CH}_2$ )<sub>3</sub>-COOR), 7.70-7.30 (br m, 3a·H, *Ph*-( $\text{CH}_2$ )<sub>3</sub>-COOR), 6.90-6.10 (br m, 4(a+b)·H,  $H_{\text{ar}}$ ), 3.90-3.55 (br s, 3b·H,  $H_{\text{OMe}}$ ), 3.06-2.92 (br m, 2a·H, *Ph-CH}\_2\text{-CH}\_2\text{-CH}\_2\text{-COOR}), 2.81-2.66 (br m, 2a·H, *Ph-CH}\_2\text{-CH}\_2\text{-CH}\_2\text{-COOR}), 2.32-2.20 (br m, 2a·H, *Ph-CH}\_2\text{-CH}\_2\text{-CH}\_2\text{-COOR}), 2.20-0.8 (br m,  $H_{\text{backbone}}$ ,  $H_{\text{CTA}}$ ,  $H_{\text{Octyl}}$ ).  $T_{\text{dec},1} = 180\text{--}190 \text{ }^\circ\text{C}$ ,  $T_{\text{dec},2} = 395 \text{ }^\circ\text{C}$ .***

### Synthesis of PPCBM 2

$M_n = 11.6 \text{ kg mol}^{-1}$ ,  $M_w/M_n = 1.21$ ,  $M_n = 25.8 \text{ kg mol}^{-1}$ ,  $M_{p,1} = 16.1 \text{ kg mol}^{-1}$  (MALDI-TOF MS).  $^1\text{H-NMR}$  (300 MHz,  $\text{CDCl}_3$ ,  $\delta$ ): 8.00-7.87 (br m, 2a·H, *Ph*-( $\text{CH}_2$ )<sub>3</sub>-COOR), 7.70-7.30 (br m, 3a·H, *Ph*-( $\text{CH}_2$ )<sub>3</sub>-COOR), 6.90-6.10 (br m, 4(a+b)·H,  $H_{\text{ar}}$ ), 3.90-3.55 (br s, 3b·H,  $H_{\text{OMe}}$ ), 3.06-2.90 (br m, 2a·H, *Ph-CH}\_2\text{-CH}\_2\text{-CH}\_2\text{-COOR}), 2.81-2.63 (br m, 2a·H, *Ph-CH}\_2\text{-CH}\_2\text{-CH}\_2\text{-COOR}), 2.37-2.18 (br m, 2a·H, *Ph-CH}\_2\text{-CH}\_2\text{-CH}\_2\text{-COOR}), 2.10-0.8 (br m,  $H_{\text{backbone}}$ ,  $H_{\text{CTA}}$ ,  $H_{\text{Octyl}}$ ).  $T_{\text{dec},1} = 184 \text{ }^\circ\text{C}$ ,  $T_{\text{dec},2} = 391 \text{ }^\circ\text{C}$ .***

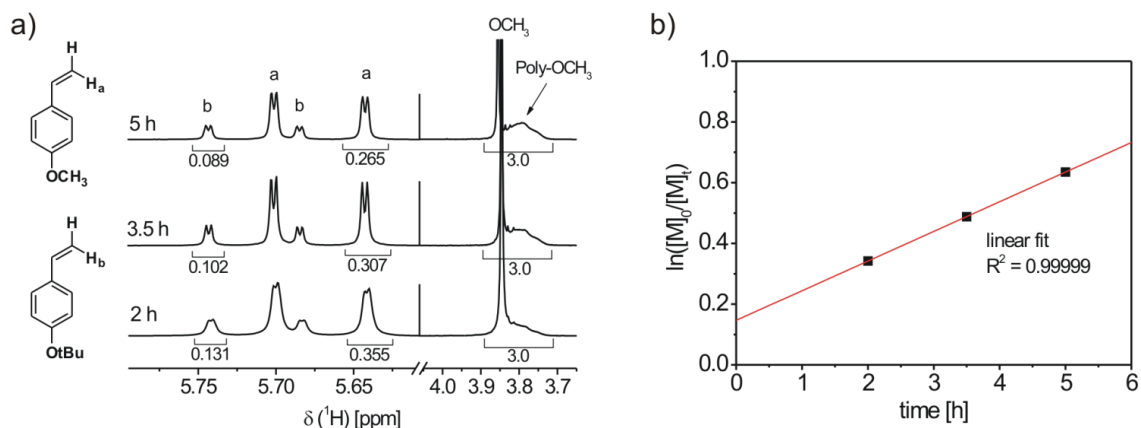
### Synthesis of PPCBM 3 and PPCBM 4

$M_n = 7.6 \text{ kg mol}^{-1}$ ,  $M_w/M_n = 1.21$  (CB),  $M_n = 19.6 \text{ kg mol}^{-1}$ ,  $M_{p,1} = 13.0 \text{ kg mol}^{-1}$ ,  $M_{p,2} = 26.6 \text{ kg mol}^{-1}$  (MALDI-TOF MS).  $^1\text{H-NMR}$  (300 MHz,  $\text{oDCB-D}_4$ ,  $\delta$ ): 7.80-7.67 (br m, 2a·H, *Ph-C*-( $\text{CH}_2$ )<sub>3</sub>-COOR), 7.32-7.05 (br m, 3a·H, *Ph-C*-( $\text{CH}_2$ )<sub>3</sub>-COOR), 6.65-6.00 (br m, 4(a+b)·H,  $H_{\text{ar}}$ ), 3.55-3.27 (br s, 3b·H,  $H_{\text{OMe}}$ ), 2.84-2.68 (br m, 2a·H, *Ph-C-CH}\_2\text{-CH}\_2\text{-CH}\_2\text{-COOR}), 2.56-2.38 (br m, 2a·H, *Ph-C-CH}\_2\text{-CH}\_2\text{-CH}\_2\text{-COOR}), 2.19-2.01 (br m, 2a·H, *Ph-C-CH}\_2\text{-CH}\_2\text{-CH}\_2\text{-COOR}), 1.95-0.55 (br m,  $H_{\text{backbone}}$ ,  $H_{\text{CTA}}$ ,  $H_{\text{Octyl}}$ ).  $T_{\text{dec},1} = 180 \text{ }^\circ\text{C}$ ,  $T_{\text{dec},2} = 382 \text{ }^\circ\text{C}$ .***

The large amount of solid residues in the reaction flask after synthesis of PPCBM 3 was collected (198 mg) and dissolved by stirring for 3 h at 100 °C in DCB. The polymer PPCBM 4 was isolated by precipitation into 400 mL toluene:methanol (5:2/v:v) and then 400 ml methanol. Yield: 78 mg of a deep brown solid.  $M_n = 25.2 \text{ kg mol}^{-1}$ ,  $M_{p,1} = 17.8 \text{ kg mol}^{-1}$ ,  $M_{p,2} = 35.0 \text{ kg mol}^{-1}$  (MALDI-TOF MS).  $^1\text{H-NMR}$  (300 MHz,  $\text{oDCB-D}_4$ ,  $\delta$ ): 7.82-7.65 (br m, 2a·H, *Ph-C*-( $\text{CH}_2$ )<sub>3</sub>-COOR), 7.37-7.04 (br m, 3a·H, *Ph-C*-( $\text{CH}_2$ )<sub>3</sub>-COOR), 6.65-6.00 (br m, 4(a+b)·H,  $H_{\text{ar}}$ ), 3.58-3.23 (br s, 3b·H,  $H_{\text{OMe}}$ ), 2.85-2.70 (br m, 2a·H, *Ph-C-CH}\_2\text{-CH}\_2\text{-CH}\_2\text{-COOR}), 2.57-2.38 (br m, 2a·H, *Ph-C-CH}\_2\text{-CH}\_2\text{-CH}\_2\text{-COOR}), 2.57-2.38 (br m, 2a·H, *Ph-C-CH}\_2\text{-CH}\_2\text{-CH}\_2\text{-COOR}), 2.57-2.38 (br m, 2a·H, *Ph-C-CH}\_2\text{-CH}\_2\text{-CH}\_2\text{-COOR}).****

COOR), 2.19-2.01 (br m, 2a-H, Ph-C-CH<sub>2</sub>-CH<sub>2</sub>-CH<sub>2</sub>-COOR), 1.95-0.55 (br m, H<sub>backbone</sub>, H<sub>CTA</sub>, H<sub>Octyl</sub>).  $T_{\text{dec},1} = 180\text{--}190\text{ }^{\circ}\text{C}$ ,  $T_{\text{dec},2} = 386\text{ }^{\circ}\text{C}$ .

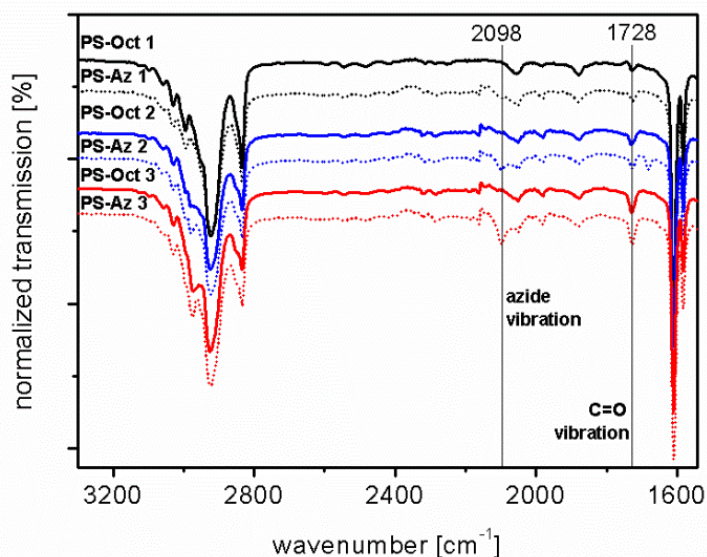
### Kinetics of the copolymerization of 4-tert-butoxystyrene and 4-methoxystyrene



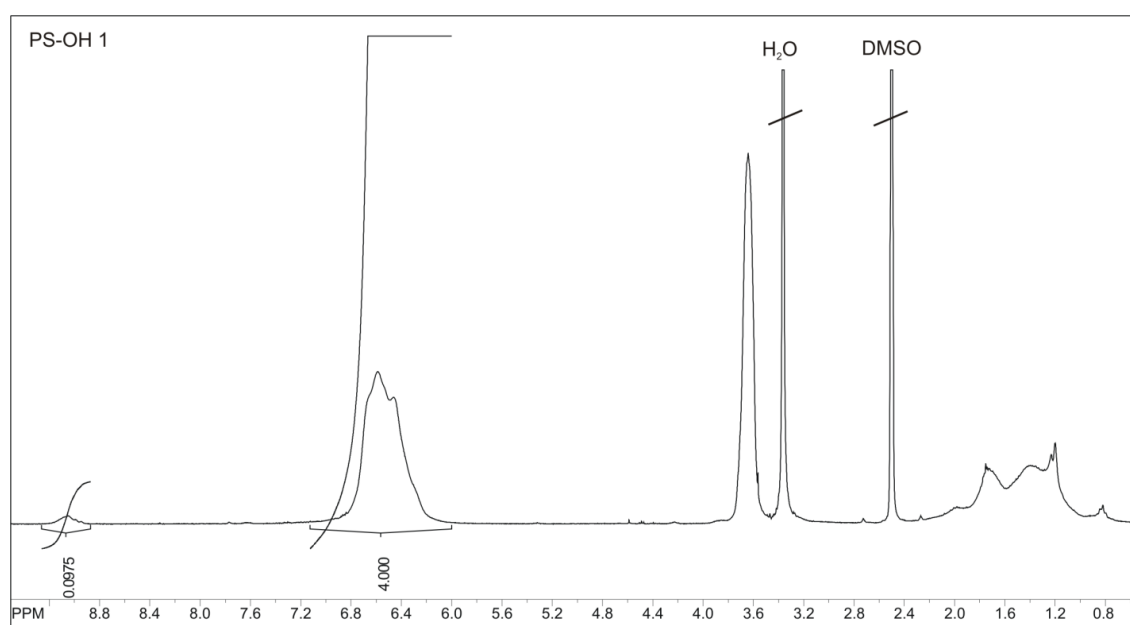
**Figure S1:** Monitoring of the kinetics of 4-tert-butoxystyrene (BS) and 4-methoxystyrene (MS) copolymerization by <sup>1</sup>H-NMR. The NMR spectra of samples taken periodically during RAFT copolymerization of PS-Az 3 are shown in (a). The integral ratio of the vinyl proton resonances a and b of the unreacted monomers represent the molar ratio of both monomers in solution. It remains almost constant and was BS:MS=73:27, 75:25 and 75:25 after 2, 3.5 and 5 hours. Thus, the consumption of both monomer species can be assumed to be equally fast. The monomer conversion was also estimated from the <sup>1</sup>H-NMR spectra. The time-conversion plot (b) nicely shows a perfect linear correlation following first order kinetics.

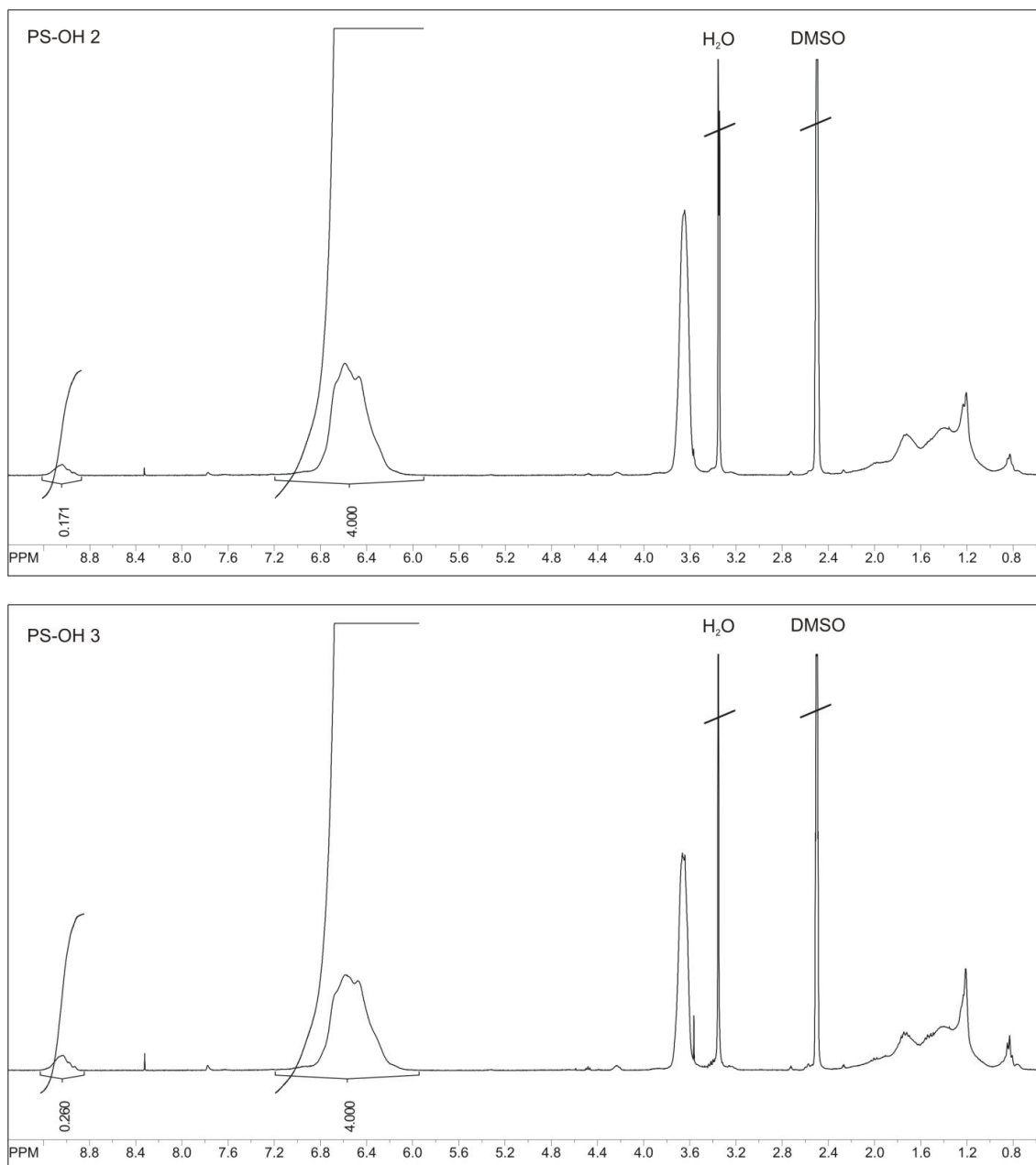
**Table S1:** Molar feed ratio and molar built-in ratio of 4-tert-butoxystyrene (BS) and 4-methoxystyrene (MS) for the copolymers PS-Az 1-3.

Polymer	Feed ratio BS:MS	Built-in ratio BS:MS
PS-Az 1	8:92	10:90
PS-Az 2	15:85	17:83
PS-Az 3	23:77	26:74

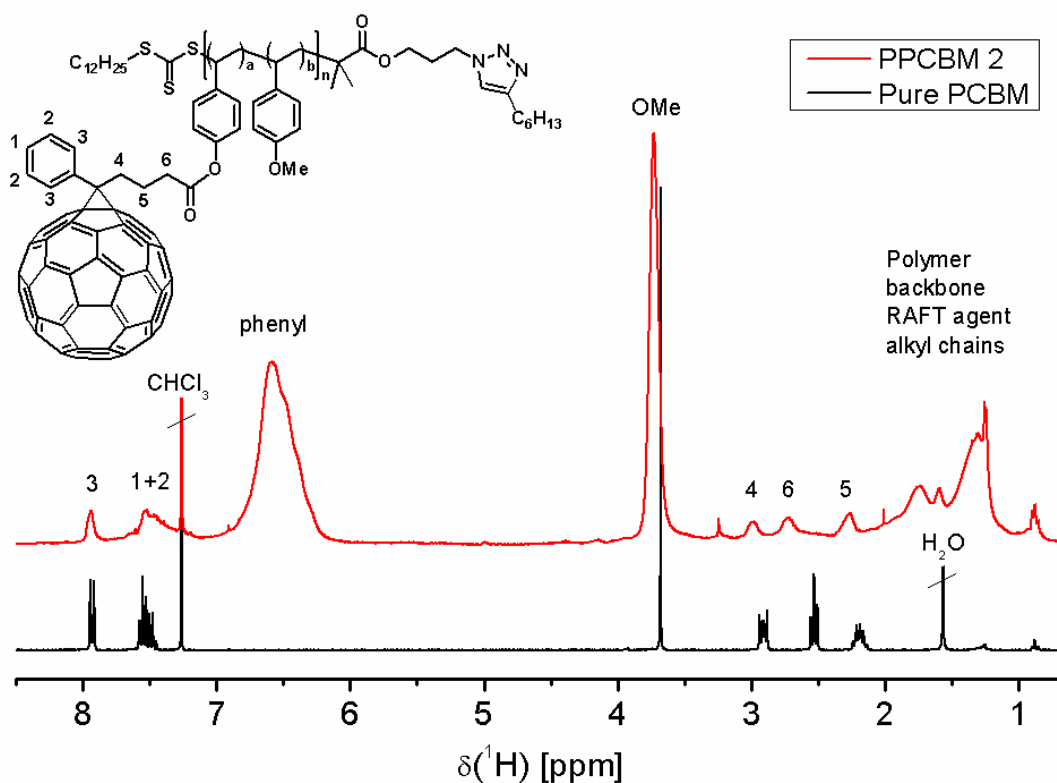
**Fourier-transform infrared spectra of PS-Az 1-3 and PS-Oct 1-3**

**Figure S2:** Magnified detail of the FTIR spectra of octyl end-capped polymers PS-Oct 1, PS-Oct 2 and PS-Oct 3 (solid lines) and their respective precursor copolymers PS-Az 1, PS-Az 2 and PS-Az 3 (dotted lines) with terminal azide groups. The azide vibration band at  $\nu = 2098 \text{ cm}^{-1}$  of the copolymers PS-Az 1, PS-Az 2 and PS-Az 3 disappears completely after the 1,3-dipolar cycloaddition (click reaction) with 1-octyne, since a triazole ring is formed. This gives evidence for a quantitative conversion of the azide end groups. The intensity of the end group dependent bands at  $2098 \text{ cm}^{-1}$  and  $1728 \text{ cm}^{-1}$  (C=O stretching band of carboxylic acid ester) correlates with the chain length in the expected indirect proportional manner due to normalization of all spectra to the polymer backbone signals.

 **$^1\text{H-NMR}$  spectra of copolymers PS-OH 1-3 after *tert*-butyl ether cleavage**

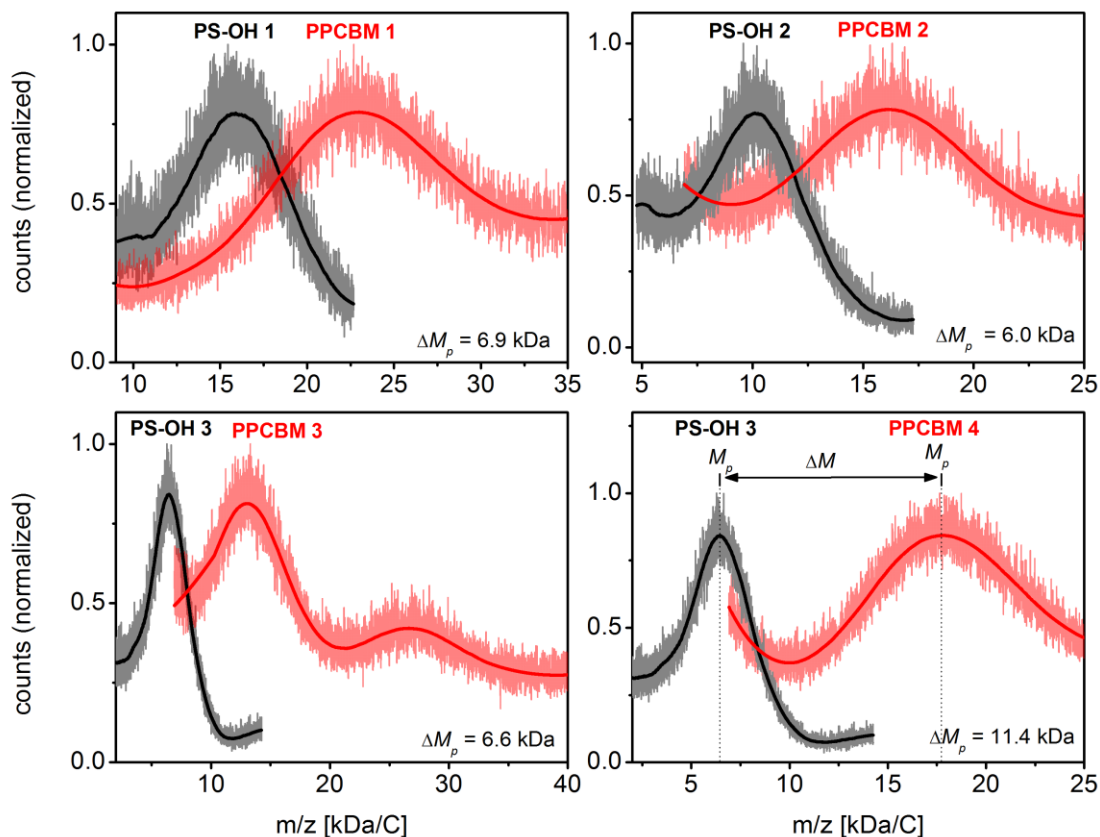


**Figure S3:**  $^1\text{H-NMR}$  spectra of the copolymers PS-OH 1-3. The proton resonances around  $\delta = 9.05$  ppm and  $\delta = 6.55$  ppm can be assigned to the hydroxyl group of 4-hydroxystyrene and to the phenyl protons of 4-methoxystyrene and 4-hydroxystyrene respectively. The integral of the phenyl protons was calibrated to 4.0, therefore the integral of the hydroxyl group corresponds to the molar ratio of 4-hydroxystyrene in the copolymers. The  $^1\text{H-NMR}$  spectra confirm a full conversion of 4-*tert*-butoxystyrene to 4-hydroxystyrene as the integral analysis give 10 mol% HS in PS-OH 1, 17 mol% HS in PS-OH 2 and 26 mol% in PS-OH 3 (values rounded off).

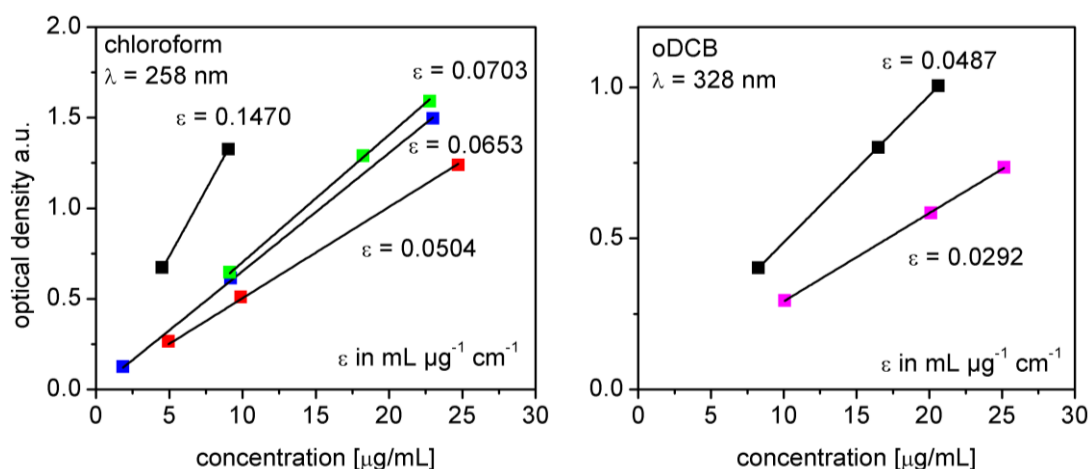
**$^1\text{H-NMR}$  spectra of PPCBM 2**

**Figure S4:**  $^1\text{H-NMR}$  spectra of PPCBM 2 in comparison to pure PCBM. While the low-molecular weight PCBM shows throughout clear multiplets for all proton resonances, these multiplets appear as broad signals in the PCBM-grafted copolymer as the fullerene moiety is covalently attached to the polymer backbone. Note also the significant shift of the methylene protons 6 for PPCBM 2 at  $\delta = 2.73$  ppm, which is adjacent to the ester bond, compared to the triplet proton signal at  $\delta = 2.53$  for pure PCBM. This further indicates the successful ester formation in the PCBM-grafted copolymer.

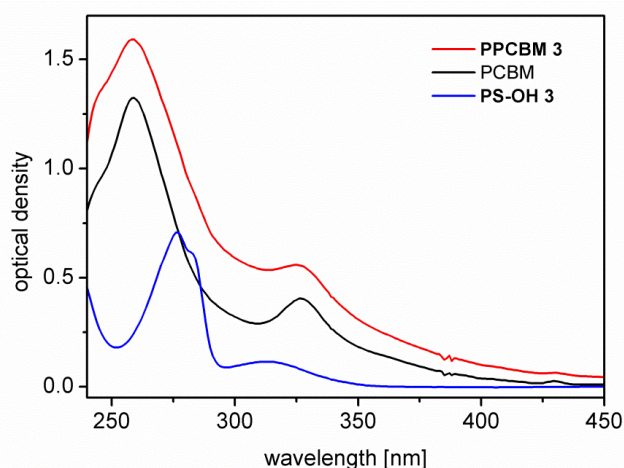
## MALDI-TOF mass spectra of PS-OH 1-3 and PPCBM 1-4



**Figure S5:** MALDI-TOF mass spectra of PCBM-grafted copolymers PPCBM 1-4 (red) and their corresponding precursor copolymers PS-OH 1-3 (black). As depicted for PPCBM 4, the PCBM content  $f_{\text{PCBM}}$  was determined from the mass difference  $\Delta M$  of the peak maxima. All mass spectra were smoothed for clarity due to the low signal-to-noise ratio. Some polymer-polymer coupling was observed leading to an additional peak at double molecular weight (see PPCBM 3).

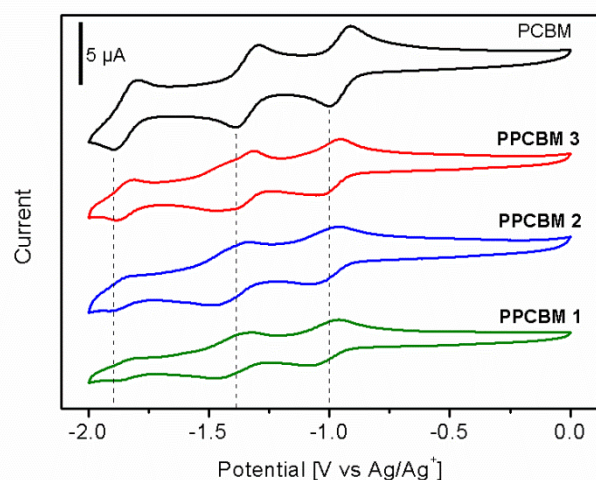
**Quantitative UV-Vis of the dilution series of PPCBM 1-4 and PCBM**

**Figure S6:** Quantitative UV-vis measurements for the determination of extinction coefficient  $\epsilon$ . Left: PCBM (black), PPCBM 1 (red), PPCBM 2 (blue) and PPCBM 3 (green) in chloroform. Right: PCBM (black) and PPCBM 4 (magenta) measured in DCB. According to the law of Lambert-Beer, the extinction coefficient  $\epsilon$  can be extracted from the slope of the linear fits. The ratio  $\epsilon_{\text{Polymer}}/\epsilon_{\text{PCBM}}$  gives the PCBM weight content of the PCBM-grafted copolymers, but is usually underestimated for high contents.

**Representative UV-Vis spectra of PPCBM 3, PCBM and PS-OH 3**

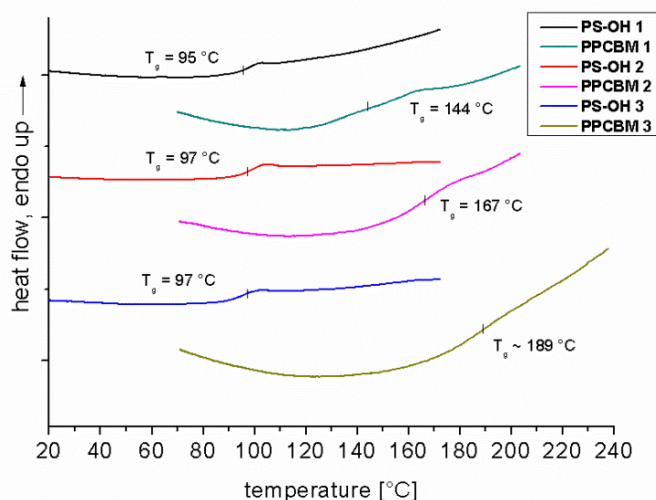
**Figure S7:** UV-Vis absorption spectra of PCBM ( $9.04 \mu\text{g/mL}$ ), PS-OH 3 ( $62.88 \mu\text{g/mL}$ ) and PPCBM 3 ( $22.79 \mu\text{g/mL}$ ). The PCBM-grafted copolymer PPCBM 3 exhibits the same optical features as PCBM, i.e. two absorption bands at 258 nm ( $\epsilon_{258 \text{ nm}} = 0.0703 \text{ mL mg}^{-1} \text{ cm}^{-1}$ ) and 328 nm. Hence, the optical properties of PCBM are not affected by the covalent attachment to the polymer backbone.

## Cyclic voltammetry curves of PPCBM 1-4 and PCBM

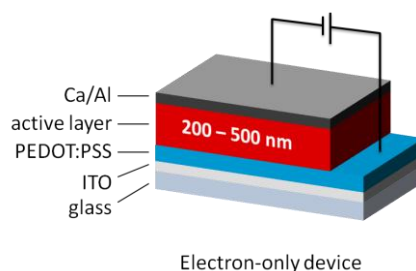


**Figure S8:** Cyclic voltammetry curves of PCBM-grafted copolymers and pristine PCBM measured at  $50 \text{ mV s}^{-1}$  in *o*DCB:AcN 5:1 (v:v) with 0.1 mM TBAPF<sub>6</sub>. The potential is given in volt using Ag/AgNO<sub>3</sub> as reference electrode.

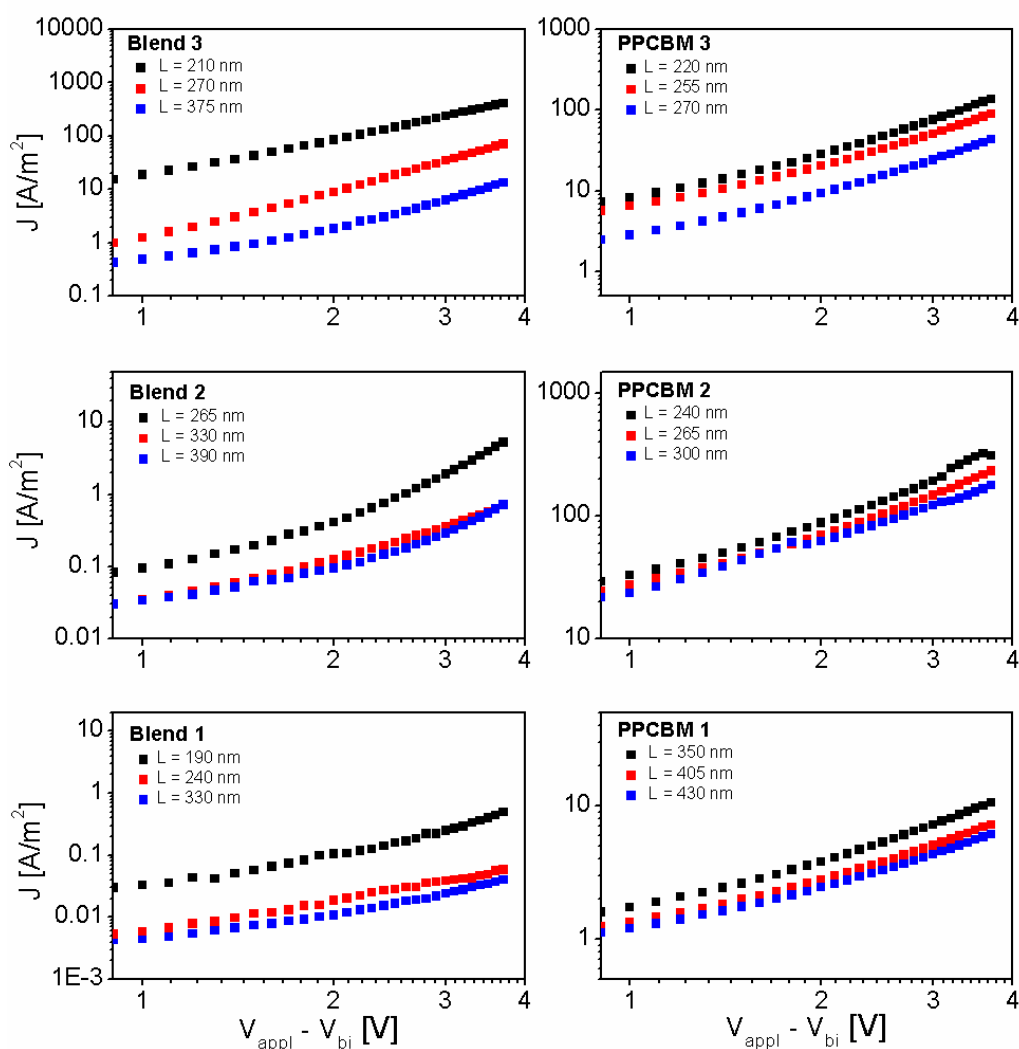
## Differential scanning calorimetry of PS-OH 1-3 and PPCBM 1-3



**Figure S9:** DSC curves (second heating cycle) of PCBM-grafted copolymers PPCBM 1-3 and the corresponding precursor copolymers PS-OH 1-3. Whereas the precursor copolymers exhibit a typical glass transition at  $T_g \approx 95\text{-}97 \text{ }^\circ\text{C}$ , the glass transition of PCBM-grafted copolymers is shifted considerably towards higher temperatures. With increasing PCBM content of 30 wt% (PPCBM 1), 37 wt% (PPCBM 2) and 51 wt% (PPCBM 3), the  $T_g$  step is broadening and increasing to  $144 \text{ }^\circ\text{C}$ ,  $167 \text{ }^\circ\text{C}$  and about  $189 \text{ }^\circ\text{C}$ , respectively.

**Electron-only device architecture for space-charge limited current (SCLC) method**

**Figure S10:** Device configuration for space-charge limited current (SCLC) measurements.

**Current-Voltage curves of SCLC devices with varying active layer thickness**

**Figure S11:** Current-voltage ( $J$ - $V$ ) curves from SCLC measurements of blends (PCBM:PS-OH 1) in different compositions in comparison to the synthesized PCBM-grafted copolymers PPCBM 1-3. A series of devices with varying film thickness  $L$  was measured for each compound.

**Experimental Data of SCLC measurements**

**Table S2:** Experimental data of the SCLC measurements of the PPCBMs and blends. The electron mobility was determined from the J-V curves using the Mott-Gurney equation from devices with different active layer thicknesses. Average mobility is given as rounded value with the standard deviation as error.

Sample	Active layer thickness [nm]	Electron mobility [ $\text{cm}^2 \text{V}^{-1} \text{s}^{-1}$ ]	Average electron mobility [ $\text{cm}^2 \text{V}^{-1} \text{s}^{-1}$ ]	Standard deviation [ $\text{cm}^2 \text{V}^{-1} \text{s}^{-1}$ ]
PPCBM 1	350	1.0E-5	1E-5	0
	405	1.0E-5		
	430	1.0E-5		
PPCBM 2	240	1.3E-4	1E-4	1.5E-5
	265	1.1E-4		
	300	1.0E-4		
PPCBM 3	220	4.6E-5	4E-5	1.1E-5
	255	4.3E-5		
	270	2.6E-5		
Blend 1	190	1.2E-7	6E-8	5.4E-8
	240	1.9E-8		
	330	3.6E-8		
Blend 2	265	4.2E-6	2E-6	1.7E-6
	330	8.4E-7		
	390	1.8E-6		
Blend 3	210	1.1E-4	6E-5	4.4E-5
	270	4.7E-5		
	375	2.5E-5		

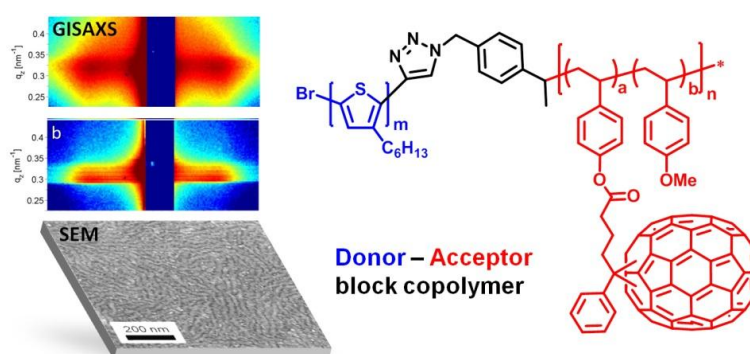
## 4 Donor-acceptor block copolymers carrying pendant PC<sub>71</sub>BM fullerenes with ordered nanoscale morphology

Martin Hufnagel<sup>a</sup>, Matthias Fischer<sup>b</sup>, Thomas Thurn-Albrecht<sup>b</sup>, Mukundan Thelakkat<sup>a,\*</sup>

<sup>a</sup>Applied Functional Polymers, Department of Macromolecular Chemistry I  
University of Bayreuth, Universitaetsstr. 30, 95440 Bayreuth (Germany)

<sup>b</sup>Experimental Polymer Physics Group, Martin-Luther University Halle-Wittenberg,  
Von-Danckelmann-Platz 3, 06120 Halle (Germany)

\*E-mail: [mukundan.thelakkat@uni-bayreuth.de](mailto:mukundan.thelakkat@uni-bayreuth.de)



**ABSTRACT**

We present a straightforward method for the preparation of a novel donor-acceptor block copolymer based on an acceptor block with pendant phenyl-C<sub>71</sub>-butyric methyl ester (PC<sub>71</sub>BM) and a regioregular poly(3-hexylthiophene) (P3HT) as donor. First, a hydroxyl-functionalized polystyrene copolymer with azide end group was synthesized *via* nitroxide-mediated radical polymerization (NMRP) and coupled with alkyne-terminated P3HT using copper(I) catalyzed azide-alkyne cycloaddition (CuAAC). The grafting reaction of phenyl-C<sub>71</sub>-butyric acid (PC<sub>71</sub>BA) to the hydroxyl groups of the polystyrene precursor was optimized to yield near-quantitative conversion which is demonstrated for a PC<sub>71</sub>BM-grafted acceptor copolymer in detail using MALDI-TOF mass spectrometry, thermogravimetric analysis (TGA) and <sup>1</sup>H-NMR spectroscopy. Owing to the incorporation of C<sub>70</sub>, the donor-acceptor block copolymer exhibits enhanced absorption in the whole visible range of 300 to 600 nm. A detailed structural analysis of the block copolymer based on small-angle X-ray scattering in transmission (SAXS) and in grazing incidence geometry (GISAXS) as well as scanning electron microscopy (SEM) gives clear evidence for the formation of a periodic nanostructure of 37 nm in bulk and in thin films.

**INTRODUCTION**

In the last decade polymeric semiconductors emerged as a leading class of organic materials with great potential in solution processable, flexible and light-weight organic electronic devices especially organic photovoltaics (OPV).<sup>[1,2]</sup> In the case of OPV the physical mixture of a donor and an acceptor material leading to a bulk-heterojunction (BHJ) delivers the highest performance in polymer devices. The short lifetime of excitons in organic semiconductors typically results in a restricted diffusion length of about 10 nm. Moreover the excitons are strongly bound due to Coulomb forces. Therefore, the morphology of the active layer should provide a large donor/acceptor interface with suitable energy levels and small domain sizes for an efficient charge separation.<sup>[3]</sup> An interpenetrating network of donor and acceptor material is additionally essential for charge transport to the electrodes. Thus, controlling the nanostructure in BHJ solar cells is a key to achieve high device performance. The blend morphology of a conjugated polymer and a fullerene derivative was extensively optimized by adequate processing conditions and post-preparation thermal treatments.<sup>[4-6]</sup> However, such optimized, kinetically frozen mesostructures are in a non-equilibrium state. It is a big challenge to control the size and

long-term stability of such mesostructures, which is essential for long-term operational stability.<sup>[7,8]</sup> These issues become in particular critical for transferring the small area, lab-scale processing of OPV devices to a large scale roll-to-roll fabrication which requires totally different drying or annealing procedures.<sup>[9]</sup>

An ideal solution to stabilize such a morphology is by the development of nanostructured systems in thermodynamic equilibrium. One of the approaches is by using a single material consisting of both donor and acceptor functions with the capability to self-assemble into the desired nanostructures. Basically, classical coil-coil block copolymers exhibit well-defined equilibrium nanostructures by microphase separation that are tunable in size and shape simply by variation of the degree of polymerization, Flory-Huggins interaction parameter and volume fraction.<sup>[10]</sup> Theoretical studies on block copolymer systems comprising donor and acceptor blocks predict an improved device performance for vertically aligned nanostructures.<sup>[11]</sup> This manuscript deals with the design of fully functionalized donor-acceptor block copolymers with a  $\pi$ -conjugated poly(3-hexylthiophene) (P3HT) and an acceptor block carrying phenyl-C<sub>71</sub>-butyric methyl ester (PC<sub>71</sub>BM) fullerenes.

Donor-acceptor block copolymers are attractive candidates for single material solar cells.<sup>[12,13]</sup> Typically, P3HT is employed as the donor block and perylene bisimides (PBI) or fullerenes as acceptor units. We have recently reported well-defined microphase separation in P3HT-b-poly(PBI) active donor-acceptor block copolymers with a lamellar or cylindrical morphology in the range of tens of nanometers.<sup>[14]</sup> Since fullerenes are so far the most efficient acceptor material in OPV, it seems reasonable to integrate fullerenes into donor-acceptor block copolymers, which was realized up to now by grafting C<sub>60</sub> and its derivatives using different synthetic approaches. The very first reports on block copolymers carrying a conjugated block and a fullerene pendant block was reported by Hadziioannou *et al.*<sup>[15]</sup>

Perrin *et al.* showed that the unique electron-acceptor/transporting capability of fullerenes is maintained in C<sub>60</sub>-grafted polymers.<sup>[16]</sup> Just recently, we could demonstrate a well-defined synthesis method for fullerene-grafted copolymers carrying phenyl-C<sub>61</sub>-butyric methyl ester (PC<sub>61</sub>BM) which show high electron mobilities up to  $1 \times 10^{-4} \text{ cm}^2 \text{ V}^{-1} \text{ s}^{-1}$  without the formation of nanocrystals.<sup>[17]</sup>

Many of the synthetic strategies which aim at a covalent attachment of fullerenes to the block copolymer rely on reactions with unmodified C<sub>60</sub> fullerenes. For example atom transfer radical addition (ATRA),<sup>[18]</sup> [3+2]-cycloaddition with azides<sup>[19,20]</sup> or routes using tosylhydrazone addition<sup>[21]</sup> to C<sub>60</sub> have been reported. Since buckminsterfullerene C<sub>60</sub> can act as a multifunctional reactant these methods often lead to polymer crosslinking by multiple additions and result in diminished solubility of the products. More complex monofunctional fullerenes have been attached to block copolymers in an azide-alkyne Huisgen cycloaddition<sup>[22,23]</sup> or Williamson ether synthesis.<sup>[24]</sup> Lee *et al.* have reported a Steglich esterification procedure using phenyl-C<sub>61</sub>-butyric acid (PC<sub>61</sub>BA)<sup>[25]</sup> which is easily accessible from commercially available PC<sub>61</sub>BM in a straight-forward acidic hydrolysis.<sup>[26]</sup> Another concept toward donor-acceptor copolymers with graft-type architecture has been reported by Sivula *et al.* based on ring opening metathesis polymerization of C<sub>60</sub>- and P3HT-bearing norbornene monomers.<sup>[27]</sup> Even though different synthetic approaches to realize fullerene containing block copolymers as discussed above are reported, no long range microphase separation was observed for C<sub>60</sub>-grafted donor-acceptor block copolymers up to now.<sup>[28]</sup> An additional issue of C<sub>60</sub> fullerenes is their low optical density and thus C<sub>60</sub> does not contribute substantially to light harvesting. But C<sub>70</sub> and its derivatives absorb much more efficiently in the visible range which considerably improves the photocurrent in solar cells.<sup>[29]</sup> Therefore, PC<sub>71</sub>BM is the state-of-the-art acceptor material in OPV exhibiting record efficiencies<sup>[30]</sup> and it is desirable to incorporate C<sub>70</sub> fullerenes also into donor-acceptor block copolymers. Up to the best of our knowledge there are no reports regarding the grafting of C<sub>70</sub> into fully functionalized donor-acceptor block copolymers.

Taking into account the above facts we address the following questions in the design and structure elucidation of PC<sub>71</sub>BM-grafted donor-acceptor block copolymers: 1. What are the optimum reactions conditions for an efficient grafting of PC<sub>71</sub>BM into a polystyrene backbone? 2. Is it feasible to incorporate PC<sub>71</sub>BM into a donor-acceptor block copolymer maintaining high solubility and high yield of grafting? 3. Does such a block copolymer self-assemble into a periodic donor-acceptor nanostructure?

In this work we present the high yield grafting of PC<sub>71</sub>BM to obtain PC<sub>71</sub>BM-grafted copolymers (PPC<sub>71</sub>BM) and the controlled synthesis of a P3HT-b-PPC<sub>71</sub>BM donor-acceptor block copolymer. Further, we study the structure formation of this block copolymer using X-ray scattering methods and scanning electron microscopy.

## RESULTS AND DISCUSSION

Our synthetic strategy for P3HT-b-PPC<sub>71</sub>BM is based on copper(I) catalyzed azide-alkyne cycloaddition (CuAAC) of two individually designed polymer blocks; a hydroxyl functionalized polystyrene copolymer with an azide end group and a P3HT-alkyne. This was followed by a Steglich esterification procedure using phenyl-C<sub>71</sub>-butyric acid (PC<sub>71</sub>BA) to obtain the target donor-acceptor block copolymers (Figure 1). The major challenge of block copolymer synthesis *via* CuAAC is the control over the end group functionalization of both polymer blocks. In the case of P3HT-alkyne high end group fidelity was achieved by termination of the Kumada transfer catalyst polymerization with ethynylmagnesium chloride.<sup>[31]</sup> For the synthesis of the azide-terminated polystyrene precursor a statistical copolymer, poly(4-methoxystyrene-*stat*-4-*tert*-butoxystyrene), was used. This was achieved by nitroxide-mediated radical polymerization (NMRP) and a subsequent polymer-analogous introduction of an azide end group. The NMRP copolymers proved to be highly tolerant toward polymer-analogous reactions.

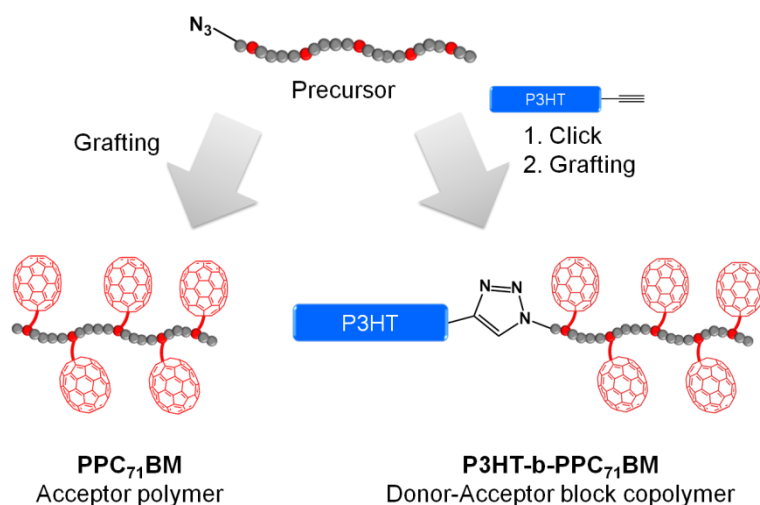
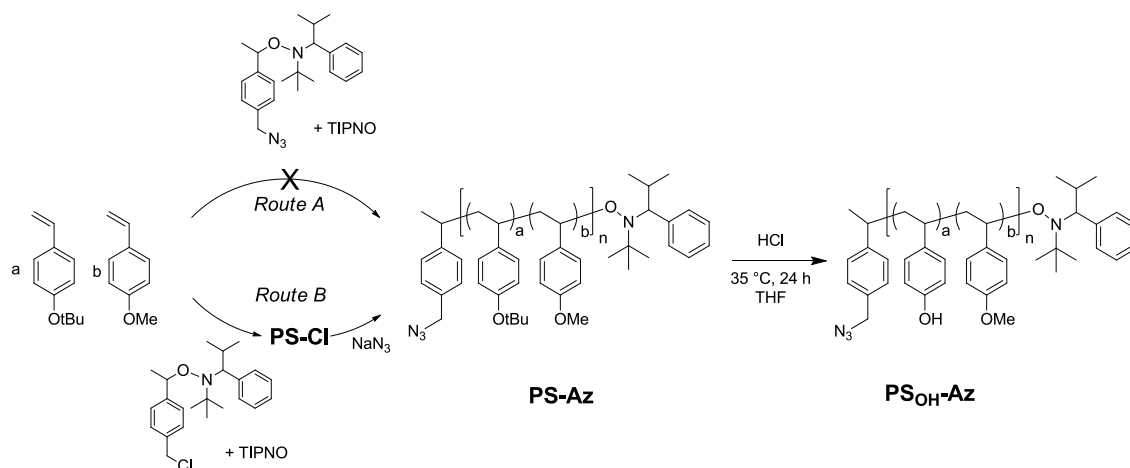


**Figure 1.** Schematic representation of the synthetic strategies toward PC<sub>71</sub>BM-grafted acceptor polymers and donor-acceptor block copolymers.

### Hydroxyl-functionalized polystyrene copolymers with azide end group

We examined two synthetic strategies toward azide terminated copolymers using NMRP (Scheme 1): Route A is intended to introduce the azide group to the copolymer directly through an azide derivatized alkoxyamine initiator. Route B is based on two steps involving the copolymerization with a chloride derivatized initiator and a subsequent polymer-analogous substitution with sodium azide (route B).



**Scheme 1.** Synthesis strategy toward the azide-terminated precursor copolymer poly(4-methoxystyrene-*stat*-4-hydroxystyrene). Introduction of the azide end group is attempted by two different methods depicted as route A and B. The hydroxyl functionality is achieved by the hydrolysis of the *tert*-butyl ether groups in PS-Az maintaining the azide end group to obtain PS<sub>OH</sub>-Az.

For both routes the feed ratio of 4-*tert*-butoxystyrene (BS) and 4-methoxystyrene (MS) BS:MS was a:b=0.08:0.92 and gave the copolymer poly(4-methoxystyrene-*stat*-4-*tert*-butoxystyrene) (PS) with a built-in ratio of a:b=0.10:0.90, which can be extracted from <sup>1</sup>H-NMR analysis (Figure S1). The particular ratio was selected to realize a ratio of 1:1 w/w of P3HT and PC<sub>71</sub>BM in the final block copolymer which is reported to be optimum for charge separation and transport.<sup>[32]</sup>

In route A, the styrene monomers were copolymerized using the azide-functionalized alkoxyamine initiator 2,2,5-trimethyl-3-(1'-*p*-azidemethylphenylethoxy)-4-phenyl-3-azahexane (Ini-Az) and 2,2,5-trimethyl-4-phenyl-3-azahexane-3-nitroxide (TIPNO) as persistent radical (Scheme 1). The copolymerization was carried out at 125 °C in *o*-dichlorobenzene (DCB) solution. The copolymerization follows a statistical incorporation of the monomers according to the evaluation of samples which were periodically taken during the copolymerization.

Here, the consumption of both monomer species BS and MS proved to be equally fast. This can be deduced from the <sup>1</sup>H-NMR spectra at different polymerization times (*i.e.* conversions), where the ratio of residual monomers in the reaction mixture remains constant (Figure S2). The size-exclusion chromatography (SEC) trace of PS shows a number-averaged molecular weight ( $M_n$ ) of 19.6 kg mol<sup>-1</sup> with a dispersity ( $\mathcal{D}$ ) of 1.19 (Figure 2a). The slightly broad molecular weight distribution results from a shoulder at roughly double molecular weight and can be assigned to a small amount of radical recombina-

tion of polymer chains. To verify the azide end group fidelity Fourier-transform infrared (FTIR) spectroscopy was performed. This analytical method is highly sensitive for the detection of organic azides since the asymmetric vibration of azides is very strong.<sup>[33]</sup> Unlike the azide initiator Ini-Az, the copolymer from route A does not show a distinct azide vibration at  $2095\text{ cm}^{-1}$  (Figure 2b). In the literature it has been proposed that the azide end group of the alkoxyamine initiator can react in an azide-alkene cycloaddition during polymerization with the styrene monomers at  $125\text{ }^{\circ}\text{C}$ .<sup>[34]</sup> This explains the lack of the FTIR azide vibration in the copolymer from route A. Additionally, this is supported by our observation that the polystyrene copolymers from route A did not form any block copolymer using click chemistry.

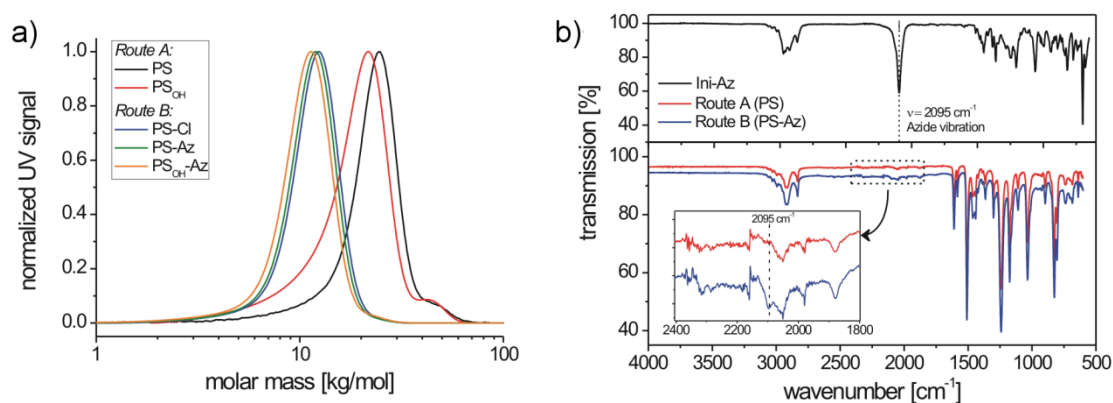


**Figure 2.** SEC traces (a) of the copolymers from route A (PS and PS<sub>OH</sub>) and route B (PS-Cl, PS-Az and PS<sub>OH</sub>-Az) obtained by NMRP. Corresponding FTIR spectra (b) of the copolymers demonstrate the degree of azide end group functionalization

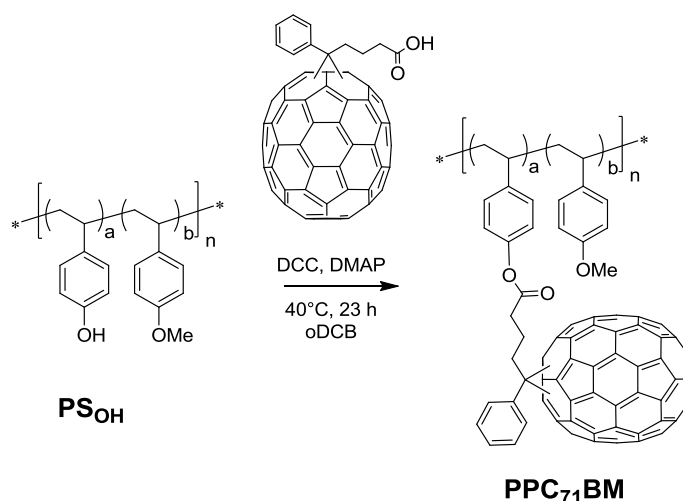
In route B, the copolymerization was performed in bulk in presence of the chlorine-functionalized alkoxyamine initiator 2,2,5-trimethyl-3-(1'-p-chloromethylphenyl-ethoxy)-4-phenyl-3-aza-hexane (Ini-Cl) and TIPNO (Scheme 1). Here also the feed ratio of BS:MS was 0.08:0.92 and copolymerization until 40% conversion gave a chlorine-terminated polystyrene copolymer (PS-Cl) with a built-in ratio of BS:MS=0.10:0.90 (Figure S3). Bulk polymerization improved the copolymerization and no high molecular weight shoulder could be observed in SEC analysis (Figure 2a). This polymerization procedure enables a perfect control of the statistical copolymerization with monomodal molecular weight distribution and very low dispersity of 1.10. PS-Cl has a molecular weight of  $M_n=9.8\text{ kg mol}^{-1}$  (Figure 2a). In a subsequent step, the chloride end group of PS-Cl was replaced in a nucleophilic substitution reaction using excess of sodium azide. The resulting azide-monoterminated copolymer PS-Az has a molecular weight of  $M_n=10.4\text{ kg mol}^{-1}$

and a narrow dispersity of 1.10 (Figure 2a). In contrast to route A, the copolymer PS-Az from route B shows a azide vibration at  $2095\text{ cm}^{-1}$ . As expected the observed signal is weak due to the high dilution of the end group. This indicates a successful end group functionalization with azide *via* the polymer-analogous substitution in route B. Additionally, the FTIR spectra of PS-Cl and PS-Az are compared in Figure S4 which also confirm the successful conversion of the halide to azide.

The next step toward the hydroxyl-functionalized poly(4-methoxystyrene-*stat*-4-hydroxystyrene) precursor copolymer (PS<sub>OH</sub>-Az) is the deprotection of the *tert*-butoxystyrene repeating units. Under acidic conditions with hydrochloric acid at a mild temperature of 35 °C, the cleavage of the *tert*-butylether groups is usually quantitative.<sup>[17]</sup> This was evidenced by <sup>1</sup>H-NMR, where the hydroxyl signal at  $\delta=9.24\text{--}8.84$  ppm indicates a successful hydrolysis of the *tert*-butoxystyrene units (Figure S5). The obtained copolymer PS<sub>OH</sub>-Az exhibit a molecular weight of  $M_n=9.8\text{ kg mol}^{-1}$  and a narrow monomodal distribution with  $D=1.11$  (Figure 2a). The precursor copolymer carries 10 mol% of 4-hydroxystyrene units which can be used for the esterification with PC<sub>71</sub>BA.

### Optimized fullerene grafting with PC<sub>71</sub>BA

To find the optimum conditions for the covalent PC<sub>71</sub>BM fullerene attachment *via* Steglich esterification, we tested the grafting reaction using a hydroxyl-functionalized polystyrene copolymer PS<sub>OH</sub> obtained *via* NMRP having a molecular weight of  $M_n=16.7\text{ kg mol}^{-1}$ ,  $D=1.19$  and containing 10 mol% hydroxystyrene. As fullerene derivative we synthesized the monofunctional reactant phenyl-C<sub>71</sub>-butyric acid (PC<sub>71</sub>BA) by hydrolysis of the commercially available phenyl-C<sub>71</sub>-butyric acid methyl ester (PC<sub>71</sub>BM) in analogy to a protocol from Hummelen *et al.*<sup>[26]</sup> Generally, toxic solvents such as carbon disulfide (CS<sub>2</sub>) are used for reactions involving PC<sub>61</sub>BA. Owing to the increased solubility of PC<sub>71</sub>BA ( $1.48\text{ mg mL}^{-1}$ ) compared to PC<sub>61</sub>BA ( $0.38\text{ mg mL}^{-1}$ ), we were able to avoid CS<sub>2</sub>. Even then the grafting yield was very high (Scheme 2). The esterification of PS<sub>OH</sub> was carried out in DCB at 40 °C for 23 h in presence of an excess of PC<sub>71</sub>BA (2 equivalents with respect to the hydroxyl groups) and *N,N'*-dicyclohexylcarbodiimide (DCC) and 4-dimethylaminopyridine (DMAP).



**Scheme 2.** Monofunctional grafting of the precursor copolymer PS<sub>OH</sub> via Steglich esterification with PC<sub>71</sub>BA.

The crude product was purified by an extensive procedure to guarantee that only covalently bound fullerenes remain in the product (see experimental part). The low molecular weight fullerene side products (*e.g.* *N*-acyl urea derivatives) were removed by several precipitation cycles into mixtures of methanol:toluene (1:2, v:v). Purity of the PC<sub>71</sub>BM-grafted copolymer PPC<sub>71</sub>BM was monitored by thin layer chromatography (TLC), where the small molecules impurities appear as distinct spots. Further, the <sup>1</sup>H-NMR spectrum (Figure S6) verifies the purity of PPC<sub>71</sub>BM, since any low-molecular weight fullerene impurity would appear as sharp multiplets in the spectrum. The obtained polymer PPC<sub>71</sub>BM is well-soluble in chlorinated solvents such as chloroform, chlorobenzene and DCB. The grafted product was further analyzed using <sup>1</sup>H-NMR to verify the grafting reaction. The <sup>1</sup>H-NMR spectrum of PPC<sub>71</sub>BM clearly supports a successful grafting reaction since all relevant resonances belonging to the polymer and the pendant fullerenes are present in the product (Figure S6). The multiplets of the methylene protons of the pendant PC<sub>71</sub>BM appear as strongly broadened signals indicating a successful covalent linkage to the polymer backbone. SEC analysis in chloroform as eluent shows a molecular weight of  $M_n=20.8 \text{ kg mol}^{-1}$  and a relatively narrow distribution with  $D=1.27$  (Figure S7). Note that there is no polymer crosslinking observed in the SEC trace, there is only the shoulder at higher molecular weight which was already present in the precursor PS<sub>OH</sub>. The peak maximum in SEC increased from  $21.7 \text{ kg mol}^{-1}$  for PS<sub>OH</sub> to  $26.3 \text{ kg mol}^{-1}$  for PPC<sub>71</sub>BM. It is typical for fullerene polymers that the effective molecular weight is underestimated in SEC most probably due to strong intrachain interactions between the pendant fullerene moieties.<sup>[15]</sup>

To quantify the extent of fullerene grafting, we favor matrix assisted laser desorption ionization mass spectrometry with time of flight detection (MALDI-TOF MS) as a very reliable method.<sup>[17]</sup> The mass spectra of the precursor copolymer PS<sub>OH</sub> and the grafted copolymer PPC<sub>71</sub>BM are depicted in Figure 3a. Here, the esterification leads to a significant mass increase of the copolymer due to the pendant fullerenes from  $M_p=24.4 \text{ kg mol}^{-1}$  for PS<sub>OH</sub> to  $M_p=42.4 \text{ kg mol}^{-1}$  for PPC<sub>71</sub>BM.  $M_p$  denotes the peak maximum of the molar mass distribution curve. The resulting mass increase,  $\Delta M$  is  $18.0 \text{ kg mol}^{-1}$  and this corresponds to the amount of attached PC<sub>71</sub>BA per polymer chain. From  $M_p$  of PS<sub>OH</sub> we can further estimate the average degree of polymerization, which is 181 repeating units per chain. Since the copolymer PS<sub>OH</sub> contains 10 mol% hydroxystyrene, the number of hydroxyl groups is 18 units on an average. Therefore, a maximum of 18 PC<sub>71</sub>BA moieties ( $M=1016.99 \text{ g mol}^{-1}$ ) can be grafted per chain which corresponds to a theoretical mass increase of  $18.3 \text{ kg mol}^{-1}$ . From this, we deduce that the efficiency of grafting is almost quantitative (98%) and yields a copolymer with 42 wt% of pendant PC<sub>71</sub>BM.

Thermogravimetric analysis (TGA) of the polymers PS<sub>OH</sub> and PPC<sub>71</sub>BM fully supports these findings (Figure 3b). Whereas the precursor copolymer PS<sub>OH</sub> is decomposed almost completely in nitrogen, the fullerene-grafted PPC<sub>71</sub>BM shows a significant amount of residual char. This residue corresponds to the C<sub>70</sub> fullerene core which is thermally very stable and does not decompose until 800 °C. Thus, we can roughly estimate the fullerene weight content of PPC<sub>71</sub>BM as 49 wt%. This is in very good agreement with the MALDI-TOF MS result since the content of PCBM in TGA is usually overestimated likely due to incomplete decomposition.<sup>[17]</sup>

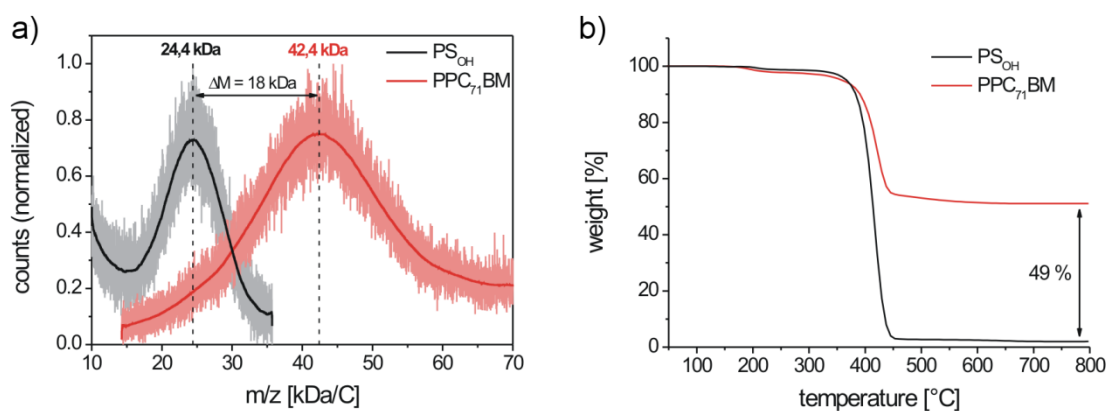


**Figure 3.** Determination of the PC<sub>71</sub>BM content in PPC<sub>71</sub>BM by (a) MALDI-TOF mass spectrometry and (b) by thermogravimetric analysis in nitrogen atmosphere.

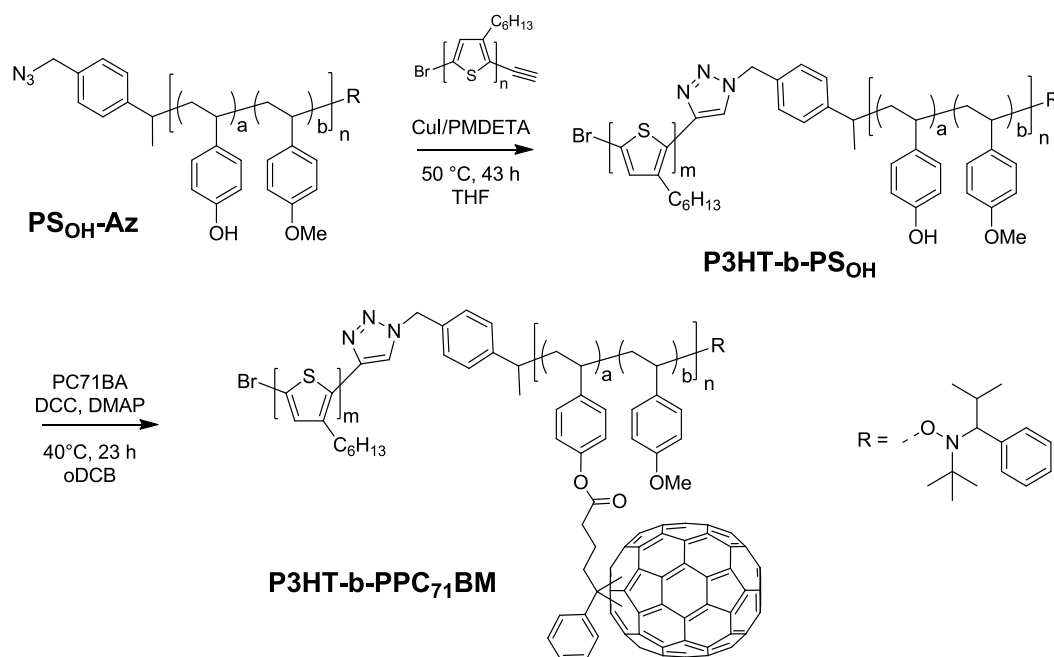
The optical absorption of PPC<sub>71</sub>BM ranges from the UV region up to 650 nm and hence, it has improved light harvesting capability with respect to optical density and wavelength range compared to the known C<sub>60</sub> fullerene polymers. This was confirmed by UV-vis spectroscopy in solution (Figure S8).

Since PC<sub>71</sub>BM is a crystalline material, we were also interested to know if the covalent attachment of these fullerene moieties to the copolymer backbone influences the crystallization or not. X-ray diffraction of a powder sample prepared by slow evaporation of a solution of PPC<sub>71</sub>BM in DCB confirmed the absence of any fullerene crystallites showing only an amorphous scattering signal (Figure S9). This is very similar to the observation of amorphous states in PPC<sub>61</sub>BM polymers.<sup>[17]</sup> This is also an important aspect regarding structure formation in block copolymers comprising a PPC<sub>71</sub>BM block, because a too strong fullerene interaction may disturb the self-assembly of the block copolymer, which is not the case here.

### **Synthesis and characterization of the donor-acceptor block copolymer with pendant PC<sub>71</sub>BM**

The target block copolymer was obtained by a polymer-polymer click reaction followed by the grafting of PC<sub>71</sub>BM on to the PS backbone. For the click reaction, ethynyl-terminated P3HT having an average molecular weight of  $M_n=19.2 \text{ kg mol}^{-1}$  (SEC) and a narrow dispersity of 1.11 (Figure 4a) and the PS<sub>OH</sub>-Az with  $9.8 \text{ kg mol}^{-1}$  and dispersity of 1.11 were used. P3HT with a molecular weight  $M_n$  around  $20 \text{ kg mol}^{-1}$  (SEC) exhibits optimum charge transport<sup>[35]</sup> and can promote phase separation in block copolymers due to its high degree of polymerization.<sup>[14]</sup> The copolymer PS<sub>OH</sub>-Az contains 10 repeating units 4-hydroxystyrene and therefore can be grafted with up to  $10 \text{ kg mol}^{-1}$  PC<sub>71</sub>BM. This yields roughly equal amounts of donor and acceptor compound in the final block copolymer, which is in analogy to the ratio typically used in blend solar cell devices.<sup>[32]</sup>

The CuAAC reaction was carried out with ethynyl-terminated P3HT and three equivalents of azide-terminated PS<sub>OH</sub>-Az in presence of copper(I) iodide/*N,N,N',N',N''*-pentamethyl-diethylenetriamine (PMDETA) as catalyst (Scheme 3). The precursor PS<sub>OH</sub>-Az was used in excess, since it can be separated easily from the block copolymer afterwards by precipitation into a mixture of methanol:acetone (2:1/v:v). We monitored the progress of block copolymer formation by SEC and stopped the reaction after 43 hours, when no further consumption P3HT could be observed.



**Scheme 3.** Synthesis route of the donor-acceptor block copolymer P3HT-b-PPC<sub>71</sub>BM via polymer-polymer click chemistry and Steglich esterification with PC<sub>71</sub>BA.

From the SEC traces shown in Figure 4 it is obvious that the polymer-polymer click reaction was successful resulting in diblock copolymer P3HT-b-PS<sub>OH</sub> with an average molecular weight  $M_n$  of 26.3 kg mol<sup>-1</sup> and  $D=1.35$ . The broad dispersity can be accounted for by taking into consideration the residual P3HT homopolymer observed as a shoulder in the SEC trace (Figure 4a). This can either be attributed to an incomplete click reaction and/or an insufficient ethynyl functionalization of P3HT. The small shoulder at higher molecular weight of the block copolymer SEC trace might be due to aggregation effects in SEC.

The composition of the block copolymer P3HT-b-PS<sub>OH</sub> can be deduced from the individual blocks that were analyzed by MALDI-TOF MS (Figure S10). Here, the mass spectrum of P3HT shows a major peak series corresponding to the ethynyl-P3HT (Figure S10a) with a  $M_p$  of 12.4 kg mol<sup>-1</sup> which equals to 74 hexylthiophene repeating units (RU). The mass spectrum of PS<sub>OH</sub>-Az (Figure S10b) shows an  $M_p$  of 13.4 kg mol<sup>-1</sup> which corresponds to 98 repeating units in the copolymer. Thus, for P3HT-b-PS<sub>OH</sub> we can expect a peak molecular weight of 25.8 kg mol<sup>-1</sup>. Exactly this molecular weight is found for the P3HT-b-PS<sub>OH</sub> block copolymer (25.9 kg mol<sup>-1</sup>). Therefore, the MALDI-TOF mass spectra analysis unambiguously proves the success of the polymer-polymer click reaction (Figure S10c).

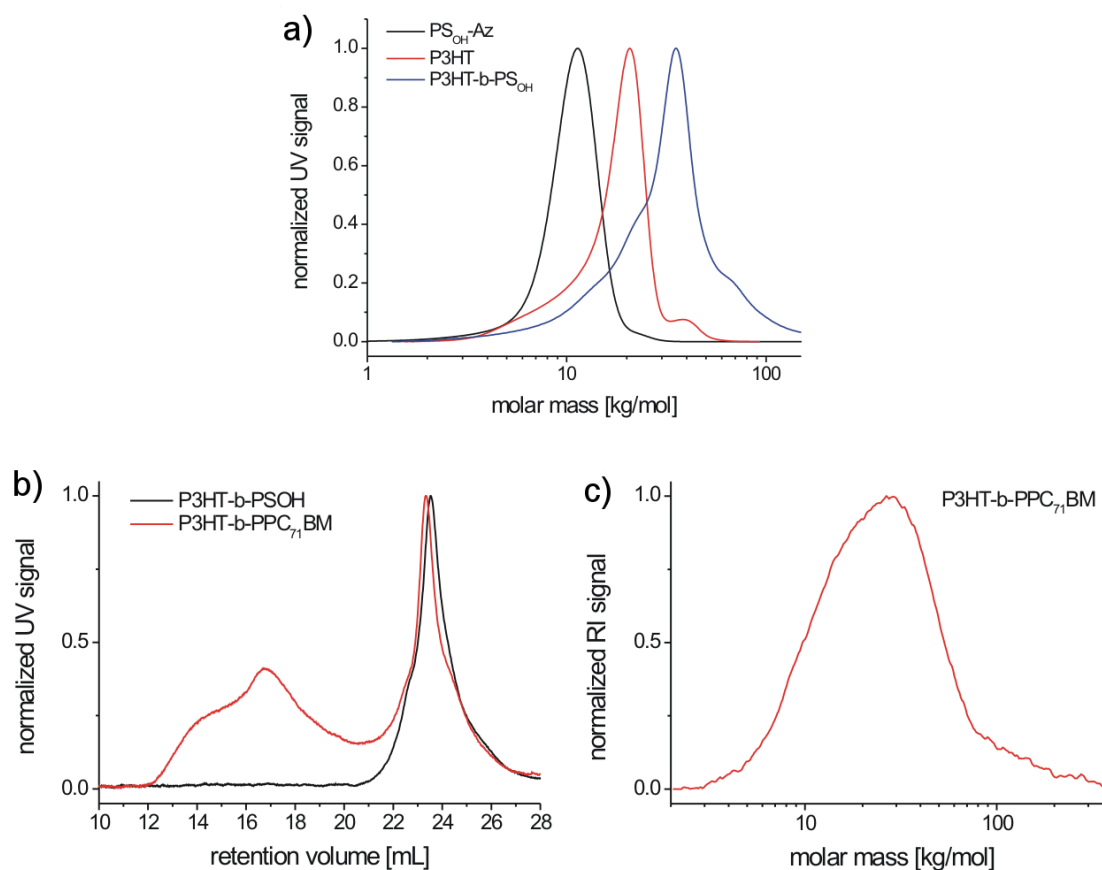


**Figure 4.** SEC traces of (a) the polymer-polymer coupling by click chemistry (THF, UV detector). Analysis of the block copolymer P3HT-*b*-PS<sub>OH</sub> and P3HT-*b*-PPC<sub>71</sub>BM via SEC in chloroform (b) and SEC in 1,2,4-trichlorobenzene at 150 °C for P3HT-*b*-PPC<sub>71</sub>BM (c).

**Table 1.** Experimentally determined molecular weight data of the block copolymers and its contributing polymer blocks.

Polymer	SEC		MALDI <sup>c)</sup>	DP	
	$M_n$ [kg mol <sup>-1</sup> ]	$D$	$M_p$ <sup>d)</sup> [kg mol <sup>-1</sup> ]	$m$	$n$
PS <sub>OH</sub> -Az <sup>a)</sup>	9.8	1.11	13.4	-	98 <sup>f)</sup>
P3HT-alkyne <sup>a)</sup>	19.2	1.11	12.4	74 <sup>g)</sup>	-
P3HT- <i>b</i> -PS <sub>OH</sub> <sup>a)</sup>	26.3	1.35	25.9	74 <sup>h)</sup>	103 <sup>h)</sup>
P3HT- <i>b</i> -PPC <sub>71</sub> BM <sup>b)</sup>	27.5	1.31	31.5 <sup>e)</sup>	74 <sup>h)</sup>	102 <sup>h)</sup>

<sup>a)</sup> SEC in tetrahydrofuran as eluent, UV (254 nm) detector, polystyrene calibration. <sup>b)</sup> SEC in chloroform as eluent, UV (254 nm) detector, polystyrene calibration excluding the aggregation region. <sup>c)</sup> Matrix-assisted laser desorption/ionization mass spectrometry with time of flight detection. <sup>d)</sup>  $M_p$  is the peak maximum of the molecular weight distribution curve. <sup>e)</sup>  $M_p$  determined from very broad mass distribution. <sup>f)</sup> Degree of polymerization (DP) determined from  $M_p$  of MALDI-TOF mass spectrum. <sup>g)</sup> DP determined from  $M_n = 12.3$  kg mol<sup>-1</sup> of MALDI-TOF MS. <sup>h)</sup> DP determined from <sup>1</sup>H-NMR spectrum.

To summarize, P3HT-*b*-PS<sub>OH</sub> in average contains 74 RU of hexylthiophene and 98 RU of styrene moieties (Table 1). Taking the composition of the PS<sub>OH</sub> block (a:b=0.10:0.90) into consideration a total number of ten 4-hydroxystyrene (HS) units per block copolymer chain is present. The composition of the block copolymer P3HT-*b*-PS<sub>OH</sub> was also verified using <sup>1</sup>H-NMR analysis. We can find all relevant proton resonances in the <sup>1</sup>H-NMR spectrum of P3HT-*b*-PS<sub>OH</sub> (Figure S11). From the integral ratio of the thiophene proton singlet at  $\delta=7.37$  ppm and the broad phenyl proton multiplet at  $\delta=7.11$ -6.52 ppm we calculated a composition of P3HT-*b*-PS<sub>OH</sub> of m:n=74:103 repeating units. Thus, the composition of the block copolymers deduced from NMR is in very good agreement with the MALDI-TOF MS data for the individual polymer blocks.

In the final step of polymer-analogous grafting we attached PC<sub>71</sub>BA to P3HT-*b*-PS<sub>OH</sub> by Steglich esterification. Similar reaction conditions using DCC and DMAP in dichlorobenzene as for PPC<sub>71</sub>BM was used here. The applied amount of PC<sub>71</sub>BA with respect to hydroxyl groups in P3HT-*b*-PS<sub>OH</sub> was adjusted to approximately 2.5 equivalents to obtain a high degree of grafting. The product was extensively purified by several precipitations into methanol:toluene (1:1, v:v) and pure methanol. The removal of small molecule fullerene side products was thoroughly monitored *via* TLC. Furthermore, the absence multiplet resonances for fullerene side products is supported by <sup>1</sup>H-NMR in deuterated DCB (Figure S12). This NMR solvent turned out to give most reasonable spectra because aggregation of the P3HT-*b*-PPC<sub>71</sub>BM in chloroform is also a challenging problem for NMR analysis. The spectrum exhibits all the expected signals corresponding to both P3HT and PPC<sub>71</sub>BM blocks. Comparing the ratio of the thiophene proton at  $\delta=7.36$  ppm (1H) with the phenyl protons of the polystyrene block at  $\delta=7.09$ -6.51 ppm (4H) we obtain a ratio of repeating units of P3HT and polystyrene of m:n=74:102, which is very close to the expected ratio of 74:98 from MALDI-TOF MS analysis. The pendant fullerene proton resonances are rather weak in the aromatic region at  $\delta=7.94$ -7.86 ppm and  $\delta=7.70$ -7.46 ppm and, additionally, strongly overlap in case of the methylene resonances.

A significant tendency of P3HT-*b*-PPC<sub>71</sub>BM toward aggregation in chloroform is observed in the SEC eluogram in Figure 4b. While P3HT-*b*-PS<sub>OH</sub> exhibits a rather narrow and monomodal eluogram, P3HT-*b*-PPC<sub>71</sub>BM is characterized by a sharp peak at 23.34 mL corresponding to the fully dissolved block copolymer and a huge amount of aggregates at very low retention volumes. The aggregation can be suppressed at elevated

temperature and by changing the eluent, which is demonstrated by high-temperature SEC in 1,2,4-trichlorobenzene at 150 °C (Figure 4c). Here, the SEC trace shows a monomodal mass distribution in the expected mass range. Using a polystyrene calibration, the molecular weights of P3HT-b-PS<sub>OH</sub> and P3HT-b-PPC<sub>71</sub>BM correspond to  $M_n=26.3 \text{ kg mol}^{-1}$  ( $M_p=34.3 \text{ kg mol}^{-1}$ ) and  $M_n=27.5 \text{ kg mol}^{-1}$  ( $M_p=36.6 \text{ kg mol}^{-1}$ ) respectively (Table 1). This expected marginal molecular weight shift in SEC is in full agreement with the contractile effects of fullerene polymers (see also PPC<sub>71</sub>BM).

To quantify the exact composition of the donor-acceptor block copolymer P3HT-b-PPC<sub>71</sub>BM we applied UV-vis spectroscopy in solution and MALDI-TOF MS. The mass spectrum of P3HT-b-PPC<sub>71</sub>BM in Figure S10c, however, is not suited to derive a clear composition of donor and acceptor blocks. Here, not only a shift toward higher molecular weight indicating a covalent grafting with PC<sub>71</sub>BA, but also a broadening of the mass distribution is observed.

A very useful method for the estimation of the PC<sub>71</sub>BM content is UV-vis spectroscopy. It is possible to calculate the content of a chromophore in polymers by comparing the extinction coefficients of polymer and the pure chromophore as reference in dilute solutions.<sup>[17,36]</sup> To determine the PC<sub>71</sub>BM content, we use the extinction coefficients of PC<sub>71</sub>BM and P3HT-b-PPC<sub>71</sub>BM at 274 nm (Figure 5a), at which PC<sub>71</sub>BM shows a shoulder with high optical density. For the calculation, the residual absorption of polystyrene and P3HT at this wavelength was subtracted. Details regarding the exact calculation of the PC<sub>71</sub>BM content in the block copolymer are given in the Supporting Information. According to our calculation, the block copolymer P3HT-b-PPC<sub>71</sub>BM contains 24 wt% of PC<sub>71</sub>BM. Taking into consideration the MALDI TOF MS value of P3HT, a composition of P3HT to PC<sub>71</sub>BM was obtained as 1:0.86. The maximum possible theoretical content of PC<sub>71</sub>BM can be estimated based on the MALDI molecular weights of the individual polymer blocks (12.4 kg mol<sup>-1</sup> for P3HT, 13.4 kg mol<sup>-1</sup> for PS<sub>OH</sub>) and the maximum possible grafting which is supposed to be ten PC<sub>71</sub>BM units per polymer chain with a total weight of 10.17 kg mol<sup>-1</sup>. This results in a theoretical PC<sub>71</sub>BM content of 28 wt%. Comparing the theoretical PC<sub>71</sub>BM content of 28 wt% in P3HT-b-PPC<sub>71</sub>BM with the experimental value of 24 wt% from UV-vis, we can conclude a very high grafting efficiency of 86 %.

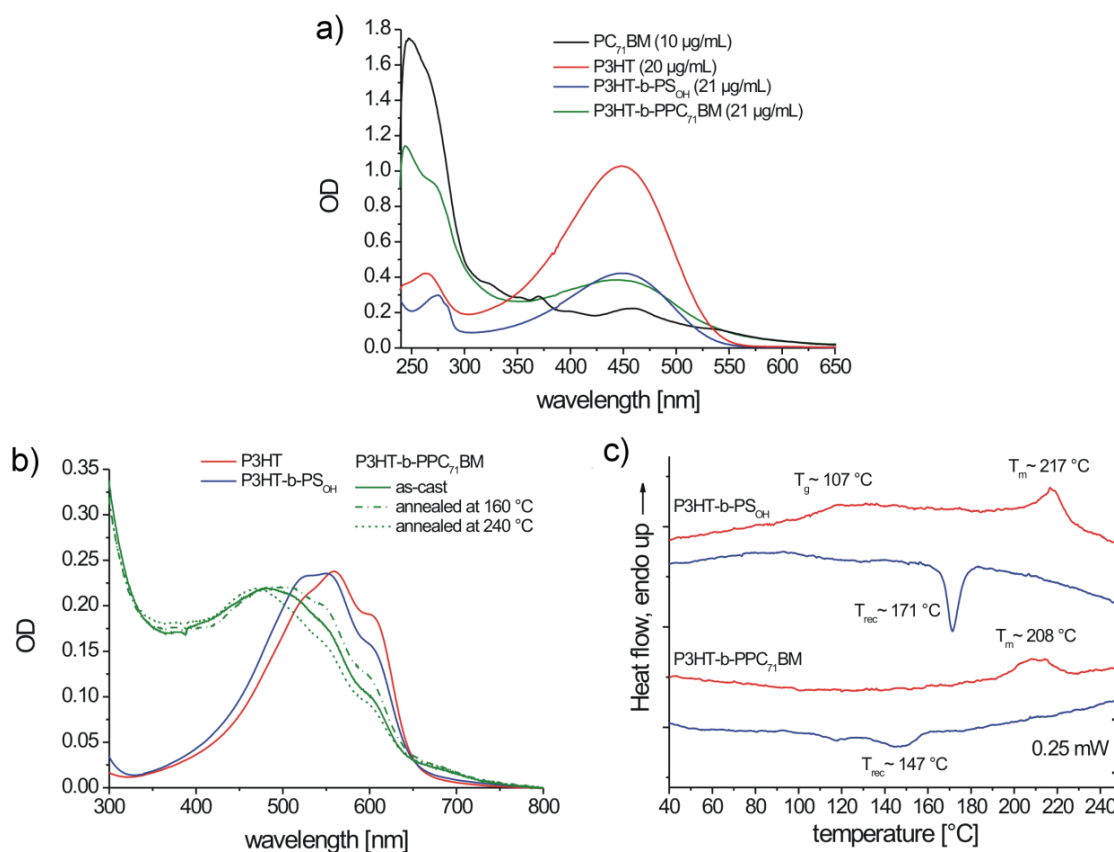


**Figure 5.** UV-vis absorption spectra (a) taken from solutions in chloroform. The spectra of PC<sub>71</sub>BM and P3HT are given as reference and for the determination of the mass fractions of P3HT and PC<sub>71</sub>BM incorporated in the block copolymers. UV-vis spectra of thin films (b) after spin-coating (solid lines) and for P3HT-b-PPC<sub>71</sub>BM additionally after thermal annealing for 2 hours at 160 °C (dash-dot) and after annealing at 240 °C with a subsequent cooling rate of approximately 10 K/min (short dash). Differential scanning calorimetry traces (c) of the block copolymers P3HT-b-PS<sub>OH</sub> and P3HT-b-PPC<sub>71</sub>BM. The DSC traces for the heating cycles are red and blue for the cooling cycles.

UV-Vis absorption studies of thin films allow for a qualitative estimation of the crystallization of P3HT (Fig. 5b). The neat P3HT shows distinct absorption bands at about 520, 560 and 605 nm which are ascribed to the formation of weak *H*-aggregates in crystals.<sup>[37]</sup> Whereas the amorphous P3HT phase exhibits a non-structured absorption band with a peak maximum at 450 nm. Both the block copolymers P3HT-b-PS<sub>OH</sub> and P3HT-b-PPC<sub>71</sub>BM exhibit the typical absorptions bands relevant for aggregates or crystallites, but the relative intensities of the aggregate bands are lower compared to that of neat P3HT. On annealing P3HT-b-PPC<sub>71</sub>BM at 160 °C for 2 hours the aggregate bands appear more pronounced. On the other hand, heating the sample just above the melting point of P3HT (240 °C) and cooling at 10 K min<sup>-1</sup> (similar to DSC cooling scan) there is a reduction of

intensity of the aggregate bands. This clearly indicates that appropriate annealing procedures need to be developed for the crystallization of P3HT in the block copolymers.

Differential scanning calorimetry (DSC) confirms that P3HT-*b*-PS<sub>OH</sub> contains a crystalline P3HT block with a peak melting temperature at 217 °C and a melting enthalpy of 4.6 J g<sup>-1</sup> (Figure 5c). Further, the amorphous polystyrene block exhibits a glass transition  $T_g$  at around 107 °C. For P3HT-*b*-PPC<sub>71</sub>BM we observe notably broadened peaks showing a melting of P3HT around 211 °C with an enthalpy of 2.3 J g<sup>-1</sup>. No  $T_g$  for the PC<sub>71</sub>BM-grafted polystyrene was observed. The glass transition in such fullerene-grafted polystyrenes is typically shifted toward higher temperature and often shows a strong broadening.<sup>[17,38]</sup>

To get an estimation on the crystallinity of the P3HT segment in the block copolymers, we compared the melting enthalpies with that of neat P3HT, which melts at 230 °C with an enthalpy of 15.1 J g<sup>-1</sup>. Considering the weight fractions of P3HT in P3HT-*b*-PS<sub>OH</sub> and P3HT-*b*-PPC<sub>71</sub>BM which are 39 wt% and 28 wt% according to UV-Vis in solution, we expect a melting enthalpy of 5.9 and 4.2 J g<sup>-1</sup> if the same degree of crystallinity as in P3HT homopolymer is maintained. The experimentally determined melting enthalpies of 4.6 and 2.3 J g<sup>-1</sup> are lower and thus indicate a decreased crystallinity of P3HT in both block copolymers as determined in DSC measurements. Since DSC scans are carried out too fast and therefore do not allow for the full crystallization in confined geometries, it is quite natural that the measured  $\Delta H_m$  values are lower than those expected for the same degree of crystallinity as a homopolymer. This is also in agreement with the varying degree of aggregation depending on annealing conditions observed in UV-vis absorption studies in thin films.

### Structural analysis by X-ray scattering and scanning electron microscopy

Structure formation of the donor-acceptor block copolymer P3HT-*b*-PPC<sub>71</sub>BM was investigated using temperature-dependent small-angle X-ray scattering (SAXS) in bulk samples. The morphology of thin films was characterized by scanning electron microscopy (SEM) and grazing-incidence small angle X-ray scattering (GISAXS). Figure 6 shows small angle x-ray scattering data obtained from bulk samples of P3HT-*b*-PPC<sub>71</sub>BM as measured at 240 °C in the melt state and at room temperature at which P3HT is in a crystalline state.

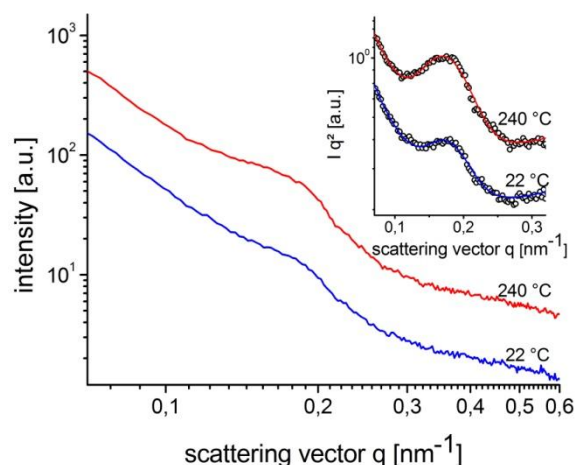


**Figure 6.** SAXS intensity of P3HT-b-PPC<sub>71</sub>BM at room temperature (blue) and at 240 °C in the melt (red). The inset shows the same data after Lorentz correction with a fit to a model function consisting of a power law background and a Gaussian.

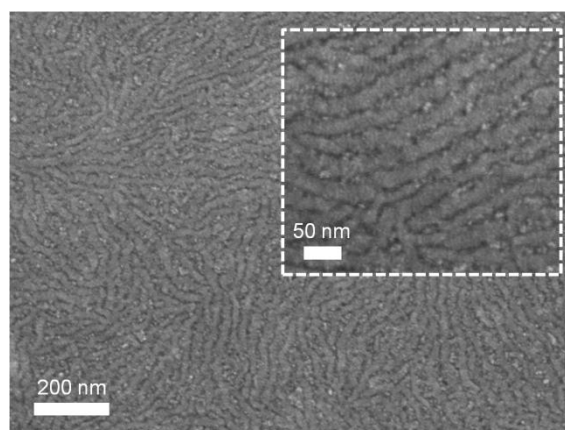


**Figure 7.** Scanning electron microscope image of P3HT-b-PPC<sub>71</sub>BM prepared by drop-casting of a 2 wt% dichlorobenzene solution. The inset shows a magnified section of the film.

Both scattering curves show a peak in the SAXS range indicating a periodic nanostructure with a periodicity  $d$  of about 37 nm at room temperature ( $d = 2\pi/q_0$ ,  $q = 0.168 \text{ nm}^{-1}$  at room temperature,  $q = 0.16 \text{ nm}^{-1}$  at 240 °C). The fact that the peak is almost unchanged after cooling to room temperature, *i.e.* after crystallization of the P3HT component, suggests that the nanostructure is already caused by a liquid-liquid phase separation in the melt.<sup>[14]</sup> The weak signal and missing higher order peaks prevent a more detailed analysis of the structure based on X-ray scattering alone. The SEM image shown in Figure 7 suggests indeed an ordered nanostructure at room temperature of probably cylindrical symmetry. Additionally, there is no indication for the presence of big fullerene aggregates or crystallites. The ordered nanostructure observed in SEM is also consistent with results obtained by GISAXS experiments of thin films as shown in Figure 8 which show a clear peak indicating a periodic lateral structure within the films. Figure 8a,b show the corresponding scattering pattern measured in grazing incidence geometry at room temperature for films prepared by drop-casting (Fig. 8a) and by spin-coating with subsequent annealing in the melt (Fig. 8b) respectively. The peak positions in the corresponding horizontal profiles (Fig. 8c) were determined to be  $q = 0.146 \text{ nm}^{-1}$  ( $d \approx 43 \text{ nm}$ ) for the melt crystallized sample and  $q = 0.156 \text{ nm}^{-1}$  ( $d \approx 40 \text{ nm}$ ) for the drop cast film. Again the peak positions were determined using an empirical model function consisting of a power law background and a Gaussian to describe the peak (see Supporting Information). Varia-

tion of the fitting parameters revealed an uncertainty of about  $0.005 \text{ nm}^{-1}$  for the peak position. We attribute the small difference in the peak position between the melt crystallized sample and the drop casted film to solvent remaining in the drop casted film which mediates the incompatibility between both blocks and leads to a smaller structure size.<sup>[39]</sup> Both samples have the peak at a similar position as the bulk samples indicating that the bulk morphology is largely preserved in thin films. In detail the peak positions in SAXS and GISAXS measurements show a deviation of about 10% probably due to either calibration errors or confinement effects.

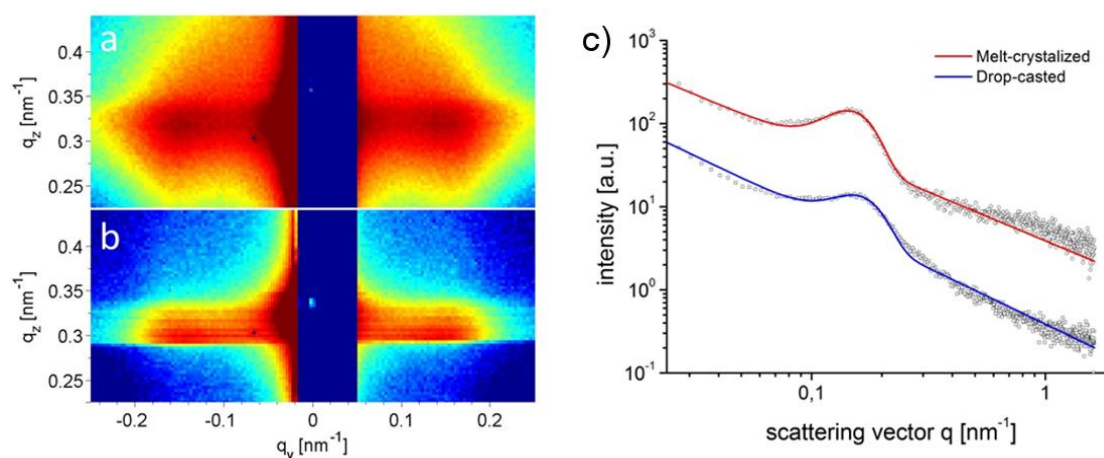


**Figure 8.** 2D-GISAXS data of P3HT-*b*-PPC<sub>71</sub>BM around the Yoneda position at room temperature of films prepared by (a) drop-casting and (b) spin-coating with subsequent annealing in the melt. Data in (a) and (b) are displayed on a logarithmic intensity scale. The Yoneda region appears at slightly different nominal  $q_z$  values due to a somewhat different angle of incidence. The horizontal intensity profiles of these samples, taken along the Yoneda position, are shown in (c) together with an empirical fit. The peak indicates a periodic nanostructure which is consistent with bulk data (data set of melt crystallized sample vertically shifted).

The aggregation of fullerene moieties was earlier reported to impede the self-assembly of fullerene-grafted block copolymers into a well-defined nanostructured morphology.<sup>[28]</sup> However, the presented block copolymer P3HT-*b*-PPC<sub>71</sub>BM does not show an aggregation of fullerene moieties. Our observation is further supported by reports of Miyanishi *et al.*<sup>[22,40]</sup> and Lee *et al.*<sup>[25]</sup> who also utilized a monofunctionalized fullerene for grafting. In the former, a crystallization driven self-assembly of the fullerene-grafted poly(3-alkylthiophene) block copolymers is suggested to result in a fibril-like surface morphology in thin films. In the latter, phase separation of P3HT-*b*-poly(acrylate) with pendant PC<sub>61</sub>BM was studied using TEM which indicated phase separation in the range of 10–

20 nm. Our findings based on GISAXS and temperature-dependent SAXS clearly show an ordered nanostructure in thin films as well as in the bulk phase of P3HT-b-PPC<sub>71</sub>BM.

## CONCLUSIONS

We demonstrated an elegant synthetic route toward PC<sub>71</sub>BM-grafted donor-acceptor block copolymers for the first time using polymer-polymer click chemistry between two tailored polymer blocks followed by a polymer-analogous fullerene grafting. PC<sub>71</sub>BM grafting was achieved from easily accessible C<sub>70</sub> carboxylic acid. The covalent incorporation of PC<sub>71</sub>BM was achieved in very high yields and it improves the optical properties of the block copolymer notably. The donor-acceptor block copolymer shows an ordered morphology on the nanoscale in bulk and in thin films independent of the processing method, *i.e.* from solution or by melt crystallization. Further, SAXS and GISAXS structural analysis correlates with the domain size observed in SEM. This pioneering work in the field of PC<sub>71</sub>BM-grafted block copolymers opens new perspectives towards the realization of further fullerene-grafted donor-acceptor block copolymers exploiting the full range of block copolymer morphologies.

## EXPERIMENTAL

### Materials

The reagents for the following synthetic procedures were purchased from Sigma-Aldrich and used as received, if not stated otherwise. Phenyl-C<sub>71</sub>-butyric acid methyl ester (PC<sub>71</sub>BM, purity 99 %) was purchased from American Dye Source (Canada). Solvents were either distilled at atmospheric pressure utilizing appropriate desiccants or purchased in p.a. (pro analysi) grade. Commercially available anhydrous solvents were purchased from Sigma Aldrich and Acros in sealed bottles with mole sieve. Prior to polymerization, 4-methoxystyrene (MS) and 4-tert-butoxystyrene (BS) were passed through a column of basic alumina to remove the inhibitor and stored at -18°C. 2,2,5-trimethyl-4-phenyl-3-azahexane-3-nitroxide, 2,2,5-trimethyl-3-(1'-*p*-chloromethylphenylethoxy)-4-phenyl-3-azahexane and 2,2,5-trimethyl-3-(1'-*p*-azidomethyl-phenylethoxy)-4-phenyl-3-azahexane were synthesized according to the literature.<sup>[41,42]</sup> Ethynyl-terminated poly(3-hexylthiophene) was prepared by Kumada catalyst transfer polymerization followed by end-capping with ethynylmagnesium chloride.<sup>[31]</sup> The stock solution of 0.07 M copper(I)

iodide/PMDETA catalyst in tetrahydrofuran was prepared according to a literature procedure<sup>[43]</sup>.

### Instrumentation

<sup>1</sup>H-NMR spectra were measured with a Bruker Avance AC250 spectrometer at 300 MHz. The obtained spectra were calibrated to the corresponding residual solvent peak (CDCl<sub>3</sub>  $\delta$ =7.26 ppm, DMSO-D<sub>6</sub>  $\delta$ =2.50 ppm). Ultraviolet-visible (UV-Vis) spectra from solutions were recorded on a Hitachi U-3000 spectrophotometer using quartz cuvettes with a path length of 1 cm. UV-vis studies of thin films were carried out on a Hitachi U-3000 spectrophotometer and a JASCO Spectrophotometer V-670. The films were prepared by spin-coating from 2 wt% chlorobenzene solution (P3HT and P3HT-b-PS<sub>OH</sub>) or 2.5 wt% 1,2-dichlorobenzene solution (P3HT-b-PPC<sub>71</sub>BM) on glass substrates. Fourier transform infrared (FTIR) spectra were recorded from solids on a Perkin Elmer Spectrum 100 FTIR spectrometer in attenuated total reflection (ATR) mode. Thermal gravimetry analysis (TGA) experiments were performed under continuous nitrogen stream using a Mettler Toledo TGA/SDTA 851. The measurement range was 30-800 °C with a heating rate of 10 K min<sup>-1</sup>. The determined decomposition temperatures T<sub>dec</sub> are onset temperatures. Size exclusion chromatography (SEC) with stabilized THF as eluent was performed using a Waters 515-HPLC pump at a flow rate of 0.5 mL min<sup>-1</sup>. A guard column (Varian, 50x0.75 cm, ResiPore, particle size 3  $\mu$ m) and two separation columns (Varian, 300x0.75 cm, ResiPore, particle size 3  $\mu$ m) are connected in series with a Waters UV detector at 254 nm and 486 nm. 1,2-dichlorobenzene (DCB) was used as an internal standard. SEC with chloroform as eluent was carried out at 25 °C with a FLOM Intelligent Pump 301 at a flow rate of 0.5 mL min<sup>-1</sup>. A guard column and four separation columns of MZ Analysentechnik with a polystyrene solid phase (particle size 5  $\mu$ m, pore sizes 10<sup>6</sup>, 10<sup>5</sup>, 10<sup>3</sup> and 10<sup>2</sup> Å) are connected in series with a Spectra Series UV150 detector at 254 nm and a Shodex RI-71 detector. Toluene was used as internal standard. High-temperature SEC analysis was carried out on an Agilent (Polymer Laboratories Ltd.) PL-GPC 220 high temperature chromatographic unit equipped with DP, RI and LS (15° and 90°) detectors and three linear mixed bed columns of PLgel 13 micrometer (Olexis) with a linear molecular weight operating range: 500 - 15,000,000 g mol<sup>-1</sup>. SEC analysis was performed at 150 °C using 1,2,4-trichlorobenzene as the mobile phase. All SEC data were calibrated in relation to polystyrene standards.

Matrix assisted laser desorption ionization mass spectroscopy with time of flight detection (MALDI-TOF MS) was performed on a Bruker Reflex III using either dithranol or trans-2-(3-(4-tert-butylphenyl)-2-methyl-2-propenyldene)malononitrile (DCTB) as matrix and, where denoted, silver trifluoroacetate as cationizing salt. Solutions of the analyte, the matrix and the cationizing salt were prepared, mixed in the given ratio and spotted onto the MALDI target plate. P3HT: chloroform, dithranol (10 mg mL<sup>-1</sup>), analyte (0.5 mg mL<sup>-1</sup>), 50:1/v:v. PS<sub>OH</sub>: THF, DCTB (10 mg mL<sup>-1</sup>), analyte (10 mg mL<sup>-1</sup>), AgTFA (10 mg mL<sup>-1</sup>), 20:5:1/v:v:v. P3HT-b-PS<sub>OH</sub>: chloroform, dithranol (10 mg mL<sup>-1</sup>), analyte (5 mg mL<sup>-1</sup>), 10:2/v:v. P3HT-b-PPC<sub>71</sub>BM: chloroform, dithranol (10 mg mL<sup>-1</sup>), analyte (5 mg mL<sup>-1</sup>), 20:2/v:v.

Small angle X-ray scattering experiments in transmission geometry were performed with a laboratory setup consisting of a Rigaku rotating anode, a focusing X-ray optics device (Osmic confocal max flux), and a Bruker 2D-detector (HI-Star). The optics also served as monochromator for Cu K<sub>α</sub> radiation ( $\lambda = 0.154$  nm). Aluminum discs with a central hole of 0.8 mm diameter were used as sample holders. The samples were mounted on a Linkam hotstage for temperature control. Heat conducting paste was used to ensure good thermal contact. Grazing incidence small angle X-ray scattering experiments (GISAXS) were performed at beamline BM 26, DUBBLE, at the ESRF, Grenoble ( $\lambda=0.104$  nm). The monochromatic beam was collimated using an assembly of slits and focused on the detector position. An angle of incidence slightly larger than the critical angle of the polymer film and the silicon substrate was used. Rectangular samples had a typical size of 90-140 mm<sup>2</sup> and were completely illuminated by the beam. 2D scattering patterns were collected using a PILATUS 1M detector. The sample to detector distance was set to 3.07 m. Samples for GISAXS measurements were prepared by spin-coating resp. drop-casting. The spin-coated samples were prepared from a 3 wt% solution in 1,2-dichlorobenzene on silicon substrates at 800 rpm, resulting in a thickness of about 125 nm. After spin-coating the samples were annealed in nitrogen atmosphere for 90 min at 240 °C and slowly cooled down (approximately 5 - 10 K min<sup>-1</sup>). The drop-casted films were prepared from a 3 wt% solution in 1,2-dichlorobenzene, covered with a beaker and dried at room temperature. They had a thickness of about 1.4 μm. The calibration of the SAXS and GISAXS data was performed by comparison with the first order ring of silver behenate measured in transmission.

Scanning electron microscopy (SEM) was performed on a Zeiss LEO 1530 (FE-SEM with Schottky-field-emission cathode; in-lens detector) using an accelerating voltage of 2.0 – 3.0 kV. The samples were prepared by drop-casting from a 2 wt% solution in 1,2-dichlorobenzene on indium-tin oxide coated glass substrates, covered with a beaker and slow drying at room temperature. Spin-casting with quick solvent evaporation and a freezing-in of structures yields shorter structural features. For the SEM measurement the samples were mounted on a standard SEM sample holder by conductive adhesion graphite-pad (Plano) and sputtered with platinum (2 nm using a Cressington HR208 sputter coater and a Cressington mtm20 thickness controller).

### Synthesis procedure of PS

To a dry 10 mL schlenk tube were added 4-methoxystyrene (4.487 g, 33.44 mmol, 410 equ.), 4-tert-butoxystyrene (0.513 g, 2.91 mmol, 36 equ.), 2,2,5-trimethyl-4-phenyl-3-azahexane-3-nitroxide (4 mg, 0.016 mmol, 0.2 equ.) and 2,2,5-trimethyl-3-(1'-p-azidemethylphenylethoxy)-4-phenyl-3-azahexane (31 mg, 0.081 mmol, 1 equ.) and dissolved in 4 mL of dry o-dichlorobenzene. The schlenk tube was sealed with a rubber septum and the reaction mixture was degassed by three freeze, pump and thaw cycles. The polymerization was subsequently started in a preheated oil bath at 125 °C under vigorous stirring. Samples were taken periodically by syringe to monitor the monomer conversion *via*  $^1\text{H-NMR}$  spectroscopy. The polymerization was stopped at a conversion of 44 % after 550 min by quenching the reaction in liquid nitrogen. The resulting polymer was isolated by precipitation of the reaction mixture three times into 600 mL methanol, filtering the white precipitate and drying under vacuum. Yield: 1.679 g of a white precipitate.  $^1\text{H-NMR}$  (300 MHz,  $\text{CDCl}_3$ ,  $\delta$ ): 7.01-6.09 (br m, 4(a+b)·H,  $\text{H}_{\text{phenyl}}$ ), 3.95-3.49 (br s, 3b·H,  $\text{H}_{\text{OMe}}$ ), 2.29-0.97 (br m, 3(a+b)·H,  $\text{H}_{\text{backbone}}$ , 9a·H,  $\text{H}_{\text{OtBu}}$ ). SEC (THF):  $M_n=19.6 \text{ kg mol}^{-1}$ ,  $M_p=24.6 \text{ kg mol}^{-1}$ ,  $M_w/M_n=1.19$ . MALDI:  $M_p=23.5 \text{ kg mol}^{-1}$ .

### Synthesis of $\text{PS}_{\text{OH}}$

A 250 mL round bottom flask was charged with PS (1.601 g) and dissolved in 160 mL THF. 20 mL of concentrated hydrochloric acid (37 wt%) were added slowly to the solution. After purging the reaction mixture with argon for 20 min *via* a glass pipette, it was stirred at 35 °C for 16 h. All volatile components were removed under reduced pressure. The hydrolyzed polymer was isolated by precipitation twice into 500 mL deionized water

and freeze-drying from 1,4-dioxane. Yield: 1.29 g of a white precipitate.  $^1\text{H-NMR}$  (300 MHz,  $\text{DMSO-d}_6$ ,  $\delta$ ): 9.25-8.86 (br s, 1a·H, OH), 7.30-5.93 (br m, 4(a+b)·H,  $\text{H}_{\text{phenyl}}$ ), 3.85-3.45 (br s, 3b·H,  $\text{H}_{\text{OMe}}$ ), 2.25-0.73 (br m, 3(a+b)·H,  $\text{H}_{\text{backbone}}$ ). SEC (THF):  $M_n=16.7 \text{ kg mol}^{-1}$ ,  $M_p=24.6 \text{ kg mol}^{-1}$ ,  $M_w/M_n=1.19$ . MALDI:  $M_p=24.4 \text{ kg mol}^{-1}$ . TGA decomposition  $T_{\text{dec}}=389 \text{ }^\circ\text{C}$ .

### Synthesis of PPC<sub>71</sub>BM

A 250 ml schlenk flask was flame dried at 600 °C under high vacuum prior. It was charged with  $\text{PS}_{\text{OH}}$  (165 mg, 0.124 mmol hydroxy groups, 1 equ.), phenyl-C71-butyric acid (250 mg, 0.246 mmol, 2 equ.), and 4-dimethylaminopyridine (49 mg, 0.401 mmol, 3.2 equ.). The flask was degassed under high vacuum and backfilled with argon twice. 85 mL of dry o-dichlorobenzene was added and the mixture was ultrasound sonicated for 30 min at room temperature. In a separate 50 mL schlenk flask under argon, N,N'-dicyclohexylcarbodiimide (178 mg, 0.862 mmol, 7 equ.) was dissolved in 15 mL of dry o-dichlorobenzene. Then the DCC solution was added dropwise to the reaction mixture, which was then stirred at 40 °C for 23 h. After removal of the solvents under reduced pressure at 60 °C, the crude product was redissolved in DCB and filtered. For polymer purification the filtrate was precipitated first into 500 mL methanol, then three times into 500 mL of methanol:toluene (2:1, v:v) and finally into 500 mL methanol. Purity of the obtained polymer was monitored by TLC ( $\text{SiO}_2$ , toluene), where the polymer remains on the start line and the impurities show distinct spots. The precipitate was dried under high vacuum. Yield: 210 mg of a deep brown precipitate.  $^1\text{H-NMR}$  (300 MHz,  $\text{CDCl}_3$ ,  $\delta$ ): 8.11-7.72 (br m, 2a·H,  $\text{Ph-C-(CH}_2)_3\text{-COOR}$ ), 7.65-7.33 (br m, 3·aH,  $\text{Ph-C-(CH}_2)_3\text{-COOR}$ ), 7.08-5.97 (br m, 4(a+b)·H,  $\text{H}_{\text{phenyl}}$ ), 3.99-3.49 (br s, 4b·H,  $\text{H}_{\text{OMe}}$ ), 2.79-2.61, 2.61-2.44 (br m, 4a·H,  $\text{Ph-C-CH}_2\text{-CH}_2\text{-CH}_2\text{-COOR}$ ), 2.36-0.94 (br m, 2aH,  $\text{Ph-C-CH}_2\text{-CH}_2\text{-CH}_2\text{-COOR}$ , 3(a+b)H,  $\text{H}_{\text{backbone}}$ ). SEC ( $\text{CHCl}_3$ ):  $M_n=20.8 \text{ kg mol}^{-1}$ ,  $M_p=26.3 \text{ kg mol}^{-1}$ ,  $M_w/M_n=1.27$ . MALDI:  $M_p=42.5 \text{ kg mol}^{-1}$ . TGA decomposition  $T_{\text{dec}}=390 \text{ }^\circ\text{C}$ .

### Synthesis of PS-Cl

To a dry 10 mL schlenk tube were added 4-methoxystyrene (4.482 g, 33.41 mmol, 260 equ.), 4-tert-butoxystyrene (0.511 g, 2.91 mmol, 23 equ.), 2,2,5-trimethyl-4-phenyl-3-azaheptane-3-nitroxide (6 mg, 0.026 mmol, 0.2 equ.) and 2,2,5-trimethyl-3-(1'-p-chloromethylphenylethoxy)-4-phenyl-3-azaheptane (48.2 mg, 0.129 mmol, 1 equ.). The

schlenk tube was sealed with a rubber septum and the reaction mixture was degassed by three freeze, pump and thaw cycles. The polymerization was subsequently started in a preheated oil bath at 125 °C under vigorous stirring. Samples were taken periodically by syringe to monitor the monomer conversion *via*  $^1\text{H-NMR}$  spectroscopy. The polymerization was stopped at a conversion of 40 % after 410 min by quenching the reaction in liquid nitrogen. The resulting polymer was isolated by precipitation of the reaction mixture three times into 600 mL methanol, filtering the white precipitate and drying under vacuum. Yield: 1.593 g of a white precipitate.  $^1\text{H-NMR}$  (300 MHz,  $\text{CDCl}_3$ ,  $\delta$ ): 6.95-6.15 (br m, 4(a+b)·H,  $\text{H}_{\text{phenyl}}$ ), 3.90-3.56 (br s, 3b·H,  $\text{H}_{\text{OMe}}$ ), 2.25-0.85 (br m, 3(a+b)·H,  $\text{H}_{\text{backbone}}$ , 9a·H,  $\text{H}_{\text{OtBu}}$ ). SEC (THF):  $M_n=10.7 \text{ kg mol}^{-1}$ ,  $M_w/M_n=1.10$ .

### Synthesis of PS-Az

A dry schlenk flask was charged with PS-Cl (1.30 g, approximately 0.07 mmol, 1 equ.) and sodium azide (0.11 g, 1.69 mmol, 24 equ.) and sealed with a rubber septum. It was degassed under high vacuum and backfilled with argon three times before adding dry N,N-dimethylformamide (20 mL) *via* a syringe. The suspension was stirred for 70 h at room temperature. The polymer was isolated by diluting the reaction mixture with a small amount of THF and precipitation into 600 mL deionized water twice. After filtering the white precipitate, it was washed with 100 mL methanol and dried in vacuum at room temperature. Yield: 1.223 g of a white precipitate.  $^1\text{H-NMR}$  (300 MHz,  $\text{CDCl}_3$ ,  $\delta$ ): 6.96-6.14 (br m, 4(a+b)·H,  $\text{H}_{\text{phenyl}}$ ), 3.87-3.59 (br s, 3b·H,  $\text{H}_{\text{OMe}}$ ), 2.25-0.83 (br m, 3(a+b)·H,  $\text{H}_{\text{backbone}}$ , 9a·H,  $\text{H}_{\text{OtBu}}$ ). SEC (THF):  $M_n=10.4 \text{ kg mol}^{-1}$ ,  $M_w/M_n=1.10$ .

### Synthesis of PS<sub>OH</sub>-Az

A 250 mL round bottom flask was charged with PS-Az (1.10 g) and dissolved in 110 mL THF. 13.8 mL of concentrated hydrochloric acid (37 wt%) were added slowly to the solution. After purging the reaction mixture with argon for 20 min *via* a glass pipette, it was stirred at 35 °C for 20 h. For work up, all volatile components were removed under reduced pressure. The hydrolyzed polymer was isolated by precipitation twice into 600 mL deionized water and freeze-drying from 1,4-dioxane. Yield: 0.92 g of a white precipitate.  $^1\text{H-NMR}$  (300 MHz,  $\text{DMSO-d}_6$ ,  $\delta$ ): 9.28-8.83 (br s, 1a·H, OH), 7.10-5.97 (br m, 4(a+b)·H,  $\text{H}_{\text{phenyl}}$ ), 3.80-3.51 (br s, 3b·H,  $\text{H}_{\text{OMe}}$ ), 2.315-0.72 (br m, 3(a+b)·H,  $\text{H}_{\text{backbone}}$ ).

SEC (THF):  $M_n=9.8 \text{ kg mol}^{-1}$ ,  $M_p=11.4 \text{ kg mol}^{-1}$ ,  $M_w/M_n=1.11$ . MALDI:  $M_p=13.4 \text{ kg mol}^{-1}$ .

### Synthesis of P3HT-b-PS<sub>OH</sub>

A dry 20 mL schlenk tube with screw cap was charged with P3HT-alkyne (75 mg, approx. 6.1  $\mu\text{mol}$ , 1 equ.) and PS<sub>OH</sub>-Az (223 mg, approx. 16.6  $\mu\text{mol}$ , 2.7 equ.). It was degassed under high vacuum and backfilled with argon three times. 20 mL of dry THF were added under argon and the solution was stirred for 20 min at 50 °C until all components were fully dissolved. After purging the mixture with argon *via* a needle for 20 min, the copper iodide/PMDETA catalyst solution (0.5 mL, 0.07M, 35  $\mu\text{mol}$ ) was added under argon. The schlenk flask was sealed with the screw cap and cautiously degassed under vacuum and backfilled with argon three times to remove any oxygen traces. The reaction mixture was stirred for 26 h at 50 °C, 0.3 mL of the catalyst solution were added and the solution was stirred for another 17 h. The reaction mixture was passed through a short column of basic aluminium oxide to remove the copper catalyst. The column was washed with 50 mL of THF, the organic fractions were combined and the solvent removed under reduced pressure. The polymer was isolated by precipitation twice into 300 mL of methanol:acetone (2:1, v:v) from THF and drying the precipitate under vacuum at room temperature. Yield: 163 mg of a black precipitate. <sup>1</sup>H-NMR (300 MHz, o-DCB-d<sub>4</sub>,  $\delta$ ): 7.37 (s, *m*·1H, H<sub>a</sub>), 7.10-6.55 (br m, *n*·4(a+b)·H, H<sub>phenyl</sub>), 4.00-3.66 (br s, *n*·3b·H, H<sub>OMe</sub>), 3.20-2.96 (br m, *m*·2H, H<sub>b</sub>), 2.00-1.85 (br m, H<sub>c</sub>), 1.68-1.55 (br m, H<sub>d</sub>), 1.54-1.38 (br m, H<sub>e</sub>, H<sub>f</sub>), 2.38-1.34 (br m, H<sub>backbone</sub>), 1.10 (tr, *m*·3H, H<sub>g</sub>). SEC (CHCl<sub>3</sub>):  $M_n=26.3 \text{ kg mol}^{-1}$ ,  $M_p=35.4 \text{ kg mol}^{-1}$ ,  $M_w/M_n=1.35$ . MALDI:  $M_p=25.9 \text{ kg mol}^{-1}$ .

### Synthesis of P3HT-b-PPC<sub>71</sub>BM

A 100 ml schlenk flask was flame dried at 600 °C under high vacuum. It was charged with P3HT-b-PS<sub>OH</sub> (50 mg, approx. 1.9  $\mu\text{mol}$  polymer, 19  $\mu\text{mol}$  hydroxy groups, 1 equ.), phenyl-C71-butyric acid (49 mg, 48  $\mu\text{mol}$ , 2.5 equ.), and 4-dimethylaminopyridine (9 mg, 68.6  $\mu\text{mol}$ , 3.6 equ.). The flask was degassed under high vacuum and backfilled with argon twice. 17 mL of dry o-dichlorobenzene were added and the mixture was ultrasound sonicated for 30 min at room temperature. In a separate 10 mL schlenk flask under argon, N,N'-dicyclohexylcarbodiimide (33 mg, 160  $\mu\text{mol}$ , 8.4 equ.) was dissolved in 3 mL of dry o-dichlorobenzene. Then the DCC solution was added dropwise to the reac-

tion mixture, which was then stirred at 40 °C for 23 h. After removal of the solvents under reduced pressure at 60 °C, the crude product was redissolved in chloroform and filtered. For polymer purification the filtrate was precipitated first into 300 mL methanol:toluene (1:1, v:v) twice and then into 300 mL methanol. Purity of the obtained polymer was monitored by TLC (SiO<sub>2</sub>, toluene), where the polymer remains on the start line and the impurities show distinct spots. The precipitate was dried under vacuum at room temperature. Yield: 61 mg of a black precipitate. <sup>1</sup>H-NMR (300 MHz, o-DCB-d<sub>4</sub>, δ): 7.94-7.87, 7.70-7.44 (br m, H<sub>h</sub>, H<sub>i</sub>), 7.36 (s, *m*·1H, H<sub>a</sub>), 7.09-6.55 (br m, *n*·4(a+b)·H, H<sub>phenyl</sub>), 3.98-3.68 (br s, *n*·3b·H, H<sub>OMe</sub>), 3.22-2.95 (br m, *m*·2H, H<sub>b</sub>), 2.01-1.84 (br m, H<sub>c</sub>), 1.69-1.55 (br m, H<sub>d</sub>), 1.54-1.36 (br m, H<sub>e</sub>, H<sub>f</sub>), 2.07-1.24 (br m, H<sub>backbone</sub>), 1.09 (m, *m*·3H, H<sub>g</sub>). SEC (CHCl<sub>3</sub>):  $M_n=27.5 \text{ kg mol}^{-1}$ ,  $M_p=36.6 \text{ kg mol}^{-1}$ ,  $M_w/M_n=1.31$ . MALDI:  $M_p=31.5 \text{ kg mol}^{-1}$ .

### Acknowledgements

We kindly acknowledge DFG (SPP1355), EU LARGECELLS (Gr. No: 291936) and Bavarian State Ministry of Science, Research, and the Arts for the Collaborative Research Network "Solar Technologies go Hybrid" for financial support of this project. M. Hufnagel also thanks the German National Academic Foundation for PhD scholarship and the Elite Network Bavaria Macromolecular Science programme at the University of Bayreuth. We also acknowledge Ruth Lohwasser for providing ethynyl-terminated poly(3-hexylthiophene). The GISAXS experiments were performed on the BM26 beamline at the European Synchrotron Radiation Facility (ESRF), Grenoble, France. We are grateful to Guiseppe Portale for providing assistance in using beamline BM26. Finally, we thank Christian Stelling and Fabian Nutz for their help in polymer synthesis.

**References**

- [1] K. M. Coakley, M. D. McGehee, *Chem. Mater.* **2004**, *16*, 4533.
- [2] J. Peet, M. L. Senatore, A. J. Heeger, G. C. Bazan, *Adv. Mater.* **2009**, *21*, 1521.
- [3] G. Yu, J. Gao, J. C. Hummelen, F. Wudl, a J. Heeger, *Science* **1995**, *270*, 1789.
- [4] J. K. J. van Duren, X. Yang, J. Loos, C. W. T. Bulle-Lieuwma, a. B. Sieval, J. C. Hummelen, R. a. J. Janssen, *Adv. Funct. Mater.* **2004**, *14*, 425.
- [5] W. Ma, C. Yang, X. Gong, K. Lee, a. J. Heeger, *Adv. Funct. Mater.* **2005**, *15*, 1617.
- [6] T. Erb, U. Zhokhavets, G. Gobsch, S. Raleva, B. Stühn, P. Schilinsky, C. Waldauf, C. J. Brabec, *Adv. Funct. Mater.* **2005**, *15*, 1193.
- [7] J. U. Lee, J. W. Jung, T. Emrick, T. P. Russell, W. H. Jo, *Nanotechnology* **2010**, *21*, 105201.
- [8] S. Bertho, G. Janssen, T. J. Cleij, B. Conings, W. Moons, A. Gadisa, J. D'Haen, E. Goovaerts, L. Lutsen, J. Manca, D. Vanderzande, *Sol. Energy Mater. Sol. Cells* **2008**, *92*, 753.
- [9] F. C. Krebs, *Sol. Energ. Mat. Sol. C.* **2009**, *93*, 394.
- [10] M. W. Matsen, F. S. Bates, *Macromolecules* **1996**, *29*, 1091.
- [11] M. Shah, V. Ganesan, *Macromolecules* **2010**, *43*, 543.
- [12] P. D. Topham, A. J. Parnell, R. C. Hiorns, *J. Polym. Sci. Part B Polym. Phys.* **2011**, *49*, 1131.
- [13] M. Sommer, S. Huettner, M. Thelakkat, *J. Mater. Chem.* **2010**, *20*, 10788.
- [14] R. H. Lohwasser, G. Gupta, P. Kohn, M. Sommer, A. S. Lang, T. Thurn-Albrecht, M. Thelakkat, *Macromolecules* **2013**, *46*, 4403.
- [15] U. Stalmach, B. de Boer, C. Videlot, P. F. van Hutten, G. Hadziioannou, *J. Am. Chem. Soc.* **2000**, *122*, 5464.
- [16] L. Perrin, A. Nourdine, E. Planes, C. Carrot, N. Alberola, L. Flandin, *J. Polym. Sci. Part B Polym. Phys.* **2013**, *51*, 291.
- [17] M. Hufnagel, M.-A. Muth, J. C. Brendel, M. Thelakkat, *Macromolecules* **2014**, *47*, 2324.
- [18] B. de Boer, U. Stalmach, P. F. van Hutten, C. Melzer, V. V. Krasnikov, G. Hadziioannou, B. De Boer, P. F. Van Hutten, *Polymer* **2001**, *42*, 9097.
- [19] M. H. van der Veen, B. de Boer, U. Stalmach, K. I. van de Wetering, G. Hadziioannou, *Macromolecules* **2004**, *37*, 3673.
- [20] B. Gholamkhash, S. Holdcroft, *Chem. Mater.* **2010**, *22*, 5371.
- [21] C. Yang, J. K. Lee, A. J. Heeger, F. Wudl, *J. Mater. Chem.* **2009**, *19*, 5416.
- [22] S. Miyanishi, Y. Zhang, K. Hashimoto, K. Tajima, *Macromolecules* **2012**, *45*, 6424.
- [23] X.-H. Dong, W.-B. Zhang, Y. Li, M. Huang, S. Zhang, R. P. Quirk, S. Z. D. Cheng, *Polym. Chem.* **2012**, *3*, 124.
- [24] M. Heuken, H. Komber, T. Erdmann, V. Senkovskyy, A. Kiriya, B. Voit, *Macromolecules* **2012**, *45*, 4101.
- [25] J. U. Lee, A. Cirpan, T. Emrick, T. P. Russell, W. H. Jo, P. Russell, W. Ho, T. P. Russell, W. H. Jo, *J. Mater. Chem.* **2009**, *19*, 1483.
- [26] J. C. Hummelen, B. W. Knight, F. LePeq, F. Wudl, J. Yao, C. L. Wilkins, *J. Org. Chem.* **1995**, *60*, 532.
- [27] K. Sivula, Z. T. Ball, N. Watanabe, J. M. J. Fréchet, *Adv. Mater.* **2006**, *18*, 206.
- [28] S. Barrau, T. Heiser, F. Richard, C. Brochon, C. Ngov, K. van de Wetering, G. Hadziioannou, D. V. Anokhin, D. A. Ivanov, *Macromolecules* **2008**, *41*, 2701.

- [29] M. M. Wienk, J. M. Kroon, W. J. H. Verhees, J. Knol, J. C. Hummelen, P. a van Hal, R. a J. Janssen, *Angew. Chem. Int. Ed.* **2003**, *42*, 3371.
- [30] Z. He, C. Zhong, S. Su, M. Xu, H. Wu, Y. Cao, *Nat. Photonics* **2012**, *6*, 593.
- [31] R. H. Lohwasser, M. Thelakkat, *Macromolecules* **2012**, *45*, 1.
- [32] C. J. Brabec, S. Gowrisanker, J. J. M. Halls, D. Laird, S. Jia, S. P. Williams, B. C. J. Brabec, *Adv. Mater.* **2010**, *22*, 3839.
- [33] E. Lieber, C. N. R. Rao, T. Chao, C. Hoffman, *Anal. Chem.* **1957**, *29*, 916.
- [34] S. Fleischmann, H. Komber, D. Appelhans, B. I. Voit, *Macromol. Chem. Phys.* **2007**, *208*, 1050.
- [35] C. R. Singh, G. Gupta, R. Lohwasser, S. Engmann, J. Balko, M. Thelakkat, T. Thurn-Albrecht, H. Hoppe, *J. Polym. Sci. Part B Polym. Phys.* **2013**, *51*, 943.
- [36] M. Thelakkat, P. Pösch, H. W. Schmidt, *Macromolecules* **2001**, *34*, 7441.
- [37] F. C. Spano, *J. Chem. Phys.* **2005**, *122*, 234701.
- [38] C. J. Hawker, *Macromolecules* **1994**, *27*, 4836.
- [39] A. Knoll, R. Magerle, G. Krausch, *J. Chem. Phys.* **2004**, *120*, 1105.
- [40] S. Miyanishi, Y. Zhang, K. Tajima, K. Hashimoto, *Chem. Commun.* **2010**, *46*, 6723.
- [41] A. W. Bosman, R. Vestberg, A. Heumann, J. M. J. Fréchet, C. J. Hawker, *J. Am. Chem. Soc.* **2003**, *125*, 715.
- [42] W. Binder, D. Gloger, H. Weinstabl, G. Allmaier, E. Pittenauer, *Macromolecules* **2007**, *40*, 3097.
- [43] A. S. Lang, M. Thelakkat, *Polym. Chem.* **2011**, *2*, 2213.

## SUPPORTING INFORMATION

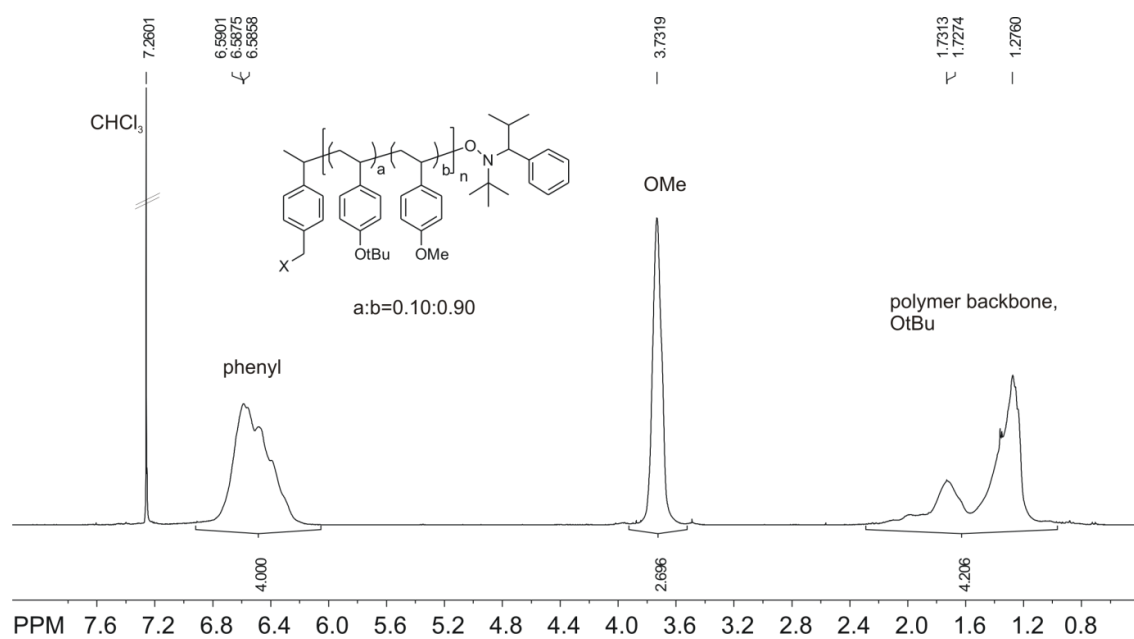


**Figure S1.** <sup>1</sup>H-NMR spectrum (300 MHz) of poly(4-methoxystyrene-stat-4-tert-butoxystyrene) PS. The built-in ratio of both monomers in the copolymer can be derived from the signal integrals giving a:b.=0.10:0.90.

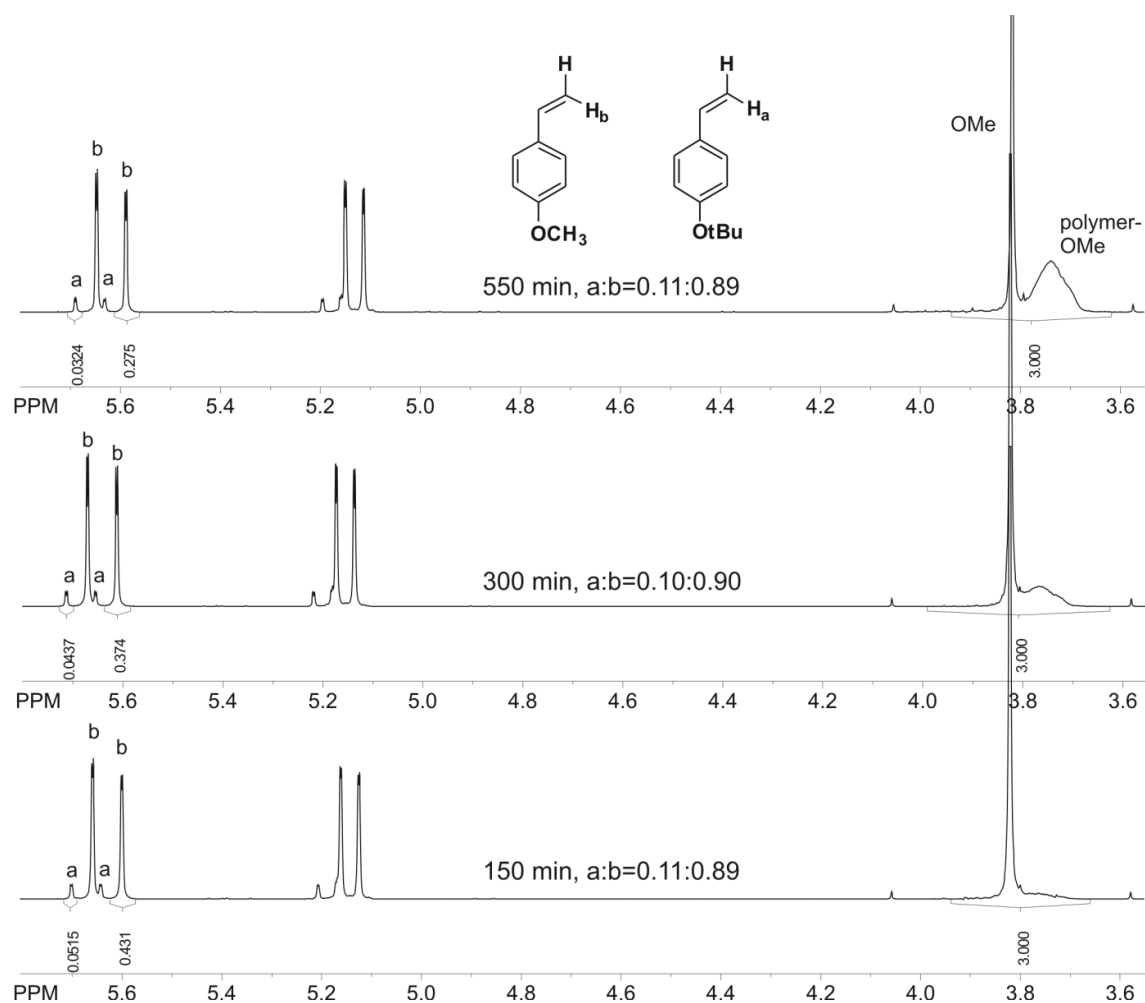


**Figure S2.**  $^1\text{H-NMR}$  monitoring of the copolymerization kinetics of 4-*tert*-butoxystyrene (BS) and 4-methoxystyrene (MS) via NMRP for PS. The integral ratio of the vinyl proton resonances a (BS at  $\delta=5.69$  ppm) and b (MS at  $\delta=5.59$  ppm) of the unreacted monomers represent the molar ratio of both monomers in solution. It remains almost constant and was a:b=0.11:0.89, 0.10:0.90 and 0.11:0.89 after 150 min, 300 min and 550 min. Therefore the consumption of both monomers is equally fast during the copolymerization. The conversion can be determined from the ratio of proton signals of the methoxy group (of monomer and polymer) with respect to the vinyl protons. Thus a conversion of 13% after 150 min, 25% after 300 min and 44% after 550 min was calculated.

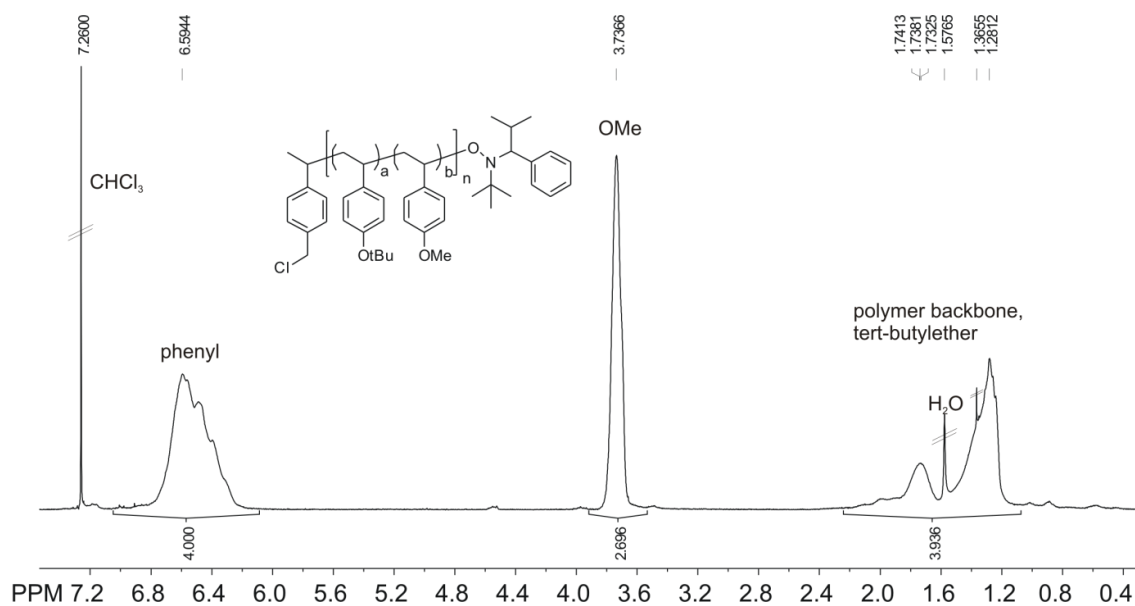


**Figure S3.**  $^1\text{H-NMR}$  spectrum of PS-Cl. The built-in ratio of the monomers BS:MS is determined from the integrals as 0.10:0.90.

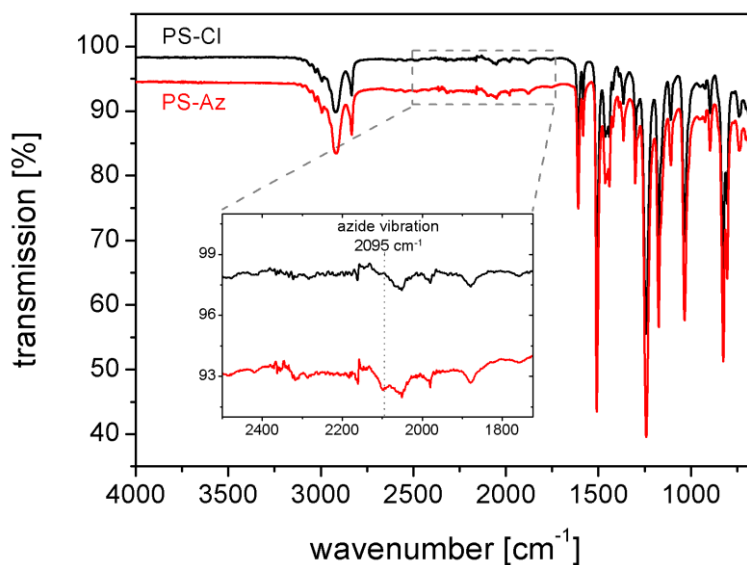


**Figure S4.** FTIR spectra of PS-Cl and the azido-monoterminated PS-Az. After substitution with sodium azide the copolymer PS-Az carries an azido end group which is evidenced by the weak vibration band at 2095  $\text{cm}^{-1}$ .

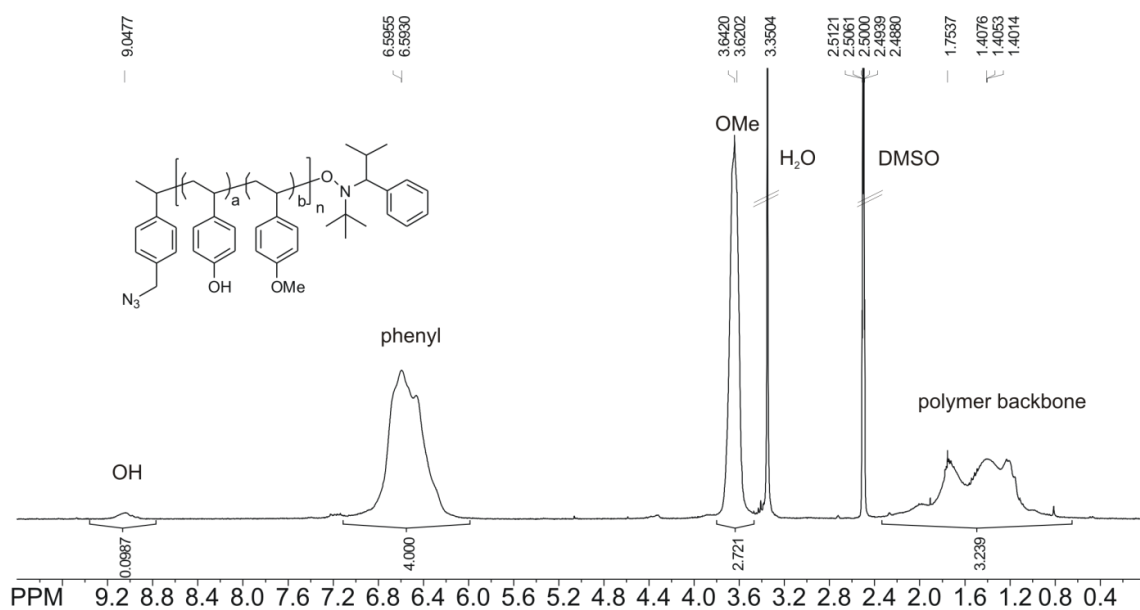
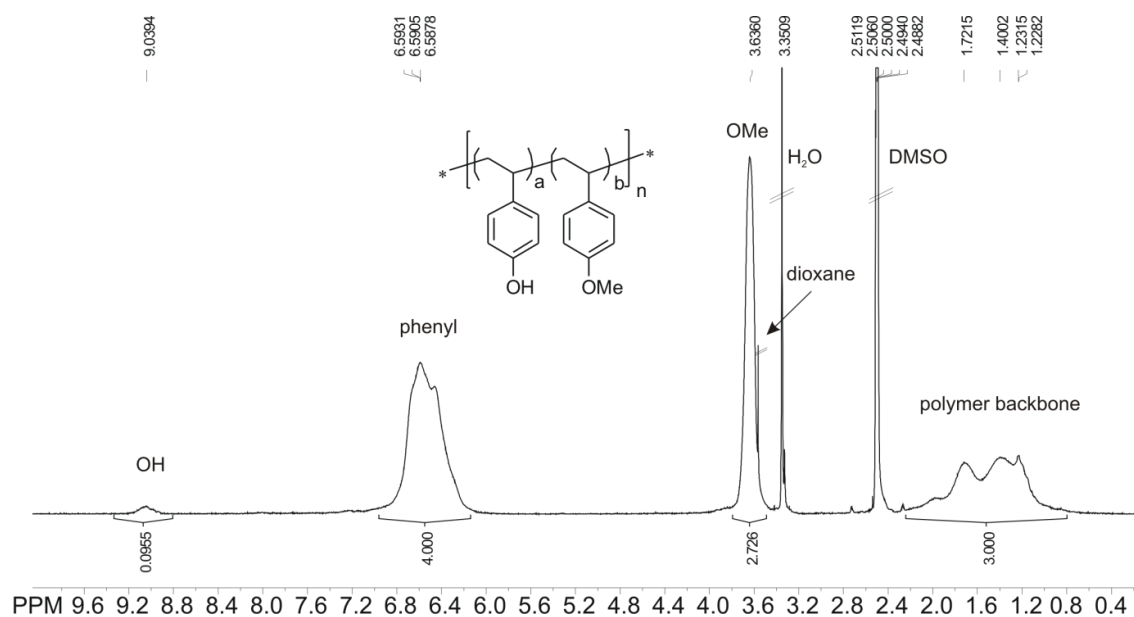


**Figure S5.**  $^1H$ -NMR spectrum of the deprotected copolymer  $PS_{OH}$  (top) and  $PS_{OH-Az}$  (bottom).

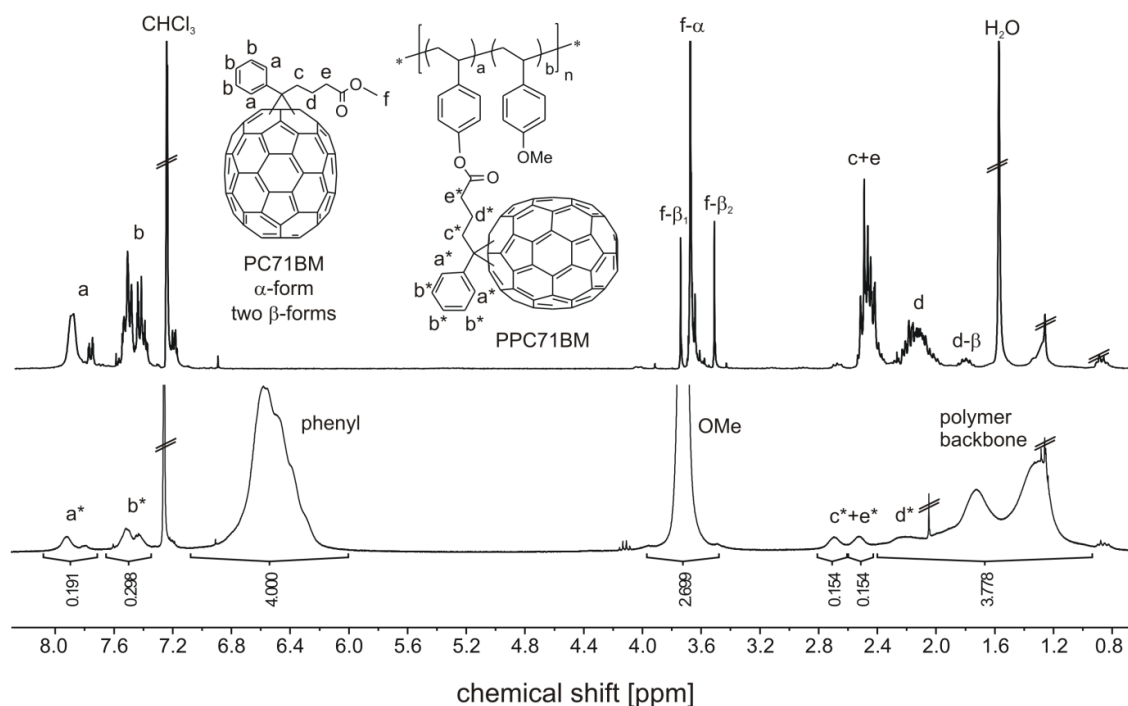


**Figure S6.** <sup>1</sup>H-NMR spectra of the small molecule compound PC<sub>71</sub>BM (top) in comparison to the PC<sub>71</sub>BM-grafted copolymer PPC<sub>71</sub>BM (bottom). Basically, the anisotropic shape of C<sub>70</sub> is the reason why the starting material phenyl-C<sub>71</sub>-butyric acid methyl ester (PC<sub>71</sub>BM), is usually obtained as isomeric mixture from synthesis with one major regioisomer, α-form [6,6]-methanofullerene, and two minor isomers, β-form achiral stereoisomers, in the ratio 85:7:8.31,32 These isomers can be distinguished in <sup>1</sup>H-NMR, where the methyl protons of PC<sub>71</sub>BM show three different singlets at δ=3.68, 3.74 and 3.51 ppm in the ratio 83:8:9 (Figure 3). The corresponding methylene protons of the major isomer appear as fine structured multiplets at δ=2.55-2.33 ppm (4H) and δ=2.27-1.94 ppm (2H) and overlap with the multiplets of the minor isomers. Now, the grafting reaction, i.e. the ester bond formation between PC<sub>71</sub>BA and the hydroxyl groups of the copolymer, can be verified by the proton NMR spectrum of PPC<sub>71</sub>BM: First, all the multiplets of PC<sub>71</sub>BM with its pronounced fine structure experience the same strong polymer-related signal broadening in PPC<sub>71</sub>BM. Second, the methylene multiplet of PC<sub>71</sub>BM at δ=2.55-2.33 ppm is split up into two separated broad resonances in PPC<sub>71</sub>BM at δ=2.79-2.61 ppm and δ=2.61-2.44 ppm with equal intensity. The middle methylene group is very broad around δ=2.21 ppm and overlaps with the resonances from the polystyrene backbone. Both aspects give strong evidence for the covalent bonding of PC<sub>71</sub>BA to the polymer backbone in PPC<sub>71</sub>BM.

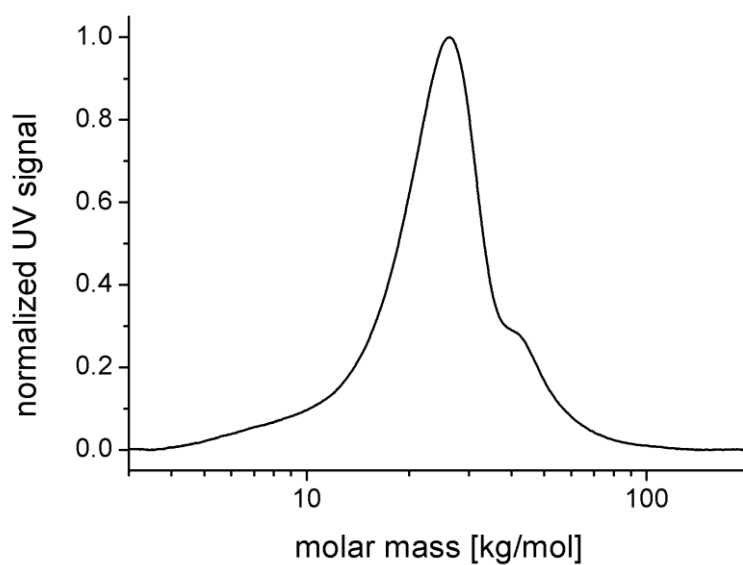


**Figure S7.** SEC trace of PPC<sub>71</sub>BM in chloroform as eluent.

**Table S1.** Experimental data on molecular weights of PS, PS<sub>OH</sub> and the PC<sub>71</sub>BM-grafted copolymer PPC<sub>71</sub>BM.

Polymer	Molar ratio a:b	SEC			MALDI
		$M_n$ [kg mol <sup>-1</sup> ]	$M_p^{c)}$ [kg mol <sup>-1</sup> ]	$M_w/M_n$	$M_p^{c)}$ [kg mol <sup>-1</sup> ]
PS <sup>a)</sup>	0.1:0.9	19.6	24.6	1.19	
PS <sub>OH</sub> <sup>a)</sup>	0.1:0.9	16.7	21.7	1.19	24.4
PPC <sub>71</sub> BM <sup>b)</sup>	0.1:0.9	20.8	26.3	1.27	42.5

<sup>a)</sup> SEC in tetrahydrofuran as eluent. <sup>b)</sup> SEC in chloroform as eluent. <sup>c)</sup>  $M_p$  is the peak maximum of the MW distribution curve.

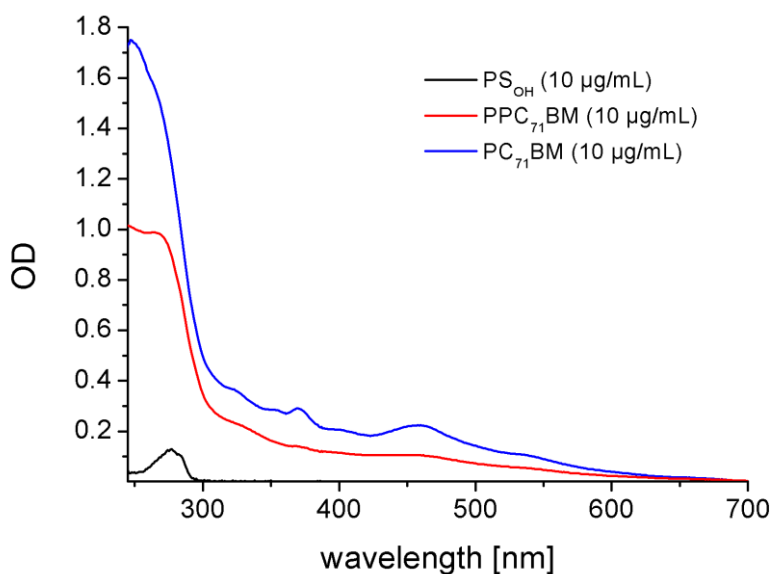


**Figure S8.** UV-vis absorption spectra in chloroform solution of PPC<sub>71</sub>BM and the precursor copolymer PS<sub>OH</sub>. The spectrum of PC<sub>71</sub>BM is given as reference.

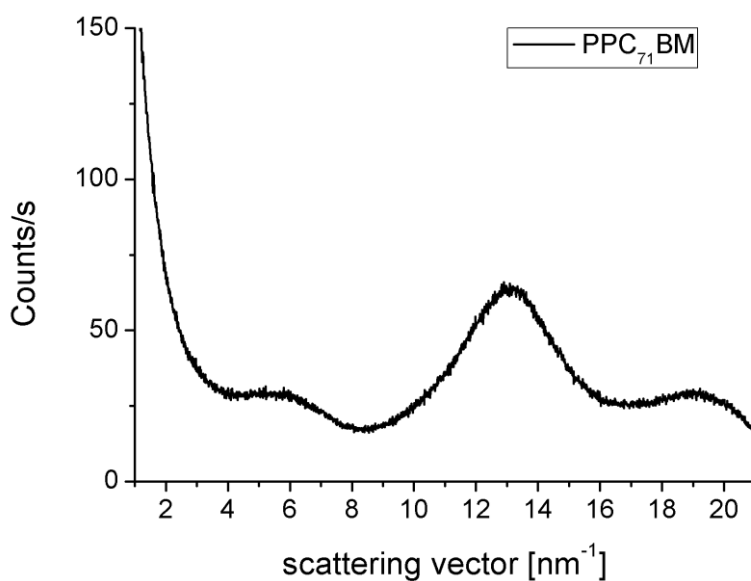


**Figure S9.** X-ray diffractogram of PPC<sub>71</sub>BM prepared by film-casting from DCB at 70 °C in vacuum. The film was scratched and the powder filled into a glass capillary for XRD measurement.

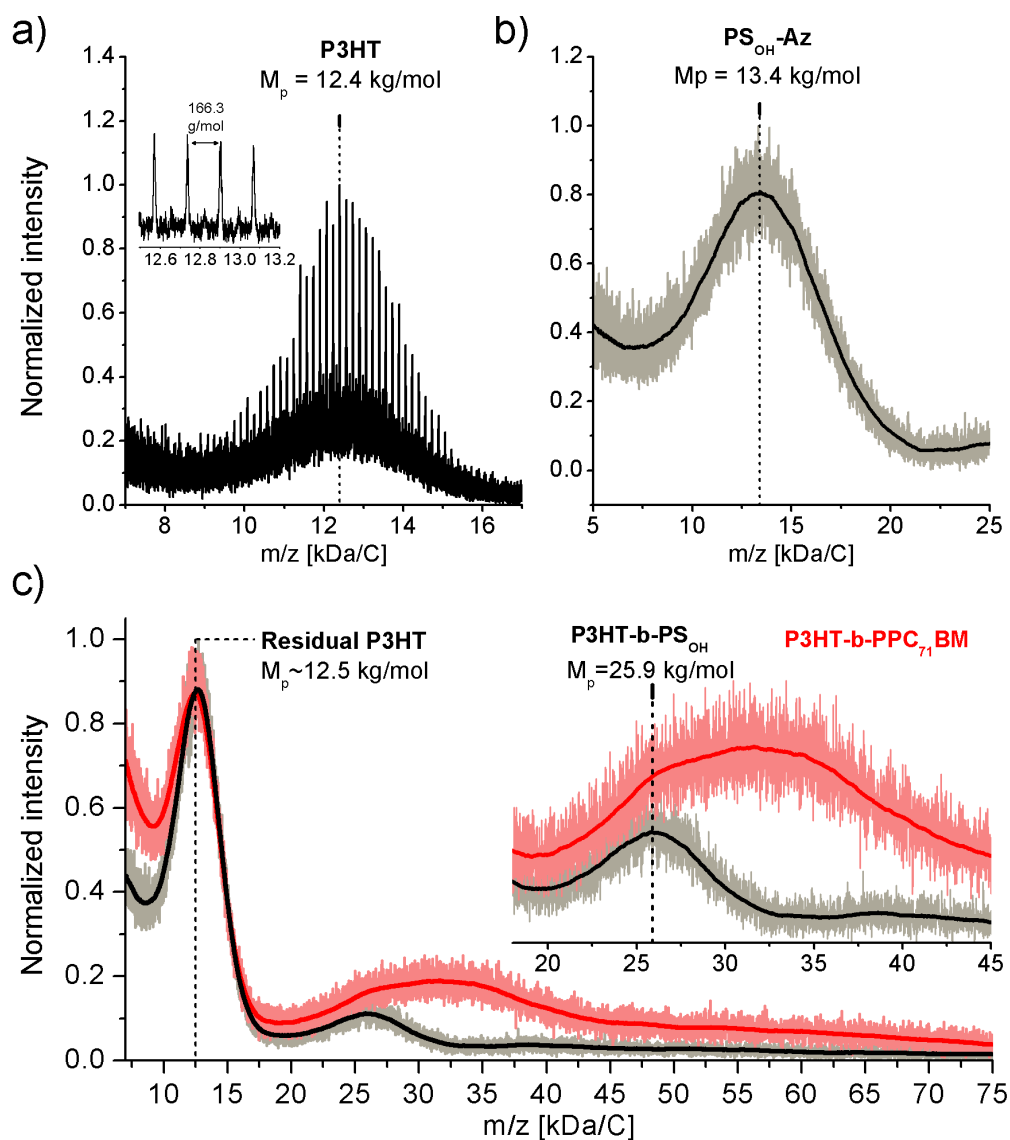


**Figure S10.** MALDI-TOF mass spectra of the polymer blocks (a) P3HT and (b)  $PS_{OH}$ -Az with the individual peak maxima  $M_p$  of 12.4 and 13.4 kg mol<sup>-1</sup>, respectively. The block copolymers  $P3HT$ -b- $PS_{OH}$  (black) and  $P3HT$ -b-PPC<sub>71</sub>BM (red) are shown in the mass spectra in (c) containing residual P3HT and the block copolymer signal (magnified detail in the inset).

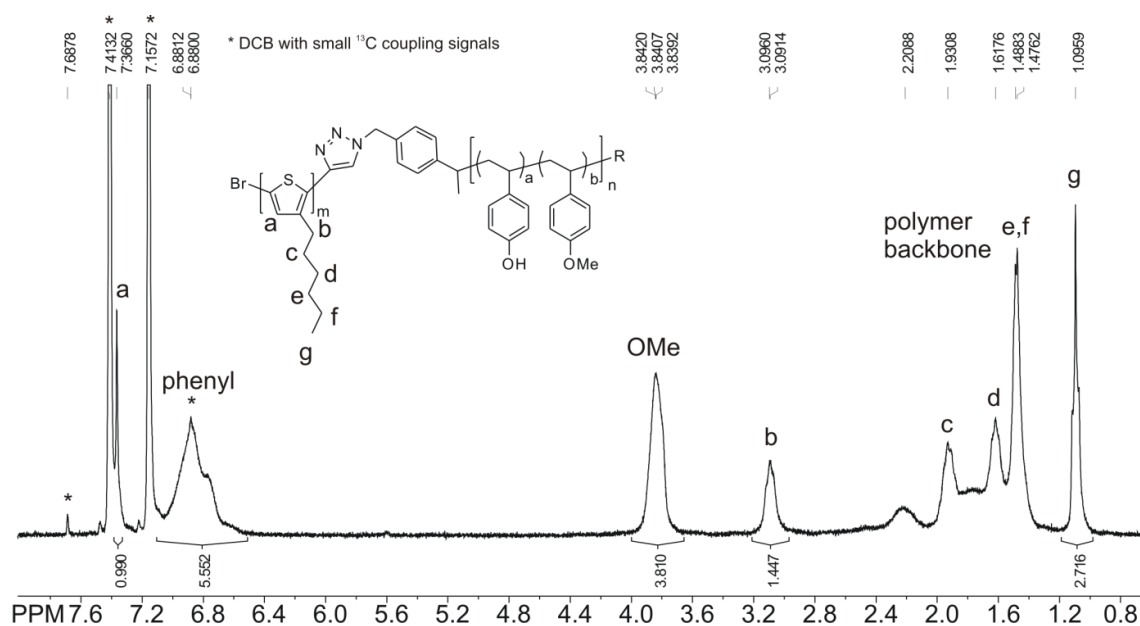


**Figure S11.**  $^1\text{H-NMR}$  spectrum of blockcopolymer  $\text{P3HT-b-PS}_{\text{OH}}$  in  $\text{DCB-d}_4$ . The solvent residue signals of DCB were calibrated to  $\delta=7.4132$  ppm and  $\delta=7.1572$  ppm.

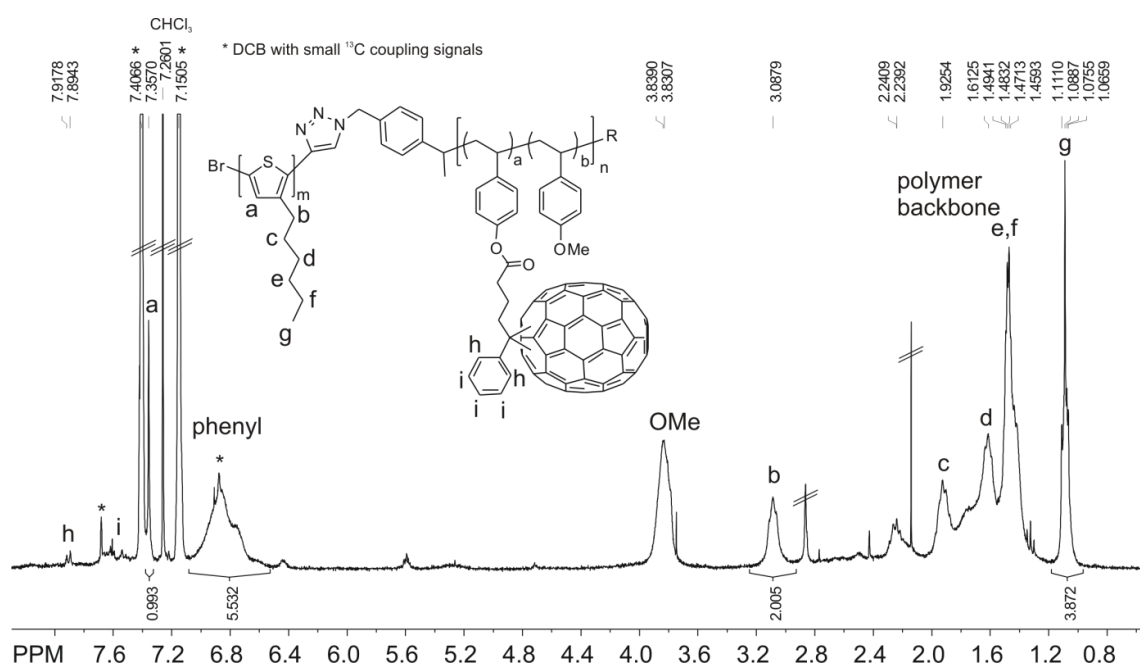


**Figure S12.**  $^1\text{H-NMR}$  spectrum of donor-acceptor block copolymer  $\text{P3HT-b-PPC}_{71}\text{BM}$  measured in  $\text{DCB-d}_4$ . The solvent  $\text{CDCl}_3$  was added for calibration.

**Quantitative UV-Vis spectroscopy for the determination of P3HT and PC<sub>71</sub>BM content in the block copolymers**

*P3HT-b-PS<sub>OH</sub>*: The weight content of P3HT was calculated by the ratio of mass extinction coefficients  $\epsilon(\text{P3HT-b-PS}_{\text{OH}})/\epsilon(\text{P3HT})$  at the absorption maximum of 450 nm (Figure 6a). The calculated amount of P3HT is 39 wt%.

*P3HT-b-PPC<sub>71</sub>BM*: To determine the PC<sub>71</sub>BM content, we use the mass extinction coefficients at 274 nm (Figure 6a) for PC<sub>71</sub>BM and P3HT-b-PPC<sub>71</sub>BM in solution due to the high absorption of the C<sub>70</sub> fullerene in the UV range. Further, it is necessary to subtract the absorption originating from polystyrene, which is clearly visible in the UV-vis spectrum of P3HT-b-PS<sub>OH</sub> (Figure 6a). We can now estimate the PC<sub>71</sub>BM content in P3HT-b-PPC<sub>71</sub>BM from the ratio  $[\epsilon(\text{P3HT-b-PPC}_{71}\text{BM}) - 0.75 \times \epsilon(\text{P3HT-b-PS}_{\text{OH}})]/\epsilon(\text{PC}_{71}\text{BM})$  which is 24 wt% PC<sub>71</sub>BM in the block copolymer.

Similar approach was done for P3HT, but at a wavelength of 424 nm. Here, a correction of  $\epsilon(\text{P3HT-b-PPC}_{71}\text{BM})$  by  $\epsilon(\text{PC}_{71}\text{BM})$  is required due to overlapping absorption with PC<sub>71</sub>BM. Note that the wavelength 424 nm is not at the absorption maximum of P3HT but shifted slightly to avoid correction errors from the distinct vibration band in PC<sub>71</sub>BM which is weaker when PC<sub>71</sub>BM is grafted to a polymer. The P3HT content is then calculated using  $[\epsilon(\text{P3HT-b-PPC}_{71}\text{BM}) - 0.25 \times \epsilon(\text{PC}_{71}\text{BM})]/\epsilon(\text{P3HT})$ . From this calculation a weight fraction of 28 wt% of P3HT in P3HT-b-PPC<sub>71</sub>BM is obtained.

### Analysis of the SAXS and GISAXS scattering curves

The SAXS experiments were performed in transmission geometry on bulk samples with a typical thickness of around 1-2 mm. We performed in addition GISAXS measurements on thin film samples prepared in different ways (crystallization from the melt and drop cast, *i.e.* dried from solution). We analyzed the GISAXS data in a quantitative way using a similar model function as for the analysis of the bulk SAXS data, which consists of a power law background and a Gaussian to describe the peak:

$$I = B q^{-D} + \frac{I_0}{\sqrt{2\pi} \sigma} e^{-\frac{(q-q_0)^2}{2\sigma^2}}$$

The periodicity of the structure is calculated based on Bragg's equation,  $d=2\pi/q_0$ , where  $q_0$  is the position of the first order peak. The peak position is determined by modeling the data with a function consisting of a power law background and a Gaussian describing the peak itself. The inset in the manuscript in Fig.6 shows the data after Lorentz correction, *i.e.* multiplication with a factor  $q^2$  together with the model function given below.

$$I q^2 = \left( y_0 + B q^{-D} + \frac{I_0}{\sqrt{2\pi} \sigma} e^{-\frac{(q-q_0)^2}{2\sigma^2}} \right) q^2 * q^2$$

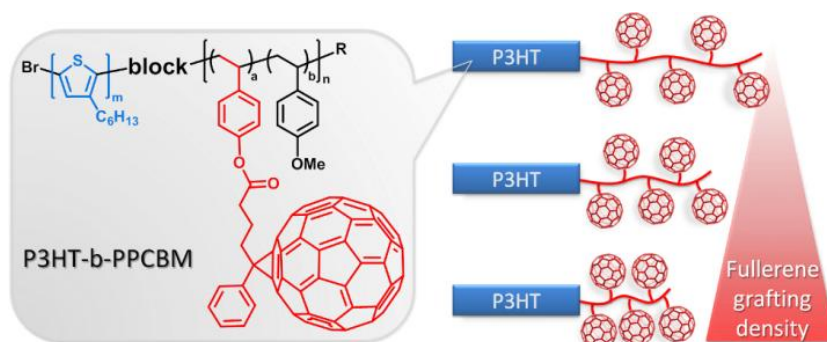
## 5 Influence of fullerene grafting density on structure, dynamics and charge transport in P3HT-b-PPC<sub>61</sub>BM block copolymers

Martin Hufnagel<sup>a</sup>, Matthias Fischer<sup>b</sup>, Thomas Thurn-Albrecht<sup>b</sup>, Mukundan Thelakkat<sup>a,\*</sup>

<sup>a</sup>Applied Functional Polymers, Department of Macromolecular Chemistry I  
University of Bayreuth, Universitaetsstr. 30, 95440 Bayreuth (Germany)

<sup>b</sup>Experimental Polymer Physics Group, Martin-Luther University Halle-Wittenberg,  
Von-Danckelmann-Platz 3, 06120 Halle (Germany)

\*E-mail: [mukundan.thelakkat@uni-bayreuth.de](mailto:mukundan.thelakkat@uni-bayreuth.de)



Under revision in *Macromolecules* **2015**.

**ABSTRACT**

A series of tailor-made P3HT-b-PPCBM block copolymers incorporating P3HT as donor and a polystyrene with pendant fullerene (PC<sub>61</sub>BM) as acceptor block (PPCBM) is presented. The grafting density of PC<sub>61</sub>BM was varied between 26 and 60 wt%. This has high impact on structure formation, molecular dynamics and charge transport. It causes considerable increase in glass transition temperature ( $T_g$  from 150 to 200 °C). The  $T_g$  of the amorphous PPCBM block restricts the dynamics of structure evolution of the block copolymer resulting in an incomplete microphase separation, even though structural studies revealed a donor-acceptor nanostructure of 30 to 40 nm in bulk and thin films. All block copolymers exhibit ambipolar charge transport in organic field-effect transistors. Further, the most densely grafted system showed two orders of magnitude higher electron mobility. Thus the fullerene grafting density turned out as a key parameter in designing P3HT-b-PPCBM systems for tuning phase separation and charge transport.

**INTRODUCTION**

Tailoring block copolymers with specific functionalities has emerged into a significant field of research. For example, the rational design of functional block copolymers which self-assemble into nanostructured materials in the range of 10-100 nm has paved the way for a variety of novel applications.<sup>[1,2]</sup> Driven by the incompatibility between two covalently connected polymer blocks, classical coil-coil block copolymers can microphase separate into well-defined equilibrium nanostructures that are tunable in size and shape by variation of the degree of polymerization, Flory-Huggins interaction parameter and volume fraction of the components.<sup>[3]</sup> Recent advances in the synthesis of  $\pi$ -conjugated polymers, *e.g.* Kumada catalyst transfer polymerization (KCTP),<sup>[4-6]</sup> considerably enhanced the ability to prepare well-defined and end-functional conjugated polymers in chain-growth type polycondensations with high end-group fidelity. This has opened new perspectives for the development of block copolymers comprising a conjugated polymer block, often referred to as rod-coil block copolymer, with attractive applications in optoelectronic devices.<sup>[7,8]</sup> For example in organic photovoltaics (OPV), the light-harvesting active layer requires a bicontinuous, interpenetrating network of donor and acceptor material on the scale of tens of nanometers for efficient charge generation and charge transport.<sup>[9-12]</sup> An ideal solution towards a long-term stable donor-acceptor morphology could be realized by the development of nanostructured materials in thermody-

dynamic equilibrium. One of the approaches is by using a single polymer material incorporating both donor and acceptor functions with the capability to self-assemble into the desired microdomains. A variety of donor-acceptor block copolymers for OPV has been reported so far.<sup>[13–17]</sup> This includes fullerene-grafted block copolymers based on poly(para-phenylene vinylene)<sup>[18]</sup> or poly(3-hexylthiophene)<sup>[19–21]</sup> as donor polymer, perylene bisimide (PBI) pendant block copolymers with P3HT<sup>[14]</sup> and all-conjugated block copolymers comprising P3HT in conjunction with poly(diketopyrrolopyrrole)<sup>[22]</sup> or poly((9,9-dioctylfluorene)-2,7-diyl-alt-[4,7-bis(thiophen-5-yl)-2,1,3-benzothiadiazole]-2',2''-diyl) (PFTBT).<sup>[23]</sup>

Unlike classical coil-coil block copolymers, the aforementioned donor-acceptor block copolymers typically have at least one crystallizable block that can affect the block copolymer self-assembly. Generally, the crystallization in these crystalline-amorphous block polymer systems depends on block copolymer composition and the interplay between crystallization temperature, glass transition of the amorphous block and the order-disorder transition.<sup>[24]</sup> Owing to this complexity and the difficulty to prepare these type of block copolymers with sufficiently narrow dispersity, the observation of highly ordered microphase separation is rather rare. Reports for donor-acceptor block copolymers show either complete loss of the nanoscale structure<sup>[18]</sup> or only weak evidence for block copolymer morphology based on atomic force microscopy, electron microscopy or X-ray scattering experiments.<sup>[21,23,25–28]</sup> However, we have recently reported a well-defined microphase separation in double-crystalline P3HT-b-poly(peryene bismide) donor-acceptor block copolymers with a lamellar and cylindrical morphology in the range of tens of nanometers.<sup>[29]</sup>

Since fullerenes are so far the most efficient acceptor material in OPV, it seems reasonable to integrate fullerenes as acceptor into donor-acceptor block copolymers, which was realized up to now by grafting C<sub>60</sub> and its derivatives using different synthetic approaches.<sup>[19,20,30–33]</sup> However, an elegant method for a controlled fullerene attachment without multiaddition or cross-linking was first shown by Jo *et al.* using Steglich esterification<sup>[25]</sup> and Hashimoto *et al.* using alkyne-azide click chemistry.<sup>[34]</sup> Just recently, we have reported a novel modular synthesis route towards donor-acceptor block copolymers incorporating P3HT and phenyl-C<sub>71</sub>-butyric acid methyl ester (PC<sub>71</sub>BM).<sup>[35]</sup> In fact, the unique electron-acceptor/transporting capability of fullerenes is maintained in C<sub>60</sub>-grafted polymers.<sup>[36,37]</sup> Polystyrene copolymers with pendant phenyl-C<sub>61</sub>-butyric acid methyl es-

ter (PC<sub>61</sub>BM) exhibit electron mobilities up to  $1 \times 10^{-4} \text{ cm}^2 \text{ V}^{-1} \text{ s}^{-1}$  (space-charge limited current method) without the formation of fullerene nanocrystals.<sup>[38]</sup>

Despite the manifold approaches towards synthesis and characterization of fullerene-grafted block copolymers, there is no clear understanding how the fullerene acceptor block governs the structure formation, molecular dynamics and charge transport properties in these block copolymers. Especially in the case of fullerenes this is highly required since a full functionalization of the fullerene block leads to solubility issues in fullerene-grafted polymers. Therefore, a copolymerization strategy is usually required. A systematic investigation focusing on the role of the rigidity/flexibility of the polymer backbone, the density of fullerene grafting and/or block copolymer composition is still lacking. However, these fundamental questions have to be addressed to identify suitable design principles for fullerene-grafted block copolymers which promote self-assembly into well-defined nanoscale donor/acceptor domains and ambipolar charge transport properties.

Therefore, we address the question of dilution of the fullerenes in the acceptor polymer and its impact on diverse properties in the resulting block copolymers. We introduce the parameter grafting density as a measure for the weight fraction of PC<sub>61</sub>BM in the PPCBM block, *i.e.* the grafting density expresses the dilution/concentration of fullerenes in the acceptor block. For this, we synthesized a series comprising three donor-acceptor block copolymers incorporating P3HT as semi-crystalline donor and a pendant PC<sub>61</sub>BM polystyrene copolymer as acceptor (PPCBM). The design of the PC<sub>61</sub>BM carrying acceptor block has been varied systematically by changing the grafting density with PC<sub>61</sub>BM moieties and the chain length. The impact of this systematic variation on structure formation of the P3HT-b-PPCBM block copolymers is studied utilizing scanning and transmission electron microscopy (SEM, TEM), temperature-dependent X-ray scattering techniques in bulk (SAXS, WAXS) and in films (grazing-incidence SAXS). Crystallization and glass transition has been studied by differential scanning calorimetry (DSC) to obtain an insight into the interaction of molecular dynamics and self-assembly of these rod-coil block copolymers. Moreover, the influence of PC<sub>61</sub>BM grafting density on charge transport is investigated in organic field-effect transistors (OFET).

## RESULTS AND DISCUSSION

### Block copolymer synthesis

The donor-acceptor block copolymers discussed in this report are based on a regioregular P3HT block as donor and a polystyrene copolymer with pendant PC<sub>61</sub>BM fullerenes as acceptor block PPCBM. A rational design of the block copolymer is required to meet the major targets of nanostructure formation and sufficient charge transport of both holes and electrons. Regarding P3HT as donor block it has been already reported that optimum hole transport is achieved at a molecular weight of 20 kg mol<sup>-1</sup> (determined from size-exclusion chromatography, SEC),<sup>[39]</sup> and further, this high molecular weight showed in previous materials systems that it can promote donor-acceptor block copolymer microphase separation.<sup>[29]</sup> Second, the acceptor block PPCBM can be tailored with regard to length and dilution of PC<sub>61</sub>BM along the polystyrene backbone<sup>[38]</sup> which can influence the solubility, structure and charge carrier transport. And third, a constant ratio of donor and acceptor moieties has to be maintained for a comparison of properties. For this, we aimed at the highly optimized ratio of P3HT:PC<sub>61</sub>BM in polymer blend solar cells of roughly 1:1<sup>[40]</sup> also for the block copolymers. Bringing these three considerations together, we have prepared a series of block copolymers P3HT-b-PPCBM 1-3. This block copolymer series was synthesized with a 20 kg mol<sup>-1</sup> P3HT block and coupled with systematically varied PPCBM blocks, where the fullerene grafting density was increased simultaneously with reducing the chain length of PPCBM. This design strategy is in particular helpful to investigate the influence of fullerene grafting density in P3HT-b-PPCBM on the structural and electrical properties.

To realize such a demanding polymer design we have applied a modular synthesis strategy for the block copolymers (Figure 1a). It is a striking benefit that the individual polymer blocks P3HT and PS<sub>OH</sub> 1-3 were precisely tailored prior to the coupling which forms the block copolymers P3HT-b-PS<sub>OH</sub> 1-3 in a simple and efficient copper(I)-catalyzed azide-alkyne cycloaddition (CuAAC) click reaction. In a subsequent step, the fullerene PC<sub>61</sub>BM was introduced by a Steglich esterification to yield the fully-functionalized P3HT-b-PPCBM block copolymer. The scheme of synthesis is given in Figure 1a and the detailed synthesis route with reaction conditions is given in Figure S1.

First, the individual polymer blocks were prepared using established synthetic protocols. Ethynyl end-capped P3HT was achieved by termination of the Kumada transfer cat-

alyst polymerization with ethynylmagnesium chloride.<sup>[41]</sup> The polystyrene copolymers poly(4-hydroxystyrene-stat-4-methoxystyrene) PS<sub>OH</sub> 1-3 were prepared either by nitroxide-mediated radical polymerization (NMRP) or reversible addition-fragmentation chain transfer polymerization (RAFT) followed by a polymer-analogous deprotection reaction.<sup>[35,38]</sup> Both methods allow the introduction of an azide end group and an excellent control over molecular weight and narrow dispersity as shown in the SEC traces in Figure 1b. Moreover, the copolymerization of the styrene monomers proceeds in a statistical manner and allows a precise tailoring of the 4-hydroxystyrene content. In the series PS<sub>OH</sub> 1-3, the ratio of 4-hydroxystyrene and 4-methoxystyrene *a:b* was stepwise varied from 0.10:0.90, 0.17:0.83 to 0.26:0.74, while the degree of polymerization *n* was reduced from 98 to 70 and 46, respectively. This allows for a similar number of functionalizable OH-groups despite a difference in dilution. Thus, the number of 4-hydroxystyrene repeating units that can later carry a fullerene moiety is controlled to be 10, 12 and 12, respectively. The CuAAC reaction was carried out between the ethynyl end-capped P3HT and with an excess of up to 3 equivalents of azide-endcapped PS<sub>OH</sub> 1-3 in the presence of copper(I) iodide/*N,N,N,N,N*-pentamethyl-diethylenetriamine (PMDETA) as catalyst in THF. The precursor PS<sub>OH</sub> 1-3 was used in excess to promote both reaction rate and yield of block copolymer. Further, a maximum incorporation of P3HT-alkyne into the block copolymer helps to avoid a tedious removal of unreacted P3HT in the resulting block copolymer. Progress of the polymer-polymer click reaction was monitored by SEC and the reaction was stopped after about 42 hours by passing the mixture over a short plug of neutral aluminium oxide. The residual PS<sub>OH</sub> polymer was completely removed by precipitation of the crude block copolymer into a mixture of methanol:acetone (2:1/v:v). The obtained precursor block copolymers P3HT-b-PS<sub>OH</sub> show monomodal molar mass distributions and narrow dispersity between 1.19 and 1.35 with THF as eluent. SEC traces of P3HT-b-PS<sub>OH</sub> 1-3 measured in 1,2,4-trichlorobenzene at 150 °C are depicted in Figure 1c.

The functionalization of the precursor block copolymers P3HT-b-PS<sub>OH</sub> 1-3 was achieved by an esterification reaction between the 4-hydroxystyrene units and phenyl-C<sub>61</sub>-butyric acid (PCBA). A Steglich esterification protocol<sup>[35,38]</sup> with dicyclohexylcarbodiimide (DCC) and 4-*N,N*-dimethylaminopyridine (DMAP) yields the corresponding PC<sub>61</sub>BM-grafted block copolymers with a good grafting efficiency in the range of 68, 88 and 97 % for P3HT-b-PPCBM 1-3. The crude product was purified by an extensive precipitation procedure (see Experimental part) to guarantee that only covalent-

ly bound fullerenes remain in the product. Thin layer chromatography (TLC) was applied to make sure that the product does not contain any low molecular weight fullerenes such as *N*-acyl urea fullerene derivatives (byproduct of esterification) which show distinct spots in TLC.

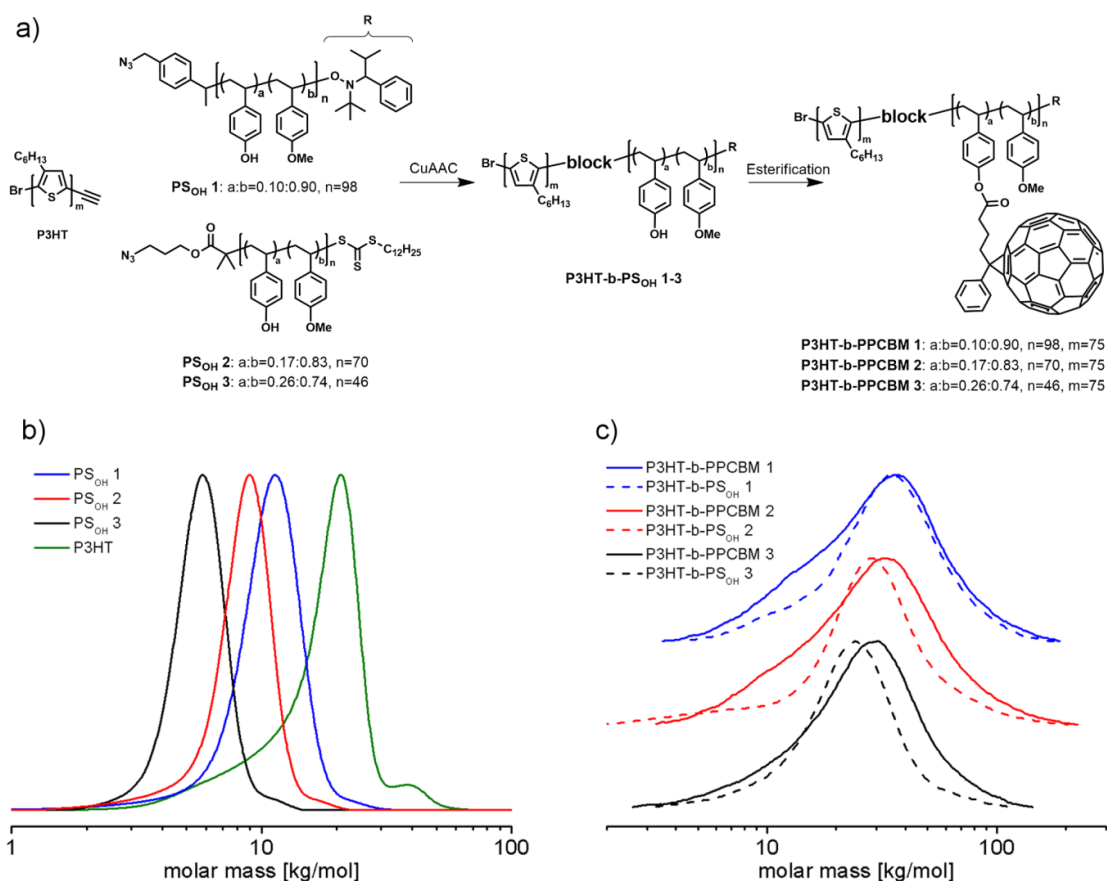


**Figure 1.** Synthesis strategy (a) for the block copolymers using preformed polymer blocks. Ethynyl end-capped P3HT is coupled via click chemistry with a poly(4-hydroxystyrene-*stat*-4-methoxystyrene) carrying an azide end group (PS<sub>OH</sub> 1-3). The polystyrene copolymer PS<sub>OH</sub> was either prepared by NMRP (PS<sub>OH</sub> 1) or RAFT polymerization (PS<sub>OH</sub> 2,3). Subsequent Steglich esterification with PC<sub>61</sub>BA yields the donor-acceptor block copolymers P3HT-b-PPCBM 1-3. The SEC traces given in Figure 1 show the molar mass distribution for (b) the individual polymer blocks P3HT and PS<sub>OH</sub> 1-3 (eluent THF, UV detector at 254 nm) and (c) the block copolymers P3HT-b-PS<sub>OH</sub> 1-3 and their PC<sub>61</sub>BM-grafted analogues P3HT-b-PPCBM 1-3 (eluent 1,2,4-trichlorobenzene at 150 °C, refractive index detector).

The increase of molar weight of the block copolymer is indicated in the SEC traces in Figure 1c, which show a slight shift of the peak maximum from 24.2 to 30.1 kg mol<sup>-1</sup> for P3HT-b-PPCBM 3 and 28.3 to 32.0 kg mol<sup>-1</sup> for P3HT-b-PPCBM 2. The strong contractile effects in fullerene polymers cause only a small shift of the apparent molecular weight in SEC and, in case of P3HT-b-PPCBM 1, this contraction effect overrules the mass in-

crease fully.<sup>[38,42]</sup> A slight broadening of the SEC traces can presumably be attributed to some residual P3HT homopolymer, indicated by a broadening of the molecular weight distribution in the range of 10 to 20 kg mol<sup>-1</sup>. We know from our detailed optimization of the synthesis of P3HT-alkyne that ethynyl end-functionalization of P3HT, in particular for high molecular weight polymers, is not quantitative giving rise to some non-functional P3HT residue. The molecular weights of  $M_p=35.7$ , 32.0 to 30.1 kg mol<sup>-1</sup> for P3HT-b-PPCBM 1-3 follows the targeted length variation of the PPCBM block; the dispersity ranges between 1.5 and 1.6.

Our synthetic work suggests that both controlled radical polymerization techniques, RAFT and NMRP, are well suited for the presented block copolymers synthesis since they allow excellent control and very good end group fidelity.

**Table 1.** Polymer characterization including monomer ratio 4-hydroxystyrene and 4-methoxystyrene a:b, degree of polymerization (DP), number-average molecular weight  $M_n$ , peak molecular weight  $M_p$  and the dispersity  $D$ .

Polymer	Ratio a:b	DP <sup>a)</sup> n:m	$M_n$ [kg mol <sup>-1</sup> ]	$M_p$ [kg mol <sup>-1</sup> ]	$D$
P3HT	-	-/75	19.2 <sup>b)</sup>	20.8 <sup>b)</sup>	1.11 <sup>b)</sup>
PS <sub>OH</sub> 1	0.10:0.90	98/-	9.8 <sup>b)</sup>	11.4 <sup>b)</sup>	1.11 <sup>b)</sup>
PS <sub>OH</sub> 2	0.17:0.83	70/-	7.5 <sup>b)</sup>	9.0 <sup>b)</sup>	1.14 <sup>b)</sup>
PS <sub>OH</sub> 3	0.26:0.74	46/-	5.0 <sup>b)</sup>	5.8 <sup>b)</sup>	1.12 <sup>b)</sup>
P3HT-b-PS <sub>OH</sub> 1	0.10:0.90	98/75	26.3 <sup>b)</sup> /26.5 <sup>c)</sup>	35.4 <sup>b)</sup> /35.7 <sup>c)</sup>	1.35 <sup>b)</sup> /1.41 <sup>c)</sup>
P3HT-b-PS <sub>OH</sub> 2	0.17:0.83	70/75	24.5 <sup>b)</sup> /20.4 <sup>c)</sup>	31.4 <sup>b)</sup> /28.3 <sup>c)</sup>	1.25 <sup>b)</sup> /1.60 <sup>c)</sup>
P3HT-b-PS <sub>OH</sub> 3	0.26:0.74	46/75	24.3 <sup>b)</sup> /19.1 <sup>c)</sup>	29.5 <sup>b)</sup> /24.2 <sup>c)</sup>	1.19 <sup>b)</sup> /1.32 <sup>c)</sup>
P3HT-b-PPCBM 1	0.10:0.90	98/75	23.2 <sup>c)</sup>	35.7 <sup>c)</sup>	1.55 <sup>c)</sup>
P3HT-b-PPCBM 2	0.17:0.83	70/75	21.6 <sup>c)</sup>	32.0 <sup>c)</sup>	1.62 <sup>c)</sup>
P3HT-b-PPCBM 3	0.26:0.74	46/75	19.8 <sup>c)</sup>	30.1 <sup>c)</sup>	1.50 <sup>c)</sup>

<sup>a)</sup> Determined by MALDI-TOF mass spectrometry.

<sup>b)</sup> Determined by SEC with eluent THF, UV detector, polystyrene calibration.

<sup>c)</sup> Determined by high-temperature SEC in 1,2,4-trichlorobenzene at 150 °C, polystyrene calibration.

### Determination of block copolymer composition

A crucial aspect of the P3HT-b-PPCBM donor-acceptor block copolymers characterization is the exact quantification of the individual weight fractions of P3HT, PPCBM and PC<sub>61</sub>BM. For this we applied UV-vis spectroscopy in solution (Figure 2). The content of a chromophore in polymers can be calculated by comparing the extinction coefficients of the polymer and the pure chromophore as a reference in dilute solutions.<sup>[38,43]</sup> The absorption spectra of the block copolymers P3HT-b-PPCBM 1-3 show the characteristic broad P3HT band at  $\lambda_{\text{peak}}=448$  nm and the absorption of PC<sub>61</sub>BM in the UV range at  $\lambda_{\text{peak}}=258$  nm. This is exemplarily shown for P3HT-b-PPCBM 3 in Figure 2a. The weight content of P3HT was determined by the relative extinction at 448 nm in P3HT-b-PPCBM 1-3 compared to that of pure P3HT homopolymer, which reveals that the P3HT weight content increases from 27, 34 to 42 wt% in the series P3HT-b-PPCBM 1-3. Further, the absorption of PC<sub>61</sub>BM increases corresponding to a growing PC<sub>61</sub>BM weight fraction of 19, 31 to 35 wt%. To express the dilution of PC<sub>61</sub>BM molecules in the acceptor block PPCBM, we introduce the grafting density as a measure for the weight fraction of PC<sub>61</sub>BM in the PPCBM block. For instance in P3HT-b-PPCBM 1, the weight content of the PPCBM block is 73 wt% (since P3HT was determined to be 27 wt%) with 19 wt% of pendant PC<sub>61</sub>BM moieties in the whole block copolymer. Thus, the weight fraction of PC<sub>61</sub>BM in the PPCBM polymer block alone, *i.e.* the grafting density, is calculated to be 26 wt%. For P3HT-b-PPCBM 2 and 3 the grafting density is increasing to 47 and 60 wt%. The increase of grafting density in the block copolymers was feasible due to the growing molar ratio of the esterified 4-hydroxystyrene repeating units in the polystyrene backbone, that is 10, 17 and 26 mol% in PS<sub>OH</sub> 1-3 (see Table 1).

Another target of the initial polymer design was to realize a constant weight ratio of donor and acceptor compounds in the block copolymer. Considering the weight ratio of P3HT versus PC<sub>61</sub>BM obtained from UV-vis spectroscopy, we have achieved a similar ratios of P3HT:PC<sub>61</sub>BM between 1:0.70 and 1:0.92. The absorption spectra in Figure 2b clearly demonstrate that the relative amount of P3HT and PC<sub>61</sub>BM in all the block copolymers is similar, while reducing the polystyrene chain length leads to an overall growing optical density from block copolymer P3HT-b-PPCBM 1 to 3.

Another widely-used method to characterize the content of incorporated fullerenes in polymers is thermogravimetric analysis (TGA).<sup>[38,42]</sup> We found, however, that TGA is not

accurate enough for our purposes to estimate the exact composition of these complex block copolymers (Figure S7). Although the general trends regarding both PC<sub>61</sub>BM and P3HT contents are confirmed by TGA, a precise quantification seems not rational due to incomplete decomposition and cross-linking reactions during the heating process.

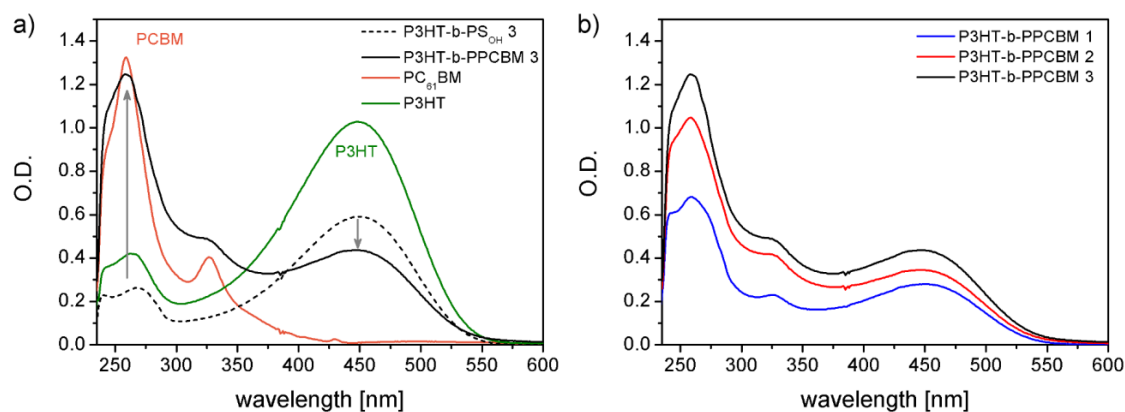


**Figure 2.** UV-vis absorption spectra of solutions in chloroform showing (a) the optical properties of P3HT-b-PS<sub>OH</sub> 3 ( $20 \mu\text{g mL}^{-1}$ ) and P3HT-b-PPCBM 3 ( $20 \mu\text{g mL}^{-1}$ ) in comparison to PC<sub>61</sub>BM ( $9 \mu\text{g mL}^{-1}$ ) and P3HT ( $20 \mu\text{g mL}^{-1}$ ). The growing optical density of P3HT-b-PPCBM 1-3 ( $20 \mu\text{g mL}^{-1}$ ) solutions in (b) correlates with the different polymer design. With a decreasing length of the non-absorbing polystyrene backbone from P3HT-b-PPCBM 1 to P3HT-b-PPCBM 3, the absorption of both PC<sub>61</sub>BM moieties and P3HT block is steadily increasing.

**Table 2.** Composition of the block copolymers P3HT-b-PPCBM 1-3 determined by quantitative UV-vis spectroscopy.

Polymer	P3HT block <sup>a)</sup> [wt%]	PPCBM block <sup>b)</sup> [wt%]	PC <sub>61</sub> BM <sup>a)</sup> [wt%]	Grafting density <sup>c)</sup> [wt%]	Ratio P3HT:PC <sub>61</sub> BM [wt:wt]
P3HT-b-PPCBM 1	27	73	19	26	1:0.70
P3HT-b-PPCBM 2	34	66	31	47	1:0.92
P3HT-b-PPCBM 3	42	58	35	60	1:0.83

<sup>a)</sup> Determined by UV-vis spectroscopy.

<sup>b)</sup> Weight fraction of acceptor block  $f_{\text{PPCBM}}$  calculated from  $f_{\text{PPCBM}} = 100 - f_{\text{P3HT}}$ .

<sup>c)</sup> The grafting density represents the weight content of PC<sub>61</sub>BM  $f_{\text{PC61BM}}$  in the acceptor block PPCBM and was calculated by  $f_{\text{PC61BM}} / f_{\text{PPCBM}} \times 100 \text{ wt\%}$ .

## Crystallization and glass transition

Crystallization in block copolymers can compete with the structure formation *via* phase separation. Generally, in crystalline-amorphous block copolymers, the crystallization depends on three important parameters: crystallization temperature  $T_c$  of the crystalline block, the glass transition temperature  $T_g$  of the amorphous block and the order-disorder transition of the block copolymer.<sup>[24]</sup> Furthermore, the crystallinity of P3HT also strongly improves the hole transport.<sup>[39,44]</sup> Therefore, we investigate in the following the thermal properties of the block copolymers P3HT-b-PS<sub>OH</sub> 1-3 and P3HT-b-PPCBM 1-3 using differential scanning calorimetry (DSC).

As a reference material to study crystallization in neat P3HT, we took a well-defined P3HT without alkyne end group,  $M_n=18.3 \text{ kg mol}^{-1}$  and  $D=1.1$  (SEC) which is very similar to that used for the synthesis. The DSC results of this P3HT were compared with those of the block copolymers where the crystallization of P3HT occurs under multiple constraints: Reduced chain mobility due to the block copolymer architecture, high glass transition temperature of the amorphous acceptor polymer block and possible confinement effects from the block copolymer morphology.

The neat P3HT sample melts between 228-247 °C and crystallizes upon cooling at 195 °C at a rate of 10 K min<sup>-1</sup> with a melting enthalpy  $\Delta H_m$  of 23.2 J g<sup>-1</sup>. After attaching the PS<sub>OH</sub> polymer block to P3HT giving the P3HT-b-PS<sub>OH</sub> block copolymers, the recordable enthalpy of the P3HT melting transition is naturally lower due to the dilution of the crystallizable polymer block. We can now calculate the expected  $\Delta H_{m, \text{theor.}}$  in P3HT-b-PS<sub>OH</sub> 1-3 assuming the same degree of crystallization compared to the pure P3HT but taking the reduced weight fraction of P3HT into account (Table 3). Under the given conditions of heating/cooling from 25 to 260 °C at a rate of 10 K min<sup>-1</sup>, the found melting enthalpies  $\Delta H_m$  of P3HT in the block copolymers remained below  $\Delta H_{m, \text{theor.}}$  for P3HT-b-PS<sub>OH</sub> 1-3 (Figure S8 and Table 3). The reason for this reduced crystallinity is most likely caused by the cross-linking of the PS<sub>OH</sub> polymer block upon heating above 200 °C. In the temperature range of 200-250 °C, the hydroxyl moieties in PS<sub>OH</sub> undergo a condensation reaction and form ether linkages between the polymer chains resulting in a cross-linked polymer network.<sup>[45]</sup> We found clear evidence for this cross-linking reaction in TGA (Figure S9), SEC (Figure S10) and DSC (Figure S11). Even though the 4-hydroxystyrene is diluted in the PS<sub>OH</sub> copolymers, the molar ratio is appreciably high (10-26%).

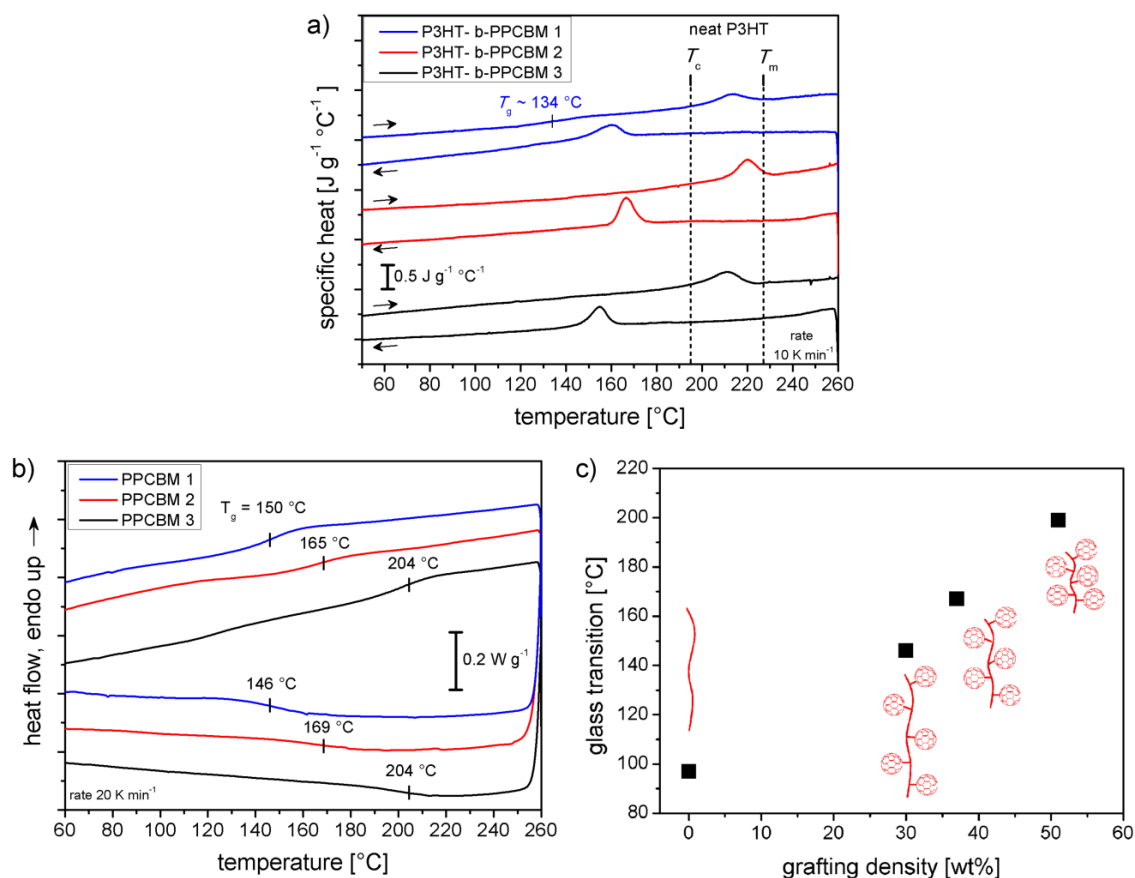


**Figure 3.** DSC traces (a) of P3HT-*b*-PPCBM 1-3 showing the melting and crystallization of the conjugated P3HT block and (b) of PPCBM 1-3 homopolymers which are very identical regarding fullerene grafting density and molecular weight of those in the block copolymers. (c) Glass transitions of the PPCBM homopolymers and precursor polymer PSoH 4 in correlation with the fullerene grafting density determined at a rate of 10 K min<sup>-1</sup>.

**Table 3.** Thermal properties and crystallization of the block copolymers in bulk.

Polymer	P3HT [wt%]	Ratio P3HT: PC <sub>61</sub> BM	$T_{m,peak}$ [°C]	$\Delta H_m$ [J g <sup>-1</sup> ]	$\Delta H_m, theor.$ <sup>a)</sup> [J g <sup>-1</sup> ]
P3HT reference	100	-	228, 236, 247	23.2	-
P3HT- <i>b</i> -PSoH 1	41	-	217	4.5	9.5
P3HT- <i>b</i> -PSoH 2	48	-	228	7.2	11.1
P3HT- <i>b</i> -PSoH 3	57	-	234	8.8	13.2
P3HT- <i>b</i> -PPCBM 1	27	1:0.70	213	2.5	6.3
P3HT- <i>b</i> -PPCBM 2	34	1:0.92	220	3.6	7.9
P3HT- <i>b</i> -PPCBM 3	42	1:0.83	210	4.7	9.7

<sup>a)</sup> Calculated according to the weight fraction of P3HT in the block copolymers assuming the same degree of crystallinity as in P3HT homopolymer.

Nevertheless, the block copolymers P3HT-b-PS<sub>OH</sub> 1-3 show a distinct glass transition  $T_g$  between 107-109 °C, corresponding to the amorphous PS<sub>OH</sub> block (Figure S8). The presence of both the crystallization of P3HT and the glass transition of the amorphous polystyrene block indicates an immiscibility-driven phase separation/segregation of the block copolymer, although a detailed investigation with scattering experiments turned out to be difficult due to the crosslinking reaction taking place at elevated temperatures.

The DSC studies of P3HT-b-PPCBM 1-3 clearly show the melting and crystallization of P3HT in the block copolymers (Figure 3a). The melting enthalpies  $\Delta H_m$  of the PC<sub>61</sub>BM-grafted block copolymers in comparison to the expected  $\Delta H_{m, \text{theor.}}$  are considerably reduced (Table 3). This finding seems in agreement with the strong shift of the P3HT crystallization temperature  $T_c$  in P3HT-b-PPCBM 1-3, from 195 °C, for neat P3HT to 155-166 °C for the block copolymers, suggesting a kinetic inhibition for crystallization under the given experimental conditions.

Here, the glass transition of the PPCBM block must be considered as a crucial factor which can influence the crystallization and structure formation. In P3HT-b-PPCBM 1 with the largest weight fraction of PPCBM and lowest degree of grafting, a weak glass transition is observable at 134 °C (Figure 3a), considerably higher than in the precursor polymer P3HT-b-PS<sub>OH</sub> 1 with 107 °C. Since the glass transition step in the DSC traces of P3HT-b-PPCBM 2-3 is hardly detectable, a series of homopolymers PPCBM 1-3 (Table 4) was separately investigated to determine the  $T_g$  of the fullerene blocks (Figure 3b and S12). PPCBM 1-3 are nearly chemically identical to those incorporated into P3HT-b-PPCBM 1-3. The grafting densities of the homopolymers are 30, 37 and 51 wt% for PPCBM 1-3. Evidently, the grafting density significantly increases the glass transition temperature  $T_g$  in the PPCBMs, ranging from 97 °C for the non-functionalized polystyrene copolymer PS<sub>OH</sub> 4 to 146, 167 and 198 °C for PPCBM 1-3 (Figure 3c). It is well known that bulky side groups in polymers such as pendant adamantane<sup>[46]</sup>, carbazole<sup>[47]</sup> or fullerenes<sup>[48]</sup> hinder the rotational freedom of the polymer backbone and lead to a notably increased  $T_g$ . Since the shape of the glass transition in the PPCBMs is rather broad, we have plotted the DSC traces with a heating rate of 20 K min<sup>-1</sup> in Figure 3b for better clarity, while those for 10 K min<sup>-1</sup> are given in the Supporting Information (Figure S12a). As the comparison of Figure 3a and 3c shows, the crystallization temperature of the P3HT block lies either in the same range or below the respective  $T_g$  values of the PPCBM block as determined from the measurements of the homopolymers. While in P3HT-b-PPCBM 1

a  $T_g$  at 134 °C was observed (26 wt% grafting density in PPCBM block), which is fitting roughly into the grafting density -  $T_g$  correlation in Figure 3c, the glass transition of P3HT-b-PPCBM 2-3 is expected around 190 °C and above 200 °C for 47 and 60 wt% grafting density, respectively. This can hinder the crystallization of P3HT on cooling from the melt due to a restricted chain mobility of the liquid-like P3HT segments in the solidifying PPCBM matrix. The reduced crystallinity of P3HT in the P3HT-b-PPCBM block copolymers (see Table 3) might also originate from a cross-linking of unreacted hydroxyl groups in the block copolymers. However, the good grafting efficiency leaves only very few OH groups which are highly diluted, their accessibility is drastically reduced by the huge PCBM pendants along the polymer chain, and further, the dynamics in the PPCBM block is decreased. These aspects strongly reduce the probability for cross-linking of any residual OH groups, therefore we suggest that the glass transition is likely the main factor governing P3HT crystallization and structure formation in P3HT-b-PPCBM.

**Table 4.** Fullerene-grafted copolymers PPCBM and a corresponding precursor copolymer PS<sub>OH</sub> 4 for the examination of the glass transition. Details on synthesis and characterization of these polymers have been reported earlier.<sup>[38]</sup>

Polymer	Ratio a:b	DP <sup>a)</sup> n:m	$M_n$ [kg mol <sup>-1</sup> ]	$D$	Grafting density [wt%]	$T_g$ <sup>d)</sup> [°C]
PS <sub>OH</sub> 4	0.10:0.90	117	9.3 <sup>b)</sup>	1.29 <sup>b)</sup>	0	97
PPCBM 1	0.10:0.90	117	17.2 <sup>c)</sup>	1.27 <sup>c)</sup>	30	146
PPCBM 2	0.17:0.83	73	11.6 <sup>c)</sup>	1.21 <sup>c)</sup>	37	167
PPCBM 3	0.26:0.74	45	7.6 <sup>c)</sup>	1.21 <sup>c)</sup>	51	199

<sup>a)</sup> Determined from MALDI-TOF mass spectrometry.

<sup>b)</sup> Determined from SEC in tetrahydrofuran at room temperature.

<sup>c)</sup> Determined from SEC in chlorobenzene at 50 °C.

<sup>d)</sup> Glass transition determined from the cooling cycle at a rate of 10 K min<sup>-1</sup>.

### Structure analysis of the donor-acceptor block copolymers

The microscopic structure in the P3HT-b-PPCBM block copolymers 1-3 and in the PPCBM homopolymers 1-3 in the bulk was investigated by temperature dependent small and wide-angle X-ray scattering (SAXS/WAXS), scanning and transmission electron microscopy (SEM, TEM). Grazing incidence small-angle X-ray scattering (GISAXS) was used to obtain complementary information about the structure in thin films.

To confirm the suppression of crystallization of PC<sub>61</sub>BM in the acceptor polymer we studied the model homopolymers PPCBM 1-3 independently by temperature dependent small- and wide-angle X-ray scattering. Figure 4 shows X-ray scattering patterns of PPCBM 1-3 at room temperature after an annealing step of around 45 min in the molten state at 240 °C. For comparison also the data of pure PC<sub>61</sub>BM in the molten state at 300 °C are shown. The absence of Bragg reflections in the scattering pattern of PPCBM 1-3 together with the similarity with the molten PC<sub>61</sub>BM at higher scattering vector  $q$  confirms that even during annealing above the glass transition temperature the PPCBM stays amorphous. All samples show Porod-scattering (intensity  $\sim q^{-4}$ ) below about 0.7 nm<sup>-1</sup>, which can be attributed to the remaining powder structure of the samples.

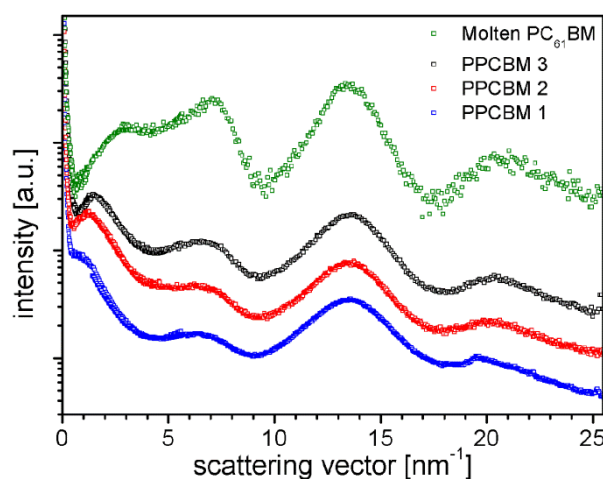


**Figure 4.** Scattering intensity versus scattering vector  $q$  of PPCBM 1-3 at room temperature and of pure PC<sub>61</sub>BM in the molten state (300 °C). Data from different measurements taken at two sample to detector distances in transmission ( $q \approx 0.07$ - 1.25 nm<sup>-1</sup>,  $q \approx 0.4$ - 5.6 nm<sup>-1</sup>) and a measurement in reflection ( $q \approx 1.4$ - 25.5 nm<sup>-1</sup>) were shifted to make them overlap. In addition data sets from different samples are shifted vertically.

The most prominent difference between the data of the molten PC<sub>61</sub>BM and PPCBM 1-3 are the scattering features below 10 nm<sup>-1</sup>. As the peak of the melt signal at 7 nm<sup>-1</sup> corresponds roughly to the size of a PC<sub>61</sub>BM molecule of about 0.9 nm we assume that it reflects a next neighbor distance. As expected this peak is weaker and shifted towards smaller  $q$ -values in the polymeric samples. Surprisingly there is an additional peak at significantly smaller  $q$  (1 nm<sup>-1</sup>, 1.2 nm<sup>-1</sup> and 1.5 nm<sup>-1</sup>, for PPCBM 1-3 respectively). This peak cannot be explained as a next neighbor peak shifted due to the dilution of PC<sub>61</sub>BM molecules in the polymer, as a simple estimate shows: Neglecting differences in density between PC<sub>61</sub>BM and PPCBM, the weight fractions given in Table 4 show that the vol-

ume per PC<sub>61</sub>BM molecule is by about a factor of around three larger for PPCBM 1, the polymer with the lowest grafting fraction, than for pure PC<sub>61</sub>BM. This dilution would correspond to a shift of the next neighbor peak in  $q$  by a factor of about  $1/3^{1/3} \approx 0.69$ . Given that we only expect contrast between PC<sub>61</sub>BM and the polymer backbone, we are led to the conclusion that the PC<sub>61</sub>BM aggregates at least partially in the polymeric sample.

To investigate the donor-acceptor nanostructure in the P3HT-b-PPCBM block copolymer we performed small angle X-ray scattering over a large  $q$ -range at different temperatures. Figure 5 shows the corresponding scattering patterns of samples P3HT-b-PPCBM 1-3 at 240 °C, *i.e.* above the melting temperature of P3HT and above the glass transition temperature of PPCBM, together with a measurement taken at room temperature.

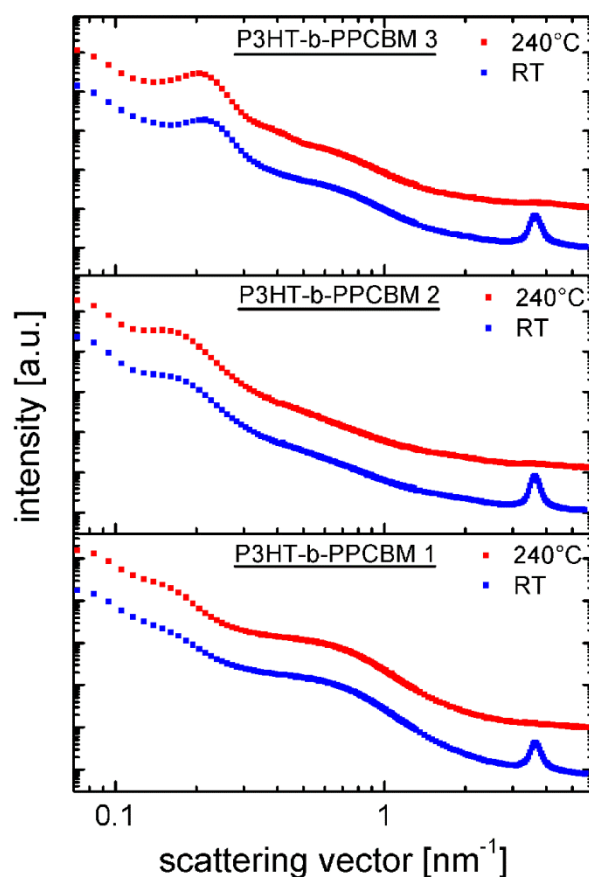


**Figure 5.** Scattering intensity vs. scattering vector  $q$  of P3HT-b-PPCBM 1-3 in the molten state (240 °C, red) and back at room temperature (blue). Data were joined from two measurements at two sample to detector distances (curves shifted for clarity).

Before measuring the samples were annealed for 75 min at 240 °C. These scattering data show basically three distinct features. The peak at  $q=3.64 \text{ nm}^{-1}$  corresponds to the (100)-Bragg reflection of P3HT. The diffuse signal around  $1 \text{ nm}^{-1}$  can be attributed to the

above mentioned aggregate scattering of the PPCBM component, which is here shifted towards smaller  $q$  due to the uneven background intensity; while the peak around  $0.2 \text{ nm}^{-1}$  reflects the nanoscopic two phase structure of the block copolymer.

We performed a more detailed analysis of this peak for P3HT-b-PPCBM 1-3 in the molten state (Figure 6). To determine position and width of the peak an empirical model function consisting of a power law background and a Gaussian for the peak was used. The model function describes the peak well, but at higher scattering vectors deviations between the model function and the experimental data are visible because of the broad PC<sub>61</sub>BM aggregate signal. The intensity of the peak decreases with decreasing grafting density, obviously due to diminishing contrast. The resulting peak positions are given in Table 5 and correspond to a periodicity ( $d=2\pi/q_{\text{max}}$ ) in the range of 30 nm to 40 nm. A shift of the peak towards higher scattering vectors can be observed from P3HT-b-PPCBM 1 to 3 consistent with the decrease of the PPCBM block length. For all three samples the peak could be well described by a Gaussian with a common full width half maximum of  $0.071 \text{ nm}^{-1}$  which is about a factor of 1.9 above the resolution limit of the instrument.

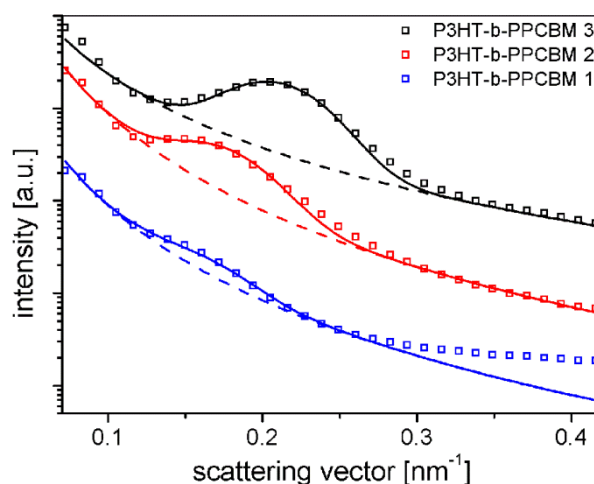


**Figure 6.** SAXS data of P3HT-b-PPCBM 1-3 with a model function consisting of a power law background intensity (dashed line) and a Gaussian (solid line) used to describe the peak. Curves are shifted for clarity.

While typically a microphase separated structure leads to resolution limited peak we still believe the peak shape to be indicative of a microphase separation due to the fact that the peak does not show the Lorentzian shape typical for a disordered block copolymer. Also the fact that the crystallization of the P3HT component occurring during cooling

leaves the position of this peak and therefore the microstructure unchanged is a strong indication that a microphase separation of the two components takes place already in the melt at higher temperatures.<sup>[29]</sup> Missing higher order peaks on the other hand suggest that the structure formed shows no long range order and might be quenched due to the slow molecular dynamics of the high  $T_g$  PPCBM component. Such a scenario is also consistent with the TEM and SEM images of Figure 7 which show a clearly visible but irregular two-phase structure at least for P3HT-b-PPCBM 2-3.

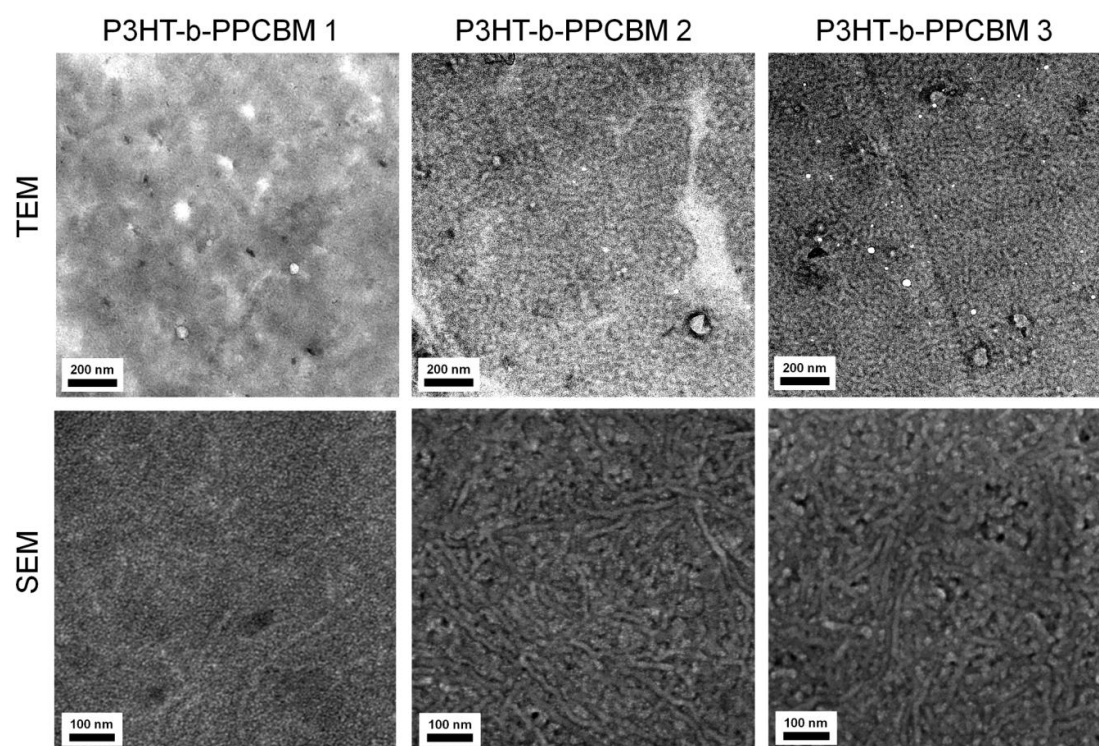


**Figure 7.** TEM images of bulk samples of P3HT-b-PPCBM 1-3 (top) after melt-crystallization and SEM surface images of drop-casted films of P3HT-b-PPCBM 1-3 (bottom).

While the phase diagram and processes of structure formation in block copolymers are often most simply analyzed by bulk experiments, the thin film structures, in most cases prepared from solution, are relevant for devices. We therefore performed GISAXS experiment to test if the results from bulk experiments can be transferred to thin film samples. Figure 8 shows reciprocal space maps of the intensity around the Yoneda position of P3HT-b-PPCBM 2 and 3, while the data for P3HT-b-PPCBM 1 are shown in Figure S13. The maxima left and right of the beamstop along  $q_y$  prove the existence of a periodic nanostructure in melt-crystallized films as well as in drop-cast films. Directly after spin-coating the peak is not visible. Remarkably, the position of the scattering maxima of the

drop-cast films and the melt-crystallized thin films is basically unchanged with respect to the bulk value leading to the conclusion that the formation of the periodic nanostructure is independent of the processing conditions (Figure S14).

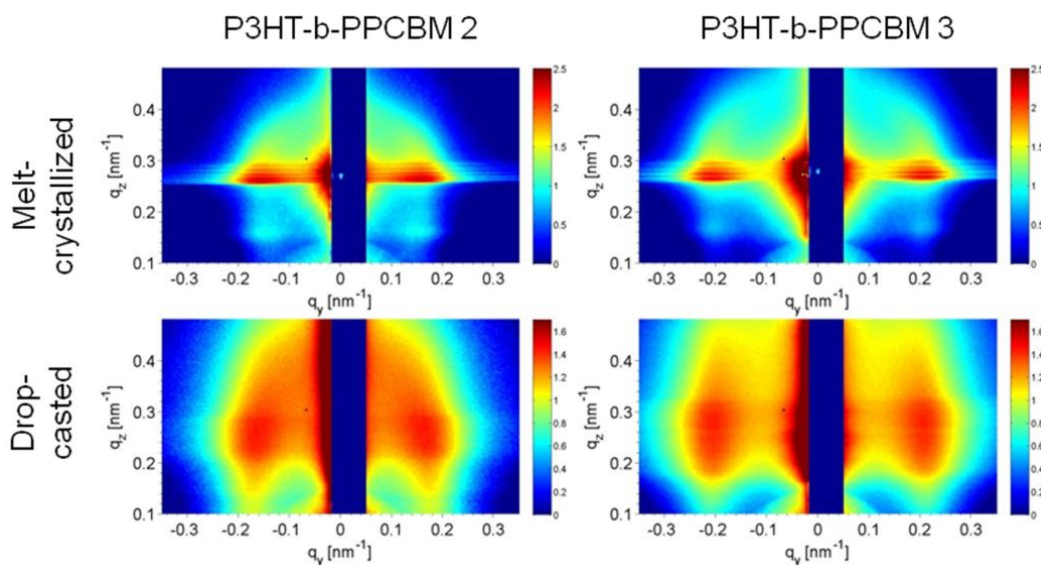


**Figure 8.** 2D-GISAXS data of P3HT-b-PPCBM 2 (left) and P3HT-b-PPCBM 3 (right) around the Yoneda position at room temperature of films prepared by spin-coating with subsequent annealing in the melt (top) or drop-casting (bottom). Data are displayed on a logarithmic intensity scale.

**Table 5.** Long period of the observed nanostructure in P3HT-b-PPCBM 1-3.

Polymer	SAXS		GISAXS	
	$q$ [nm <sup>-1</sup> ]	$d (=2\pi/q)$ [nm]	$q$ [nm <sup>-1</sup> ]	$d (=2\pi/q)$ [nm]
P3HT-b-PPCBM 1	0.150	42	0.145	43
P3HT-b-PPCBM 2	0.165	38	0.160	39
P3HT-b-PPCBM 3	0.205	31	0.210	30

### Crystallization in thin films

In order to understand the behavior of the block copolymers in thin films such as organic field-effect transistors (OFET), we have studied the degree of P3HT aggregation in thin films using UV-vis absorption spectroscopy. Since the film preparation for OFETs from chloroform solutions by spin-coating at 5000 rpm results in a rapidly frozen morphology, all block copolymer films were subsequently annealed for 2 hours at 160 °C to enable a sufficient crystallization of P3HT. While the as-cast films of P3HT-b-PPCBM 1-

3 show a broad, unstructured absorption band around 500 nm indicating mostly amorphous P3HT, the annealed films exhibit additional vibrational shoulders at 555 nm and 600 nm corresponding to the 0-1 and 0-0 vibration of weakly interacting H-aggregates in P3HT (Figure 9a).<sup>[49,50]</sup> This characteristic absorption pattern confirms the presence of a semi-crystalline P3HT block. Further, the photoluminescence (PL) spectra of the block copolymers at an excitation of P3HT at  $\lambda=500$  nm indicate a notable change in thin film morphology (Figure 9b). After annealing, the PL intensity increases strongly, which can be explained by an improved phase separation of donor and acceptor domains, likely accompanied by a higher phase purity.

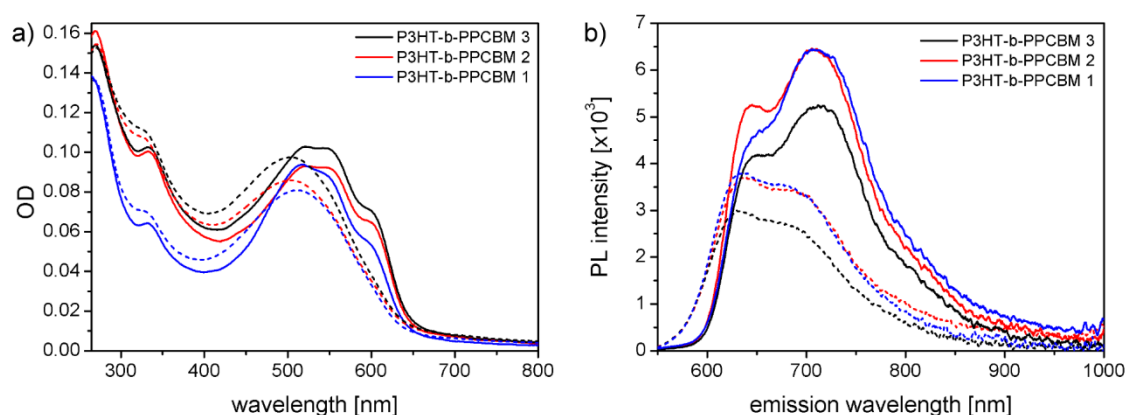


**Figure 9.** (a) Absorption spectra and (b) photoluminescence spectra of thin films of P3HT-b-PPCBM 1-3 after spin-coating from  $4 \text{ mg mL}^{-1}$  chloroform solutions at 5000 rpm (dashed lines) and after annealing for 2 h at  $160^\circ\text{C}$  (solid lines). The photoluminescence (PL) spectra were measured with an excitation wavelength of 500 nm; the PL intensity was scaled to  $\text{OD}=1.0$  at 500 nm of the film absorption.

### Charge transport in field-effect transistors

In general, the donor-acceptor block copolymers are designed to allow for charge transport of both holes and electrons *via* individual microdomains in a single material. While P3HT is an established p-type semiconductor with maximum reported hole mobility in the range of  $0.01 \text{ cm}^2/\text{Vs}$  in organic field-effect transistors (OFET),<sup>[44]</sup> the n-type character of PPCBM was not yet studied in OFET. In a previous work, we could demonstrate that PPCBM is a decent n-type semiconductor using the space-charge limited current (SCLC) method with electron mobility reaching  $1 \times 10^{-4} \text{ cm}^2 \text{ V}^{-1} \text{ s}^{-1}$  for 37 wt% PC<sub>61</sub>BM content.<sup>[38]</sup> Studying the charge transport of ambipolar materials in OFET is in particular attractive since hole and electron mobility can be determined in a single device structure.<sup>[51]</sup>

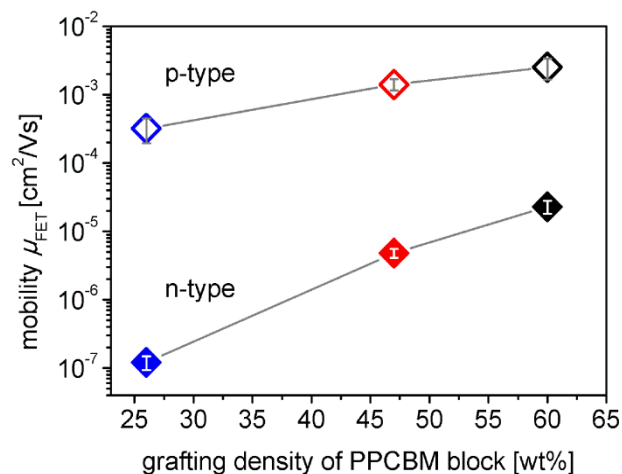


**Figure 10.** Field-effect transistor mobilities for p-type (open diamonds) and n-type (filled diamonds) transport of P3HT-b-PPCBM 1 (blue), P3HT-b-PPCBM 2 (red) and P3HT-b-PPCBM 3 (black) after annealing for 2 hours at 160 °C.

To clarify the role of fullerene grafting density in P3HT-b-PPCBM block copolymers on charge transport, we have analyzed thin film OFETs with bottom-gate, bottom-contact configuration. The OFET devices were annealed for 2 hours at 160 °C after spin-coating to enable a sufficient crystallization of P3HT as demonstrated in the spectroscopic thin film studies. All the annealed samples exhibit ambipolar charge transport characteristics (Figure 10, S15 and Table S2). The extracted OFET mobilities for p-type charge transport are  $3 \times 10^{-4}$ ,  $1.4 \times 10^{-3}$  to  $3 \times 10^{-3} \text{ cm}^2 \text{ V}^{-1} \text{ s}^{-1}$  for P3HT-b-PPCBM 1-3, respectively. The increasing hole mobility correlates with the growing weight fraction of P3HT in the block copolymer series, *i.e.* 27, 34 and 43 wt%, and remains only one order of magnitude lower than the maximum reported value for pristine P3HT. The electron mobility is notably increasing by orders of magnitude from  $1 \times 10^{-7}$ ,  $5 \times 10^{-6}$  to  $2 \times 10^{-5} \text{ cm}^2 \text{ V}^{-1} \text{ s}^{-1}$  for P3HT-b-PPCBM 1-3. It is evident that the determining factor for electron mobility must be the increasing density of fullerene grafting, which was determined as 26, 47 and 60 wt% in this block copolymer series which goes hand in hand with a decreasing polystyrene content as well. Note that the weight fraction of PPCBM in the block copolymers is diminishing at the same time from 73, 66 to 57 wt% in this series. Hence, the increasing grafting density is more than compensating the decreasing fraction of the PPCBM polymer phase in the block copolymer. This allows us to conclude that the grafting density of fullerenes plays a more significant role than the relative composition of the donor/acceptor blocks in determining the electron mobility. Conclusively, the reduced fullerene-fullerene distance

in the PPCBM block realized by an increasing grafting density improves electron transport by two orders of magnitude.

## CONCLUSIONS

We have presented a feasible route towards tailoring P3HT-b-PPCBM block copolymers with high control over molecular weight, donor-acceptor composition and fullerene grafting density. The rational design of the block copolymers enabled us to study the fundamental impact of the fullerene grafting density ranging from 26, 47 to 60 wt% while the overall ratio of P3HT:PC<sub>61</sub>BM was kept within a narrow range between 1:0.70 and 1:0.92. The block copolymers exhibit a donor-acceptor nanostructure of 30 to 40 nm in bulk and thin films independent of the processing method, *i.e.* from solution or melt crystallization. P3HT shows confined crystallization during cooling from the liquid-liquid phase separated melt. Most likely, a long-range ordered block copolymer morphology is hindered by the high  $T_g$  of the amorphous PPCBM block. We found a strongly increasing  $T_g$  for the PPCBM homopolymers based on an increasing grafting density. As desired for applications, all block copolymers P3HT-b-PPCBM show ambipolar charge transport in organic field-effect transistors, and importantly, the high fullerene grafting density emerged as the fundamental design parameter to improve the electron mobility by two orders of magnitude.

## ASSOCIATED CONTENT

**Supporting Information.** Detailed synthesis route, <sup>1</sup>H-NMR spectra, data from thermogravimetric analysis (TGA), differential scanning calorimetry (DSC), SEC, GISAXS, OFET output and transfer characteristics and device statistics. This material is available free of charge *via* the Internet at <http://pubs.acs.org>.

## ACKNOWLEDGEMENTS

We kindly acknowledge the Bavarian State Ministry of Science, Research, and the Arts for the Collaborative Research Network "Solar Technologies go Hybrid" and the Bavarian State Ministry of Environment and Consumer Protection (UMWELT-nanoTECH) for financial support of this project. M. Hufnagel also thanks the German National Academic Foundation for a PhD scholarship and the Elite Network Bavaria Macromolecular Science programme at the University of Bayreuth. We also acknowledge Ruth Lohwasser for providing ethynyl-terminated poly(3-hexylthiophene). The GISAXS

experiments were performed on the BM26 beamline at the European Synchrotron Radiation Facility (ESRF), Grenoble, France. We are grateful to Guiseppe Portale for providing assistance in using beamline BM26. We also thank Fabian Nutz and Christian Stelling who were involved as practical assistants in the synthesis as well as Martina Heider and Melanie Förtsch for electron microscopy measurements.

## EXPERIMENTAL SECTION

### Materials

The reagents for the following synthetic procedures were purchased from Sigma-Aldrich and used as received, if not stated otherwise. Phenyl-C<sub>61</sub>-butyric acid methyl ester (PC<sub>61</sub>BM, purity 99 %) was purchased from Solenne (Groningen, NL). Solvents were either distilled at atmospheric pressure utilizing appropriate desiccants or purchased in p.a. (pro analysi) grade. Commercially available anhydrous solvents were purchased from Sigma Aldrich and Acros in sealed bottles with mole sieve. The precursor copolymers Poly(4-methoxystyrene-stat-4-hydroxystyrene) PS<sub>OH</sub> 1-3 were prepared by NMRP or RAFT polymerization with subsequent polymer-analogous reactions following published synthesis protocols.<sup>[35,38]</sup> Note that in case of PS<sub>OH</sub> 2 and 3, the azide end-group was not end-capped as shown in the reference but used as it is for the click reaction. Ethynyl terminated poly(3-hexylthiophene) was prepared by Kumada catalyst transfer polymerization followed by end-capping with ethynylmagnesium chloride.<sup>[41]</sup> The stock solution of 0.07 M copper(I) iodide/PMDETA catalyst in tetrahydrofuran was prepared according to a literature procedure.<sup>[52]</sup>

### Instrumentation and Analysis

<sup>1</sup>H-NMR spectra were measured with a Bruker Avance AC250 spectrometer at 300 MHz. The obtained spectra were calibrated to the corresponding residual solvent peak (CDCl<sub>3</sub>  $\delta$ =7.26 ppm). Ultraviolet-visible (UV-vis) spectra from solutions were recorded on a Hitachi U-3000 spectrophotometer using quartz cuvettes with a path length of 1 cm. Thin films for absorption and photoluminescence spectra of P3HT-b-PPCBM 1-3 were prepared by spin-coating of 4 mg mL<sup>-1</sup> solutions in chloroform at 5000 rpm on glass substrates and measured with a JASCO Spectrophotometer V-670 and a JASCO FP-8600 spectrofluorometer at an excitation wavelength of  $\lambda$ =450 nm for solutions. Thermal gravimetry analysis (TGA) experiments were performed under continuous nitrogen

stream using a Mettler Toledo TGA/SDTA 851. The measurement range was 30-800 °C with a heating rate of 10 K min<sup>-1</sup>. Size exclusion chromatography (SEC) with stabilized THF as eluent was performed using a Waters 515-HPLC pump at a flow rate of 0.5 mL min<sup>-1</sup>. A guard column (Varian, 50x0.75 cm, ResiPore, particle size 3 μm) and two separation columns (Varian, 300x0.75 cm, ResiPore, particle size 3 μm) are connected in series with a Waters UV detector at 254 nm and 486 nm. 1,2-dichlorobenzene (DCB) was used as an internal standard. High-temperature SEC analysis was carried out on an Agilent (Polymer Laboratories Ltd.) PL-GPC 220 high temperature chromatographic unit equipped with DP, RI and LS (15° and 90°) detectors and three linear mixed bed columns of PLgel 13 micrometer (Olexis) with a linear molecular weight operating range: 500-15,000,000 g mol<sup>-1</sup>. SEC analysis was performed at 150 °C using 1,2,4-trichlorobenzene as the mobile phase. All SEC data were calibrated in relation to polystyrene standards.

Matrix assisted laser desorption ionization mass spectroscopy with time of flight detection (MALDI-TOF MS) was performed on a Bruker Reflex III using either dithranol for P3HT or trans-2-(3-(4-tert-butylphenyl)-2-methyl-2-propenylidene)malononitrile (DCTB) for PS<sub>OH</sub> 1-3 as a matrix and, where denoted, silver trifluoroacetate as cationizing salt. Solutions of the analyte, the matrix and the cationizing salt were prepared, mixed in the given ratio and spotted onto the MALDI target plate. P3HT: chloroform, dithranol (10 mg mL<sup>-1</sup>), analyte (0.5 mg mL<sup>-1</sup>), 50:1/v:v. PS<sub>OH</sub> 1-3: THF, DCTB (20 mg mL<sup>-1</sup>), analyte (10 mg mL<sup>-1</sup>), AgTFA (10 mg mL<sup>-1</sup>), 20:5:1/v:v:v. The molar mass  $M_p$  at the peak maximum of the mass spectra was determined and the degree of polymerization estimated based on this value.

Small angle X-ray scattering experiments in transmission were performed using a Rigaku rotating anode (RU-H3R) equipped with an Osmic confocal max flux X-ray optic acting as monochromator for Cu K<sub>α</sub> radiation ( $\lambda=0.154$  nm) and a Bruker 2D-detector (HI-Star). Two millimeter thick aluminum discs with a central hole of 1.5 mm served as sample holders for the materials and were mounted on a Linkam hotstage. Heat conducting paste was used to ensure a good thermal contact. The measurement was performed at two sample to detector distances to cover a wider  $q$ -range ( $q=0.07-1.25$  nm<sup>-1</sup> and  $q=0.4-5.6$  nm<sup>-1</sup>). Sample preparation: For P3HT-b-PPCBM 1-3 the following temperature treatment was chosen: Heating the sample to 240 °C, annealing for 75 min, measuring for 15 min, cooling down in several steps to room temperature. The PPCBM homopolymers

1-3 were heated to 240 °C, annealed for 30-60 min and cooled back down to room temperature. The heating/cooling rate was 10 K min<sup>-1</sup>.

Grazing incidence small-angle X-ray scattering experiments (GISAXS) were performed at beamline BM 26, DUBBLE, at the ESRF, Grenoble. An assembly of slits served as collimation system for the monochromatic beam with a wavelength of 0.104 nm. For the data collection a PILATUS 1M detector was used with a sample to detector distance of 3.07 m. The angle of incidence was chosen slightly larger than the critical angle of the polymer film but below the critical angle of the silicon substrate. GISAXS samples were prepared from a 3 wt% solution in 1,2-dichlorobenzene by spin-coating and drop-casting. The spin-coating was done with 800 rpm on silicone substrates with a typical size of 90-140 mm<sup>2</sup> resulting in a film thickness of about 125 nm. Subsequently, the samples were annealed in nitrogen atmosphere for 90 min at 240 °C and cooled down with a cooling rate of approximately 5-10 K min<sup>-1</sup>. The drop-casted films were prepared by slow evaporation of the solution on the silicon substrates at room temperature covered with a beaker. The resulting samples had a thickness about 1.4 μm. The calibration of the X-ray scattering data measured in transmission and grazing incidence small-angle X-ray scattering data was performed by comparison with the first order ring of silver behenate measured in transmission.

Wide-angle X-ray diffraction was carried out using an EMPYREAN diffractometer from PANalytical using a multilayer X-ray mirror for Cu K<sub>α</sub> radiation (λ=0.154 nm) and a parallel plate collimator in front of the PIXcel detector (PANalytical). The powder samples were placed on silicone substrates in a TTK 450 temperature chamber (PANalytical). PPCBM 1-3 was annealed in nitrogen atmosphere for around 45 min at 240 °C before cooling down to room temperature with 5 K min<sup>-1</sup>.

A Perkin-Elmer DSC 7 was used to investigate the thermal properties of P3HT-b-PPCBM 1-3. A heating and cooling rate of 10 K min<sup>-1</sup> under nitrogen atmosphere was chosen. The data were corrected by this baseline resulting in the measurement of the apparent heat capacity. The glass transitions in PPCBM 1-3 and PS<sub>OH</sub> 4 were measured with a METTLER TOLEDO DSC 2 in nitrogen atmosphere at rates of 10 and 20 K min<sup>-1</sup>.

Transmission electron microscopy (TEM) was carried out on a Zeiss EM922 Omega. The block copolymer samples were either melt-crystallized (10 min at 250 °C, cooling 10 K min<sup>-1</sup> in inert atmosphere) or prepared from 10 mg mL<sup>-1</sup> chlorobenzene solution in

glass vials with subsequent slow evaporation of the solvent at 40 °C (at least overnight). Small pieces of polymer were cut into thin sections using an ultramicrotome and placed on commercial TEM copper grids. Prior to the TEM measurement the polymer samples were stained in osmium tetroxide vapour.

Scanning electron microscopy (SEM) was performed on a Zeiss LEO 1530 (FE-SEM with Schottky-field-emission cathode; in-lens detector) using an accelerating voltage of 2.0–3.0 kV. The samples were prepared by drop-casting from a 2 wt% solution in 1,2-dichlorobenzene on indium-tin oxide coated glass substrates, covered with a beaker and slow drying at room temperature. For the SEM measurement the samples were mounted on a standard SEM sample holder by conductive adhesion graphite-pad (Plano) and sputtered with platinum (2 nm using a Cressington HR208 sputter coater and a Cressington mtm20 thickness controller).

Organic thin films transistor substrates in bottom-gate, bottom-contact configuration were purchased from Fraunhofer IPMS (Dresden/Germany). The substrate and gate electrode is n-doped silicon (doping at wafer surface:  $n \sim 3 \times 10^{17} \text{ cm}^{-3}$ ) with a thermally grown 230 nm  $\pm$  10 nm SiO<sub>2</sub> dielectric top layer. 30 nm Gold electrodes with 10 nm ITO as high work function adhesion layer were used as drain/source contact. The channel width was 1 mm for all devices with a channel length varying between 5 to 20  $\mu\text{m}$ . The substrates were cleaned in an ultrasonic bath in acetone and 2-propanol for 10 min each. After ozone treatment for 20 min at 50 °C, the substrates were immersed into a solution of 1 vol% of octadecyltrichlorosilane in toluene at 60 °C for 45 min. After rinsing the substrates with toluene and 2-propanol, the substrates were dried in nitrogen stream and the polymer was spin-coated from a 4 mg/ml chloroform solution at 5000 rpm under ambient conditions. The devices were annealed at 160 °C for 2 hours in nitrogen atmosphere and measured with an Agilent B1500 Semiconductor Parameter Analyzer. Mobilities were calculated from the slope in the  $V_g - (I_d)^{0.5}$  plots in the saturation regime using the following equation:

$$I_d = \frac{W}{2L} C_i \mu (V_g - V_{th})^2$$

$I_d$  is the drain current,  $W$  is the channel width,  $L$  is the channel length,  $C_i$  is the capacitance,  $V_g$  is the gate voltage and  $V_{th}$  is the threshold voltage.

### General synthetic procedure for P3HT-b-PS<sub>OH</sub> 1-3

A 100 ml schlenk flask was flame dried at 600 °C under high vacuum and charged with ethynyl-terminated poly(3-hexylthiophene) P3HT (1 equ.) and PS<sub>OH</sub> (~3 equ.). It was degassed under high vacuum and backfilled with argon three times. Dry THF was added and the solution stirred for 20 min at 40 °C until all compounds were fully dissolved. After purging the solution with argon for 30 min, the CuI/PMDETA stock solution in THF was added *via* syringe and the reaction mixture was stirred at 40 °C for 42-43 hours. The progress of polymer coupling was monitored by SEC analysis. When full conversion was observed, the reaction mixture was passed through a short column of neutral aluminium oxide to remove the copper catalyst. After washing the column with 50 mL of THF, the organic fractions were combined and the solvent removed under reduced pressure. The polymer was isolated by precipitation into methanol:acetone (2:1, v:v) from THF and drying the precipitate under vacuum at room temperature.

### Synthesis procedure of P3HT-b-PS<sub>OH</sub> 1

P3HT (75 mg, approx. 6.1 μmol, 1 equ.) and PS<sub>OH</sub> 1 (223 mg, approx. 16.6 μmol, 2.7 equ.) dissolved in 20 mL of THF were reacted in presence of 0.5 mL copper(I) iodide/PMDETA catalyst solution (0.07 M in THF, 35 μmol). After 26 h, 0.3 mL catalyst solution were added under argon to the reaction mixture and stirred for another 17 h. Purification was performed as described above and precipitation was done into 300 mL of methanol:acetone (2:1, v:v) twice. Yield: 163 mg of a black precipitate. <sup>1</sup>H-NMR (300 MHz, CDCl<sub>3</sub>, δ): 6.98 (s, m·H, H<sup>1</sup>), 6.82-6.10 (br m, 4(a+b)·H, H<sup>10</sup>), 3.82-3.54 (br s, 3b·H, H<sup>8</sup>), 2.85-2.70 (br t, 2m·H, H<sup>2</sup>), 2.00-1.10 (br m, H<sup>3</sup>, H<sup>4-6,9</sup>, H<sup>CTA</sup>), 0.95-0.73 (br m, 3m·H, H<sup>7</sup>). SEC (THF):  $M_n=26.3 \text{ kg mol}^{-1}$ ,  $M_p=35.4 \text{ kg mol}^{-1}$ ,  $D=1.35$ . SEC (TCB, 150°C):  $M_n=26.5 \text{ kg mol}^{-1}$ ,  $M_p=35.7 \text{ kg mol}^{-1}$ ,  $D=1.41$ . MALDI-TOF MS:  $M_p=25.7 \text{ kg mol}^{-1}$ .

### Synthesis procedure of P3HT-b-PS<sub>OH</sub> 2

P3HT (130 mg, approx. 10.6 μmol, 1 equ.) and PS<sub>OH</sub> 2 (355 mg, approx. 31.7 μmol, 3 equ.) dissolved in 49 mL dry THF were reacted in presence of 0.45 mL copper(I) iodide/PMDETA catalyst solution (0.07 M in THF, 32 μmol). Purification was performed as described above and precipitation was done into 500 mL of methanol:acetone (2:1, v:v) three times. Yield: 210 mg of a black precipitate. <sup>1</sup>H-NMR (300 MHz, CDCl<sub>3</sub>, δ): 6.98 (s,

m·H, H<sup>1</sup>), 6.85-6.10 (br m, 4(a+b)·H, H<sup>10</sup>), 3.85-3.55 (br s, 3b·H, H<sup>8</sup>), 2.88-2.71 (br t, 2m·H, H<sup>2</sup>), 2.10-1.10 (br m, H<sup>3</sup>, H<sup>4-6,9</sup>, H<sup>CTA</sup>), 0.95-0.75 (br m, 3m·H, H<sup>7</sup>). SEC (THF):  $M_n=24.5$  kg mol<sup>-1</sup>,  $M_p=31.4$  kg mol<sup>-1</sup>,  $D=1.25$ . SEC (TCB, 150°C):  $M_n=20.4$  kg mol<sup>-1</sup>,  $M_p=28.3$  kg mol<sup>-1</sup>,  $D=1.60$ . MALDI-TOF MS:  $M_p=23.0$  kg mol<sup>-1</sup>.

### Synthesis procedure of P3HT-b-PS<sub>OH</sub> 3

P3HT (130 mg, approx. 10.6 μmol, 1 equ.) and PS<sub>OH</sub> 3 (231 mg, approx. 31.7 μmol, 3 equ.) dissolved in 45 mL dry THF were reacted in presence of 0.45 mL copper(I) iodide/PMDETA catalyst solution (0.07 M in THF, 32 μmol). Purification was performed as described above and precipitation was done into 500 mL of methanol:acetone (2:1, v:v) three times. Yield: 167 mg of a black precipitate. <sup>1</sup>H-NMR (300 MHz, CDCl<sub>3</sub>, δ): 6.98 (s, m·H, H<sup>1</sup>), 6.82-6.05 (br m, 4(a+b)·H, H<sup>10</sup>), 3.90-3.55 (br s, 3b·H, H<sup>8</sup>), 2.90-2.65 (br t, 2m·H, H<sup>2</sup>), 2.10-1.15 (br m, H<sup>3</sup>, H<sup>4-6,9</sup>, H<sup>CTA</sup>), 0.95-0.75 (br m, 3m·H, H<sup>7</sup>). SEC (THF):  $M_n=24.3$  kg mol<sup>-1</sup>,  $M_p=29.5$  kg mol<sup>-1</sup>,  $D=1.19$ . SEC (TCB, 150°C):  $M_n=19.1$  kg mol<sup>-1</sup>,  $M_p=24.2$  kg mol<sup>-1</sup>,  $D=1.32$ . MALDI-TOF MS:  $M_p=18.5$  kg mol<sup>-1</sup>.

### General synthesis procedure of P3HT-b-PPCBM

A 100 ml schlenk flask was flame dried at 600 °C under high vacuum and charged with P3HT-b-PS<sub>OH</sub>, phenyl-C<sub>61</sub>-butyric acid (PC<sub>61</sub>BA), 4-dimethylaminopyridine (DMAP) and - in case of P3HT-b-PPCBM 2 and 3, additionally with 4-dimethylaminopyridine hydrochloride (DMAP·HCl). The flask was degassed under high vacuum and backfilled with argon twice. A solvent mixture of dry o-dichlorobenzene (DCB) and carbon disulfide (CS<sub>2</sub>) (1:1, v:v) was added (in case of P3HT-b-PPCBM 2 and 3 a mixture of dry DCB:CS<sub>2</sub>:acetonitrile (3:3:1, v:v:v)) and the mixture was sonicated for 30 min at room temperature. In a separate 10 mL schlenk flask under argon, *N,N'*-dicyclohexylcarbodiimide (DCC) was dissolved in DCB:CS<sub>2</sub> (1:1, v:v). The DCC solution was added to the reaction mixture *via* syringe, which was then stirred at 40 °C for 24-70 h. After removal of CS<sub>2</sub> under reduced pressure, the reaction mixture was transferred to a round bottom flask and the residual DCB was removed at 60 °C using a rotary evaporator. The crude product was redissolved in chloroform and filtered. For polymer purification the filtrate was precipitated several times. Purity of the obtained polymer was monitored by TLC (SiO<sub>2</sub>, eluent toluene:ethyl acetate 1:1), where the polymer remains on the

start line and the impurities show distinct spots. The precipitate was dried under vacuum at room temperature.

### Synthesis procedure for P3HT-b-PPCBM 1

P3HT-b-PS<sub>OH</sub> 1 (80 mg, approx. 3.1  $\mu\text{mol}$ , 31  $\mu\text{mol}$  hydroxy groups, 1 equ.), PC<sub>61</sub>BA (69 mg, 73  $\mu\text{mol}$ , 2.4 equ.) and DMAP (12 mg, 100  $\mu\text{mol}$ , 3.2 equ) were dissolved in 22 mL of dry DCB:CS<sub>2</sub> (1:1, v:v) and reacted for 24 h in presence of a solution of DCC (54 mg, 256  $\mu\text{mol}$ , 8.5 equ.) in 4 mL in dry DCB:CS<sub>2</sub> (1:1, v:v). Purification was done by precipitation from concentrated solution in chloroform into 300 mL toluene:MeOH=1:1 twice, 300 mL toluene:MeOH=5:2 and finally into 300 mL methanol. Yield: 79 mg of a black precipitate. <sup>1</sup>H-NMR (300 MHz, CDCl<sub>3</sub>,  $\delta$ ): 8.02-7.85 (br m, H<sup>c</sup>), 7.60-7.29 (br m, H<sup>a</sup>, H<sup>b</sup>), 6.98 (s, m·H, H<sup>1</sup>), 6.88-6.09 (br m, 4(a+b)·H, H<sup>10</sup>), 3.90-3.53 (br s, 3b·H, H<sup>8</sup>), 3.10-2.90 (br m, H<sup>d</sup>), 2.90-2.70 (br t, 2m·H, H<sup>2</sup>), H<sup>f</sup> and H<sup>e</sup> not clearly resolved, 2.05-1.15 (br m, H<sup>3</sup>, H<sup>4-6,9</sup>, H<sup>CTA</sup>), 0.98-0.75 (br m, 3m·H, H<sup>7</sup>). SEC (TCB, 150 °C):  $M_n=23.2 \text{ kg mol}^{-1}$ ,  $M_p=35.7 \text{ kg mol}^{-1}$ ,  $D=1.55$ . MALDI-TOF MS:  $M_p=30.0 \text{ kg mol}^{-1}$ .

### Synthesis procedure for P3HT-b-PPCBM 2

P3HT-b-PSOH 2 (120 mg, approx. 5  $\mu\text{mol}$ , 60  $\mu\text{mol}$  hydroxy groups, 1 equ.), PC<sub>61</sub>BA (83 mg, 93  $\mu\text{mol}$ , 1.6 equ.), DMAP (26 mg, 213  $\mu\text{mol}$ , 3.6 equ), DMAP·HCl (23 mg, 145  $\mu\text{mol}$ , 2.4 equ.) were dissolved in 24 mL of dry DCB:CS<sub>2</sub>:AcN (3:3:1, v:v:v) and reacted for 70 h in presence of a solution of DCC (103 mg, 500  $\mu\text{mol}$ , 8.3 equ.) in 4 mL in of dry DCB:CS<sub>2</sub>:AcN (3:3:1, v:v:v). Purification was done by precipitation from a concentrated solution in chloroform into 400 mL toluene:MeOH=5:2 twice and finally into 400 mL of methanol. Yield: 167 mg of a deep-brown precipitate. <sup>1</sup>H-NMR (300 MHz, CDCl<sub>3</sub>,  $\delta$ ): 8.00-7.86 (br m, H<sup>c</sup>), 7.60-7.30 (br m, H<sup>a</sup>, H<sup>b</sup>), 6.98 (s, m·H, H<sup>1</sup>), 6.85-6.07 (br m, 4(a+b)·H, H<sup>10</sup>), 3.90-3.50 (br s, 3b·H, H<sup>8</sup>), 3.10-2.90 (br m, H<sup>d</sup>), 2.90-2.66 (br t, 2m·H, H<sup>2</sup>), 2.65-2.45 (br m, H<sup>f</sup>), 2.35-2.18 (br m, H<sup>e</sup>), 2.10-1.15 (br m, H<sup>3</sup>, H<sup>4-6,9</sup>, H<sup>CTA</sup>), 0.95-0.75 (br m, 3m·H, H<sup>7</sup>). SEC (TCB, 150 °C):  $M_n=21.6 \text{ kg mol}^{-1}$ ,  $M_p=32.0 \text{ kg mol}^{-1}$ ,  $D=1.62$ . MALDI-TOF MS:  $M_p=28.5 \text{ kg mol}^{-1}$ .

### Synthesis procedure for P3HT-b-PPCBM 3

P3HT-b-PSOH 3 (100 mg, approx. 5  $\mu\text{mol}$ , 60  $\mu\text{mol}$  hydroxy groups, 1 equ.), PC<sub>61</sub>BA (83 mg, 93  $\mu\text{mol}$ , 1.6 equ.), DMAP (26 mg, 213  $\mu\text{mol}$ , 3.6 equ), DMAP·HCl (23 mg,

145  $\mu\text{mol}$ , 2.4 equ.) were dissolved in 24 mL of dry DCB:CS<sub>2</sub>:AcN (3:3:1, v:v:v) and reacted for 70 h in presence of a solution of DCC (103 mg, 500  $\mu\text{mol}$ , 8.3 equ.) in 4 mL in of dry DCB:CS<sub>2</sub>:AcN (3:3:1, v:v:v). Purification was done by precipitation from a concentrated solution in chloroform into 400 mL toluene:MeOH=5:2 twice and finally into 400 mL of methanol. Yield: 128 mg of a deep-brown precipitate. <sup>1</sup>H-NMR (300 MHz, o-DCB-d<sub>4</sub>,  $\delta$ ): 7.78-7.65 (br m, H<sup>c</sup>), H<sup>a</sup> and H<sup>b</sup> overlap with solvent signal, 6.91 (s, m·H, H<sup>1</sup>), 6.65-6.05 (br m, 4(a+b)·H, H<sup>10</sup>), 3.55-3.26 (br s, 3b·H, H<sup>8</sup>), 2.80-2.49 (br t, 2m·H, H<sup>2</sup>), 1.58-1.38 (m, 2m·H, H<sup>3</sup>), 1.30-0.85 (br m, H<sup>3</sup>, H<sup>4-6,9</sup>, H<sup>CTA</sup>), 0.74-0.53 (m, 3m·H, H<sup>7</sup>). H<sup>d-f</sup> not clearly resolved. SEC (TCB, 150 °C):  $M_n=19.8 \text{ kg mol}^{-1}$ ,  $M_p=30.1 \text{ kg mol}^{-1}$ ,  $D=1.50$ . MALDI-TOF MS:  $M_p=25.3 \text{ kg mol}^{-1}$ .

## REFERENCES

- [1] C. Park, J. Yoon, E. L. Thomas, *Polymer* **2003**, *44*, 6725.
- [2] F. H. Schacher, P. a. Rugar, I. Manners, *Angew. Chem. Int. Ed.* **2012**, *51*, 7898.
- [3] M. W. Matsen, F. S. Bates, *Macromolecules* **1996**, *29*, 1091.
- [4] E. E. Sheina, J. Liu, M. C. Iovu, D. W. Laird, R. D. McCullough, *Macromolecules* **2004**, *37*, 3526.
- [5] R. Miyakoshi, A. Yokoyama, T. Yokozawa, *J. Am. Chem. Soc.* **2005**, *127*, 17542.
- [6] R. H. Lohwasser, M. Thelakkat, *Macromolecules* **2011**, *1*, 3388.
- [7] A. de Cuendias, R. C. Hiorns, E. Cloutet, L. Vignau, H. Cramail, *Polym. Int.* **2010**, *59*, 1452.
- [8] C.-L. Liu, C.-H. Lin, C.-C. Kuo, S.-T. Lin, W.-C. Chen, *Prog. Polym. Sci.* **2011**, *36*, 603.
- [9] G. Yu, J. Gao, J. C. Hummelen, F. Wudl, a J. Heeger, *Science* **1995**, *270*, 1789.
- [10] K. M. Coakley, M. D. McGehee, *Chem. Mater.* **2004**, *16*, 4533.
- [11] H. Hoppe, N. S. Sariciftci, *J. Mater. Chem.* **2006**, *16*, 45.
- [12] J. Peet, M. L. Senatore, A. J. Heeger, G. C. Bazan, *Adv. Mater.* **2009**, *21*, 1521.
- [13] S. B. Darling, *Energy Environ. Sci.* **2009**, *2*, 1266.
- [14] M. Sommer, S. Huettner, M. Thelakkat, *J. Mater. Chem.* **2010**, *20*, 10788.
- [15] P. D. Topham, A. J. Parnell, R. C. Hiorns, *J. Polym. Sci. Part B Polym. Phys.* **2011**, *49*, 1131.
- [16] A. Yassar, L. Miozzo, R. Gironda, G. Horowitz, *Prog. Polym. Sci.* **2013**, *38*, 791.
- [17] K. Nakabayashi, H. Mori, *Materials* **2014**, *7*, 3274.
- [18] S. Barrau, T. Heiser, F. Richard, C. Brochon, C. Ngov, K. van de Wetering, G. Hadziioannou, D. V. Anokhin, D. A. Ivanov, *Macromolecules* **2008**, *41*, 2701.
- [19] K. Sivula, Z. T. Ball, N. Watanabe, J. M. J. Fréchet, *Adv. Mater.* **2006**, *18*, 206.
- [20] C. Yang, J. K. Lee, A. J. Heeger, F. Wudl, *J. Mater. Chem.* **2009**, *19*, 5416.
- [21] S. Miyanishi, Y. Zhang, K. Hashimoto, K. Tajima, *Macromolecules* **2012**, *45*, 6424.
- [22] S.-Y. Ku, M. A. Brady, N. D. Treat, J. E. Cochran, M. J. Robb, E. J. Kramer, M. L. Chabiny, C. J. Hawker, *J. Am. Chem. Soc.* **2012**, *134*, 16040.
- [23] C. Guo, Y.-H. Y. Lin, M. D. M. Witman, K. K. a Smith, C. Wang, A. Hexemer, J. Strzalka, E. D. Gomez, R. Verduzco, *Nano Lett.* **2013**, *13*, 2957.

- [24] W.-N. He, J.-T. Xu, *Prog. Polym. Sci.* **2012**, *37*, 1350.
- [25] J. U. Lee, A. Cirpan, T. Emrick, T. P. Russell, W. H. Jo, P. Russell, W. Ho, T. P. Russell, W. H. Jo, *J. Mater. Chem.* **2009**, *19*, 1483.
- [26] R. C. Hiorns, E. Cloutet, E. Ibarboure, A. Khoukh, H. Bejbouji, L. Vignau, H. Cramail, *Macromolecules* **2010**, *43*, 6033.
- [27] B. Gholamkhash, T. J. Peckham, S. Holdcroft, *Polym. Chem.* **2010**, *1*, 708.
- [28] Y.-H. Lin, K. G. Yager, B. Stewart, R. Verduzco, *Soft Matter* **2014**, *10*, 3817.
- [29] R. H. Lohwasser, G. Gupta, P. Kohn, M. Sommer, A. S. Lang, T. Thurn-Albrecht, M. Thelakkat, *Macromolecules* **2013**, *46*, 4403.
- [30] B. de Boer, U. Stalmach, P. F. van Hutten, C. Melzer, V. V. Krasnikov, G. Hadziioannou, B. De Boer, P. F. Van Hutten, *Polymer* **2001**, *42*, 9097.
- [31] M. H. van der Veen, B. de Boer, U. Stalmach, K. I. van de Wetering, G. Hadziioannou, *Macromolecules* **2004**, *37*, 3673.
- [32] B. Gholamkhash, S. Holdcroft, *Chem. Mater.* **2010**, *22*, 5371.
- [33] M. Heuken, H. Komber, T. Erdmann, V. Senkovskyy, A. Kiri, B. Voit, *Macromolecules* **2012**, *45*, 4101.
- [34] S. Miyanishi, Y. Zhang, K. Tajima, K. Hashimoto, *Chem. Commun.* **2010**, *46*, 6723.
- [35] M. Hufnagel, M. Fischer, T. Thurn-Albrecht, M. Thelakkat, *Polym. Chem.* **2015**, *6*, 813.
- [36] G. Adamopoulos, T. Heiser, U. Giovanella, S. Ouldsaad, K. Vandewetering, C. Brochon, T. Zorba, K. Paraskevopoulos, G. Hadziioannou, *Thin Solid Films* **2006**, *511-512*, 371.
- [37] L. Perrin, A. Nourdine, E. Planes, C. Carrot, N. Alberola, L. Flandin, *J. Polym. Sci. Part B Polym. Phys.* **2013**, *51*, 291.
- [38] M. Hufnagel, M.-A. Muth, J. C. Brendel, M. Thelakkat, *Macromolecules* **2014**, *47*, 2324.
- [39] C. R. Singh, G. Gupta, R. Lohwasser, S. Engmann, J. Balko, M. Thelakkat, T. Thurn-Albrecht, H. Hoppe, *J. Polym. Sci. Part B Polym. Phys.* **2013**, *51*, 943.
- [40] C. J. Brabec, S. Gowrisanker, J. J. M. Halls, D. Laird, S. Jia, S. P. Williams, B. C. J. Brabec, *Adv. Mater.* **2010**, *22*, 3839.
- [41] R. H. Lohwasser, M. Thelakkat, *Macromolecules* **2012**, *45*, 1.
- [42] U. Stalmach, B. de Boer, C. Videlot, P. F. van Hutten, G. Hadziioannou, *J. Am. Chem. Soc.* **2000**, *122*, 5464.
- [43] M. Thelakkat, P. Pösch, H. W. Schmidt, *Macromolecules* **2001**, *34*, 7441.
- [44] J.-F. Chang, B. Sun, D. W. Breiby, M. M. Nielsen, T. I. Sölling, M. Giles, I. McCulloch, H. Sirringhaus, *Chem. Mater.* **2004**, *16*, 4772.
- [45] K. Zhu, T. Kwei, E. Pearce, *J. Appl. Poly. Sci.* **1989**, *37*, 573.
- [46] A. Matsumoto, S. Tanaka, T. Otsu, *Macromolecules* **1991**, *24*, 4017.
- [47] J. V. Grazulevicius, P. Stroehriegl, J. Pielichowski, K. Pielichowski, *Prog. Polym. Sci.* **2003**, *28*, 1297.
- [48] C. J. Hawker, *Macromolecules* **1994**, *27*, 4836.
- [49] F. C. Spano, *J. Chem. Phys.* **2005**, *122*, 234701.
- [50] C. Scharsich, R. H. Lohwasser, M. Sommer, U. Asawapirom, U. Scherf, M. Thelakkat, D. Neher, A. Köhler, *J. Polym. Sci. Part B Polym. Phys.* **2012**, *50*, 442.
- [51] S. Huettner, M. Sommer, J. Hodgkiss, P. Kohn, T. Thurn-Albrecht, R. H. Friend, U. Steiner, M. Thelakkat, *ACS Nano* **2011**, *5*, 3506.
- [52] A. S. Lang, M. Thelakkat, *Polym. Chem.* **2011**, *2*, 2213.

**SUPPORTING INFORMATION**

**Scheme S1.** Detailed synthesis route for PPCBM-b-P3HT 1-3.

**Figure S1.**  $^1\text{H-NMR}$  spectrum of P3HT-b-PS<sub>OH</sub> 1.

**Figure S2.**  $^1\text{H-NMR}$  spectrum of P3HT-b-PS<sub>OH</sub> 2.

**Figure S3.**  $^1\text{H-NMR}$  spectrum of P3HT-b-PS<sub>OH</sub> 3.

**Figure S4.**  $^1\text{H-NMR}$  spectrum of P3HT-b-PPCBM 1.

**Figure S5.**  $^1\text{H-NMR}$  spectrum of P3HT-b-PPCBM 2.

**Figure S6.**  $^1\text{H-NMR}$  spectrum of P3HT-b-PPCBM 3.

**Figure S7.** Thermogravimetric analysis (TGA) of P3HT-b-PPCBM 2-3 and their precursor polymers.

**Figure S8.** Differential scanning calorimetry (DSC) traces of P3HT-b-PSOH 1-3.

**Table S1.** DSC results for P3HT-b-PSOH 1-3.

**Figure S9.** TGA traces of PS<sub>OH</sub> 3 and P3HT-b-PS<sub>OH</sub> 3 indicating cross-linking.

**Figure S10.** Size exclusion chromatography (SEC) trace of a PS<sub>OH</sub> copolymer after thermal cross-linking.

**Figure S11.** DSC traces of a PS<sub>OH</sub> copolymer indicating cross-linking.

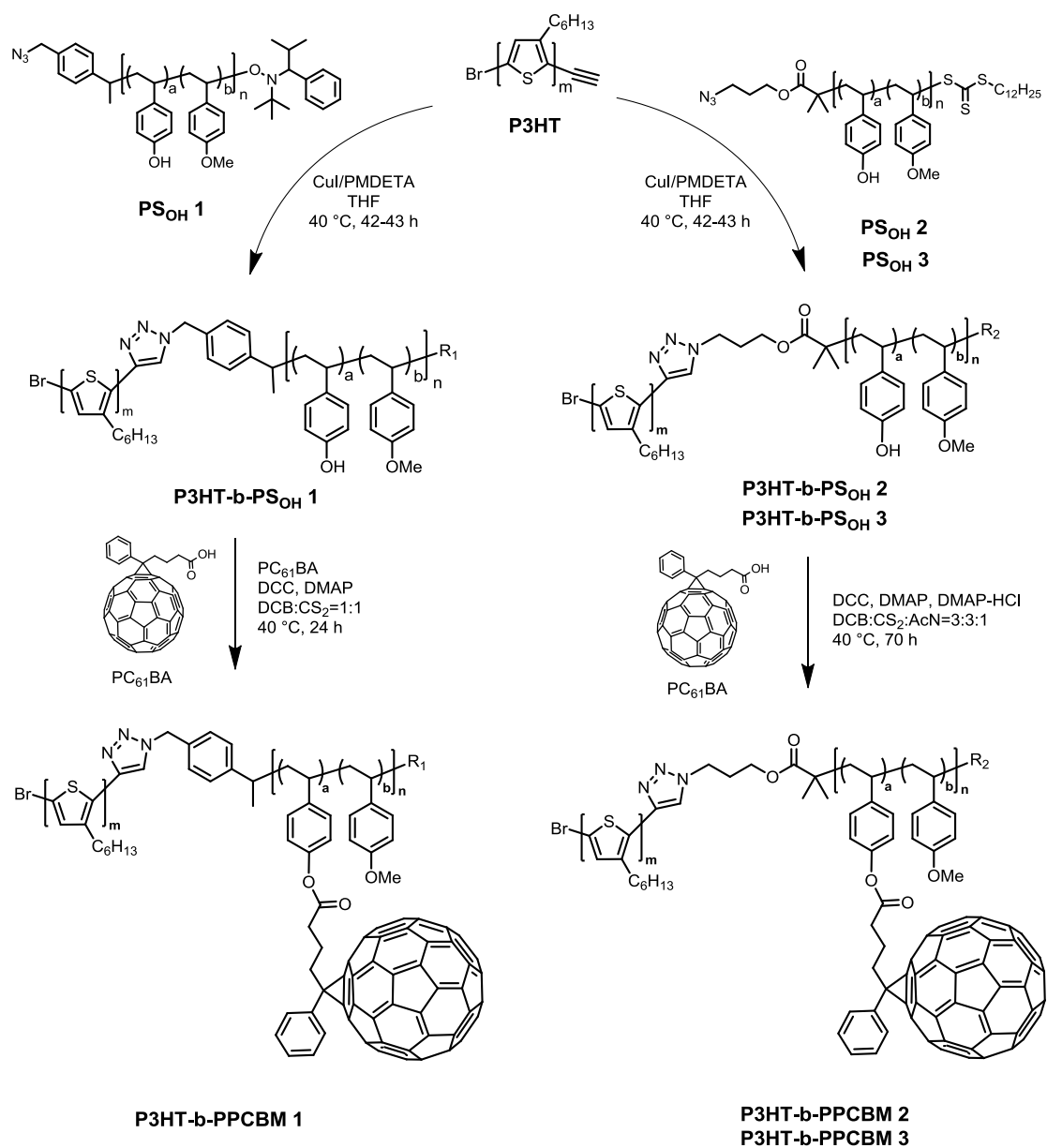
**Figure S12.** DSC traces of a) the PS<sub>OH</sub> 1 polystyrene copolymer and (b) the PC<sub>61</sub>BM-grafted homopolymers PPCBM 1-3.

**Figure S13.** 2D-GISAXS data of P3HT-b-PPCBM 1 around the Yoneda position at room temperature of films prepared by spin-coating with subsequent annealing in the melt (left) or drop-casting (right). Data are displayed on a logarithmic intensity scale

**Figure S14.** GISAXS data of P3HT-b-PPCBM 1-3: horizontal intensity profiles of drop casted samples and melt crystallized thin films taken along the Yoneda position.

**Figure S15.** Exemplary set of OFET output and transfer characteristics for P3HT-b-PPCBM 1-3.

**Table S2.** Results of the OFET measurements for P3HT-b-PPCBM 1-3.



**Scheme S1.** Synthesis strategy towards the donor-acceptor block copolymers P3HT-b-PPCBM 1-3.

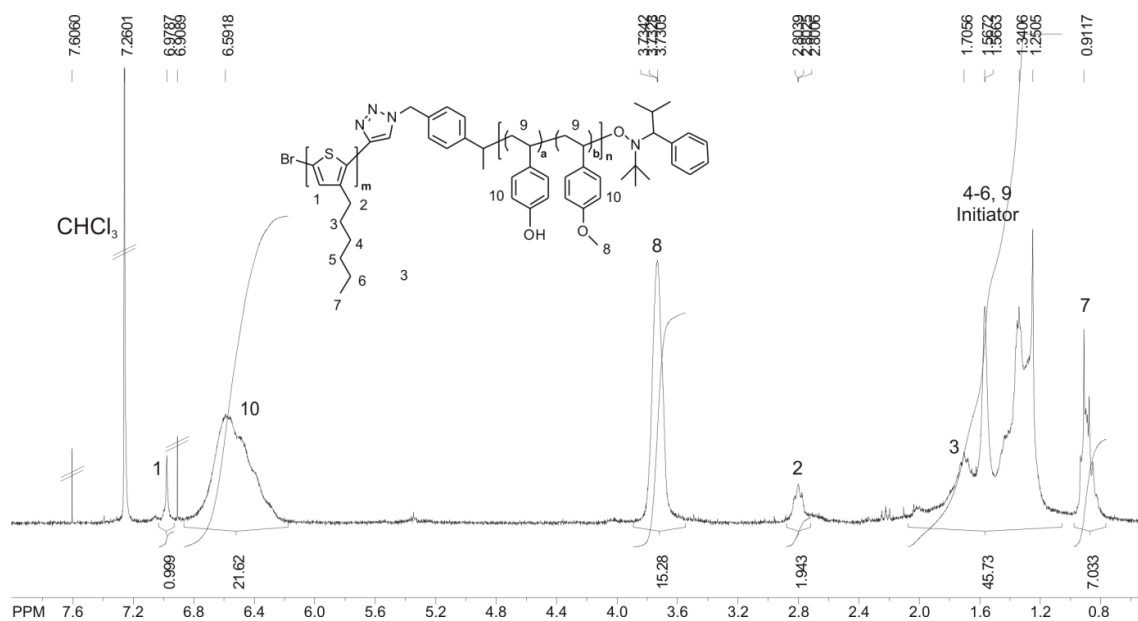


Figure S1.  $^1\text{H-NMR}$  spectrum of P3HT-b-PS<sub>OH</sub> 1.

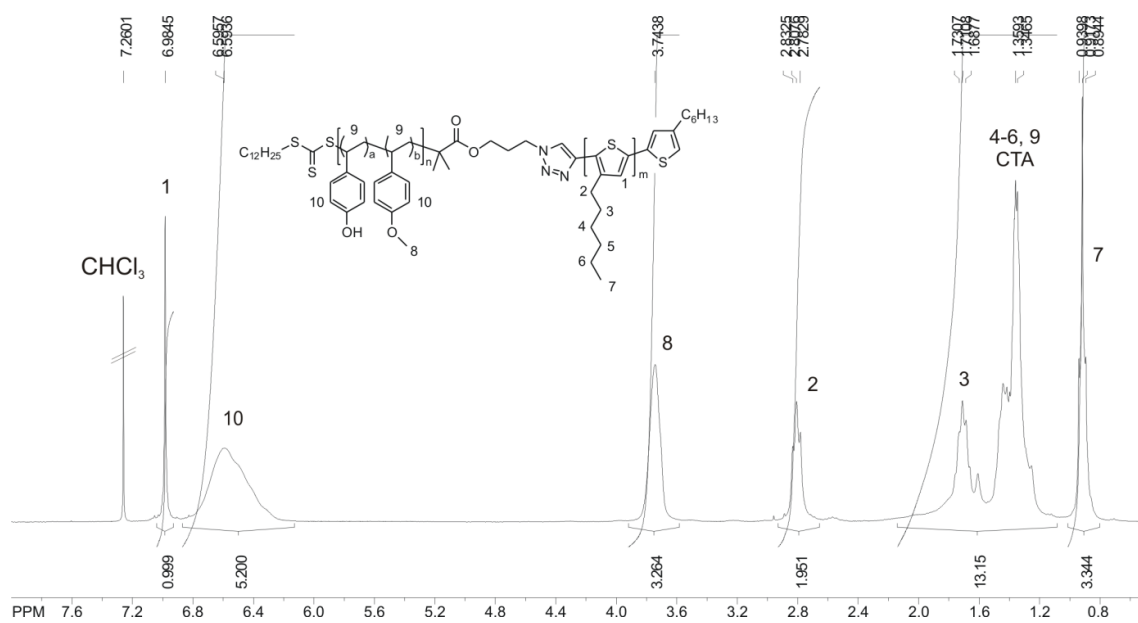


Figure S2.  $^1\text{H-NMR}$  spectrum of P3HT-b-PS<sub>OH</sub> 2.

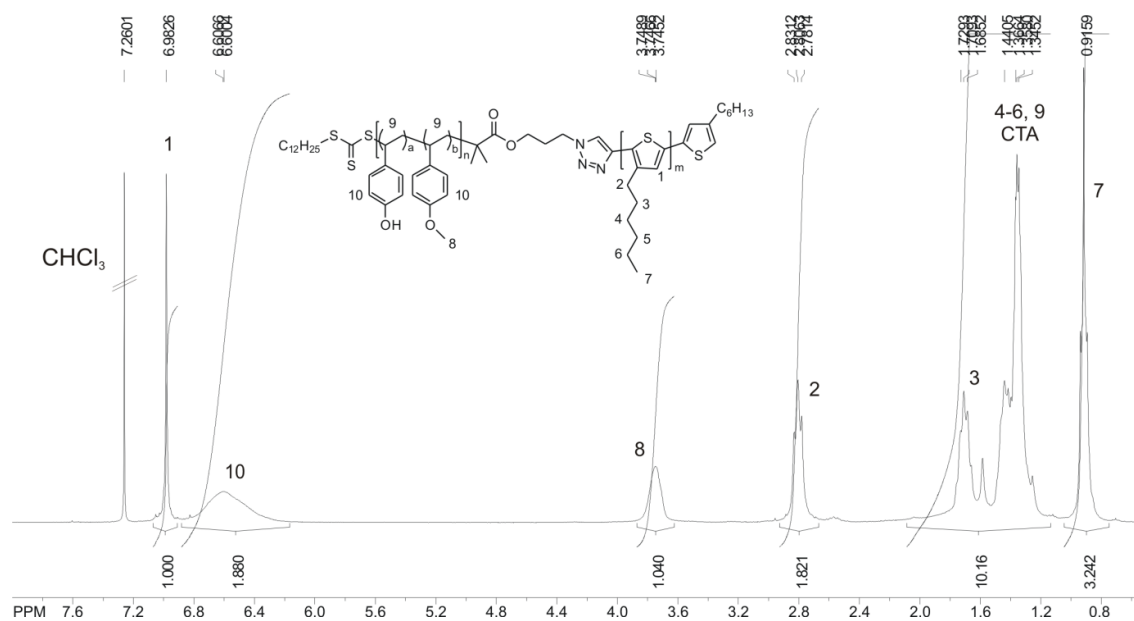


Figure S3.  $^1\text{H-NMR}$  spectrum of P3HT-b-PS<sub>OH</sub> 3.

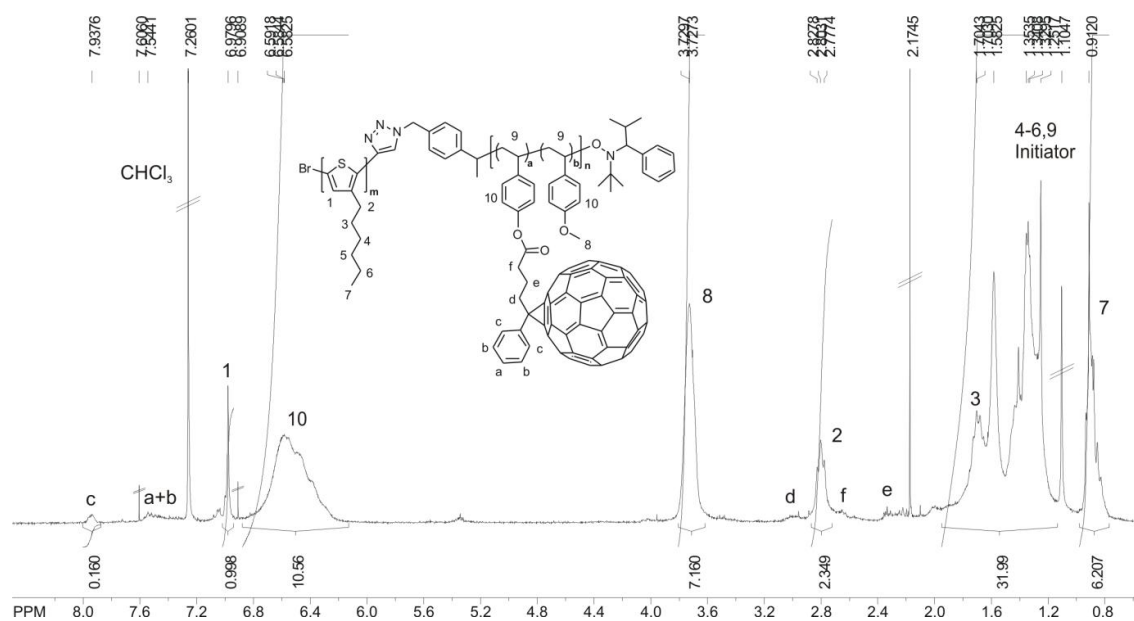


Figure S4.  $^1\text{H-NMR}$  spectrum of P3HT-b-PPCBM 1.

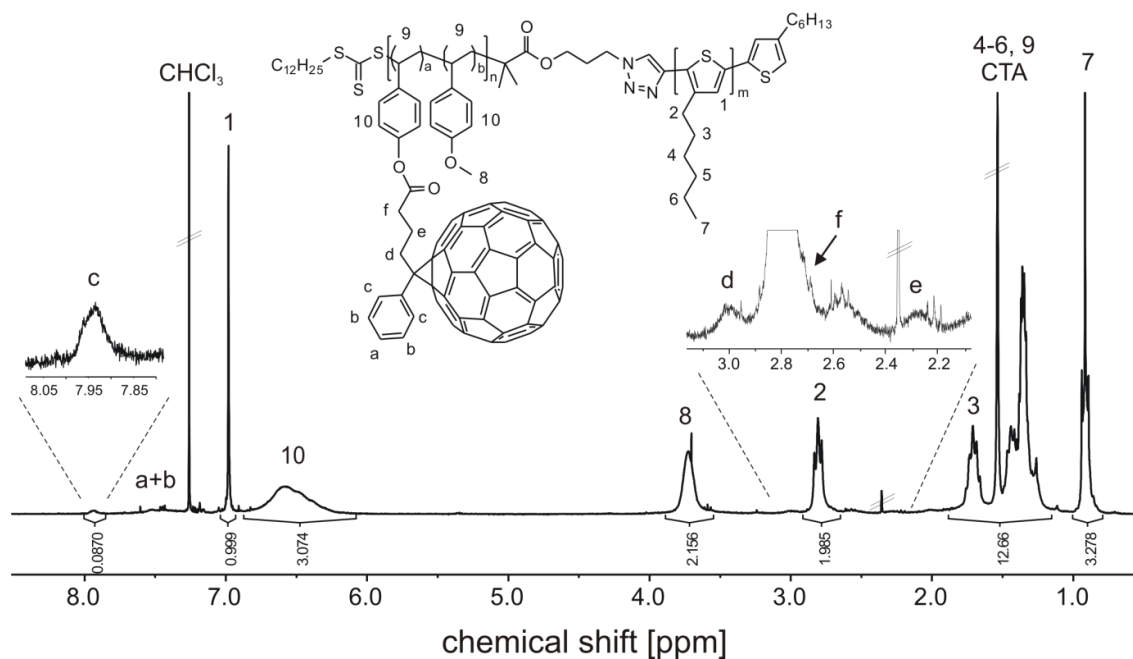


Figure S5.  $^1\text{H-NMR}$  spectrum of P3HT-b-PPCBM 2.

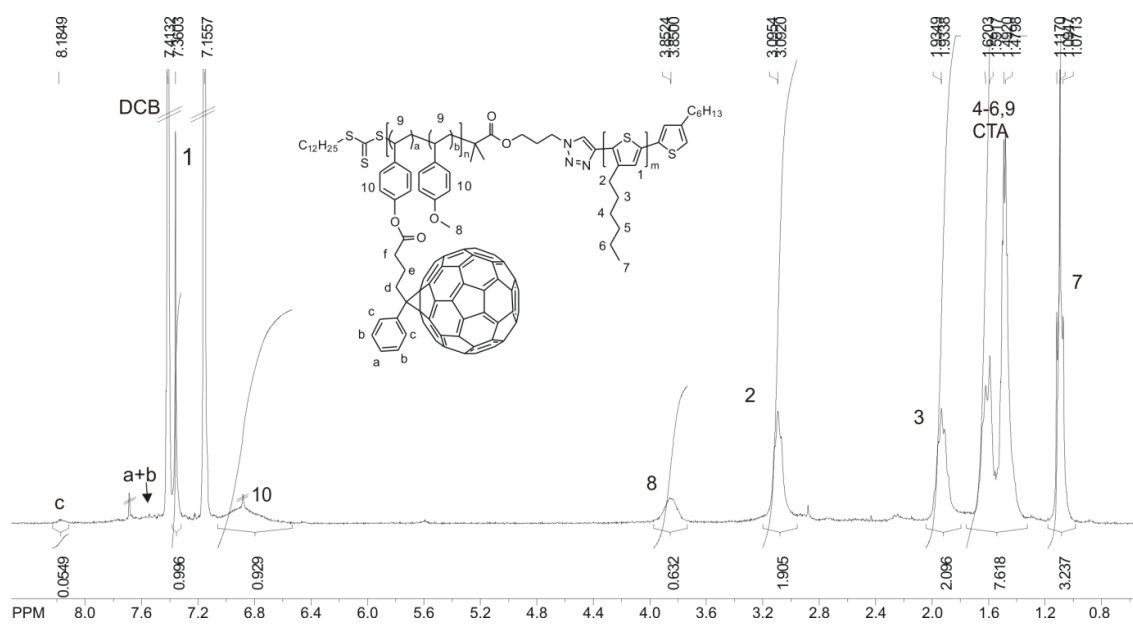
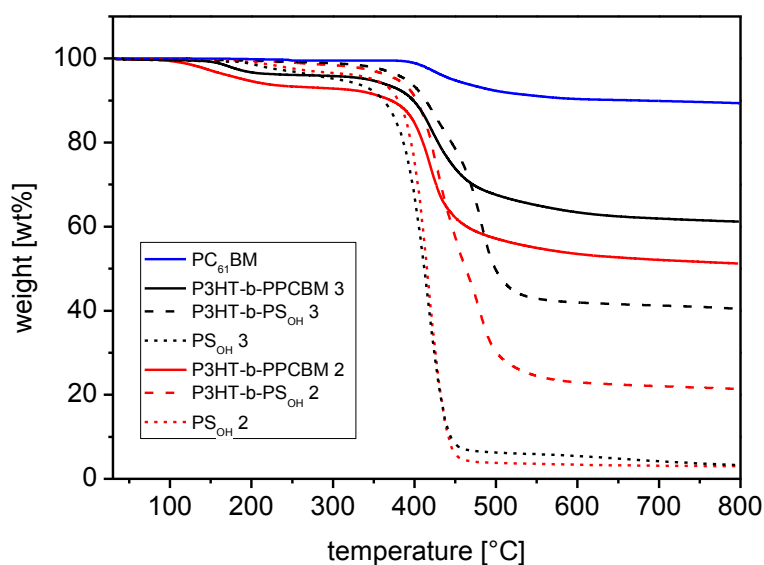
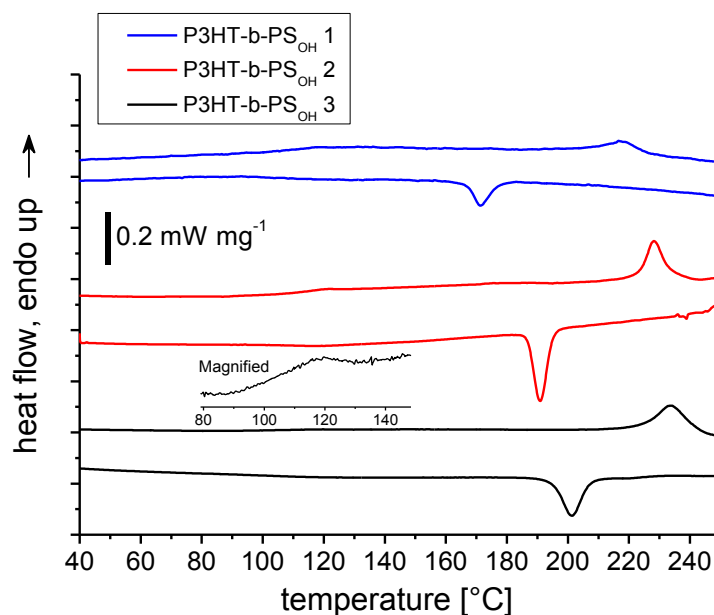


Figure S6.  $^1\text{H-NMR}$  spectrum of P3HT-b-PPCBM 3.



**Figure S7.** Thermogravimetric analysis (TGA) of the polymers in nitrogen atmosphere with a heating rate of  $10 \text{ K min}^{-1}$ . The  $\text{PC}_{61}\text{BM}$  fullerene shows a decomposition step around  $400 \text{ }^\circ\text{C}$  related to the loss of the phenyl butyric ester handle. The  $\text{C}_{60}$  fullerene core is stable up to  $800 \text{ }^\circ\text{C}$ , therefore, the residual char of the block copolymers P3HT-b-PPCBM 2 and 3 roughly correlates with the increasing amount of incorporated PCBM.



**Figure S8.** DSC traces of P3HT-b-PSOH 1-3 at a heating/cooling rate of  $10 \text{ K min}^{-1}$ .

**Table S1.** DSC data for P3HT-b-PS<sub>OH</sub> 1-3.

Polymer	Melting $T_{m,peak}$ [°C]	Crystallization $T_{c,peak}$ [°C]	Glass transition $T_g$ [°C]
P3HT-b-PS <sub>OH</sub> 1	217	172	107
P3HT-b-PS <sub>OH</sub> 2	228	191	112
P3HT-b-PS <sub>OH</sub> 3	233	201	108

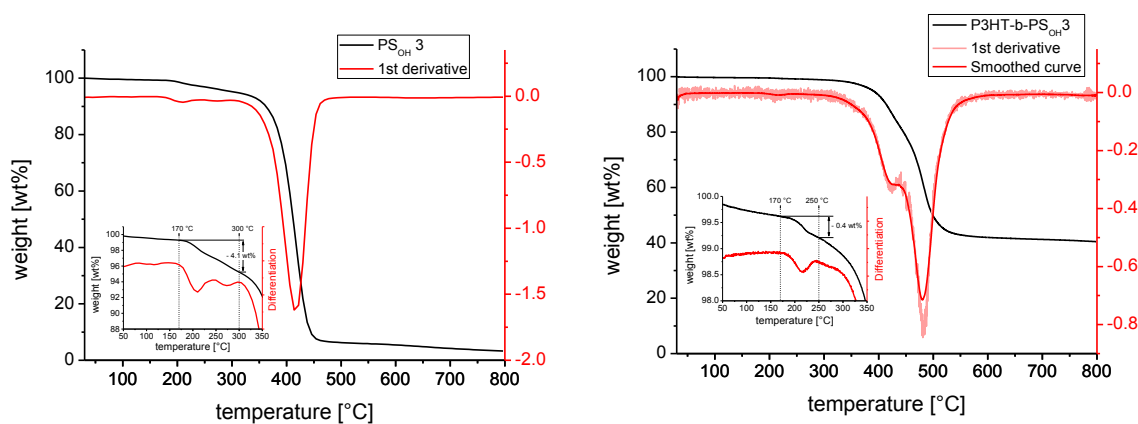


**Figure S9.** TGA traces of PS<sub>OH</sub> 3 (left) and P3HT-b-PS<sub>OH</sub> 3 recorded at a heating rate of 10 K min<sup>-1</sup> in nitrogen atmosphere. The cross-linking of the polymer via condensation of the hydroxyl groups is in agreement with the weight loss of 4.1 wt% between 170-250°C (PS<sub>OH</sub> 3) and 0.4 wt% between 170-300°C (P3HT-b-PS<sub>OH</sub> 3). The differentiation of the weight loss curve clearly illustrates the expulsion of condensation products in the range of 170 to 300°C.

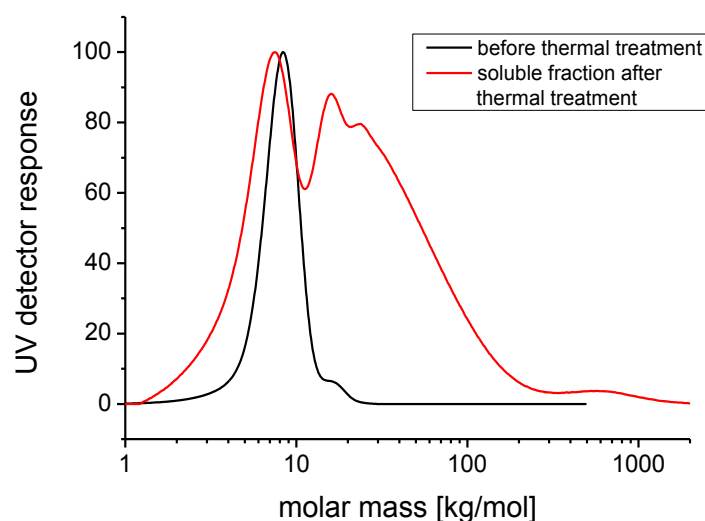


**Figure S10.** SEC trace of a  $PS_{OH}$  polymer without azide end group ( $M_n=7.5 \text{ kg mol}^{-1}$  and 26 mol% 4-hydroxystyrene) before (black) and after the thermal treatment (red) in DSC up to 260 °C (see Figure S11). The polymer after DSC measurement was mostly insoluble due to the cross-linking; only the soluble fraction was applied to SEC.

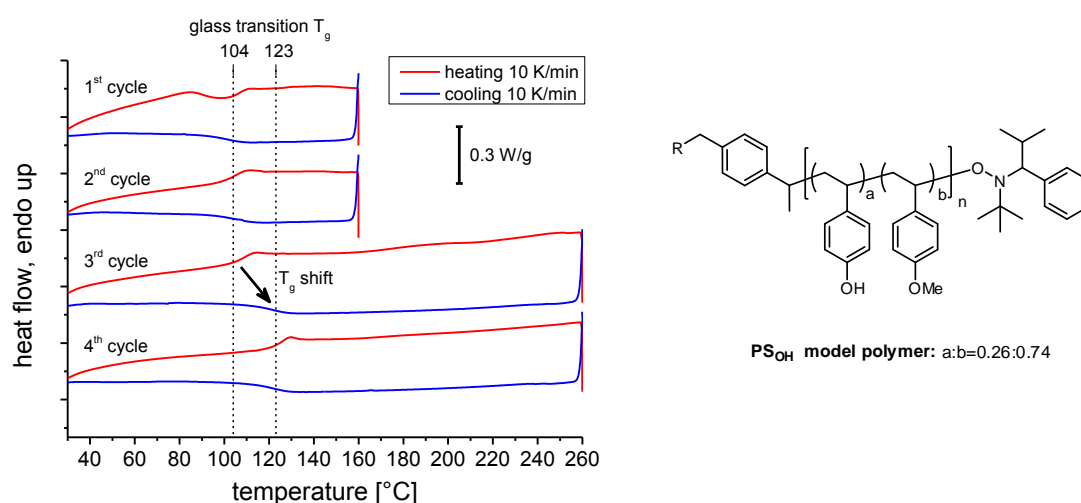


**Figure S11.** DSC traces of a  $PS_{OH}$  model polymer without azide end group ( $M_n=7.5 \text{ kg mol}^{-1}$  and monomer ratio a:b=0.26:0.74). This polymer is highly comparable to  $PS_{OH}$  3. In the measurement range 25-160 °C the  $PS_{OH}$  polymer shows a glass transition  $T_g$  of 104 °C (cycles 1 and 2). As soon as the polymer in cycle 3 is once heated above 200 °C in the range of 25-260 °C, the subsequent cooling curve of cycle 3 shows an increased  $T_g$  of 123 °C, which is attributed to the formation of cross-links in the  $PS_{OH}$  polymer. The increased  $T_g$  is maintained in the following heating/cooling cycles (see 4th cycle).

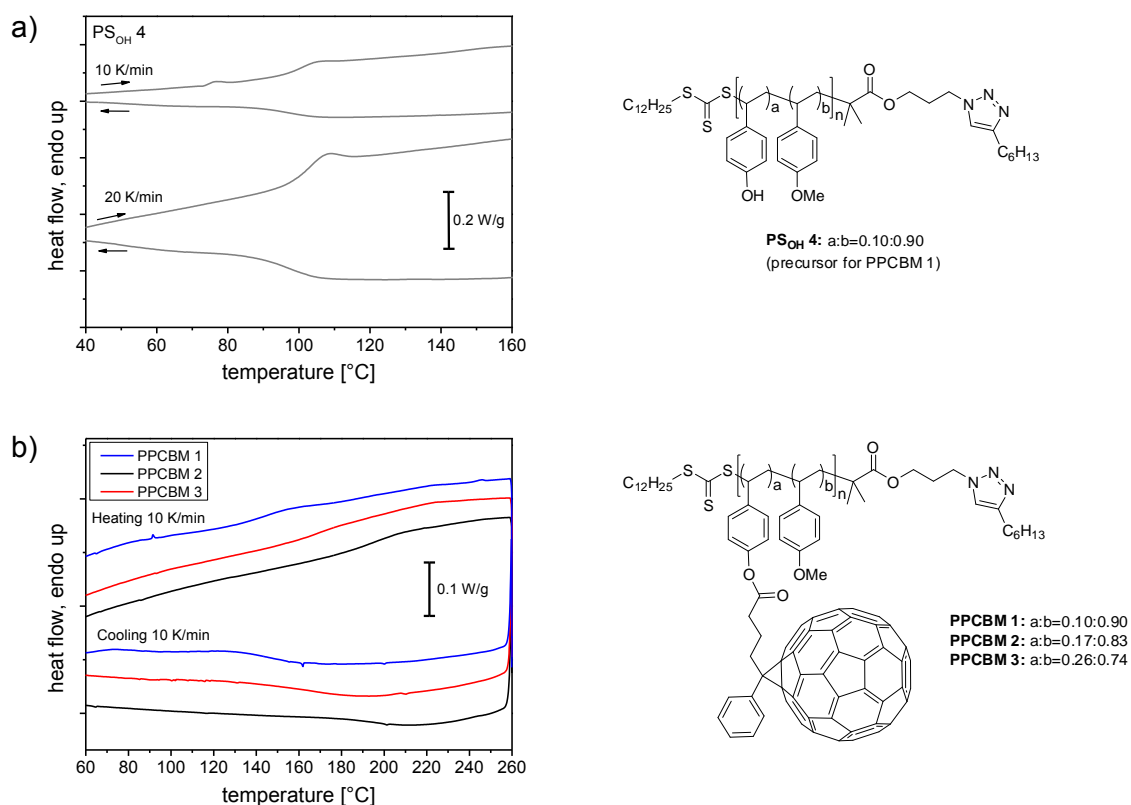


**Figure S12.** Differential scanning calorimetry traces of a) the PS<sub>OH</sub> 4 polystyrene copolymer and b) the PC<sub>61</sub>BM-grafted homopolymers PPCBM 1-3 with a heating/cooling rate of 10 K min<sup>-1</sup>.

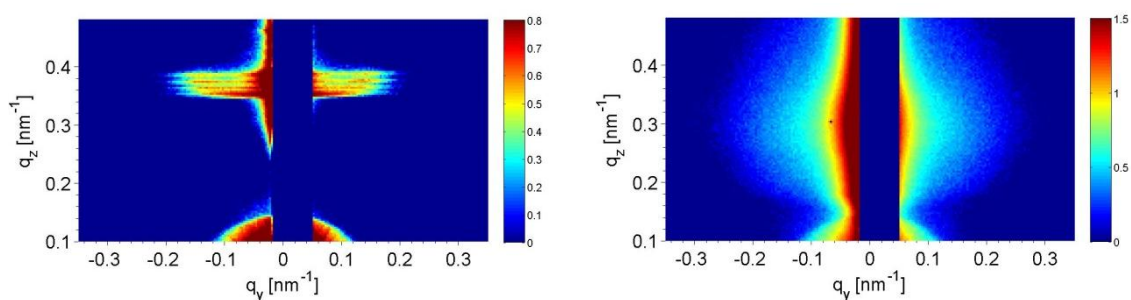


**Figure S13.** 2D-GISAXS data of P3HT-*b*-PPCBM 1 around the Yoneda position at room temperature of films prepared by spin-coating with subsequent annealing in the melt (left) or drop-casting (right). Data are displayed on a logarithmic intensity scale

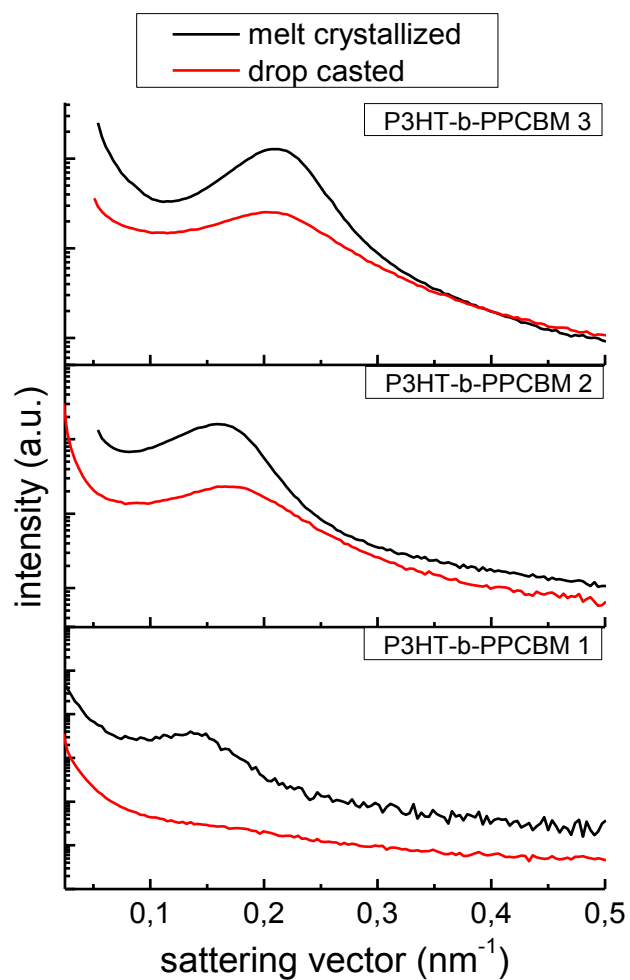


**Figure S14.** GISAXS data of P3HT-b-PPCBM 1-3: horizontal intensity profiles of drop casted samples and melt crystallized thin films taken along the Yoneda position.

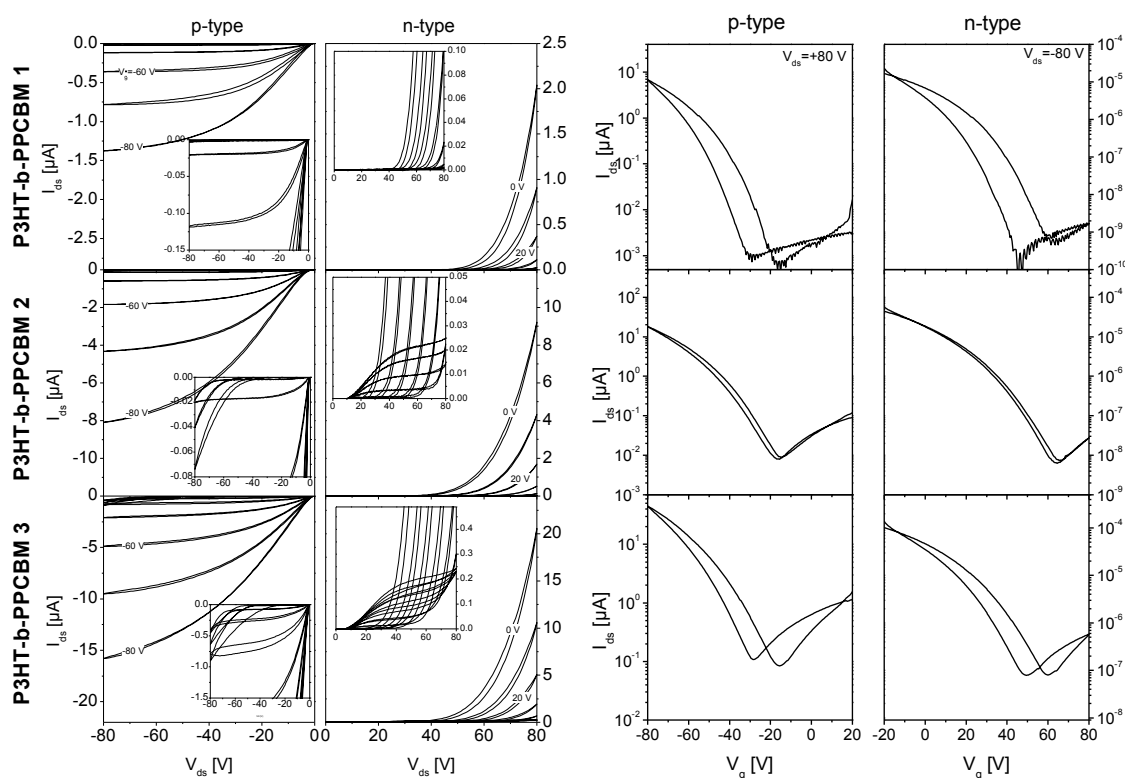


**Figure S15.** Exemplary set of OFET output characteristics for P3HT-b-PPCBM 1-3 measured in as-cast state after thermal annealing for 2 hours at 160 °C (left). The insets for the output characteristics of the annealed transistors show magnified details of the respective set of output curves. Corresponding transfer characteristics measured under p-type (source-drain voltage  $V_{ds}=+80$  V) and n-type ( $V_{ds}=-80$  V) conditions clearly support ambipolar charge transport (right). The OFET transistor architecture was bottom-gate, bottom-contact on a n-doped silicon substrate with a 230 nm  $\text{SiO}_2$  insulating gate dielectric passivated with an octadecyltrichlorosilane (ODTS) layer and 40 nm source/drain gold contacts. The transistor channel length for this set of data is 10  $\mu\text{m}$  with a width of 10 mm.

**Table S2.** Results of the OFET measurements. The average mobility was determined based on 4 different transistors with varying channel length. The mobility was extracted from the square-root of drain-source current of the transfer curves in the saturation regime.

Polymer	Type	No.	Channel length [ $\mu\text{m}$ ]	Fitted mobility [ $\text{cm}^2\text{V}^{-1}\text{s}^{-1}$ ]	Average mobility [ $\text{cm}^2\text{V}^{-1}\text{s}^{-1}$ ]
P3HT-b-PPCBM 1	p	1	10	5.33E-04	$3.20\text{E-}04 \pm 1.26\text{E-}04$
		2	20	2.68E-04	
		3	20	2.05E-04	
		4	20	2.73E-04	
	n	1	10	7.94E-08	$1.21\text{E-}07 \pm 2.79\text{E-}08$
		2	20	1.15E-07	
		3	20	1.36E-07	
		4	20	1.54E-07	
P3HT-b-PPCBM 2	p	1	10	1.19E-03	$1.41\text{E-}03 \pm 2.69\text{E-}04$
		2	10	1.15E-03	
		3	5	1.49E-03	
		4	5	1.82E-03	
	n	1	10	5.87E-06	$4.81\text{E-}06 \pm 7.16\text{E-}07$
		2	10	5.02E-06	
		3	5	4.36E-06	
		4	5	3.98E-06	
P3HT-b-PPCBM 3	p	1	20	2.30E-03	$2.53\text{E-}03 \pm 8.61\text{E-}04$
		2	10	2.45E-03	
		3	20	1.49E-03	
		4	10	3.88E-03	
	n	1	20	2.93E-05	$2.29\text{E-}05 \pm 4.89\text{E-}06$
		2	10	1.77E-05	
		3	20	2.60E-05	
		4	10	1.87E-05	



## 6 Influence of composition on structure formation and charge transport in P3HT-b-PPC<sub>71</sub>BM block copolymers

*Martin Hufnagel<sup>a</sup>, Matthias Fischer<sup>b</sup>, Anne Browa<sup>a</sup>, Thomas Thurn-Albrecht<sup>b</sup>, Mukundan  
Thekkat<sup>a,\*</sup>*

<sup>a</sup>Applied Functional Polymers, Department of Macromolecular Chemistry I  
University of Bayreuth, Universitaetsstr. 30, 95440 Bayreuth (Germany)

<sup>b</sup>Experimental Polymer Physics Group, Martin-Luther University Halle-Wittenberg,  
Von-Danckelmann-Platz 3, 06120 Halle (Germany)

\*E-mail: [mukundan.thekkat@uni-bayreuth.de](mailto:mukundan.thekkat@uni-bayreuth.de)

**ABSTRACT**

Balancing charge transport between holes and electrons in donor-acceptor block copolymers is a major challenge on the way towards their application in optoelectronic devices. One promising approach to match hole and electron mobilities could be by tailoring the molecular weights of donor and acceptor block to vary the composition between p-type and n-type semiconductor in the block copolymer. We demonstrate this strategy using a series of P3HT-b-PPC<sub>71</sub>BM block copolymers which incorporate poly(3-hexylthiophene) (P3HT) as donor and a polystyrene copolymer with pendant phenyl-C<sub>71</sub>-butyric acid methyl ester (PC<sub>71</sub>BM) fullerenes as acceptor block (PPC<sub>71</sub>BM). The composition of P3HT:PPC<sub>71</sub>BM in the block copolymers is varied between 1:0.43, 1:1.70 and 1:3.55 by increasing the polymer chain length of the acceptor block PPC<sub>71</sub>BM. We study in detail the consequences of composition on the crystallization of P3HT in bulk as well as in thin films and the structure formation through microphase separation using differential scanning calorimetry (DSC), absorption and photoluminescence (PL) spectroscopy and small angle X-ray scattering (SAXS). Various thermal annealing procedures in thin films are investigated to find ideal conditions for crystallization of the hole transporting P3HT block and to achieve high phase purity and phase separation of the donor and acceptor domains. With these optimized post-processing conditions in hand, we study the composition dependence of charge transport in P3HT-b-PPC<sub>71</sub>BM block copolymers in organic field-effect transistors (OFET).

**INTRODUCTION**

Block copolymers incorporating a  $\pi$ -conjugated polymer block have emerged into an attractive material class for novel applications in optoelectronic devices.<sup>[1,2]</sup> In the field of organic photovoltaics, the light-harvesting active layer requires a bicontinuous network of donor and acceptor material on the scale of tens of nanometers, called bulk heterojunction (BHJ), for an efficient charge generation and charge transport.<sup>[3-6]</sup> An ideal solution towards a long-term stable donor-acceptor BHJ could be realized by self-assembling nanomaterials which exhibit a thermodynamic equilibrium morphology. One approach are single polymer materials incorporating both donor and acceptor functions integrated in a block copolymer architecture with the capability to self-assemble into the desired microdomains. A variety of such donor-acceptor block copolymers for OPV has been reported so far including block copolymers which carry acceptor blocks grafted with C<sub>60</sub>

or its derivatives.<sup>[7–11]</sup> Recently, also C<sub>70</sub> has been incorporated into polymer chains as acceptors.<sup>[12]</sup> Compared to C<sub>60</sub>, the C<sub>70</sub> fullerene has an inherent advantage due to its improved absorption in the visible range which considerably can enhance the photocurrent in blend solar cells.<sup>[13]</sup> For the attachment of fullerenes onto the polymer chains monofunctionalized fullerene derivatives are preferred in order to avoid multi-adduct reactions which may lead to cross-linking or insoluble polymers.<sup>[14–16]</sup>

One of the key parameters driving the performance of optoelectronic devices such as organic light-emitting diodes (OLED), organic photovoltaics (OPV) or organic field-effect transistors (OFET) is the charge carrier mobility. The mobility  $\mu$  indicates how fast a charge carrier, an electron or hole, can travel through a semiconductor. As a rule of thumb, sufficiently high and balanced charge carrier mobilities are favorable for the power conversion efficiency in OPV, since non-geminate recombination of charges is reduced by a fast carrier extraction and the formation of space-charge in the photoactive layer is almost negligible.<sup>[17–21]</sup>

Donor-acceptor block copolymers often do not exhibit balanced charge carrier mobilities.<sup>[22,23]</sup> For block copolymers with a  $\pi$ -conjugated polymer as p-type semiconductor and a fullerene-grafted polymer block as n-type semiconductor we suggest three different methods to balance the charge transport: First, variation of the fullerene grafting density in the PPCBM block. This approach has been studied in a series of P3HT-b-PPC<sub>61</sub>BM block copolymers and resulted in a notably narrowed gap between hole and electron mobility.<sup>[23]</sup> Second, variation of the donor-acceptor composition in the block copolymer. And third, blending small molecules with high mobility into the block copolymer to match the hole and electron mobility.<sup>[24]</sup> This blend approach is a simple but efficient route towards balanced mobilities. In this work, we focus on the composition variation of donor and acceptor blocks in a series of P3HT-b-PPC<sub>71</sub>BM block copolymers. It is well known from the extensively studied P3HT:PCBM blends that charge transport is highly composition dependent. Thus, many efforts have been done so far to find the optimum composition of P3HT:PCBM for balanced charge transport.<sup>[18,25,26]</sup> Here, we raise the following questions: 1. Does the charge transport in P3HT-b-PPC<sub>71</sub>BM block copolymers show a composition dependence of P3HT and PPC<sub>71</sub>BM blocks? 2. Can we achieve balanced charge carrier mobilities by tailoring the polymer design in this block copolymer series by varying the composition? 3. What is the impact of varying the P3HT:PPC<sub>71</sub>BM composition on the crystallization of P3HT and how is the nanoscale

structure formation in P3HT-b-PPC<sub>71</sub>BM influenced by composition? 4. What are ideal thermal annealing conditions for this block copolymer system for charge carrier transport?

To answer these question we have synthesized a well-defined series of three P3HT-b-PPC<sub>71</sub>BM block copolymers with varying composition. Crystallization and morphological properties in bulk and thin films are studied using a combination of DSC, UV-vis and PL spectroscopy. Temperature-dependent SAXS analysis is performed to understand the structure formation of the block copolymers and to elucidate any structure dependence on composition. Various annealing procedures are screened to find ideal conditions for the fabrication of OFETs, which allow us to determine the charge transport properties of the P3HT-b-PPC<sub>71</sub>BM block copolymers.

## RESULTS AND DISCUSSION

### Synthesis of P3HT-*b*-PPC<sub>71</sub>BM block copolymers

The donor-acceptor block copolymers P3HT-*b*-PPC<sub>71</sub>BM investigated in this report are based on a regioregular poly(3-hexylthiophene) (P3HT) block as donor and a polystyrene copolymer with pendant phenyl-C<sub>71</sub>-butyric acid methyl ester (PC<sub>71</sub>BM) fullerenes as acceptor block (PPC<sub>71</sub>BM). To study the charge transport properties in dependence of the block copolymer composition P3HT:PPC<sub>71</sub>BM, we have prepared a series of three block copolymers: By using a modular synthesis route we are able to combine the same P3HT block with different PPC<sub>71</sub>BM blocks of varying chain lengths, *i.e.* the weight fractions of P3HT and PPC<sub>71</sub>BM were gradually changed in this polymer series (Figure 1) keeping the degree of polymerization for P3HT constant.

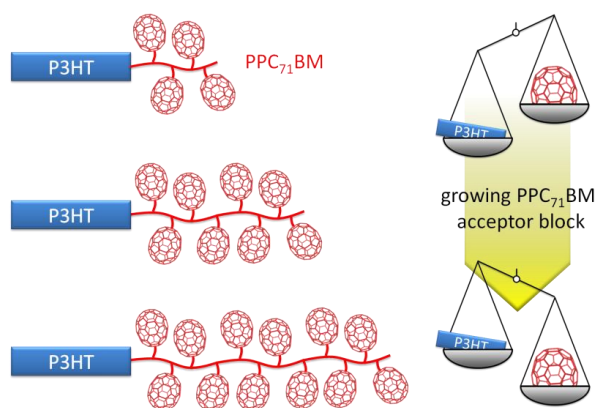
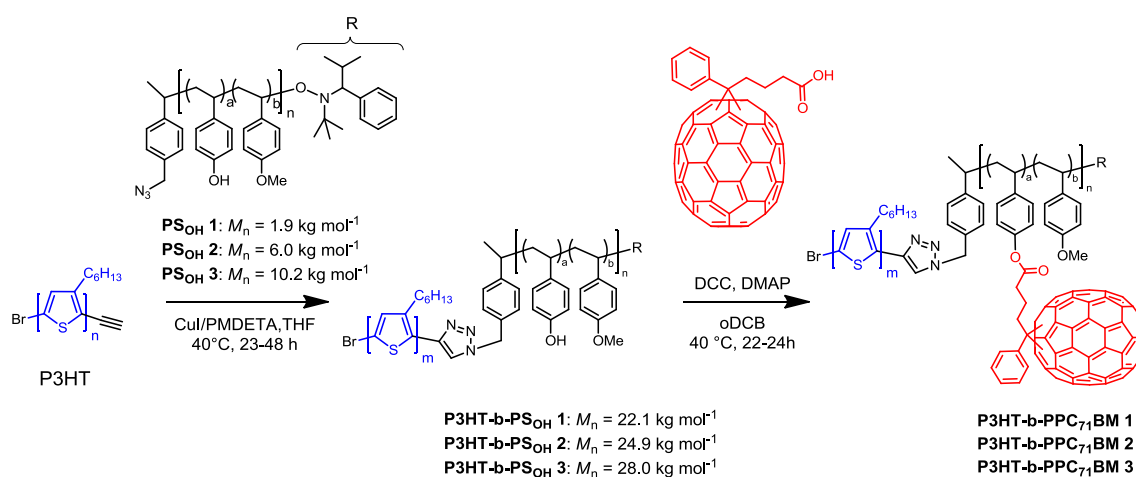


**Figure 1.** Schematic illustration of the P3HT-*b*-PPC<sub>71</sub>BM block copolymer series showing the composition variation of P3HT:PPC<sub>71</sub>BM by extending the PPC<sub>71</sub>BM acceptor block.

Ethynyl end-capped P3HT was prepared by termination of the Kumada catalyst transfer polycondensation with ethynylmagnesium chloride.<sup>[27]</sup> The obtained P3HT has high regioregularity, a molecular weight of  $M_n=20.6 \text{ kg mol}^{-1}$  (SEC) and a low dispersity of  $D=1.14$ . These factors are beneficial for hole transport<sup>[28]</sup> and can further promote microphase separation in block copolymers.<sup>[29]</sup> The acceptor counterpart is based on a polystyrene precursor, poly(4-*tert*-butyloxystyrene-*stat*-4-methoxystyrene) which was synthesized by nitroxide-mediated radical polymerization (NMRP) followed by a polymer-analogous deprotection of the *tert*-butyl ether groups and the azide substitution at the polymer chain end.<sup>[12,30]</sup> The resulting copolymers poly(4-hydroxystyrene-*stat*-4-

methoxystyrene) PS<sub>OH</sub> 1-3 have an equal built-in monomer ratio of 4-hydroxystyrene:4-methoxystyrene of a:b=0.25:0.75. This ratio was found as the upper limit to achieve soluble fullerene-grafted polymers after a high degree of esterification.<sup>[30]</sup> The preformed polymers PS<sub>OH</sub> 1-3 and P3HT were then coupled by a simple and efficient copper(I)-catalyzed azide-alkyne cycloaddition (CuAAC) to yield the P3HT-b-PS<sub>OH</sub> 1-3 block copolymers (Scheme 1). The success of the block copolymer formation is evidenced by the size exclusion chromatography (SEC) traces, which unambiguously show the molar mass growth of P3HT from  $M_p=22.3 \text{ kg mol}^{-1}$  to 24.3, 30.6 and 35.1  $\text{kg mol}^{-1}$  for P3HT-b-PS<sub>OH</sub> 1-3 after coupling with the 2.1, 6.8 and 11.5  $\text{kg mol}^{-1}$  PS<sub>OH</sub> 1-3 polystyrenes (Figure 2a). In the final polymer-analogous reaction, the fullerene derivative phenyl-C<sub>71</sub>-butyric acid (PC<sub>71</sub>BA) was introduced by a Steglich esterification to yield the fully-functionalized block copolymers P3HT-b-PPC<sub>71</sub>BM 1-3. The corresponding SEC traces were measured with high-temperature SEC in 1,2,4-trichlorobenzene and show a monomodal molar mass distribution with  $M_p=28.9$ , 26.4 and 28.4  $\text{kg mol}^{-1}$  and, particularly for P3HT-b-PPC<sub>71</sub>BM 2 and 3, only a surprisingly small increase of the  $M_p$  was observed compared to P3HT (Figure 2b and Table 1). This counterintuitive SEC behavior is a well-known issue for fullerene polymers and is usually ascribed to aggregation effects of the fullerenes in SEC. A detailed description of the general synthetic procedure including those for the polystyrene precursor has been reported earlier.<sup>[12]</sup>



**Scheme 1.** Synthesis route towards the P3HT-b-PPC<sub>71</sub>BM 1-3 block copolymers.

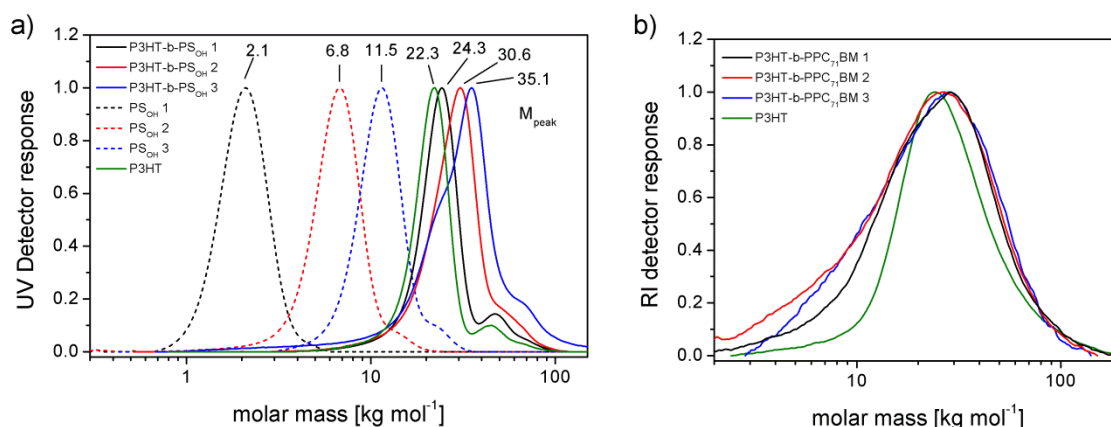


**Figure 2.** SEC traces showing (a) the block copolymer formation of P3HT-b-PS<sub>OH</sub> 1-3 via CuAAC between PS<sub>OH</sub> 1-3 and P3HT (eluent THF, room temperature) and (b) the P3HT-b-PPC<sub>71</sub>BM 1-3 block copolymers after esterification with PC<sub>71</sub>BA fullerenes (eluent 1,2,4-trichlorobenzene, 150 °C).

**Table 1.** SEC results of the synthesized polymers including number-average molecular weight  $M_n$ , peak molecular weight  $M_p$  and dispersity  $D$ .

Polymer	Ratio	$M_n$ <sup>a)</sup>	$M_p$ <sup>a)</sup>	$D$ <sup>a)</sup>	$M_n$ <sup>b)</sup>	$M_p$ <sup>b)</sup>	$D$ <sup>b)</sup>
	a:b	[kg mol <sup>-1</sup> ]	[kg mol <sup>-1</sup> ]		[kg mol <sup>-1</sup> ]	[kg mol <sup>-1</sup> ]	
P3HT alkyne		20.6	22.3	1.14	22.4	24.1	1.43
PS <sub>OH</sub> 1	0.24:0.76	1.90	2.13	1.12			
P3HT-b-PS <sub>OH</sub> 1		22.1	24.3	1.20	22.4	29.7	1.44
P3HT-b-PPC <sub>71</sub> BM 1					17.5	28.9	1.68
PS <sub>OH</sub> 2	0.26:0.74	6.04	6.81	1.13			
P3HT-b-PS <sub>OH</sub> 2		24.9	30.5	1.22	20.7	27.6	1.54
P3HT-b-PPC <sub>71</sub> BM 2					13.5	26.4	1.97
PS <sub>OH</sub> 3	0.25:0.75	10.2	11.5	1.16			
P3HT-b-PS <sub>OH</sub> 3		28.0	35.1	1.23	17.7	24.5	1.55
P3HT-b-PPC <sub>71</sub> BM 3					17.3	28.4	1.63

<sup>a)</sup> SEC in THF as eluent at room temperature, UV detector, polystyrene calibration.

<sup>b)</sup> SEC in 1,2,4-trichlorobenzene as eluent at 150 °C, refractive index detector, polystyrene calibration.

### Determination of the block copolymer composition

To estimate the composition of the block copolymers P3HT-b-PPC<sub>71</sub>BM 1-3 we used UV-vis spectroscopy in solution (Figure 3a) and thermogravimetric analysis (TGA, Figure 3b). PC<sub>71</sub>BM shows a strong absorption in the UV range. Therefore, for the determination of the PC<sub>71</sub>BM content, we use the ratio of optical densities (OD) at  $\lambda=274$  nm of P3HT-b-PPC<sub>71</sub>BM and PC<sub>71</sub>BM solutions with equal concentrations. Since the precursor

block copolymer P3HT-b-PS<sub>OH</sub> also absorbs in the UV range, the absorption spectrum of P3HT-b-PPC<sub>71</sub>BM contains contributions of PC<sub>71</sub>BM and additionally that of the P3HT block. Therefore, the OD of P3HT-b-PPC<sub>71</sub>BM at  $\lambda=274$  nm requires a correction. Details regarding the calculation of the PC<sub>71</sub>BM content in the block copolymer are given in the Supporting Information. According to our calculation, the block copolymers P3HT-b-PPC<sub>71</sub>BM 1-3 contain 22, 33 and 40 wt% of PC<sub>71</sub>BM. A similar approach was used to estimate the P3HT weight content by the ratio of OD at  $\lambda=450$  nm of P3HT-b-PPC<sub>71</sub>BM and P3HT. Again, the strong spectral overlap of the PC<sub>71</sub>BM absorption with P3HT makes a correction necessary (Details in Supporting Information). Accordingly, the P3HT content estimated in P3HT-b-PPC<sub>71</sub>BM 1-3 is 70, 37 and 22 wt% (Table 2). This implies that the weight content of the PPC<sub>71</sub>BM block is then roughly 30, 63 and 78 wt%.

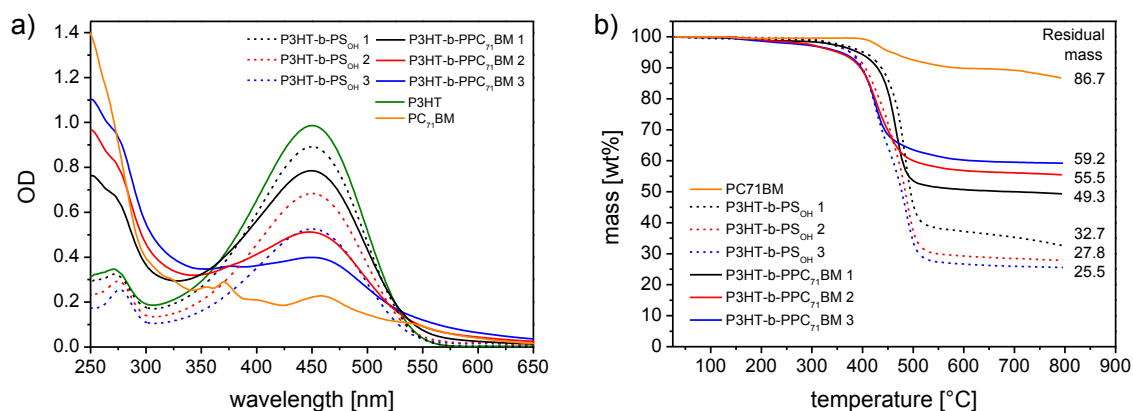


**Figure 3.** (a) UV-vis absorption spectra in chloroform solution for P3HT-b-PS<sub>OH</sub> 1-3 and the corresponding P3HT-b-PPC<sub>71</sub>BM 1-3 (polymers  $0.02 \text{ mg mL}^{-1}$ , PC<sub>71</sub>BM  $0.01 \text{ mg mL}^{-1}$ ). (b) Thermogravimetric analysis of the block copolymers performed at a heating rate of  $10 \text{ K min}^{-1}$  in nitrogen atmosphere.

To express the dilution of fullerene moieties along the polystyrene backbone, we introduce the grafting density as the ratio of weight fraction between PC<sub>71</sub>BM and the PPC<sub>71</sub>BM block. The calculated fullerene grafting density in this series is 73, 52 and 51 wt%. Assuming 100% efficiency for esterification and knowing the a:b ratio in the precursor PS<sub>OH</sub> 1-3 (Table 1), the theoretically attainable grafting densities would be 63, 67 and 66 wt%, respectively. The maximum grafting density is on the one hand restricted by the monomer ratio a:b in the polystyrene backbone, the realized grafting density, on the other hand, depends on the efficiency of esterification and is lower for long polymer chains. This is why the calculated grafting density in P3HT-b-PPC<sub>71</sub>BM 2 and 3 is lower with 52 and 51 wt% compared to the maximum achievable PC<sub>71</sub>BM content of 67 and

66 wt%. The calculated grafting density from absorption spectroscopy for P3HT-b-PPC<sub>71</sub>BM 1 with 73 wt% exceeds the maximum value of 63 wt% and indicates a certain inaccuracy of the measurement method specifically for this polymer sample.

**Table 2.** Composition of the block copolymers estimated from absorption spectroscopy.

Polymer	P3HT block <sup>a)</sup> [wt%]	PPC <sub>71</sub> BM block <sup>b)</sup> [wt%]	PC <sub>71</sub> BM [wt%]	Grafting density <sup>d)</sup> [wt%]	Ratio P3HT:PPC <sub>71</sub> BM [wt:wt]	Ratio P3HT:PC <sub>71</sub> BM [wt:wt]
P3HT-b- PPC <sub>71</sub> BM 1	70	30	22 <sup>a)</sup> /19 <sup>c)</sup>	73 / 63	1:0.43	1:0.27 <sup>e)</sup>
P3HT-b- PPC <sub>71</sub> BM 2	37	63	33 <sup>a)</sup> /32 <sup>c)</sup>	52 / 51	1:1.70	1:0.89 <sup>f)</sup>
P3HT-b- PPC <sub>71</sub> BM 3	22	78	40 <sup>a)</sup> /39 <sup>c)</sup>	51 / 50	1:3.55	1:1.82 <sup>f)</sup>

<sup>a)</sup> Determined by UV-vis absorption in solution.

<sup>b)</sup> Content of PPCBM block calculated by  $f = 100 \text{ wt\%} - \text{P3HT block wt\%}$ .

<sup>c)</sup> Determined by TGA.

<sup>d)</sup> Grafting density calculated as  $(\text{PCBM wt\%} / \text{PPCBM block wt\%}) \times 100 \text{ wt\%}$ . First value based on UV-vis, second value based on TGA.

<sup>e)</sup> Ratio based on PC<sub>71</sub>BM content determined from TGA.

<sup>f)</sup> Ratio based on PC<sub>71</sub>BM content determined by UV-Vis absorption spectroscopy.

Therefore, we have analyzed the block copolymers *via* TGA to get an additional estimation of the PC<sub>71</sub>BM content. As demonstrated in Figure 3b, the PC<sub>71</sub>BM reference exhibits only very low mass loss up to 800 °C in nitrogen atmosphere, since the fullerene core is highly temperature stable. Therefore, the residual char in the P3HT-b-PPC<sub>71</sub>BM block copolymers correlates with the incorporated PC<sub>71</sub>BM weight content. However, the precursor block copolymers P3HT-b-PS<sub>OH</sub> 1-3 also leave a notable amount of char, and consequently, need to be considered for the calculation. The resulting PC<sub>71</sub>BM content determined from TGA is then 19, 32 and 39 wt% (Table 2, Table S2). While the PC<sub>71</sub>BM content of 32 and 39 wt% for P3HT-b-PPC<sub>71</sub>BM 2 and 3 determined by TGA is in very good agreement with the UV-Vis results of 33 and 40 wt%, the value for P3HT-b-PPC<sub>71</sub>BM 1 is slightly lower with 19 wt% (TGA) instead of 22 wt% (UV-Vis). Taking this value (19 wt%) to calculate the grafting density in P3HT-b-PPC<sub>71</sub>BM 1, we obtain exactly 63 wt% which corresponds to a quantitative grafting yield. This excellent degree of grafting can be attributed to the very short PS<sub>OH</sub> 1 polymer block making esterification very efficient due to improved solubility and good accessibility of the hydroxyl groups.

Finally, the weight ratio of donor and acceptor polymer blocks P3HT:PPC<sub>71</sub>BM realized in the block copolymer varies from 1:0.43, 1:1.70 and 1:3.55, similarly the weight ratio reduced to the active semiconducting components P3HT:PC<sub>71</sub>BM is 1:0.27, 1:0.89 and 1:1.82 for P3HT-b-PPC<sub>71</sub>BM 1-3, respectively. Hence, tailoring of the molecular weights of the polymer blocks and their modular combination by click chemistry has yielded a series of well-defined block copolymers that cover a broad range of donor-acceptor compositions. But it is to be noted that the P3HT-b-PPC<sub>71</sub>BM 2 and 3 possess fullerene blocks which are more diluted than in P3HT-b-PPC<sub>71</sub>BM 1.

### Crystallization of the P3HT-b-PPC<sub>71</sub>BM block copolymers

We have earlier shown that in P3HT-b-PPC<sub>71</sub>BM the P3HT block is semi-crystalline whereas the fullerene block remains amorphous.<sup>[12]</sup> In general, the crystallization of P3HT in such crystalline-amorphous block copolymers depends on three important parameters: crystallization temperature  $T_c$  of the crystalline block, the glass transition temperature  $T_g$  of the amorphous block and the order-disorder transition of the block copolymer.<sup>[31,32]</sup> Crystallization of the conjugated polymer segment is of fundamental interest, because it can strongly affect the material properties such as charge transport.<sup>[28,33]</sup> In the following, we investigate the thermal properties of the block copolymers P3HT-b-PPC<sub>71</sub>BM 1-3 using differential scanning calorimetry (DSC). As a reference to study crystallization in neat P3HT, we took a well-defined P3HT without alkyne end group,  $M_n=18.3 \text{ kg mol}^{-1}$  (SEC) and  $D=1.1$  which is very similar to that used for the synthesis of the block copolymers. The neat P3HT sample melts at 228-247 °C and crystallizes upon cooling at a rate of 10 K min<sup>-1</sup> at 195 °C with a melting enthalpy  $\Delta H_m$  of 23.2 J g<sup>-1</sup>. In the P3HT-b-PPC<sub>71</sub>BM block copolymers the recordable enthalpy of the P3HT melting transition is naturally lower due to the dilution of the crystallizable polymer block arising from the composition in the block copolymer. We can now calculate the expected  $\Delta H_{m, \text{theor.}}$  in P3HT-b-PPC<sub>71</sub>BM 1-3 assuming the same degree of crystallization compared to the pure P3HT but taking the reduced weight fraction of P3HT into account (Table 3). At a heating rate of 10 K min<sup>-1</sup> the observed melting enthalpies  $\Delta H_m$  of P3HT remained below  $\Delta H_{m, \text{theor.}}$  for P3HT-b-PPC<sub>71</sub>BM 1-2 and is even hardly detectable for P3HT-b-PPC<sub>71</sub>BM 3 (Figure 4, Table 3). Further, the crystallization temperature  $T_c$  is decreasing from 195 °C in neat P3HT to 172, 149/121 and 122 °C in P3HT-b-PPC<sub>71</sub>BM 1-3, respectively. This implies that crystallization of P3HT in these block copolymers occurs under multiple con-

straints: Reduced chain mobility due to the block copolymer architecture, high glass transition temperature of the amorphous acceptor polymer block and possibly confinement effects from the phase-separated morphology in the block copolymer. A confinement, however, can also support crystallization since the phase-separation generates pure polymer phases. In our case, the PPC<sub>71</sub>BM segments used in this block copolymer series have a high grafting density and thus exhibit a very high glass transition around 200 °C and above.<sup>[23]</sup> This can hinder the crystallization of P3HT during cooling from the melt due to a restricted mobility of the liquid-like P3HT segments in the early solidifying PPC<sub>71</sub>BM matrix. Moreover, the remarkable decrease of  $T_c$  in the block copolymers suggests a strong kinetic inhibition for crystallization for the given experimental conditions in DSC.

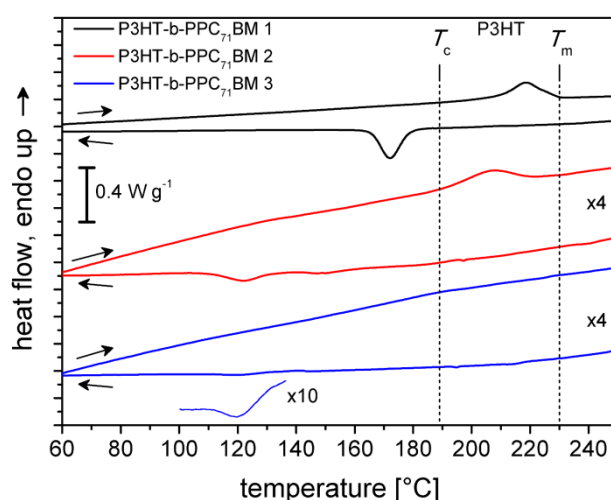


**Figure 4.** DSC traces of P3HT-b-PPC<sub>71</sub>BM 1-3 at a heating/cooling rate of 10 K min<sup>-1</sup> in nitrogen atmosphere. The melting temperature  $T_m$  and crystallization temperature  $T_c$  of neat P3HT is given as reference. For better clarity, some DSC traces were magnified by the given factors.

**Table 3.** Crystallization of the block copolymers determined by DSC at a heating/cooling rate of 10 K min<sup>-1</sup> in nitrogen atmosphere.

Polymer	P3HT [wt%]	$T_{m,peak}$ [°C]	$\Delta H_m$ [J g <sup>-1</sup> ]	$\Delta H_{m,theor}^a)$ [J g <sup>-1</sup> ]	$T_{c,peak}$ [°C]	$\Delta H_c$ [J g <sup>-1</sup> ]
P3HT reference	100	228, 236, 247	23.2	-	195	-
P3HT-b-PPC <sub>71</sub> BM 1	70	219	10.3	16.2	172	10.4
P3HT-b-PPC <sub>71</sub> BM 2	37	207	2.7	8.6	121, 149	2.1
P3HT-b-PPC <sub>71</sub> BM 3	22	- <sup>b)</sup>	- <sup>b)</sup>	5.1	122	0.4

<sup>a)</sup> Calculated according to the weight fraction of P3HT in the block copolymers assuming the same degree of crystallinity as in P3HT homopolymer. <sup>b)</sup> Very weak peak with very low melting enthalpy  $\Delta H_m$ .

### Structure analysis of the donor-acceptor block copolymers

To investigate the donor-acceptor nanostructure of P3HT-b-PPC<sub>71</sub>BM 1-3 temperature dependent small angle X-ray scattering was applied. Depicted in Figure 5 are the scattering data in the molten state at 240 °C as well as at room temperature after an annealing for 105 min at 240 °C. Similar to the investigation of P3HT-b-PPC<sub>61</sub>BM<sup>[23]</sup> three different features can be found in the scattering pattern. Namely the (100)-Bragg reflection of P3HT, the signal of the donor-acceptor nanostructure between 0.2 nm<sup>-1</sup> and 0.3 nm<sup>-1</sup> and in between a broad scattering signal attributed to PC<sub>71</sub>BM aggregates.

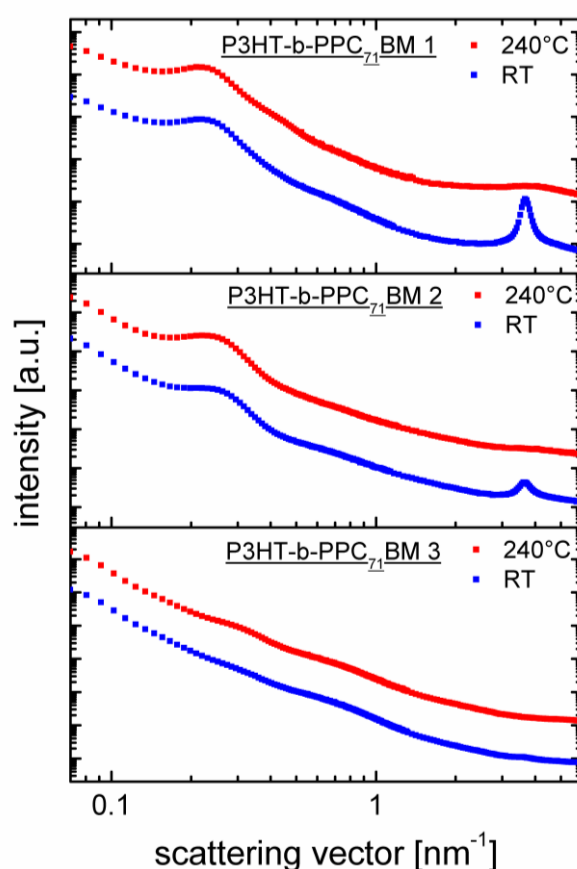


**Figure 5.** Scattering intensity vs. scattering vector  $q$  of P3HT-b-PPC<sub>71</sub>BM 1-3 in the molten state (240 °C, red) and back at room temperature (blue). Data were joined from two measurements at two sample to detector distances (curves shifted for clarity).

Comparing the (100)-Bragg signal of P3HT between P3HT-b-PPC<sub>71</sub>BM 1 and 2 one notices a strong decrease in intensity in P3HT-b-PPC<sub>71</sub>BM 2 which can only partially be explained by the reduction of the P3HT fraction. This reduction of intensity continues to P3HT-b-PPC<sub>71</sub>BM 3 where nearly no crystalline signal of P3HT is present. This finding is in good agreement with the significantly reduced crystallinity observed in the DSC

measurements and underlines the importance of the above mentioned constraints for the structure formation.

In order to investigate the signal of the BCP nanostructure more deeply a fitting procedure was applied (Figure 6). The model used consists of a power law background and either a Gaussian or a Lorentzian to describe the peak. From this fitting procedure the position and the width of the scattering signal was determined. The resulting peak positions, listed in Table 4, correspond to a long period ( $d=2\pi/q_{\max}$ ) between 20 nm and 30 nm. While the reason for the shift to larger scattering vectors, *i.e.* smaller structure sizes, with increasing molecular weight is unclear, the common full width half maximum of the Gaussian and Lorentzian used for the fitting is  $0.1 \text{ nm}^{-1}$ . This value is a factor of 2.8 above the resolution limit of the instrument, which normally indicates that the samples are rather not microphase separated. For P3HT-b-PPC<sub>71</sub>BM 1 this finding is in full agreement with the Lorentzian shape of the peak typical for a disordered block copolymer.<sup>[34]</sup> However, we still believe that the fact that the SAXS peak of P3HT-b-PPC<sub>71</sub>BM 2 can be described reasonably good by a Gaussian instead of a Lorentzian shape and is unchanged during cooling and crystallization of the P3HT is a strong indication for a microphase separated state in P3HT-b-PPC<sub>71</sub>BM 2.<sup>[34]</sup> The different peak shape is consistent with the increased PPC<sub>71</sub>BM block length from P3HT-b-PPC<sub>71</sub>BM 1 to P3HT-b-PPC<sub>71</sub>BM 2 which can possibly promote microphase separation. Note that the missing of higher order peaks together with the peak width of the scattering signal suggest a rather low long range order, which might be attributed to the high  $T_g$  of the PPCBM block. In case of P3HT-b-PPC<sub>71</sub>BM 3, the weakness of the scattering signal makes a clear distinction between Gaussian and Lorentzian shape impossible. Further, the absence of a distinct peak in the SAXS range suggests that the block copolymer P3HT-b-PPC<sub>71</sub>BM 3 is not capable to segregate possibly because of the PPC<sub>71</sub>BM majority phase. The missing phase segregation is in agreement with the DSC results that indicated virtually no crystallization of P3HT in this block copolymer. In conclusion, the structure formation in this series of block copolymers with varying chain length of PPC<sub>71</sub>BM clearly demonstrates the importance of a rather balanced donor-acceptor composition: While a too short PPC<sub>71</sub>BM block generates only a weakly segregated, disordered morphology, a very long PPC<sub>71</sub>BM block completely inhibits the phase segregation. Block copolymer P3HT-b-PPC<sub>71</sub>BM 2 with 37 wt% PPC<sub>71</sub>BM and 63 wt% P3HT exhibits microphase separated morphology albeit without long-range order.

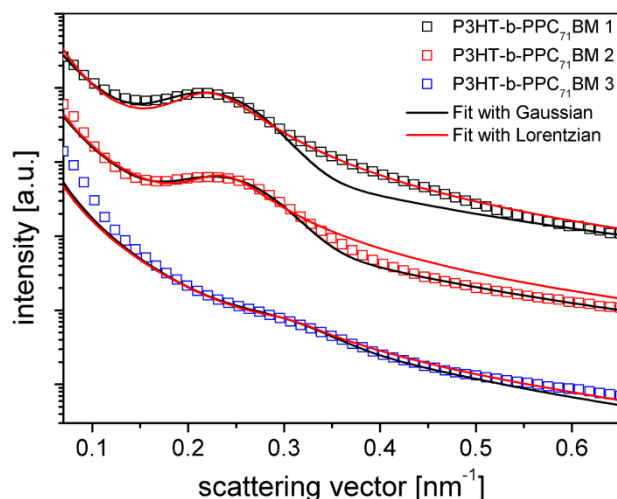


**Figure 6.** SAXS data of P3HT-b-PPC<sub>71</sub>BM 1-3 with a model function consisting of a power law background intensity and either a Gaussian (black line) or Lorentzian (red line) used to describe the peak. The curves are shifted for clarity.

**Table 4.** Peak position  $q_{\max}$  and corresponding long period  $d$  of the observed nanostructure in P3HT-b-PPC<sub>71</sub>BM 1-3 determined by SAXS.

Polymer	$q_{\max}$ [nm <sup>-1</sup> ]	$d$ ( $=2\pi/q_{\max}$ ) [nm]
P3HT-b-PPC <sub>71</sub> BM 1	0.221	28.4
P3HT-b-PPC <sub>71</sub> BM 2	0.235	26.7
P3HT-b-PPC <sub>71</sub> BM 3	0.290	21.7

### Absorption and photoluminescence in solution and thin films

A fundamental property of the donor-acceptor P3HT-b-PPC<sub>71</sub>BM block copolymers is the interplay of aggregation and electron transfer between the donor and acceptor units in solution and, with regard to device application, in thin films. Absorption spectroscopy in semiconductors films give an estimate on the aggregation/crystallization of the  $\pi$ -conjugated component. While photoluminescence (PL) studies in solution are mainly affected by the donor-acceptor composition itself, the PL quenching studies in films further give an important insight into structural aspects such as phase separation and phase purity of the block copolymer.

The PL spectra of solutions of P3HT-b-PPC<sub>71</sub>BM 1-3 compared to P3HT-b-PS<sub>OH</sub> 1-3 without fullerene acceptors give a clear picture on PL quenching for an excitation at

$\lambda=450$  nm. As depicted in Figure 7a, the PL intensity for P3HT-b-PPC<sub>71</sub>BM is reduced in comparison to their non-grafted precursors indicating a more efficient PL quenching by electron or energy transfer, likely from P3HT to PC<sub>71</sub>BM. The extent of quenching correlates with the relative amount of fullerene moieties present in solution, *i.e.* P3HT-b-PPC<sub>71</sub>BM 3 with P3HT:PC<sub>71</sub>BM=1:1.82 shows the strongest PL quenching, P3HT-b-PPC<sub>71</sub>BM 1 with 1:0.27 the weakest (see Table 2). Note that all PL spectra were scaled to equal photon absorption at the excitation wavelength, *i.e.* OD=1.0 at  $\lambda=450$  nm in the absorption curve (Figure 3a) for comparability. The solution studies clearly indicate a strong effect of the block copolymer composition on the photophysical properties.

Thin films on glass substrates have been prepared by a similar procedure as used for the organic field-effect transistors (OFET) to study the degree of P3HT aggregation using absorption spectroscopy. The as-cast films after spin-coating at 5000 rpm from chloroform solutions show a broad, unstructured absorption band around 520, 480 and 470 nm for P3HT-b-PPC<sub>71</sub>BM 1-3 respectively, indicating mostly amorphous P3HT in particular for 2 and 3 (Figure 7b-d). Whereas P3HT-b-PPC<sub>71</sub>BM 1 has some partially aggregated species, the absorption band of P3HT in films is approaching the completely non-aggregated solution structure with 450 nm peak maximum of P3HT-b-PPC<sub>71</sub>BM 3 (compare to Figure 3a). This is consistent with the decreasing amount of P3HT in the block copolymer series and a gradually reduced crystallinity in bulk as observed in the DSC studies. Note that the increasing amount of PC<sub>71</sub>BM in this series and its strong contribution to the absorption in the UV region can further cause a blue-shift of the absorption spectrum. As a result, the fast spin-coating possibly lead to a widely disordered film morphology of the block copolymer with no or negligible aggregation of P3HT. Therefore, the block copolymer films were subsequently annealed in nitrogen atmosphere under various conditions to enable a crystallization of P3HT: Annealing was done below the melting temperature of P3HT at 160 °C for 120 min and at 200 °C for 30 min, and melt-crystallization at 240 °C for 5 min with a slow cooling at 10 K min<sup>-1</sup>. Obviously, the annealed films of P3HT-b-PPC<sub>71</sub>BM 1-2 exhibit additional vibrational shoulders at 555 nm and 600 nm corresponding to the 0-1 and 0-0 vibration of weakly interacting H-aggregates in P3HT (Figure 7b-c).<sup>[35,36]</sup> This characteristic absorption pattern confirms the presence of a semi-crystalline P3HT block. Thermal annealing for 30 min at 200 °C shows the most pronounced fine structure resulting in the highest degree of P3HT aggregation. In contrast, the absorption spectra for the P3HT-b-PPC<sub>71</sub>BM 3 films do not show

structural changes upon annealing (Figure 7d). Accordingly, the minor fraction of P3HT in P3HT-b-PPC<sub>71</sub>BM 3 is not able to crystallize, which might be attributed to the restrictions in polymer dynamics caused by the high  $T_g$  of the surrounding PPC<sub>71</sub>BM majority phase and the low amount of P3HT (22 wt%). This result is fully consistent with the DSC and SAXS analysis.

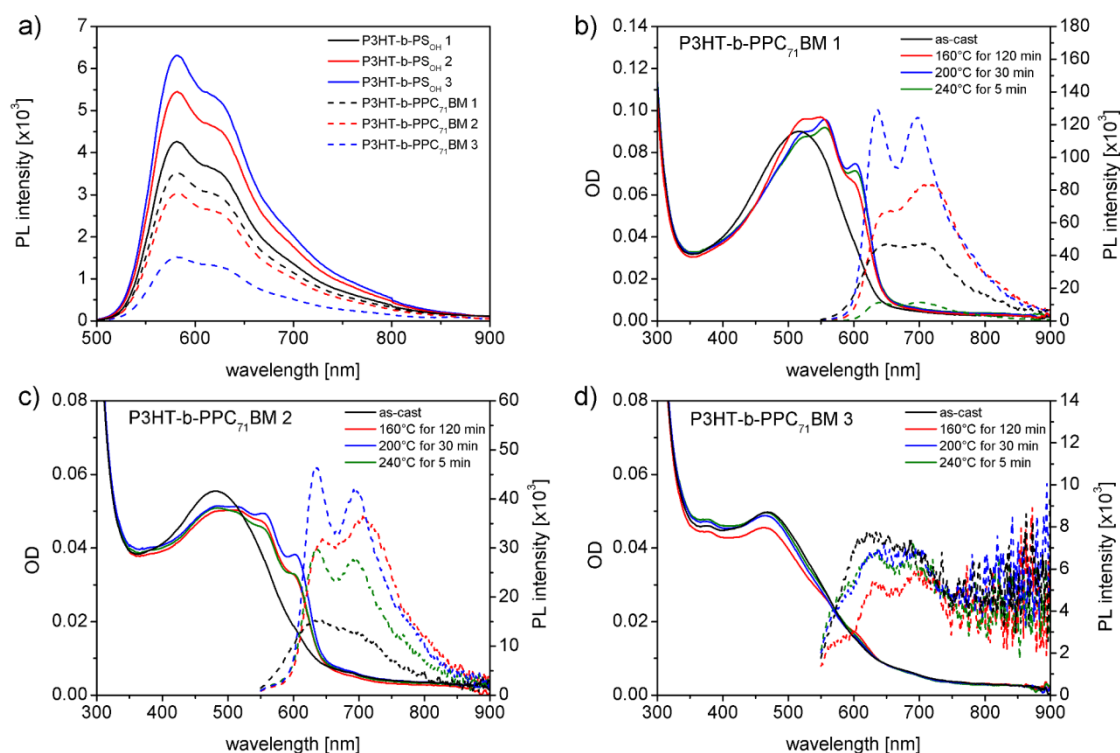


**Figure 7.** (a) Photoluminescence spectra in solution ( $0.02 \text{ mg mL}^{-1}$  in chloroform) for P3HT-b-PS<sub>OH</sub> 1-3 (solid lines) and P3HT-b-PPC<sub>71</sub>BM 1-3 (dashed lines) by excitation at  $\lambda=450 \text{ nm}$ . (b-d) Absorption spectra (solid lines) and photoluminescence spectra (dashed lines) by excitation at  $\lambda=500 \text{ nm}$  in thin films for P3HT-b-PPC<sub>71</sub>BM 1-3. Annealing conditions were varied from as-cast (black),  $160^\circ\text{C}$  for 120 min (red),  $200^\circ\text{C}$  for 30 min (blue) to  $240^\circ\text{C}$  for 5 min (green) with subsequent cooling at  $10 \text{ K min}^{-1}$  in nitrogen atmosphere. The PL intensity was scaled to equal photon absorption at the excitation wavelength, i.e. optical density of  $OD=1.0$  at  $450 \text{ nm}$  in (a) and  $500 \text{ nm}$  in (b-d) of the corresponding absorption spectra.

Further, the PL spectra of the block copolymers P3HT-b-PPC<sub>71</sub>BM 1-2 at an excitation of  $\lambda=500 \text{ nm}$  indicate a notable change in thin film morphology (Figure 7b-c). For all cases of annealing, the PL intensity increases strongly which can be explained by an improved phase separation of donor and acceptor domains through crystallization of P3HT, typically accompanied by a higher phase purity. In addition, the growth of PL intensity after annealing is remarkable since the crystallization of P3HT intrinsically causes a reduction of photoluminescence. The best results were achieved for the annealing procedure

for 30 min at 200 °C. Interestingly, after melt-crystallization at 240 °C the block copolymers P3HT-b-PPC71BM 1 and 2 show a crucial difference: Whereas the PL signal drastically drops in case of block copolymer 1, the PL signal improves for block copolymer 2. This finding goes hand in hand with the structural investigation indicating a weakly segregated, rather disordered morphology after melt-crystallization for P3HT-b-PPC<sub>71</sub>BM 1, causing an increased quenching, and a microphase separated morphology for P3HT-b-PPC<sub>71</sub>BM 2 with rather pure domains and lower quenching rate compared to the as-cast film. In contrast, P3HT-b-PPC<sub>71</sub>BM 3 shows only a negligible PL signal very close to the detection limit. The strong PL quenching in this block copolymer independent of the annealing procedure is in agreement with the absence of phase segregation observed in the SAXS analysis.

In conclusion, the annealing of P3HT-b-PPC<sub>71</sub>BM films at 200 °C for 30 min significantly improved the crystallization of P3HT in block copolymer 1 and 2 leading to a higher phase purity and possibly better phase separation/segregation of donor and acceptor domains, at least in block copolymer 2.

### **Charge transport of P3HT-b-PPC<sub>71</sub>BM in field-effect transistors**

The block copolymer design of P3HT-b-PPC<sub>71</sub>BM with varying weight fractions of P3HT:PPC<sub>71</sub>BM was intended to study the influence of composition on the charge carrier mobilities. To study the charge transport in these donor-acceptor block copolymers, we utilized organic field-effect transistors (OFET) because the hole and electron mobility can be determined in a single device structure.<sup>[37]</sup> The OFETs were fabricated using a bottom-gate, bottom-contact configuration by spin-coating the polymer solutions from chloroform at 5000 rpm. Device characterization and thermal annealing at 200 °C for 30 min was performed in nitrogen atmosphere. Output characteristics were measured for a drain-source voltage  $V_d$  from -80 to 0 V for p-type operation and 0 to +80 V for n-type operation with a stepwise varied gate voltage  $V_g$ . The transfer curves were measured for  $V_g$  in the range of -80 to +20 V in p-type and -20 to +80 V in n-type operation in the saturation regime of  $V_d=-80$  and +80 V. The field-effect mobility  $\mu_h$  for holes and  $\mu_e$  for electrons was then determined from the linear fit of the square root of the drain-source current  $I_d^{1/2}$  in the saturation regime of the corresponding transfer curve.

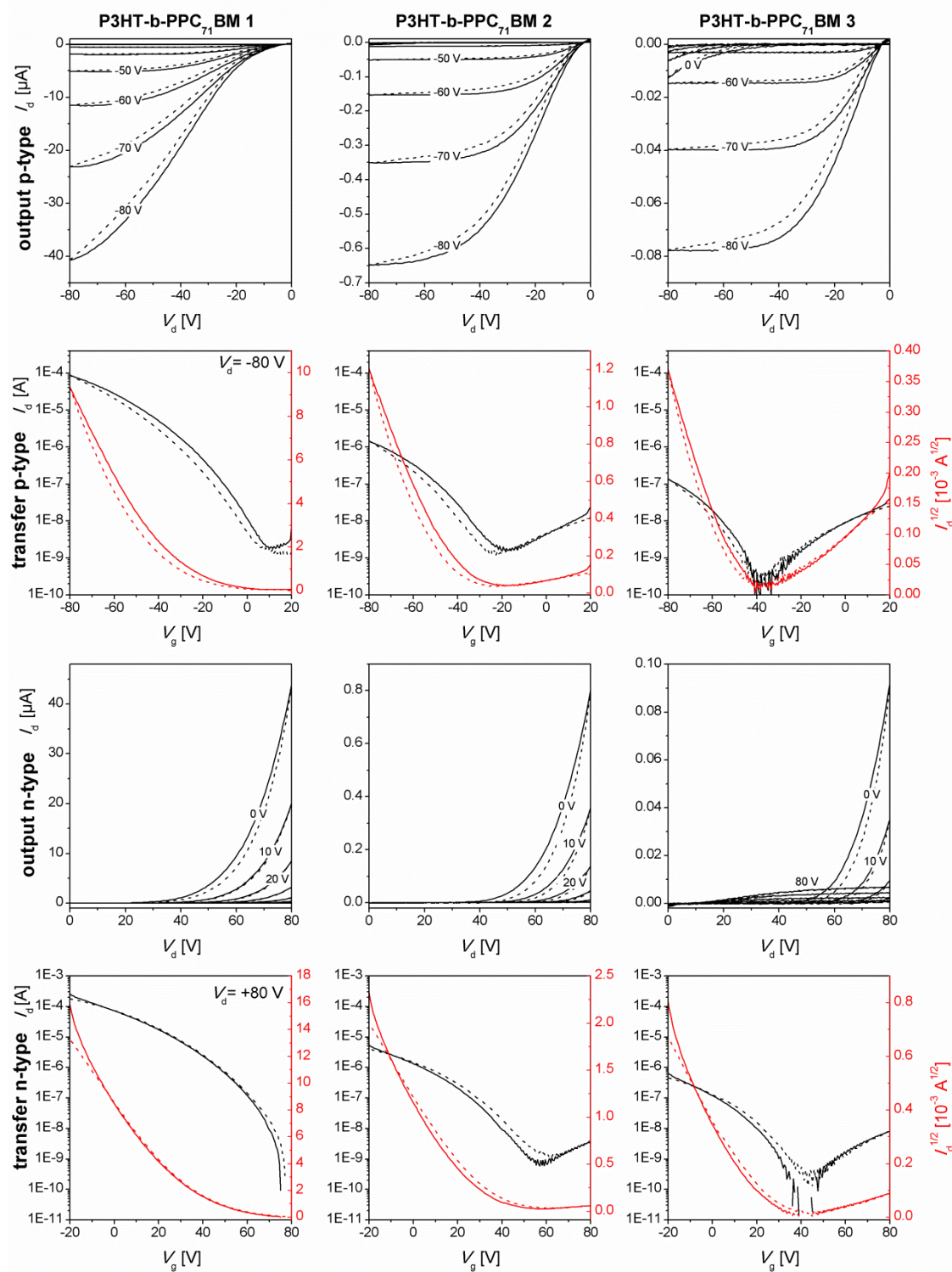


**Figure 8.** Representative OFET I-V curves for the P3HT-b-PPC<sub>71</sub>BM block copolymer series measured in p- and n-type operation for devices with a channel length of 10 μm. The transfer characteristics were determined in the saturation regime at  $V_d = -80$  V and  $V_d = +80$  V for p-channel and n-channel, respectively. Solid lines represent forward scans, dashed lines are reverse scans. The red curves correspond to the square-root of the drain-source current  $I_d^{1/2}$  from which the charge carrier mobilities  $\mu_h$  and  $\mu_e$  were extracted.

P3HT-b-PPC<sub>71</sub>BM 1 exhibits exclusively p-type transport in OFETs as shown in the representative output and transfer characteristics in Figure 8. The block copolymers P3HT-b-PPC<sub>71</sub>BM 2-3 show drain-source currents  $I_d$  reduced by one or two orders of magnitude, but an additional contribution indicating also electron transport. This is clearly visible in the p- and n-type transfer characteristics which show the V-shaped  $I_d$  curve typical for ambipolar semiconductors. The hole mobility  $\mu_h$  related to the charge transport in P3HT is decreasing from  $(3.9 \pm 0.8) \times 10^{-3}$ ,  $(1.3 \pm 0.1) \times 10^{-4}$  to  $(1.8 \pm 0.6) \times 10^{-5} \text{ cm}^2 \text{ V}^{-1} \text{ s}^{-1}$  for P3HT-b-PPC<sub>71</sub>BM 1-3, respectively (Table 5, Table S3). This is consistent with the P3HT weight fraction in the block copolymers which is 70, 37 and 22 wt%, *i.e.* the reduction of P3HT by one half roughly leads to a drop in hole mobility of one order of magnitude (Figure 9). The decreasing hole mobility can also be affected by the reduced or negligible crystallinity of P3HT in this series which is detrimental for hole transport. While in P3HT-b-PPC<sub>71</sub>BM 1 the minor fraction of only 30 wt% PPC<sub>71</sub>BM is not sufficient for electron transport, the block copolymers 2 and 3 show a low electron mobility  $\mu_e$  of  $(5.2 \pm 2.4) \times 10^{-7}$  and  $(6.7 \pm 2.0) \times 10^{-7} \text{ cm}^2 \text{ V}^{-1} \text{ s}^{-1}$ . This indicates first that there is a certain threshold for the PPC<sub>71</sub>BM content required to built up n-type channels in the OFET, and second, that PPC<sub>71</sub>BM exhibits a relatively low electron mobility which shows the maximum at 63 wt% PPC<sub>71</sub>BM in the block copolymer. The low  $\mu_e$  values can be understood taking into account that the fullerene moieties are diluted in the polystyrene matrix.

This low  $\mu_e$  for P3HT-b-PPC<sub>71</sub>BM is surprising since the reference material PC<sub>71</sub>BM, the state-of-the-art acceptor in organic photovoltaics, exhibits electron mobilities in the range of  $3 \times 10^{-3} \text{ cm}^2 \text{ V}^{-1} \text{ s}^{-1}$  in OFET device configuration. But for grafting densities of about 50 wt% decreased mobilities can be expected. The OFET studies of P3HT-b-PPC<sub>71</sub>BM 1-3 illustrate the importance of the P3HT:PPC<sub>71</sub>BM composition on the charge transport. The decrease in hole mobility with a decreasing P3HT content is also discussed in terms of a reduced effective channel width  $W$  in OFETs, originating from a smaller contact area to the electrodes.<sup>[25]</sup> Thus, the determined hole mobility might underestimate the real mobility in the P3HT blocks. Due to the low electron mobility in the investigated P3HT-b-PPC<sub>71</sub>BM block copolymer series it is difficult to predict if there is a relevant composition dependence of the acceptor block on the electron mobility.

The concept of composition variation by increasing length of the fullerene block results in reduced real contents of both P3HT and PC<sub>71</sub>BM species in the final block copol-

ymers. For instance, in P3HT-b-PPC<sub>71</sub>BM 3 only 22 wt% of P3HT is present whereas the PPC<sub>71</sub>BM content was about 40 wt%. Further, the degree of phase separation in the block copolymer plays an important role for the hole and electron mobilities.

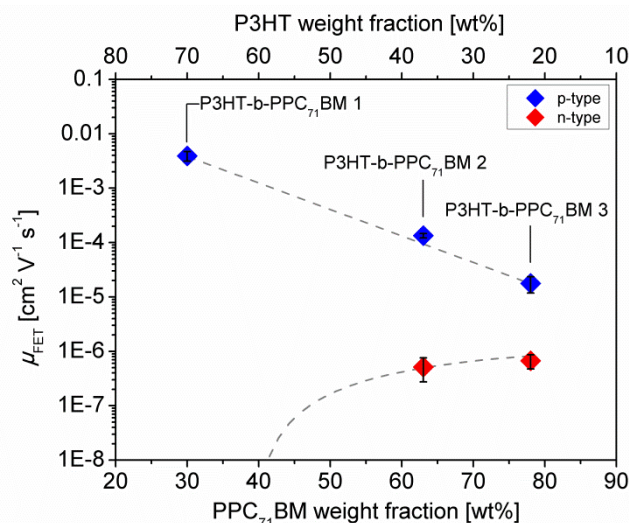


**Figure 9.** OFET hole and electron mobilities  $\mu_{FET}$  of the P3HT-b-PPC<sub>71</sub>BM series in bottom-gate, bottom contact configuration after annealing of the devices at 200 °C for 30 min. The dashed lines represent a guide to the eye.

**Table 5.** Average OFET hole mobilities  $\mu_h$  and electron mobilities  $\mu_e$  of P3HT-b-PPC<sub>71</sub>BM 1-3 after annealing for 30 min at 200 °C using a bottom-contact, bottom-gate device configuration.

Polymer	P3HT [wt%]	PPC <sub>71</sub> BM [wt%]	$\mu_h$ [cm <sup>2</sup> V <sup>-1</sup> s <sup>-1</sup> ]	$\mu_e$ [cm <sup>2</sup> V <sup>-1</sup> s <sup>-1</sup> ]
P3HT-b-PPC <sub>71</sub> BM 1	70	30	(3.9 ± 0.8) × 10 <sup>-3</sup>	-
P3HT-b-PPC <sub>71</sub> BM 2	37	63	(1.3 ± 0.1) × 10 <sup>-4</sup>	(5.2 ± 2.4) × 10 <sup>-7</sup>
P3HT-b-PPC <sub>71</sub> BM 3	22	78	(1.8 ± 0.6) × 10 <sup>-5</sup>	(6.7 ± 2.0) × 10 <sup>-7</sup>

## CONCLUSIONS

We have demonstrated a feasible synthesis approach to vary the composition of P3HT and PPC<sub>71</sub>BM in the donor-acceptor block copolymers P3HT-b-PPC<sub>71</sub>BM. While the molecular weight of P3HT was fixed at the optimum for hole transport (~20 kg mol<sup>-1</sup> in SEC), the acceptor block length of PPC<sub>71</sub>BM was stepwisely increased yielding compositions of P3HT:PPC<sub>71</sub>BM of 1:0.43, 1:1.70 and 1:3.55. With a growing weight fraction of PPC<sub>71</sub>BM the crystallization of P3HT in the block copolymer is increasingly hindered in bulk and in thin films. Very likely the high glass transition of the fullerene-grafted accep-

tor block drastically restricts the polymer dynamics. The annealing of thin films at 200 °C can promote P3HT crystallization as long as the PPC<sub>71</sub>BM block is not too large leading to a severe suppression of crystallization due to the negligible chain mobility and high dilution of P3HT as observed for P3HT-*b*-PPC<sub>71</sub>BM 3. The structural studies in bulk underlines the significance of a roughly balanced composition of the P3HT-*b*-PPC<sub>71</sub>BM block copolymer to achieve the desired periodic donor-acceptor nanostructure induced by microphase separation. The correspondingly rather pure donor/acceptor domains are crucial for any optoelectronic application. The charge transport, however, could not be balanced only by varying the composition. On the one hand, the C<sub>70</sub>-grafted block copolymers show in general low electron mobilities compared to the hole mobility. On the other hand, the correlation of composition and charge transport is strongly influenced by the structure formation in these block copolymers. With increasing PPC<sub>71</sub>BM block length, the morphology is first weakly segregated with rather isolated PPC<sub>71</sub>BM domains, then microphase separated with a donor-acceptor nanostructure and reaches finally for large blocks a dynamically frozen state without any nanoscale order. This work clearly shows the limitations and complexity of polymer design to tailor a specific material property. In particular, the high glass transition temperature of the PPC<sub>71</sub>BM block is a recurring issue that reinforces the need for tailoring the polymer backbone towards low  $T_g$  systems.

## EXPERIMENTAL PART

### Materials

The reagents for the following synthetic procedures were purchased from Sigma-Aldrich and used as received, if not stated otherwise. Solvents were either distilled at atmospheric pressure utilizing appropriate desiccants or purchased in p.a. (pro analysi) grade. Commercially available anhydrous solvents were purchased from Sigma Aldrich and Acros in sealed bottles with mole sieve. Phenyl-C<sub>71</sub>-butyric acid methyl ester (PC<sub>71</sub>BM, purity 99 %) was purchased from American Dye Source (Canada). The precursor copolymers poly(4-methoxystyrene-*stat*-4-hydroxystyrene) PS<sub>OH</sub> 1-3 were prepared by NMRP with subsequent polymer-analogous reactions following published synthesis protocols.<sup>[12]</sup> Ethynyl-terminated poly(3-hexylthiophene) was prepared by Kumada catalyst transfer polymerization followed by end-capping with ethynylmagnesium chloride.<sup>[27]</sup> The stock solution of 0.07 M copper(I) iodide/PMDETA catalyst in tetrahydrofuran was prepared according to a literature procedure.<sup>[38]</sup>

### Instrumentation and analysis

$^1\text{H-NMR}$  spectra were measured with a Bruker Avance AC250 spectrometer at 300 MHz. The obtained spectra were calibrated to the corresponding residual solvent peak ( $\text{CDCl}_3$   $\delta=7.26$  ppm or *o*-DCB- $d_4$   $\delta=7.41, 7.16$  ppm). Size exclusion chromatography (SEC) with stabilized THF as eluent was performed using a Waters 515-HPLC pump at a flow rate of  $0.5 \text{ mL min}^{-1}$ . A guard column (Varian,  $50 \times 0.75$  cm, ResiPore, particle size  $3 \mu\text{m}$ ) and two separation columns (Varian,  $300 \times 0.75$  cm, ResiPore, particle size  $3 \mu\text{m}$ ) are connected in series with a Waters UV detector at 254 nm and 486 nm. 1,2-dichlorobenzene (DCB) was used as an internal standard. High-temperature SEC analysis was carried out on an Agilent (Polymer Laboratories Ltd.) PL-GPC 220 high temperature chromatographic unit equipped with DP, RI and LS ( $15^\circ$  and  $90^\circ$ ) detectors and three linear mixed bed columns of PLgel  $13 \mu\text{m}$  (Olexis) with a linear molecular weight operating range:  $500\text{-}15,000,000 \text{ g mol}^{-1}$ . SEC analysis was performed at  $150^\circ\text{C}$  using 1,2,4-trichlorobenzene as the mobile phase. All SEC data were calibrated in relation to polystyrene standards. Ultraviolet-visible (UV-vis) spectra from solutions of the polymers in chloroform were recorded on a JASCO Spectrophotometer V-670 using quartz cuvettes with a path length of 1 cm. The corresponding photoluminescence (PL) spectra were measured on a JASCO FP-8600 spectrofluorometer at an excitation wavelength of  $\lambda=450 \text{ nm}$  for solutions. Thermal gravimetry analysis (TGA) experiments were performed under continuous nitrogen stream using a Mettler Toledo TGA/SDTA 851. The measurement range was  $30\text{-}800^\circ\text{C}$  with a heating rate of  $10 \text{ K min}^{-1}$ . A Mettler Toledo DSC 2 was used to investigate the thermal properties of P3HT-b-PPC $_{71}$ BM 1-3. A heating and cooling rate of  $10 \text{ K min}^{-1}$  in nitrogen atmosphere was chosen. UV-vis absorption spectra of thin films prepared by spin-coating of  $4 \text{ mg mL}^{-1}$  solutions in chloroform at 5000 rpm were recorded on a JASCO spectrophotometer V-670 and the corresponding photoluminescence (PL) spectra on a JASCO FP-8600 spectrofluorometer at an excitation wavelength of  $\lambda=500 \text{ nm}$ . The thermal annealing of thin films was performed in nitrogen atmosphere on a precision hotplate. Organic thin films transistor (OFET) substrates in bottom-gate, bottom-contact configuration were purchased from Fraunhofer IPMS (Dresden/Germany). The substrate and gate electrode is n-doped silicon (doping at wafer surface:  $n \sim 3 \times 10^{17} \text{ cm}^{-3}$ ) with a thermally grown  $230 \text{ nm} \pm 10 \text{ nm}$   $\text{SiO}_2$  dielectric top layer. 30 nm Gold electrodes with 10 nm ITO as high work function adhesion layer were used as drain/source contact. The channel width was 1 mm for all devices with a channel

length varying between 5 to 20  $\mu\text{m}$ . The substrates were cleaned in an ultrasonic bath in acetone and 2-propanol for 10 min each. After ozone treatment for 20 min at 50  $^{\circ}\text{C}$ , the substrates were immersed into a solution of 1 vol% of octadecyltrichlorosilane in toluene at 60  $^{\circ}\text{C}$  for 45 min. After rinsing the substrates with toluene and 2-propanol, the substrates were dried in nitrogen stream and the polymer was spin-coated from a 4  $\text{mg mL}^{-1}$  chloroform solution at 5000 rpm under ambient conditions. The OFET devices were transferred to a glovebox in nitrogen atmosphere, annealed for 30 min at 200  $^{\circ}\text{C}$  and the transistor characteristics measured with an Agilent B1500 Semiconductor Parameter Analyzer. Mobilities were calculated from the slope of the  $V_g-(I_d)^{1/2}$  plots in the saturation regime using the following equation,

$$I_d = \frac{W}{2L} C_i \mu (V_g - V_{th})^2$$

where  $I_d$  is the drain current,  $W$  is the channel width,  $L$  is the channel length,  $C_i$  is the capacitance,  $V_g$  is the gate voltage and  $V_{th}$  is the threshold voltage.

### General synthetic procedure for P3HT-b-PS<sub>OH</sub> 1-3

A 250 ml schlenk flask was flame dried at 600  $^{\circ}\text{C}$  under high vacuum and charged with ethynyl-terminated poly(3-hexylthiophene) P3HT (1 equ.) and PS<sub>OH</sub> (2 equ.). It was degassed under high vacuum and backfilled with argon three times. Dry THF was added and the solution stirred for 15 min at 40  $^{\circ}\text{C}$  until all compounds were fully dissolved. After purging the solution with argon for 30 min, the CuI/PMDETA stock solution in THF was added *via* syringe and the reaction mixture was stirred at 40  $^{\circ}\text{C}$  for 23-48 hours. The progress of polymer coupling was monitored by SEC analysis. When full conversion was observed, the reaction mixture was passed through a short column of neutral aluminium oxide to remove the copper catalyst. After washing the column with 50 mL of THF, the organic fractions were combined and the solvent removed under reduced pressure. The polymer was isolated by precipitation into methanol:acetone (2:1, v:v) from THF or chloroform and drying the precipitate under high vacuum at room temperature.

**Synthesis procedure of P3HT-b-PS<sub>OH</sub> 1**

P3HT (250 mg, approx. 21.4  $\mu\text{mol}$ , 1 equ.) and PS<sub>OH</sub> 1 (89 mg, approx. 42.7  $\mu\text{mol}$ , 2 equ.) dissolved in 80 mL of THF were reacted in presence of 2 mL copper(I) iodide/PMDETA catalyst solution (0.07 M in THF, 140  $\mu\text{mol}$ ). After 24.5 h full conversion was observed by SEC, the purification was performed as described above and precipitation was done into 500 mL of methanol:acetone (2:1, v:v) twice. Yield: 257 mg. <sup>1</sup>H-NMR (300 MHz, CDCl<sub>3</sub>,  $\delta$ ): 6.98 (s, m·H, H<sup>1</sup>), 6.82-6.15 (br m, 4(a+b)·H, H<sup>10</sup>), 3.85-3.60 (br s, 3b·H, H<sup>8</sup>), 2.88-2.65 (br t, 2m·H, H<sup>2</sup>), 1.80-1.15 (br m, H<sup>3</sup>, H<sup>4-6,9</sup>, H<sup>ini</sup>), 0.95-0.73 (br m, 3m·H, H<sup>7</sup>). SEC (THF):  $M_n=22.1 \text{ kg mol}^{-1}$ ,  $M_p=24.3 \text{ kg mol}^{-1}$ ,  $D=1.20$ . SEC (TCB, 150°C):  $M_n=22.4 \text{ kg mol}^{-1}$ ,  $M_p=29.7 \text{ kg mol}^{-1}$ ,  $D=1.44$ .

**Synthesis procedure of P3HT-b-PS<sub>OH</sub> 2**

P3HT (350 mg, approx. 29.9  $\mu\text{mol}$ , 1 equ.) and PS<sub>OH</sub> 2 (435 mg, approx. 60.4  $\mu\text{mol}$ , 2 equ.) dissolved in 100 mL dry THF were reacted in presence of 2 mL copper(I) iodide/PMDETA catalyst solution (0.07 M in THF, 140  $\mu\text{mol}$ ). After 17 h and 24 h the reaction mixture was purged with argon for 15 min and 1 ml catalyst solution was added respectively. Purification was performed after 48 h as described above and precipitation was done into 500 mL of methanol:acetone (2:1, v:v) twice. Yield: 477 mg. <sup>1</sup>H-NMR (300 MHz, o-DCB-d<sub>4</sub>,  $\delta$ ): 7.37 (s, m·H, H<sup>1</sup>), 7.05 -6.55 (br m, 4(a+b)·H, H<sup>10</sup>), 3.90-3.70 (br s, 3b·H, H<sup>8</sup>), 3.18-2.90 (br t, 2m·H, H<sup>2</sup>), 2.00-1.25 (br m, H<sup>3</sup>, H<sup>4-6,9</sup>, H<sup>ini</sup>), 1.15-0.95 (br m, 3m·H, H<sup>7</sup>). SEC (THF):  $M_n=24.9 \text{ kg mol}^{-1}$ ,  $M_p=30.5 \text{ kg mol}^{-1}$ ,  $D=1.22$ . SEC (TCB, 150°C):  $M_n=20.7 \text{ kg mol}^{-1}$ ,  $M_p=27.6 \text{ kg mol}^{-1}$ ,  $D=1.54$ .

**Synthesis procedure of P3HT-b-PS<sub>OH</sub> 3**

P3HT (250 mg, approx. 21.4  $\mu\text{mol}$ , 1 equ.) and PS<sub>OH</sub> 3 (598 mg, approx. 42.8  $\mu\text{mol}$ , 2 equ.) dissolved in 80 mL THF were reacted in presence of 2 mL copper(I) iodide/PMDETA catalyst solution (0.07 M in THF, 140  $\mu\text{mol}$ ). After 16.5 h the reaction mixture was purged with argon for 15 min and 1 ml catalyst solution was added. Purification was performed after 24 h as described above and precipitation was done into 500 mL of methanol:acetone (2:1, v:v) twice. Yield: 410 mg. <sup>1</sup>H-NMR (300 MHz, o-DCB-d<sub>4</sub>,  $\delta$ ): 7.37 (s, m·H, H<sup>1</sup>), 7.08 -6.50 (br m, 4(a+b)·H, H<sup>10</sup>), 3.95-3.65 (br s, 3b·H, H<sup>8</sup>), 3.20-2.90 (br t, 2m·H, H<sup>2</sup>), 2.10-1.30 (br m, H<sup>3</sup>, H<sup>4-6,9</sup>, H<sup>ini</sup>), 1.15-0.95 (br m, 3m·H, H<sup>7</sup>). SEC

(THF):  $M_n=28.0 \text{ kg mol}^{-1}$ ,  $M_p=35.1 \text{ kg mol}^{-1}$ ,  $D=1.23$ . SEC (TCB,  $150^\circ\text{C}$ ):  
 $M_n=17.7 \text{ kg mol}^{-1}$ ,  $M_p=24.5 \text{ kg mol}^{-1}$ ,  $D=1.55$ .

### General synthesis procedure of P3HT-b-PPC<sub>71</sub>BM

A 250 ml schlenk flask was flame dried at  $600^\circ\text{C}$  under high vacuum and charged with P3HT-b-PS<sub>OH</sub>, phenyl-C<sub>71</sub>-butyric acid (PC<sub>71</sub>BA), and 4-dimethylaminopyridine (DMAP). The flask was degassed under high vacuum and backfilled with argon twice. Dry o-dichlorobenzene (DCB) and the mixture was sonicated for 30 min at room temperature. In a separate flame dried 10 mL schlenk flask under argon, *N,N'*-dicyclohexylcarbodiimide (DCC) was dissolved in dry o-DCB. The DCC solution was added to the reaction mixture *via* syringe, which was stirred at  $40^\circ\text{C}$  for 22-24 h. The reaction mixture was transferred to a round bottom flask and the solvent DCB was removed at  $60^\circ\text{C}$  under vacuum using a rotary evaporator until a highly concentrated, viscous solution was reached. This crude product was then precipitated into a mixture of toluene:ethyl acetate (EE) (1:1,v:v), the precipitate filtered or centrifuged, dried in vacuum and redissolved in DCB. The precipitation cycles were done twice in toluene:ethyl acetate and then in methanol. Purity of the polymer was monitored by TLC (SiO<sub>2</sub>, eluent toluene:EE 1:1), where the polymer remains on the start line and the impurities show distinct spots. The precipitate was dried under high vacuum at room temperature.

### Synthesis procedure for P3HT-b-PPC<sub>71</sub>BM 1

P3HT-b-PS<sub>OH</sub> 1 (210 mg, approx.  $15.4 \mu\text{mol}$ ,  $61.8 \mu\text{mol}$  hydroxy groups, 1 equ.), PC<sub>71</sub>BA (94 mg,  $92.6 \mu\text{mol}$ , 1.5 equ.) and DMAP (23 mg,  $185 \mu\text{mol}$ , 3 equ) were dissolved in 22 mL of dry DCB and reacted for 24 h in presence of a solution of DCC (64 mg,  $309 \mu\text{mol}$ , 5 equ.) in 3 mL of dry DCB. Purification was done by precipitation of the crude product from a concentrated solution in DCB following the above described protocol twice into 300 mL toluene:EE and finally into 300 mL of methanol. Yield: 220 mg of a black precipitate. <sup>1</sup>H-NMR (300 MHz, CDCl<sub>3</sub>,  $\delta$ ): 7.55-7.30 (br m, H<sup>a</sup>, H<sup>b</sup>), 6.98 (s, m·H, H<sup>1</sup>), 6.85-6.30 (br m, 4(a+b)·H, H<sup>10</sup>), 3.85-3.60 (br s, 3b·H, H<sup>8</sup>), 2.90-2.65 (br t, 2m·H, H<sup>2</sup>), 1.90-1.12 (br m, H<sup>3</sup>, H<sup>4-6,9</sup>, H<sup>Imi</sup>), 0.98-0.75 (br m, 3m·H, H<sup>7</sup>). H<sup>c</sup>, H<sup>d</sup>, H<sup>f</sup> and H<sup>e</sup> were not clearly resolved. SEC (TCB,  $150^\circ\text{C}$ ):  $M_n=17.5 \text{ kg mol}^{-1}$ ,  $M_p=28.9 \text{ kg mol}^{-1}$ ,  $D=1.68$ .

**Synthesis procedure for P3HT-b-PPC<sub>71</sub>BM 2**

P3HT-b-PS<sub>OH</sub> 2 (302 mg, approx. 16.0 μmol, 224 μmol hydroxy groups, 1 equ.), PC<sub>71</sub>BA (341 mg, 336 μmol, 1.5 equ.) and DMAP (82 mg, 671 μmol, 3 equ) were dissolved in 75 mL of dry DCB and reacted for 22 h in presence of a solution of DCC (231 mg, 1.12 mmol, 5 equ.) in 5 mL in of dry DCB. Purification was done by precipitation of the crude product from a concentrated solution in DCB following the above described protocol twice into 400 mL toluene:EE and finally into 300 mL of methanol. Yield: 365 mg of a black precipitate. <sup>1</sup>H-NMR (300 MHz, o-DCB-d<sub>4</sub>, δ): 8.20-8.05 (br m, H<sup>c</sup>), 7.75-7.45 (br m, H<sup>a</sup>, H<sup>b</sup>), 7.37 (s, m·H, H<sup>1</sup>), 7.05-6.50 (br m, 4(a+b)·H, H<sup>10</sup>), 4.00-3.65 (br s, 3b·H, H<sup>8</sup>), 3.20-2.95 (br m, H<sup>2</sup>), 2.95-2.80, 2.80-2.65 (br m, H<sup>f</sup>, H<sup>d</sup>), 2.30-1.25 (br m, H<sup>e</sup>, H<sup>3</sup>, H<sup>4-6,9</sup>, H<sup>CTA</sup>), 1.15-0.95 (br m, 3m·H, H<sup>7</sup>). SEC (TCB, 150 °C):  $M_n=13.5 \text{ kg mol}^{-1}$ ,  $M_p=26.4 \text{ kg mol}^{-1}$ ,  $D=1.97$ .

**Synthesis procedure for P3HT-b-PPC<sub>71</sub>BM 3**

P3HT-b-PS<sub>OH</sub> 3 (300 mg, approx. 12.7 μmol, 278 μmol hydroxy groups, 1 equ.), PC<sub>71</sub>BA (425 mg, 418 μmol, 1.5 equ.) and DMAP (102 mg, 835 μmol, 3 equ) were dissolved in 95 mL of dry DCB and reacted for 23 h in presence of a solution of DCC (287 mg, 1.39 mmol, 5 equ.) in 5 mL of dry DCB. The reaction mixture was transferred to a round bottom flask and the solvent completely removed in vacuum at 60 °C using a rotary evaporator. The crude product was washed with chloroform at room temperature to remove P3HT homopolymer and low-molecular weight block copolymer. The resulting crude product was then purified by precipitation from a concentrated solution in DCB following the above described protocol twice into 400 mL toluene:EE and finally into 300 mL of methanol. Yield: 190 mg of a black precipitate. <sup>1</sup>H-NMR (300 MHz, o-DCB-d<sub>4</sub>, δ): 8.20-8.05 (br m, H<sup>c</sup>), 7.75-7.45 (br m, H<sup>a</sup>, H<sup>b</sup>), 7.37 (s, m·H, H<sup>1</sup>), 7.05-6.45 (br m, 4(a+b)·H, H<sup>10</sup>), 3.95-3.65 (br s, 3b·H, H<sup>8</sup>), 3.20-2.95 (br m, H<sup>2</sup>), 2.95-2.80, 2.80-2.65 (br m, H<sup>f</sup>, H<sup>d</sup>), 2.30-1.25 (br m, H<sup>e</sup>, H<sup>3</sup>, H<sup>4-6,9</sup>, H<sup>CTA</sup>), 1.15-0.95 (br m, 3m·H, H<sup>7</sup>). SEC (TCB, 150 °C):  $M_n=17.3 \text{ kg mol}^{-1}$ ,  $M_p=28.4 \text{ kg mol}^{-1}$ ,  $D=1.63$ .

## REFERENCES

- [1] A. de Cuendias, R. C. Hiorns, E. Cloutet, L. Vignau, H. Cramail, *Polym. Int.* **2010**, *59*, 1452.
- [2] C.-L. Liu, C.-H. Lin, C.-C. Kuo, S.-T. Lin, W.-C. Chen, *Prog. Polym. Sci.* **2011**, *36*, 603.
- [3] G. Yu, J. Gao, J. C. Hummelen, F. Wudl, a J. Heeger, *Science* **1995**, *270*, 1789.
- [4] K. M. Coakley, M. D. McGehee, *Chem. Mater.* **2004**, *16*, 4533.
- [5] H. Hoppe, N. S. Sariciftci, *J. Mater. Chem.* **2006**, *16*, 45.
- [6] J. Peet, M. L. Senatore, A. J. Heeger, G. C. Bazan, *Adv. Mater.* **2009**, *21*, 1521.
- [7] S. B. Darling, *Energy Environ. Sci.* **2009**, *2*, 1266.
- [8] M. Sommer, S. Huettner, M. Thelakkat, *J. Mater. Chem.* **2010**, *20*, 10788.
- [9] P. D. Topham, A. J. Parnell, R. C. Hiorns, *J. Polym. Sci. Part B Polym. Phys.* **2011**, *49*, 1131.
- [10] A. Yassar, L. Miozzo, R. Gironda, G. Horowitz, *Prog. Polym. Sci.* **2013**, *38*, 791.
- [11] K. Nakabayashi, H. Mori, *Materials* **2014**, *7*, 3274.
- [12] M. Hufnagel, M. Fischer, T. Thurn-Albrecht, M. Thelakkat, *Polym. Chem.* **2015**, *6*, 813.
- [13] M. M. Wienk, J. M. Kroon, W. J. H. Verhees, J. Knol, J. C. Hummelen, P. a van Hal, R. a J. Janssen, *Angew. Chem. Int. Ed.* **2003**, *42*, 3371.
- [14] U. Stalmach, B. de Boer, C. Videlot, P. F. van Hutten, G. Hadziioannou, *J. Am. Chem. Soc.* **2000**, *122*, 5464.
- [15] A. Nourdine, L. Perrin, R. De Bettignies, S. Guillerez, L. Flandin, N. Alberola, *Polymer* **2011**, *52*, 6066.
- [16] C. Yang, J. K. Lee, A. J. Heeger, F. Wudl, *J. Mater. Chem.* **2009**, *19*, 5416.
- [17] S. M. Tuladhar, D. Poplavskyy, S. a. Choulis, J. R. Durrant, D. D. C. Bradley, J. Nelson, *Adv. Funct. Mater.* **2005**, *15*, 1171.
- [18] A. Baumann, J. Lorrman, C. Deibel, V. Dyakonov, *Appl. Phys. Lett.* **2008**, *93*, 252104.
- [19] V. D. Mihailitchi, H. X. Xie, B. de Boer, L. J. a. Koster, P. W. M. Blom, *Adv. Funct. Mater.* **2006**, *16*, 699.
- [20] J. Huang, G. Li, Y. Yang, *Appl. Phys. Lett.* **2005**, *87*, 112105.
- [21] R. Mauer, M. Kastler, F. Laquai, *Adv. Funct. Mater.* **2010**, *20*, 2085.
- [22] S. Huettner, M. Sommer, J. Hodgkiss, P. Kohn, .
- [23] M. Hufnagel, M. Fischer, T. Thurn-Albrecht, M. Thelakkat, *Submitted to Macromolecules* **2015**.
- [24] M. Hufnagel, M. Thelakkat, *Submitt. to J. Polym. Sci. Part B Polym. Phys.* **2015**.
- [25] E. von Hauff, J. Parisi, V. Dyakonov, *J. Appl. Phys.* **2006**, *100*, 043702.
- [26] M. T. Dang, L. Hirsch, G. Wantz, J. D. Wuest, *Chem. Rev.* **2013**, *113*, 3734.
- [27] R. H. Lohwasser, M. Thelakkat, *Macromolecules* **2012**, *45*, 1.
- [28] C. R. Singh, G. Gupta, R. Lohwasser, S. Engmann, J. Balko, M. Thelakkat, T. Thurn-Albrecht, H. Hoppe, *J. Polym. Sci. Part B Polym. Phys.* **2013**, *51*, 943.
- [29] R. H. Lohwasser, G. Gupta, P. Kohn, M. Sommer, A. S. Lang, T. Thurn-Albrecht, M. Thelakkat, *Macromolecules* **2013**, *46*, 4403.
- [30] M. Hufnagel, M.-A. Muth, J. C. Brendel, M. Thelakkat, *Macromolecules* **2014**, *47*, 2324.
- [31] W.-N. He, J.-T. Xu, *Prog. Polym. Sci.* **2012**, *37*, 1350.
- [32] E. C. Davidson, B. S. Beckingham, V. Ho, R. a. Segalman, *J. Polym. Sci. Part B Polym. Phys.* **2015**, DOI: 10.1002/polb.23904.

- [33] J.-F. Chang, B. Sun, D. W. Breiby, M. M. Nielsen, T. I. Sölling, M. Giles, I. McCulloch, H. Sirringhaus, *Chem. Mater.* **2004**, *16*, 4772.
- [34] S. M. Mai, J. P. A. Fairclough, I. W. Hamley, M. W. Matsen, R. C. Denny, B. X. Liao, C. Booth, A. J. Ryan, *Macromolecules* **1996**, *29*, 6212.
- [35] F. C. Spano, *J. Chem. Phys.* **2005**, *122*, 234701.
- [36] C. Scharsich, R. H. Lohwasser, M. Sommer, U. Asawapirom, U. Scherf, M. Thelakkat, D. Neher, A. Köhler, *J. Polym. Sci. Part B Polym. Phys.* **2012**, *50*, 442.
- [37] S. Huettner, M. Sommer, J. Hodgkiss, P. Kohn, T. Thurn-Albrecht, R. H. Friend, U. Steiner, M. Thelakkat, *ACS Nano* **2011**, *5*, 3506.
- [38] A. S. Lang, M. Thelakkat, *Polym. Chem.* **2011**, *2*, 2213.

## SUPPORTING INFORMATION

**Figure S1.**  $^1\text{H-NMR}$  spectrum of P3HT-b-PS<sub>OH</sub> 1.

**Figure S2.**  $^1\text{H-NMR}$  spectrum of P3HT-b-PS<sub>OH</sub> 2.

**Figure S3.**  $^1\text{H-NMR}$  spectrum of P3HT-b-PS<sub>OH</sub> 3.

**Figure S4.**  $^1\text{H-NMR}$  spectrum of P3HT-b-PPC<sub>71</sub>BM 1.

**Figure S5.**  $^1\text{H-NMR}$  spectrum of P3HT-b-PPC<sub>71</sub>BM 2.

**Figure S6.**  $^1\text{H-NMR}$  spectrum of P3HT-b-PPC<sub>71</sub>BM 3.

**Calculation of the block copolymer composition based on UV-Vis absorption spectroscopy**

**Table S1.** Calculated weight fractions from UV-Vis absorption spectroscopy.

**Table S2.** Thermogravimetric data for the estimation of the PC71BM content.

**Table S3.** OFET results for p- and n-type operation of the P3HT-b-PPC<sub>71</sub>BM block copolymers.

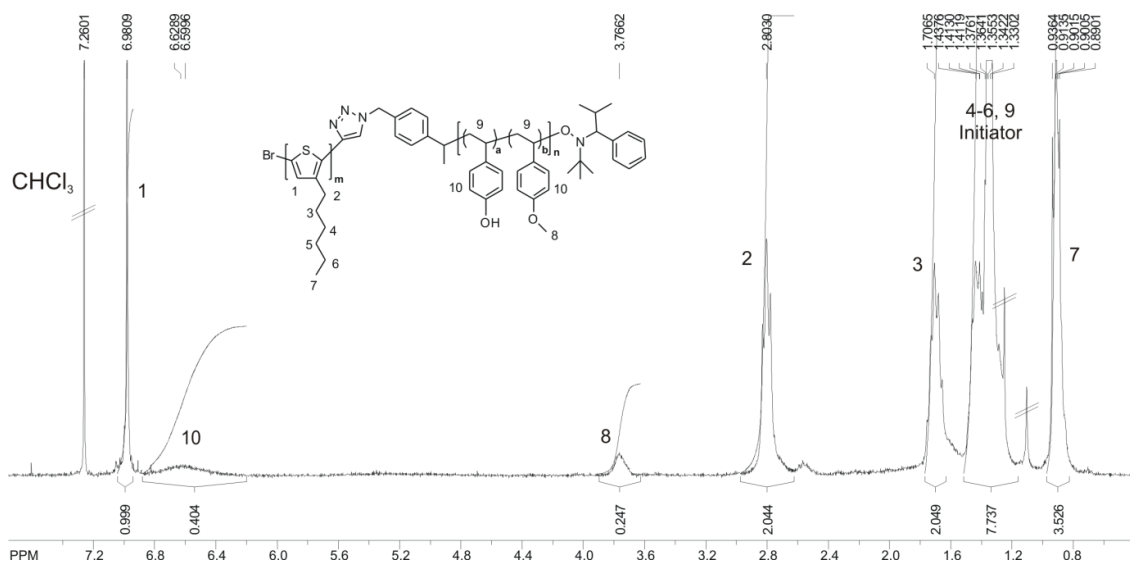


**Figure S1.**  $^1\text{H-NMR}$  spectrum of P3HT-b-PS<sub>OH</sub> 1.

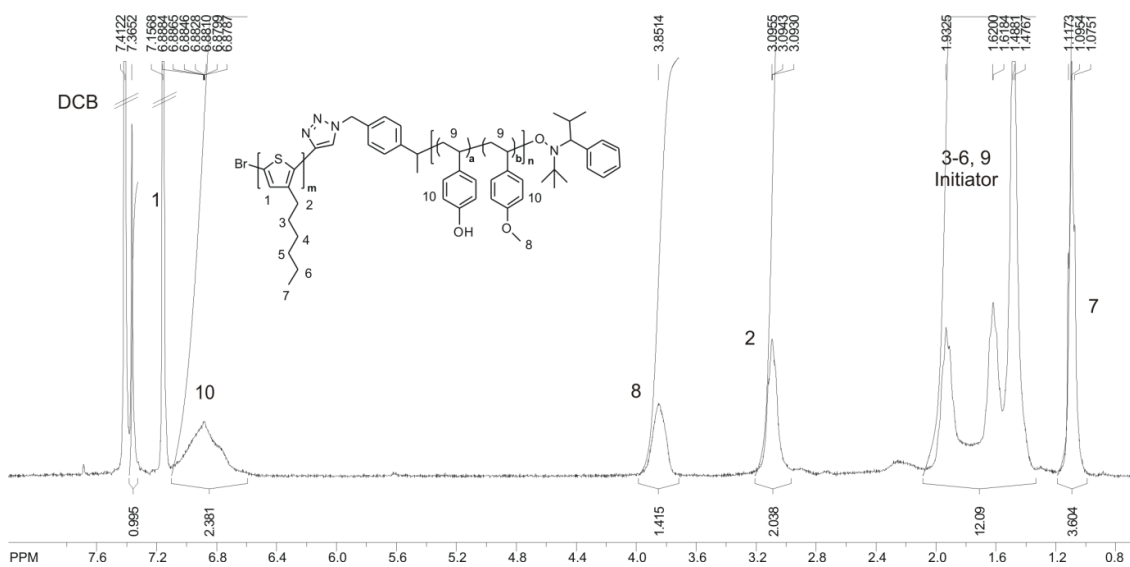


**Figure S2.**  $^1\text{H-NMR}$  spectrum of P3HT-b-PS<sub>OH</sub> 2.

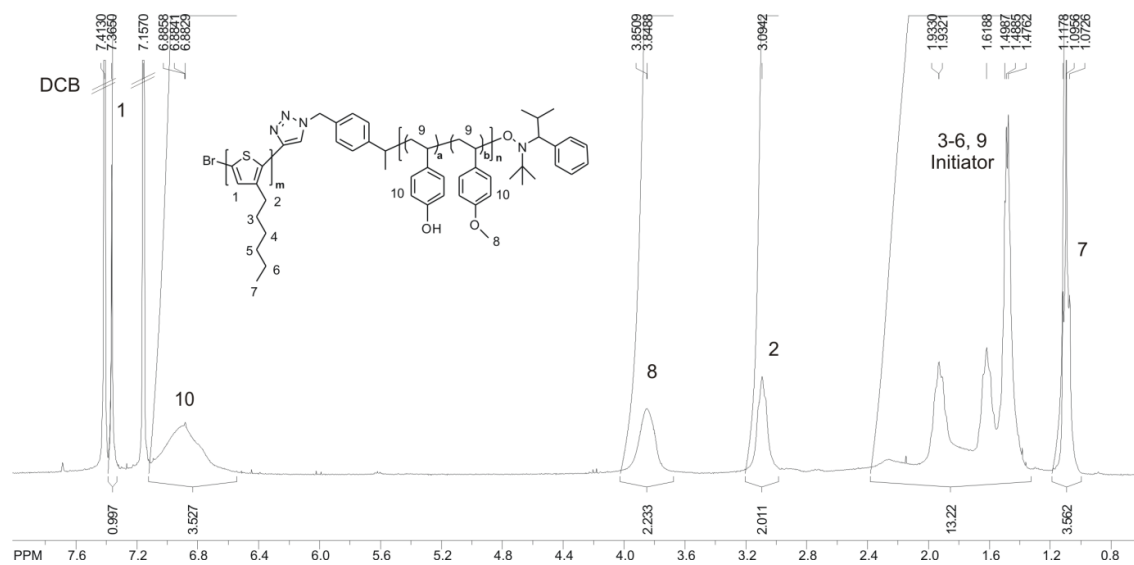


Figure S3.  $^1\text{H-NMR}$  spectrum of P3HT-*b*-PS<sub>OH</sub> 3.

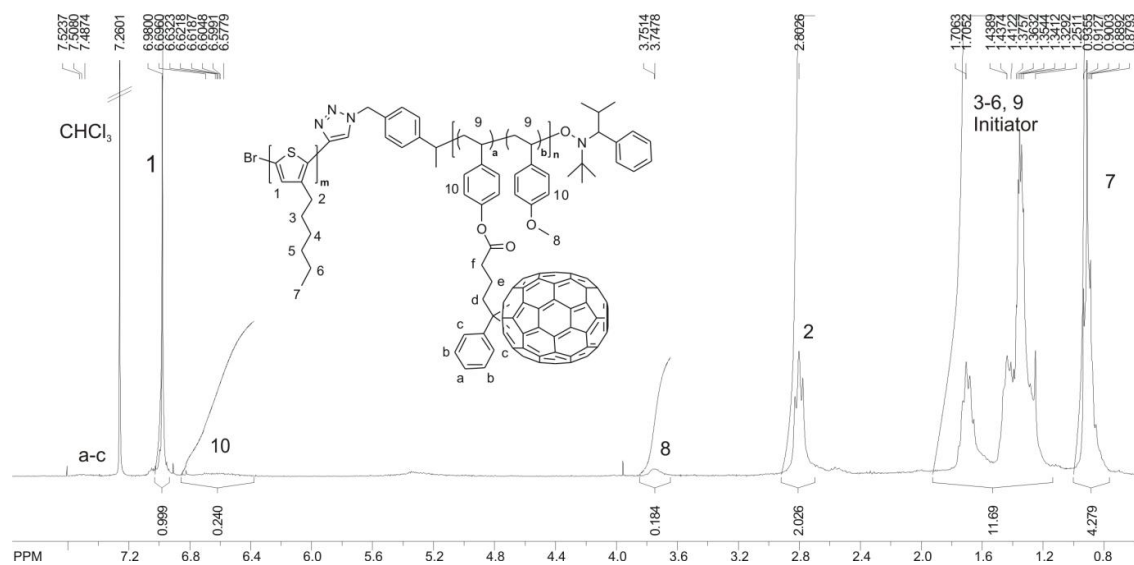


Figure S4.  $^1\text{H-NMR}$  spectrum of P3HT-*b*-PPC<sub>71</sub>BM 1.

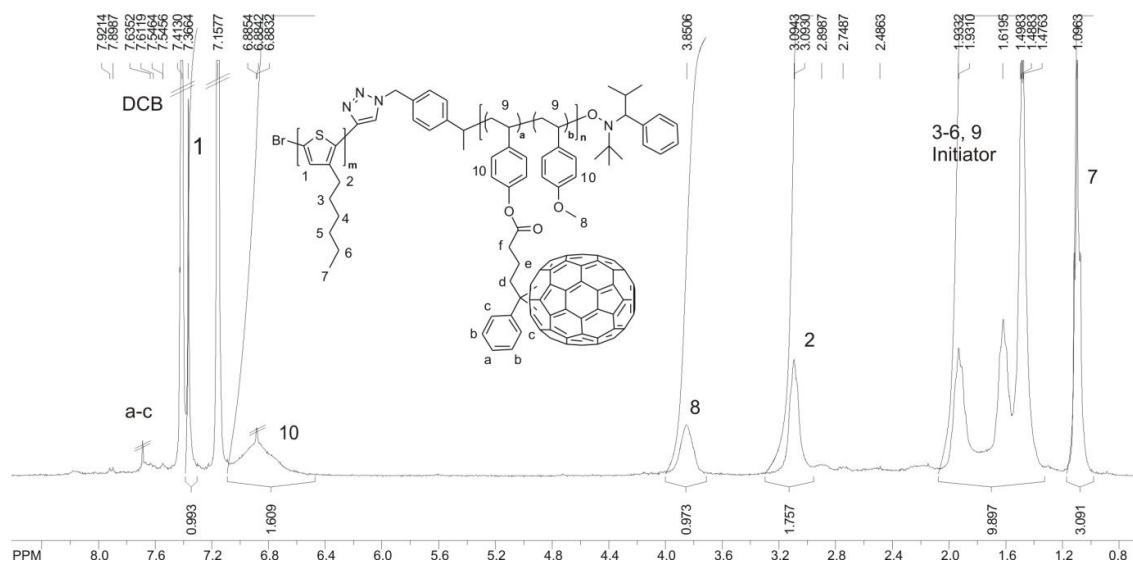


Figure S5.  $^1\text{H-NMR}$  spectrum of P3HT-b-PPC<sub>71</sub>BM 2.

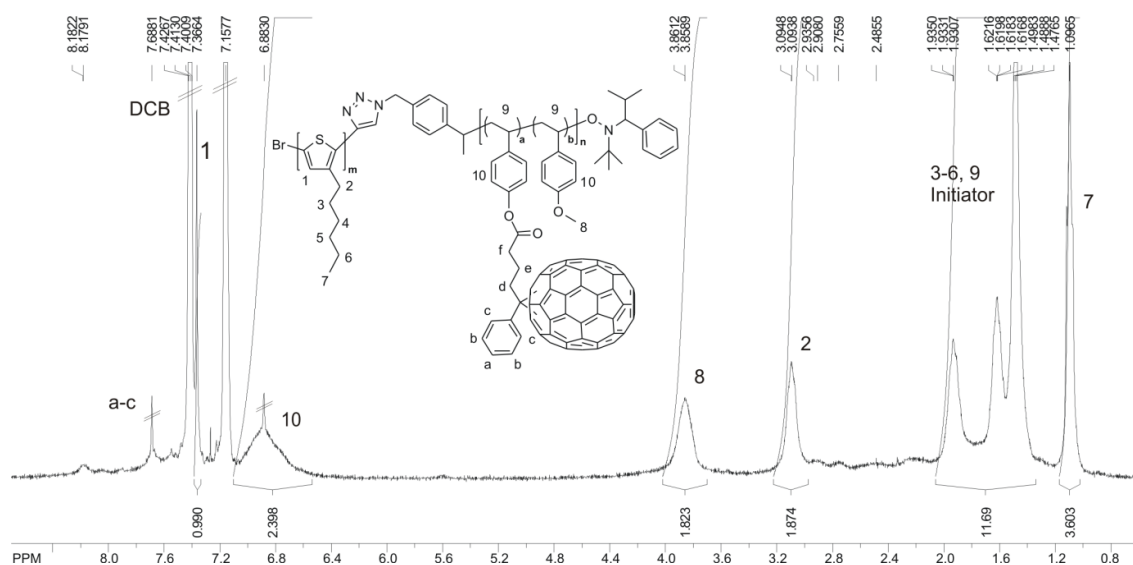


Figure S6.  $^1\text{H-NMR}$  spectrum of P3HT-b-PPC<sub>71</sub>BM 3.

### Calculation of the block copolymer composition

The absorption spectra of the polymers in 0.02 mg/mL chloroform solution (Figure 2a) were taken to calculate the P3HT and PC<sub>71</sub>BM content of the block copolymers P3HT-b-PPC<sub>71</sub>BM 1-3. It is possible to calculate the content of a chromophore in polymers by comparing the extinction coefficients of polymer and the pure chromophore as reference in dilute solutions.<sup>[1,2]</sup>

#### PC<sub>71</sub>BM content in P3HT-b-PC<sub>71</sub>BM:

$$f(\text{PC}_{71}\text{BM}) = \frac{[\text{OD}_{274}(\text{P3HT-b-PPC}_{71}\text{BM}) - f(\text{P3HT-b-PS}_{\text{OH}}) * \text{OD}_{274}(\text{P3HT-b-PS}_{\text{OH}})]}{\text{OD}_{274}(\text{PC}_{71}\text{BM})}$$

The optical densities OD at  $\lambda=274$  nm were extracted from the UV-vis absorption spectra of P3HT-b-PPC<sub>71</sub>BM, P3HT-b-PS<sub>OH</sub> and pure PC<sub>71</sub>BM for solutions with the same concentration. Due to spectral overlap, OD<sub>274</sub>(P3HT-b-PPC<sub>71</sub>BM) has contributions from PC<sub>71</sub>BM and P3HT-b-PS<sub>OH</sub>. Therefore, OD<sub>274</sub>(P3HT-b-PPC<sub>71</sub>BM) was corrected by  $f(\text{P3HT-b-PS}_{\text{OH}}) * \text{OD}_{274}(\text{P3HT-b-PS}_{\text{OH}})$ , where  $f(\text{P3HT-b-PS}_{\text{OH}})$  stands for the weight fraction of P3HT-b-PS<sub>OH</sub> in the P3HT-b-PPC<sub>71</sub>BM block copolymer and OD<sub>274</sub>(P3HT-b-PS<sub>OH</sub>) for the absorption at  $\lambda=274$  nm. The weight fractions  $f(\text{P3HT-b-PS}_{\text{OH}})$  were 0.77, 0.67 and 0.59.

#### P3HT content in P3HT-b-PPC<sub>71</sub>BM:

$$f(\text{P3HT}) = \frac{[\text{OD}_{450}(\text{P3HT-b-PPC}_{71}\text{BM}) - f(\text{PC}_{71}\text{BM}) * \text{OD}_{450}(\text{PC}_{71}\text{BM})]}{\text{OD}_{450}(\text{P3HT})}$$

The optical densities OD at  $\lambda=450$  nm were extracted from the UV-vis absorption spectra of P3HT-b-PPC<sub>71</sub>BM, PC<sub>71</sub>BM, and pure P3HT. Due to spectral overlap, OD<sub>450</sub>(P3HT-b-PPC<sub>71</sub>BM) has contributions from P3HT and PC<sub>71</sub>BM. Therefore, OD<sub>450</sub>(P3HT-b-PPC<sub>71</sub>BM) was corrected by  $f(\text{PC}_{71}\text{BM}) * \text{OD}_{450}(\text{PC}_{71}\text{BM})$ , where  $f(\text{PC}_{71}\text{BM})$  are the weight fractions for PC<sub>71</sub>BM determined above, 0.22, 0.33 and 0.40 for P3HT-b-PPC<sub>71</sub>BM 1-3.

**Table S1.** Calculated weight fractions from UV-Vis absorption spectroscopy.

Polymer	$f(\text{PC}_{71}\text{BM})$	$f(\text{P3HT})$
P3HT-b-PPC <sub>71</sub> BM 1	0.22	0.70
P3HT-b-PPC <sub>71</sub> BM 2	0.33	0.37
P3HT-b-PPC <sub>71</sub> BM 3	0.40	0.22

[1] M. Hufnagel, M.-A. Muth, J. C. Brendel, M. Thelakkat, *Macromolecules* **2014**, *47*, 2324.

[2] M. Thelakkat, P. Pösch, H. W. Schmidt, *Macromolecules* **2001**, *34*, 7441.

**Table S2.** Thermogravimetric data for the estimation of the PC<sub>71</sub>BM content.

Polymer	Residual mass at 800 °C	$\Delta m$ <sup>a)</sup>	PC <sub>71</sub> BM <sup>b)</sup>
	[wt%]	[wt%]	[wt%]
P3HT-b-PS <sub>OH</sub> 1	32.7		
P3HT-b-PPC <sub>71</sub> BM 1	49.3	16.6	19
P3HT-b-PS <sub>OH</sub> 2	27.8		
P3HT-b-PPC <sub>71</sub> BM 2	55.5	27.7	32
P3HT-b-PS <sub>OH</sub> 3	25.5		
P3HT-b-PPC <sub>71</sub> BM 3	59.2	33.7	39

<sup>a)</sup> Difference of the residual masses of P3HT-b-PS<sub>OH</sub> and the corresponding P3HT-b-PPC<sub>71</sub>BM.

<sup>b)</sup> Estimated PC<sub>71</sub>BM weight content in P3HT-b-PPC<sub>71</sub>BM corrected by a weight loss of 13 wt% of PC<sub>71</sub>BM at 800 °C. The correction factor applied is  $f=1.149$ .

**Table S3.** OFET results for *p*- and *n*-type operation of the P3HT-*b*-PPC<sub>71</sub>BM block copolymers after annealing for 30 min at 160 °C. The average mobility was determined based on several different transistors with varying channel length.

Polymer	Type	No.	Channel length [μm]	Fitted mobility [cm <sup>2</sup> V <sup>-1</sup> s <sup>-1</sup> ]	Average mobility [cm <sup>2</sup> V <sup>-1</sup> s <sup>-1</sup> ]
P3HT- <i>b</i> -PPC <sub>71</sub> BM 1	p	1	20	3.58 x 10 <sup>-3</sup>	(3.9±0.8) x 10 <sup>-3</sup>
		2	10	3.21 x 10 <sup>-3</sup>	
		3	10	2.89 x 10 <sup>-3</sup>	
		4	10	3.38 x 10 <sup>-3</sup>	
		5	10	5.13 x 10 <sup>-3</sup>	
		6	10	4.28 x 10 <sup>-3</sup>	
		7	20	4.12 x 10 <sup>-3</sup>	
		8	20	4.73 x 10 <sup>-3</sup>	
	n	1	20	0	0
		2	10	0	
		3	10	0	
		4	10	0	
		5	10	0	
		6	10	0	
		7	20	0	
		8	20	0	
P3HT- <i>b</i> -PPC <sub>71</sub> BM 2	p	9	20	1.46 x 10 <sup>-4</sup>	(1.3±0.1) x 10 <sup>-4</sup>
		10	10	1.46 x 10 <sup>-4</sup>	
		11	10	1.34 x 10 <sup>-4</sup>	
		12	20	1.27 x 10 <sup>-4</sup>	
		13	20	1.48 x 10 <sup>-4</sup>	
		14	10	1.18 x 10 <sup>-4</sup>	
	n	15	10	1.22 x 10 <sup>-4</sup>	(5.2±2.4) x 10 <sup>-7</sup>
		9	20	-	
		10	10	3.43 x 10 <sup>-7</sup>	
		11	10	3.38 x 10 <sup>-7</sup>	
		12	20	8.29 x 10 <sup>-7</sup>	
		13	20	8.23 x 10 <sup>-7</sup>	
		14	10	3.75 x 10 <sup>-7</sup>	
		15	10	3.81 x 10 <sup>-7</sup>	
		P3HT- <i>b</i> -PPC <sub>71</sub> BM 3	p	16	
17	20			2.17 x 10 <sup>-5</sup>	
18	10			1.89 x 10 <sup>-5</sup>	
19	10			1.80 x 10 <sup>-5</sup>	
20	20			2.14 x 10 <sup>-5</sup>	
21	10			2.25 x 10 <sup>-5</sup>	
n	22		10	1.55 x 10 <sup>-5</sup>	(6.7±2.0) x 10 <sup>-7</sup>
	16		20	-	
	17		20	9.74 x 10 <sup>-7</sup>	
	18		10	5.54 x 10 <sup>-7</sup>	
	19		10	7.49 x 10 <sup>-7</sup>	
	20		20	7.71 x 10 <sup>-7</sup>	
21	10	5.23 x 10 <sup>-7</sup>			
22	10	4.54 x 10 <sup>-7</sup>			

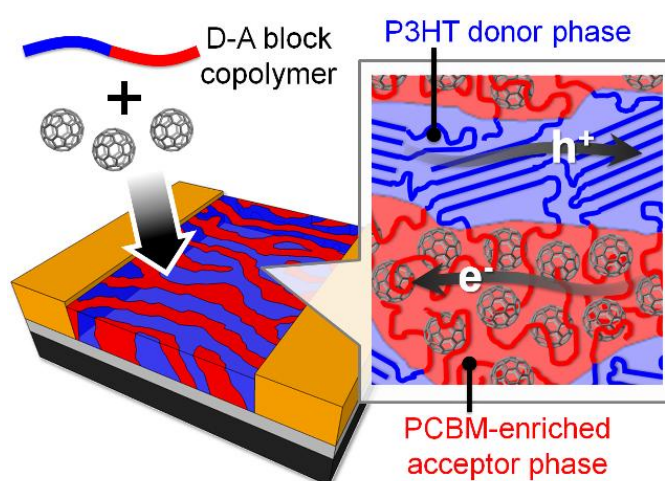


## 7 Simultaneous morphological stability and high charge carrier mobilities in donor-acceptor block copolymer/PCBM blends

*Martin Hufnagel and Mukundan Thelakkat\**

Applied Functional Polymers, Department of Macromolecular Chemistry I  
University of Bayreuth, Universitaetsstr. 30, 95440 Bayreuth (Germany)

\*Corresponding author: [mukundan.thelakkat@uni-bayreuth.de](mailto:mukundan.thelakkat@uni-bayreuth.de)



Submitted to *Journal of Polymer Science, Part B: Polymer Physics* in 2015.

**ABSTRACT**

Donor-acceptor block copolymers (BCP), incorporating poly(3-hexylthiophene) (P3HT) and a polystyrene copolymer with pendant fullerenes (PPCBM) provide desired stable nanostructures, but mostly do not exhibit balanced charge carrier mobilities. This work presents an elegant approach to match hole and electron transport in BCP by blending with molecular PCBM without causing any macrophase separation. An insufficient electron mobility of PPCBM can be widely compensated by adding PCBM which is monitored by the space-charge limited current (SCLC) method. Using X-ray diffraction (XRD), atomic force microscopy (AFM) and differential scanning calorimetry (DSC), we verify the large miscibility of the PPCBM:PCBM blend up to 60 wt% PCBM load forming an amorphous, molecularly mixed fullerene phase without crystallization. Thus, blending BCP with PCBM substantially enhances charge transport achieving an electron mobility of  $\mu_e=3.2 \times 10^{-4} \text{ cm}^2\text{V}^{-1}\text{s}^{-1}$  and hole mobility of  $\mu_h=1.8 \times 10^{-3} \text{ cm}^2\text{V}^{-1}\text{s}^{-1}$  in organic field effect transistors (OFET). The BCP:PCBM blend provides a similarly high ambipolar charge transport compared to the established P3HT:PCBM system, but with the advantage of an exceptionally stable morphology even for prolonged thermal annealing. This work demonstrates the feasibility of high charge transport and stable morphology simultaneously in a donor-acceptor block copolymer by a blend approach.

**INTRODUCTION**

One of the key parameters determining the performance of optoelectronic devices such as organic light-emitting diodes (OLED), organic photovoltaics (OPV) or organic field-effect transistors (OFET) is the charge carrier mobility. The effective drift velocity  $v$  of charge carriers depends on the intrinsic charge carrier mobility  $\mu$  and the applied electrical field  $E$ , generally expressed by  $v = \mu E$ .<sup>[1]</sup> Polymer solar cells typically have an active layer which is a physical mixture of a hole transporting donor material and an electron transporting acceptor material and the resulting bicontinuous blend is referred to as bulk heterojunction (BHJ).<sup>[2,3]</sup> So far, blends of poly(3-hexylthiophene) (P3HT) and phenyl-C<sub>61</sub>-butyric acid methyl ester (PCBM) constitute one of the most studied active layer materials in OPV.<sup>[4]</sup> As a rule of thumb, sufficiently high and balanced charge carrier mobilities are favorable for the power conversion efficiency in OPV, since non-geminate recombination of charges is reduced by a fast carrier extraction and the formation of space-charge in the photoactive layer is widely suppressed.<sup>[5-9]</sup>

A fundamental requirement for ambipolar charge carrier transport in donor:acceptor blends is the formation of phase separated domains that allow both hole and electron transport. Basically, the miscibility of a blend of two or more components is described by the Gibbs free enthalpy of mixing  $\Delta G_m = \Delta H_m - T\Delta S_m$ .<sup>[10]</sup> Hence,  $\Delta G_m$  is decisive for the compatibility of the blend and is mostly driven by the entropy of mixing  $\Delta S_m$  and the enthalpy of mixing  $\Delta H_m$ , which is negative only for strong attractive interactions such as ion, acid-base, hydrogen or dipole-dipole interactions. Against the assumption that blends of conjugated polymers and fullerenes simply phase separate into pure polymer and fullerene domains, they often exhibit very complex phase diagrams. On the one hand, the intercalation of fullerenes into polymers resulting in bimolecular crystals is observed when there is enough free volume between the polymer side-chains to accommodate the fullerene molecules.<sup>[11,12]</sup> On the other hand, molecular mixing of fullerenes into the amorphous polymer phase can also occur, *e.g.* in P3HT:PCBM blends.<sup>[12–14]</sup> The phase diagram of these binary blends is in particular dominated by the donor:acceptor composition. Several studies have confirmed that the optimum composition of binary blends for BHJ devices coincides with phase separation into coexisting phases that allow both hole and electron transport through interconnected domains.<sup>[11,13,15–17]</sup>

Such blend systems, however, rely on kinetically frozen active layer mesostructures in a non-equilibrium state that makes morphology control and long-term stability of the device difficult.<sup>[18–21]</sup> These issues become in particular critical for transferring the small area, lab-scale processing of OPV devices to a large scale roll-to-roll fabrication which requires totally different drying or annealing procedures.<sup>[22]</sup> The morphological evolution of polymer:PCBM blends during thermal annealing is strongly influenced by the enhanced diffusion of the PCBM molecules. Although the diffusion of fullerenes initially improve phase separation on the nanoscale generating domains between 10 and 100 nm, the growth of micron-sized fullerene crystals is usually observed for longer annealing times and higher temperatures with detrimental effects for the device.<sup>[23–25]</sup> In consequence, several strategies have been developed to stabilize the blend nanomorphology towards enhanced long-term stability, *e.g.* by cross-linking of either donor or acceptor material,<sup>[26]</sup> increasing the glass transition temperature<sup>[27]</sup> or by compatibilization of the blend using small amounts of block copolymers.<sup>[19,28–33]</sup> Several reports on block copolymer stabilized polymer:fullerene blends demonstrate the improved but still limited morphological stability and only a partial suppression of PCBM crystallization.<sup>[19,32,34]</sup>

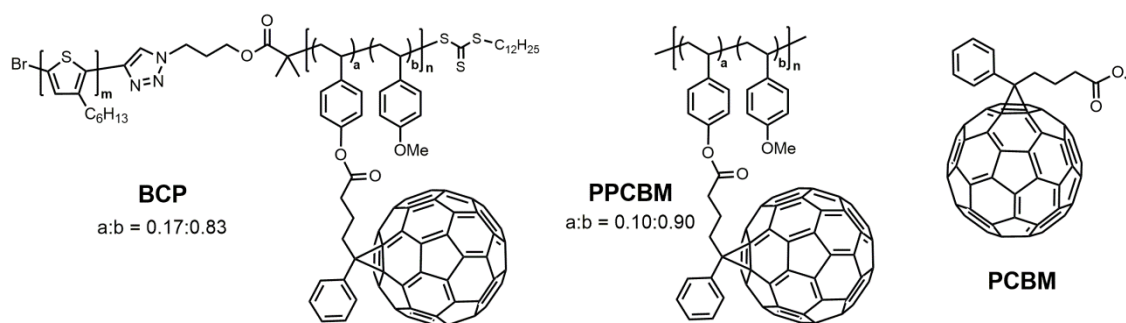
Here, donor–acceptor block copolymers are attractive candidates as single material since they can self-assemble into well-defined nanoscale BHJ morphologies which are in a stable thermodynamic equilibrium.<sup>[35–38]</sup> To achieve balanced and high charge carrier mobilities in both polymer blocks, it often requires tremendous synthetic efforts. For example, the fullerene grafting density in side-chain functionalized acceptor polymers such as PCBM-grafted polystyrene (PPCBM) is limited due to solubility issues, and in consequence, the resulting electron mobility is less compared to pristine PCBM.<sup>[39,40]</sup> A feasible route to close the gap of hole and electron mobility in such single-component donor-acceptor block copolymer is the addition of a small molecule (or polymeric) semiconductors with high mobility.<sup>[34,41,42]</sup> We favor a blend with the block copolymer as the majority phase to preserve the nanoscale and stable block copolymer morphology by enriching one polymer block with small molecules. Fortunately, the microphase separated morphology of block copolymers is often maintained or even can be specifically modified by blending.<sup>[43]</sup> In this way, the charge carrier mobilities can be balanced with beneficial effects for device application without adversely affecting the nanoscale phase separation realized in a block copolymer.

This work focuses on balancing the hole and electron mobility in a typical block copolymer BCP carrying a p-type P3HT block and a n-type PPCBM using a blend approach. We study first in detail the consequences of PCBM blending on both morphology and charge carrier mobility in fullerene-grafted polymers. For this, the miscibility, phase behavior and charge carrier transport in blends of the homopolymer PPCBM with molecular PCBM is systematically investigated in dependence of the blend composition. The molecular mixing observed for the PPCBM:PCBM blends is then investigated in blends of the nanostructured donor-acceptor block copolymer BCP which is carrying a PPCBM polymer block. The charge transport in OFETs of the BCP:PCBM blends is studied as a function of the added PCBM weight fraction. Further, we compare the optimized BCP:PCBM blend with the benchmark P3HT:PCBM blend regarding charge transport and morphological stability. The approach presented here offers a solution to the dilemma of not achieving high fullerene content in grafted polymers due to solubility limitation and the lack of morphology control in binary blends. We clearly demonstrate how to maintain the desired morphological stability and simultaneously achieve balanced charge carrier mobilities in a donor-acceptor system. This has a general validity and it serves as a universal approach for polymer:fullerene blend systems.

## RESULTS AND DISCUSSION

The donor-acceptor block copolymer (BCP) investigated here consists of a poly(3-hexylthiophene) (P3HT) segment as donor and a polystyrene copolymer with pendant phenyl- $C_{61}$ -butyric acid methyl ester (PCBM) fullerenes as acceptor block (PPCBM) as depicted in **Scheme 1**. BCP has a molecular weight of  $M_n=21.6 \text{ kg mol}^{-1}$  and  $M_p=32.0 \text{ kg mol}^{-1}$  with a dispersity of  $D=1.62$ . The conjugated P3HT block exhibits excellent regioregularity, a molecular weight of  $M_n=19.2 \text{ kg mol}^{-1}$  (SEC) and  $D=1.11$  owing to the well-controlled Kumada catalyst transfer polymerization. The PPCBM acceptor block is based on a statistical polystyrene copolymer backbone with  $M_n=7.5 \text{ kg mol}^{-1}$  with a monomer ratio of a:b=0.17:0.83. A detailed description for the synthesis of this block copolymer has been reported earlier.<sup>[40]</sup> The composition of BCP is 34 wt% P3HT and 66 wt% of PPCBM; considering only the fullerene content it corresponds to a weight fraction of 31 wt% for PCBM. The fullerene grafting density in the acceptor block, *i.e.* the weight ratio between pendant PCBM and the PPCBM block, is 47 wt%. The ratio of the semiconducting components P3HT:PCBM in this block copolymer is 1:0.92. BCP exhibits a nanoscale phase separation with amorphous PPCBM domains and a semi-crystalline P3HT phase.<sup>[40]</sup> For the blend studies phenyl- $C_{61}$ -butyric acid methyl ester (PCBM) as the state-of-the-art electron transport material in organic photovoltaics (OPV) was added to the BCP to enhance the electron mobility.

For the miscibility and mobility studies of blends of PPCBM with PCBM an acceptor copolymer (Scheme 1, PPCBM) with  $M_n=17.2 \text{ kg mol}^{-1}$ ,  $M_p=19.6 \text{ kg mol}^{-1}$  (SEC) and a dispersity  $D=1.27$  was used here. The copolymer ratio a:b=0.10:0.90 was selected which delivers a fullerene content of 30 wt%. Details of the synthesis are published elsewhere.<sup>[39]</sup>



**Scheme 1.** Donor-acceptor block copolymer BCP, fullerene-grafted copolymer PPCBM and the electron transport material phenyl- $C_{61}$ -butyric acid methyl ester (PCBM).

### Miscibility and morphology of PPCBM:PCBM blends

We first study the phase behavior and miscibility of the binary blend of PPCBM acceptor polymer and molecular PCBM. This is in particular important to understand whether the PPCBM:PCBM blend forms a homogeneous, molecularly mixed phase or a macrophase separated system with amorphous PPCBM polymer domains and PCBM crystallites. With regard to the block copolymer blend BCP:PCBM, it is desirable that the small molecule PCBM selectively settles into the PPCBM polymer domains. To preserve later the nanoscale block copolymer structure with P3HT and PPCBM domains, the added PCBM should remain within the PPCBM phase without a macrophase separation resulting in the formation of PCBM crystals. The electron transport polymer PPCBM used for the following experiments has a grafting density of 30 wt% of pendant PCBM (Scheme 1). This relatively low PCBM content in PPCBM was selected to prove whether the required miscibility and morphology is obtained even for a low degree functionalized PPCBM and if the charge carrier mobility can be tuned over a broad range.

We have studied the miscibility of PPCBM (Scheme 1) with molecular PCBM over a broad range by analyzing the compositions of PPCBM:PCBM=100:0, 80:20, 60:40, 40:60, 20:80 and 0:100 (wt:wt) in wide-angle X-ray diffraction (WAXS). All the samples were first dissolved in 1,2-dichlorobenzene (DCB) and then the solvent was slowly evaporated at 70 °C. The dried material was collected and studied as powder samples by WAXS in transmission geometry (**Figure 1a**, dotted lines for as-cast samples). PCBM was measured as received from the supplier. While pure PPCBM is fully amorphous, pure PCBM shows a clear scattering pattern corresponding to a crystalline solid. The blends 80:20, 60:40 and 40:60 remain amorphous and especially the last blend with its miscibility is a big surprise despite a fraction of molecular PCBM up to 60 wt%. When reaching 80 wt% of PCBM in the blend 20:80, the crystallization of PCBM is no longer inhibited by the minor fraction of PPCBM polymer. Here, a distinct two phase morphology of crystalline PCBM domains and amorphous PPCBM polymer domains is therefore expected. All samples were further annealed for 2 h at 120 °C to facilitate PCBM diffusion and crystallization (Figure 1a, solid lines). Although this temperature is below the glass transition of PPCBM of 150 °C, it is sufficient to promote the crystallinity as indicated in the PPCBM:PCBM=20:80 blend where the increased intensity of the reflections due to PCBM crystals can be observed. However, the blends 80:20, 60:40, and 40:60 stay completely amorphous. The WAXS results clearly show the high miscibility of PPCBM with

up to 60 wt% of PCBM retaining an amorphous blend system. This is in contrast to observations of blending PCBM into polystyrene matrix. In non-functionalized polystyrene, the PCBM demixes rapidly even for small wt% of added PCBM content resulting in macrophase separated systems.<sup>[39]</sup> Thus, the covalent attachment of a small amount of PCBM (30 wt%) onto the polystyrene chain stabilizes the polystyrene:PCBM blend even up to 60 wt% of added PCBM.

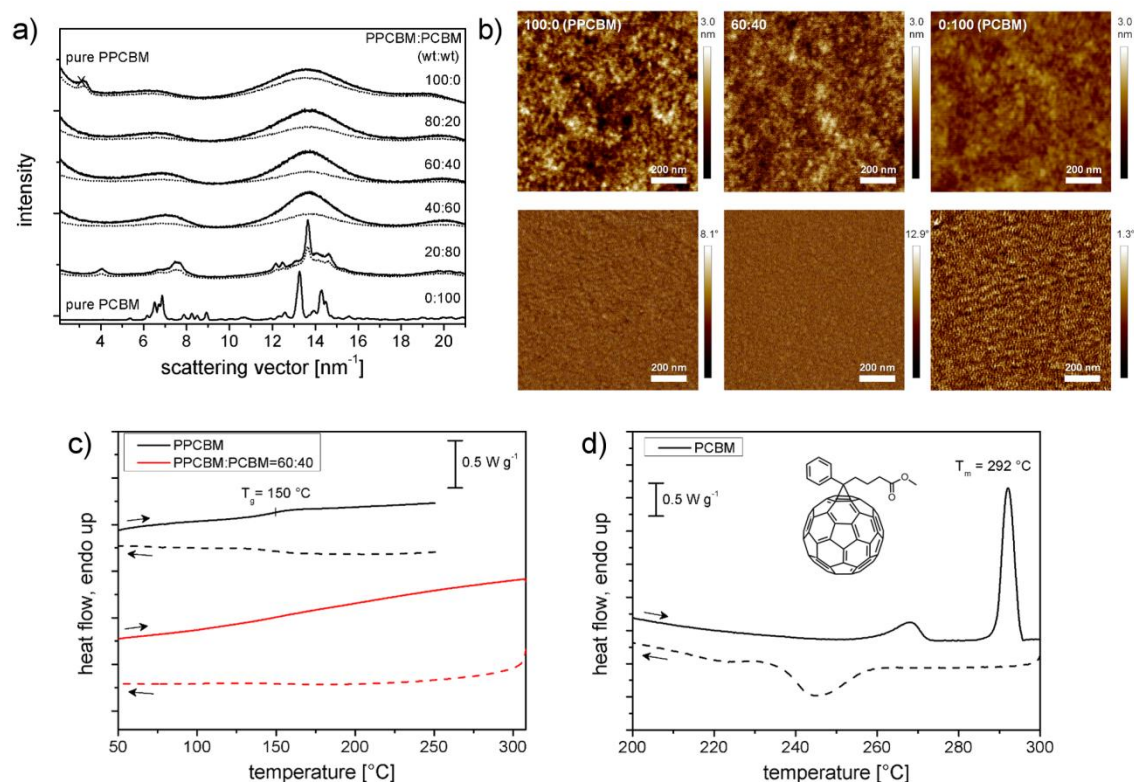


**Figure 1.** (a) Wide-angle X-ray scattering curves of PPCBM (100:0, wt:wt), the PPCBM:PCBM blends 80:20, 60:40, 40:60 and 20:80 and pure PCBM as powder samples. Except of PCBM, all samples have been measured as-prepared (dotted lines) and after thermal annealing (solid lines) for 3 h at 180 °C (PPCBM) and for 2 h at 120 °C (PCBM:PCBM blends). (b) 1x1  $\mu\text{m}^2$  AFM topography (top) and phase images (bottom) of as-cast films of pure PPCBM, PPCBM:PCBM=60:40 blend and pure PCBM. (c) DSC traces of PPCBM (black line) and a typical blend PPCBM:PCBM=60:40 blend (red line) in comparison to (d) the pristine PC<sub>61</sub>BM. Heating cycles are depicted as solid lines, cooling cycles are dashed and were recorded in nitrogen atmosphere at a rate of 20 K min<sup>-1</sup> for PPCBM and the PPCBM:PCBM blend and 10 K min<sup>-1</sup> for PCBM.

The phase morphology was further investigated by atomic force microscopy (AFM). For this, films with the composition PPCBM:PCBM=100:0, 80:20, 60:40, 20:80 and 0:100 were blade-cast from DCB solutions at 70 °C. According to the topography images of AFM, all films are very smooth with a low surface roughness between 0.191 and 0.447 nm (Figure 1b and S1). The phase images do not indicate a two phase morphology,

even not for PPCBM:PCBM=20:80 (Figure S1). But take into account that a two phase system, for instance PPCBM:PCBM=20:80, could also accumulate one phase preferentially at the film surface making it difficult to observe in topography images in AFM. Regarding the PCBM film, the very low surface roughness can only be explained by a compact layer of randomly oriented PCBM nanocrystals, possibly distributed in a glassy PCBM matrix.<sup>[20,44]</sup>

To complete the investigation of PPCBM:PCBM blend morphology, differential scanning calorimetry (DSC) of the pure materials PPCBM and PCBM in comparison to two typical blend ratios of PPCBM:PCBM=60:40 and 20:80 was performed. These blends were selected since they have shown different morphologies in XRD, *i.e.* homogeneous for 60:40 and a crystalline-amorphous two-phase morphology for 20:80. First, the DSC analysis of pure PPCBM polymer confirms the amorphous nature with a glass transition at 150 °C (Figure 1c). In contrast, the small molecule PCBM shows first an endothermic crystal structure transition around 268 °C and then a melting peak at 292 °C (Figure 1d).<sup>[45]</sup> The DSC traces of PPCBM:PCBM=60:40 and 20:80 remain both featureless even after several heating (up to 310 °C) and cooling cycles. This is exemplarily shown for PPCBM:PCBM=60:40 blend in Figure 1c and the full dataset of the DSC analysis for 60:40 and 20:80 can be found in Figure S2. This strongly suggests that the molecular PCBM does not crystallize in the polymer blend although the recrystallization temperature of PCBM during cooling is around 245 °C, *i.e.* far above the glass transition of 150 °C of PPCBM. Evidently, the thermal processing during the DSC experiments favors the mixing of the blend even for PPCBM:PCBM=20:80 and a complete suppression of PCBM crystallization is observed. These results are consistent with the previous findings in XRD and AFM studies indicating that the PPCBM polymer forms a homogeneous phase with PCBM and inhibits the crystallization fully. Even in the PPCBM polymer melt above 150 °C, where no or only negligible diffusional or kinetic hindrance for fullerene crystallization is supposed, the blend remains a homogeneous and amorphous physical mixture on cooling from an isotropic melt at 310 °C.

In conclusion, the analysis of the PPCBM:PCBM blends using X-ray scattering, AFM and DSC consistently demonstrates a molecularly mixed blend up to 60 wt% of added PCBM for solution-processed blends that remains homogeneous even upon thermal annealing. In case of cooling after thermal annealing up to 310 °C, even the blend with 80 wt% PCBM forms a homogeneous phase. This molecularly mixed phase consisting of

fullerenes and the amorphous PPCBM copolymer strongly resembles the phase behavior observed for several polymer:fullerene blends, where the fullerenes intermix with the amorphous domains of the semi-crystalline polymer, *e.g.* P3HT:PCBM,<sup>[46]</sup> poly(2-methoxy-5-(3'-7'- dimethyl-octyloxy)-1,4-phenylenevinylene) (MDMO-PPV):PCBM<sup>[47]</sup> and PCDTBT:PCBM.<sup>[48]</sup> The DSC scans up to 310 °C, which is more than 150 °C above the glass transition temperature of the PPCBM matrix, suggest that the molecular mixing of PCBM with PPCBM is thermodynamically preferred over crystallization of the PCBM component. The next important question is regarding the consequence of this blending without macrophase separation on the charge carrier mobility.

### Electron mobility in PPCBM blended with molecular PCBM

The influence of adding PCBM to the PPCBM polymer on the electron mobility was studied using the space-charge limited current (SCLC) method. SCLC allows the determination of the bulk charge carrier transport properties of a semiconductor sandwiched as film with 150-500 nm thickness between two electrodes. Electron-only devices with a layer stack of glass/ITO/ZnO/active layer/Ca/Al were fabricated using blade-casting of DCB solutions at 70 °C to deposit pure PPCBM and blends of PPCBM:PCBM. Devices with various film thicknesses were prepared to verify the  $L^{-3}$  dependence of the current density  $J$  (Figure S3). The blend ratios PPCBM:PCBM=80:20 and 60:40 were selected to stay in the molecularly mixed phase observed in the DCB cast samples of the XRD measurements. Owing to the field-dependency in the  $J$ - $V$  characteristics of the SCLC devices, the electron mobility was extracted using the Murgatroyd equation (**Figure 2a** and S3).<sup>[49]</sup> The electron mobility  $\mu_e$  found was  $(1.2 \pm 0.1) \times 10^{-6}$ ,  $(9.9 \pm 3.9) \times 10^{-6}$ ,  $(1.8 \pm 0.9) \times 10^{-4}$  and  $(4.3 \pm 1.0) \times 10^{-3} \text{ cm}^2 \text{ V}^{-1} \text{ s}^{-1}$  at a representative electrical field of  $1.5 \times 10^7 \text{ V m}^{-1}$  for PPCBM, the blends of PPCBM:PCBM=80:20, 60:40 and the reference PCBM, respectively. Thus, the enrichment of the PPCBM polymer phase with molecular PCBM strongly enhances the mobility  $\mu_e$  roughly by one order of magnitude per 20 wt% of added PCBM (Figure 2b). Since the PPCBM used for this SCLC study has only a low grafting density of 30 wt% PCBM, we can assume that  $\mu_e$  for PPCBMs with higher grafting densities (*e.g.* 47 wt% in the block copolymer BCP) and their blends with PCBM are shifted towards higher mobility values. Thus, blending of PCBM into PPCBM offers a new route towards stabilized fullerene systems with high contents of fullerenes leading to appreciably high electron mobility. This is not feasible either by grafting the required fullerene

content (due to solubility issues) or just by blending into polymers (due to macrophase separation).

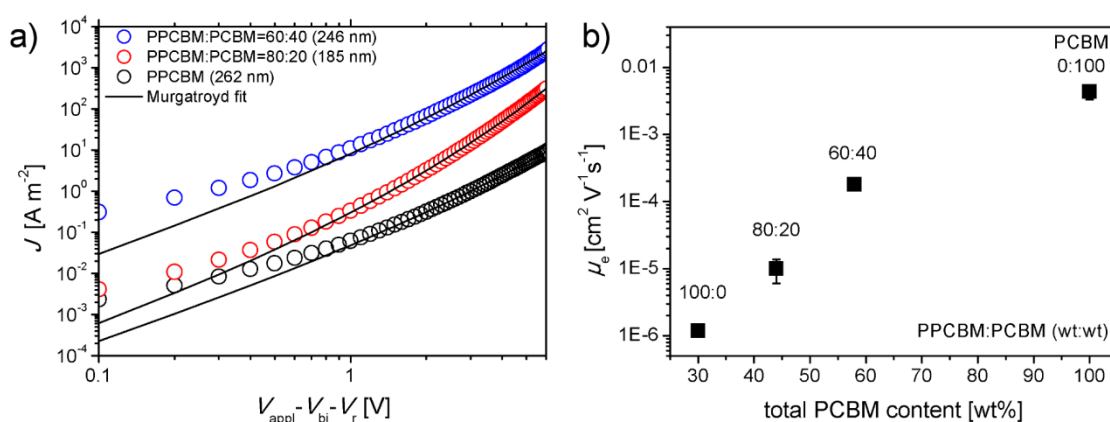


**Figure 2.** (a)  $J$ - $V$  characteristics of SCLC measurements of PPCBM and the blends PPCBM:PCBM=80:20 and 60:40 in electron-only devices. The electron mobility  $\mu_e$  was extracted using the Murgatroyd equation. (b) Electron mobility  $\mu_e$  at a field of  $1.5 \times 10^7$  V m<sup>-1</sup> in dependence of the total PCBM content starting from a 30 wt% fullerene-grafted PPCBM polymer and subsequent addition of PCBM. Pure PCBM is given as reference.

### Crystallinity and photoluminescence in thin films of BCP:PCBM blends

After confirming the positive effects of blending PCBM into PPCBM in terms of morphology and charge transport, the next question concerns the blending of PCBM into donor-acceptor block copolymers containing a PCBM-grafted polymer block. For this, we selected the block copolymer BCP (Scheme 1) incorporating 31 wt% of attached PCBM molecules. Different amounts of PCBM were blended into the block copolymer to study the morphology and charge carrier transport in these blend systems. The blend ratios of BCP:PCBM were selected in such a way that the added PCBM is fully miscible within the PPCBM block of the block copolymer. Since the PPCBM fraction of the block copolymer is 66 wt%, the blends of BCP:PCBM=80:20, 70:30 and 60:40 (wt:wt) correspond to a ratio of PPCBM:PCBM=73:27, 61:39 and 50:50 (wt:wt), respectively. This accounts to a total PCBM content of 45, 52 and 59 wt%, respectively. The blended PCBM is expected to form a molecularly mixed phase with the PPCBM block based on the previous studies where the PPCBM copolymer blend confirmed a homogeneous phase even up to PPCBM:PCBM=40:60 (wt:wt) for solution-processed samples.

First, the thin film properties of BCP and the BCP:PCBM blends (80:20, 70:30 and 60:40, wt:wt) were studied to optimize spin-coating and thermal annealing procedures for

efficient operation in OFETs. For this, thin films were prepared in a similar way as for the OFET devices by spin-coating from chloroform solutions at 5000 rpm on glass substrates. Owing to the rapid solvent evaporation, the film morphology and the crystallization of P3HT is kinetically trapped in a non-equilibrium, frozen state. Therefore, all the polymer/blend films were annealed at 160 °C in nitrogen atmosphere for 2 hours. The importance of this thermal annealing procedure becomes clear regarding the thin film absorption spectra of BCP and its various blends of BCP:PCBM in **Figure 3a**. PCBM absorbs mainly in the UV range, whereas P3HT shows different absorption features depending on the crystallinity of the polymer. While the as-cast films for BCP, BCP:PCBM=80:20, 70:30 and 60:40 (dashed lines) exhibit only a broad absorption band around 450-500 nm corresponding to mainly non-aggregated, amorphous P3HT, the annealed polymer films (solid lines) show the characteristic absorption bands at 555 and 600 nm corresponding to the 0-1 and 0-0 vibration of P3HT aggregates.<sup>[50]</sup> Hence, the annealing procedure notably improves the P3HT crystallinity. Furthermore, the impact of annealing on the nanomorphology of the block copolymer and the blends can be understood regarding the photoluminescence (PL) spectra obtained for an excitation of the films at 500 nm (Figure 3b). PL measurements are a very sensitive method to study the miscibility, phase separation and phase purity of donor:acceptor blends.<sup>[51]</sup> The intensity of PL is a measure for the degree of excited state quenching: If the PL intensity is low, the quenching efficiency is high indicating fast electron or energy transfer between adjacent donor and acceptor moieties and vice versa. In contrast, a spatial separation through separated donor and acceptor domains increases the probability for a radiative decay of the exciton which results in a increased PL intensity. The PL intensity of the as-cast blends is remarkably low compared to the as-cast BCP. Hence, the low PL of the blends must be attributed to a certain amount of free PCBM molecules distributed in the P3HT phase and acting as efficient quenching sites. After annealing, the PL intensity significantly increases both for BCP and the blends (solid lines) indicating a reorganization of the phase domains in the film. Phase-separation upon thermal annealing of blends, *e.g.* P3HT:PCBM<sup>[24,46,52]</sup> or MDMO-PPV:PCBM,<sup>[47]</sup> is a well-known issue and the corresponding increase of the PL signal has been attributed to a non-intercalating blend morphology.<sup>[53]</sup> In our case, the crystallization of P3HT on the one hand expels residual PCBM and improves the phase purity, and on the other hand, PCBM molecules can diffuse to the PPCBM phase of the block copolymer. This is in close agreement with the

observed miscibility and morphological stability of the PPCBM:PCBM blends. The increasing PL of the films after annealing strongly indicates a rearrangement of the initially frozen microstructure towards a block copolymer templated nanostructure with crystalline P3HT domains and PCBM-enriched PPCBM domains. In addition, the increase of PL intensity after annealing is remarkable since the crystallization of P3HT intrinsically causes a reduction of photoluminescence.

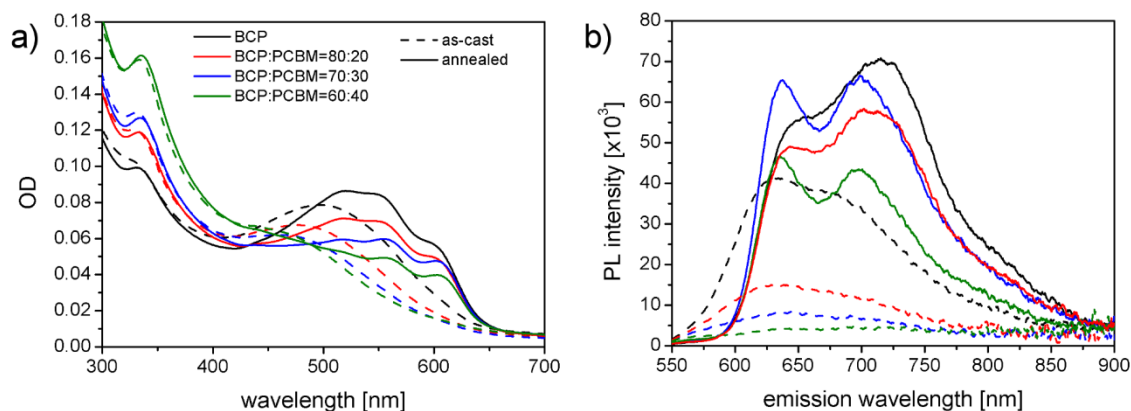


**Figure 3.** (a) Thin film absorption spectra and (b) photoluminescence spectra of BCP:PCBM blends. Dashed lines represent as-cast films, solid lines the films after annealing for 2 hours at 160 °C. The photoluminescence spectra were obtained by excitation at  $\lambda=500$  nm; the PL intensity was scaled to equal photon absorption at the excitation wavelength, i.e. an optical density of  $OD=1.0$  at 500 nm of the absorption spectra.

### Charge transport of BCP:PCBM blends in field-effect transistors

The donor-acceptor block copolymer BCP is designed to allow charge transport of both holes and electrons *via* individual microdomains in a single material. While P3HT is an established p-type semiconductor with a maximum reported hole mobility in the range of  $0.01 \text{ cm}^2 \text{ V}^{-1} \text{ s}^{-1}$  in organic field-effect transistors (OFET),<sup>[54]</sup> the n-type character of PPCBM was not yet studied in OFET devices. However, the bulk electron mobility  $\mu_e=1.2 \times 10^{-6} \text{ cm}^2 \text{ V}^{-1} \text{ s}^{-1}$  of a 30 wt% grafted PPCBM in SCLC was demonstrated in Figure 2 and in an earlier report.<sup>[39]</sup> Studying the charge transport of ambipolar materials such as donor-acceptor block copolymers in OFET is in particular attractive since hole and electron mobility can be determined in a single device structure.<sup>[55]</sup> To study the influence of PCBM blending into the block copolymer on charge carrier mobility, a series of morphologically stable blends of BCP:PCBM=80:20, 70:30 and 60:40 (wt:wt) was analyzed in as-cast and annealed OFET devices. Blends with more than 40 wt% of PCBM were not considered in this study to remain in the molecularly mixed range regarding the ratio of PPCBM:PCBM. The OFETs were fabricated using a bottom-gate, bottom-contact

configuration by spin-coating the polymer/blend solutions from chloroform at 5000 rpm to achieve a good film formation on the octadecylsilane passivated devices in ambient conditions. Device characterization and thermal annealing at 160 °C for 2 hours was performed in nitrogen atmosphere. Output characteristics were measured for a drain-source voltage  $V_d$  from -80 to 0 V for p-type operation and 0 to +80 V for n-type operation with a stepwise varied gate voltage  $V_g$ . The transfer curves were measured for  $V_g$  in the range of -80 to +20 V in p-type and -20 to +80 V in n-type operation in the saturation regime of  $V_d=-80$  and +80 V, respectively. The field-effect mobility  $\mu_h$  for holes and  $\mu_e$  for electrons was then determined from the linear fit of the square root of the drain-source current  $I_d^{1/2}$  in the saturation regime of the corresponding transfer curve.

The pure block copolymer BCP exhibits in the as-cast device exclusively hole transport with  $\mu_h=(4.0 \pm 1.6) \times 10^{-4} \text{ cm}^2 \text{ V}^{-1} \text{ s}^{-1}$ , whereas after annealing the transistor shows ambipolar character with  $\mu_h=(7.9 \pm 4.4) \times 10^{-3} \text{ cm}^2 \text{ V}^{-1} \text{ s}^{-1}$  and  $\mu_e=(4.1 \pm 0.8) \times 10^{-6} \text{ cm}^2 \text{ V}^{-1} \text{ s}^{-1}$  (**Figure 4** and Table 1). Evidently, the thermal annealing induces the formation of p- and n-type channels enabling an ambipolar charge transport. The crystallization of P3HT during thermal annealing, contributed to a notably increased hole mobility by more than one order of magnitude.

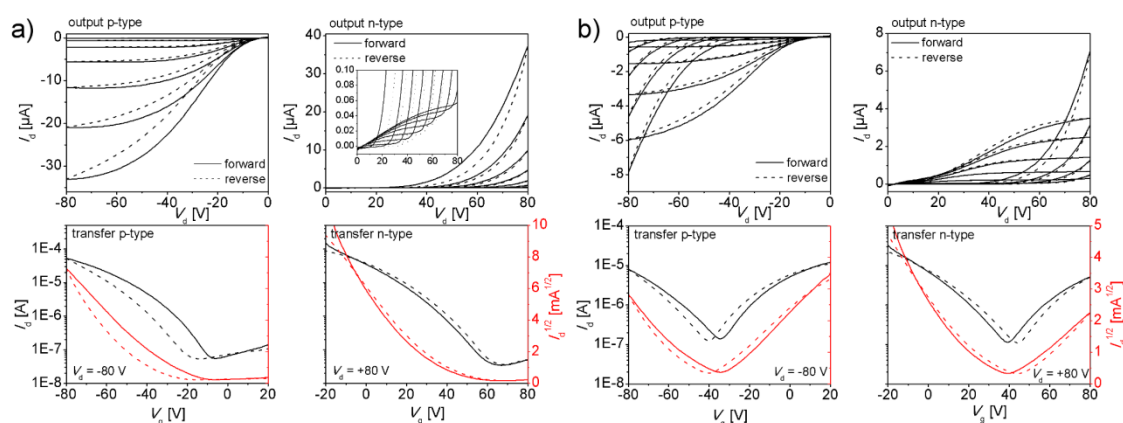


**Figure 4.** Representative OFET I-V curves of annealed (a) BCP and (b) BCP:PCBM=60:40 blend measured in p-type and n-type operation. The transfer characteristics were determined in the saturation regime at  $V_d=-80$  V and  $V_d=+80$  V for p-channel and n-channel, respectively. Solid lines represent forward scans, dashed lines are reverse scans. The red curves correspond to the square-root of the drain-source current  $I_d^{1/2}$  from which the charge carrier mobilities  $\mu_h$  and  $\mu_e$  were extracted.

Remarkably, all the blends show ambipolar transport even in the as-cast devices with an increasing electron mobility and slightly decreasing hole mobility for increasing the amount of added PCBM from 20, 30 to 40 wt%. This corresponds to a total PCBM con-

tent in the BCP:PCBM blend of 45, 52 and 59 wt%. Between 30 to 40 wt% of added PCBM the charge transport between holes and electrons in as-cast films is balanced (**Figure 5**). Moreover, the transport for both charge carriers can be significantly improved by annealing: With increasing amount of blended PCBM, the electron transport steadily increases from  $(4.1 \pm 0.8) \times 10^{-6} \text{ cm}^2 \text{ V}^{-1} \text{ s}^{-1}$  for pure BCP to  $(3.2 \pm 1.7) \times 10^{-4} \text{ cm}^2 \text{ V}^{-1} \text{ s}^{-1}$  for BCP:PCBM=60:40.

**Table 1.** Average OFET hole mobilities  $\mu_h$  and electron mobilities  $\mu_e$  of BCP:PCBM blends using a bottom-contact, bottom-gate device configuration.

BCP [wt%]	PCBM (added) [wt%]	as-cast		annealed <sup>a)</sup>	
		$\mu_h$ [ $\text{cm}^2 \text{ V}^{-1} \text{ s}^{-1}$ ]	$\mu_e$ [ $\text{cm}^2 \text{ V}^{-1} \text{ s}^{-1}$ ]	$\mu_h$ [ $\text{cm}^2 \text{ V}^{-1} \text{ s}^{-1}$ ]	$\mu_e$ [ $\text{cm}^2 \text{ V}^{-1} \text{ s}^{-1}$ ]
100	0	$(4.0 \pm 1.6) \times 10^{-4}$	0	$(7.9 \pm 4.4) \times 10^{-3}$	$(4.1 \pm 0.8) \times 10^{-6}$
80	20	$(2.0 \pm 0.2) \times 10^{-4}$	$(1.8 \pm 0.9) \times 10^{-5}$	$(6.1 \pm 2.5) \times 10^{-3}$	$(2.6 \pm 1.8) \times 10^{-5}$
70	30	$(1.0 \pm 0.1) \times 10^{-4}$	$(3.8 \pm 0.8) \times 10^{-5}$	$(2.9 \pm 0.9) \times 10^{-3}$	$(1.1 \pm 0.5) \times 10^{-4}$
60	40	$(5.4 \pm 1.2) \times 10^{-5}$	$(1.3 \pm 0.5) \times 10^{-4}$	$(1.8 \pm 0.6) \times 10^{-3}$	$(3.2 \pm 1.7) \times 10^{-4}$

<sup>a)</sup> Annealing for 2 hours at 160 °C in nitrogen atmosphere.

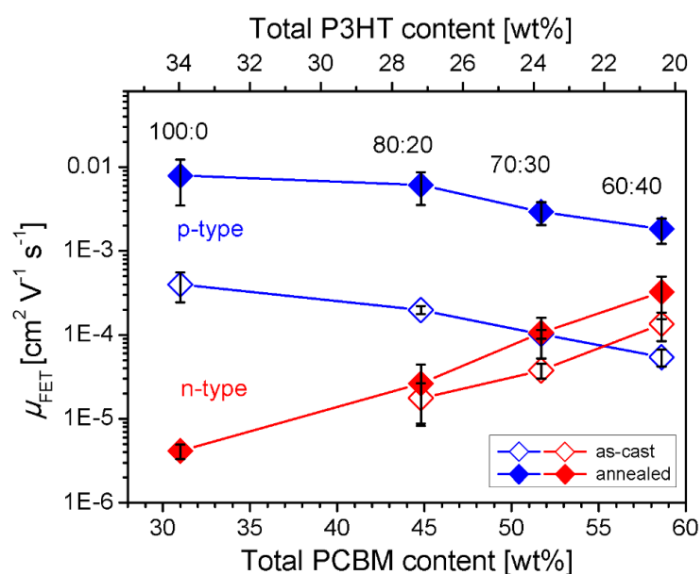


**Figure 5.** OFET hole mobilities (blue) and electron mobilities (red) of BCP:PCBM blends given in wt:wt ratio in as-cast (open symbols) and annealed devices (filled symbols). The total content of P3HT and PCBM was calculated assuming an initial composition of the pristine block copolymer P3HT-*b*-PPCBM of 34 wt% P3HT and 31 wt% PCBM.

At the same time, the hole mobility  $\mu_h$  is slightly reduced from  $(7.9 \pm 4.4) \times 10^{-3} \text{ cm}^2 \text{ V}^{-1} \text{ s}^{-1}$  to  $(1.8 \pm 0.6) \times 10^{-3} \text{ cm}^2 \text{ V}^{-1} \text{ s}^{-1}$  likely due to the decreasing

fraction of P3HT from 34 wt% to roughly 20 wt% in the blend. While the hole mobility  $\mu_h$  can be improved by one order of magnitude through annealing, the electron mobility  $\mu_e$  increases by a factor of 2-3 (Table 1).

The improved charge carrier transport can be attributed to the crystallization of P3HT on the one hand, enhancing p-type mobility, and on the other hand to the increased PCBM content in the fullerene-enriched PPCBM polymer phase. The diffusion of PCBM molecules into the amorphous PPCBM domains possibly reduces the average distance between fullerene moieties, and thus, promotes hopping transport of electrons. The blend BCP:PCBM=60:40 with the highest amount of PCBM therefore exhibits pronounced ambipolar character in output and transfer curves, exemplarily shown in Figure 4b. Despite the addition of 40 wt% of PCBM to the block copolymer, the p-type transport still exceeds the n-type transport by one order of magnitude. However, the blending approach facilitates to narrow the gap considerably between hole and electron mobility in BCP blend devices reaching appreciably high charge carrier mobilities of  $\mu_h \sim 10^{-3} \text{ cm}^2 \text{ V}^{-1} \text{ s}^{-1}$  and  $\mu_e \sim 10^{-4} \text{ cm}^2 \text{ V}^{-1} \text{ s}^{-1}$ .

### Block copolymer and blend morphology in films

The polymer films used for the OFET devices were studied using AFM to obtain an insight into the film morphology. Although the block copolymer film is smooth and featureless in the topography image with surface roughnesses of  $R_q=1.43$  and  $0.79$  nm in the as-cast and annealed device, the phase images indicate an initial two-phase nanostructure in the as-cast film which changes after annealing (**Figure 6a**). A similar surface morphology is found for the BCP:PCBM=60:40 blend film. While the as-cast and annealed films have a very low roughness of  $R_q=1.14$  and  $0.47$  nm, the phase image reveals again a distinct two-phase morphology in the as-cast film which completely disappears after annealing. In particular, the blend film does not show a macrophase separated structure or crystals from PCBM. Consequently, the BCP efficiently stabilizes the blend and preserves a bicontinuous donor-acceptor morphology which is required for the observed ambipolar charge transport.

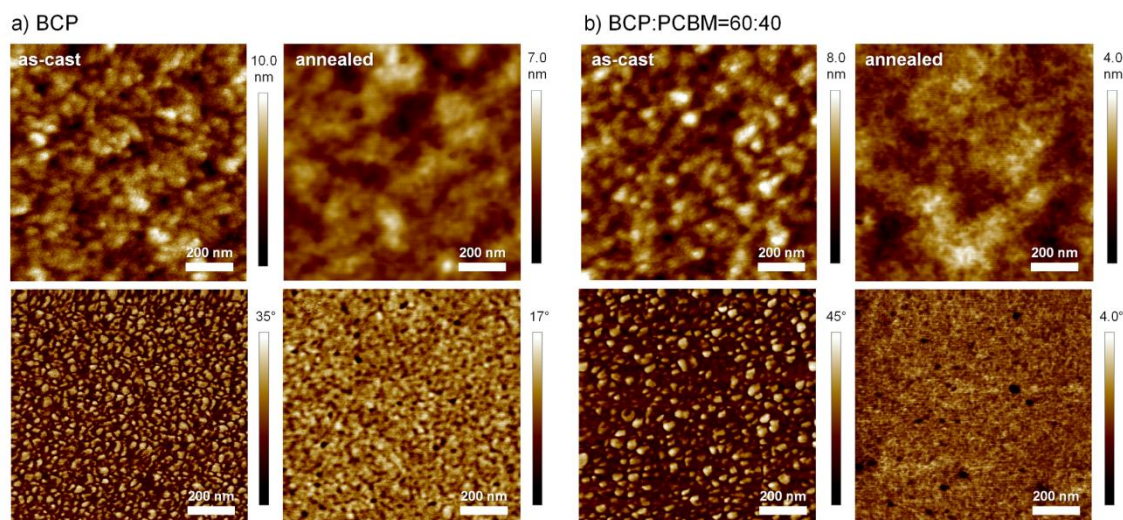


**Figure 6.**  $1 \times 1 \mu\text{m}^2$  AFM topography (top) and phase images (bottom) of thin films of the OFET devices: (a) Block copolymer BCP and (b) the blend BCP:PCBM=60:40 with the highest content of PCBM in this series in as-cast state and after annealing for 2 h at  $160^\circ\text{C}$ .

### Charge transport and blend stability of BCP:PCBM in comparison to P3HT:PCBM

The chemical design of the block copolymer BCP was selected to tune and control the morphology of donor-acceptor systems based on the well-studied P3HT:PCBM blend in organic photovoltaics. Hence, a fundamental target in the donor-acceptor block copolymer is to achieve sufficiently high charge carrier mobility for holes and electrons that is competitive with the P3HT:PCBM blend and additionally maintaining long-term morphological stability. A classical approach is to blend small amounts of a relevant block copolymer into the P3HT:PCBM blend of optimum composition in order to improve the stability.<sup>[19,28–33]</sup> However, this approach did not deliver the desired effect in particular at high temperatures or upon prolonged annealing.<sup>[19,32]</sup>

Therefore, we have studied the charge transport in OFETs of a P3HT:PCBM blend with an optimized composition of 1:0.8 (wt:wt)<sup>[56]</sup> in comparison with a BCP:PCBM=60:40 blend. Usually the blends in active layers of OPV are thermally annealed to improve the charge transport<sup>[6,57–59]</sup> and performance in solar cells.<sup>[4]</sup> Therefore we annealed also the OFET devices at  $160^\circ\text{C}$  for 5, 30, 60 and 120 min in nitrogen atmosphere and measured the transistor characteristics to monitor the evolution of hole and electron mobility. As **Figure 7a** shows, the hole mobility of the P3HT:PCBM blend device improves after annealing at  $160^\circ\text{C}$  due to the crystallization of P3HT by one order of magnitude and remains roughly constant at  $\mu_{\text{h}}=1 \times 10^{-2} \text{ cm}^2 \text{ V}^{-1} \text{ s}^{-1}$ . The best ambipolar

transport in P3HT:PCBM is achieved after 5 min annealing with  $\mu_h=(1.1 \pm 0.1) \times 10^{-2} \text{ cm}^2 \text{ V}^{-1} \text{ s}^{-1}$  and  $\mu_e=(2.5 \pm 1.0) \times 10^{-4} \text{ cm}^2 \text{ V}^{-1} \text{ s}^{-1}$ . This result is in agreement with the optimized annealing procedures for P3HT:PCBM blends in OPV.<sup>[60]</sup> However, the electron mobility in OFET drastically drops after 30 min of annealing and is completely lost for longer annealing times (Figure 7a and S4, Table S2). The loss of electron transport can be attributed to the limited morphological stability of the P3HT:PCBM blend caused by a demixing of P3HT and PCBM and the formation of micron-sized PCBM crystals.<sup>[23,61–63]</sup> The P3HT:PCBM film on the OFET after 120 min of annealing was covered with rice-grain like PCBM crystals with a length of roughly 10  $\mu\text{m}$  (Figure 7a). The crystals were surrounded by a bright depletion zone indicating a local diffusion and diminution of PCBM in the film, consequently, the percolation paths for electrons are widely lost.

In contrast to that, the charge transport in the BCP:PCBM=60:40 blend steadily improves up to 60 min of annealing and remains excellent even after 120 min of thermal treatment (Figure 7b and S5, Table S3). While the hole mobility shows the expected improvement due to P3HT crystallization, the electron mobility increases slowly possibly due to the diffusion of the fullerene into the PPCBM phase of the block copolymer. The best ambipolar transport for BCP:PCBM=60:40 was observed after 60 min of annealing with  $\mu_h=(4.2 \pm 1.0) \times 10^{-3} \text{ cm}^2 \text{ V}^{-1} \text{ s}^{-1}$  and  $\mu_e=(2.2 \pm 0.6) \times 10^{-4} \text{ cm}^2 \text{ V}^{-1} \text{ s}^{-1}$ . This is an excellent result considering that the total weight fractions of P3HT and PCBM are only 20.4 and 58.6 wt% in BCP:PCBM=60:40 compared to 56 and 44 wt% in P3HT:PCBM blend. In contrast to the classical P3HT:PCBM blend, the block copolymer blend BCP:PCBM exhibits a permanently high charge transport even upon prolonged annealing with similar high mobility values (Table 2). This property must be attributed to the outstanding morphological stability of the BCP:PCBM blend arising from the compatibilizing effect of the PPCBM block on the added PCBM and the inherent nanoscale morphology of the pristine BCP at thermodynamic equilibrium. Consistently, the films of BCP:PCBM=60:40 on the OFET substrate are fully homogeneous after annealing for 120 min despite 40 wt% of added molecular PCBM (Figure 7b). Furthermore, this finding also suggests that electron transport in PCBM can also proceed efficiently through a non-crystalline, amorphous PCBM-enriched PPCBM polymer phase.

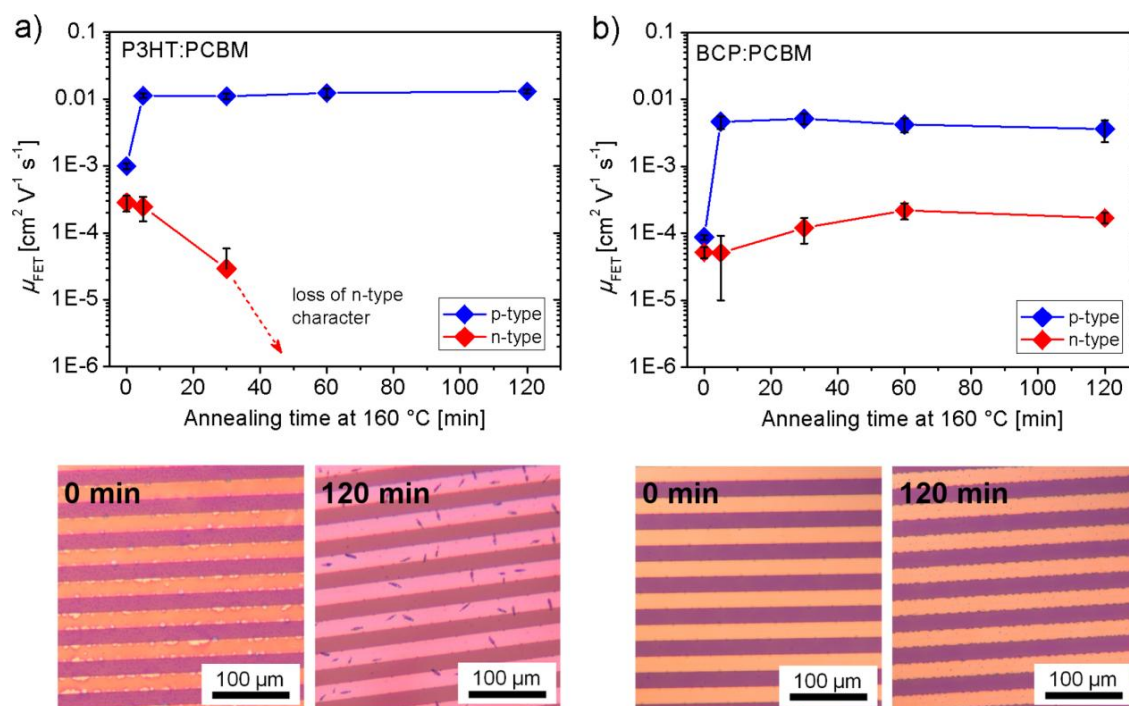


**Figure 7.** Hole and electron field-effect mobilities in dependence of the annealing time at 160 °C for (a) the P3HT:PCBM blend (1:0.8, wt:wt) and (b) the BCP:PCBM=60:40 blend. The optical microscopy images (bottom) show a section of the interdigitating 20  $\mu\text{m}$  channel gold electrodes of the OFET devices covered with the polymer blend films. The images were taken in as-cast state, 0 min, and after 120 min of annealing at 160 °C.

**Table 2.** Average OFET hole mobilities  $\mu_h$  and electron mobilities  $\mu_e$  of P3HT:PCBM and BCP:PCBM=60:40 blend in dependency of the annealing time at 160 °C in nitrogen atmosphere.

Annealing time [min]	P3HT:PCBM		BCP:PCBM=60:40	
	$\mu_h$ [ $\text{cm}^2 \text{V}^{-1} \text{s}^{-1}$ ]	$\mu_e$ [ $\text{cm}^2 \text{V}^{-1} \text{s}^{-1}$ ]	$\mu_h$ [ $\text{cm}^2 \text{V}^{-1} \text{s}^{-1}$ ]	$\mu_e$ [ $\text{cm}^2 \text{V}^{-1} \text{s}^{-1}$ ]
0	$(1.0 \pm 0.1) \times 10^{-3}$	$(2.8 \pm 0.8) \times 10^{-4}$	$(8.7 \pm 0.7) \times 10^{-5}$	$(5.2 \pm 1.0) \times 10^{-5}$
5	$(1.1 \pm 0.1) \times 10^{-2}$	$(2.5 \pm 1.0) \times 10^{-4}$	$(4.6 \pm 1.0) \times 10^{-3}$	$(5.1 \pm 4.1) \times 10^{-5}$
30	$(1.1 \pm 0.1) \times 10^{-2}$	$(2.9 \pm 2.9) \times 10^{-5}$	$(5.1 \pm 0.9) \times 10^{-3}$	$(1.2 \pm 0.5) \times 10^{-4}$
60	$(1.2 \pm 0.2) \times 10^{-2}$	0	$(4.2 \pm 1.0) \times 10^{-3}$	$(2.2 \pm 0.6) \times 10^{-4}$
120	$(1.3 \pm 0.1) \times 10^{-2}$	0	$(3.6 \pm 1.3) \times 10^{-3}$	$(1.7 \pm 0.3) \times 10^{-4}$

## CONCLUSIONS

We have demonstrated an elegant approach to match hole and electron transport in P3HT-b-PPCBM by blending molecular PCBM into the block copolymer. Adding PCBM to fullerene-grafted styrene copolymers PPCBM can widely compensate the issue of diminished electron mobility in the acceptor block. In fact, the large miscibility of the PPCBM:PCBM blend up to 60 wt% PCBM load, while still remaining an amorphous solid without crystallization of PCBM, forms the basis for application in block copolymers. The electron transport in BCP:PCBM blends in OFETs is substantially enhanced by two orders of magnitude achieving  $\mu_e=(3.2 \pm 1.7) \times 10^{-4} \text{ cm}^2 \text{ V}^{-1} \text{ s}^{-1}$  while the hole transport with  $\mu_h=(1.8 \pm 0.6) \times 10^{-3} \text{ cm}^2 \text{ V}^{-1} \text{ s}^{-1}$  remains appreciably high. Accordingly, the mobility gap was reduced from three orders of magnitude in pure BCP to only one order in the BCP:PCBM=60:40 blend. This BCP:PCBM blend provides not only similar high ambipolar charge transport compared to the established P3HT:PCBM system, but furthermore, exhibits an exceptional stable morphology upon prolonged annealing at elevated temperature which results in permanently high hole and electron mobilities.

This work demonstrates the feasibility of obtaining high charge carrier transport and a stable morphology in a donor-acceptor block copolymer by a blend approach and thus opens new perspectives for their integration in devices with long-term stability. Such an excellent morphological stability maintaining high charge carrier mobilities is not otherwise easily achievable. This overcomes the inherent solubility limitations in designing fullerene-grafted polymers with high fullerene content which is required for high electron mobility.

## EXPERIMENTAL SECTION

### Materials

Phenyl- $\text{C}_{61}$ -butyric acid methyl ester ( $\text{PC}_{61}\text{BM}$ , purity 99 %) was purchased from Solenne (Groningen, NL). Anhydrous solvents were purchased from Sigma Aldrich and Acros in sealed bottles with mole sieve. The block copolymer BCP and the polymer PPCBM were prepared following literature protocols.<sup>[39,40]</sup> All the blends were prepared by dissolving the materials in the respective composition in solvent. Films were prepared directly by deposition of the solution, powder samples were obtained from drying 3 wt% DCB solutions of the blend at 70 °C and subsequent storage in vacuum overnight.

## Instrumentation

Powder X-ray analysis (XRD) was carried out with a Huber/Seifert Iso-Debyeflex 3003, using a Guinier diffractometer system (Cu  $K_{\alpha}$ :  $\lambda=1.5418 \text{ \AA}$ ) with the powder sample in a sealed glass tube for temperature-dependent measurements. The powder samples were prepared by collecting the material from casting 3 wt% solutions of the blends from DCB at 70 °C with subsequent drying in vacuum at room temperature. Atomic force microscopy (AFM) was performed on a Dimension 3100 NanoScope IV in tapping mode. The films of PPCBM and the PPCBM:PCBM blends were prepared by blade-casting 20-40 mg/mL solutions with a gap width of 100  $\mu\text{m}$  at 70 °C on zinc oxide coated glass substrates. The films of BCP and BCP:PCBM=60:40 on OFET substrates were spin-coated at 5000 rpm from 8 mg/mL solutions in chloroform; annealing for 2 h at 160 °C was done in nitrogen atmosphere on a precision hot plate. A Mettler Toledo DSC 2 was used to investigate the thermal properties of the materials in nitrogen atmosphere at heating/cooling rates of 10 or 20 K/min.

Electron-only devices for space-charge limited current (SCLC) measurements were fabricated using the following device structure: glass/ITO/ZnO/active layer/Ca/Al. The 40 nm zinc oxide layer was deposited onto cleaned, patterned ITO coated glass substrates with 10 Ohm  $\text{sq}^{-1}$  sheet resistance by spin-coating 100  $\mu\text{L}$  of precursor solution (110 mg zinc acetate dihydrate, 31  $\mu\text{L}$  ethanol amine, 1000  $\mu\text{L}$  methoxyethanole) at 4000 rpm for 50 s with subsequent annealing for 5 min at 150 °C on a hotplate. The active layer was doctor-bladed under inert conditions at 70 °C from solutions of 20-40 mg/mL concentration in 1,2-dichlorobenzene resulting in film thicknesses of 150 to 400 nm. Deposition of the top electrodes was performed by thermal evaporation of 30 nm calcium and 100 nm aluminum under high vacuum through a shadow mask giving active devices areas of 9  $\text{mm}^2$  or 16  $\text{mm}^2$ . The current-voltage characteristics of the devices were measured using a Keithley 2400 (J-V) Digital SourceMeter at 25 °C in nitrogen atmosphere. The electron mobility was extracted from the obtained forward  $J$ - $V$  curves using the field-dependent Murgatroyd equation,<sup>[49]</sup>

$$J = \frac{9}{8} \varepsilon \varepsilon_0 \mu_0 e^{(0.89\gamma\sqrt{F})} \frac{V^2}{L^3}$$

where  $J$  is the current density,  $\varepsilon$  the dielectric constant ( $\sim 3$  for organic semiconductors),  $\varepsilon_0$  the permittivity of free space,  $\mu_0$  the zero field charge carrier mobility,  $V$  the ef-

fective voltage,  $L$  the active layer thickness and  $\gamma$  is the parameter that represents the field-dependence of the mobility. The effective voltage  $V$  is obtained by correction of the applied voltage  $V_{\text{appl}}$  by the built-in voltage  $V_{\text{bi}}$  and the voltage drop by internal resistance  $V_{\text{r}} = I \cdot R_{\text{s}}$ , *i.e.*  $V = V_{\text{appl}} - V_{\text{bi}} - V_{\text{r}}$ . The contact resistance  $R_{\text{s}}$  was determined from a reference device and was 64 Ohm for 9 mm<sup>2</sup> and 34 Ohm for 16 mm<sup>2</sup> active area. We assume a built-in voltage of  $V_{\text{bi}}=0$  V since forward and reverse voltage scans delivered the same current density indicating a negligible built-in potential. The electron mobility  $\mu_{\text{e}}(F)$  is given at a representative field of  $F=1.5 \times 10^7$  V m<sup>-1</sup> using the Poole-Frenkel equation:

$$\mu(F) = \mu_0 \exp(\gamma\sqrt{F})$$

Film thicknesses were determined on a Dektak surface profilometer.

UV-vis absorption spectra of thin films prepared by spin-coating of 8 mg mL<sup>-1</sup> solutions in chloroform at 5000 rpm were recorded on a JASCO spectrophotometer V-670 and the corresponding photoluminescence (PL) spectra on a JASCO FP-8600 spectrofluorometer at an excitation wavelength of  $\lambda=500$  nm. The PL spectra were scaled for comparability to OD=1.0 at the absorption at  $\lambda=500$  nm. Annealing was performed for 2 h at 160 °C in nitrogen atmosphere on a precision hot plate.

Organic field-effect transistor (OFET) substrates in bottom-gate, bottom-contact configuration were purchased from Fraunhofer IPMS (Dresden/Germany). The substrate and gate electrode is n-doped silicon (doping at wafer surface:  $n \sim 3 \times 10^{17}$  cm<sup>-3</sup>) with a thermally grown 230 nm  $\pm$  10 nm SiO<sub>2</sub> dielectric top layer. 30 nm Gold electrodes with 10 nm ITO as high work function adhesion layer were used as drain/source contact. The channel width was 1 mm for all devices with a channel length varying between 5 to 20  $\mu$ m. The substrates were cleaned in an ultrasonic bath in acetone and 2-propanol for 10 min each. After ozone treatment for 20 min at 50 °C, the substrates were immersed into a solution of 1 vol% of octadecyltrichlorosilane in toluene at 60 °C for 45 min. After rinsing the substrates with toluene and 2-propanol, the substrates were dried in nitrogen stream and the polymer was spin-coated from a 4 mg/ml chloroform solution at 5000 rpm under ambient conditions. The devices were measured with an Agilent B1500 Semiconductor Parameter Analyzer in nitrogen atmosphere in as-cast and annealed films (160 °C for 2 hours in nitrogen atmosphere). Mobilities were calculated from the slope in the  $V_{\text{g}}-(I_{\text{d}})^{0.5}$  plots in the saturation regime using the following equation

$$I_d = \frac{W}{2L} C_i \mu (V_g - V_{th})^2$$

where  $I_d$  is the drain current,  $W$  is the channel width,  $L$  is the channel length,  $C_i$  is the capacitance,  $V_g$  is the gate voltage and  $V_{th}$  is the threshold voltage.

For optical micrographs a Zeiss Axio Imager microscope was used.

### Supporting Information

Supporting Information is available from the Wiley Online Library or from the author.

### Acknowledgements

We kindly acknowledge the Bavarian State Ministry of Environment and Consumer Protection (UMWELTnanoTECH) and Bavarian State Ministry of Science, Research, and the Arts for the Collaborative Research Network "Solar Technologies go Hybrid" for financial support of this project. M. Hufnagel also thanks the German National Academic Foundation for a PhD scholarship and the Elite Network Bavaria Macromolecular Science programme at the University of Bayreuth. Mathis Muth and Chetan Raj Singh are acknowledged for their help and discussions regarding the SCLC experiments. We also thank Steffen Czich for assistance using the Guinier diffractometer and Anne Browa who was involved as practical assistant in the preparation of OFETs.

### REFERENCES

- [1] A. Köhler, H. Bässler, *Electronic Processes in Organic Semiconductors: An Introduction*; WILEY-VCH Verlag GmbH & Co. KGaA: Weinheim, Germany, 2015.
- [2] K. M. Coakley, M. D. McGehee, *Chem. Mater.* **2004**, *16*, 4533.
- [3] L. Lu, T. Zheng, Q. Wu, A. M. Schneider, D. Zhao, L. Yu, *Chem. Rev.* **2015**.
- [4] M. T. Dang, L. Hirsch, G. Wantz, *Adv. Mater.* **2011**, *23*, 3597.
- [5] S. M. Tuladhar, D. Poplavskyy, S. a. Choulis, J. R. Durrant, D. D. C. Bradley, J. Nelson, *Adv. Funct. Mater.* **2005**, *15*, 1171.
- [6] A. Baumann, J. Lorrman, C. Deibel, V. Dyakonov, *Appl. Phys. Lett.* **2008**, *93*, 252104.
- [7] V. D. Mihailechi, H. X. Xie, B. de Boer, L. J. a. Koster, P. W. M. Blom, *Adv. Funct. Mater.* **2006**, *16*, 699.
- [8] J. Huang, G. Li, Y. Yang, *Appl. Phys. Lett.* **2005**, *87*, 112105.
- [9] R. Mauer, M. Kastler, F. Laquai, *Adv. Funct. Mater.* **2010**, *20*, 2085.
- [10] J. W. Barlow, D. R. Paul, *Polym. Eng. Sci.* **1981**, *21*, 985.
- [11] A. C. Mayer, M. F. Toney, S. R. Scully, J. Rivnay, C. J. Brabec, M. Scharber, M.

- Koppe, M. Heeney, I. McCulloch, M. D. McGehee, *Adv. Funct. Mater.* **2009**, *19*, 1173.
- [12] N. C. Miller, E. Cho, R. Gysel, C. Risko, V. Coropceanu, C. E. Miller, S. Sweetnam, A. Sellinger, M. Heeney, I. McCulloch, J.-L. Brédas, M. F. Toney, M. D. McGehee, *Adv. Energy Mater.* **2012**, *2*, 1208.
- [13] J. Y. Kim, C. D. Frisbie, *J. Phys. Chem. C* **2008**, *112*, 17726.
- [14] P. Kohn, Z. Rong, K. K. H. Scherer, A. Sepe, M. Sommer, P. Müller-Buschbaum, R. H. Friend, U. Steiner, S. Hüttner, *Macromolecules* **2013**, *46*, 4022.
- [15] N. C. Miller, R. Gysel, C. E. Miller, E. Verploegen, Z. Beiley, M. Heeney, I. McCulloch, Z. Bao, M. F. Toney, M. D. McGehee, *J. Polym. Sci. Part B Polym. Phys.* **2011**, *49*, 499.
- [16] D. W. Gehrig, I. A. Howard, S. Sweetnam, T. M. Burke, M. D. McGehee, F. Laquai, *Macromol. Rapid Commun.* **2015**, *36*, 1054.
- [17] N. C. Miller, S. Sweetnam, E. T. Hoke, R. Gysel, C. E. Miller, J. a. Bartelt, X. Xie, M. F. Toney, M. D. McGehee, *Nano Lett.* **2012**, *12*, 1566.
- [18] S. Bertho, G. Janssen, T. J. Cleij, B. Conings, W. Moons, A. Gadisa, J. D'Haen, E. Goovaerts, L. Lutsen, J. Manca, D. Vanderzande, *Sol. Energy Mater. Sol. Cells* **2008**, *92*, 753.
- [19] J. U. Lee, J. W. Jung, T. Emrick, T. P. Russell, W. H. Jo, *Nanotechnology* **2010**, *21*, 105201.
- [20] X. Yang, J. K. van Duren, R. A. Janssen, M. A. Michels, J. Loos, *Macromolecules* **2004**, *37*, 2151.
- [21] M. T. Dang, L. Hirsch, G. Wantz, J. D. Wuest, *Chem. Rev.* **2013**, *113*, 3734.
- [22] F. C. Krebs, *Sol. Energ. Mat. Sol. C.* **2009**, *93*, 394.
- [23] a. Swinnen, I. Haeldermans, M. vande Ven, J. D'Haen, G. Vanhoyland, S. Aresu, M. D'Olieslaeger, J. Manca, *Adv. Funct. Mater.* **2006**, *16*, 760.
- [24] M. Campoy-Quiles, T. Ferenczi, T. Agostinelli, P. G. Etchegoin, Y. Kim, T. D. Anthopoulos, P. N. Stavrinou, D. D. C. Bradley, J. Nelson, *Nat. Mater.* **2008**, *7*, 158.
- [25] S. Bertho, B. Campo, F. Piersimoni, D. Spoltore, J. D'Haen, L. Lutsen, W. Maes, D. Vanderzande, J. Manca, *Sol. Energy Mater. Sol. Cells* **2013**, *110*, 69.
- [26] J. W. Rumer, I. McCulloch, *Mater. Today* **2015**, *18*, 425.
- [27] C. Müller, *Chem. Mater.* **2015**, *27*, 2740.
- [28] K. Sivula, Z. T. Ball, N. Watanabe, J. M. J. Fréchet, *Adv. Mater.* **2006**, *18*, 206.
- [29] M. Urien, H. Erothu, E. Cloutet, R. C. Hiorns, L. Vignau, H. Cramail, *Macromolecules* **2008**, *41*, 7033.
- [30] F. Richard, C. Brochon, N. Leclerc, D. Eckhardt, T. Heiser, G. Hadziioannou, *Macromol. Rapid Commun.* **2008**, *29*, 885.
- [31] C. Yang, J. K. Lee, A. J. Heeger, F. Wudl, *J. Mater. Chem.* **2009**, *19*, 5416.
- [32] V. Gernigon, P. Lévêque, C. Brochon, J.-N. Audinot, N. Leclerc, R. Bechara, F. Richard, T. Heiser, G. Hadziioannou, *Eur. Phys. J. Appl. Phys.* **2011**, *56*, 34107.
- [33] M. Heuken, H. Komber, T. Erdmann, V. Senkovskyy, A. Kiriya, B. Voit, *Macromolecules* **2012**, *45*, 4101.
- [34] B. Gholamkhash, S. Holdcroft, *Chem. Mater.* **2010**, *22*, 5371.
- [35] P. D. Topham, A. J. Parnell, R. C. Hiorns, *J. Polym. Sci. Part B Polym. Phys.* **2011**, *49*, 1131.
- [36] M. Sommer, S. Huettner, M. Thelakkat, *J. Mater. Chem.* **2010**, *20*, 10788.
- [37] S. B. Darling, *Energy Environ. Sci.* **2009**, *2*, 1266.
- [38] S. Miyanishi, Y. Zhang, K. Hashimoto, K. Tajima, *Macromolecules* **2012**, *45*, 6424.

- [39] M. Hufnagel, M.-A. Muth, J. C. Brendel, M. Thelakkat, *Macromolecules* **2014**, *47*, 2324.
- [40] M. Hufnagel, M. Fischer, T. Thurn-Albrecht, M. Thelakkat, *Submitted to Macromolecules* **2015**.
- [41] C. R. Singh, M. Sommer, M. Himmerlich, A. Wicklein, S. Krischok, M. Thelakkat, H. Hoppe, *Phys. Status Solidi* **2011**, *5*, 247.
- [42] B. Gholamkhash, T. J. Peckham, S. Holdcroft, *Polym. Chem.* **2010**, *1*, 708.
- [43] V. Abetz, P. Simon, *Adv. Polym. Sci.* **2005**, *189*, 125.
- [44] X. Yang, J. K. J. van Duren, M. T. Rispens, J. C. Hummelen, R. a. J. Janssen, M. a. J. Michels, J. Loos, *Adv. Mater.* **2004**, *16*, 802.
- [45] N. R. Tummala, S. Mehraeen, Y.-T. Fu, C. Risko, J.-L. Brédas, *Adv. Funct. Mater.* **2013**, *23*, 5800.
- [46] W. Yin, M. Dadmun, *ACS Nano* **2011**, *5*, 4756.
- [47] N. C. Cates, R. Gysel, J. E. P. Dahl, A. Sellinger, M. D. McGehee, *Chem. Mater.* **2010**, *22*, 3543.
- [48] Z. M. Beiley, E. T. Hoke, R. Noriega, J. Dacuña, G. F. Burkhard, J. A. Bartelt, A. Salleo, M. F. Toney, M. D. McGehee, *Adv. Energy Mater.* **2011**, *1*, 954.
- [49] P. N. Murgatroyd, *J. Phys. D. Appl. Phys.* **1970**, *3*, 151.
- [50] C. Scharsich, R. H. Lohwasser, M. Sommer, U. Asawapirom, U. Scherf, M. Thelakkat, D. Neher, A. Köhler, *J. Polym. Sci. Part B Polym. Phys.* **2012**, *50*, 442.
- [51] N. C. Miller, E. T. Hoke, M. D. McGehee, In *Organic Photovoltaics: Materials, Device Physics, and Manufacturing Technologies*; Brabec, C. J.; Dyakonov, V.; Scherf, U., Eds.; Wiley-VCH: Weinheim, 2014; pp. 421–444.
- [52] Y. Kim, S. Cook, S. M. Tuladhar, S. A. Choulis, J. Nelson, J. R. Durrant, D. D. C. Bradley, M. Giles, I. McCulloch, C.-S. Ha, M. Ree, *Nat. Mater.* **2006**, *5*, 197.
- [53] F. C. Jamieson, E. B. Domingo, T. McCarthy-Ward, M. Heeney, N. Stingelin, J. R. Durrant, *Chem. Sci.* **2012**, *3*, 485.
- [54] J.-F. Chang, B. Sun, D. W. Breiby, M. M. Nielsen, T. I. Sölling, M. Giles, I. McCulloch, H. Sirringhaus, *Chem. Mater.* **2004**, *16*, 4772.
- [55] S. Huettner, M. Sommer, J. Hodgkiss, P. Kohn, T. Thurn-Albrecht, R. H. Friend, U. Steiner, M. Thelakkat, *ACS Nano* **2011**, *5*, 3506.
- [56] C. J. Brabec, S. Gowrisanker, J. J. M. Halls, D. Laird, S. Jia, S. P. Williams, B. C. J. Brabec, *Adv. Mater.* **2010**, *22*, 3839.
- [57] F. Laquai, D. Andrienko, R. Mauer, P. W. M. Blom, *Macromol. Rapid Commun.* **2015**, *36*, 1001.
- [58] E. von Hauff, J. Parisi, V. Dyakonov, *J. Appl. Phys.* **2006**, *100*, 043702.
- [59] V. Shrotriya, Y. Yao, G. Li, Y. Yang, *Appl. Phys. Lett.* **2006**, *89*, 063505.
- [60] G. Li, V. Shrotriya, Y. Yao, Y. Yang, *J. Appl. Phys.* **2005**, *98*, 043704.
- [61] Y. Zhang, H.-L. Yip, O. Acton, S. K. Hau, F. Huang, A. K.-Y. Jen, *Chem. Mater.* **2009**, *21*, 2598.
- [62] S. Miyaniishi, K. Tajima, K. Hashimoto, *Macromolecules* **2009**, *42*, 1610.
- [63] B. Watts, W. J. Belcher, L. Thomsen, H. Ade, P. C. Dastoor, *Macromolecules* **2009**, *42*, 8392.

## SUPPORTING INFORMATION

### Content

**Figure S1.** AFM topography and phase images for PPCBM:PCBM blends 100:0, 80:20, 60:40, 40:60, 20:80 and 0:100 (wt:wt) prepared as blade-cast films.

**Figure S2.** DSC traces for the blends PPCBM:PCBM=60:40 and 20:80 (wt:wt).

**Figure S3.** Space-charge limited current (SCLC)  $J$ - $V$  characteristics of PPCBM, PPCBM:PCBM=80:20, 60:40 and PCBM.

**Table S1.** Experimental results of SCLC electron mobility measurements.

**Figure S4.** Representative OFET  $I$ - $V$  output and transfer curves for P3HT:PCBM=1.0:0.8 after 0, 5, 30, 60 and 120 min of annealing at 160 °C in nitrogen atmosphere.

**Table S2.** OFET results for p- and n-type operation of the P3HT:PCBM blend after different annealing times at 160 °C.

**Figure S5.** Representative OFET  $I$ - $V$  output and transfer curves for BCP:PCBM=60:40 after 0, 5, 30, 60 and 120 min of annealing at 160 °C in nitrogen atmosphere.

**Table S3.** OFET results for p- and n-type operation of the BCP:PCBM=60:40 blend after different annealing times at 160 °C.

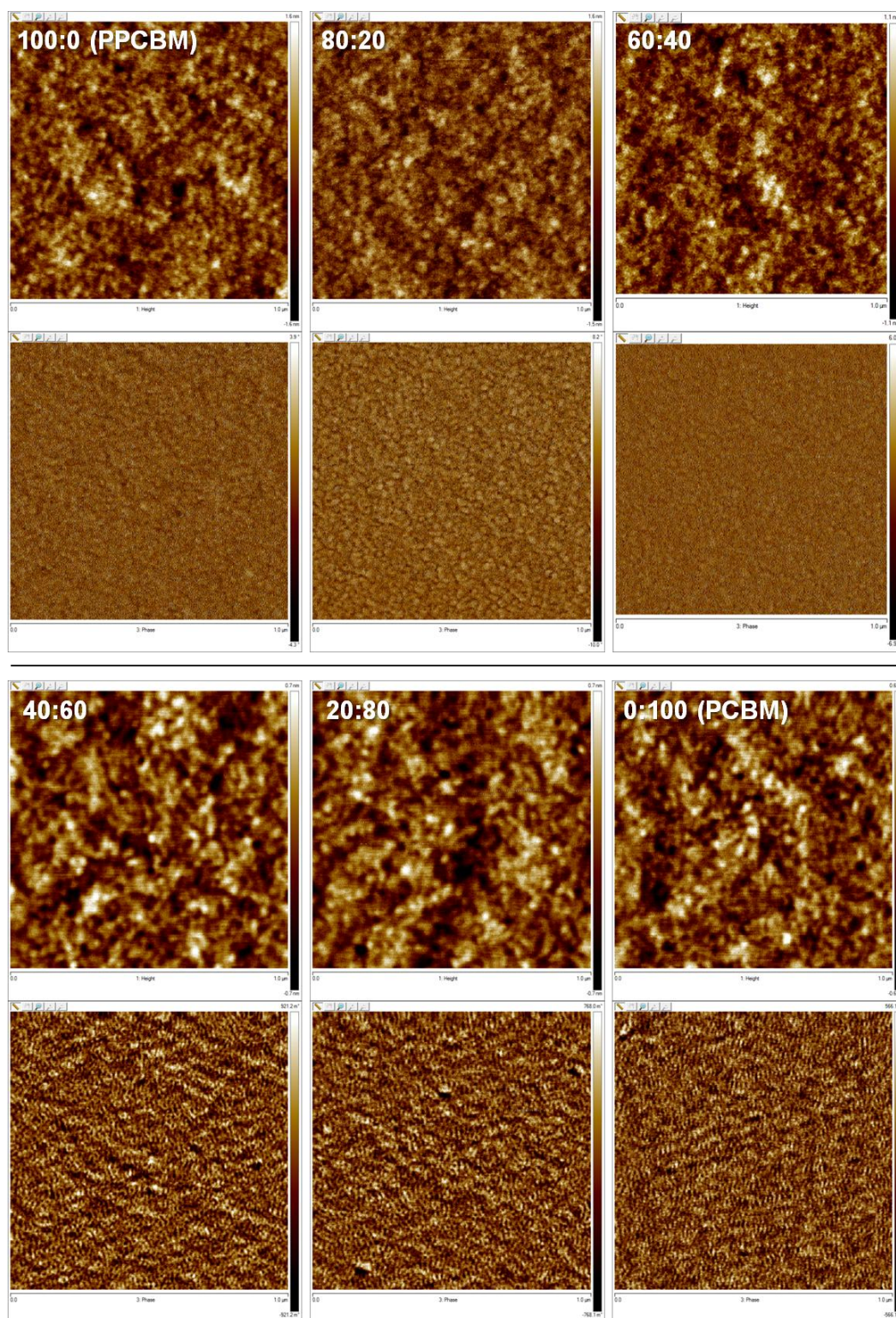


**Figure S1.**  $1 \times 1 \mu\text{m}^2$  AFM topography and phase images for PPCBM:PCBM blends 100:0, 80:20, 60:40, 40:60, 20:80 and 0:100 (wt:wt) prepared as blade-cast films.

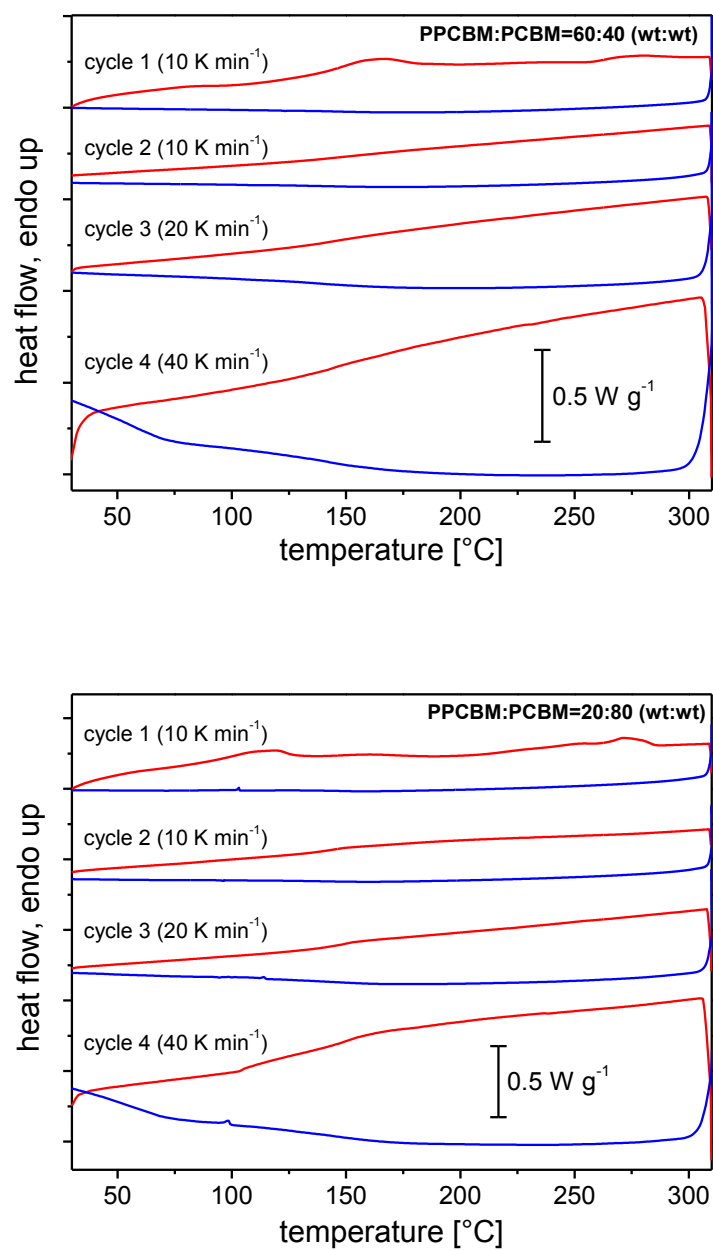


**Figure S2.** DSC traces for the blends PPCBM:PCBM=60:40 (top) and 20:80 (bottom) recorded at 10, 20 and 40 K min<sup>-1</sup> heating/cooling rate in nitrogen atmosphere. Red lines are heating curves, blue lines indicate cooling curves.

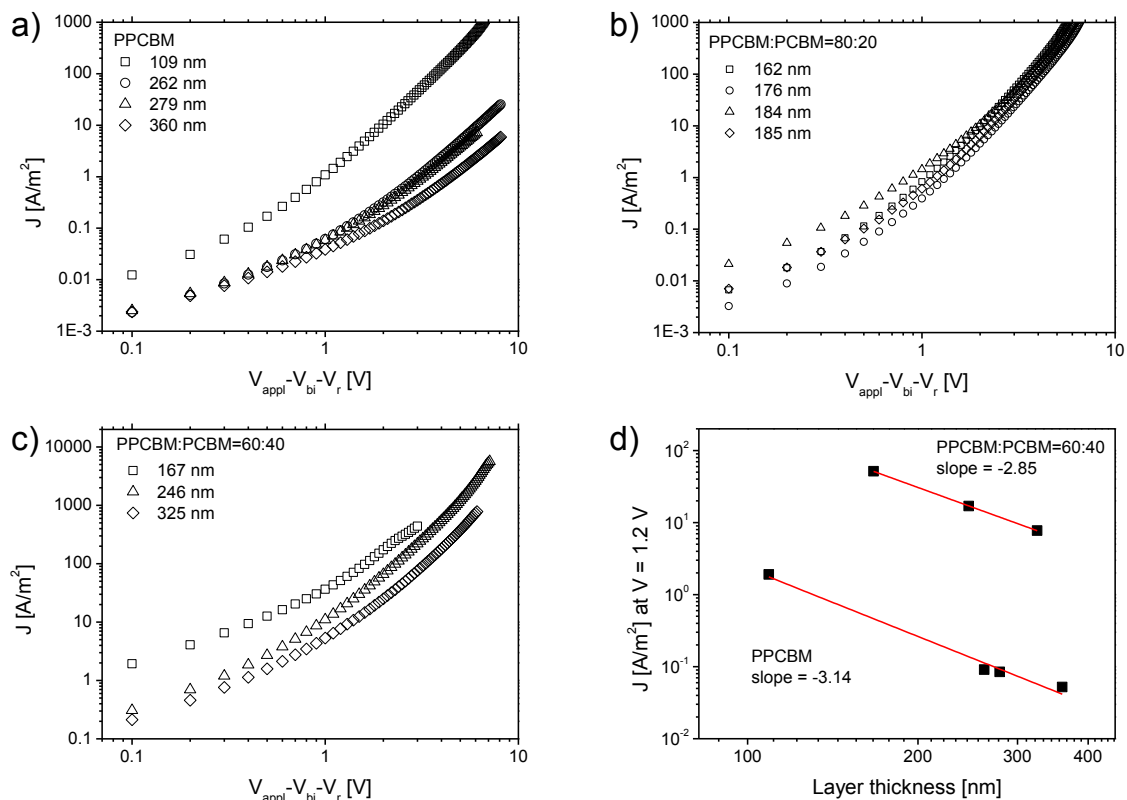


**Figure S3.** Space-charge limited current (SCLC) measurements: Log-log plots of current density  $J$  vs. effective voltage  $V_{\text{appl}} - V_{\text{bi}} - V_r$  for (a) PPCBM, (b) PPCBM:PCBM=80:20 and (c) PPCBM:PCBM=60:40 with variation of the active layer thickness. The thickness dependency of the current density  $J \propto L^{-3}$  is shown in the log-log plot of  $J$  vs.  $L$  in (d). The devices of PPCBM:PCBM=80:20 did not cover a sufficiently broad range of active layer thicknesses and were not considered in (d).

**Table S1.** Experimental results of SCLC electron mobility measurements including the active layer thickness  $L$ , zero-field electron mobility  $\mu_e(0)$ , field-dependency parameter  $\gamma$  and the electron mobility  $\mu_e(F)$  at a representative field of  $1.5 \times 10^7 \text{ V m}^{-1}$ . The mobility was extracted using the field-dependent Murgatroyd equation for fitting. The PCBM reference was analyzed using the Mott-Gurney equation, hence,  $\mu_e(0)$  and  $\gamma$  were not determined.

Material	No.	$L$ [nm]	$\mu_e(0)$ [ $\text{cm}^2\text{V}^{-1}\text{s}^{-1}$ ]	$\gamma$ [ $\text{m}^{0.5}\text{V}^{-0.5}$ ]	$\mu_e(F)$ [ $\text{cm}^2\text{V}^{-1}\text{s}^{-1}$ ]	Average $\mu_e(F)$ [ $\text{cm}^2\text{V}^{-1}\text{s}^{-1}$ ]
PPCBM	1	360	$1.97 \times 10^{-7}$	$4.462 \times 10^{-4}$	$1.11 \times 10^{-6}$	$(1.2 \pm 0.1) \times 10^{-6}$
	2	262	$9.36 \times 10^{-8}$	$6.529 \times 10^{-4}$	$1.17 \times 10^{-6}$	
	3	109	$9.98 \times 10^{-8}$	$6.526 \times 10^{-4}$	$1.25 \times 10^{-6}$	
	4	279	$1.18 \times 10^{-7}$	$5.941 \times 10^{-4}$	$1.18 \times 10^{-6}$	
PPCBM:PCBM= 80:20	1	185	$1.03 \times 10^{-7}$	$1.200 \times 10^{-3}$	$1.07 \times 10^{-5}$	$(9.9 \pm 3.9) \times 10^{-6}$
	2	162	$7.89 \times 10^{-8}$	$1.199 \times 10^{-3}$	$8.19 \times 10^{-6}$	
	3	176	$6.39 \times 10^{-8}$	$1.167 \times 10^{-3}$	$5.88 \times 10^{-6}$	
	4	184	$1.79 \times 10^{-7}$	$1.143 \times 10^{-3}$	$1.49 \times 10^{-5}$	
PPCBM:PCBM= 60:40	1	325	$1.34 \times 10^{-5}$	$7.350 \times 10^{-4}$	$2.31 \times 10^{-4}$	$(1.8 \pm 0.9) \times 10^{-4}$
	2	246	$9.24 \times 10^{-6}$	$8.280 \times 10^{-4}$	$2.28 \times 10^{-4}$	
	3	167	$3.29 \times 10^{-5}$	$2.248 \times 10^{-4}$	$7.85 \times 10^{-5}$	
PCBM reference	1	170	-	-	$3.40 \times 10^{-3}$	$(4.3 \pm 1.0) \times 10^{-3}$
	2	200	-	-	$5.40 \times 10^{-3}$	
	3	230	-	-	$4.10 \times 10^{-3}$	

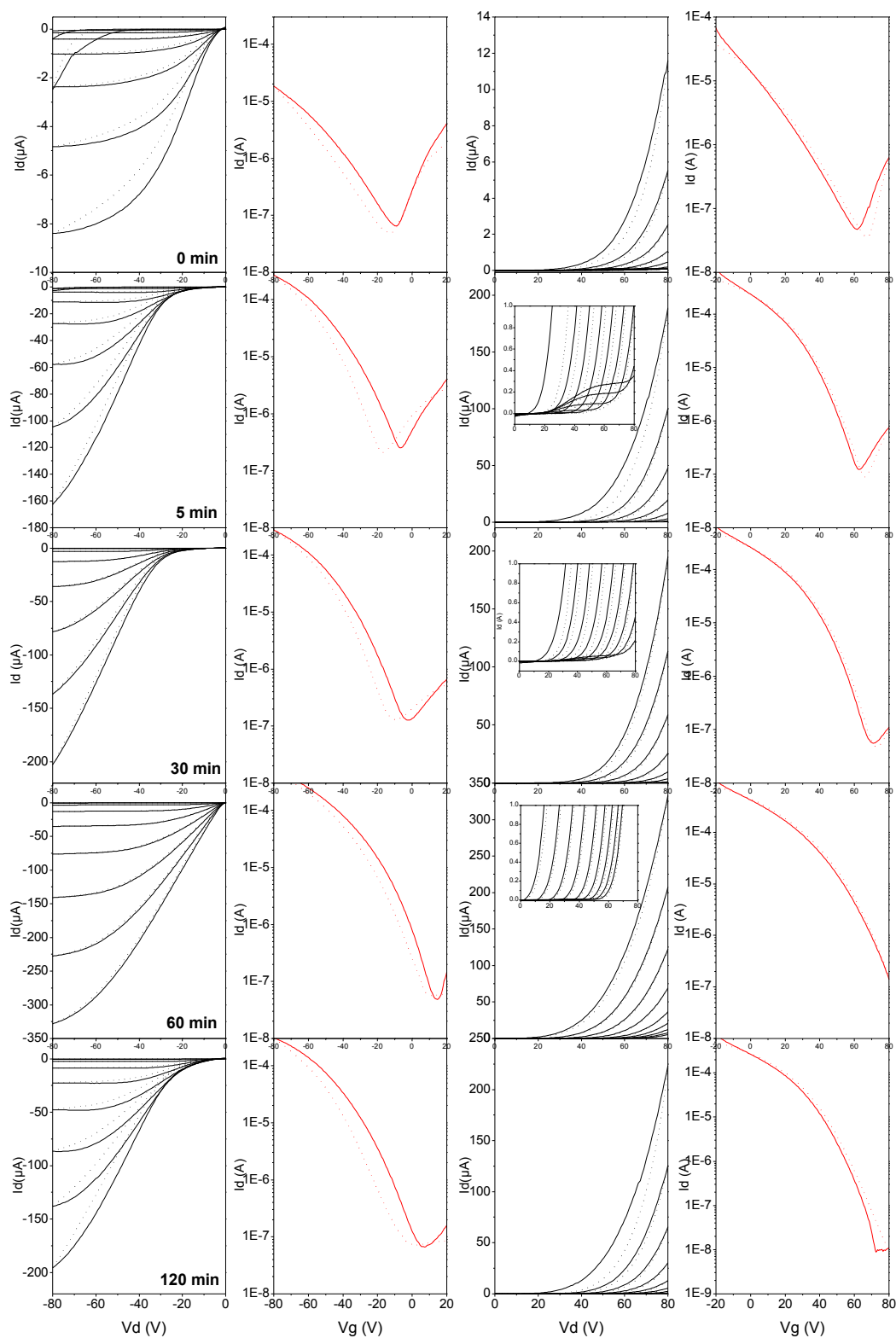


**Figure S4.** Representative OFET  $I$ - $V$  output and transfer curves for P3HT:PCBM=1.0:0.8 after 0, 5, 30, 60 and 120 min of annealing at 160 °C in nitrogen atmosphere.

**Table S2.** OFET results for p- and n-type operation of the P3HT:PCBM blend after different annealing times at 160 °C. The average mobility was determined based on several different transistors with varying channel length.

Annealing time [min]	Type	No.	Channel length [ $\mu\text{m}$ ]	Fitted mobility [ $\text{cm}^2 \text{V}^{-1} \text{s}^{-1}$ ]	Average mobility [ $\text{cm}^2 \text{V}^{-1} \text{s}^{-1}$ ]
0 min	p	1	10	$8.72 \times 10^{-4}$	$(1.0 \pm 0.1) \times 10^{-3}$
		2	20	$9.01 \times 10^{-4}$	
		3	20	$9.60 \times 10^{-4}$	
		4	20	$9.43 \times 10^{-4}$	
		5	10	$1.04 \times 10^{-3}$	
		6	10	$1.05 \times 10^{-3}$	
		7	20	$1.06 \times 10^{-3}$	
		8	20	$1.15 \times 10^{-3}$	
	n	1	10	$1.87 \times 10^{-4}$	$(2.8 \pm 0.8) \times 10^{-4}$
		2	20	$2.63 \times 10^{-4}$	
		3	20	$2.47 \times 10^{-4}$	
		4	20	$2.69 \times 10^{-4}$	
		5	10	$2.32 \times 10^{-4}$	
		6	10	$2.72 \times 10^{-4}$	
		7	20	$3.91 \times 10^{-4}$	
		8	20	$4.06 \times 10^{-4}$	
5 min	p	9	10	$1.10 \times 10^{-2}$	$(1.1 \pm 0.1) \times 10^{-2}$
		10	10	$1.25 \times 10^{-2}$	
		11	20	$1.05 \times 10^{-2}$	
		12	20	$1.12 \times 10^{-2}$	
	n	9	10	$1.54 \times 10^{-4}$	$(2.5 \pm 1.0) \times 10^{-4}$
		10	10	$1.71 \times 10^{-4}$	
		11	20	$3.27 \times 10^{-4}$	
		12	20	$3.35 \times 10^{-4}$	
30 min	p	13	10	$1.11 \times 10^{-2}$	$(1.1 \pm 0.1) \times 10^{-2}$
		14	10	$1.23 \times 10^{-2}$	
		15	20	$9.73 \times 10^{-3}$	
		16	20	$1.11 \times 10^{-2}$	
	n	13	10	$5.75 \times 10^{-6}$	$(2.9 \pm 2.9) \times 10^{-5}$
		14	10	$2.30 \times 10^{-5}$	
		15	20	$7.22 \times 10^{-5}$	
		16	20	$1.57 \times 10^{-5}$	
60 min	p	17	10	$1.08 \times 10^{-2}$	$(1.2 \pm 0.2) \times 10^{-2}$
		18	10	$1.12 \times 10^{-2}$	
		19	10	$1.53 \times 10^{-2}$	
		20	20	$1.20 \times 10^{-2}$	
	n	17	10	0	0
		18	10	0	
		19	10	0	
		20	20	0	
120 min	p	21	10	$1.24 \times 10^{-2}$	$(1.3 \pm 0.1) \times 10^{-2}$
		22	20	$1.26 \times 10^{-2}$	
		23	20	$1.42 \times 10^{-2}$	
		24	20	$1.30 \times 10^{-2}$	
	n	21	10	0	0
		22	20	0	
		23	20	0	
		24	20	0	

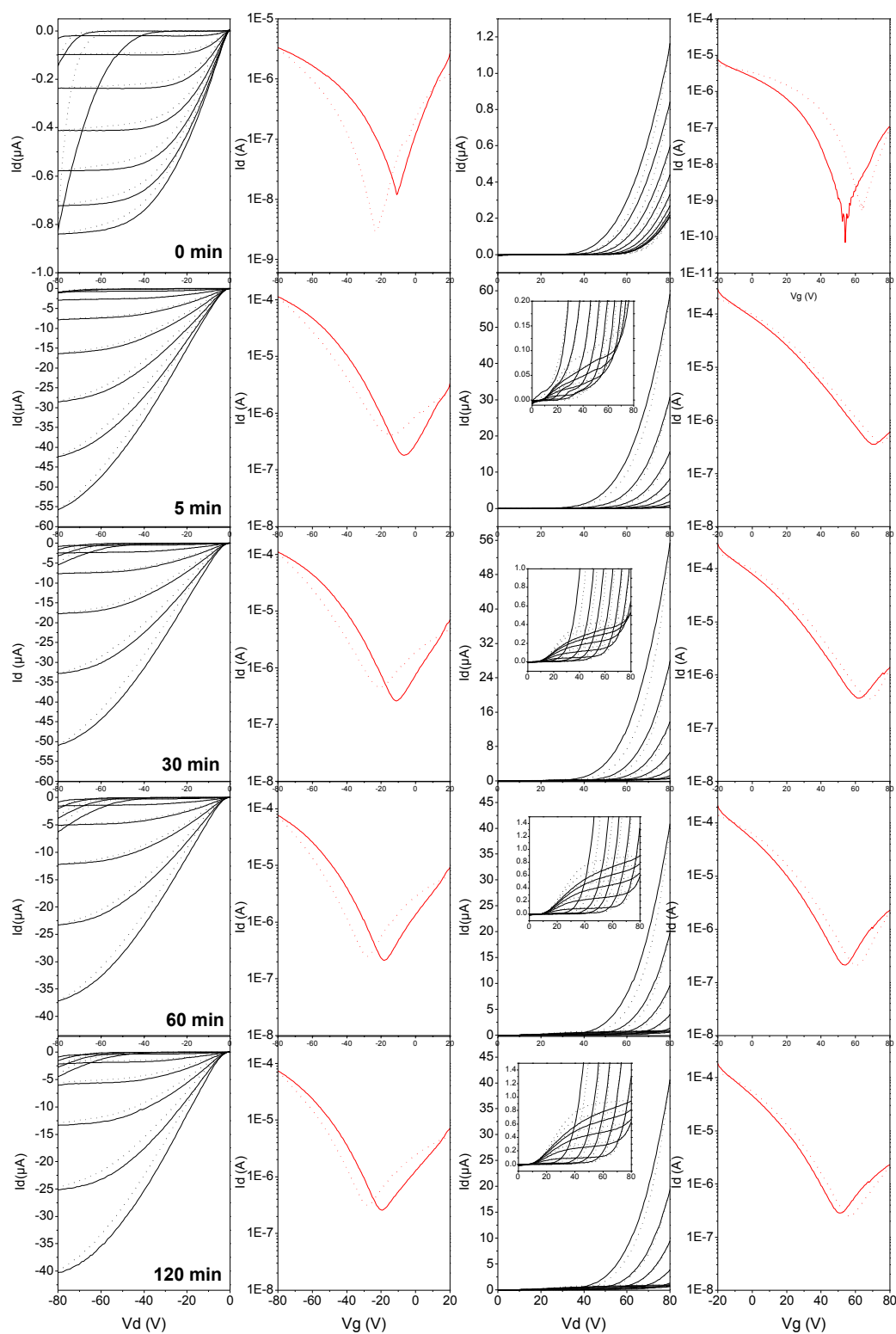


**Figure S5.** Representative OFET I-V output and transfer curves for BCP:PCBM=60:40 after 0, 5, 30, 60 and 120 min of annealing at 160 °C in nitrogen atmosphere.

**Table S3.** OFET results for p- and n-type operation of the BCP:PCBM=60:40 blend after different annealing times at 160 °C. The average mobility was determined based on several different transistors with varying channel length.

Annealing time [min]	Type	No.	Channel length [ $\mu\text{m}$ ]	Fitted mobility [ $\text{cm}^2 \text{V}^{-1} \text{s}^{-1}$ ]	Average mobility [ $\text{cm}^2 \text{V}^{-1} \text{s}^{-1}$ ]
0 min	p	1	10	$7.65 \times 10^{-5}$	$(8.7 \pm 0.7) \times 10^{-5}$
		2	10	$9.23 \times 10^{-5}$	
		3	10	$8.48 \times 10^{-5}$	
		4	10	$9.57 \times 10^{-5}$	
		5	10	$8.65 \times 10^{-5}$	
	n	1	10	$4.08 \times 10^{-5}$	$(5.2 \pm 1.0) \times 10^{-5}$
		2	10	$4.48 \times 10^{-5}$	
		3	10	$6.06 \times 10^{-5}$	
		4	10	$5.35 \times 10^{-5}$	
		5	10	$6.27 \times 10^{-5}$	
5 min	p	6	10	$4.60 \times 10^{-3}$	$(4.6 \pm 1.0) \times 10^{-3}$
		7	10	$6.24 \times 10^{-3}$	
		8	10	$3.58 \times 10^{-3}$	
		9	10	$4.73 \times 10^{-3}$	
		10	20	$3.99 \times 10^{-3}$	
	n	6	10	$2.99 \times 10^{-6}$	$(5.1 \pm 4.1) \times 10^{-5}$
		7	10	-	
		8	10	$8.64 \times 10^{-5}$	
		9	10	$8.47 \times 10^{-5}$	
		10	20	$3.12 \times 10^{-5}$	
30 min	p	11	10	$5.17 \times 10^{-3}$	$(5.1 \pm 0.9) \times 10^{-3}$
		12	10	$6.51 \times 10^{-3}$	
		13	10	$4.24 \times 10^{-3}$	
		14	10	$4.61 \times 10^{-3}$	
		15	20	$5.04 \times 10^{-3}$	
	n	11	10	$5.71 \times 10^{-5}$	$(1.2 \pm 0.5) \times 10^{-4}$
		12	10	$7.66 \times 10^{-5}$	
		13	10	$1.70 \times 10^{-4}$	
		14	10	$1.81 \times 10^{-4}$	
		15	20	$1.20 \times 10^{-4}$	
60 min	p	16	10	$4.55 \times 10^{-3}$	$(4.2 \pm 1.0) \times 10^{-3}$
		17	10	$5.84 \times 10^{-3}$	
		18	10	$3.12 \times 10^{-3}$	
		19	10	$4.07 \times 10^{-3}$	
		20	20	$3.61 \times 10^{-3}$	
	n	16	10	$1.51 \times 10^{-4}$	$(2.2 \pm 0.6) \times 10^{-4}$
		17	10	$1.72 \times 10^{-4}$	
		18	10	$2.68 \times 10^{-4}$	
		19	10	$2.75 \times 10^{-4}$	
		20	20	$2.45 \times 10^{-4}$	
120 min	p	21	10	$3.42 \times 10^{-3}$	$(3.6 \pm 1.3) \times 10^{-3}$
		22	10	$5.10 \times 10^{-3}$	
		23	10	$3.23 \times 10^{-3}$	
		24	10	$4.44 \times 10^{-3}$	
		25	10	$1.75 \times 10^{-3}$	
	n	21	10	$1.40 \times 10^{-4}$	$(1.7 \pm 0.3) \times 10^{-4}$
		22	10	$1.76 \times 10^{-4}$	
		23	10	$2.10 \times 10^{-4}$	
		24	10	$1.88 \times 10^{-4}$	
		25	10	$1.27 \times 10^{-4}$	



## 8 Nanoscale morphology from donor-acceptor block copolymers: Formation and functions

*David Heinrich<sup>a</sup>, Martin Hufnagel<sup>a</sup>, Chetan Raj Singh<sup>a</sup>, Matthias Fischer<sup>b</sup>, Shahidul Alam<sup>c</sup>, Harald Hoppe<sup>c</sup>, Thomas Thurn-Albrecht<sup>b</sup> and Mukundan Thelakkat<sup>a</sup>*

<sup>a</sup>Applied Functional Polymers, Department of Macromolecular Chemistry I  
University of Bayreuth, Universitaetsstr. 30, 95440 Bayreuth (Germany)

E-mail: [mukundan.thelakkat@uni-bayreuth.de](mailto:mukundan.thelakkat@uni-bayreuth.de)

<sup>b</sup>Experimental Polymer Physics Group, Martin-Luther University Halle-Wittenberg,  
Von-Danckelmann-Platz 3, 06120 Halle (Germany)

E-mail: [thomas.thurn-albrecht@physik.uni-halle.de](mailto:thomas.thurn-albrecht@physik.uni-halle.de)

<sup>c</sup>Institut für Physik, Technische Universität Ilmenau, 98693 Ilmenau (Germany)

E-mail: [harald.hoppe@tu-ilmenau.de](mailto:harald.hoppe@tu-ilmenau.de)

## ABSTRACT

General design principles of donor-acceptor block copolymers are reviewed and specific results arising from block copolymers consisting of semicrystalline P3HT blocks of appreciably high molecular weight and acceptor blocks carrying pendant perylene bisimides or fullerene derivatives are summarized. The chapter is structured according to the building blocks, P3HT, PPerAcr, and PPCBM used for the synthesis of the corresponding block copolymers and in each part the synthetic challenges, structure formation and the consequences for charge transport and in some cases photovoltaic properties are addressed.

## INTRODUCTION

Conjugated polymer-based organic solar cells have been successfully developed over the last 20 years<sup>[1-7]</sup> reaching nowadays power conversion efficiencies of over 10%.<sup>[8-15]</sup> One major requirement, arising from the fact that organic semiconductors generally exhibit strong exciton binding energies one order of magnitude above the thermal energy ( $k_B T$ ) and only small exciton diffusion lengths (a few nanometers), constitutes the existence of a so-called donor-acceptor interface to facilitate exciton dissociation and thus charge generation at this heterojunction interface. Thus only an intimate blend of donor and acceptor phases enables efficient charge generation throughout the bulk of the photoactive layer. Here the acceptor can be distinguished from the donor simply by having a larger electron affinity, thus forming a type II heterojunction. In other words, both the lowest unoccupied molecular orbital (LUMO) as well as the highest occupied molecular orbital (HOMO) of the acceptor need to be lower in energy as of the donor. Besides charge generation, also their efficient extraction at the two opposing selective electrodes displays a second requirement for successful photovoltaic operation. Hence, donor and acceptor phases need to form a bicontinuous interpenetrating network of a certain coarse grained lateral extend, providing percolation paths for both charge carrier types, holes and electrons. For minimizing charge recombination events, these phases need to be well-separated at a length scale roughly corresponding to the exciton diffusion length,<sup>[16]</sup> and both the charge generation and extraction benefit from the existence of semicrystalline phases. This three-dimensional mixing of donor and acceptor phases on the nanoscale is called the bulk heterojunction morphology.<sup>[17,18]</sup>

Commonly, the formation of such bulk heterojunctions is practically obtained from blending the two molecular or polymeric components in a common organic solvent and casting a film from it, resulting in a morphology governed by a kinetically locked non-equilibrium distribution of those two phases. The disadvantage of this approach lies in the fact that the scale of phase separation can be subject to coarsening processes with time, resulting in an increase of domain sizes due to phase separation<sup>[19,20]</sup> or unfavorable phase segregation towards an electrode,<sup>[21-23]</sup> reducing the amount of charge generation and extraction over time. These processes are generally termed morphological degradation and need to be prevented to ensure long-term efficient device operation. Hence several approaches have been developed in order to lock the scale of phase separation within the bulk heterojunction, among which i) cross-linking of single phases by *e.g.* epoxy-based agents,<sup>[24,19]</sup> ii) increasing the glass transition temperature of the blend,<sup>[22,25-28]</sup> iii) compatibilization of the donor and acceptor phases *via* bi-functional surfactants<sup>[29,30]</sup> and finally iv) the use of microphase separated donor-acceptor diblock copolymers as a single component with microstructures at thermodynamic equilibrium<sup>[31,32]</sup> have been pursued. In the latter approach, in addition to the viability of stable morphology, the scale of phase separation can be finely adjusted *via* precise control of the individual donor and acceptor blocks lengths to meet the restrictions of the exciton diffusion lengths. Furthermore, by definition of the respective volume fraction *via* the individual block lengths, certain phase distributions can be readily obtained, as predicted by the phase diagram of block copolymers. As an illustration, Fig. 1 summarizes various resulting phase distributions in dependence of the relative volume fractions of phase A and B:

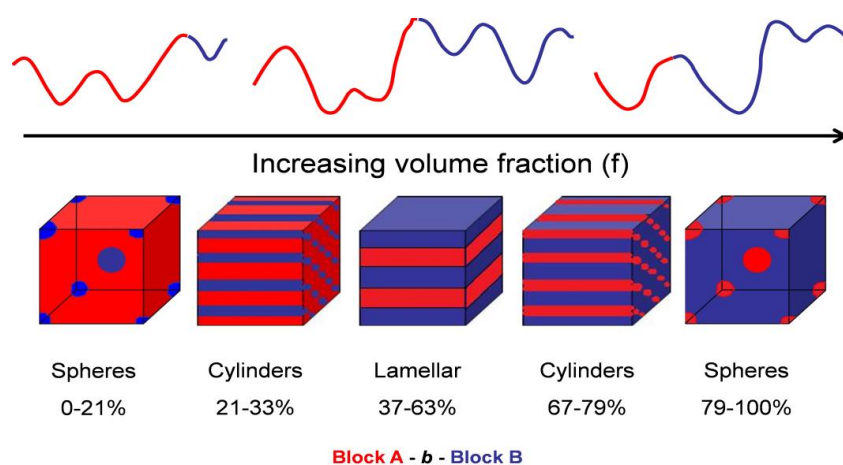


**Figure 1.** Schematic representation of most commonly observed morphologies of coil-coil block copolymers dictated by relative volume fractions. The typical range of percent volume fractions for the morphologies is also shown. Left to right: spherical, cylindrical,

*lamellar, inverse-cylindrical, inverse spherical phases. The red phase represents polymer block A, the blue phase polymer block B. Reproduced with permission from [33].*

In this chapter, this approach towards creating microstructures in donor-acceptor block copolymers will be reviewed. So far polymer physics has described mostly the phase behavior of coil-coil (amorphous or liquid-like) block copolymers, *i.e.* where both blocks exhibit a rather small persistence length (or Kuhn segment length) making them rather flexible. However, as already pointed out above, semicrystalline phases inhere the advantage of improved charge transport and generation capabilities, which triggered many authors to choose the so-called semicrystalline block copolymers (often referred to as rod-coil or rod-rod) in order to aim for well-defined phase separation in conjunction with crystallinity within the individual hole and/or electron transporting domains. With that approach, the goal of the majority of the studies was to obtain a controlled self-assembly of the donor and acceptor phases *via* molecular design of the functional blocks yielding nanostructures suitable for photovoltaics enabling efficient charge generation and transport over the whole lateral area of photovoltaic devices (compare with Fig. 2).

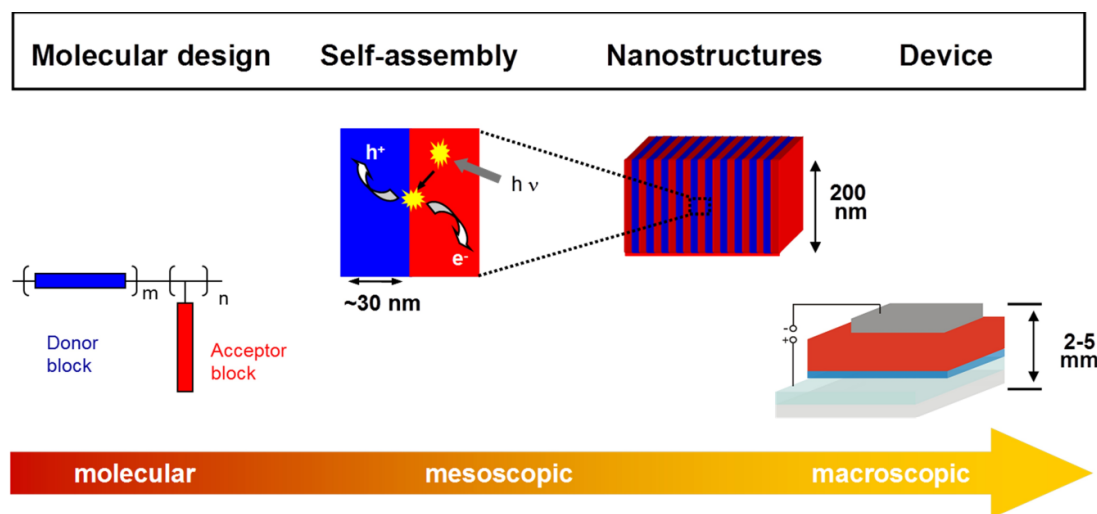


**Figure 2.** The schematic shows the goal pursued: *via* control of molecular structure by design leading to morphological control through self-assembly of nanostructures, yielding functional control in devices spanning all length scales from molecular (nanoscopic) over mesoscopic nanostructures to macroscopic device levels.

Several attempts for reaching this goal were followed and described in the literature so far, from realizing first functional block copolymers with dual function of electron and hole transporting phases,<sup>[34-43]</sup> over using of oligomers with rather small scale of phase separation<sup>[44]</sup> up to lately rather successful approaches based on diblock copolymers ex-

hibiting a poly(3-hexylthiophene-2,5-diyl) (P3HT) -based donor block combined with a fullerene-based acceptor block.<sup>[45,46]</sup> Due to the large diversity of chemical structures and a huge number of publications in this field, we limit our discussions to P3HT systems in which the acceptor block carries either perylene bisimides (PBI) or fullerene derivatives ( $C_{60}$ ,  $C_{70}$ ) as pendant groups (see Fig. 3). For reviews of different kinds of semiconductor block copolymers, we draw the attention to published work by Mori *et al.*,<sup>[43]</sup> Horowitz *et al.*,<sup>[34]</sup> Thelakkat *et al.*<sup>[39,40]</sup> and Scherf *et al.*<sup>[47]</sup>

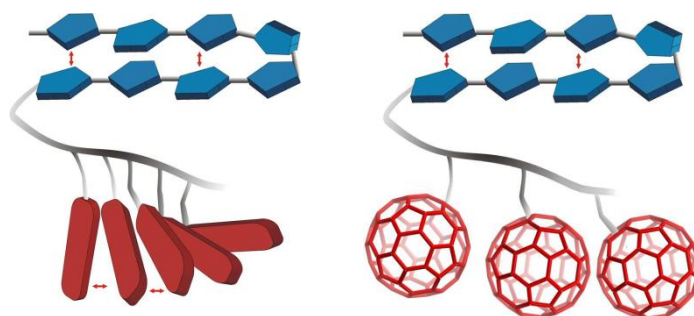


**Figure 3.** Simplified schematics of P3HT containing block copolymers carrying either perylene bisimides (PBI) or fullerene derivatives as pendant groups in the acceptor block. The double-headed red arrows indicate the  $\pi - \pi$  interaction of the thiophene units resp. perylene bisimide units leading to crystallinity and improved charge transport in these systems.

The chemical structures of some of the reported donor-acceptor block architectures are given in Fig. 4. Hashimoto *et al.* developed the most successful P3HT-b-Poly( $C_{60}$ ) systems in which the fullerenes were grafted to a P3HT copolymer backbone, delivering power conversion efficiencies of 2.46% in single layer devices using polymer 4 (Fig. 4).<sup>[48]</sup> The best performing device so far was indeed obtained using a non-fullerene-based acceptor block using a Poly(9,9-dioctylfluorene)-co-(4,7-di-2-thienyl-2,1,3-benzothiadiazole) PFTBT copolymer (polymer , approaching 3% power conversion efficiency.<sup>[49]</sup> This success was to a large part due to a considerably high open circuit voltage of more than 1.2 Volts.

In this chapter, studies are reviewed which focus towards an improved understanding of the self-assembling process by bringing the block copolymers first into the melt, accompanied by the formation of the microphase separation and followed by a controlled crystallization upon slow cooling. A major challenge which still remains to be solved, consists in obtaining the desired vertical phase orientation within the photoactive layer.

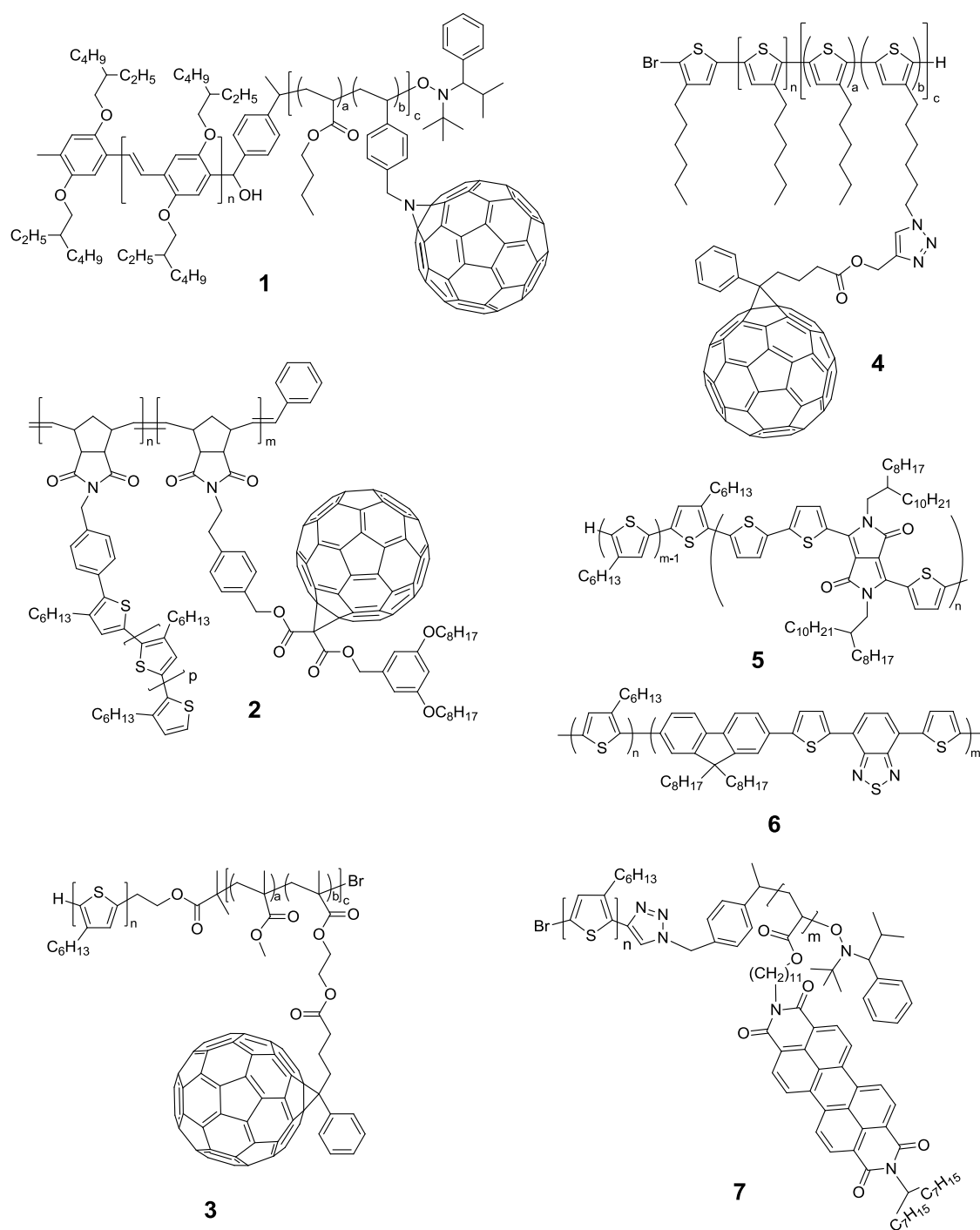


**Figure 4.** Chemical structures of some of the selected P3HT-*b*-Poly(C<sub>60</sub>) systems (polymers 1-4),<sup>[48,50-52]</sup> all conjugated polymers (polymers 5,6),<sup>[49,53]</sup> and a P3HT-*b*-PPerAcr system 7,<sup>[40]</sup> which were tested in polymer solar cells.

To understand and control the donor-acceptor nanostructure in block copolymer systems as introduced above, it is important to identify the driving forces responsible for structure formation. The classical microphase separation refers to systems with two amorphous blocks and is driven by their incompatibility, quantified by the product  $\chi N$  ( $N$  - degree of polymerization,  $\chi$  - Flory–Huggins interaction parameter). In addition, the phase diagram depends on the volume fraction, cf. Fig. 1. The situation becomes more complex, if additional ordering processes take place within the individual blocks which can also lead to a separation of the components. Crystallization is such an ordering process, but also the formation of liquid-crystalline phases can influence microphase separation.<sup>[54]</sup> The complexity of microphase separation in crystalline–amorphous systems as well as in double-crystalline block copolymers has *e.g.* been studied in detail by Register *et al.* using polyethylene as a model block.<sup>[55,56]</sup> In general, it is useful to first study the individual components of such a complex block copolymer system by themselves, before studying structure formation in the fully functionalized block copolymers. As P3HT can crystallize and as most donor-acceptor block copolymers synthesized until now contain P3HT as donor block, the case of crystallization is most important. Schematically this situation is illustrated in Fig. 5.

An additional aspect to be taken into account, when considering structure formation in donor-acceptor block copolymers, is the dependence on processing pathways. Drying from solution and cooling from the melt might not necessarily lead to the same nanostructure. Nevertheless it makes sense attempting at first to determine the equilibrium structure and to study deviations from it in a second step. To get information about phase diagrams temperature dependent in-situ techniques are necessary, as *e.g.* scattering techniques, complemented by imaging techniques used mostly at room temperature. For understanding the structure formation in donor-acceptor block copolymers, first the controlled synthesis leading to structure formation in individual blocks is discussed in detail in the following.

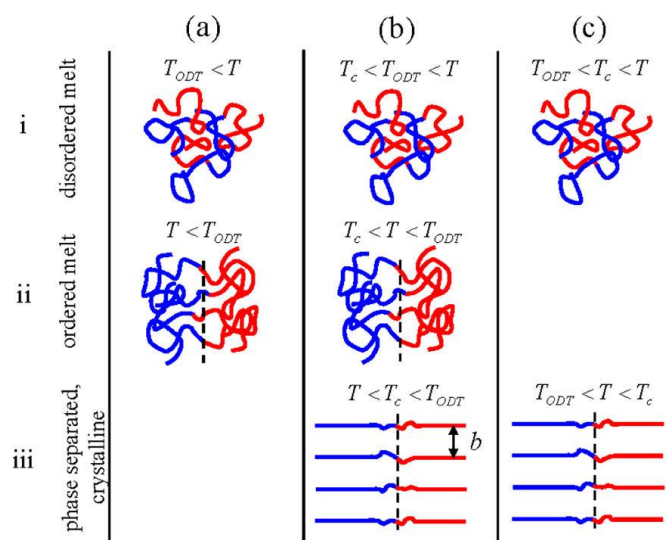


**Figure 5.** Schematic illustration of possible ordering scenarios for block copolymers upon cooling (top to bottom): (a) A block copolymer with two noncrystallizable blocks forms a disordered melt at temperatures above the order–disorder temperature  $T_{ODT}$  (i), while for  $T < T_{ODT}$  (ii) in the ordered melt the well-known microphase separated morphologies develop. For block copolymers with one or two crystallizable blocks, the crystallization of the individual blocks either occurs from an ordered melt (b) or directly from the disordered melt (c) depending on the relative locations of  $T_{ODT}$  and  $T_c$ . Here, for simplicity, only one melting/crystallization temperature  $T_c$  was assumed. For case (b) very often crystallization overrides the existing microphase structure leading to a nanostructure consisting of lamellar crystals as in case (c). The case where for (b) the microphase structure stays intact upon crystallization, is called *confined crystallization*. Reproduced with permission from [112].

## 1. Donor building block: poly(3-hexylthiophene-2,5-diyl) P3HT

### 1.1. Controlled Synthesis as a key for structure formation

Polythiophene, one of the most commonly used and most studied conjugated polymer, was earlier synthesized as unsubstituted and insoluble derivative.<sup>[57,58]</sup> Later irregular alkyl substituted polythiophene<sup>[59]</sup> and in the last years regioregular poly(3-hexylthiophene-2,5-diyl), P3HT was prepared by Ni-catalyzed syntheses.<sup>[60,61]</sup> A further development was the synthesis of the active Grignard monomer species through Grignard metathesis reaction.<sup>[62]</sup> This route which starts from 2,5-dibromo-3-hexylthiophene will be referred to as McCullough route whereas the Yokozawa route uses 2-bromo-3-hexyl-5-iodothiophene as starting component (Fig. 6). Yokozawa *et al.* and Mc Cullough *et al.* were able to show that the Ni-catalyzed polymerization of **2a** follows a chain growth mechanism and gives an increased control over the properties of the targeted polymer.<sup>[63-66]</sup> With this method, it was possible to synthesize regioregular P3HT with narrow distributions and predictable

molecular weights which can be seen from the SEC curves of a series of P3HTs with different molecular weights (Fig. 7a). The method is generally termed as Kumada catalyst transfer polymerization.

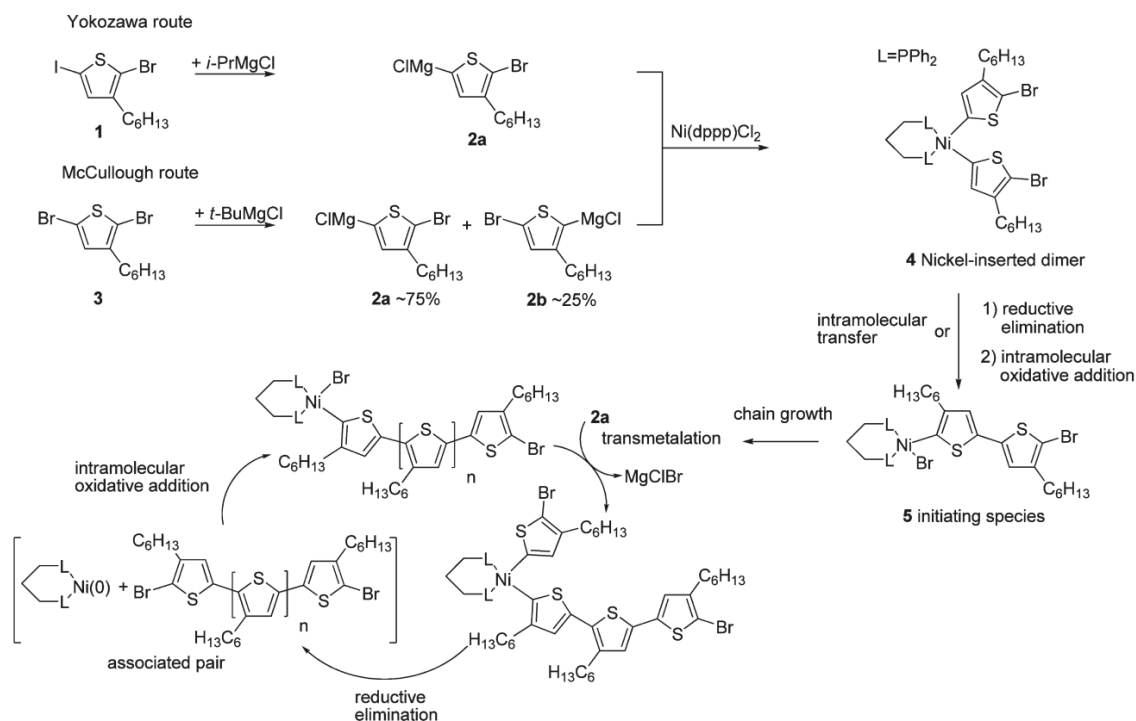


**Figure 6.** Formation of the active Grignard monomer **2a** by Yokozawa and McCullough route, and chain growth mechanism of the Kumada catalyst transfer polymerization. Reproduced with permission from [67].

Upon addition of the nickel catalyst the active species **2a** forms the nickel inserted dimer **4**, the species **2b** does not take part in the polymerization because of the sterical hindrance of the hexyl chain. One regio-defect is always generated at the initial step from the inserted dimer **4** to the initiating species **5**. In the additional chain growth step, only head to tail couplings occur. After the monomer is consumed, the living chain remains active until the reaction is quenched with a suitable reagent. If P3HT is intended to be used in block copolymer systems or other more complex architectures, it is important to control the end groups of the obtained polymers. Lohwasser *et al.* showed that a detailed understanding of the mechanism involved makes it possible to perfectly control the end groups of P3HT.<sup>[67]</sup> It has been shown that the quenching agent has a great effect on the final product.<sup>[68]</sup> Methanol as quenching agent was shown to lead to chain-chain coupling *via* disproportionation which has a detrimental effect that cannot be observed after quenching the polymerization in dilute HCl. It has also been shown that a complete Grignard monomer formation was crucial to achieve almost 100 % H/Br end groups. When

LiCl was used as an additive the complete consumption of  $t\text{-BuMgCl}$  and the complete formation of the active species could be assured.<sup>[69]</sup> LiCl is accelerating the active monomer formation and increasing the molecular weight of the final polymer by also incorporating the second sterically disfavored monomer species **2b**. Wu *et al.* found that the detrimental effect of the incorporation of the second monomer on the regioregularity is minimal.<sup>[70]</sup>

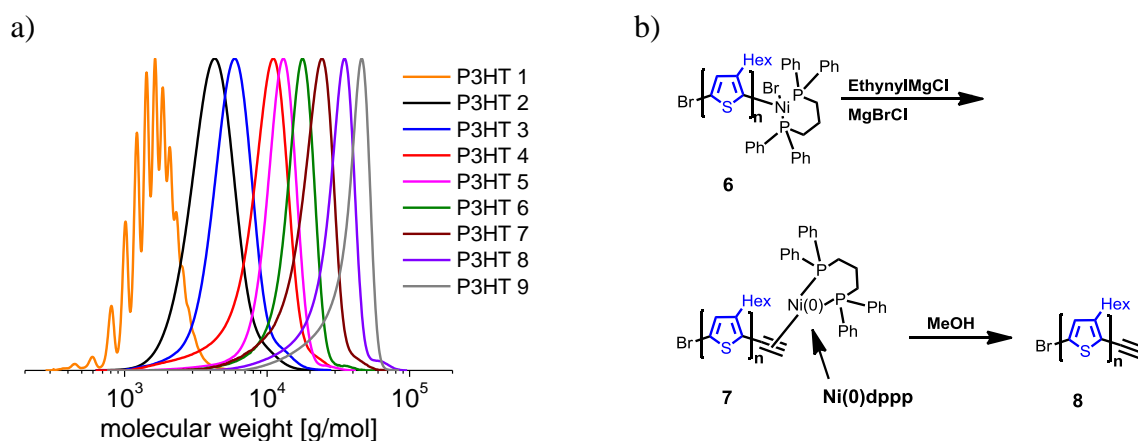


**Figure 7.** a) SEC curves of a series of P3HTs with different molecular weights and narrow distributions. The SEC was calibrated against polystyrene standards. b) Formation of P3HT-alkyne via endcapping with ethynyl magnesium chloride and quenching in methanol.

This is due to the lower reactivity of the sterically hindered monomer **2b** which is only incorporated into the polymer chain, once most of the majority species **2a** is consumed. A simple way to obtain functional end groups is highly advantageous when P3HT is intended to be part of a block copolymer or more complex polymer architectures. Jeffries *et al.* reported a straightforward method to obtain a series of end groups, simply by adding a functional Grignard reagent in order to end cap the polymer.<sup>[71]</sup> While this method proved to be highly versatile and efficient, it did only lead to monocapped products for a variety of the end capping agents. Only end groups like vinyl or alkyne, which form stable  $\pi$ -complexes with the nickel catalyst, were not leading to dicapped products. The formation of dicapped products in cases where the catalyst was not bound to the end group can be explained by the effect of random catalyst walking along the polymer chain which was observed by Tkachov *et al.*<sup>[72]</sup> The authors were able to show that the catalyst is not bound to one chain end but can move along the chain and initiate the polymerization at the other end of the polymer. This process, aside from having possibly negative effects on end capping, also leads to a change of position of regiodefects, which will not stay at one

chain end but may rather be in the middle of the chain at the end of the polymerization. Especially alkyne-functionalized P3HT can be an interesting starting material for the synthesis of block copolymers containing P3HT. To obtain such polymers in high yield it is again crucial to quench the polymerization in the appropriate media. Lohwasser *et al.* showed that, in the case of alkyne functionalization, dilute HCl leads to a hydration and hydrohalogenation of the end group.<sup>[73]</sup> Methanol on the other hand appeared to be a good choice in this particular case. The nickel is now in the Ni(0) state and no disproportionation reaction with the methanol is therefore possible (see Fig. 7b).

## 1.2. Structure elucidation in bulk and thin films of P3HT

### Temperature dependent phase diagram

The structure of P3HT has been studied in detail by many authors.<sup>[74-76]</sup> Depending on the conditions of sample preparation such as solvent, temperature and molecular weight and it can exist in an amorphous phase with coiled chain conformations or in an aggregated phase containing planarized chains with a tendency to form semicrystalline domains. It is also now well established that P3HT can adopt different morphologies.<sup>[76]</sup> Using selected samples of P3HT with well-defined molecular weight and high regioregularity from the series of materials mentioned above, Wu *et al.* performed temperature dependent in-situ small and wide angle X-ray scattering experiments complemented by DSC and AFM experiments.<sup>[77]</sup> Fig. 8 shows the results of DSC measurements on a series of P3HTs with varying molecular weights. Apart from the sample with the lowest molecular weight, all samples melt in a similar temperature range around 220°C. P3HT 3 shows an additional peak around 60°C, whose structural origin becomes clear when considering the temperature dependent wide angle X-ray scattering patterns shown in Fig. 9 together with a sketch of the microstructure of P3HT. As described in the figure caption, the reflections indicating order in the crystal across the layers separated by side chains disappear around 60°C, in line with the observed transition in the DSC. The samples with higher molecular weight do not show this transition, most likely because the corresponding ordering process at low temperatures is kinetically suppressed. This interpretation of the phase transition was later on confirmed by NMR experiments, in which also a structural disordering process of the alkyl side chains, not affecting rigidity and conformation of the backbones, could be observed.<sup>[78]</sup>

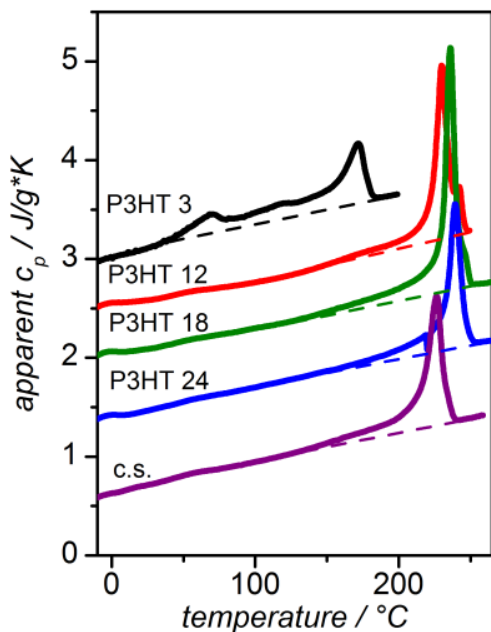


**Figure 8.** DSC thermograms of samples of P3HT with well-defined molecular weight. The sample names indicate the molecular weight  $M_n$  as obtained by MALDI-TOF MS, polydispersities are about 1.15. C.S. is a commercial sample with a broader molecular weight distribution. All data were obtained during a second heating run with a rate of  $20 \text{ K min}^{-1}$ . Apart from P3HT 24, all curves are shifted vertically for clarity. Straight lines below the melting peaks are used as background signal subtracted for integrations to determine the melting enthalpy  $\Delta H_m$ . Note the transition around  $60^\circ\text{C}$  for P3HT 3 caused by side chain melting. Reproduced with permission from [79].

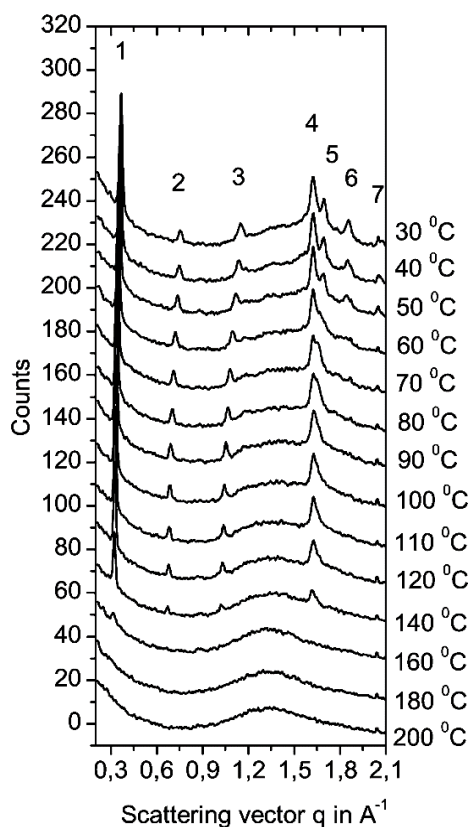
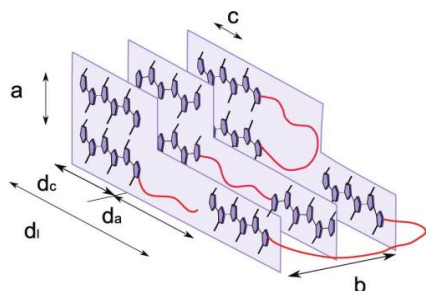


**Figure 9.** Top: Temperature dependent wide angle X-ray powder scattering diagrams of P3HT 3 reflecting the crystal structure. All data were taken during heating. Bragg reflections are numbered from low to high scattering vector. Peak 1-3 are caused by alternating layers of main and side chains in  $a$ -direction, while peak 4 reflects the  $\pi$ -stacking. Peak 5 and 6 carry mixed indices ( $hk0$ ) and can only exist if crystal packing in different layers of main chains is in register. This kind of order is lost at the phase transition at  $60^\circ\text{C}$ , which can therefore be attributed to side chain disordering. Peak 7 contains a contribution from the substrate and remains therefore visible up to the highest temperatures. Bottom: Scheme of the typical microstructure of regioregular P3HT.  $a$ ,  $b$ ,  $c$ , crystal lattice parameters;  $d_c$ , thickness of lamellar crystals;  $d_a$ , thickness of amorphous layers,  $d_l$ , long period, (scheme not to scale: the long period is about on order of magnitude larger than the lattice parameters  $a$ ,  $b$ ,  $c$ ). Reproduced with permission from [77].



### Semicrystalline morphology of P3HT

That P3HT is semicrystalline, is confirmed by the observation of a diffuse scattering signal in the X-ray diffraction pattern appearing underneath the Bragg reflections reflecting the crystalline fraction of the sample (Fig. 9). The corresponding morphology can be visualized by AFM. In the lower row of Fig. 10, a well-developed semicrystalline morphology, consisting of lamellar or fibrous crystals separated by amorphous domains on a scale of some ten nanometers, is visible.

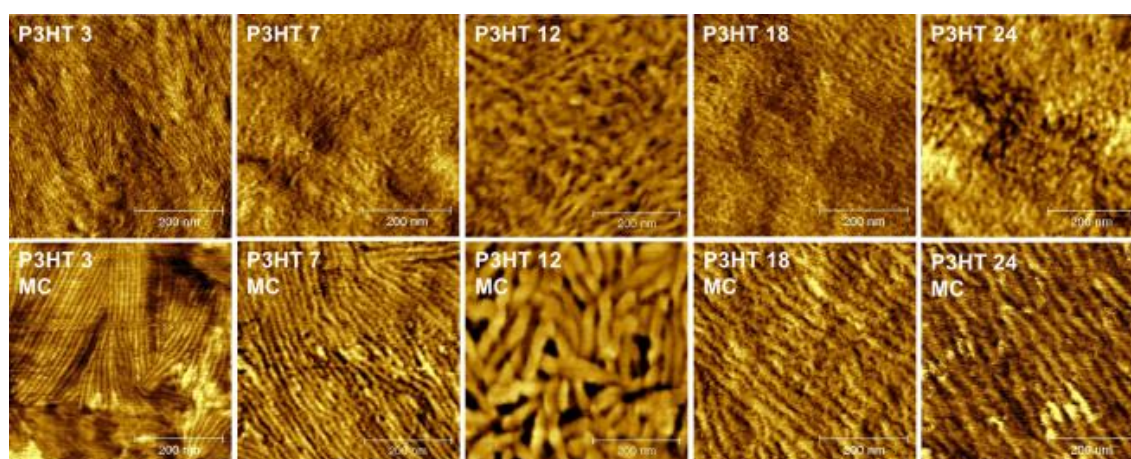


**Figure 10.** AFM phase images of spin-cast (top) and melt crystallized (bottom) films of P3HT with different molecular weights. The scan area for each sample is  $500 \times 500 \text{ nm}^2$ . Reproduced with permission from [80].

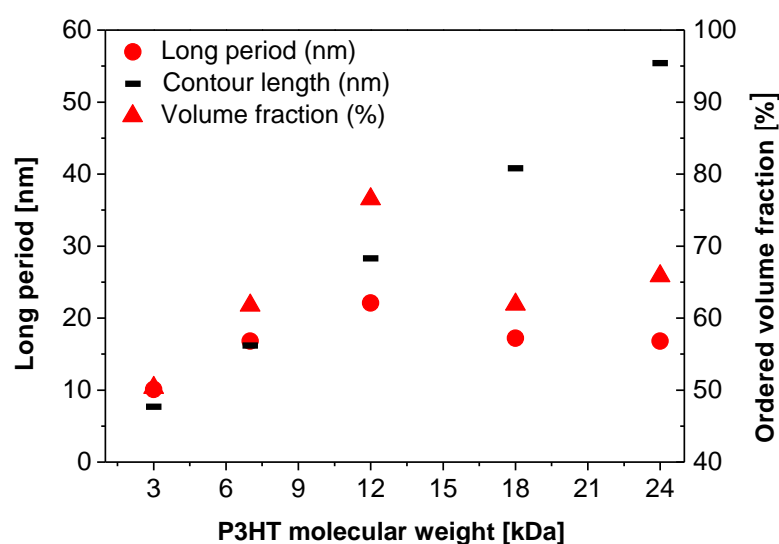


**Figure 11.** Left axis: Long period (circles) as measured by SAXS in bulk samples and calculated contour lengths (black bars) versus molecular weight of P3HT (MALDI-TOF MS). Right axis: Volume fraction (triangle) of more ordered P3HT domains in melt crystallized films determined by analysis of ellipsometric data. Reproduced with permission from [80].

These samples were crystallized by cooling from the melt. Directly after spincoating, crystallization is largely suppressed, as the images in the upper row show. A more quantitative analysis of the semicrystalline morphology is possible with small angle X-ray scattering, which allows a measurement of the long period of the semicrystalline structure. The result is shown in Fig. 11 together with the contour length of the corresponding molecular weight. The results show that for low molecular weight the polymer crystallizes as extended chain crystals, but starts to form folded chain crystals around a molecular weight of  $12 \text{ kg mol}^{-1}$  (MALDI-TOF MS).

### Quantitative determination of crystallinity

A common method for the determination of the crystallinity of a semicrystalline polymer is based on the comparison of the melting enthalpy as determined by DSC to the melting enthalpy of a 100% crystalline sample. The latter value has to be determined independently by an absolute method like *e.g.* X-ray diffraction or NMR. We therefore attempted a quantitative determination of the crystallinity based on temperature-dependent small-angle and wide angle X-ray scattering (SAXS/WAXS) measurements on the above mentioned series of P3HT with different molecular weights. The analysis is based on the evaluation of the scattered intensity from the amorphous regions as shown in Fig. 12 providing an easy and fast method for the determination of the crystallinity in the class of side chain substituted polymers. The resulting values for the crystallinity of our P3HTs are in the range of 68–80% at room temperature depending on the molecular weight. Based on these values, an extrapolated reference melting enthalpy of a 100% crystalline material was determined ( $\Delta H_{m,\infty} = 33 \pm 3 \text{ J g}^{-1}$ ) for use in DSC measurements. This value is consistent with a previous estimation based on NMR measurements<sup>[79]</sup> and it includes a substantial correction to previously used values.<sup>[81]</sup> For higher molecular weights a decrease of the crystallinity was observed which can be explained by the onset of chain folding as deduced from the analysis of the SAXS patterns. An in-depth analysis of the scattering patterns indicated that the crystalline regions of P3HT exhibit a large amount of internal disorder, considerably larger than typically found in other synthetic polymers. The results are described in detail in ref. [78].

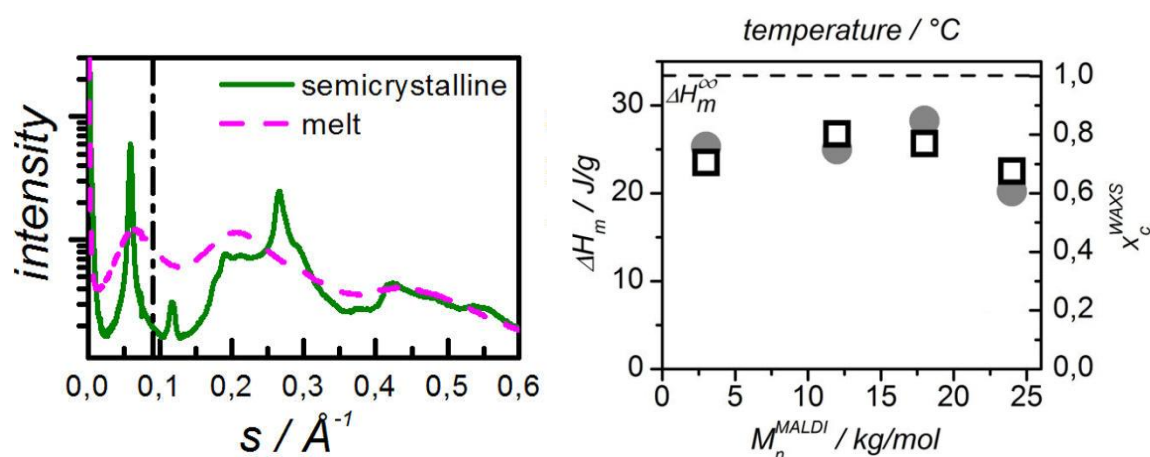


**Figure 12.** Left: X-ray diffraction pattern of P3HT 18 in the semicrystalline state at 40 °C (solid line) after cooling from the melt and in the melt (dashed line). The vertical dot-dashed line indicates the range in which the intensities were compared to determine the crystallinity. Right: crystallinities determined by WAXS (squares) and DSC melting enthalpies (gray circles) of P3HT showing the same trend with molecular weight. The broken horizontal line indicates the extrapolated melting enthalpy of a 100% crystalline sample. Reproduced with permission from [78].

### 1.3. Structure correlation with charge transport in bulk and thin films

Based on the results described above the effect of crystallinity and molecular weight on hole mobility in P3HT was investigated in a single carrier devices using the space charge limited current (SCLC) method.<sup>[80]</sup> To vary the crystallinity in otherwise identical materials two samples were prepared, one remained in the disordered state after spincoating, while the other was crystallized from the melt. As Fig. 10 shows and as it was confirmed by X-ray scattering, crystallization is largely suppressed after spincoating due to the fast drying process. The results of charge transport investigation in Fig. 13 show that there is a strong increase of up to one order of magnitude in hole mobility upon crystallization. Even stronger was the effect of molecular weight displaying a strong rise over nearly 3 orders of magnitude from the lowest to intermediate molecular weights. Beyond  $12 \text{ kg mol}^{-1}$  the hole mobility decreased again and leveled off for highest molecular weights. This reduction occurred thus at molecular weight, where chain folding sets in, resulting in a decrease of the overall crystallinity and an increase in the amorphous volume fraction. This result is in good agreement with the general model of chain organization leading to predicted changes in certain materials properties according to Vikar *et al.*<sup>[82]</sup> In this case, however, the dependency is of exponential nature, whereas the crystallinity itself displays the same behavior on a linear scale (compare with Fig. 11 above).

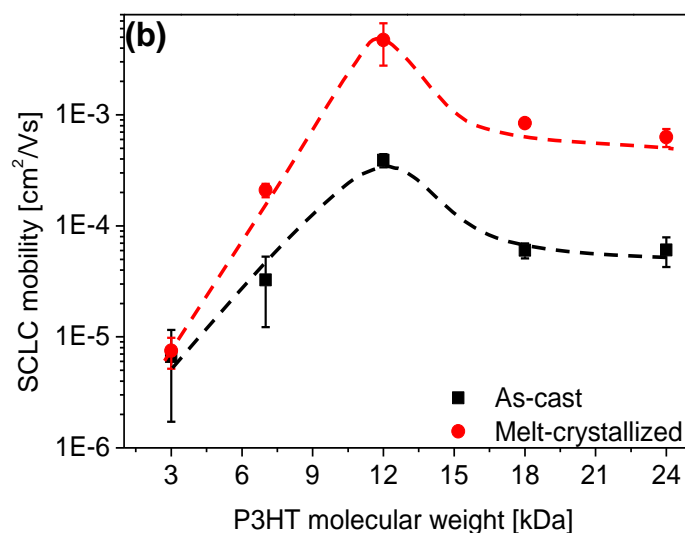


**Figure 13.** SCLC charge carrier mobility of holes in as-cast (square) and melt crystallized (circle) P3HT films of different molecular weight (MALDI-TOF MS). Each data point represents the average of 3–4 sets of devices produced for varying film thicknesses in the range of 250–350 nm. Dashed lines are shown as a guide to the eye for the observed trend of charge carrier mobility. Reproduced with permission from [80].

It should be noted that the charge carrier mobility obtained for the melt crystallized P3HT sample with 12 kg mol<sup>-1</sup> is one of the highest reported values for bulk charge transport through a film, thus reflecting the extraordinary quality of the material synthesized as described above. Based on these charge carrier mobility studies, the intermediate molecular weight sample could be identified as an ideal building block for the donor within block copolymers.

## 2. Acceptor building block: Poly(Perylene bisimide acrylate) PPerAcr/Poly(PBI)

### 2.1. Controlled Synthesis

Polymers with pendant perylene bisimide side chains (PPBI) were first reported by Linder *et al.* in 2004.<sup>[83]</sup> The authors synthesized an unsymmetrical perylene bisimide monomer with a solubilizing swallow-tail substituent and an acrylate group for polymerization. This acrylate monomer was polymerized with nitroxide mediated radical polymerization (NMRP).<sup>[84]</sup> It was possible to obtain moderate molecular weights by this method, and even block copolymers were obtained *via* sequential polymerization.<sup>[40]</sup> The homo-polymerization of this high molecular weight perylene bisimide monomer is not optimal. Narrow distributions, which are characteristic for controlled radical polymerizations, could not be obtained. Additionally, the polymerization has to be performed at high

monomer concentrations and the resulting polymer shows a limited solubility. This makes it difficult to achieve high molecular weights and also limits the choice of side chains that can be introduced. These synthetic restrictions were overcome by introducing the Cu-catalyzed azide-alkyne “click”-chemistry (CuAAC) concept<sup>[85]</sup> and combining it with controlled radical polymerization. The first attempt to obtain pendant perylene bisimide polymer using this concept was reported by Tao *et al.* in 2009.<sup>[86]</sup>

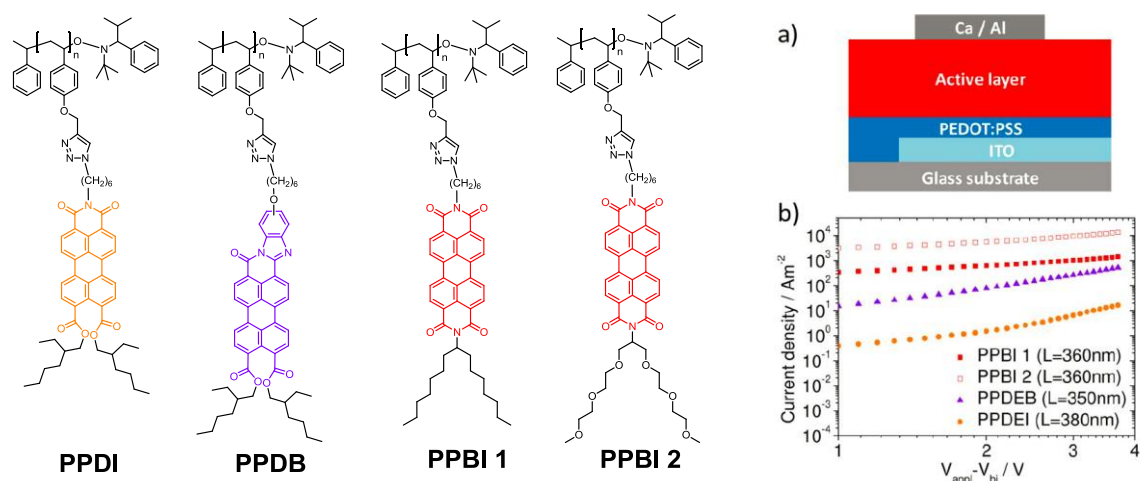


**Figure 14.** (left) Pendant perylene side chains synthesized via “click chemistry” and (right) a) schematic of an electron-only device and b)  $J$ - $V$  characteristics for electron-only devices of compounds PPBI 1, PPBI 2, PPDB, and PPDI with active layer thickness  $L$ . Reproduced with permission from [89].

Lang *et al.* investigated this concept in detail and compared it to the conventional synthesis approach.<sup>[87]</sup> The polymer backbone is synthesized independently and afterwards decorated with the perylene bisimide moieties. The authors synthesized poly(propargyloxystyrene) *via* NMRP with alkyne functionality at each monomer unit and also perylene bisimides with azide functionality. Alkynes can undergo a very efficient reaction at room temperature with azides in the presence of a Cu(I) catalyst and form stable 1,4-substituted triazoles.<sup>[86]</sup> It was reported that the polymer backbone can be almost quantitatively decorated with the perylene bisimide moieties as proven by FTIR and  $^1\text{H-NMR}$  spectroscopy. These polymers had very narrow distributions as good as 1.16 and molecular weights of up to  $15,000 \text{ g mol}^{-1}$ . The “clicked” polymers were compared with poly(peryene acrylate bisimides) (synthesized directly *via* NMRP) with different alkyl spacers. The comparison of the phase behavior showed a strong dependence on spacer lengths. In a further study, Lang *et al.* investigated the effect of the spacer

length and different phase behavior of perylene bisimide pendant polymers with hydrophilic side chains.<sup>[88]</sup> Two sets of polymers were synthesized as shown in Fig. 14. Polymers with pendant perylene bisimides with hydrophobic alky swallow-tails: **PPBI 1** and a set with hydrophilic oligo ethylene glycol swallow-tails **PPBI 2**. In both cases three polymers were synthesized each, using three different spacers ((CH<sub>2</sub>)<sub>6</sub>, (CH<sub>2</sub>)<sub>8</sub> and (CH<sub>2</sub>)<sub>11</sub>). The systematic investigation of the influence of the perylene bisimide substitutions could be done because the approach of a polymer analogous introduction of different pendant groups to one single precursor polymer made it possible to obtain a set of highly comparable polymers. All polymers had molecular weights up to 60.000 g mol<sup>-1</sup> (SEC) and narrow distributions below 1.09. This also showed that this modular synthesis method is reliable even for higher molecular weights.

A marked difference between hydrophilic PPBIs with OEG- and hydrophobic PPBIs with alkyl swallow-tails was reported. The hydrophilic PPBIs were all found to be amorphous with the spacer length influencing the  $T_g$  of the polymers. An increase in spacer length reduced the glass transition temperature. A similar trend was observed for the  $T_g$  of the hydrophobic polymers with generally higher transition temperatures. If the spacer length did not exceed (CH<sub>2</sub>)<sub>8</sub>, the polymers were not amorphous but liquid crystalline. The introduction of the new hydrophilic side chains claimed to increase the  $\chi$ -parameter through a polar-apolar driving force and could be interesting for a supposed block copolymer implementation. Two other new perylene derivatives were introduced utilizing this reliable concept.<sup>[89]</sup> In this case, the electronically active perylene core was modified itself tuning the absorption properties of the polymers. A poly(perylene diester benzimidazole) (**PPDB**) and poly(perylene diester imide) (**PPDI**) with a blue- respectively red-shifted absorption in respect to PBIs were successfully synthesized (see Fig. 14).

## 2.2 Charge carrier transport in polymeric PBIs

As the same parent scaffold polymer was used for “clicking” the different perylene derivatives, influence on charge transport properties by modifying the pendant perylene core and the substituents on PBI could be well compared.<sup>[89]</sup> In OFET devices, poor performance with high threshold voltages, hysteresis, and low on/off ratios were reported for each material. Electron mobility values the OFET measurements are summarized in Table 1. Since the charge transport in OFET geometry is determined by a thin channel of charge at the gate/dielectric interface, the results can be heavily influenced by the inter-

face effects, wetting/dewetting issues and unfavorable alignment of the polymers within the channel. Thus, the SCLC method is better suited to compare the bulk charge transport properties of these polymers. The SCLC electron mobilities are usually determined by fitting measured  $J$ - $V$  characteristics using the Mott-Gurney equation in electron-only SCLC devices.<sup>[90]</sup>

The mobility values obtained from the SCLC devices are also mentioned in Table 1. The typical  $J$ - $V$  curves of electron-only devices for the four polymers mentioned above are depicted in Fig. 14 together with a schematic of an electron-only device. A comparison of the mobilities shows that except of PPDI, all other polymers are good electron transport materials. The electron mobility in PPDI,  $5 \times 10^{-6} \text{ cm}^2 \text{ V}^{-1} \text{ s}^{-1}$ , was two orders of magnitude lower than that of in PPDB,  $6 \times 10^{-4} \text{ cm}^2 \text{ V}^{-1} \text{ s}^{-1}$ . Nevertheless in comparison to PPDB, better electron transport was reported for both PPBI polymers, *i.e.* PPBI 1 and PPBI 2. A direct comparison of PPBI 1 and PPBI 2 showed that not only the core of the  $\pi$ -conjugation system, but also the substituent has an impact on the charge transport properties of the material. Pendant perylene bisimides with hydrophilic OEG, PPBI 2, showed a major increase of one order of magnitude in electron mobility over PPBI 1 with hydrophobic alky tails. The reported electron mobility in PPBI 2 was  $1 \times 10^{-2} \text{ cm}^2 \text{ V}^{-1} \text{ s}^{-1}$ , which is among the highest bulk electron mobility values ever reported for polymers.<sup>[91,92]</sup> However the XRD data suggested a LC SmC structure for PPBI 1, whereas amorphous phase for PPBI 2.<sup>[93]</sup> Thus the less ordered PPBI 2 was surprisingly superior in terms of electron mobility.

**Table 1.** OFET and SCLC (Obtained from Single Carrier Devices with an Active Layer Thickness of ca. 350 nm) mobility values for PDEB, PDEI, PPBI 1, and PPBI 2.<sup>[89,90]</sup>

Polymer	OFET	SCLC
	electron mobility ( $\mu_e$ ) [ $\text{cm}^2 \text{ V}^{-1} \text{ s}^{-1}$ ]	electron mobility ( $\mu_e$ ) [ $\text{cm}^2 \text{ V}^{-1} \text{ s}^{-1}$ ]
PPDB	n.d.	$6 \times 10^{-4}$
PPDI	n.d.	$5 \times 10^{-6}$
PPBI 1	$2 \times 10^{-6}$	$1 \times 10^{-3}$
PPBI 2	$1 \times 10^{-6}$	$1 \times 10^{-2}$

### 2.3. Effect of polymer architecture on structure of perylene bisimide

From the different types of acceptor polymers introduced above, one, namely an acrylate with pendant perylene bisimides with hydrophobic alkyl swallow-tails was selected for detailed structural investigations. This type of polymer was later on used in the donor-acceptor block copolymers. To study the effect of the polymer architecture on structure a low molecular weight model compound, PBI was included as a reference material (cf. Fig. 15).<sup>[94]</sup>

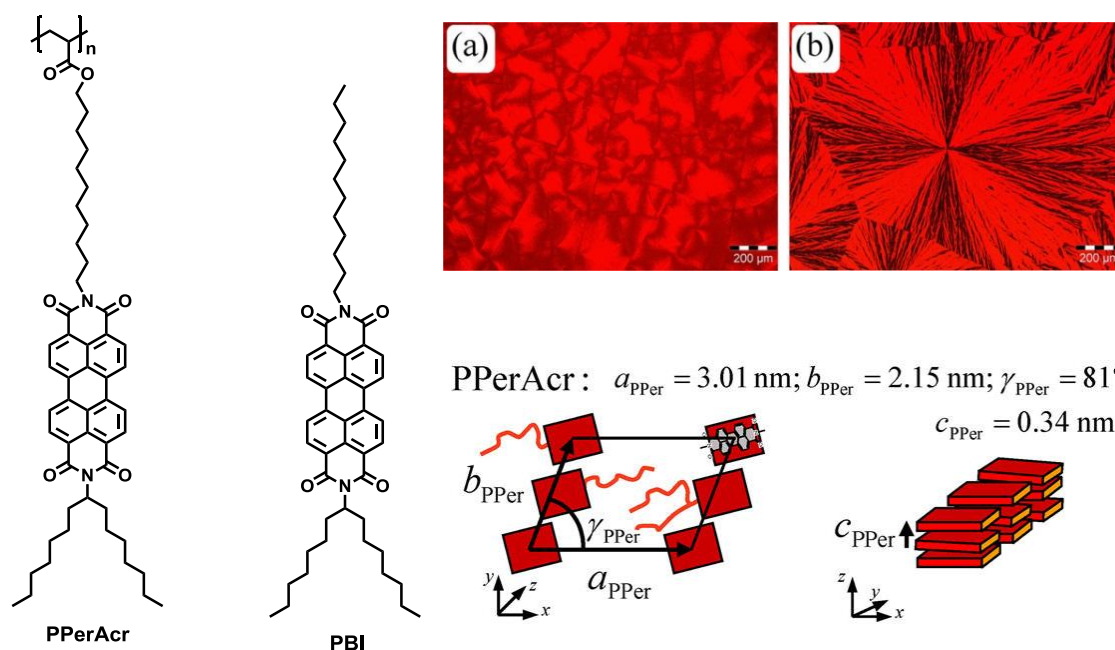


**Figure 15.** (Left) Chemical structures of the investigated materials: (a) Perylenebisimide side-chain polymer with polyacrylate backbone (PPerAcr); (b) asymmetrically substituted low molecular weight perylenebisimide (PBI; right above: Polarized light optical microscopy: PPerAcr (a) and PBI (b) at room temperature after cooling from the melt. Scale bar represents 200 μm in both cases; right bottom: Proposed lamella-columnar liquid crystalline structure for the polymer PPerAcr at  $T=20^\circ\text{C}$ . Packing in the  $a$ - $b$ -plane is not correlated with stacking in  $c$ -direction. Reproduced with permission from [94].

Already the results of polarized light microscopy suggest that there are structural differences between the low molecular weight model compound PBI and the corresponding polymer PPerAcr (cf. Fig. 15 right). By combination of DSC, optical microscopy, and temperature-dependent small angle and wide angle X-ray scattering, it was shown that both compounds display a lamello-columnar packing. While the PBI crystallizes, the PPerAcr suppresses order, leading to an only 2D lamello-columnar liquid crystalline phase as schematically shown in Fig. 15. Most likely the reduced order in the polymeric compound is due to the quenched chemical disorder in the atactic polymer. In thin films,

the a-axis is oriented perpendicularly to the substrate. Similarly as for P3HT ordering is suppressed directly after spincoating and higher order is beneficial for charge transport, here electron transport.

### 3. Acceptor building block: Poly(fullerenes)/PPCBM

#### 3.1. Controlled Synthesis

Basically, the preparation of pendant fullerene polymers can be achieved either by polymer-analogous modification of a preformed polymer<sup>[95-100]</sup> or directly by polymerization of fullerene-derivatized monomers using organometallic catalysis.<sup>[101-104]</sup> While many polymer-analogous approaches involve C<sub>60</sub> as reagent which is often leading to polymer cross-linking and multiaddition, we applied a well-controlled fullerene grafting method using Steglich esterification.<sup>[105]</sup> A series of well-soluble fullerene-grafted copolymers PPCBMs with high contents of pendant phenyl-C<sub>61</sub>-butyric acid methyl ester (PCBM) between 30 and 64 wt% were synthesized (Fig. 16).<sup>[106]</sup>

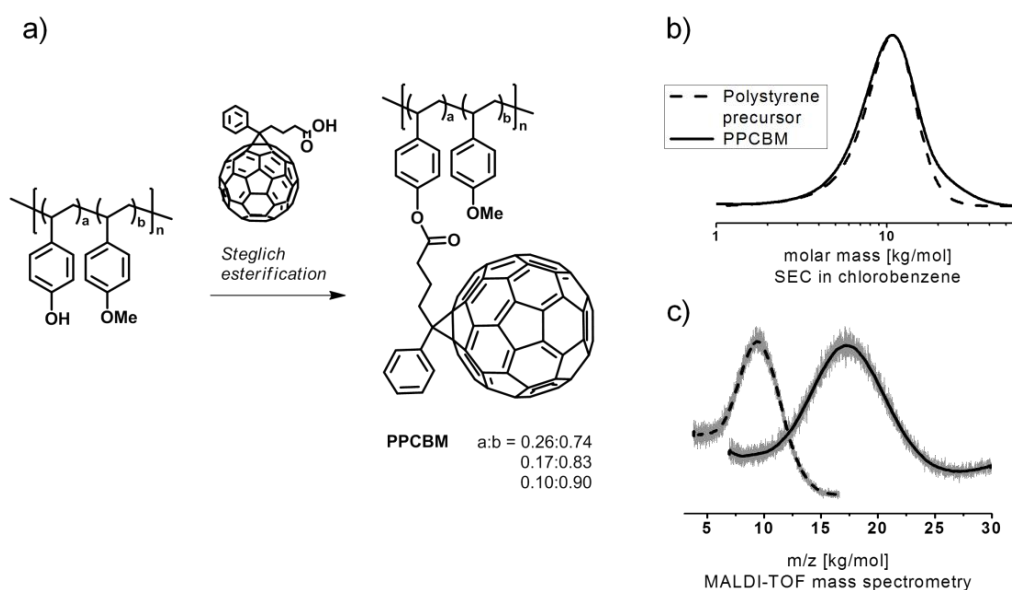


**Figure 16.** (a) Synthesis route towards PPCBM acceptor polymers starting from a poly(4-tert-butoxystyrene-stat-4-methoxystyrene) copolymer with subsequent tert-butylether deprotection. The hydroxyl-functionalized precursor copolymer is grafted with phenyl-C<sub>61</sub>-butyric acid (PC<sub>61</sub>BA) using an optimized Steglich esterification protocol. (b) Characteristic size-exclusion chromatography (SEC) traces in chlorobenzene at 50 °C of a PPCBM polymer (solid line) with a monomer ratio of a:b=0.23:0.77 and 46 wt% PCBM in comparison to the corresponding precursor copolymer (dashed line). (c) MALDI-TOF mass spectra confirming the molar mass growth after successful grafting of the precursor (dashed line) with PC<sub>61</sub>BA moieties yielding PPCBM (solid line).

Herein, the tailor-made precursor copolymers poly(4-methoxystyrene-*stat*-4-*tert*-butoxystyrene) obtained by reversible addition fragmentation chain transfer (RAFT) polymerization were functionalized *via* an efficient polymer-analogous esterification. Both grafting density and PCBM content could easily be tuned by the monomer ratio in the precursor copolymers. The resulting PCBM-grafted copolymers exhibit low molecular-weight dispersity and no cross-linking owing to the controlled monofunctional grafting reaction, *i.e.* Steglich esterification<sup>[105]</sup> of phenyl-C<sub>61</sub>-butyric acid with the hydroxyl moieties of the precursor copolymer. The synthesized acceptor copolymers retain the optical and electrochemical properties of the incorporated PCBM independent of their fullerene weight fraction.

### 3.2. Structure formation and charge transport

Earlier studies on side chain polymers carrying pendant C<sub>60</sub> have shown a correlation of increasing electron mobility with increasing C<sub>60</sub> content.<sup>[107]</sup> In these systems, for a C<sub>60</sub> content of 23-60 wt%, a rather low electron mobility of 10<sup>-9</sup> to 10<sup>-7</sup> cm<sup>2</sup> V<sup>-1</sup> s<sup>-1</sup> was determined by the space charge limited current method (SCLC).<sup>[14,108]</sup> Further, these fullerene polymers exhibit a C<sub>60</sub> aggregation starting at a threshold of 12-13 vol% of incorporated C<sub>60</sub>. Improved charge transport reported by Fang *et al.* of pendant C<sub>60</sub> polynorbornenes in organic field effect transistors (OFET) was attributed to the confined organization of fullerenes along the polymer chain.<sup>[104]</sup> The potential for the application of pendant fullerene polymers as suitable acceptor material in polymer solar cells was successfully demonstrated by Eo *et al.*<sup>[103]</sup>

Our structural studies using AFM, TEM, and XRD reveal a homogeneous and amorphous morphology of the PPCBMs both in thin films and in bulk phase. In contrast to pristine PCBM or blends of polystyrene and PCBM, the strong tendency for nanocrystal formation of PCBM is fully suppressed in the PCBM-grafted copolymers. Additionally, the absence of nanocrystal formation in PPCBM was maintained even after prolonged thermal annealing (Fig. 17).

The electron transport properties were studied using the space-charge limited current (SCLC) method. The maximum electron mobility  $\mu_e$  of 1 x 10<sup>-4</sup> cm<sup>2</sup> V<sup>-1</sup> s<sup>-1</sup> is achieved for 37 wt% of incorporated PC<sub>61</sub>BM. Despite the dilution of the electronically active fullerene moieties with the insulating polymer backbone, the PC<sub>61</sub>BM-grafted copolymers exhibit exceptional high charge transport in reference to blend systems between polystyrene

copolymers and PC<sub>61</sub>BM. For 30 wt% PC<sub>61</sub>BM content, the grafted copolymer exhibits three orders of magnitude better mobility than the corresponding blend. Thus, an efficient charge carrier percolation is facilitated by the homogeneous distribution of PC<sub>61</sub>BM in the copolymer. Charge transport in the blends relies on nanocrystal formation and is improved with an increasing PC<sub>61</sub>BM content. On the other hand, the PC<sub>61</sub>BM-grafted copolymers exhibit excellent mobility and no nanocrystal formation even after thermal annealing. This can be of great advantage if issues of long term stability in devices have to be addressed using fullerene materials. The modular synthetic approach presented here can also be transferred to other fullerene derivatives.

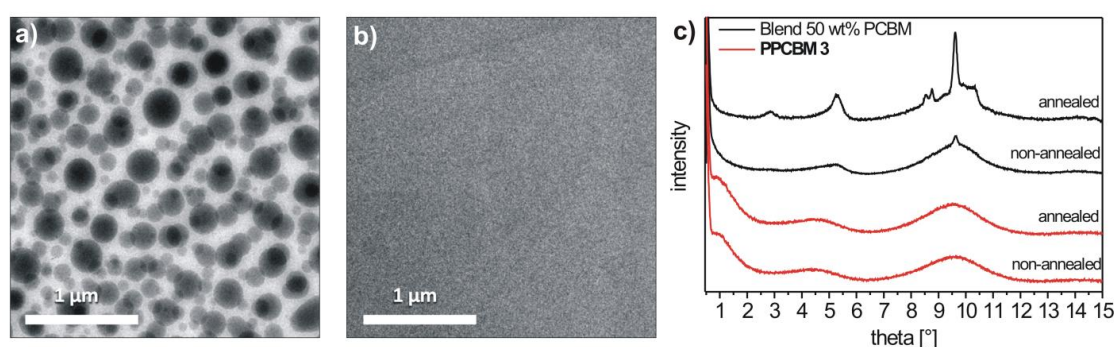


**Figure 17.** Transmission electron microscopy (TEM) images representing thin films made of (a) a blend consisting of 50 wt% PCBM content and 50 wt% polystyrene precursor and (b) a PPCBM acceptor polymer with 51 wt% of incorporated PC<sub>61</sub>BM. By the covalent attachment of the PC<sub>61</sub>BM moieties to the polymer backbone, the demixing of the fullerenes and polymer is fully restrained leading to a homogenous morphology. (c) Powder X-ray diffractograms of the blend sample and PPCBM before and after annealing at 140 °C for 3 hours indicating a suppression of nanocrystal formation in the PPCBM acceptor polymer. Reproduced with permission from [106].

## 4. Donor-acceptor block copolymers: P3HT-*block*-PPerAcr

### 4.1. Synthesis of P3HT-*block*-PPerAcr

P3HT-*b*-PPerAcr copolymers constitute one of the fully-functionalized block copolymers carrying both donor and acceptor moieties obtained by controlled synthesis of the individual blocks, maintaining appreciable solubility in common solvents.<sup>[86,109-111]</sup> The synthetic strategy of this system can be taken as a general criterion for the design of donor-acceptor block copolymer systems. P3HT-*b*-PPerAcr polymers were first synthesized by Sommer *et al.* from a P3HT macroinitiator.<sup>[109]</sup> For this, P3HT with a molecular weight of 8900 g mol<sup>-1</sup> (SEC) and a narrow PDI was first synthesized by a modified version of the aforementioned Yokozawa route and in situ functionalized to obtain a

macroinitiator suitable for NMRP. This macroinitiator was then used to polymerize a perylene bisimide acrylate. A set of block copolymers with small polydispersities and different perylene bisimide contents were obtained. The low degree of polymerization of these block copolymers prevented them from phase separating into well-defined and ordered structures in the melt.

By a modified synthetic strategy, Lohwasser *et al.* obtained higher molecular weights which lead to a sufficient increase of the  $\chi_N$ -parameter.<sup>[112]</sup> P3HT with a high molecular weight (19.7 kg mol<sup>-1</sup> in SEC equivalent to a MALDI-TOF MS molecular weight of 12.4 kg mol<sup>-1</sup>) and an alkyne end group was synthesized and converted into a macro initiator suitable for NMRP *via* CuACC “click”-chemistry. This macroinitiator was then used to polymerize the perylene bisimide acrylate monomer. This new method also prevented the formation of triblocks, which can occur when the macro initiator is synthesized in-situ as reported before. In this way, the synthesis of a series of donor-acceptor block copolymers P3HT-*b*-PPerAcr with sufficient purity, narrow distribution (PDI <1.20) and high molecular weights was realized (see Fig. 18). The structure formation and microphase separation in two selected block copolymers with 47 and 64 wt% of PPerAcr are discussed in detail in the following.

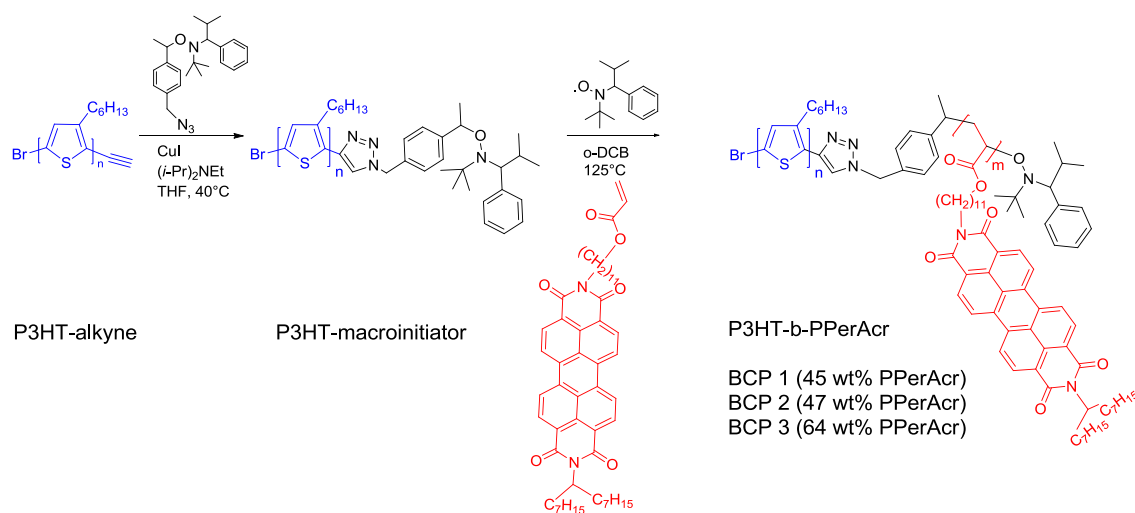


**Figure 18.** Synthetic scheme for P3HT-*b*-PPerAcr block copolymers starting from P3HT-alkyne and its conversion to a macroinitiator suitable for NMRP of PerAcr monomer. The samples BCP 1-3 are used for further investigations described below.

## 4.2. Structural elucidation of P3HT-*b*-PPerAcr

Transmission electron microscopy images of two exemplary block copolymers of the type introduced above are shown in Fig. 19. The patterns are very similar to classical microphase structures as they had not been observed before on donor-acceptor block copolymers. Combined small angle and wide angle X-ray scattering measurements showed that indeed these samples microphase separate at elevated temperatures where both components are in the molten state.

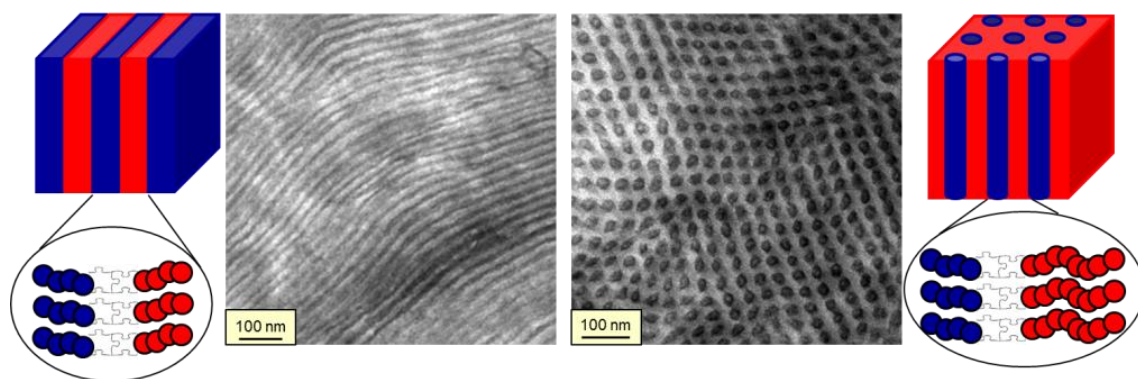


**Figure 19.** Illustration of the microphase separation in donor-acceptor block copolymers, P3HT-*b*-PPerAcr with different volume fractions of PPerAcr and transmission electron micrographs of the two exemplary block copolymers exhibiting lamellar (BCP 2) and cylindrical (BCP 3) microphase structures.

The data in Fig. 20 demonstrate that subsequent cooling leads to crystallization but leaves the microphase structure intact, as it becomes obvious from the unchanged position of the peak in the SAXS pattern reflecting the nanostructure. These results show that in order to achieve well-defined classical microphase structures, high molecular weight leading to a large enough incompatibility  $\chi N$  is the key as it induces microphase separation at high temperatures with subsequent confined crystallization. The observed microstructures fitted well to the respective volume fractions and the crystalline packing within the individual blocks was analogous to those in the respective homopolymers. For the first time, typical lamellar or cylindrical phase separated structures as known for amorphous coil-coil systems were realized for a crystalline-liquid crystalline, donor-acceptor block copolymer.<sup>[112]</sup> A similar block copolymer synthesized with the above mentioned earlier method exhibited only crystallization-induced microphase separation (cf. Fig. 5).

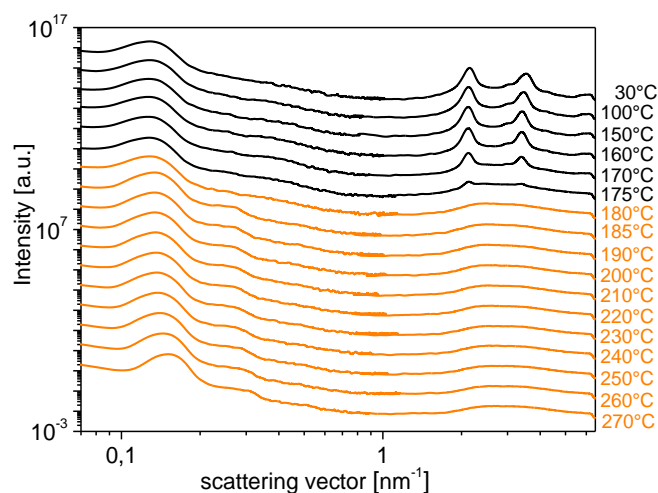


**Figure 20.** Combined small angle and wide angle X-ray diffraction pattern of the asymmetric P3HT-*b*-PPerAcr (BCP 3) (cylindrical microstructures) recorded during cooling from the melt. Temperatures at which the block copolymer is in the molten state are marked in orange. Note that the position of the small angle peak reflecting the nanostructure remains unchanged upon crystallization (Bragg peaks at high scattering vector) indicating confined crystallization. Reproduced with permission from [112].

Next, structural and electronic properties of thin films prepared from these block copolymers using a combination of X-ray scattering, AFM and vertical charge transport measurements in diode devices were studied.<sup>[113]</sup> Exemplary results are shown in Fig. 21. Generally the well-defined microphase structures found in bulk could also be prepared in thin films, but block copolymer self-assembly and crystallization of the individual components are interrelated and well-developed microdomains form only after an annealing step above the melting temperature of both components. In addition, alignment parallel to the substrate induced by interfacial interactions was observed. The copolymers sustain ambipolar charge transport, but experiments on samples prepared with different thermal treatment show that the exact values of electron and hole mobilities depend strongly on orientation and connectivity of the microdomains as well as the molecular order within the domains. Generally, the measured mobilities were lower than in pure homopolymers, similarly as in blend morphologies, as they are used for organic solar cells. Apart from optimization of domain sizes, an important further step toward usage of the investigated materials in solar cell devices will be to achieve vertical alignment of the microphase structure.

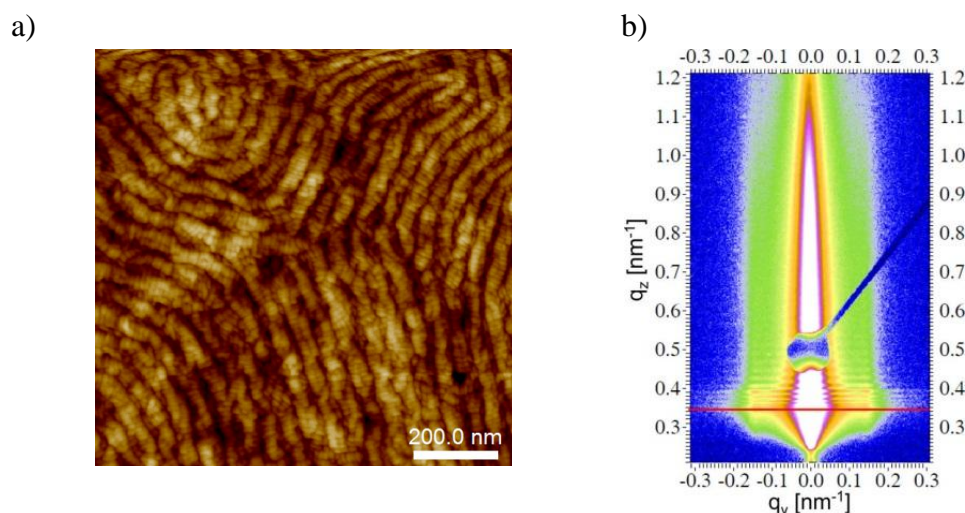


**Figure 21.** a) AFM height image of an annealed thin film of P3HT-*b*-PPerAcr with cylindrical microdomains (BCP3) measured with a Bruker MultiMode 8 using PeakForce Tapping<sup>TM</sup> mode (nanoscope 5 controller) and showing cylindrical microstructures lying flat on the substrate. We attribute the small scale structure within the cylinders to P3HT crystals. b) 2D GISAXS image of a similarly prepared film. The specular reflection is masked by the beam stop. The red line indicates the Yoneda position. The two peaks around  $q_y=0.14 \text{ nm}^{-1}$  reflect the lateral arrangement of cylindrical microdomains. Reproduced with permission from [113].

### 4.3. Solar cell devices based on P3HT-*b*-PPerAcr

In general, the photovoltaic performance of the P3HT-*b*-PPerAcr systems investigated up to now was weak due to a variety of reasons as discussed below. First photovoltaic devices based on the P3HT-*b*-PPerAcr diblock copolymers<sup>[114]</sup> were realized with a PPerAcr weight fraction of 55 wt% and two different block lengths of the P3HT block of 8.9 and 17.0 kg mol<sup>-1</sup>. Here a strong dependence on the block length was found: whereas the smaller molecular weight block copolymer yielded only about 3% maximum external quantum efficiency (EQE), the larger resulted in a maximum of 31% EQE and thus produced one order of magnitude larger photocurrent. However, overall device efficiencies remained low at 0.007 and 0.17% power conversion efficiency, due to small open circuit voltages and small fill factors. Nevertheless, an important lesson has been learned: for efficient charge transport a certain scale of coarse graining in the donor and acceptor domains is required.

The next step of improvement was reported about 2 years later with the same kind of block copolymer, exhibiting a PPerAcr weight fraction of 45% and a higher total molecular weight of about 27 kg mol<sup>-1</sup>.<sup>[115]</sup> The corresponding results are shown in Fig. 22. While the pristine block copolymer delivered a power conversion efficiency of 0.1% on-

ly, addition of PPerAcr homopolymer yielded a three-fold improvement, yielding an overall power conversion efficiency of about 0.34%. This improvement was largely based on doubling the photocurrent to  $2 \text{ mA cm}^{-2}$  and a relative increase of the open circuit voltage by another 60%. Using steady state photoluminescence measurements, this increase could be in part assigned to a statistically increased PPerAcr domain size, as the strong rise in the corresponding luminescence signal shows.

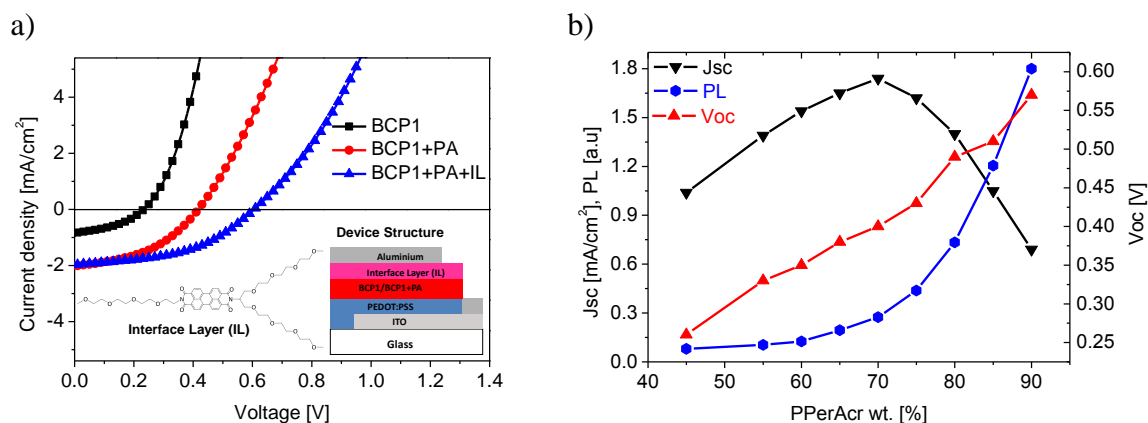


**Figure 22.** a) Current-voltage characteristics of photovoltaic devices based on pristine P3HT-*b*-PPerAcr (BCP1) (black squares), the same with additional PPerAcr (PA) homopolymers (red circles) and finally the device with an additional perylene bisimide (PBI) interface layer (IL). b) Dependence of the short circuit photocurrent, open circuit voltage and photoluminescence intensity of P3HT-*b*-PPerAcr:PPerAcr block copolymer:homopolymer blends. Reproduced with permission from [115].

A surprising result was the steady increase of the open circuit voltage with increasing PPerAcr fraction, reaching a maximum of 575 mV for the largest investigated weight fraction (90 wt.%). The key for the understanding of the rise in open circuit voltage was provided by X-ray photoelectron spectroscopy (XPS) measurements on identically processed films, by which it was found that the PPerAcr surface fraction was increasing over-stoichiometrically as compared to the bulk fraction. Since the electron extracting electrode of the photovoltaic devices was situated at this interface with the photoactive layer, an enrichment of the electron transporting PPerAcr-phase could be related to the formation of an hole blocking layer, thus preventing charge recombination at the electron extracting electrode and so improving the open circuit voltage by a higher maintained quasi Fermi level of the electrons. To prove this hypothesis, an alcohol soluble perylene derivative, PBI, was deposited as extra layer to function as a hole blocking electron transporting layer on top of the photoactive layer. At the optimum blend ratio yielding the maximum photocurrent, the application of this PBI interlayer resulted in an increase of

the open circuit voltage yielding reasonable 610 mV and a power conversion efficiency of 0.56%.<sup>[115]</sup> Table 2 collects the device parameters from these experiments.

**Table 2.** Summary of the photovoltaic parameters obtained for the P3HT-*b*-PPerAcr system (BCP 1), upon domain coarsening via homopolymer blending and blocking layer insertion using the PBI interlayer.<sup>[115]</sup>

Active layer	$J_{sc}$ [mA cm <sup>-2</sup> ]	$V_{oc}$ [V]	FF [%]	$\eta$ [%]	$R_s$ [ $\Omega$ ]	$R_{SH}$ [ $\Omega$ ]
BCP 1	0.84	0.23	41	0.08	12.1	1277
BCP 1+PPerAcr	2.00	0.41	45	0.34	18.5	1851
BCP 1+PPerAcr+IL	1.96	0.61	47	0.56	26.7	3002

The block copolymers BCP 2 (lamellar morphology, 47 wt% PPerAcr) and BCP 3 (cylindrical morphology, 64 wt% PPerAcr) were used to undertake a first study of the interrelation between morphology and solar cell performance. To vary the morphology different thermal treatments were applied: in the film as obtained after spincoating microphase separation as well as crystallization of the components is largely suppressed by the fast drying process. One film was annealed above the melting temperature of PPerAcr but below the melting temperature of P3HT. In this film both components crystallize but there is no time for the development of a well-defined and ordered microphase structure due to the fast crystallization of the P3HT component. A third film was first annealed at a high temperature where both components are molten leading to the development of a well-defined microphase structure with subsequent crystallization during cooling. Of course, this latter treatment also leads to an orientation of the microdomains parallel to the substrate preventing a good charge transport to the electrodes; a well performing photovoltaic devices is not yet produced in this way. As an example, the results of the photovoltaic characterization of BCP 3, for which the structural analysis is shown above, are shown in Fig. 23. Clearly, the increase in crystallinity induced by the thermal treatment at the intermediate temperature led to a considerable increase of the photocurrent, whereas the unfavourable orientation of the microdomains induced by annealing in the melt state again suppresses charge transport leading to a very low short circuit current and an even worse photovoltaic performance than in the ‘as cast’ case. These results demonstrate the combined influence of crystallinity and block copolymer morphology upon photovoltaic parameters.

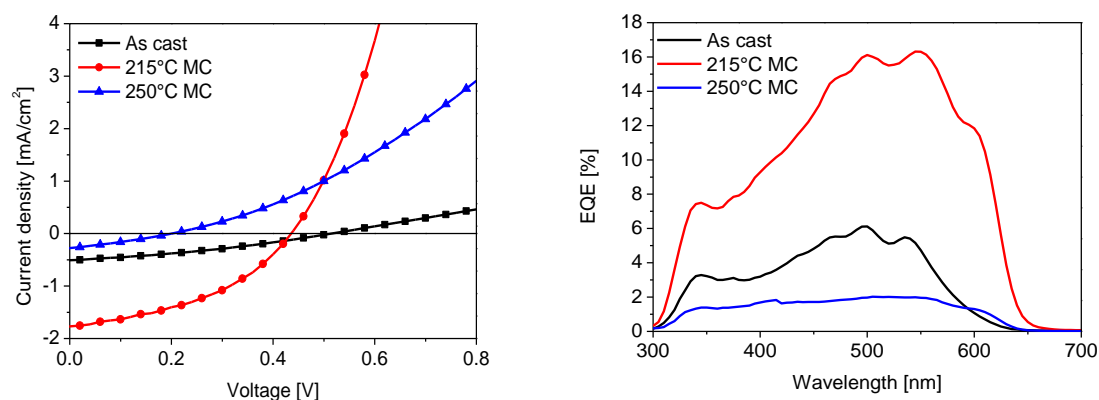


**Figure 23.** Current-voltage characteristics ( $J$ - $V$ , left) and external quantum efficiency (EQE, right) obtained from BCP 3 prepared in the following way: i) as cast (black squares), ii) annealing at an intermediate temperature ( $215^{\circ}\text{C}$ ) leading to crystallization without well-ordered microphase separation (red circles) and iii) annealing at high temperatures ( $250^{\circ}\text{C}$ ) leading the formation of well-defined microdomains oriented parallel to the substrate (blue triangles). Clearly the unfavourable orientation of the lying cylinders results in the worst photovoltaic performance of all cases. Reproduced with permission from [ 33].

As an outlook for further studies, therefore either a more favourable vertical microphase orientation or a bicontinuous phase like the gyroid structure may be most beneficial for obtaining high performing organic photovoltaic devices based on self-assembling single component block copolymers.

## 5. Donor-acceptor block copolymer: P3HT-*block*-PPCBM

### 5.1. Controlled Synthesis without cross-linking

The very first reports on block copolymers carrying a poly(*p*-phenylene vinylene) conjugated block and a fullerene pendant block are related to the work of Hadziioannou *et al.*<sup>[95]</sup> Then, the development of controlled poly(3-hexylthiophene) (P3HT) polymerization and the capability of specific end functionalization of P3HT opened new perspectives for the synthesis of donor-acceptor block copolymers comprising fullerene-grafted acceptor blocks. A variety of  $\text{C}_{60}$ -decorated block copolymers was reported.<sup>[35,38,116-118]</sup> However, an elegant method for a controlled fullerene attachment without multiaddition or cross-linking was first shown by Russel *et al.* using Steglich esterification<sup>[105]</sup> and Hashimoto *et al.* using alkyne-azide click chemistry.<sup>[119]</sup>

We present a straightforward method for the preparation of novel donor-acceptor block copolymers based on an acceptor block with pendant phenyl- $\text{C}_{61}$ -butyric methyl

ester (PC<sub>61</sub>BM) or its C<sub>70</sub> analogue PC<sub>71</sub>BM and a regioregular poly(3-hexylthiophene) (P3HT) as donor.<sup>[120]</sup> Our strategy is based on a modular combination of azide-terminated polystyrene copolymers with alkyne-terminated P3HT using copper(I)-catalyzed alkyne-azide cycloaddition (CuAAC) to form the block copolymer. The polystyrene precursor poly(4-*tert*-butoxystyrene-*stat*-4-methoxystyrene) can be tailored precisely using controlled radical polymerization methods such as reversible addition-fragmentation chain transfer (RAFT) polymerization or nitroxide mediated radical polymerization (NMRP). Subsequent acidic hydrolysis was used to deprotect the *tert*-butylether group yielding a hydroxyl functionalized copolymer. Polymer coupling with ethynyl-terminated regioregular P3HT<sup>[73]</sup> using CuAAC proceeds equally well for both RAFT and NMRP precursor copolymers. Owing to the modularity of the P3HT-*b*-PS<sub>OH</sub> block copolymer synthesis, a wide range of individual polymer designs can be realized regarding the block lengths, grafting density with fullerene moieties and the final donor/acceptor composition after PCBM grafting. Lastly, the fullerene acceptors are covalently attached to the pre-formed block copolymer to give the P3HT-*b*-PPCBM donor-acceptor block copolymers.

To enhance the optical properties of the block copolymers, PC<sub>71</sub>BM as the state-of-the-art acceptor in organic photovoltaics was introduced to these polymer system. The esterification reaction of phenyl-C<sub>71</sub>-butyric acid (PC<sub>71</sub>BA) to the hydroxyl groups of the polystyrene precursor was first optimized in homopolymers and yielded near-quantitative conversion. Analogous grafting reaction with P3HT-*b*-PS<sub>OH</sub> yielded the fully functionalized donor-acceptor block copolymer P3HT-*b*-PPC<sub>71</sub>BM (Fig. 24). Owing to the incorporation of C<sub>70</sub>, the donor-acceptor block copolymer exhibits enhanced absorption in the whole visible range of 300 to 600 nm.

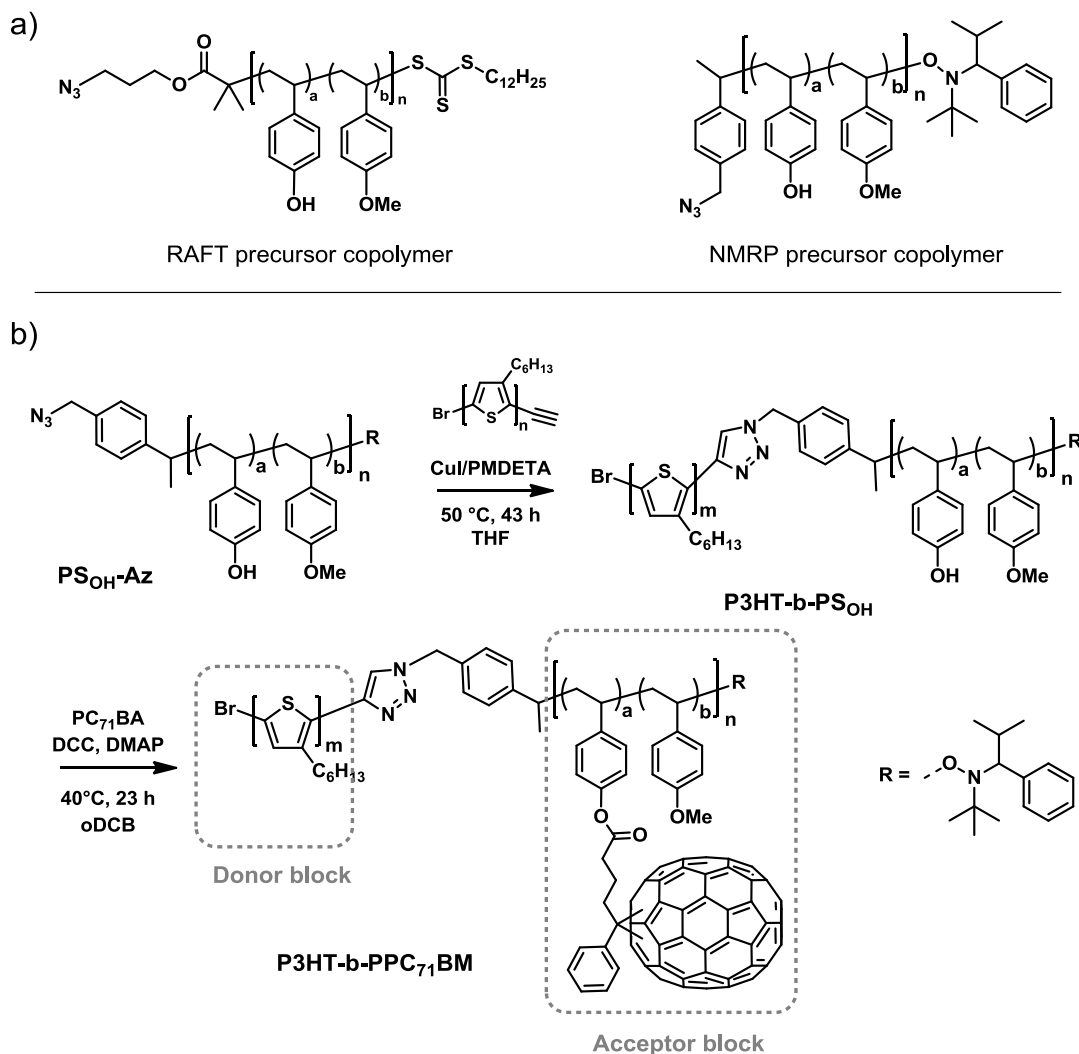


**Figure 24.** (a) Azide-terminated poly(4-hydroxystyrene-*stat*-4-methoxystyrene) copolymers obtained either by reversible addition-fragmentation chain transfer polymerization (RAFT) or nitroxide mediated radical polymerization (NMRP) of 4-methoxystyrene and 4-*tert*-butoxystyrene with subsequent polymer-analogous deprotection of the *tert*-butyl ether group. (b) Synthesis route of the donor-acceptor block copolymer P3HT-*b*-PPC<sub>71</sub>BM via copper(I)-catalyzed alkyne-azide cycloaddition (CuAAC) and Steglich esterification with PC<sub>71</sub>BA.

## 5.2. Structure formation

Even though different synthetic approaches to realize fullerene containing block copolymers have been reported, no microphase separation with ordered donor/acceptor domains was observed for C<sub>60</sub>-grafted donor-acceptor block copolymers up to now. Structural investigations on these block copolymers are rare and show either a loss of nanoscale structure due to fullerene aggregation<sup>[121]</sup> or a disordered phase-separated morphology.<sup>[105,122]</sup>

In contrast, our structural analysis of the P3HT-*b*-PPC<sub>71</sub>BM block copolymer based on small angle X-ray scattering in transmission (SAXS) and in grazing incidence geometry (GISAXS) as well as scanning electron microscopy (SEM) gave clear evidence for the formation of a periodic nanostructure of 37 nm in bulk and in thin films (Fig. 25). Temperature-dependent SAXS measurements both in the melt at 240°C and in solid state at room temperature show the same periodic nanostructure. The fact that the SAXS peak is almost unchanged after cooling to room temperature, *i.e.* after crystallization of the P3HT component, suggests that the nanostructure is already caused by a liquid-liquid phase separation in the melt.<sup>[112]</sup> Compared to the block copolymers described above, the high  $T_g$  in the acceptor block here seems to be a hurdle for the formation of equally well-developed microdomains on cooling from melt. Remarkably, the observed nanoscale morphology is nearly independent of the processing method, *i.e.* from solution or by melt crystallization above the melting point of P3HT at 240°C. SAXS and GISAXS structural analysis correlates with the domain size observed in SEM.

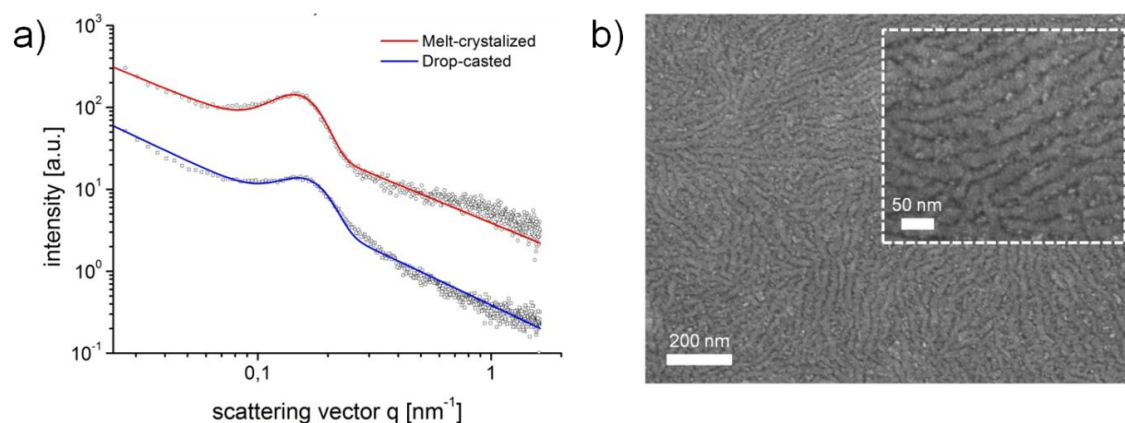


**Figure 25.** (a) GISAXS data of P3HT-*b*-PPC<sub>71</sub>BM showing horizontal intensity profiles around the Yoneda position at room temperature of films prepared by drop-casting and spincoating with subsequent annealing in the melt at 240 °C. The peaks indicate a periodic nanostructure which is consistent with bulk data from SAXS measurements. (b) Scanning electron microscope image of P3HT-*b*-PPC<sub>71</sub>BM prepared by drop-casting of a 2 wt% dichlorobenzene solution. The inset shows a magnified section of the film. Reproduced with permission from [41].

## CONCLUSION & OUTLOOK

The biggest challenges in designing and synthesizing block copolymers carrying semicrystalline P3HT segments of appreciably high molecular weight and acceptor blocks carrying pendant perylene bisimides or fullerene derivatives have been successfully accomplished. Some of the initial problems such as end group fidelity of the first block is no more an issue and the problems of subsequent polymerization using P3HT macroinitiator have been resolved by making use of the modular approach provided by click chemistry. This has led to well-defined P3HT-*b*-PPerAcr block polymers with required volume fractions and low polydispersity. One of the biggest tasks in the synthesis of pendant fullerene polymers is the attainment of sufficient fullerene content without compromising on solubility. Additionally the multivalent attachment of fullerene to polymer backbone leading to cross-linking and insoluble materials reported earlier could be avoided by adopting a polymer analogous esterification. Thus a combination of all these synthetic techniques involving NMRP, KCTP and click chemistry has facilitated the tailored synthesis of such complex donor-acceptor structures exhibiting microphase separation and thus suitable for structure-property correlation studies. It is to be emphasized that using two P3HT-*b*-PPerAcr block copolymers of sufficient molecular weight and either 47 or 64 wt% PPerAcr in the acceptor block, microphase separation and subsequent confined crystallization could be obtained *via* cooling from the melt crystallization yielding lamellar in the former and cylindrical microdomains in the latter case. In the synthesis, further efforts are needed to obtain controlled lengths of novel low band gap donor segments with low polydispersity and to integrate them into block copolymers.

Concerning the microscopic structure, the basic result of our investigations is, that the crystalline-liquid crystalline donor-acceptor block copolymers, P3HT-*b*-PPerAcr under study are in fact very complex systems, but the driving forces and principles underlying structure formation are very similar to more conventional materials. There is generally a competition between liquid-liquid microphase separation and the formation of order on a molecular scale *via* crystallization or formation of a liquid crystalline phase. P3HT shows the typical features of semicrystalline polymers, PPerAcr forms a side chain liquid crystal. The morphology of block copolymers from such materials depends on the relative values of the different transitions temperatures and on the mobility of the materials involved. In addition, there is not necessarily one well-defined equilibrium structure and the structure may depend on the processing conditions (thermal history, melt or solvent pro-

cessing). Also the effect of the thin film geometry on self-assembly is rather similar to more simple systems studied in the past. Because of interfacial interactions, microdomains tend to align parallel to the plane of the film. Moreover, crystallization under the constraints set by the microphase structure can lead to orientation of the crystals. It is important to note, that for the systems studied, the crystallization of the individual components did not destroy the microdomains, *i.e.* crystallization was confined.

With respect to application of diblock copolymers in photovoltaic devices substantial progress in understanding the underlying principles has been made. At first, a certain scale of phase separation appeared to be required in order to allow efficient charge extraction. This has been shown by comparison of donor-acceptor block copolymers bearing different molecular weights and *via* blending in a PPerAcr homopolymer, where the original block composition included only 45 wt% of PPerAcr before and 70 wt% after homopolymer addition. In the case of microphase separated block copolymers, the preferential alignment of the microdomains parallel to the electrode surface unfortunately constitute a major hindrance for efficient charge extraction. However, as desired, the block copolymers exhibit ambipolar charge transport, but as transport and structure are coupled, further optimization is necessary and probably also possible. An important further step toward usage of the investigated materials in solar cell devices will be to achieve vertical alignment of the microphase structure. This task is not trivial, as the two most established methods to orient thin film block copolymers cannot be applied without difficulties. Electric field induced alignment is not efficient most likely due to the residual conductivity of the materials, and solvent annealing is difficult in crystalline systems, as it would require compatibilization of the components as well as dissolution of the crystals. Nevertheless, already at this point it became clear that the block copolymer architecture allows the preparation of well-defined and stable donor-acceptor nanostructures with shape and size of the domains determined by the architecture and molecular weight of the polymer.

#### ACKNOWLEDGEMENTS

We acknowledge financial support from the German Research Foundation (DFG) within the priority program SPP1355, projects HO 3981/6, Th 807/3, and TH 1281/1. Part of the results were obtained from experiments on beamlines ID10 and Dubble at the European Synchrotron Radiation Facility (ESRF), Grenoble, France.

## REFERENCES

- <sup>1</sup> N. S. Sariciftci, L. Smilowitz, A. J. Heeger, F. Wudl, *Science* **258**, 1476 (1992)
- <sup>2</sup> N. S. Sariciftci, D. Braun, C. Zhang, V. I. Srdanov, A. J. Heeger, G. Stucky, F. Wudl, *Applied Physics Letters* **62**, 585 (1993)
- <sup>3</sup> G. Yu, J. Gao, J. C. Hummelen, F. Wudl, A. J. Heeger, *Science* **270**, 789 (1995)
- <sup>4</sup> G. Yu, A. J. Heeger, *Journal of Applied Physics* **78**, 4510 (1995)
- <sup>5</sup> J. J. M. Halls, C. A. Walsh, N. C. Greenham, E. A. Marseglia, R. H. Friend, S. C. Moratti, A. B. Holmes, *Nature* **376**, 498 (1995)
- <sup>6</sup> H. Hoppe, N. S. Sariciftci, *Journal of Materials Research* **19**, 1924 (2004)
- <sup>7</sup> H. Hoppe, N. S. Sariciftci, *Photoresponsive Polymers II*, **214**, 1 (2008).
- <sup>8</sup> J. D. Chen, C. H. Cui, Y. Q. Li, L. Zhou, Q. D. Ou, C. Li, Y. F. Li, J. X. Tang, *Advanced Materials* **27**, 1035 (2015)
- <sup>9</sup> C. Liu, C. Yi, K. Wang, Y. L. Yang, R. S. Bhatta, M. Tsige, S. Y. Xiao, X. Gong, *ACS Applied Materials & Interfaces* **7**, 4928 (2015)
- <sup>10</sup> F. Huang, *Science China-Chemistry* **58**, 190 (2015)
- <sup>11</sup> Y. H. Liu, J. B. Zhao, Z. K. Li, C. Mu, W. Ma, H. W. Hu, K. Jiang, H. R. Lin, H. Ade, H. Yan, *Nature Communications* **5** (2014)
- <sup>12</sup> S. Q. Zhang, L. Ye, W. C. Zhao, B. Yang, Q. Wang, J. H. Hou, *Science China-Chemistry* **58**, 248 (2015)
- <sup>13</sup> H. B. Wu, *Science China-Chemistry* **58**, 189 (2015)
- <sup>14</sup> Y. F. Li, *Science China-Chemistry* **58**, 188 (2015)
- <sup>15</sup> I. Etxebarria, J. Ajuria, R. Pacios, *Organic Electronics* **19**, 34 (2015)
- <sup>16</sup> R. G. E. Kimber, A. B. Walker, G. E. Schröder-Turk, D. J. Cleaver, *Phys. Chem. Chem. Phys.*, **12**, 844 (2010)
- <sup>17</sup> H. Hoppe, N. S. Sariciftci, *Journal of Materials Chemistry* **16**, 45 (2006)
- <sup>18</sup> H. Hoppe, T. Glatzel, M. Niggemann, W. Schwinger, F. Schaeffler, A. Hinsch, M. C. Lux-Steiner, N. S. Sariciftci, *Thin Solid Films* **511**, 587 (2006)
- <sup>19</sup> M. Drees, H. Hoppe, C. Winder, H. Neugebauer, N. S. Sariciftci, W. Schwinger, F. Schaeffler, C. Topf, M. C. Scharber, Z. G. Zhu, R. Gaudiana, *Journal of Materials Chemistry* **15**, 5158 (2005)
- <sup>20</sup> L. H. Nguyen, H. Hoppe, T. Erb, S. Gunes, G. Gobsch, N. S. Sariciftci, *Advanced Functional Materials* **17**, 1071 (2007)
- <sup>21</sup> S. S. van Bavel, M. Barenklau, G. de With, H. Hoppe, J. Loos, *Advanced Functional Materials* **20**, 1458 (2010)
- <sup>22</sup> O. Synooka, K. R. Eberhardt, C. R. Singh, F. Hermann, G. Ecke, B. Ecker, E. von Hauff, G. Gobsch, H. Hoppe, *Advanced Energy Materials* **4**, 10 (2014)
- <sup>23</sup> I. T. Sachs-Quintana, T. Heumüller, W. R. Mateker, D. E. Orozco, R. Cheacharoen, S. Sweetnam, C. J. Brabec, M. D. McGehee, *Advanced Functional Materials* **24**, 3978 (2014)
- <sup>24</sup> G. Wantz, L. Derue, O. Dautel, A. Rivaton, P. Hudhomme, C. Dagron-Lartigau, *Polymer International* **63**, 1346 (2014)
- <sup>25</sup> J. Vandenberg, B. Conings, S. Bertho, J. Kesters, D. Spoltore, S. Esiner, J. Zhao, G. Van Assche, M. M. Wienk, W. Maes, L. Lutsen, B. Van Mele, R. A. J. Janssen, J. Manca, D. J. M. Vanderzande, *Macromolecules* **44**, 8470 (2011)
- <sup>26</sup> I. Cardinaletti, J. Kesters, S. Bertho, B. Conings, F. Piersimoni, J. D'Haen, L. Lutsen, M. Nesladek, B. Van Mele, G. Van Assche, K. Vandewal, A. Salleo, D. Vanderzande, W. Maes, J. V. Manca, *Journal of Photonics for Energy* **4** (2014)

- <sup>27</sup> L. Derue, O. Dautel, A. Tournebize, M. Drees, H. L. Pan, S. Berthumeyrie, B. Pavageau, E. Cloutet, S. Chambon, L. Hirsch, A. Rivaton, P. Hudhomme, A. Facchetti, G. Wantz, *Advanced Materials* **26**, 5831 (2014)
- <sup>28</sup> S. Khiev, L. Derue, G. Ayenew, H. Medlej, R. Brown, L. Rubatat, R. C. Hiorns, G. Wantz, C. Dagron-Lartigau, *Polymer Chemistry* **4**, 4145 (2013)
- <sup>29</sup> K. Sivula, Z. T. Ball, N. Watanabe, J. M. J. Fréchet, *Advanced Materials* **18**, 206 (2006)
- <sup>30</sup> E. Biccocchi, M. Haeussler, E. Rizzardo, A. D. Scully, K. P. Ghiggino, *Journal of Polymer Science Part a-Polymer Chemistry* **53**, 888 (2015)
- <sup>31</sup> M. Heuken, H. Komber, T. Erdmann, V. Senkoosky, A. Kiri, B. Voit, *Macromolecules* **45**, 4101 (2012)
- <sup>32</sup> K. Johnson, Y. S. Huang, S. Huettner, M. Sommer, M. Brinkmann, R. Mulherin, D. Niedzialek, D. Beljonne, J. Clark, W. T. S. Huck, R. H. Friend, *Journal of the American Chemical Society* **135**, 5074 (2013)
- <sup>33</sup> C. R. Singh, Dissertation, TU-Ilmenau, Germany (2013)
- <sup>34</sup> A. Yassar, L. Miozzo, R. Girona, G. Horowitz, *Progress in Polymer Science* **38**, 791 (2013)
- <sup>35</sup> B. de Boer, U. Stalmach, P. F. van Hutten, C. Melzer, V. V. Krasnikov, G. Hadziioannou, *Polymer* **42**, 9097 (2001)
- <sup>36</sup> B. de Boer, U. Stalmach, C. Melzer, G. Hadziioannou, *Synthetic Metals* **121**, 1541 (2001)
- <sup>37</sup> Q. L. Zhang, A. Cirpan, T. P. Russell, T. Emrick, *Macromolecules* **42**, 1079 (2009)
- <sup>38</sup> M. H. van der Veen, B. de Boer, U. Stalmach, K. I. van de Wetering, G. Hadziioannou, *Macromolecules* **37**, 3673 (2004)
- <sup>39</sup> M. Sommer, S. Huettner, M. Thelakkat, *Complex Macromolecular Systems II* **228**, 123 (2010)
- <sup>40</sup> M. Sommer, S. Huettner, M. Thelakkat, *Journal of Materials Chemistry* **20**, 10788 (2010)
- <sup>41</sup> M. Hufnagel, M. Fischer, T. Thurn-Albrecht, M. Thelakkat, *Polymer Chemistry* **6**, 813, (2015)
- <sup>42</sup> S. B. Darling, *Energy & Environmental Science* **2**, 1266 (2009)
- <sup>43</sup> K. Nakabayashi, H. Mori, *Materials* **7**, 3274 (2014)
- <sup>44</sup> L. J. Bu, X. Y. Guo, B. Yu, Y. Qu, Z. Y. Xie, D. H. Yan, Y. H. Geng, F. S. Wang, *Journal of the American Chemical Society* **131**, 13242 (2009)
- <sup>45</sup> N. Sary, F. Richard, C. Brochon, N. Leclerc, P. Leveque, J. N. Audinot, S. Berson, T. Heiser, G. Hadziioannou, R. Mezzenga, *Advanced Materials* **22**, 763 (2010)
- <sup>46</sup> S. Miyanishi, Y. Zhang, K. Tajima, K. Hashimoto, *Chemical Communications* **46**, 6723 (2010)
- <sup>47</sup> U. Scherf, A. Gutacker, N. Koenen, *Acc. Chem. Res.*, **41** (9), 1086 (2008)
- <sup>48</sup> S. Miyanishi, Y. Zhang, K. Hashimoto, K. Tajima, *Macromolecules* **45**, 6424 (2012)
- <sup>49</sup> C. H. Guo, Y. H. Lin, M. D. Witman, K. A. Smith, C. Wang, A. Hexemer, J. Strzalka, E. D. Gomez, R. Verduzco, *Nano Letters* **13**, 2957 (2013)
- <sup>50</sup> S. Barrau, T. Heiser, F. Richard, C. Brochon, C. Ngov, K. van de Wetering, G. Hadziioannou, D. V. Anokhin, D. A. Ivanov, *Macromolecules* **41**, 2701 (2008)
- <sup>51</sup> K. Sivula, Z. T. Ball, N. Watanabe, J. M. J. Fréchet, *Adv. Mater.* **18**, 206 (2006).
- <sup>52</sup> J. U. Lee, A. Cirpan, T. Emrick, P. Russell, W. Ho, T. P. Russell, W. H. Jo, *J. Mater. Chem.* **19**, 1483. (2009)

- <sup>53</sup> S.-Y. Ku,; M.A. Brady, N.D. Treat, J.E. Cochran, M.J. Robb, E.J. Kramer, , M.L. Chabiny, C.J. Hawker, *J. Am. Chem. Soc.* **134**, 16040 (2012).
- <sup>54</sup> B. D. Olsen, R. A. Segalman, *Materials Science & Engineering R-Reports* **62**, 37 (2008)
- <sup>55</sup> Y. L. Loo, R. A. Register, A. J. Ryan, *Macromolecules* **35**, 2365 (2002)
- <sup>56</sup> S. Li, S. B. Myers, R. A. Register, *Macromolecules* **44**, 8835 (2011)
- <sup>57</sup> T. Yamamoto, K. Sanechika, A. J. Yamamoto, *Polym. Sci., Polym. Lett. Ed.* **18**, 9 (1980)
- <sup>58</sup> J. W. P. Lin, L. P. Dudek, *J. Polym. Sci. Polym. Part A Polym. Chem. Ed.* **18**, 2869 (1980)
- <sup>59</sup> K.-Y. Jen, G. G. Miller, R. L. Elsenbaumer, *J. Chem. Soc., Chem. Commun.* **17**, 1346 (1986)
- <sup>60</sup> R. D. McCullough, R. D. Lowe, *J. Chem. Soc., Chem. Commun.* **1**, 70 (1992)
- <sup>61</sup> T.-A. Chen, R. D. Rieke, *J. Am. Chem. Soc.* **114**, 10087 (1992)
- <sup>62</sup> R. S. Loewe, S. M. Khersonsky, R. D. McCullough, *Adv. Mater.* **11**, 250 (1999)
- <sup>63</sup> A. Yokoyama, R. Miyakoshi, T. Yokozawa, *Macromolecules* **37**, 1169 (2004)
- <sup>64</sup> E. E. Sheina, J. Liu, M. C. Iovu, D. W. Laird, R. D. McCullough, *Macromolecules* **37**, 3526 (2004)
- <sup>65</sup> R. Miyakoshi, A. Yokoyama, T. Yokozawa, *J. Am. Chem. Soc.* **127**, 17542 (2005)
- <sup>66</sup> M. C. Iovu, E. E. Sheina, R. R. Gil, R. D. McCullough, *Macromolecules* **38**, 8649 (2005)
- <sup>67</sup> R. H. Lohwasser, M. Thelakkat, *Macromolecules* **44**, 3388 (2011)
- <sup>68</sup> R. Miyakoshi,; A. Yokoyama, T. Yokozawa, *Macromol. Rapid Commun.* **25**, 1663 (2004)
- <sup>69</sup> A. Krasovskiy, B. F. Straub, P. Knochel, *Angew. Chem. Int. Ed.* **45**, 159 (2006)
- <sup>70</sup> S. Wu, L. Huang, H. Tian, Y. Geng, F. Wang, *Macromolecules* **44**, 7558 (2011)
- <sup>71</sup> M. Jeffries-El, G. Sauve, R. D. McCullough, *Macromolecules*, **38**, 10346 (2005)
- <sup>72</sup> R. Tkachov, V. Senkovskyy, H. Komber, J.-U. Sommer, A. Kiriy, *J. Am. Chem. Soc.* **132**, 7803 (2010)
- <sup>73</sup> R. H. Lohwasser, M. Thelakkat, *Macromolecules* **45**, 3070 (2012)
- <sup>74</sup> T. J. Prosa, M. J. Winokur, R. D. McCullough, *Macromolecules*, **29**, 3654 (1996).
- <sup>75</sup> R. J. Kline, D. M. DeLongchamp; D. A. Fischer,; E. K. Lin, L. J. Richter, M. L. Chabiny, M. F. Toney, M. Heeney, I. McCulloch, *Macromolecules*, **40**, 7960. (2007)
- <sup>76</sup> M. Brinkmann *J. Polym. Sci., Part B: Polym. Phys.* **49**, 1218 (2011).
- <sup>77</sup> Z. Y. Wu, A. Petzold, T. Henze, T. Thurn-Albrecht, R. H. Lohwasser, M. Sommer, M. Thelakkat, *Macromolecules* **43**, 4646 (2010)
- <sup>78</sup> O. F. Pascui, R. H. Lohwasser, M. Sommer, M. Thelakkat, T. Thurn-Albrecht, K. Saalwachter, *Macromolecules* **43**, 9401 (2010)
- <sup>79</sup> J. Balko, R. H. Lohwasser, M. Sommer, M. Thelakkat, T. Thurn-Albrecht, *Macromolecules* **46**, 9642 (2013).
- <sup>80</sup> C. R. Singh, G. Gupta, R. H. Lohwasser, S. Engmann, J. Balko, M. Thelakkat, T. Thurn-Albrecht, H. Hoppe, *J. Polym. Sci.; Part B Polymer Physics* **51**, 943 (2013)
- <sup>81</sup> S. Malik, A. K. Nandi, *J. Polym. Sci., Part B* **40**, 2073 (2002)
- <sup>82</sup> A. A. Virkar, S. Mannsfeld, Z. A. Bao, N. Stingelin, *Advanced Materials* **22**, 3857 (2010)
- <sup>83</sup> S. M. Lindner, M. Thelakkat, *Macromolecules* **37**, 8832 (2004)
- <sup>84</sup> C. J. Hawker, A. W. Bosman, E. Harth, *Chem. Rev.* **101**, 3661 (2001)
- <sup>85</sup> H. C. Kolb, M. G. Finn, K. B. Sharpless, *Angew. Chem., Int. Ed.* **40**, 2004 (2001)

- <sup>86</sup> Y. Tao, B. McCulloch, S. Kim, R. A. Segalman, *Soft Matter* **5**, 4219 (2009)
- <sup>87</sup> A. S. Lang, A. Neubig, M. Sommer, M. Thelakkat, *Macromolecules* **43**, 7001 (2010)
- <sup>88</sup> A. S. Lang, M. Thelakkat, *Polym. Chem.* **2**, 2213 (2011)
- <sup>89</sup> A. S. Lang, M.-A. Muth, C. D. Heinrich, M. Carassco-Orozco, M. Thelakkat, *J. Polym. Sci.; Part B: Polymer Physics* **51**, 1480 (2013)
- <sup>90</sup> N. F. Mott, R. W. Gurney, *Electronic Processes in Ionic Crystals*, (The Clarendon Press, Oxford, U.K., 1940)
- <sup>91</sup> R. Steyrlleuthner, M. Schubert, F. Jaiser, J. C. Blakesley, Z. Chen, A. Facchetti, D. Neher, *Adv. Mater.* **22**, 2799 (2010)
- <sup>92</sup> C. J. Mueller, C. R. Singh, M. Fried, S. Huettner, M. Thelakkat, *Adv. Funct. Mater.* (2015), in press
- <sup>93</sup> S. M. Lindner, S. Huettner, A. Chiche, M. Thelakkat, G. Krausch, *Angew. Chem. Int. Ed. Engl.* **45**, 3364 (2006)
- <sup>94</sup> P. Kohn, L. Ghazaryan, G. Gupta, M. Sommer, A. Wicklein, M. Thelakkat, T. Thurn-Albrecht *Macromolecules* **45**, 5676 (2012)
- <sup>95</sup> Stalmach, U.; de Boer, B.; Videlot, C.; van Hutten, P. F.; Hadziioannou, G. *J. Am. Chem. Soc.* **2000**, *122*, 5464–5472.
- <sup>96</sup> Hawker, C. J. *Macromolecules* **1994**, *27*, 4836–4837.
- <sup>97</sup> Liu, B.; Bunker, C. E.; Sun, Y.-P. *Chem. Commun.* **1996**, 1241.
- <sup>98</sup> Yang, C.; Lee, J. K.; Heeger, A. J.; Wudl, F. *J. Mater. Chem.* **2009**, *19*, 5416–5423.
- <sup>99</sup> Heuken, M.; Komber, H.; Voit, B. *Macromol. Chem. Phys.* **2012**, *213*, 97–107.
- <sup>100</sup> Miyanishi, S.; Zhang, Y.; Tajima, K.; Hashimoto, K. *Chem. Commun.* **2010**, *46*, 6723–6725.
- <sup>101</sup> Zhang, N.; Schrickler, S.; Wudl, F.; Prato, M. *Chem. Mater.* **1995**, *7*, 441–442.
- <sup>102</sup> Kim, J.; Yun, M. H.; Lee, J.; Kim, J. Y.; Wudl, F.; Yang, C. *Chem. Commun.* **2011**, *47*, 3078–80.
- <sup>103</sup> Eo, M.; Lee, S.; Park, M. H.; Lee, M. H.; Yoo, S.; Do, Y. *Macromol. Rapid Commun.* **2012**, *33*, 1119–25.
- <sup>104</sup> Fang, L.; Liu, P.; Sveinbjornsson, B. R.; Atahan-Evrenk, S.; Vandewal, K.; Osuna, S.; Jiménez-Osés, G.; Shrestha, S.; Giri, G.; Wei, P.; Salleo, A.; Aspuru-Guzik, A.; Grubbs, R. H.; Houk, K. N.; Bao, Z. *J. Mater. Chem. C* **2013**, *1*, 5747.
- <sup>105</sup> J. U. Lee, A. Cirpan, T. Emrick, P. Russell, W. Ho, T. P. Russell, W. H. Jo, *J. Mater. Chem.* **19**, 1483 (2009)
- <sup>106</sup> M. Hufnagel, M.-A. Muth, J. C. Brendel, M. Thelakkat, *Macromolecules* **47**, 2324 (2014)
- <sup>107</sup> Adamopoulos, G.; Heiser, T.; Giovanella, U.; Ouldsaad, S.; Vandewetering, K.; Brochon, C.; Zorba, T.; Paraskevopoulos, K.; Hadziioannou, G. *Thin Solid Films* **2006**, *511-512*, 371–376.
- <sup>108</sup> Perrin, L.; Nourdine, A.; Planes, E.; Carrot, C.; Alberola, N.; Flandin, L. *J. Polym. Sci., Part B: Polym. Phys.* **2013**, *51*, 291–302.
- <sup>109</sup> M. Sommer, A. S. Lang, M. Thelakkat, *Angew. Chem. Int. Ed.* **47**, 7901 (2008)
- <sup>110</sup> S. Rajaram, P. B. Armstrong, B. J. Kim, J. M.J. Fréchet, *Chem. Mater.*, **21**, 1775 (2009)
- <sup>111</sup> Zhang, Q.; Cirpan, A.; Russel, T. P.; Emrick, T. *Macromolecules*, **42**, 1079 (2009).
- <sup>112</sup> R. H. Lohwasser, G. Gupta, P. Kohn, M. Sommer, A. S. Lang, T. Thurn-Albrecht, M. Thelakkat, *Macromolecules* **46**, 4403 (2013)

- <sup>113</sup> G. Gupta, C. R. Singh, R. H. Lohwasser, M. Himmerlich, S. Krischok, P. Müller-Buschbaum, M. Thelakkat, H. Hoppe, T. Thurn-Albrecht, *ACS Applied Materials & Interfaces* (2015), DOI: 10.1021/am5049948
- <sup>114</sup> M. Sommer, S. Hüttner, U. Steiner, M. Thelakkat, *Appl. Phys. Lett.* **95**, 183308(1-3) (2009)
- <sup>115</sup> C. R. Singh, M. Sommer, M. Himmerlich, A. Wicklein, S. Krischok, M. Thelakkat, H. Hoppe, *Physica Status Solidi-Rapid Research Letters* **5**, 247 (2011)
- <sup>116</sup> B. Gholamkhash and S. Holdcroft, *Chem. Mater.*, 2010, **22**, 5371–5376.
- <sup>117</sup> C. Yang, J. K. Lee, A. J. Heeger, and F. Wudl, *J. Mater. Chem.*, 2009, **19**, 5416–5423.
- <sup>118</sup> M. Heuken, H. Komber, T. Erdmann, V. Senkovskyy, A. Kiriy, and B. Voit, *Macromolecules*, 2012, **45**, 4101–4114.
- <sup>119</sup> S. Miyanishi, Y. Zhang, K. Hashimoto, and K. Tajima, *Macromolecules*, 2012, **45**, 6424–6437.
- <sup>120</sup> M. Hufnagel, M. Fischer, T. Thurn-Albrecht, M. Thelakkat, *Polym. Chem.* **6**, 813 (2015)
- <sup>121</sup> S. Barrau, T. Heiser, F. Richard, C. Brochon, C. Ngov, K. van de Wetering, G. Hadziioannou, D. V. Anokhin, and D. A. Ivanov, *Macromolecules*, 2008, **41**, 2701–2710.
- <sup>122</sup> S. Miyanishi, Y. Zhang, K. Hashimoto, and K. Tajima, *Macromolecules*, 2012, **45**, 6424–6437.

## List of publications

1. M. Hufnagel, M.-A. Muth, J. C. Brendel, M. Thelakkat, "Fullerene-grafted copolymers exhibiting high electron mobility without nanocrystal formation" *Macromolecules* **2014**, *47*, 2324-2332.
2. M. Hufnagel, M. Fischer, T. Thurn-Albrecht, M. Thelakkat, "Donor-acceptor block copolymers carrying pendant PC<sub>71</sub>BM fullerenes with an ordered nanoscale morphology", *Polym. Chem.* **2015**, *6*, 813-826.
3. M. Hufnagel, M. Fischer, T. Thurn-Albrecht, M. Thelakkat, "Influence of fullerene grafting density on structure, dynamics and charge transport in P3HT-b-PPC<sub>61</sub>BM block copolymers", under revision in *Macromolecules* **2015**.
4. M. Hufnagel, M. Fischer, A. Browa, T. Thurn-Albrecht, M. Thelakkat, "Influence of composition on structure formation and charge transport in P3HT-b-PPC<sub>71</sub>BM block copolymers", intended for submission.
5. M. Hufnagel, M. Thelakkat, "Simultaneous morphological stability and high charge carrier mobilities in donor-acceptor block copolymer/PCBM blends", submitted to *J. Polym. Sci. Part B Polym. Phys.* **2015**.
6. D. Heinrich, M. Hufnagel, C. R. Singh, M. Fischer, S. Alam, H. Hoppe, T. Thurn-Albrecht, M. Thelakkat, "Nanoscale morphology from donor-acceptor block copolymers: Formation and functions", submitted to *Advances in Polymer Science* **2015**.



## Danksagung

Ein herzliches Dankeschön an alle, die durch ihr direktes Mitwirken, durch Hilfestellungen, Ratschläge, Diskussionen oder anderweitige Unterstützung zum Gelingen dieser Arbeit beigetragen haben.

Ganz besonderer Dank gilt meinem Doktorvater Prof. Dr. Mukundan Thelakkat, der mir dieses spannende und anspruchsvolle Thema anvertraut hat. Seine große Diskussionsbereitschaft, konstruktive Kritik und kreativen Impulse waren für diese Arbeit überaus wertvoll. Außerdem möchte ich mich für die Bereitstellung eines hervorragend ausgestatteten Labors bedanken und die zahlreichen Möglichkeiten meine Ergebnisse auf nationalen und internationalen Konferenzen vorstellen zu können. Mukus sehr persönliche und familiäre Art schaffte eine sehr motivierende und angenehme Atmosphäre in der Arbeitsgruppe.

Die Studienstiftung des deutschen Volkes hat mich zwei Jahre lang mit einem Promotionsstipendium finanziell unterstützt. Vielen Dank! Herrn Dr. Peter Antes von der Studienstiftung danke ich für sein offenes Ohr und die Unterstützung in der Endphase meiner Doktorarbeit.

Das Elitenetzwerk Bayern ermöglichte mir die Teilnahme an zahlreichen Seminaren, Workshops und Tagungen, die ich als große Bereicherung empfand. Danke!

Herzlich bedanken möchte ich mich auch bei meinen Kooperationspartnern Prof. Dr. Thomas Thurn-Albrecht und Matthias Fischer von der Universität Halle-Wittenberg. Durch die intensive Zusammenarbeit und auch die Möglichkeit dort eigenständig Messungen durchzuführen konnten wir viel Neues über meine Arbeit lernen.

Danken möchte ich auch meinen Arbeitskollegen vom Lehrstuhl Makromolekulare Chemie 1 für die gute Arbeitsatmosphäre, die Hilfsbereitschaft und Diskussionsfreude. Besonders hervorheben möchte ich Paul Reichstein, Katharina Neumann und Klaus Kreger für die GPC-Messungen, Chetan Raj-Singh und Mathis Muth für die Unterstützung bei SCLC-Messungen, Christian Müller für die Ratschläge bei den OFET-Messungen, David Heinrich für die Tipps am UV-Vis/PL-Spektrometer, Christoph Hunger für die Einführung in die Solarzellen-Präparation, Marina Behr und Steffen Czich für die Messungen am Guinier-Diffraktometer. Darüber hinaus möchte ich auch Martina Fried, Sandra Ganzleben, Jonas Mayer, Alexander Kern, Petra Weiss und Christina Wunderlich für ihre technische oder administrative Unterstützung im Hintergrund danken.

Von großer Bedeutung war auch die tatkräftige Unterstützung durch das Team der Elektronenmikroskopie: Martina Heider und Dr. Beate Förster am REM, sowie Melanie Förtsch, Annika Pfaffenberger und Carmen Kunert am TEM. Markus Hund aus der Physikalischen Chemie 2 möchte ich für die Einführung und Betreuung am AFM danken.

Meinen Praktikanten und Bacheloranden Christian Stelling, Fabian Nutz, Simon Schötz, Thomas Schmitt, Martin Demleitner, Philip Schmode und Anne Browa gebührt großes Lob für ihre fleißige Unterstützung im Labor.

Meinen Kollegen und Freunden am Lehrstuhl möchte ich für die vielen gemeinsamen Abende und Ausflüge danken, besonders hervorheben möchte ich hier auch meine Büro- und Laborkollegen im Gebäude B6, Katja Gräf, Johannes Brendel, Christian Müller, Christoph Hunger, Tanaji Gujar, Tina Weller und Hubertus Burchardt. Vielen Dank für die schöne Zeit!

Ein ganz großer Dank geht auch an Elli, die mir in all den Jahren stets liebevoll zur Seite gestanden ist, mir Rückhalt und neue Energie gegeben hat. Zuletzt möchte ich meinen Eltern dafür danken, dass sie mich mit großer Geduld bei meinem langen akademischen Ausbildungsweg begleitet und unterstützt haben. Das ist als Erstakademiker keine Selbstverständlichkeit und verdient meine größte Anerkennung. Vielen Dank!

## **(Eidesstattliche) Versicherungen und Erklärungen**

(§ 8 S. 2 Nr. 6 PromO)

Hiermit erkläre ich mich damit einverstanden, dass die elektronische Fassung meiner Dissertation unter Wahrung meiner Urheberrechte und des Datenschutzes einer gesonderten Überprüfung hinsichtlich der eigenständigen Anfertigung der Dissertation unterzogen werden kann.

(§ 8 S. 2 Nr. 8 PromO)

Hiermit erkläre ich eidesstattlich, dass ich die Dissertation selbständig verfasst und keine anderen als die von mir angegebenen Quellen und Hilfsmittel benutzt habe.

(§ 8 S. 2 Nr. 9 PromO)

Ich habe die Dissertation nicht bereits zur Erlangung eines akademischen Grades anderweitig eingereicht und habe auch nicht bereits diese oder eine gleichartige Doktorprüfung endgültig nicht bestanden.

(§ 8 S. 2 Nr. 10 PromO)

Hiermit erkläre ich, dass ich keine Hilfe von gewerblichen Promotionsberatern bzw. -vermittlern in Anspruch genommen habe und auch künftig nicht nehmen werde.

.....  
Ort, Datum, Unterschrift